ASNR26 ABSTRACT PROCEEDINGS

SCIENTIFIC ORAL PRESENTATIONS

Critical Updates in HN Cancer Staging

4:00 - 5:00pm Sunday, 17th May, 2026

987 Visualization of metabolic-vascular uncoupling in Head and Neck Cancer- potential multimodal imaging of tumor hypoxia

Jocelyn Wu MD, John Roberts PhD, Seon-Eun KIm PhD, Yoshimi Anzai MD MPH
University of Utah, Salt Lake City, UT, USA

Purpose

Tumor cells that thrive in hypoxic environments exhibit the ability to facilitate glucose metabolism despite inefficient/low vascular perfusion, known as metabolic-vascular uncoupling. This occurs through a cascade of biochemical/transcriptional responses leading to the creation of disorganized and leaky vessels that are inefficient in delivering oxygen. In head and neck cancer (HNC), tumor hypoxia is an important characteristic as it confers treatment resistance and poor prognosis related to inefficient drug delivery and proliferation of these aggressive tumor cells. Determination of regional metabolic-vascular uncoupling within tumors has the potential to characterize the degree of tumor hypoxia, as well as to identify subregions of hypoxia within a cancer, allowing for increased radiation dose delivery. Furthermore, hypoxia-activated prodrugs and radiation sensitizer or target therapy for HIF-1 alpha can be explored as treatment options. The goal of this study is to visualize metabolic-vascular uncoupling in patients with newly diagnosed HNC that can be incorporated at the individual patient level.

Materials & Methods

In a multicenter, prospective trial, 20 patients with newly diagnosed HNC were enrolled. Patients underwent DCE MRI and FDG PET/CT prior to initiation of CRT. FDG PET/CT was performed 3-4 months following CRT to assess treatment response. In addition, F-MISO-PET/CT was performed in the most recent 2 patients. An expert neuroradiologist annotated primary tumors and nodal metastases on T2W images. Composites of FDG-PET and Ktrans map on DCE MRI images were created using an RGB color model. Statistical analysis of the annotated pixels across all subjects was performed to determine the median values of SUV and Ktrans. The pixels were then assigned a color to indicate whether they fell above or below the median. The co-registered Ktrans and PET images were then transferred to RGB (red, green, and blue) color maps, where FDG activity was displayed in the green channel. In contrast, the quantitative Ktrans map was assigned to a combination of blue and red channels (2D color map). Furthermore, all tumor pixels from an individual patient were divided into 4 quadrants: high FDG/low Ktrans (hypoxia quadrant), high FDG/high Ktrans, low FDG/high Ktrans, and low FDG/low Ktrans. A 2D histogram of all tumor pixels was displayed in terms of glucose metabolism on the Y axis, and perfusion was measured by Ktrans on the X axis. The distribution of hypoxia quadrants was compared with F-MISO-PET/CT using two different thresholds: TBR (tumor-to-blood ratio) of 1.2 and 1.6.

Results

Image co-registration and creation of the color map enable the visualization of tumor heterogeneity in individual tumors, including both primary tumors and lymph node metastases (Figure). Lesions with higher hypoxia quadrant pixels correlate with FMISO-PET activity at a higher threshold TBR of 1.6, as well as lower Ktrans values, suggesting hypoxic tumors with higher FDG uptake and poor perfusion.

Conclusion

The old concept of the Warburg effect, which is the acceleration of glycolysis despite the presence of oxygen (aerobic glycolysis), can be visualized at the individual patient level using multiparametric imaging. Further validation with FMISO-PET is currently undergoing.

References

1. Vaupel P, Multhoff G. Revisiting the Warburg effect: historical dogma versus current understanding. *J Physiol* 2021; **599**(6): 1745-57.
2. Carmona-Bozo JC, Manavaki R, Woitek R, et al. Hypoxia and perfusion in breast cancer: simultaneous assessment using PET/MR imaging. *Eur Radiol* 2021; **31**(1): 333-44.
3. Simonsen TG, Lund KV, Hompland T, Kristensen GB, Rofstad EK. DCE-MRI-Derived Measures of Tumor Hypoxia and Interstitial Fluid Pressure Predict Outcomes in Cervical Carcinoma. *Int J Radiat Oncol Biol Phys* 2018; **102**(4): 1193-201.
4. Halle C, Andersen E, Lando M, et al. Hypoxia-induced gene expression in chemoradioresistant cervical cancer revealed by dynamic contrast-enhanced MRI. *Cancer Res* 2012; **72**(20): 5285-95.
5. Rasey JS, Casciari JJ, Hofstrand PD, Muzi M, Graham MM, Chin LK. Determining hypoxic fraction in a rat glioma by uptake of radiolabeled fluoromisonidazole. *Radiat Res* 2000; **153**(1): 84-92.

Images/Tables

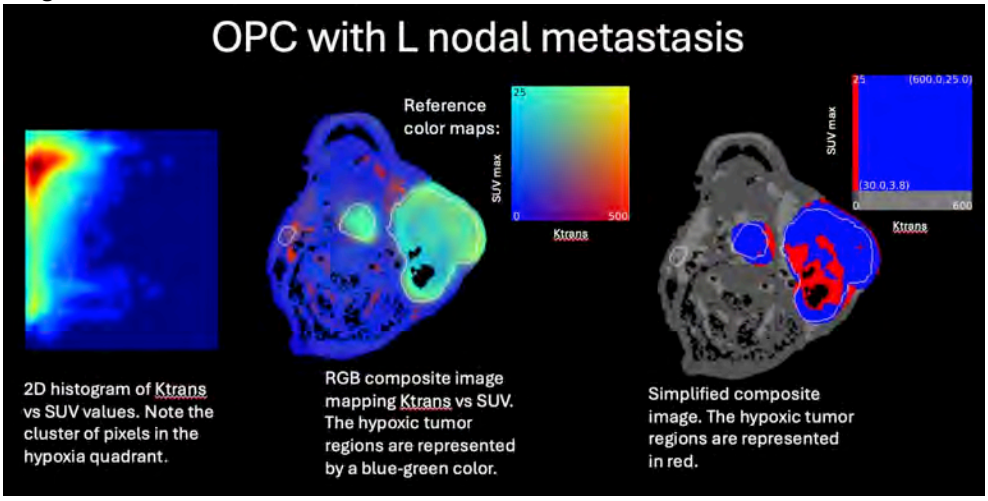

Blueprints of the Developing Brain: Mapping Malformations, Metabolism & More

9:55 - 10:55am Monday, 18th May, 2026

414 Nanoparticle-Enhanced MR Imaging of T-Cell Trafficking

Hossein Nejadnik MD, PhD[1], Sina Bagheri MD[1], Ali Nabavizadeh MD[2]

[1]University of Pennsylvania, Philadelphia, PA, USA. [2]Univenrity of Pennsylvania, Philadelphia, PA, USA

Purpose

Magnetic resonance imaging (MRI) provides a powerful, noninvasive approach for visualizing and tracking therapeutic cells in vivo. Superparamagnetic iron oxide nanoparticles (SPIONs), known for their biocompatibility and strong magnetic susceptibility, serve as effective MRI cell-labeling agents. This study utilizes a custom microfluidic mechanoporation platform to label human T cells with SPIONs, enabling rapid, uniform, and efficient intracellular delivery while preserving cell viability and function.

Materials & Methods

A novel, custom-engineered microfluidic device was developed to enhance intracellular delivery of SPIONs via mechanoporation, which combines transient mechanical deformation with convective nanoparticle transport. Human T cells were passed through microchannels containing angular chevron ridges that transiently increased membrane permeability, facilitating nanoparticle entry. Intracellular iron uptake was confirmed using Prussian blue staining and quantified by a colorimetric iron assay. Both labeled and unlabeled T cells were imaged in vitro using a high-field MRI system, and T_2 relaxation times were compared using an unpaired Student's t-test ($p < 0.05$).

Results

SPION uptake was significantly higher in labeled T cells compared to unlabeled controls (0.250 ± 0.048 pg/cell vs. 0.009 ± 0.003 pg/cell, $p < 0.001$). Cellular SPION internalization was confirmed by positive Prussian blue staining. Labeled T cells demonstrated markedly shorter T_2 relaxation times (50.49 ± 7.19 ms) relative to unlabeled cells (89.35 ± 11.03 ms, $p = 0.007$), confirming successful magnetic labeling and detectability by MRI.

Conclusion

This study establishes an efficient, microfluidic-based method for labeling human T cells with SPIONs, producing strong MRI contrast while maintaining cell integrity. The approach provides a foundation for developing MRI-traceable therapeutic T cells, including CAR T-cell products, enabling noninvasive in vivo tracking of immune-cell biodistribution and persistence. Such imaging capability could substantially improve the precision, safety, and translational monitoring of T-cell–based immunotherapies in both preclinical and clinical settings.

References

1. Nejadnik H, Jung KO, Theruvath AJ, Kiru L, Liu A, Wu W, et al. Instant labeling of therapeutic cells for multimodality imaging. Theranostics. 2020;10(13):6024-34.

2. Kiru L, Zlitni A, Tousley AM, Dalton GN, Wu W, Lafortune F, et al. In vivo imaging of nanoparticle-labeled CAR T cells. Proc Natl Acad Sci U S A. 2022;119(6).

Images/Tables

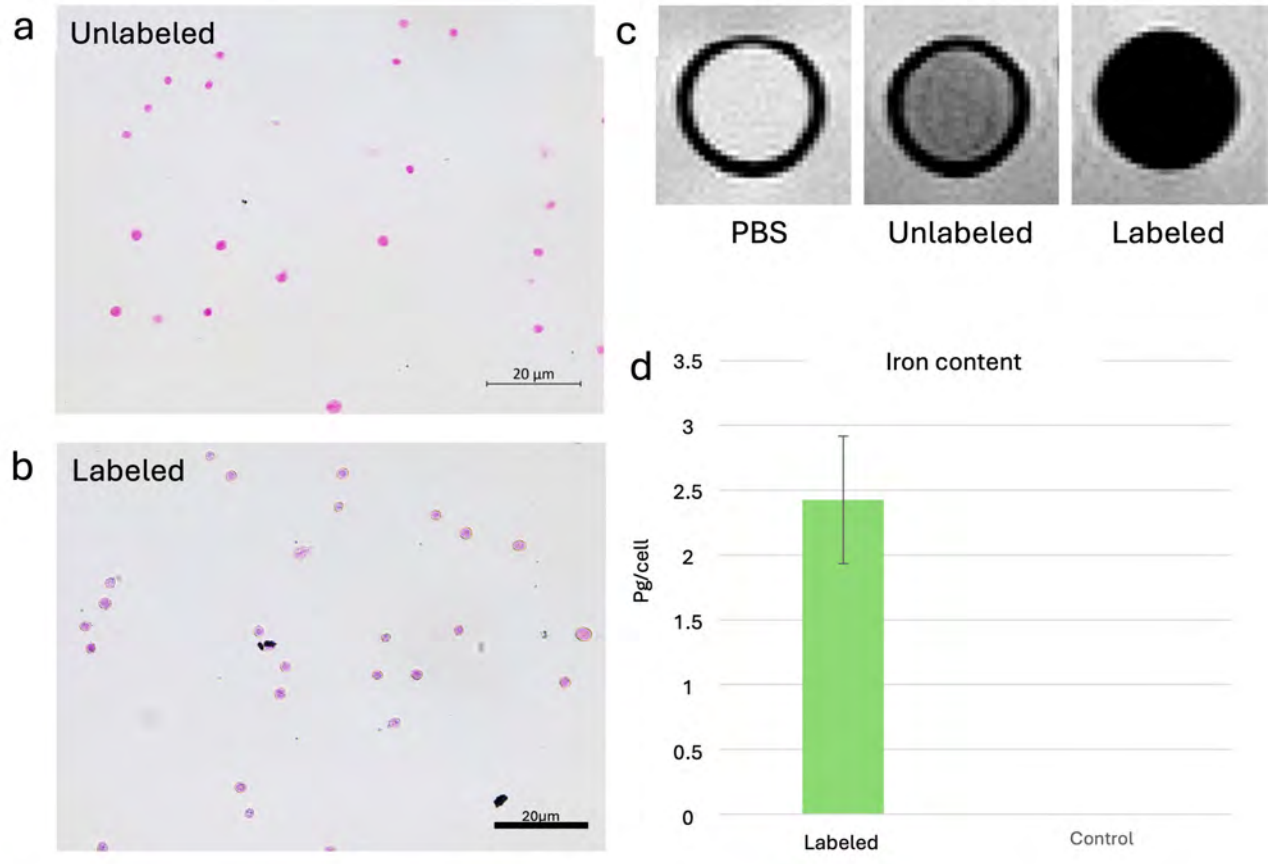

Scientific Abstract Power Pitches & Luminary Speaker: Advanced Imaging Biomarkers in Adult Brain Disorders

9:55 - 10:55am Monday, 18th May, 2026

740 Validation of diffusion imaging and radio-pathomic maps for the prediction of histological cell density in image-guided biopsies obtained from human brain gliomas

Francesco Sanvito[1], Gianluca Nocera[2], Jingwen Yao[1], Sonoko Oshima[3], Samuel A Bobholz[4], Ashley M Teraishi[1], Catalina Raymond[1], Richard G Everson[1], Linda M Liau[1], Jennifer Connelly[4], Antonella Castellano[2], Noriko Salamon[1], Timothy F Cloughesy[1], Peter S LaViolette[4], Benjamin M Ellingson[1]
[1]UCLA, Los Angeles, CA, USA. [2]San Raffaele University, Milan, MI, Italy. [3]Kyoto University, Kyoto, Kyoto, Japan. [4]Medical College of Wisconsin, Milwaukee, WI, USA

Purpose

In brain gliomas, non-invasive imaging metrics reflecting regional cell density would aid in planning "supramarginal" surgical resections [1], by identifying the high-cellularity infiltrative tumor components would guide the boundaries of resection, and in planning stereotactic biopsies in inoperable tumors [2], by identifying the high-grade components for tissue sampling. While the apparent diffusion coefficient (ADC) from diffusion MRI is considered a marker of tumor cell density [3], a dedicated machine learning (ML) algorithm [4] has recently been developed to generate voxel-wise cellularity prediction maps (CPM) from multiparametric MRI. This study evaluates the association between histological cellularity from surgical biopsies with ADC and with CPM regional values, respectively.

Materials & Methods

A cohort of patients with treatment-naïve or recurrent gliomas were prospectively imaged before surgery. This cohort was independent and external, compared to the original cohort used for the ML algorithm development [4]. All patients underwent pre-surgical MRI according to the standardized brain tumor imaging protocol [5]. The surgical sampling sites were planned based on image-guided biopsy targets, and the imaging coordinates of the planned biopsy sites were retained. The sampled tissue was stained with hematoxylin-eosin, and cell density was quantified with semi-automated software (QuPath). CPM maps were retrospectively generated based on T1w, T2w-FLAIR, post-contrast T1w, and ADC, using the previously developed algorithm [4]. Regional CPM and ADC values corresponding to the biopsy sites were extracted from a 10 mm spherical region of interest centered on the biopsy coordinates. The correlation between regional histological cellularity and regional MRI-derived CPM and ADC values, respectively, was evaluated both assuming independent observations (i.e., as all biopsy samples were independent) and accounting for non-independent observations (i.e., accounting for the non-independence of biopsies belonging to the same patient).

Results

66 biopsy samples from 27 patients were collected: 13 with treatment-naïve tumors and 14 with recurrent gliomas. Assuming independent observations, both CPM (R^2=0.20 p=0.009; rho=0.41 p=0.016, **Figure1A**) and ADC values (R^2=0.22 p=0.007; rho=-0.37 p=0.03, **Figure1B**) accurately predicted histological cell density in treatment-naïve patients, with no significant difference between CPM and ADC correlations with histology (z=0.27, p=0.79). Conversely, neither CPM nor ADC values were associated with cell density in recurrent gliomas (**Figure1C–D**). When accounting for non-independent observations, too, CPM (p=0.013) and ADC (p=0.010) were significantly associated with histological cell density only in the treatment-naïve group (**Figure1E**). Representative cases are shown in **Figure1F–G**.

Conclusion

Machine learning generated CPM maps provided a non-invasive estimate of tumor cellularity in treatment-naïve glioma patients, although CPM did not clearly outperform ADC alone in this cohort.

References

1. Karschnia, P., et al., *Prognostic validation of a new classification system for extent of resection in glioblastoma: A report of the RANO resect group*. Neuro Oncol, 2023. **25**(5): p. 940-954.
2. Weller, M., et al., *EANO guidelines on the diagnosis and treatment of diffuse gliomas of adulthood.* Nat Rev Clin Oncol, 2021. **18**(3): p. 170-186.
3. Ellingson, B.M., et al., *Validation of functional diffusion maps (fDMs) as a biomarker for human glioma cellularity.* J Magn Reson Imaging, 2010. **31**(3): p. 538-48.
4. Bobholz SA, et al. *Radio-Pathomic Maps of Cell Density Identify Brain Tumor Invasion beyond Traditional MRI-Defined Margins*. AJNR Am J Neuroradiol. 2022 May;43(5):682-688.
5. Sanvito F., et al. *Standardized brain tumor imaging protocols for clinical trials: current recommendations and tips for integration*. Front Radiol. 2023 Dec 13;3:1267615.

Images/Tables

Correlation between imaging metrics and histological cell density (assuming independent observations)

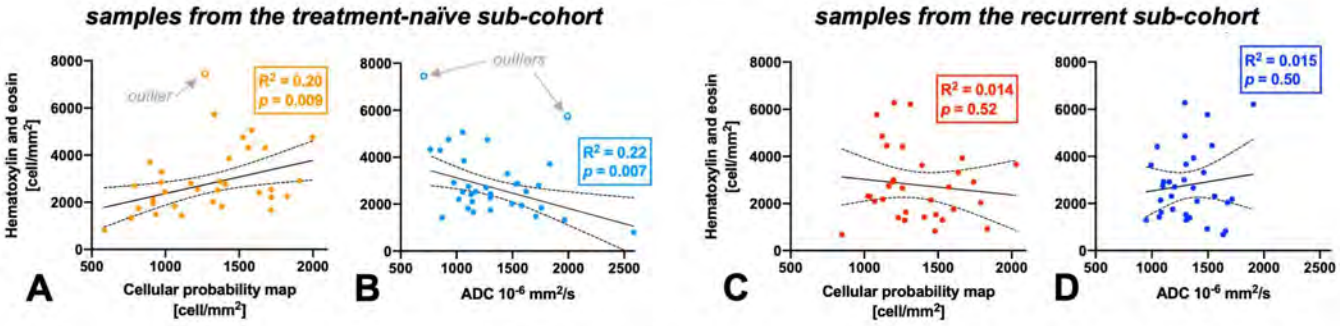

Correlation between imaging metrics and histological cell density (assuming non-independent observations)

a distribution of ρ coefficients was obtained with 1000 iterations of Spearman's correlations on random combinations of n=27 observations (one per patient) →

dependent variable = H&E cell density
fixed effect = imaging metrics
random effect = patient ID →

E	Treatment-naïve sub-cohort		Recurrent sub-cohort	
	CPM	ADC	CPM	ADC
Iterative Spearman's	mean ρ = 0.51	mean ρ = -0.37	mean ρ = 0.02	mean ρ = -0.08
Mixed effects model	β=1.4; p=0.013*	β= -1.2; p=0.010*	β= -0.4; p=0.70	β=1.07; p=0.013*

Representative Cases

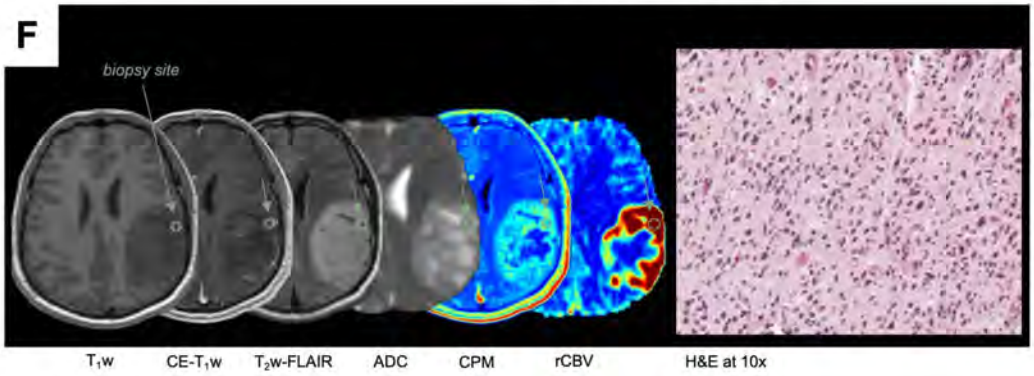

Elevated CPM
Intermediate-low ADC
High H&E cellularity

> good agreement between MRI and histology

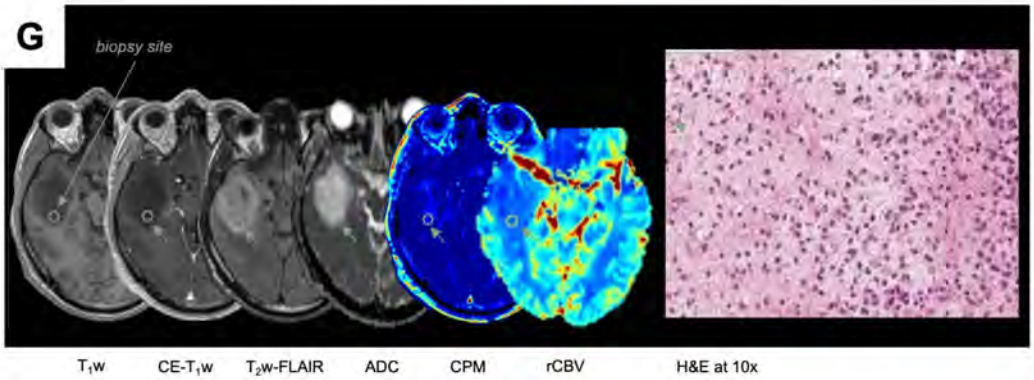

Low CPM
High ADC
High H&E cellularity

> poor agreement between MRI and histology

684 Prognostic value of pre- and post-treatment imaging metrics in primary central nervous system lymphoma treated with high-dose methotrexate

Irina Kryukov[1], Francesco Sanvito[1], Giulio Cassanello[2], Patricia A Young[1], Gianluca Nocera[2], Noriko Salamon[1], Benjamin M Ellingson[1]
[1]UCLA, Los Angeles, CA, USA. [2]University San Raffaele, Milan, MI, Italy

Purpose

The induction treatment for primary central nervous system lymphoma (PCNSL) is based on high-dose methotrexate (HD-MTX) [1]. While patient stratification is commonly based on clinical prognostic variables, the role of imaging metrics in PCNSL is under-investigated. This study aims to assess the prognostic value of imaging variables before and after HD-MTX induction treatment in predicting progression-free (PFS) and overall survival (OS).

Materials & Methods

After reviewing institutional patient data from 2004 to 2025, 67 patients were retrospectively selected for analyses. Inclusion criteria were: immunocompetent status, histologically-confirmed diffuse large B-cell PCNSL, HD-MTX induction therapy, availability of either pre-treatment (n=48 patients) or post-treatment (n=48) imaging (for n=29 both timepoints were available). Contrast-enhancing (CE) and non-enhancing lesion components were automatically segmented [2].

OS data was retrieved for all patients, while PFS was calculated only for a subset of patients with available follow-up MRI scans (n=47 of the group with pre-treatment MRI, and n=35 of the group with post-treatment MRI). PFS was defined based on enhancing progression, as per current guidelines [3], using a ≥40% volumetric increase compared to nadir as in RANO 2.0 [4,5]. Bivariate Cox proportional hazards models were used to evaluate the association between imaging metrics (as continuous variables) and PFS/OS, while adjusting for age (covariate). Complementary Kaplan-Meier curves and log-rank tests were calculated by dichotomizing continuous variables based on their median value. Finally, exploratory survival analyses were also performed on a small subset of patients with available diffusion datasets, to evaluate the prognostic role of the apparent diffusion coefficient (ADC).

Results

Pre-treatment tumor volumes were not associated with OS (**Figure 1A–B**). A larger pre-treatment CE volume (**Figure 1C**), but not whole-lesion volume (**Figure 1D**), was associated with shorter PFS when analyzed as a continuous variable adjusted for age (p=0.032, HR 1.04).

Post-treatment tumor volumes were strongly associated with OS. A larger post-treatment CE volume was associated with shorter OS both when analyzed as continuous variable adjusted for age (p<0.001, HR 1.07), and with dichotomization (p=0.004, **Figure 1E**). A similar effect was seen with larger post-treatment whole-lesion volume (continuous variable adjusted for age: p<0.0001, HR 1.013; with dichotomization: p=0.094, **Figure 1F**). Conversely, post-treatment volumes were not associated with PFS (**Figure 1G–H**).

Exploratory analyses on a subset of patients, pre-treatment ADC values did not appear to be significantly associated with PFS and OS (**Figure 1I–J**).

Conclusion

Post-treatment enhancing and whole-lesion volumes emerged as strong predictors of overall survival in MTX-treated PCNSL (**Figure 1K–L**). If confirmed on larger independent cohorts, post-treatment volume may be used as an early radiographic endpoint in clinical trials testing new induction schemes. The apparent lack of prognostic value of other imaging metrics may be partly due to the inconsistent sample composition across sub-analyses, and to limited statistical power due to the high prevalence of censored data in survival analyses.

References

[1] Ferreri AJM, Illerhaus G, Doorduijn JK, et al. Primary central nervous system lymphomas: EHA-ESMO Clinical Practice Guideline for diagnosis, treatment and follow-up. Ann Oncol. 2024 May 14:S0923-7534(23)05074-3. doi: 10.1016/j.annonc.2023.11.010. PMID: 38839484

[2] Abayazeed AH, Abbassy A, Müeller M et al (2023) NS-HGlio: A generalizable and repeatable HGG segmentation and volumetric measurement AI algorithm for the longitudinal MRI assess- ment to inform RANO in trials and clinics. Neuro-oncology Adv 5:vdac184. https://doi.org/10.1093/noajnl/vdac184 PMID: 36685009

[3] Abrey LE, Batchelor TT, Ferreri AJ, et al. International Primary CNS Lymphoma Collaborative Group. Report of an international workshop to standardize baseline evaluation and response criteria for primary CNS lymphoma. J Clin Oncol. 2005 Aug 1;23(22):5034-43. doi: 10.1200/JCO.2005.13.524. Epub 2005 Jun 13. PMID: 15955902.

[4] Wen PY, van den Bent M, Youssef G, et al. RANO 2.0: Update to the Response Assessment in Neuro-Oncology Criteria for High- and Low-Grade Gliomas in Adults. J Clin Oncol. 2023 Nov 20;41(33):5187-5199. doi: 10.1200/JCO.23.01059. Epub 2023 Sep 29. PMID: 37774317; PMCID: PMC10860967.

[5] Ellingson BM, Sanvito F, Cloughesy TF,et al. A Neuroradiologist's Guide to Operationalizing the Response Assessment in Neuro-Oncology (RANO) Criteria Version 2.0 for Gliomas in Adults. AJNR Am J Neuroradiol. 2024 Dec 9;45(12):1846-1856. doi: 10.3174/ajnr.A8396. PMID: 38926092; PMCID: PMC11630866.

Images/Tables

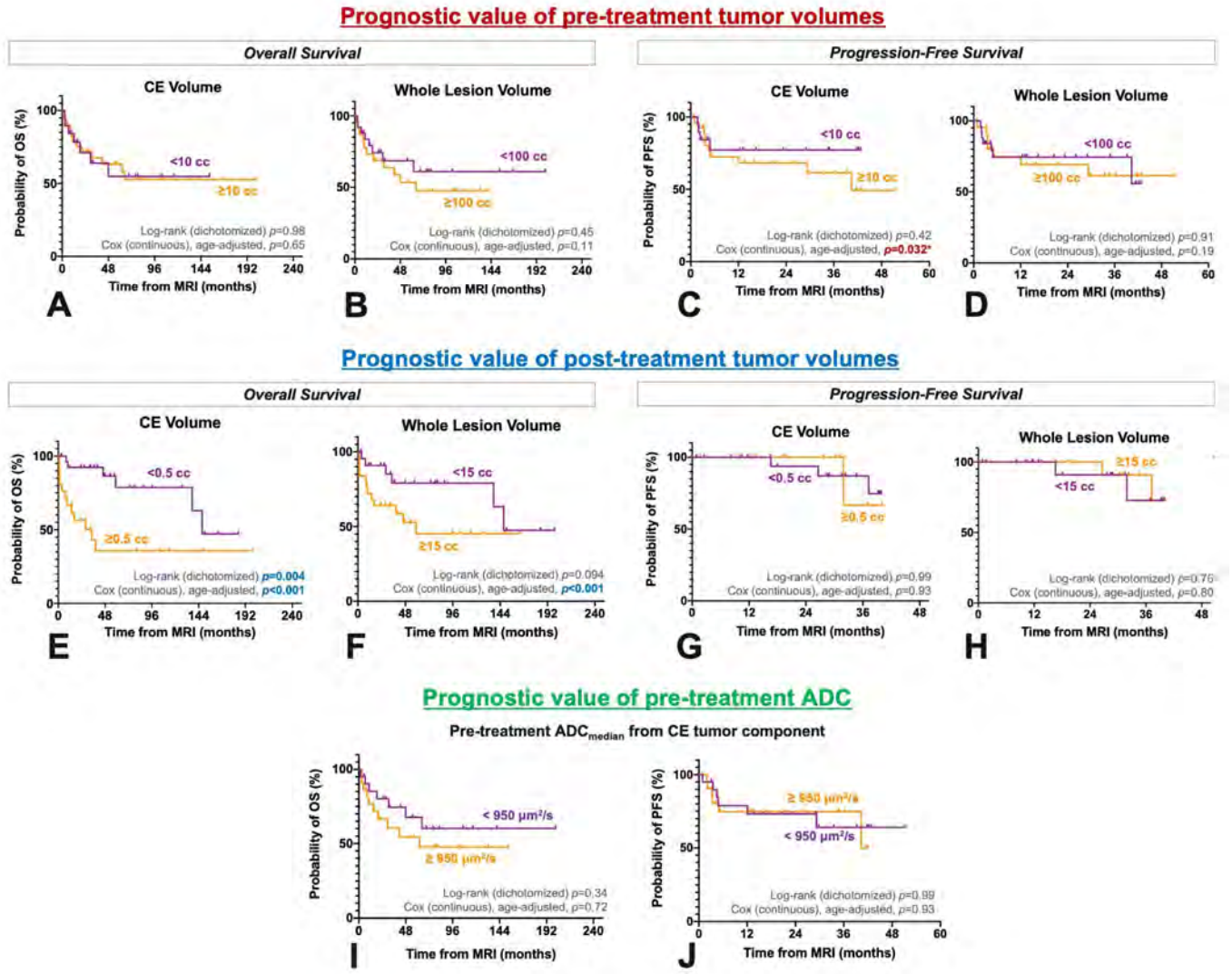

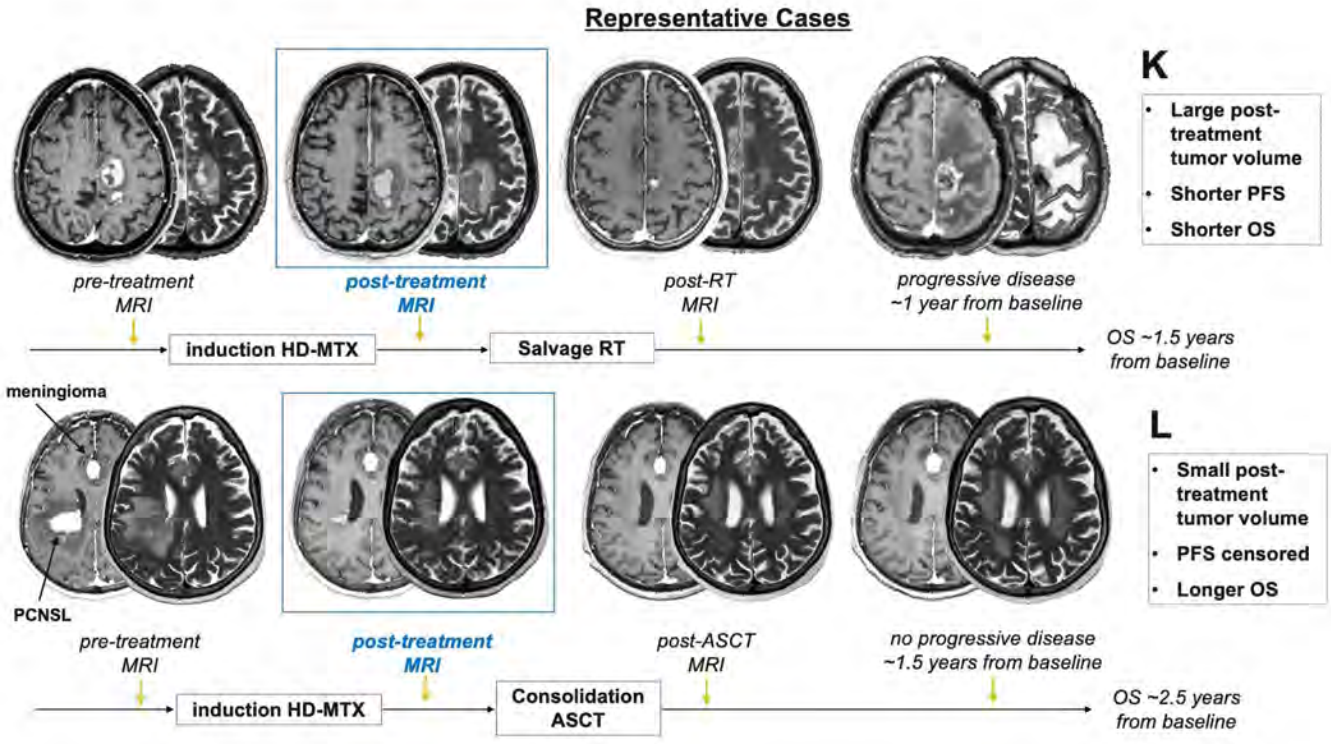

209 MRI-derived cortical thinning complements blood-based biomarker detection of Alzheimer's pathology in cognitively normal individuals

Mohammad Khalafi, Krista Wartchow PhD, Seyed Hani Hojjati PhD, Tracy Butler MD, Xiuyuan Hugh Wang MS, Emily Tanzi MS, Liangdong Zhou PhD, Qolamreza Ray Razlighi PhD, William Dartora PhD, Lidia Glodzik MD, PhD, Nancy Foldi PhD, Laura Beth J McIntire PhD, Gloria C Chiang MD
Weill Cornell Medicine, New York, NY, USA

Purpose

Blood-based biomarkers, specifically phosphorylated tau 217 (p-tau217) and the ratio of amyloid b-peptide 42 to 40 (Ab42/40) have emerged as validated biomarkers for Alzheimer's disease (AD) [1]. However, their ability to detect early preclinical AD in cognitively normal individuals is less clear. We assessed the utility of these plasma biomarkers in the preclinical setting, then evaluated whether MRI-derived cortical thinning in AD-vulnerable temporal and parietal regions could enhance their predictive accuracy.

Materials & Methods

We measured plasma p-tau217, Aβ42, and Aβ40 using the Fujirebio Lumipulse platform in 60 prospectively enrolled cognitively normal participants (mean age 67 ± 11.3 years; 26% APOE ε4 carriers). All underwent amyloid positron emission tomography (PET) scanning, with positivity defined by a quantitative threshold of 18 Centiloids. We also assessed tau PET positivity in a subset of 40 participants using a standardized uptake value ratio (SUVR) threshold of 1.35 [2, 3]. Freesurfer segmentation was used on 3T MRI scans to obtain regional cortical thickness [4, 5]. We then calculated the area under the curve (AUC) for the plasma biomarkers alone, and then combined with regional cortical thickness. Paired receiver operating characteristic (ROC) curves were compared using the DeLong's test to assess improved accuracy.

Results

In detecting amyloid positivity on PET, p-tau217 had high accuracy (AUC=0.92), which improved further to AUC=0.97 when including entorhinal cortical thickness (ERC). The p-tau217/Aβ42 ratio had the highest baseline AUC (0.94), which rose to an AUC of 0.99 when including the ERC. The Aβ42/Aβ40 ratio showed slightly lower accuracy for detecting amyloid positivity (AUC 0.89), but this improved to an AUC of 0.96 when including cortical thickness of the left inferior temporal gyrus (Delong's p=0.03).

In detecting tau positivity on PET, p-tau217 alone had a baseline AUC of 0.67, which improved to an AUC of 0.89 when the right parahippocampal gyrus (PHG) thickness was included (Delong's p=0.02). The p-tau217/Aβ42 ratio had an accuracy of AUC 0.66 for detecting tau, which increased to an AUC of 0.82 with left posterior cingulate cortical thickness. The Aβ42/Aβ40 ratio had an AUC of 0.71, which rose to an AUC of 0.88 when the right PHG was included.

Conclusion

Blood-based biomarkers have high accuracy for detecting amyloid deposition on PET, even at the preclinical disease stage. However, detection of tau deposition on PET can be improved by incorporating MRI measures of cortical thickness. This provides evidence for complementary approach using both accessible blood biomarkers and noncontrast MRI for early detection of preclinical AD, paving the way for more cost-effective screening.

References

1. Palmqvist S, Janelidze S, Quiroz YT, et al. Discriminative Accuracy of Plasma Phospho-tau217 for Alzheimer Disease vs Other Neurodegenerative Disorders. *Jama* 2020;324:772-781
2. Khalafi M, Hojjati SH, Wang XH, et al. Concordance between Centiloid quantification and visual interpretation of amyloid PET scans across the Alzheimer's disease continuum. *AJNR Am J Neuroradiol* 2025
3. Klunk WE, Koeppe RA, Price JC, et al. The Centiloid Project: standardizing quantitative amyloid plaque estimation by PET. *Alzheimers Dement* 2015;11:1-15.e11-14
4. Jack CR, Jr., Andrews JS, Beach TG, et al. Revised criteria for diagnosis and staging of Alzheimer's disease: Alzheimer's Association Workgroup. *Alzheimers Dement* 2024;20:5143-5169
5. Jenkinson M, Beckmann CF, Behrens TE, et al. FSL. *Neuroimage* 2012;62:782-790

Images/Tables

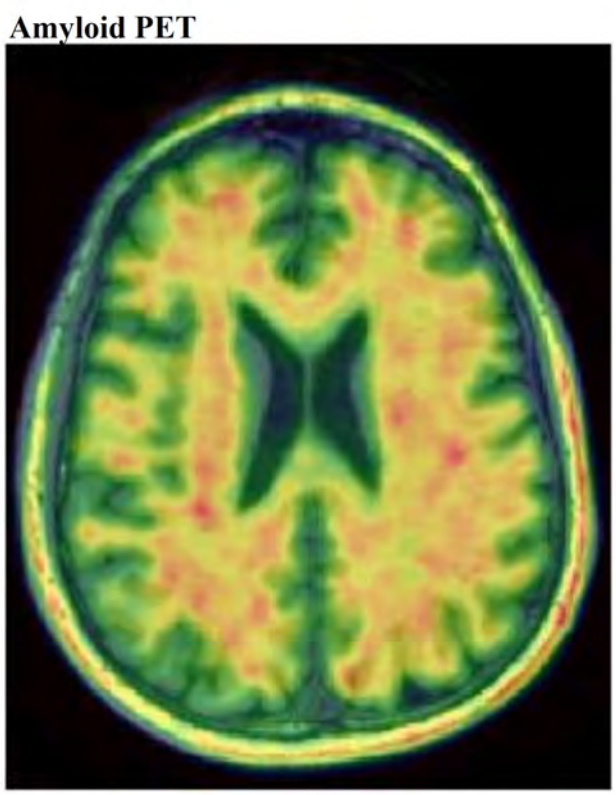

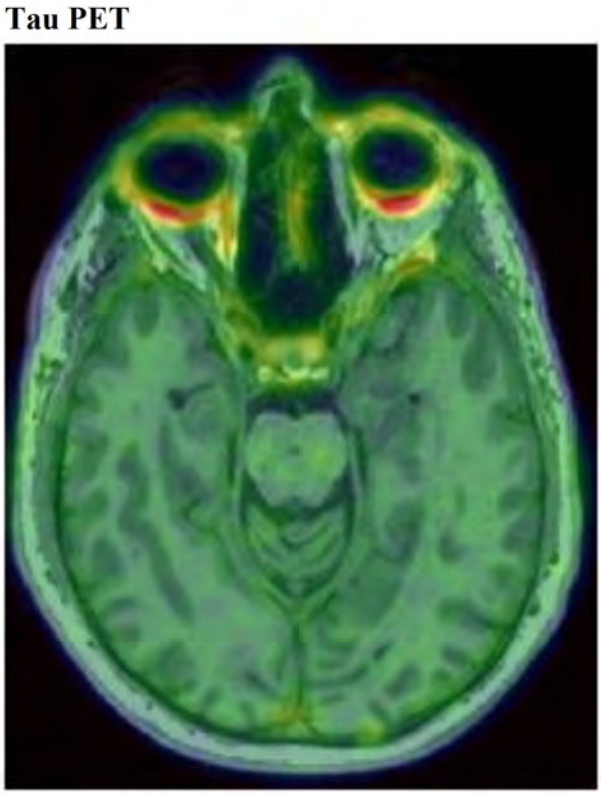

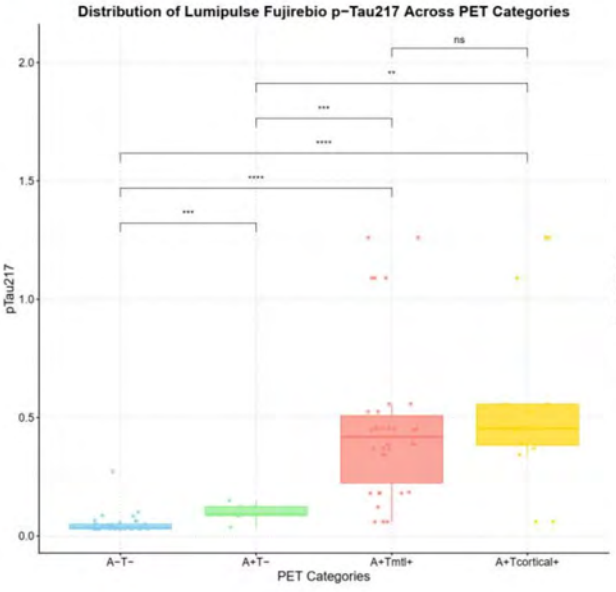

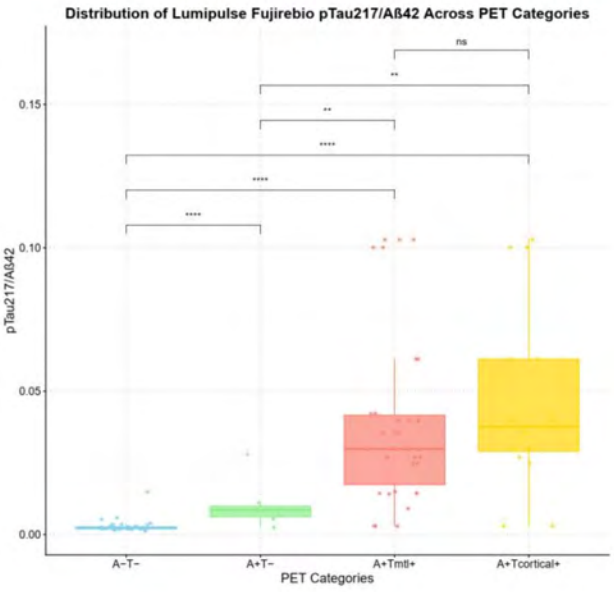

---

874 The impact of brain MRI surveillance in advanced non-small cell lung cancer without baseline CNS metastasis

Hye Hyeon Moon MD, PhD[1], Ji Eun Park MD, PhD[2], Ho Sung Kim MD, PhD[1], Shinkyo Yoon MD, PhD[1]
[1]Asan Medical Center, Seoul, Seoul, Korea, Republic of. [2]Johns Hopkins University, Baltimore, Maryland, USA

Purpose

Brain metastases are common in patients with non-small cell lung cancer (NSCLC), yet the role of brain MRI surveillance in patients without initial brain metastases remains uncertain. We tried to evaluate the cumulative incidence of brain metastases, and the impact of brain MRI surveillance, on survival outcomes of NSCLC patients without brain metastases at initial diagnosis.

Materials & Methods

We conducted a retrospective, single-institution cohort study of NSCLC patients diagnosed between September 2014 and December 2019. Patients who underwent staging brain MRI without evidence of brain metastases were categorized into surveillance and non-surveillance groups based on follow-up MRI. Propensity score matching was used to balance clinical stage, histology, and actionable genetic alterations (AGAs). The primary outcome was the cumulative incidence of brain metastases. The secondary end-point was overall survival (OS).

Results

In total, 6,448 patients met the inclusion criteria, and 2,236 (34.7%) underwent brain MRI surveillance. The cumulative incidence of brain metastases was higher in patients with advanced-stage disease (0.4% *vs*. 4.8% *vs*. 6.9% at 1 year, and 1.4% *vs*. 12.0% *vs*. 20.1% at 2 years, for stages I–II, III, and IV, respectively), particularly those with adenocarcinoma with specific AGAs (EGFR, ALK, ROS1 alterations). After propensity score matching, brain MRI surveillance was associated with significantly improved OS at stage IIIB/C (HR = 0.604; 95% CI = 0.389–0.936; *P* = 0.024) and stage IV (HR = 0.470; 95% CI = 0.390–0.566; *P* < 0.001). Subgroup analysis revealed that survival benefit was linked to increased utilization of gamma knife radiosurgery, and longer duration of tyrosine kinase inhibitor therapy.

Conclusion

Brain MRI surveillance of NSCLC patients without initial brain metastases was associated with improved survival outcomes, particularly for advanced-stage disease, suggesting that a risk-adapted approach to brain MRI surveillance may be beneficial.

References

1. Wu J, Ding V, Luo S, et al. Predictive model to guide brain magnetic resonance imaging surveillance in patients with metastatic lung cancer: impact on real-world outcomes. *JCO Precis Oncol* 2022; 6: e220022

2. Villano JL, Durbin EB, Normandeau C, et al. Incidence of brain metastasis at initial presentation of lung cancer. *Neuro Oncol* 2015; 17: 122-128.

3. Kim M, Suh CH, Lee SM, et al. Development of brain metastases in patients with non-small cell lung cancer and no brain metastases at initial staging evaluation: cumulative incidence and risk factor analysis. *AJR Am J Roentgenol* 2021; 217: 1184-1193.

Images/Tables

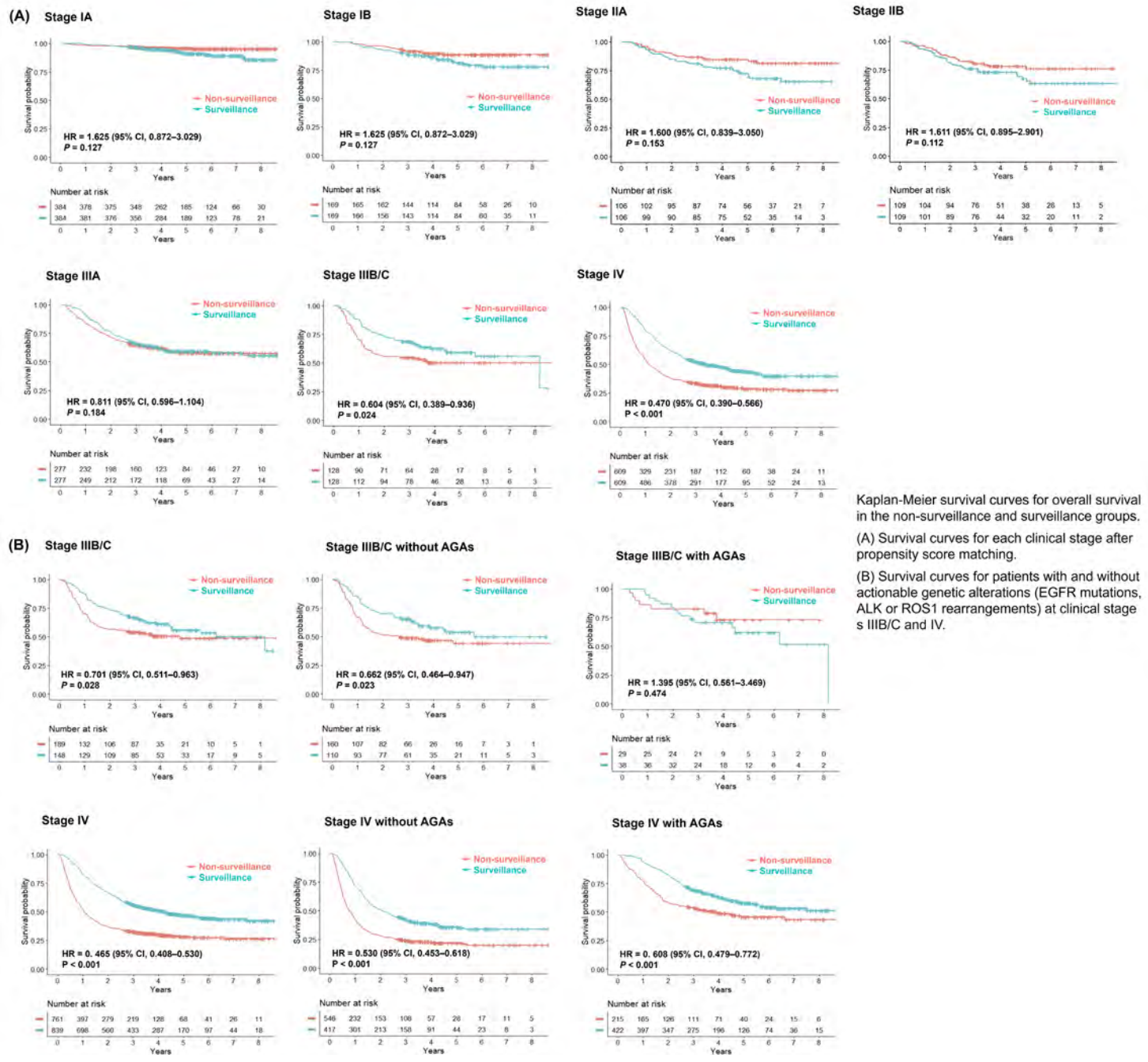

Kaplan-Meier survival curves for overall survival in the non-surveillance and surveillance groups.

(A) Survival curves for each clinical stage after propensity score matching.

(B) Survival curves for patients with and without actionable genetic alterations (EGFR mutations, ALK or ROS1 rearrangements) at clinical stage s IIIB/C and IV.

978 Arterial Spin Labeling-Derived Fractional Tumor Burden Differentiates Tumor Recurrence from Radiation Necrosis in Brain Metastases After Stereotactic Radiosurgery

Rafail C Christodoulou MD[1], Elham Rahimi MD[2], Erqi Liu Pollom MD[3], Melanie Hayden Gephart MD[4], Seema Nagpal MD[5], Scott Soltys MD[2], Michael Iv MD[6]

[1]Division of Neuroimaging and Neurointervention, Department of Radiology, Stanford University, Stanford, CA, Stanford, Califronia, USA. [2]Department of Radiation Oncology, Stanford University, Stanford, CA,Stanford Brain Tumor Center, Stanford University, Stanford, CA, Stanford, California, USA. [3]Department of Radiation Oncology, Stanford University, Stanford, CA, Stanford, California, USA. [4]Department of Neurosurgery, Stanford University, Stanford, CA,Stanford Brain Tumor Center, Stanford University, Stanford, CA, Stanford, California, USA. [5]Division of Neuro-Oncology, Department of Neurology, Stanford University, Stanford, CA,Stanford Brain Tumor Center, Stanford University, Stanford, CA, Stanford, California, USA. [6]Division of Neuroimaging and Neurointervention, Department of Radiology, Stanford University, Stanford, CA,Stanford Brain Tumor Center, Stanford University, Stanford, CA, Stanford, California, USA

Purpose

Accurate differentiation between tumor recurrence and radiation necrosis (RN) remains challenging in patients with brain metastases (BrMs) after stereotactic radiosurgery (SRS). Fractional tumor burden (FTB) derived from dynamic susceptibility contrast perfusion MRI has shown diagnostic value,[1-3] but interpretation can be limited by susceptibility artifacts. Arterial spin labeling (ASL) provides quantitative perfusion assessment and can overcome these limitations.[4]This study validates ASL-derived cerebral blood flow (CBF) metrics and introduces ASL-derived FTB for differentiating RN from recurrent tumor.

Materials & Methods

We retrospectively included patients with BrMs treated with SRS who had suspicious contrast-enhancing lesions $\geq$ 1 cm on follow-up ASL-MRI. Absolute and normalized mean and maximum CBF, as well as FTB-low and FTB-high voxel percentages, were measured within enhancing lesion volumes. Ground truth was determined by longitudinal imaging follow-up or histopathology. Previously validated CBF thresholds[4] were applied to generate FTB maps. Group differences were assessed with the Mann-Whitney U test, and diagnostic performance with AUROC and DeLong's test. Logistic regression modeled tumor probability as a function of FTB.

Results

Eighty-six patients (mean age 60.3 years; 57 female) with 102 BrMs (68 RN, 34 tumor) were analyzed. Compared with RN, recurrent tumors showed higher CBF_{mean} (median 42.5 vs 25.2 mL/100 g/min) and CBF_{max} (81.9 vs 48.3 mL/100 g/min; all $p < 0.0001$). RN lesions contained predominantly **FTB-low voxels** (mean 92.4%) and minimal **FTB-high**(7.4%), whereas recurrent tumors exhibited reduced FTB-low (65.6%) and elevated FTB-high (34%; all $p < 0.0001$). AUROCs were similar across CBF_{mean}, CBF_{max}, FTB-low, and FTB-high (0.78-0.83). Normalized metrics slightly outperformed absolute measurements (0.82-0.83 vs 0.78-0.82), although significance was only detected with CBF_{mean}($p = 0.012$). Logistic regression demonstrated significant associations between FTB and lesion classification: each 1% increase in FTB-high raised tumor odds by 4-5% (OR 1.04-1.05), and each 1% increase in FTB-low lowered tumor odds by 4-5% (OR 0.95-0.96, all $p < 0.0001$).

Conclusion

ASL-derived CBF and FTB metrics, both absolute and normalized, reliably differentiate RN from recurrent tumor in BRMs after SRS. These findings support ASL as a robust alternative to contrast-enhanced DSC perfusion for posttreatment lesion characterization.

References

1. Kuo F, Ng NN, Nagpal S, Pollom EL, Soltys S, Hayden-Gephart M, Li G, Born M, **Iv M**. DSC Perfusion MRI-Derived Fractional Tumor Burden and Relative CBV Differentiate Tumor Progression and Radiation Necrosis in Brain Metastases Treated with Stereotactic Radiosurgery. *AJNR Am J Neuroradiol*. 2022 May;43(5):689-695.
2. **Iv M**, Liu X, Lavezo J, Gentles AJ, Ghanem R, Lummus S, Born DE, Soltys SG, Nagpal S, Thomas R, Recht L, Fischbein N. Perfusion MRI-based fractional tumor burden differentiates between tumor and treatment effect in recurrent glioblastomas and informs clinical decision-making. *AJNR Am J Neuroradiol*, 2019 Oct;40(10):1649-1657.
3. Yamin G, Tranvinh E, Lanzman BA, Tong E, Hashmi SS, Patel CB, **Iv M**. Arterial Spin-Labeling and DSC- Perfusion Metrics Improve Agreement and Confidence in Neuroradiologists' Clinical Interpretations of Posttreatment High-Grade Glioma Surveillance MRI: An Institutional Experience. *AJNR Am J Neuroradiol*. 2024 Apr;45(4):453-460.

4.Nguyen HH, Ng NN, Awasthi S, Vogel H, **Iv M**. Arterial Spin Labeling Perfusion MRI Differentiates Between Radiation Necrosis and Tumor in Brain Metastases Treated with Stereotactic Radiosurgery. *Neurooncol Adv*. 2025 May 7;7(1):vdaf091.

Images/Tables

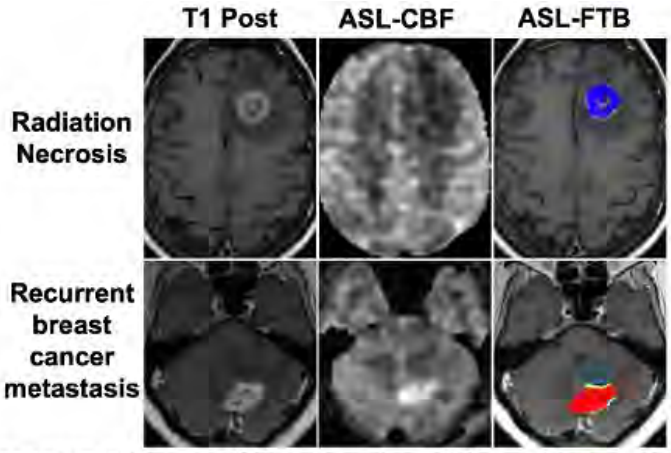

Figure 1: Representative post-SRS examples of RN and tumor. FTB-low (blue) and FTB-high (red) voxels represent higher likelihood of RN and tumor, respectively.

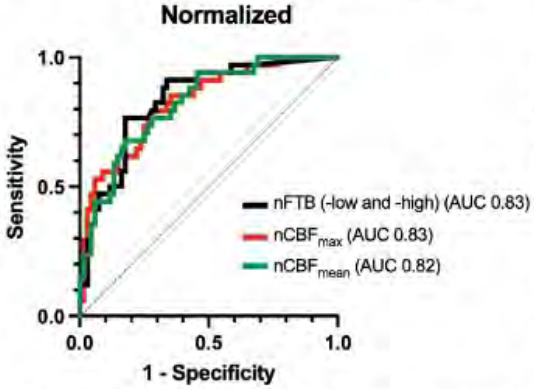

Figure 2: ROC curves show comparable performance of ASL-derived metrics.

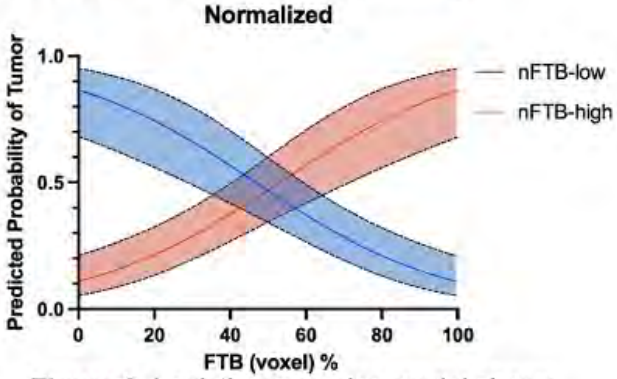

Figure 3: Logistic regression model shows opposing trends of FTB-low and FTB-high. Shaded regions represent 95% CI.

485 **Utility of Magnetic Resonance Spectroscopy for Differentiating Tumor Recurrence and Posttreatment Changes: An Institutional Experience**

Matthew D'Antuono B.S., Logan Sutton M.D., Arshan Goudarzi B.S., Anousheh Saya M.D., Earn-Chun C Lee M.D.
MedStar Georgetown University Hospital, Washington, D.C., USA

Purpose

Early identification and differentiation between post-radiation changes and tumor recurrence is essential for optimal patient care and management. Both processes exhibit similar conventional imaging features, and perfusion is routinely used to aid in distinguishing between the two. Even still, there are instances of clinical uncertainty, and our institute performs magnetic resonance spectroscopy (MRS) in combination with conventional imaging and perfusion to provide diagnostic clarity in those cases. Here, we seek to describe our institutional experience using MRS to differentiate between post-radiation changes and recurrence.

Materials & Methods

We conducted a retrospective review of MRS imaging conducted at our institute between January 2023 and August 2025, reviewed those studies, and examined the final radiology report and clinical notes. Tumor recurrence and post-radiation changes were defined by the results of 3-6 month follow up. Generally, a Choline (Cho) to N-acetylaspartate (NAA) ratio >2:1 by MRS is accepted as predictive of recurrence. We grouped patients who met inclusion criteria into four categories: Group 1 with Cho:NAA ratio >2:1 and progression, Group 2 with Cho:NAA ratio >2:1 and post-radiation changes, Group 3 with Cho:NAA ratio <2:1 and progression, and Group 4 with Cho:NAA ratio <2:1 and post-radiation changes.

Results

We identified 77 MRS studies performed on 60 patients with brain tumors. Of these 60 patients, 29 (48.3%) received radiation prior to their MRS study. Eight studies were non-diagnostic owing to poor study quality or the presence of two distinct neoplasms. Of the remaining 21 patients, 9 (42.9%) belonged to Group 1, 3 (14.3%) belonged to Group 2, 4 (19.0%) belonged to Group 3, and 5 (23.8%) belonged to Group 4. Overall, a Cho:NAA ratio >2:1 accurately predicted tumor recurrence in 75% (9/12) of patients, whereas a low Cho:NAA ratio accurately predicted radiation changes in 55.6% (5/9) of patients. In total, MRS was incongruent with the final diagnosis in 33% of cases (7/21). These patients, belonging to Groups 2 and 3, had diagnoses of low-grade oligodendrogliomas and astrocytomas (4/7, 57.1%), brain metastases (2/7, 28.6%), or lymphoma (1/7, 14.3%). In these 7 instances, conventional imaging and perfusion were more accurate at distinguishing between posttreatment changes and tumor progression (6/7, 85.7%). Moreover, of 10 total low-grade primary brain tumors, MRS accurately distinguished between recurrence and posttreatment changes in 4 (40%), whereas 88.9% (8/9) of high-grade primary brain tumors were accurately differentiated by MRS.

Conclusion

In our experience, MRS Cho:NAA ratios are best at differentiating tumor recurrence and post-radiation changes for patients with high-grade gliomas. In cases of low-grade neoplasms, Cho:NAA ratios were not accurate in predicting recurrence or radiation changes. Radiologists require better tools and

supplemental imaging modalities for early and accurate differentiation between brain tumor recurrence and posttreatment changes. Examining differences in Cho:Creatinine (Cr) or NAA:Cr ratios may help as well as supplementation with nuclear medicine studies like DOPA PET. Larger retrospective studies examining both MRS results in conjunction with these methods and clinical outcomes are desperately needed to improve accurate and early detection of brain tumor progression.

References

1. Dagher R, Gad M, da Silva de Santana P, et al. Umbrella review and network meta-analysis of diagnostic imaging test accuracy studies in differentiating between brain tumor progression versus pseudoprogression and radionecrosis. *J Neurooncol* 2024;166:1-15. DOI: https://doi.org/10.1007/s11060-023-04528-8
2. Galijasevic M, Steiger R, Mangesius S, et al. Magnetic resonance spectroscopy in diagnosis and follow-up of gliomas: State-of-the-art. *Cancers* 2022;14(13):3197. DOI: https://doi.org/10.3390/cancers14133197
3. Gurbani S, Weinberg B, Cooper L, et al. The Brain Imaging Collaboration Suite (BrICS): A cloud platform for integrating whole-brain spectroscopic MRI into the radiation therapy planning workflow. *Tomography* 2019;5(1):184-191. DOI: https://doi.org/10.18383/j.tom.2018.00028
4. Naser RKA, HAssan AAK, Shabana AM, Omar NN. Role of magnetic resonance spectroscopy in grading of primary brain tumors. *Egyptian Journal of Radiology and Nuclear Medicine* 2016;47(2)577-584. DOI: https://doi.org/10.1016/j.ejrnm.2016.03.011
5. Smith EA, Carlos RC, Junck LR, et al. Developing a clinical decision model: MR spectroscopy to differentiate between recurrent tumor and radiation change in patients with new contrast-enhancing lesions. *AJR Am J Roentgenol* 2009;192(2):45-52. DOI: https://doi.org/10.2214/AJR.07.3934

---

764 Clinical Ultra-High Field 7 Tesla MRI Proton Density Compliments Noncontrast Time-of-Flight MRA Brain to Increase Diagnostic Accuracy for Cases of Aneurysm Versus Infundibulum: An Innovation for Noninvasive Neurovascular Answers.

Jace Buxton M.D., Yuxiang Zhou Ph.D., Nick Koontz M.D., Ameet Patel M.D., Alicia Chen M.D., Ichiro Ikuta M.D., Justin Cramer M.D.
Mayo Clinic, Scottsdale, AZ, USA

Purpose

Differentiation between an intracranial aneurysm and infundibulum is crucial for guiding patient management. Prior studies have shown that 7 Tesla (T) MRA offers superior diagnostic accuracy compared to 3T MRA1. However, time-of-flight (TOF) sequences can have limitations, particularly for small or complex lesions and vessels oriented along the imaging plane2. High-resolution sequences like proton density (PD) provide exquisite vascular detail with high signal-to-noise3 regardless of intraluminal plaque / thrombus, and were anecdotally observed to show tiny arteries not apparent on TOF MRA. This study investigates the comparative diagnostic performance of 7T TOF MRA versus 7T PD MRI in differentiating intracranial aneurysms from infundibula.

Materials & Methods

This retrospective study reviewed the first 35 7T MRA examinations since June 1, 2024 that utilized both TOF MRA and PD sequences and identified 25 distinct intracranial aneurysms or infundibula. Two radiologists independently classified each sequence as: definite aneurysm or infundibulum, indeterminate, or normal. Discrepancies were resolved by consensus. The dominant vessel orientation (transverse or craniocaudal) was also recorded.

Results

Of the 25 lesions, 16 (64%) were definitively characterized by both TOF MRA and PD MRI. In cases of discordance, PD MRI provided a definitive diagnosis in 6 instances (24%) where TOF MRA was indeterminate, particularly for transversely oriented vessels such as the posterior communicating artery (PCOM). In those cases, PD clearly demonstrated a tiny PCOM which was not visible on TOF MRA. Conversely, TOF MRA provided definitive diagnoses in 3 instances (12%) where PD MRI was indeterminate, for example, the periophthalmic region and the posterior cerebral artery P1 segment. The PD sequence was limited in the cavernous and paraclinoid regions, and in cases where tiny vascular structures abut other hypointense structures such as nerves and vessels.

Conclusion

High resolution PD is a complementary sequence for intracranial vascular imaging, particularly in evaluating transversely oriented arteries such as the posterior communicating artery. PD is limited in the cavernous sinus and paraclinoid regions, where TOF remains more diagnostic.

References

1. MJ W, MA vW, A G, et al. 7Tesla MRA for the differentiation between intracranial aneurysms and infundibula - PubMed. Magnetic resonance imaging 2017 Apr;37
2. X Z, YZ C, XH M, et al. Highly accelerated compressed sensing time-of-flight magnetic resonance angiography may be reliable for diagnosing head and neck arterial steno-occlusive disease: a comparative study with digital subtraction angiography - PubMed. European radiology 2020 Jun;30
3. Y Y, SC J, JY K, et al. Added diagnostic values of three-dimensional high-resolution proton density-weighted magnetic resonance imaging for unruptured intracranial aneurysms in the circle-of-Willis: Comparison with time-of-flight magnetic resonance angiography - PubMed. PloS one 12/03/2020;15

Images/Tables

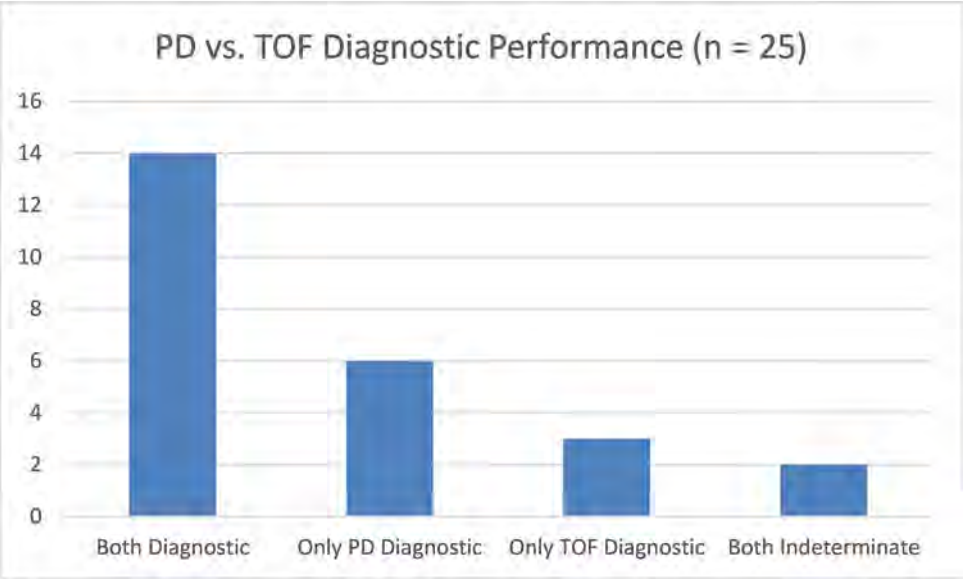

1118 Comparison of Probabilistic Tractography Methods in Infiltrative Edema for Guiding Supratotal Resection of Glioblastoma

Nima Broomand Lomer M.D., Drew Parker, Ragini Verma
University of Pennsylvania, Philadelphia, Pennsylvania, USA

Purpose

In high-grade gliomas (HGGs), the non-enhancing tumor (NET) region often harbors infiltrative tumor cells and peritumoral edema. This infiltrative component is a major driver of disease progression and recurrence through invasion of adjacent white matter (WM) tracts. Supratotal resection (SpTR) has therefore emerged as an optimal surgical strategy, extending resection beyond the contrast-enhancing tumor (CET) to encompass infiltrative margins while preserving eloquent WM pathways [1]. Diffusion MRI tractography provides valuable preoperative insights into WM architecture; however, accurate reconstruction within NET remains challenging due to free water contamination and complex fiber crossings. Although free-water corrected tensor models (e.g., FERNET) mitigate some of these effects, they are limited by single-fiber assumptions [2]. Integrating probabilistic tracking with higher-order diffusion modeling may overcome these challenges. Since clinical protocols vary between single-shell and multi-shell diffusion MRI acquisitions, it remains unclear which modeling strategy best preserves WM architecture within edematous or infiltrated regions. This case study aims to evaluate existing methods to determine their ability to resolve peritumoral WM architecture and their suitability for surgical planning in HGGs.

Materials & Methods

Three patients with pathologically confirmed glioblastoma were selected, each with tumors located in comparable regions (left temporal or temporoparietal) to ensure consistent anatomical conditions for comparison (Figure 1). Probabilistic tractography based on constrained spherical deconvolution (CSD) was performed using three diffusion modeling strategies: (1) single-shell single-tissue with b=800 s/mm^2 (SSST-b800), (2) SSST with b=2000 s/mm^2 (SSST-b2000), and (3) multi-shell multi-tissue with b=800 and 2000 s/mm^2 (MSMT-b800-2000). Whole brain tractograms were generated for each model using identical tracking parameters to ensure methodological consistency. Regions of interest (ROIs) were manually delineated by an experienced physician to reconstruct the corticospinal tract (CST) and arcuate fasciculus (AF) within peritumoral regions. Tracts were evaluated qualitatively (visual inspection) and quantitatively using metrics including track count, tract volume, and coverage, defined as the proportion of peritumoral edema volume intersected by the tracts (Tables 1-2). Corresponding tracts were also delineated in the contralateral hemisphere to serve as reference controls for comparison between tumor-affected and contralateral white matter.

Results

Figure 2 illustrates representative CST and AF reconstructions in Case 3 obtained using the three tractography methods. Across all cases, MSMT-b800-2000 consistently yielded smaller tract volumes on the ipsilateral side compared to the other two methods, whereas the SSST-b800 produced the largest volumes. On the contralateral side, tractography results were largely comparable across models, although SSST-b800 occasionally generated a greater number of streamlines. These findings were further supported by merged coverage (Table 2), which demonstrated that MSMT-b800-2000 achieved the lowest overall coverage, while SSST-b800 consistently exhibited the highest.

Conclusion

This study provides preliminary evidence on the performance of higher-order probabilistic tractography models for resolving white matter pathways within the NET regions of HGGs. Our findings suggest that while multi-shell modeling offers theoretical advantages, single-shell acquisitions demonstrated comparable or superior ability to delineate peritumoral tracts, including regions of complex fiber crossings between the CST and AF. These results highlight the potential clinical feasibility of single-shell diffusion protocols with higher-order probabilistic tractography models for preoperative surgical planning for glioblastoma.

References

1. Lasocki A, Gaillard F. Non-contrast-enhancing tumor: a new frontier in glioblastoma research. *American Journal of Neuroradiology* 2019;40:758-765

2. Parker D, Ould Ismail AA, Wolf R, et al. Freewater estimatoR using iNtErpolated iniTialization (FERNET): Characterizing peritumoral edema using clinically feasible diffusion MRI data. *Plos one* 2020;15:e0233645

Images/Tables

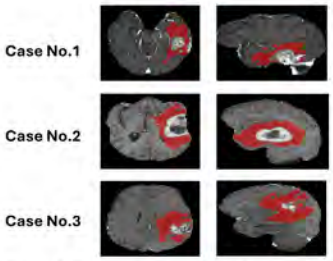

Figure 1. Representative axial and coronal MR images from three patients with glioblastoma. The red mask delineates the peritumoral edema, while the central core represents the contrast-enhancing tumor.

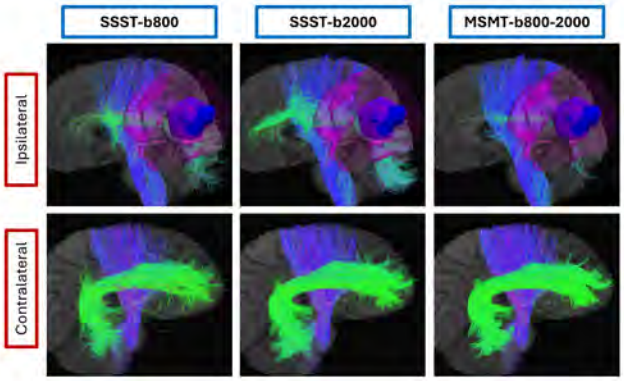

Figure 2. Visualization of manually delineated corticospinal tract (CST) and arcuate fasciculus (AF) in both hemispheres (tumor-affected and contralateral) for Case 3. The top row shows the ipsilateral (tumor) side, and the bottom row shows the contralateral side. All three tractography methods used identical regions of interest (ROIs) for reconstruction. As illustrated, the three methods yielded comparable tracts on the healthy side, whereas on the tumor side, the SSST-b2000 model more closely resembled the contralateral tract, while the MSMT-b800-2000 model produced the smallest tract volume.

Table 1. Summary of crude statistics for ipsilateral and contralateral tracts

Subject	Tract	Method	Track count		Tract volume	
			Ipsilateral	Contralateral	Ipsilateral	Contralateral
No.1	AF	SSST-b800	1101	1411	75.048	87.168
		SSST-b2000	2743	2080	58.752	63.44
		MSMT-b800-2000	1873	1583	37.232	47.848
	CST	SSST-b800	462	800	61.488	72.728
		SSST-b2000	895	1356	58.096	65.496
		MSMT-b800-2000	1005	1595	56.848	65.168
No.2	AF	SSST-b800	2060	2366	122.312	100.768
		SSST-b2000	2515	3086	76.472	72.36
		MSMT-b800-2000	1589	3105	49.712	62.392
	CST	SSST-b800	879	1151	87.056	75.76
		SSST-b2000	1584	1202	85.528	65.152
		MSMT-b800-2000	1723	1373	77.064	63.528
No.3	AF	SSST-b800	937	840	79.944	68.68
		SSST-b2000	1281	1124	65.688	62.672
		MSMT-b800-2000	1782	1375	63.768	60.184
	CST	SSST-b800	262	947	31.128	54.608
		SSST-b2000	902	2319	37.912	55.72
		MSMT-b800-2000	55	2102	7.824	47.312

Table 2. Details of coverage for each track and combination of both

Subject	Method	AF	CST	Merged
No.1	SSST800	0.1987	0.0551	0.2301
	SSST2000	0.165	0.0244	0.1847
	MSMT	0.0737	0.0384	0.1013
No.2	SSST800	0.3212	0.1154	0.3728
	SSST2000	0.1843	0.1008	0.2446
	MSMT	0.0883	0.0833	0.1495
No.3	SSST800	0.1246	0.1964	0.286
	SSST2000	0.1229	0.1331	0.2316
	MSMT	0.0355	0.1046	0.1387

Scientific Abstract Power Pitches & Luminary Speaker: Precision Neuroradiology: Advanced Imaging, AI, and Biomarkers in Clinical Practice

9:55 - 10:55am Monday, 18th May, 2026

212 Opportunistic Deep Learning-Based Prediction of Brain Tau Burden Using MRI

Donghoon Kim Ph.D., Brandon C. Ho BS, Henk van Voorst MD, Ph.D., Yongkai Liu PhD, Sharon Sha MD, MS, Elizabeth Mormino Ph.D., Victor W. Henderson MD, MS, Greg Zaharchuk MD, Ph.D.
Stanford University, Stanford, CA, USA

Purpose

Most people with Alzheimer's disease remain undiagnosed until cognitive symptoms become clinically apparent, by which time substantial pathology has already developed, often too late for meaningful intervention. Surprisingly, several recent studies have revealed that approximately 10% of cognitively normal individuals over age 60 have significant brain tau burden, and that they progress to dementia at a much faster rate than their tau-negative peers.[1,2] These findings highlight a critical need for a scalable approach to identify individuals with preclinical tau pathology. To address this, we developed a deep learning model that infers brain tau burden directly from routinely acquired MRI, potentially enabling opportunistic detection of at-risk individuals without additional procedures or cost.

Materials & Methods

A total of 3,180 MRI–tau PET pairs were collected across five publicly available datasets, each with T1-weighted and T2-FLAIR MRI scans acquired within one year of PET imaging. Data from ADNI, OASIS-3, A4, and HABS were split for network development (80%) and internal testing (20%), with 342 cases from the SCAN reserved as an external test set. Tau-PET standardized-uptake-value ratios (SUVRs) were quantified in each Braak region and combined into early (Braak I–IV) and late (Braak V–VI) stages.[3,4] MRIs underwent skull-stripping, co-registration, reorientation, resampled, and intensity normalization.

The SUVR prediction model was developed using a 3D DenseNet-264 architecture with a combined loss function optimizing both local accuracy and global consistency across Braak stages. Additionally, predicted SUVRs were binarized using a threshold of the mean SUVR + 2 standard deviations from cognitively normal subjects. Opportunistic screening cutoffs were derived from the internal receiver operating characteristic (ROC) curve for Braak I–IV regions, incorporating known prevalence[2] to achieve a target positive predictive value (PPV) above 50% in the external test set. Different cutoff values were also explored.

Results

On the internal test set, the model predicted composite SUVRs with Pearson correlations of 0.60 (Braak I–IV) and 0.46 (Braak V–VI); area under the curve values (AUC) for binary tau positivity were 0.86 and 0.82 at Youden's *J* index point, respectively. External validation demonstrated strong generalizability, with Pearson correlations of 0.73 for Braak I–IV and 0.76 for Braak V–VI, and corresponding AUCs of 0.90 and 0.87 (**Fig. 1-A**). The opportunistic screening approach maintained a minimum PPV of 50%, with robust negative predictive values (NPVs), even in this external cohort with lower cognitively normal tau-positive prevalence than population estimates[2] (**Fig. 1-B**). The effects of varying cutoff thresholds are illustrated in **Fig. 1-C**.

Conclusion

Prediction of brain tau burden from routine MRI provides a scalable and quantitative approach for noninvasive estimation of regional and global tau pathology. This study offers a practical pathway for early detection, risk stratification, and clinical trial enrichment. Screening cutoffs can be tailored to specific goals. For instance, clinical trial recruitment may adopt a lower threshold with higher sensitivity to include a broader pool of potentially eligible participants. With further validation in population-based settings, MRI-based tau prediction could enable opportunistic identification of individuals with preclinical Alzheimer's disease, supporting timely referral for neurological evaluation or confirmatory PET imaging.

References

1. Ossenkoppele R, Pichet Binette A, Groot C, et al. Amyloid and tau PET-positive cognitively unimpaired individuals are at high risk for future cognitive decline. *Nat Med* 2022;28:2381–7.
2. Ossenkoppele R, Coomans EM, Apostolova LG, et al. Tau PET positivity in individuals with and without cognitive impairment varies with age, amyloid-β status, APOE genotype and sex. *Nat Neurosci* https://doi.org/10.1038/s41593-025-02000-6.
3. Carlson ML, Smith V, Johns E, et al. MRI-free processing of tau PET images for early detection. *Imaging Neuroscience* 2024;2:1–14.
4. Landau SM, Ward TJ, Murphy A, et al. Quantification of amyloid beta and tau PET without a structural MRI. *Alzheimers Dement* 2023;19:444–55.

Images/Tables

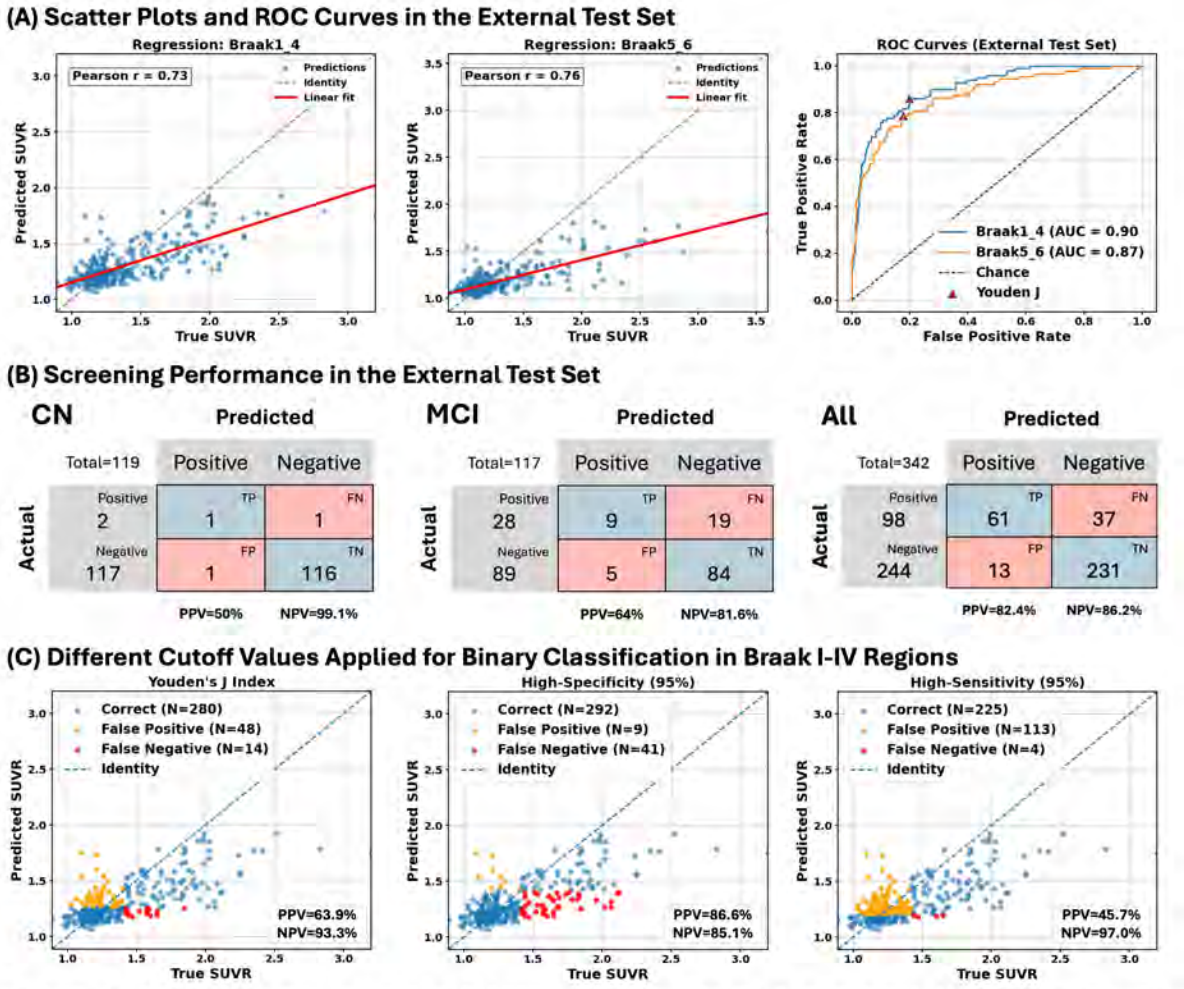

Figure 1. (A) True versus predicted SUVRs for Braak I–IV (left) and Braak V–VI (middle), with corresponding ROC curves (right) in the external test set. **(B)** Confusion matrices from the external test set showing screening performance at the high specificity cutoff for cognitively normal (left), mild cognitive impairment (middle), and all included SCAN participants (right). **(C)** Scatter plots showing correct (blue) and incorrect binary predictions (false positive in orange and false negative in red) in Braak I-IV regions when different cutoff values were applied, from left to right: Youden's *J* index, high specificity, and high sensitivity cutoffs.

---

410 **Integrating Anatomical Location with Radiomic Features Improves Risk Stratification of Pediatric High-Grade Gliomas**

Paul F D'Cunha MD[1], Abhishek Midya PhD[2], Adam Goldman-Yassen MD[1], Sheila McThenia MD[3], Frank Chien MD[3], Ujjwal Baid PhD[2], Bhakti Baheti PhD[2], Eswar Damaraju MS[3], Anant Madabhushi PhD[2], Kartik Reddy MD[1]

[1]Emory University, Department of Radiology, Atlanta, Georgia, USA. [2]Emory University, Atlanta, Georgia, USA. [3]Children's Healthcare of Atlanta, Atlanta, Georgia, USA

Purpose

To develop and validate an automated risk and survival prediction model for pediatric high-grade gliomas (pHGGs). We hypothesize that a model combining radiomic and automated anatomical location features will provide more robust and generalizable risk stratification for overall survival (OS) compared to a model built on radiomic features or location alone.

Materials & Methods

We retrospectively identified children (2009-2023) with biopsy-proven pediatric high-grade glioma (pHGG), or radiologically-diagnosed diffuse intrinsic pontine glioma who had pretreatment multi-sequence MRIs (T1, T1c, T2, T2-FLAIR, ADC) and available overall survival (OS) data. MRIs were preprocessed following BraTS guidelines, and a 3D U-Net performed automated tumor segmentations, which were validated against manual contours from one of two board-certified pediatric neuroradiologists using a lesion-wise DICE score (n=41). Anatomical location was determined by non-linearly registering T1-contrast images to a pediatric atlas and mapping the segmentations to identify the dominant structure, categorized as thalamus, brainstem, cerebral white matter, cerebellum, basal ganglia, or ventricles. An in-house, IBSI-compliant pipeline extracted 119 radiomic features including first-order (Gray), Haralick, Laws' texture measures, and CoLlAGe features from all 5 sequences. Prior to modeling, radiomic features were filtered by removing highly correlated features and applying a univariable Cox screen. We then developed three models: (1) a Location-Only Cox model, (2) a Radiomics-Only Elastic Net (ENet) Cox model selecting 10 features via 5-fold cross-validation, and (3) an early-fusion Radiomics+Location (Rad-Loc) hybrid ENet Cox model. In this third model, the 6 anatomical location variables were fused into Enet Cox model and

the 10 radiomic features were selected via standard L1/L2 regularization. All models were evaluated on a held-out test set using Harrell's C-index, time-dependent AUROC at 730 days, and Kaplan-Meier survival analysis with log-rank tests based on median risk-score stratification.

Results

A total of 193 children (training = 116; test = 77; average age 7.3 years with median OS 457 days) were included. The automated segmentation validation, compared against manual contours from two expert neuroradiologists, yielded a DICE score of 0.85. The baseline Location-Only model demonstrated strong prognostic value on the test set (C-index of 0.654), and significant risk stratification (HR: 2.71 [95% CI 1.52–4.83], $p < 0.001$); it also showed no signs of overfitting (Training C-index: 0.553). In comparison, the Radiomics-Only model was prognostic (Test HR: 1.91 [95% CI 1.12–3.26], $p = 0.017$), but it demonstrated a performance gap between the training (C-index: 0.726) and test datasets (C-index: 0.642), with a lower test performance than the Location-Only model. The final Rad-Loc model demonstrated the strongest and most generalizable performance. This combined model achieved the highest test C-index (0.681), the most significant risk stratification (HR: 3.55 [95% CI 1.98–6.35], $p < 0.001$), and the smallest gap between training (C-index: 0.714) and test performance. This improvement was supported by a trending, though not statistically significant, increase in the time-dependent AUROC at 730 days over the Radiomics-Only model (Rad-Loc: 0.78 vs. Rad-Only: 0.72, p=0.08).

Conclusion

Our final early-fusion Rad-Loc model, which integrated radiomics and location based features, yielded the most robust and accurate stratification for overall survival in pHGGs.

References

1. Prasanna, P., Tiwari, P. & Madabhushi, A. Co-occurrence of Local Anisotropic Gradient Orientations (CoLlAGe): A new radiomics descriptor. *Sci Rep* **6**, 37241 (2016). https://doi.org/10.1038/srep37241
2. Kazerooni, Anahita Fathi, et al. "The brain tumor segmentation in pediatrics (BraTS-PEDs) challenge: focus on pediatrics (CBTN-CONNECT-DIPGR-ASNR-MICCAI BraTS-PEDs)." *arXiv preprint arXiv:2404.15009* (2024).
3. VS Fonov, AC Evans, RC McKinstry, CR Almli and DL Collins Unbiased nonlinear average age-appropriate brain templates from birth to adulthood NeuroImage, Volume 47, Supplement 1, July 2009, Page S102 Organization for Human Brain Mapping 2009 Annual Meeting, DOI: 10.1016/S1053-8119(09)70884-5
4. Simon N, Friedman J, Hastie T, Tibshirani R. Regularization Paths for Cox's Proportional Hazards Model via Coordinate Descent. J Stat Softw. 2011 Mar;39(5):1-13. doi: 10.18637/jss.v039.i05. PMID: 27065756; PMCID: PMC4824408.
5. Eisenstat DD, Pollack IF, Demers A, Sapp MV, Lambert P, Weisfeld-Adams JD, Burger PC, Gilles F, Davis RL, Packer R, Boyett JM, Finlay JL. Impact of tumor location and pathological discordance on survival of children with midline high-grade gliomas treated on Children's Cancer Group high-grade glioma study CCG-945. J Neurooncol. 2015 Feb;121(3):573-81. doi: 10.1007/s11060-014-1669-x. Epub 2014 Nov 28. PMID: 25431150; PMCID: PMC4323766.

Images/Tables

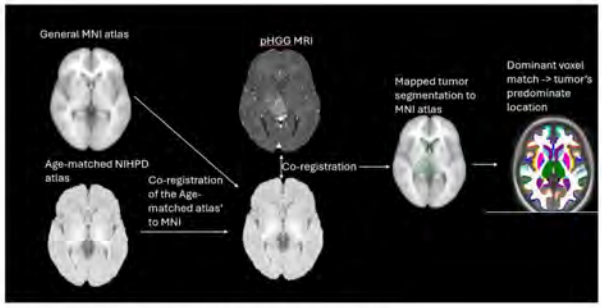

Figure 1: Location based automated feature extraction method

Figure 2: Radiomic heat map of one of the top 10 selected Features from FLAIR: CoLlAGe Energy

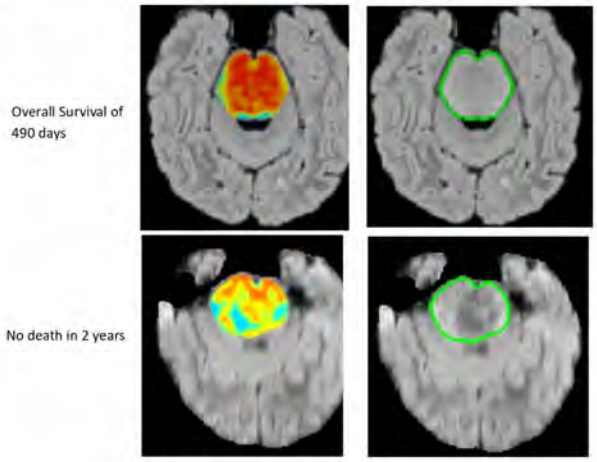

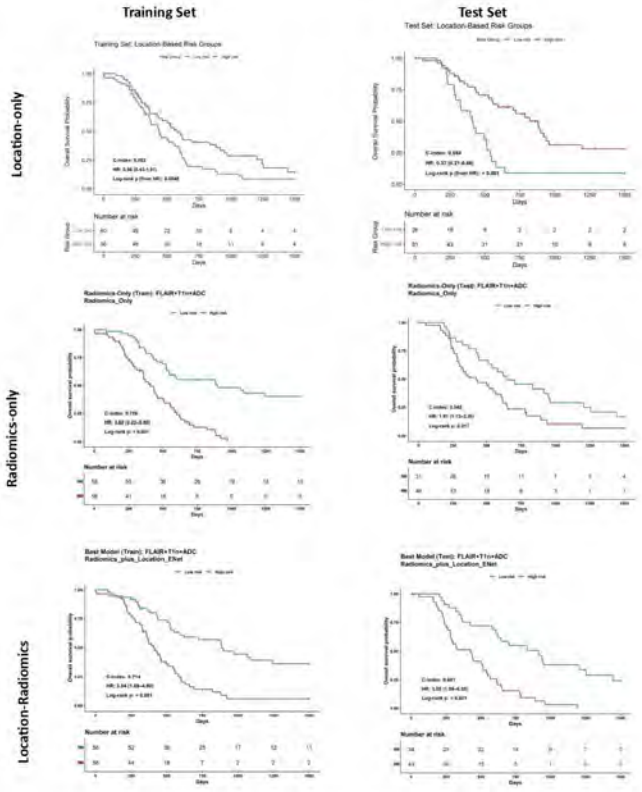

Figure 3: Kaplan Meier Plots for risk stratification of the 3 models.

504 Multiclass Radiomics-Based Prediction of BRAF Mutation Status in Pediatric Low-Grade Gliomas Using Multisequence MRI

Anat Yahav-Dovrat MD[1], Khashayar Namdar Ph.D., M.Sc., MEng, P.Eng[1], Matthias W Wagner1 MD[1], Min Sheng[1], Mitra Naseri MD[1], Matheus D Soldatelli MD[1], Peter Dirks MD[1], Kristen W Yeom MD[2], Cynthia Hawkins MD[1], Uri Tabori MD[1], Farzad Khalvati MSc, Ph.D.[1], Birgit B Ertl-Wagner MD[1]
[1]The Hospital for Sick Children, Toronto, Ontario, Canada. [2]Stanford School of Medicine, Palo Alto, CA, USA

Purpose

Pediatric low-grade gliomas (pLGGs) are the most common brain tumors in children and frequently harbor BRAF alterations, most commonly KIAA1549-BRAF fusions and BRAF V600E mutations. Differentiating between these subtypes is clinically important as therapeutic response differs substantially. The aim of our study was to assess multiclass radiomics-based prediction of BRAF mutation status in children with pLGG using multi-sequence MRI.

Materials & Methods

This retrospective, bi-institutional study, included pediatric patients with pLGG and known BRAF mutation status who underwent pre-surgical MRI between January 2009 and January 2023. Tumors were manually segmented, and radiomics features were extracted using PyRadiomics following multiple normalization strategies and bin widths. Random Forest classifiers were trained for three-class classification (BRAF fusion vs BRAF V600E vs non-BRAF) using clinical-only, radiomics-only, and combined models. Performance was evaluated with leave-one-out cross-validation, and results were compared across single-sequence and multisequence approaches

Results

511 children were included (mean age 8.5 ± 5.1 years; 45% female). FLAIR sequences were available for 495, T2WI for 454, contrast-enhanced T1WI (CE-T1WI) for 285 and ADC maps for 252 children. All sequences were available for 180 children. FLAIR was the best-performing single sequence (AUC 0.82), followed by T2WI (0.80), ADC (0.77), and CE-T1WI (0.75). Combined clinical-radiomics models consistently outperformed single-source models. In the 180-patient multisequence cohort, multisequence integration significantly improved performance: radiomics feature concatenation (macro-AUC 0.79) and ensemble modeling (0.79) both outperformed single-sequence approaches ($p < 0.001$). Feature analysis showed FLAIR-derived features dominated, but adding T2, ADC, and CE-T1WI improved balanced classification across subtypes.

Conclusion

MRI-based machine learning models can predict BRAF mutation status in pLGG. FLAIR is the best-predicting single sequence, but multisequence integration provides significantly superior and more balanced performance. These findings support multisequence radiomics as a promising tool to guide precision treatment in pLGG, particularly when tissue sampling is not feasible.

References

1. Wisoff JH, Sanford RA, Heier LA, et al. Primary neurosurgery for pediatric low-grade gliomas: A prospective multi-institutional study from the children's oncology group. *Neurosurgery* 2011;68:1548–54.
2. Plant-Fox AS, Tabori U. Future perspective of targeted treatments in pediatric low-grade glioma (pLGG): the evolution of standard-of-care and challenges of a new era. *Child's Nervous System* https://doi.org/10.1007/s00381-024-06504-7.
3. Ryall S, Tabori U, Hawkins C. Pediatric low-grade glioma in the era of molecular diagnostics. *Acta Neuropathol Commun* 2020;8.
4. Soldatelli MD, Namdar K, Tabori U, et al. Identification of Multiclass Pediatric Low-Grade Neuroepithelial Tumor Molecular Subtype with ADC MR Imaging and Machine Learning. *American Journal of Neuroradiology* 2024;45:753–60.

Images/Tables

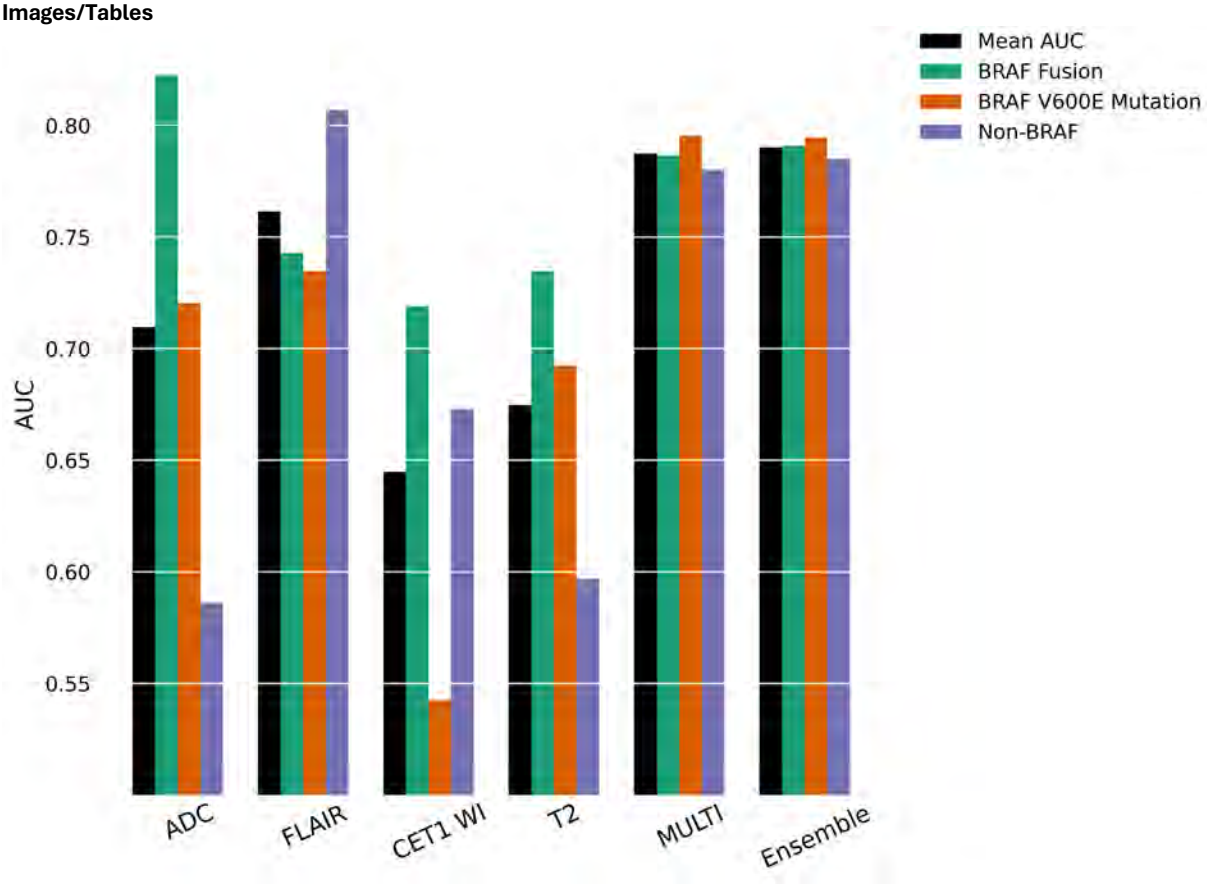

1087 Personalizing Radiation Planning Using a Transformer-Based Segmentation Approach to Predict Glioblastoma Recurrence from Metabolic MRI and White Matter Infiltration Maps

Harshita Kukreja[1], Bo Liu[1], Nate Tran[1], Angela Jakary[1], Oluwaseun Adegbite[1], Tracy L Luks[1], Yan Li[1], Annette M Molinaro[2], Javier E Villanueva-Meyer[2], Steve E Braunstein[3], Hui Lin[3], Janine M Lupo[1]

[1]Department of Radiology & Biomedical Imaging, UCSF, San Francisco, California, USA. [2]Department of Neurological Surgery, UCSF, San Francisco, California, USA. [3]Department of Radiation Oncology, UCSF, San Francisco, California, USA

Purpose

Standard-of-care (SoC) radiation therapy (RT) planning utilizes a uniform, isotropic 2cm-expansion of the T1-contrast-enhancing or T2-hyperintensity lesion (CEL, T2L) to generate a clinical target volume (CTV), without considering anisotropic tumor infiltration. We have previously demonstrated the benefit of using segmentation-based deep-learning approaches to generate progression CTVs from either the combination of anatomic, metabolic and diffusion-weighted imaging from MRI exams acquired pre-RT[1] or white matter infiltration maps from DTI acquired pre-surgical resection[2] that covered the progressed region while sparing more normal brain. This study aims to i) integrate these approaches to leverage their joint predictive power, ii) double the size of our training dataset by incorporating spatially-weighted loss functions, and iii) evaluate the ability to improve sensitivity to the progressed lesion compared to two SoC guidelines.

Materials & Methods

White matter infiltration maps from DTI, along with anatomical, diffusion-weighted, and metabolic MRI from 92 patients with glioblastoma acquired presurgical resection, were retrospectively used to predict regions of new contrast-enhancement or T2-hyperintensity at recurrence (60/30/10% train/validation/test split). Two segmentation-based predictive deep-learning approaches (UNet and Vision Transformer) with personalized loss functions and evaluation metrics that incorporate tumor size were employed, and their performance was compared to that of the SOC-2cm expansion CTVs in terms of sensitivity, specificity, and a personal progression coverage coefficient (PCC) that incorporates both sensitivity and specificity while accounting for class imbalance due to lesion size in one single metric.

Additionally, we developed an approach for combining imaging from pre-surgical and post-surgical pre-RT time points that incorporated spatially-weighted loss functions that ignored portions of the original lesion and resection cavity when making predictions in training. This allowed us to combine anatomical, diffusion-weighted, and metabolic MRI from 193 patients with glioblastoma (92 acquired pre-surgery, 101 post-surgery, pre-chemoradiation) to jointly predict the CEL + T2L at the time of recurrence. The benefit of using this approach was evaluated using two segmentation-based predictive deep-learning approaches (UNet and Vision Transformer), and their performance was compared to the two common SOC-2cm expansion CTV guidelines.

Results

Spatially-weighting the loss function to ignore the original CEL provided similar performance measures but allows for future training on larger cross-domain datasets (Figure 1A, left). Including white matter infiltration maps from DTI acquired pre-surgical resection significantly improved specificity and PCC over using only anatomical, diffusion-weighted, and metabolic MRI (0.87 vs 0.82; $p<0.001$), while maintaining a similarly high sensitivity (Figure 1A, right). Both our deep learning approaches significantly outperformed the aggressive RTOG-SOC in terms of specificity and PCC while having comparable sensitivity, with significantly improved sensitivity compared to the more conservative EORTC-SOC (0.90 vs 0.77; $p<0.01$) with comparable specificity. Figure 1B visually confirms the CTVs generated using these models, illustrating the benefit of these approaches.

Conclusion

This study demonstrates the potential benefit of using a segmentation-based, deep-learning approach for personalized RT planning that leverages vision-transformers, white matter infiltrative maps from DTI in combination with anatomical, diffusion-weighted, and metabolic MRI, and spatially-weighted loss to improve CTV definition.

References

1. Tran, N., Luks, T.L., Li, Y. *et al.* Novel radiotherapy target definition using AI-driven predictions of glioblastoma recurrence from metabolic and diffusion MRI. *npj Digit. Med.* **8**, 508 (2025).

2. Liu, B., Tran, N., Rowley, P. et al. Pre-RT Fiber Density-Weighted White Matter Pathlength Maps Can Predict Tumor Progression in Patients with Glioblastoma Multiforme. ISMRM (2024).

Images/Tables

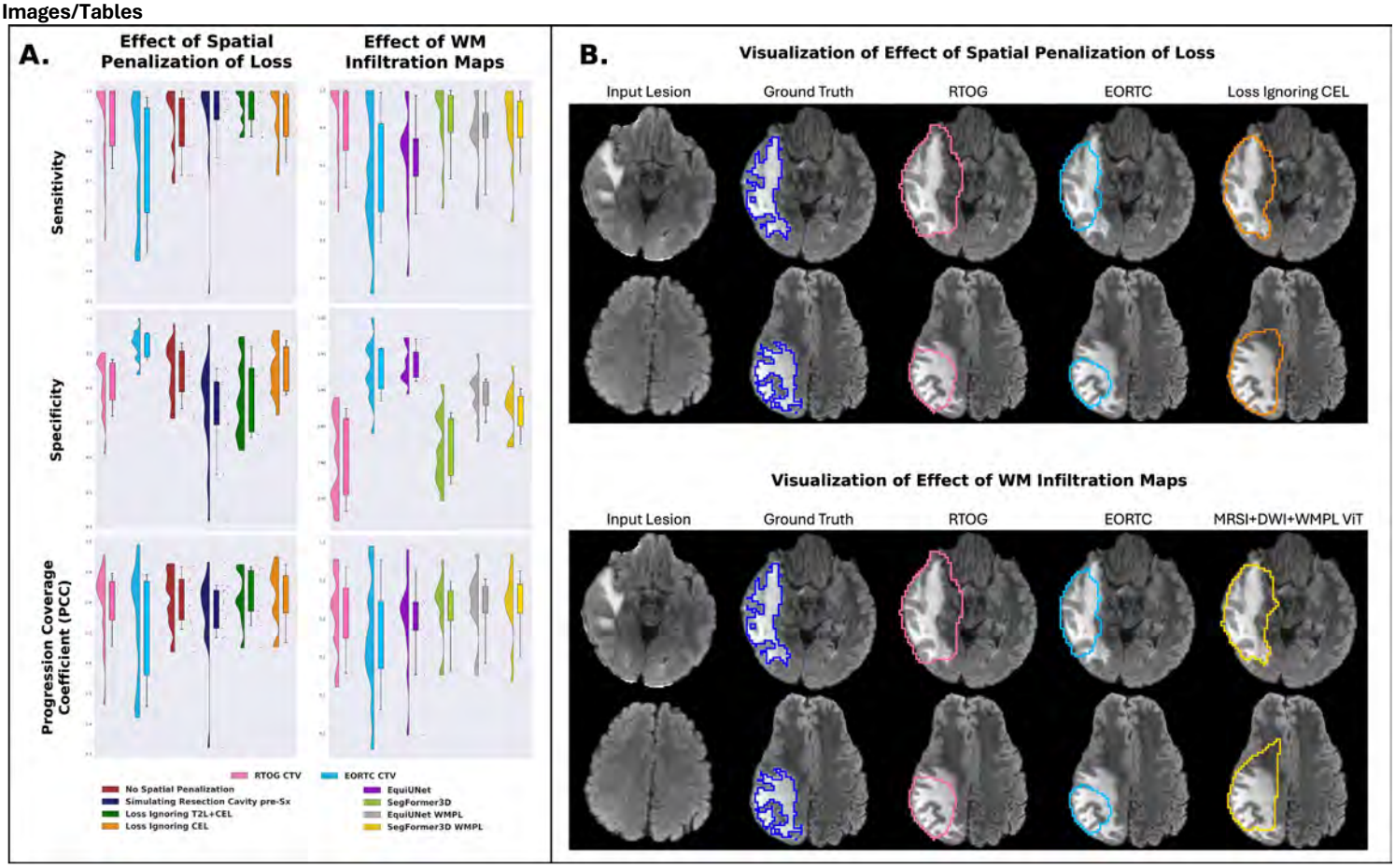

713 ASLNet: An Explainable Deep Learning Framework for Glioma Grading and Survival Prediction

Rafail C Christodoulou MD[1], Georgios Vamvouras[2], Michalis F Georgiou PhD[3]

[1]Department of Radiology, Stanford University School of Medicine, Stanford, California, USA, Stanford, California, USA. [2]Department of Electrical and Computer Engineering, National Technical University of Athens NTUA, Athens, Greece, Athens, Greece, Greece. [3]Department of Radiology, University of Miami Miller School of Medicine, Miami, Florida, USA, Miami, Florida, USA

Purpose

Arterial spin labeling (ASL) MRI combined with deep learning (DL) appears promising in providing a noninvasive prediction of glioma grade and overall survival (OS). ASL provides quantitative perfusion information and may capture vascular heterogeneity related to tumor aggressiveness and prognosis[1,2]. This study aimed to develop and validate ASLNet, an interpretable three-dimensional ResNet framework trained on ASL raw images to predict histopathologic grade and OS in glioma patients.

Materials & Methods

Patients with histologically confirmed diffuse glioma who underwent ASL-MRI between 2015 and 2024 were retrospectively included (n = 471; mean age 56.9 ± 13.1 years; 41 % female). Original, 3D ASL volumes were used as inputs, along with isotropically resampled, Gaussian-smoothed, and z-score normalized versions. Two custom three-dimensional Residual Network (3D ResNet) architectures were trained: one for WHO II–IV grading and a FiLM-type intermediate fusion variant, integrating demographic (Age, Sex) and clinical variables (EOR) for OS classification (< 12 months vs ≥ 12 months). Models were implemented in Python TensorFlow and optimized with Adam, class-balanced sampling, learning-rate scheduling, and early stopping under five-fold stratified cross-validation. Performance was assessed on held-out test sets using ROC AUC, PR AUC, macro-F1, accuracy, and recall. Integrated gradients saliency maps were computed to visualize influential perfusion regions.

Results

Our framework on the grading model achieved a macro-ROC AUC of 0.79 (95 % CI 0.75–0.83), Precision-Recall (PR) AUC 0.77, macro-F1 0.72, and accuracy 0.60. The OS model reached ROC AUC 0.70 (95 % CI 0.66–0.74), PR AUC 0.69, macro-F1 0.73, accuracy 0.66, and recall 0.94 for the long-survival class. Saliency analysis highlighted coregistered with T1-weighted image revealed hyper-perfused tumor cores as the most influential regions for grading, while also including peri-tumoral zones for survival prediction, consistent with perfusion heterogeneity patterns in gliomas[3,4]

Conclusion

ASLNet enables interpretable, perfusion-based assessment of glioma grade and survival. The approach demonstrates that arterial spin labeling carries clinically relevant information on tumor vascular characteristics, supporting its integration into neuro-oncology

References

1. Romano A, Romano A, Moltoni G, et al. Does arterial spin labelling represent a valid alternative to other MR perfusion techniques in neuro-oncology? *Radiol med* 2025;130:1489–502.

2. Haller S, Zaharchuk G, Thomas DL, et al. Arterial Spin Labeling Perfusion of the Brain: Emerging Clinical Applications. *Radiology* 2016;281:337–56.

3. Qiu J, Zhu M, Chen CY, et al. Diffusion heterogeneity and vascular perfusion in tumor and peritumoral areas for prediction of overall survival in patients with high-grade glioma. *Magnetic Resonance Imaging* 2023;104:23–8.
4. Furtner J, Bender B, Braun C, et al. Prognostic Value of Blood Flow Measurements Using Arterial Spin Labeling in Gliomas. Elder JB, ed. *PLoS ONE* 2014;9:e99616.

Images/Tables

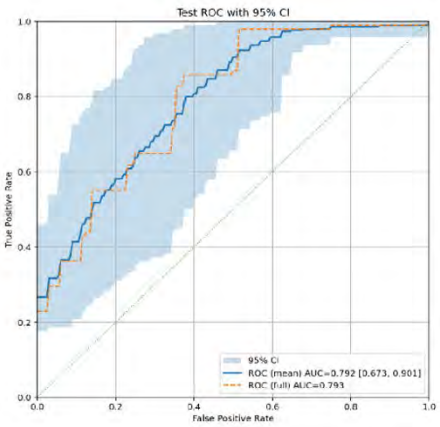

Figure 2: [Grade] ROC AUC curve for test set, with 95% CI.

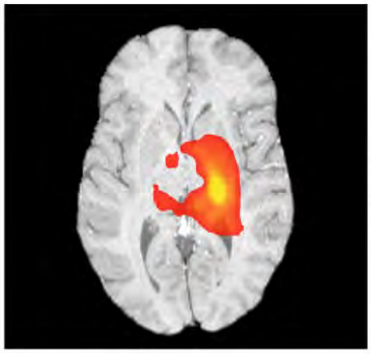

Figure 1: Voxel-wise saliency map derived from integrated gradients, demonstrating the most influential ASL regions associated with model output. The map is co-registered and overlaid on the subject's T1-weighted MRI for anatomical reference.

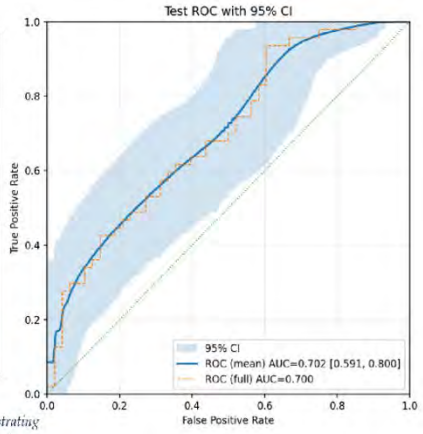

Figure 3: [OS] ROC AUC curve for test set, with 95% CI.

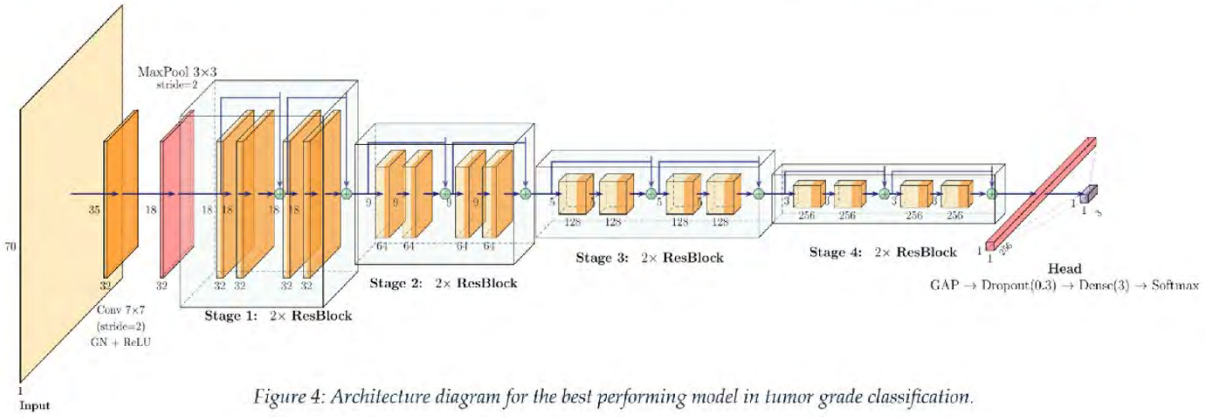

Figure 4: Architecture diagram for the best performing model in tumor grade classification.

1030 MRI-Based Volumetric Profiling of Skull Base Chordomas for Surgical Decision-Making and Outcome Prediction

Mohammadreza Amjadzadeh MD[1], Zachary Gersey MD[2], Yassine Alami Idrissi MD[1], Priyadarshini Mamindla MS[1], Vishal Peddagangireddy MS[1], Afrooz Zandifar MD[2], Nasim Batavani MD[2], Sakibul Huq MD[1], Serafettin Zenkin MD[2], Ayla Buyukkaya MD[2], Ozlem Tugce Kalayci MD[1], Ramazan Buyukkaya MD[1], Walaa Hamza MD[2], Sinef Huvaj Aksoy MD[2], Georgios A. Zenonos MD[3], Rivka R. Colen MD[2]

[1]Hillman Cancer Center, University of Pittsburgh Medical Center, Pittsburgh, Pennsylvania, USA. [2]Hillman Cancer Center, University of Pittsburgh Medical Center, Pittsburgh, PA, USA. [3]Department of Neurological Surgery, University of Pittsburgh Medical Center, Pittsburgh, PA, USA

Purpose

Skull base chordomas (SBCs) are rare, locally aggressive tumors that remain surgically challenging due to their proximity to critical neurovascular structures and propensity for recurrence (1, 2). While maximal safe resection is the cornerstone of management, the extent of resection (EOR) thresholds that significantly correlate with postoperative progression-free survival (PFS) have not been clearly determined. This study aimed to determine an optimal volumetric EOR threshold predictive of PFS in patients with treatment-naïve SBCs using quantitative MRI-based analysis at a high-volume tertiary center.

Materials & Methods

We retrospectively reviewed patients with newly diagnosed SBCs who underwent resection and pre- and postoperative MRI at our institution. All MRIs were acquired using standardized 1.5T or 3.0T protocols. Volumetric segmentation of T2-weighted sequences was performed by an experienced team of radiologists using 3D Slicer (version 4.10.2), a validated open-source platform. The EOR was calculated as the percentage reduction in tumor volume between pre- and postoperative MRIs. To determine the optimal EOR cutpoint predictive of PFS, maximally selected rank statistics with 10,000 bootstrap iterations were applied. The median cutpoint derived from this analysis was used for binary categorization of patients into high and low EOR groups. Kaplan–Meier survival analysis with log-rank testing was performed to compare PFS between these groups. Multivariable Cox proportional hazards regression was used to assess the independent prognostic value of EOR after adjusting for age, sex, molecular subtype, and postoperative radiation. All analyses were conducted in R (packages: *survminer*, *ggplot2*, *dplyr*).

Results

The study cohort included 104 patients (mean age: 44.22 years ± 19.52 [SD]; 58% male). The mean and median EOR were 95.9% and 100%, respectively, while the mean and median PFS were 35.3 months and 29.3 months, respectively. The optimal EOR threshold predictive of improved PFS was determined to be >98.9%, dividing the cohort into 21 patients with ≤98.9% resection (low-EOR group) and 83 patients with >98.9% resection (high-EOR group). This cutoff effectively differentiated patients who achieved gross total resection (0% residual volume) from those with

residual tumor, and the Kaplan-Meier analysis demonstrated a statistically significant difference in PFS between the groups (log-rank p = 0.0016). On multivariable Cox regression analysis, achieving an EOR >98.9% remained a significant independent predictor of prolonged PFS after controlling for demographic, molecular, and treatment-related variables ($p < 0.05$).

Conclusion

Volumetric MRI analysis demonstrated that an EOR threshold of >98.9% is significantly associated with improved progression-free survival in patients with skull base chordomas. These findings support the use of precise volumetric assessment to guide surgical strategy and postoperative prognostication. Quantitative imaging metrics such as volumetric EOR may serve as valuable tools for personalized surgical planning and longitudinal outcome prediction in skull base chordoma management.

References

1. Amit M, Na'ara S, Binenbaum Y, et al. Treatment and outcome of patients with skull base chordoma: a meta-analysis. J Neurol Surg B Skull Base 2014;75(6):383–90. DOI: https://doi.org/10.1055/s-0034-1376197. [Epub 2014 May 27]
2. Bai J, Li M, Shi J, et al. Mid-term follow-up surgical results in 284 cases of clival chordomas: risk factors for outcome and tumor recurrence. Neurosurg Rev 2022;45(2):1451–62. DOI: https://doi.org/10.1007/s10143-021-01576-4. [Epub 2021 Oct 8]

Images/Tables

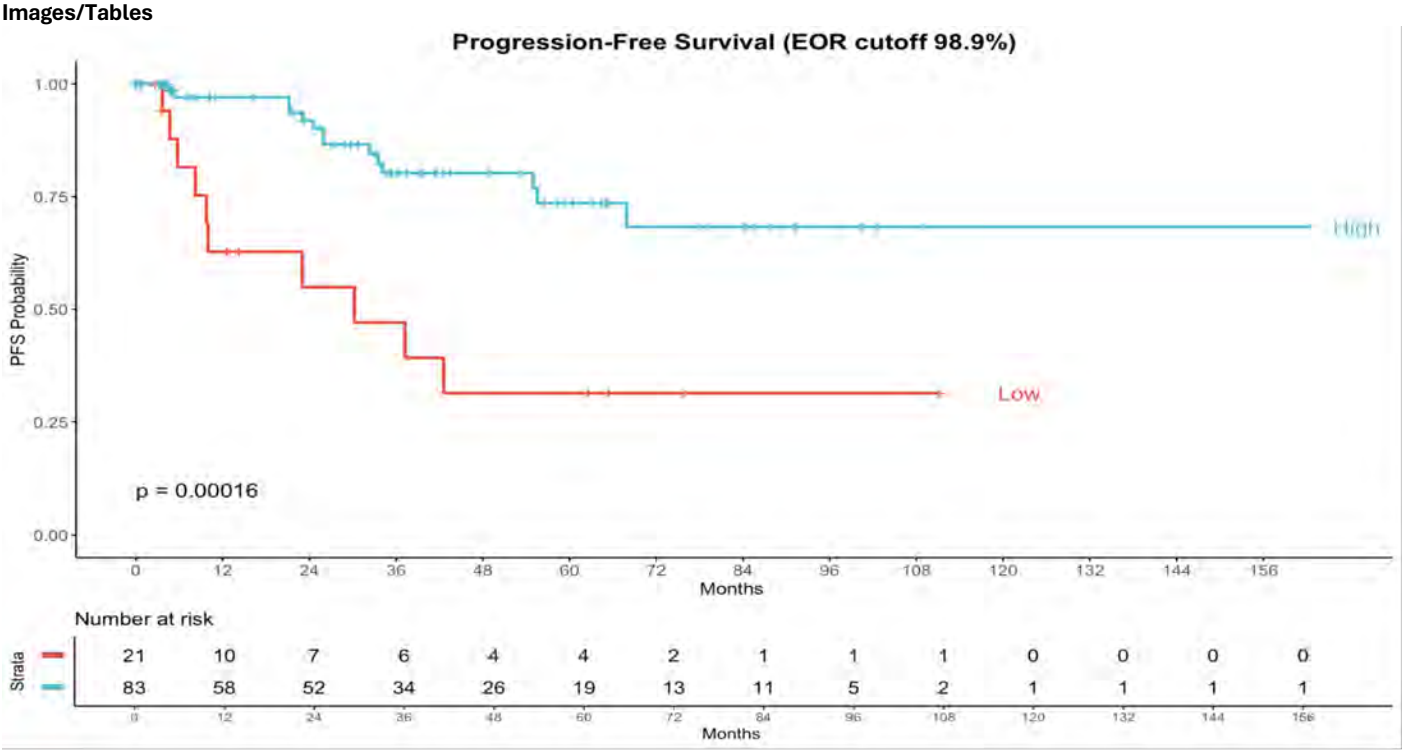

Figure B. The Kaplan-Meier curve demonstrating differences in progression-free survival (PFS) between the low-EOR and high-EOR groups. EOR = Extent of resection

---

457 Explainable Deep Learning Framework for CNS Lymphoma vs Non-Lymphoma Classification on MRI

Utkarsh Sharma MBBS, MD, Jayadevan ER MBBS, MD, DM, Abhishek Nayak MBBS, DNB, Bejoy Thomas MBBS, MD, Kesavadas C MBBS, MD

Sree Chitra Tirunal Institute for Medical Sciences & Technology, Trivandrum, Kerela, India

Purpose

Accurate differentiation between primary central nervous system lymphoma (PCNSL) and non-lymphomatous brain tumors such as gliomas or metastases usually poses diagnostic challenges on MRI due to overlapping imaging features. Conventional imaging features may not always provide sufficient discriminatory evidence, often requiring invasive biopsy for confirmation.

Recent advances in deep learning, particularly convolutional neural networks (CNNs), have demonstrated high potential for automated lesion classification from brain MRI. However, the “black-box” nature of these models limits clinical adoption, as radiologists require transparency and interpretability to validate algorithmic predictions.

This study aimed to develop a CNN-based model for classifying CNS lymphoma versus non-lymphoma using post-contrast T1WI and to systematically evaluate multiple explainability methods through neuroradiologist assessment, providing a human-centered interpretability benchmark.

Materials & Methods

MRI data from patients with histopathological confirmed diagnoses were collected, including 80 lymphoma and 111 non-lymphoma cases. All images underwent preprocessing to remove skull and soft tissues using a segmentation model, for focusing the model solely on intracranial structures.

A ResNet-18 CNN architecture was used to train the images. Data divided into training, validation, and test sets. The model’s performance was evaluated using accuracy, precision, recall, F1-score, and area under the receiver operating characteristic curve (ROC-AUC) (Fig 1).

Explainability (XAI) assessment employed eight widely used XAI methods: Grad-CAM, Grad-CAM++, Score-CAM, Ablation-CAM, Saliency Map, SHAP, LIME, and Integrated Gradients.

To quantify interpretability, an explainability evaluation scoring system was devised. Two senior neuroradiologists evaluated the generated heatmaps for localization accuracy, visual clarity, clinical interpretability and consistency across cases—using a 1–5 Likert scale. The final interpretability score for each XAI method represented the mean of the raters' assessments.

Results

The ResNet-18 CNN achieved high classification performance (Fig 2):

- Validation: Accuracy: 0.9407, Precision: 0.9357, Recall: 0.9299, F1: 0.9328, ROC-AUC: 0.9864
- Testing: Accuracy: 0.9372, Precision: 0.9342, Recall: 0.9252, F1-Score: 0.9297, ROC-AUC: 0.9851

With external validation data, the model accurately distinguished lymphoma from non-lymphoma lesions, achieving an accuracy of 86.6 across 92 test cases (including 33 lymphoma and 59 non-lymphoma).

Explainability evaluation revealed distinct differences among XAI techniques. Integrated Gradients and Saliency Maps achieved the highest interpretability scores, being rated as the most clinically and visually meaningful by the neuroradiologists. All the CAM based methods demonstrated good lesion localization but showed higher visual noise and partial lesion coverage. The SHAP and LIME were less consistent across cases (Fig 3).

Conclusion

The developed CNN model demonstrated good performance in differentiating lymphoma from non-lymphoma brain tumors using post-contrast T1WI. Beyond high classification accuracy, explainability assessment by experienced neuroradiologists provided a clinically grounded evaluation of multiple XAI techniques.

The findings highlight that Integrated Gradients and Saliency Maps yield the most clinically interpretable visual explanations, aligning closely with expected tumor anatomy, while CAM-based methods offer reasonable localization but reduced clarity.

This study underscores the feasibility of combining AI performance with human-validated interpretability, advancing the integration of explainable deep learning in neuro-oncologic imaging and promoting greater clinical trust in AI-assisted diagnostics.

References

1. C Petersen GI, Shatalov J, Verma T et al: A Systematic Review, Reporting Quality & Risk of Bias Assessment. AJNR Am J Neuroradiol. 2022 Apr;43(4):526-533. doi: 10.3174/ajnr.A7473.
2. Naser PV, Maurer MC, Fischer M et al: Deep learning aided preoperative diagnosis of primary central nervous system lymphoma. iScience. 2024 Jan 24;27(2):109023. doi: 10.1016/j.isci.2024.109023.

Images/Tables

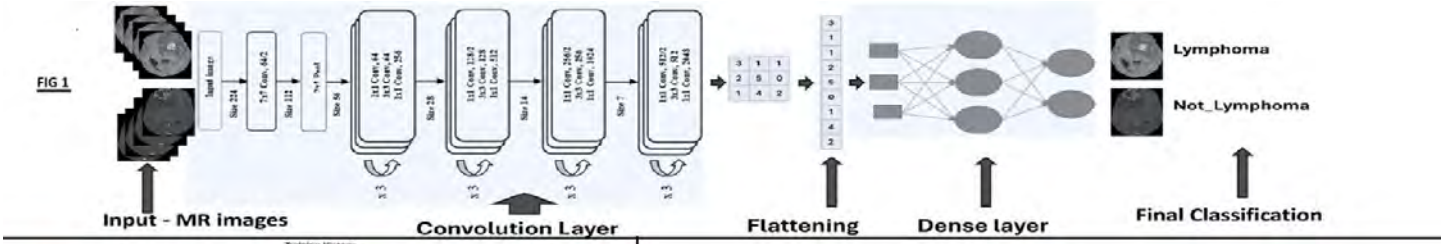

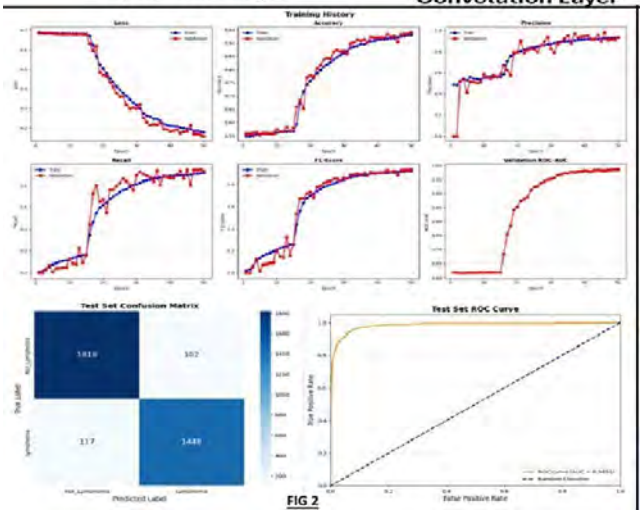

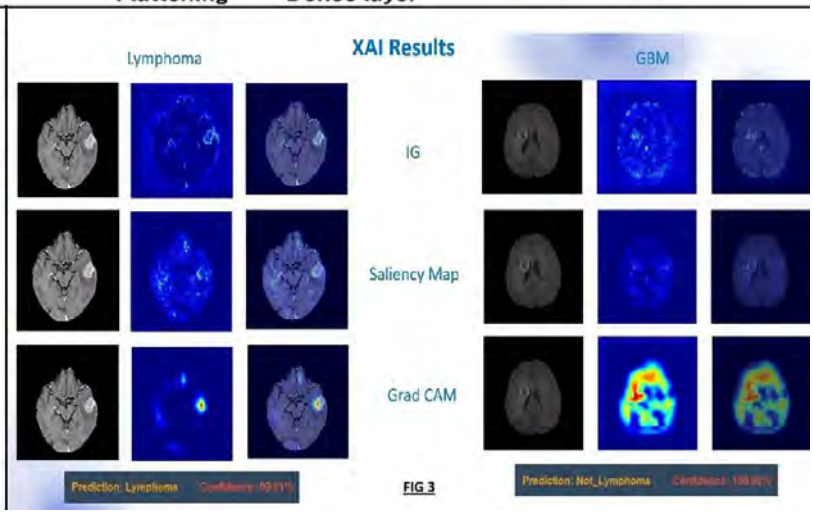

522 Differential White Matter Integrity Along the Corpus Callosum in 16p11.2 Deletion and Duplication Carriers

Yash A. Thacker BS[1], Lanya T. Cai PhD[2], Pratik Mukherjee MD, PhD[2], Shinjini Kundu MD, PhD[1]

[1]Washington University in St. Louis, St. Louis, Missouri, USA. [2]University of California San Francisco, San Francisco, California, USA

Purpose

Copy number variation (CNV) at the 16p11.2 locus is a well-established genetic risk factor for autism, with both deletions and duplications associated with distinct neurodevelopmental and behavioral phenotypes. Recent studies have reported altered white matter organization in individuals with 16p11.2 CNVs, particularly in the corpus callosum (CC), where deletions are linked to greater structural alterations in posterior regions and duplications with more anterior changes[1,2,3]. However, most studies have not examined diffusion metrics across distinct CC subregions or used anatomically informed methods for extracting localized white matter differences. Building on these results, the current study investigates spatial gradients of white matter microstructure along the corpus callosum in individuals with 16p11.2 deletions and duplications. We hypothesize that deletion and duplication carriers will have distinct patterns of callosal microarchitecture along the anteroposterior axis.

Materials & Methods

We analyzed diffusion imaging data from 78 individuals (*N* = 40 deletion carriers; *N* = 38 duplication carriers) from the Simons Variation in Individuals Project (Simons VIP). We adapted MaPPeRTrac, a high-throughput diffusion MRI processing pipeline, to generate high-resolution, anatomically informed structural connectomes[4] for each subject. Preprocessing was followed by probabilistic tractography to estimate fiber orientations and connection probabilities, retaining only bidirectionally validated connections between brain regions to increase anatomical specificity and interpretability. We employed a customized Tract-Based Spatial Statistics (TBSS) pipeline to extract average fractional anisotropy (FA) and mean diffusivity (MD) values, using the JHU ICBM-DTI-81 atlas registered to each subject's native space. This approach allowed us to quantify mean FA values in 48 white matter regions, with a specific focus on corpus callosum subregions: Genu (GCC), Body (BCC), and Splenium (SCC). Unlike prior studies that report only global or anterior CC differences, we examined spatial gradients along the anterior-posterior axis to detect region-specific alterations in microstructural integrity.

Results

Our results revealed significant differences in mean FA values between deletion and duplication carriers in both the GCC and BCC. After correcting for multiple comparisons using the Benjamini-Hochberg False Discovery Rate (BH-FDR), FA differences remained highly significant for GCC (p = 7.5e-06) and BCC (p = 2.6e-4). Across both regions, individuals with duplications consistently exhibited lower mean FA compared to deletion carriers, suggesting reduced axon diameter and myelination[5]. The average FA values, computed across the full extent of each region, further support this pattern of anterior-dominant disruption in deletion and duplication carriers. We additionally trained a random forest classifier to separate deletion and duplication carriers based on FA of all white matter regions, achieving 88% accuracy on testing data set; ranking GCC as the most relevant feature in distinguishing 16p11.2 CNV.

Conclusion

We demonstrate a novel application of atlas-based TBSS combined with tractography to evaluate spatially specific white matter alterations in 16p11.2 CNV carriers. To our knowledge, no prior studies have systematically extracted regional FA values from CC subregions using this approach. Our findings underscore the importance of corpus callosum white matter gradient in genetically-mediated autism. In the future, the corpus callosum may be a valuable marker for precision medicine in autism.

References

1. Kundu S, Sair H, Sherr EH, Mukherjee P, Rohde GK. Discovering the gene-brain-behavior link in autism via generative machine learning. *Sci Adv*. 2024;10(24):eadl5307. doi:10.1126/sciadv.adl5307

2. Owen JP, Chang YS, Pojman NJ, et al. Aberrant White Matter Microstructure in Children with 16p11.2 Deletions. *J Neurosci*. 2014;34(18):6214-6223. doi:10.1523/JNEUROSCI.4495-13.2014

3. Qureshi AY, Mueller S, Snyder AZ, et al. Opposing Brain Differences in 16p11.2 Deletion and Duplication Carriers. *J Neurosci*. 2014;34(34):11199-11211. doi:10.1523/JNEUROSCI.1366-14.2014

4. Cai LT, Moon J, Camacho PB, et al. MaPPeRTrac: A Massively Parallel, Portable, and Reproducible Tractography Pipeline. *Neuroinformatics*. 2024;22(2):177-191. doi:10.1007/s12021-024-09650-0

5. Bertero A, Liska A, Pagani M, et al. Autism-associated 16p11.2 microdeletion impairs prefrontal functional connectivity in mouse and human. *Brain*. 2018;141(7):2055-2065. doi:10.1093/brain/awy111

Images/Tables

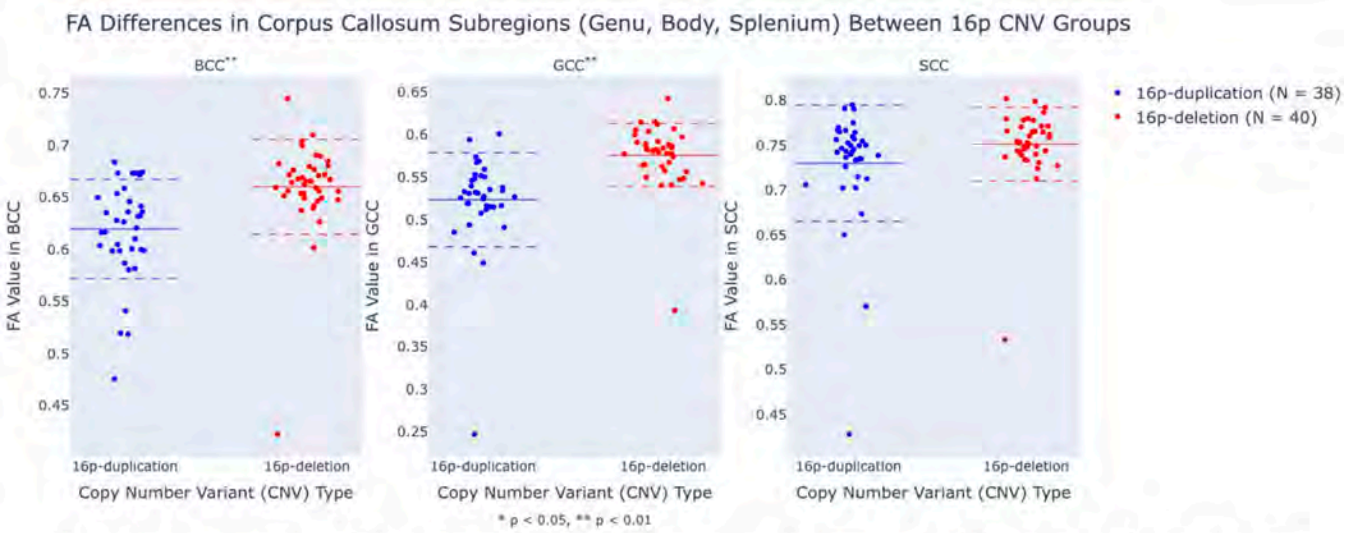

(a) Fractional Anisotropy (FA) values across three regions of the corpus callosum: body (BCC), genu (GCC), and splenium (SCC) in 16p11.2 deletion and duplication carriers. Significant group differences were observed in the BCC ($p = 3.9 \times 10^{-4}$) and GCC ($p = 2.3 \times 10^{-5}$), while the SCC did not show a statistically significant difference ($p = 9.03 \times 10^{-2}$) post BH–FDR correction.

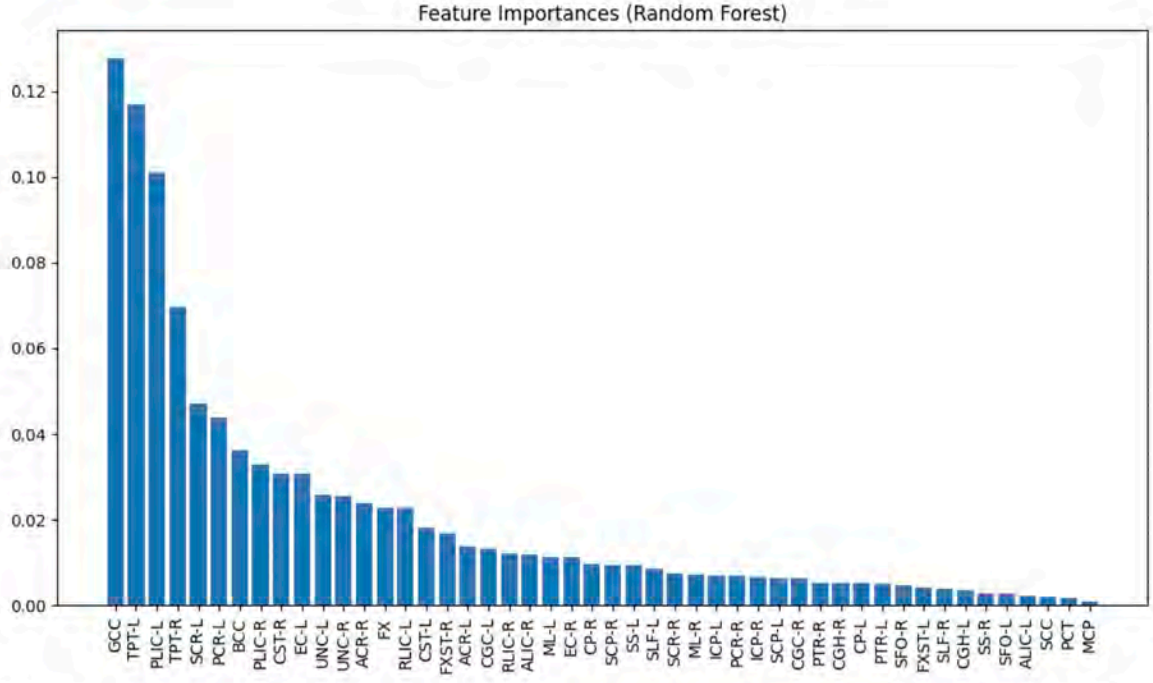

(b) Feature importance plot from a random forest classifier demonstrating the relative contribution of individual white matter regions to distinguishing 16p11.2 deletion and duplication carriers. The genu of the corpus callosum (GCC) emerged as the most important feature, contributing the highest weight to the model's decision-making process. The body of the corpus callosum (BCC) also ranked highly, underscoring the relevance of specific subregions of the corpus callosum in distinguishing between carrier groups.

Cerebrovascular Imaging in Dementia

11:00am - 12:00pm Monday, 18th May, 2026

645 Cerebral Oxygen Extraction Fraction in Vascular Cognitive Impairment: Associations with Cognition, Vascular Risk, and Tau Pathology

Jie Song MS[1], Wen Shi BS[1], Kaisha Hazel MS[2], George Pottanat MS[2], Ebony Jones MPH[2], Tyler Deane BS[2], Cuimei Xu MS[2], Kumiko Oishi PhD[2], Yifan Gou MS[1], Doris Lin MD, PhD[2], Hanzhang Lu PhD[2], Dengrong Jiang PhD[2]

[1]Department of Biomedical Engineering, Johns Hopkins University School of Medicine, Baltimore, MD, USA. [2]Department of Radiology, Johns Hopkins University School of Medicine, Baltimore, MD, USA

Purpose

Vascular cognitive impairment and dementia (VCID) is the second most common cause of dementia in older adults, yet reliable biomarkers remain limited. Cerebral oxygen-extraction-fraction (OEF) is a key hemodynamic parameter of brain function. Elevated OEF has been observed in cerebrovascular disorders such as carotid steno-occlusive disease and ischemic stroke[1]. In this study, we employed a novel non-invasive, non-contrast MRI technique, accelerated-T2-relaxation-under-phase-contrast (aTRUPC)[2], to measure regional OEF in a VCID-enriched cohort. We hypothesized that elevated OEF would be associated with worse cognition and explored its relationships with vascular-risk-score (VRS) and tau pathology.

Materials & Methods

Experimental procedure: Eighty-one older adults (mean age=71.2±6.2years; 63% female) were enrolled from the MarkVCID cohort, enriched for individuals with vascular risk factors and neuroimaging evidence of cerebral-small-vessel-disease (e.g., white matter lesions and cerebral microbleeds)[3]. Table 1 summarizes the demographic information. Cortical and subcortical OEF values were measured using aTRUPC MRI[2]. All participants underwent neuropsychological tests covering five cognitive domains : episodic memory, executive function, processing speed, attention, and language. A composite cognitive score was computed by averaging the Z-scores of each domain. VRS was calculated as the number of vascular risk factors (hypertension, hypercholesterolemia, diabetes, smoking or obesity) present in each patient. Phosphorylated-tau217 (p-tau217) levels were measured from plasma samples.

Statistical Analysis: Linear regression models with Bonferroni multiple comparison correction were used to analyze the associations between regional OEF, cognitive scores, VRS, and p-tau217.

Results

Figure 1 displays representative aTRUPC MRI data. As illustrated in Figure 2, OEF was negatively associated with the composite cognitive score (cortical OEF: β=-0.034±0.011, p=0.0034; subcortical OEF: β=-0.030±0.011, p =0.015). Further analyses of domain-specific Z-scores revealed significant negative associations between executive function and regional OEF(cortical OEF: β=–0.043±0.012, p=0.0084; subcortical OEF: β=–0.039±0.013, p=0.033), as summarized in Table 2. Notably, elevated OEF correlated with declines in executive function (characteristic of VCID) but not with declines in episodic memory (characteristic of AD)[4]. These findings suggest that elevated OEF is related to VCID rather than AD in this cohort. This notion was further supported by a significant positive association between VRS and cortical OEF (β=1.47±0.63, p=0.045, Figure 3). A possible underlying mechanism is that small vessel disease may cause microinfarcts, vessel stiffening, microhemorrhages, and vascular tortuosity, reducing cerebral blood flow and oxygen delivery, thereby elevating OEF.

Furthermore, we observed a significant negative association between p-tau217 and OEF (subcortical OEF: β=–5.62±2.3, p=0.034, Model 1 in Table 3). This association remained significant after adjusting for VRS (Model 2 in Table 3). These findings suggest that AD pathology leads to reduced OEF, possibly due to diminished glucose and oxygen metabolism resulting from neurodegeneration. These opposing effects of vascular pathology (elevate OEF) and AD pathology (reduce OEF) align with prior evidence[5], and underscore the complex interplay of mixed pathologies in VCID.

Conclusion

We demonstrated that elevated cortical and subcortical OEF were associated with poorer cognition (particularly executive function) in older adults with vascular risks, suggesting that OEF may serve as a useful biomarker for VCID.

References

1. Fan AP, Khalil AA, Fiebach JB, et al. Elevated brain oxygen extraction fraction measured by MRI susceptibility relates to perfusion status in acute ischemic stroke. *J Cereb Blood Flow Metab* 2020;40:539-551

2. Jiang D, Lu H, Parkinson C, et al. Vessel-specific quantification of neonatal cerebral venous oxygenation. *Magn Reson Med* 2019;82:1129-1139

3. Wilcock D, Jicha G, Blacker D, et al. MarkVCID cerebral small vessel consortium: I. Enrollment, clinical, fluid protocols. *Alzheimers Dement* 2021;17:704-715

4. Tierney MC, Black SE, Szalai JP, et al. Recognition memory and verbal fluency differentiate probable Alzheimer disease from subcortical ischemic vascular dementia. *Arch Neurol* 2001;58:1654-1659

5. Jiang D, Lin Z, Liu P, et al. Brain Oxygen Extraction Is Differentially Altered by Alzheimer's and Vascular Diseases. *J Magn Reson Imaging* 2020;52:1829-1837

Images/Tables

Table 1. Characteristics of the participants.

	Normal	SCD	MCI	Dementia	Total
N	11	20	46	4	81
Age (years)*	71.1 ± 4.8	70.5 ± 7.0	71.1 ± 6.2	75.4 ± 4.8	71.16 ± 6.19
Females (percentage)†	6 (54.5%)	17 (85.0%)	26 (56.5%)	2 (50.0%)	51 (63.0%)
Education (years)*	17.4 ± 1.8	15.6 ± 2.7	16.2 ± 2.4	16.0 ± 2.8	16.17 ± 2.41
Episodic memory Z-Score*	0.61 ± 0.57	0.32 ± 0.58	-0.15 ± 0.69	-1.54 ± 1.51	-0.00 ± 0.82
Executive Function Z-Score*	0.41 ± 0.51	0.33 ± 0.51	-0.14 ± 0.62	-1.34 ± 0.86	-0.01 ± 0.70
Processing Speed Z-Score*	0.19 ± 0.40	0.30 ± 0.58	-0.08 ± 0.75	-1.35 ± 0.84	-0.01 ± 0.75
Attention Z-Score*	0.17 ± 0.45	0.22 ± 0.50	-0.01 ± 0.83	-1.40 ± 1.34	0.00 ± 0.81
Language Z-Score*	0.64 ± 0.56	0.24 ± 0.58	-0.18 ± 0.64	-0.92 ± 0.97	0.00 ± 0.71
Composite cognitive Score*	0.40 ± 0.34	0.28 ± 0.34	-0.11 ± 0.50	-1.31 ± 0.92	-0.00 ± 0.59
Vascular risk score‡	2 (1-4)	2 (1-5)	2 (1-4)	3.5 (2-4)	2 (1-5)
Cortical OEF (%)*	37.0 ± 4.0	38.0 ± 7.1	37.2 ± 5.6	44.5 ± 6.2	37.70 ± 5.94
Subcortical OEF (%)*	30.3 ± 4.8	30.5 ± 7.8	29.9 ± 5.2	34.9 ± 6.4	30.33 ± 5.93
P-tau217#	-0.25 ± 0.25	-0.43 ± 0.24	-0.36 ± 0.29	-0.23 ± 0.39	-0.35 ± 0.26

SCD: subjective cognitive decline; MCI: mild cognitive impairment; OEF: oxygen extraction fraction; P-tau217: phosphorylated at threonine 217;.
*Data are means ± standard deviations.
†Data are numbers of participants, followed by percentages in parentheses.
‡Data are medians, with ranges in parentheses.
#Data are unitless, concentration is log-transformed.

Figure 1. Representative aTRUPC data of one participant

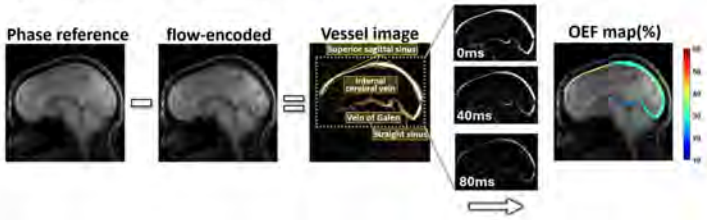

Table 2. Associations of cortical and subcortical OEF with cognitive domains

	Cortical OEF		Subcortical OEF	
Cognitive domain	β±SE for OEF	p value†	β±SE for OEF	p value†
Episodic memory Z-score	-0.011 ± 0.015	1.00	-0.017 ± 0.014	1.00
Executive function Z-score	-0.043 ± 0.012	0.0084	-0.039 ± 0.013	0.033
Processing speed Z-score	-0.026 ± 0.014	0.67	-0.029 ± 0.014	0.46
Attention Z-score	-0.018 ± 0.013	1.00	-0.014 ± 0.013	1.00
Language Z-score	-0.037 ± 0.013	0.49	-0.028 ± 0.013	0.35

OEF: oxygen extraction fraction
β±SE: standardized beta coefficient ± standardized error
All models included age, sex, and education as covariates.
†Bonferroni correction was applied to account for multiple comparisons across cognitive domains and OEF regions

Figure 2. Relationship of regional OEF with cognition

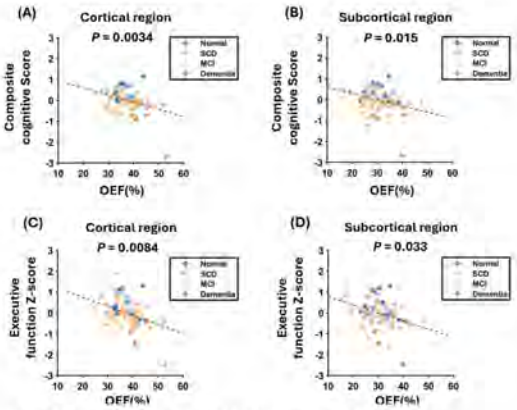

Figure 3. Associations of regional OEF with vascular risk factors

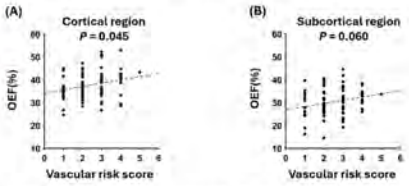

Table 3. Associations of regional OEF with plasma p-tau217 and VRS

	Independent variables	Cortical OEF		Subcortical OEF	
		β±SE	p value†	β±SE	p value†
Model 1	log10(ptau217)	-5.20 +- 2.34	0.060	-5.62 +- 2.31	0.034
	Age	0.19 +- 0.11	0.16	0.24 +- 0.10	0.05
	Sex	0.95 +- 1.33	0.96	0.42 +- 1.31	1.00
Model 2	log10(ptau217)	-4.87 +- 2.29	0.074	-5.32 +- 2.26	0.042
	VRS	1.38 +- 0.62	0.056	1.29 +- 0.61	0.074
	Age	0.17 +- 0.10	0.22	0.22 +- 0.10	0.074
	Sex	1.33 +- 1.31	0.62	0.78 +- 1.29	1.00

OEF: oxygen extraction fraction; p-tau217; phosphorylated at threonine 217; VRS: Vascular risk score
†Bonferroni correction was applied to account for multiple comparisons across OEF regions

Scientific Abstract Power Pitches & Luminary Speaker: Advanced Neurovascular Imaging and Stroke Outcomes

11:00am - 12:00pm Monday, 18th May, 2026

425 Quantitative Intracranial Vessel Wall Imaging Features Differentiate Atherosclerosis, Vasculitis, and RCVS

Dan Cheng MD[1], Yin Guo PhD[2], Mona Kharaji MD[2], Beibei Sun MD[2], Hisham Alfarra MD[1], Mohamad H Mosi MD[2], Zhiwei Tan PhD[2], Xin Wang PhD[2], SeyyedKazem HashemizadehKolowri MD[3], Chun Yuan PhD[2], Niranjan Balu PhD[2], Mahmud Mossa-Basha MD[1]

[1]University of Alabama at Birmingham, Birmingham, Alabama, USA. [2]Univeristy of Wahington, Seattle, Washington, USA. [3]Univerisity of Utah, Salt Lake, Utah, USA

Purpose

Intracranial vasculopathy differentiation is one of the most frequent clinical indications for intracranial vessel wall MR (IVW)[1]. Qualitative criteria using multi-contrast IVW have been established to aid in diagnosing conditions such as atherosclerosis, vasculitis, and Reversible Cerebral Vasoconstriction Syndrome (RCVS)[2]. However, qualitative features have varying definitions in the literature and limited reproducibility. This study evaluates the capability of IVW features to distinguish between atherosclerosis, vasculitis, and RCVS using a semi-automated quantitative IVW tool.

Materials & Methods

Patients with established intracranial vasculopathies (atherosclerosis, vasculitis, and RCVS) based on clinical criteria underwent IVW with and without gadolinium contrast administration. First, the arterial segments were independently traced on TOF-MRA by VesselVoyager[3]. Next, the cases were divided among three radiologists, who manually segmented the vessel lumen and outer wall boundary where lesions were present using a multi-contrast, multi-planar framework (MOCHA) software[4]. The detailed image processing pipeline has been described previsously[4]. Finally, a contrast enhancement color map was created by normalizing the vessel wall signal intensity on post-contrast IVW relative to the signal intensity measured in the genu of the corpus callosum[5].

For each lesion, the following quantitative features were calculated: lesion length, maximum wall thickness[6], percent wall volume (wall volume / total vessel volume × 100%), eccentricity index ([maximum wall thickness–minimum wall thickness]/maximum wall thickness), mean enhancement ratio (mean signal intensity on normalized post-contrast IVW), and percent enhancing volume. Enhancing regions were defined as voxels where the difference between post-contrast and median pre-contrast T1-weighted signal intensity exceeded 0.4 , and percent enhancing volume was calculated as the total enhancing volume divided by wall volume×100%.

Quantitative IVW features were compared across the three vasculopathy types using generalized estimating equation-based univariate regression to account for multiple lesions identified within the same patient. Statistical significance was defined as $p<0.017$ (Bonferroni correction for three pairwise comparisons: 0.05/3).

A multinomial logistic regression model was developed to classify lesions into three diagnostic categories. Stratified 5-fold cross-validation was employed to ensure balanced representation of all diagnostic categories across training and test sets.

Results

Among 55 patients, 25 were clinically diagnosed with intracranial atherosclerosis, 22 with vasculitis, and 8 with RCVS. A total of 279 lesions were identified: 162 atherosclerotic plaques, 94 vasculitis lesions, and 23 RCVS lesions. Figure 1 illustrate examples of atherosclerotic, vasculitis, and RCVS lesions.

Maximum wall thickness differed significantly across all three pairwise comparisons: atherosclerosis had the greatest wall thickness (1.95±0.42 mm), followed by vasculitis (1.62±0.36 mm) and RCVS (1.03±0.23 mm) (all $p<0.001$). Eccentricity index also differed significantly across all groups, with atherosclerosis showing the highest eccentricity (0.64±0.08), followed by vasculitis (0.58±0.08) and RCVS (0.53±0.07) (all $p\leq0.015$). RCVS lesions demonstrated significantly lower percent wall volume.

The multinomial logistic regression model achieved an overall accuracy of 82.1%±2.3% in distinguishing between the three vasculopathies using stratified 5-fold cross-validation.

Conclusion

Quantitative IVW features revealed distinct imaging signatures for the three vasculopathies: RCVS demonstrated the thinnest walls, lowest eccentricity, and minimal enhancement. A multinomial logistic regression model achieved 82% accuracy in three-way classification.

References

1. Mossa-Basha M, Zhu C, Yuan C, et al. Survey of the American Society of Neuroradiology Membership on the Use and Value of Intracranial Vessel Wall MRI. *AJNR Am J Neuroradiol*. 2022;43(7):951-957. doi:10.3174/ajnr.A7541

2. Mossa-Basha M, Hwang WD, De Havenon A, et al. Multicontrast High-Resolution Vessel Wall Magnetic Resonance Imaging and Its Value in Differentiating Intracranial Vasculopathic Processes. *Stroke*. 2015;46(6):1567-1573. doi:10.1161/STROKEAHA.115.009037

3. (ISMRM 2024) VesselVoyager: An Interactive 3D Intracranial Vessel Tracing Software. https://archive.ismrm.org/2024/0235.html. Accessed May 30, 2025.

4. Guo Y, Canton G, Chen L, et al. Multi-Planar, Multi-Contrast and Multi-Time Point Analysis Tool (MOCHA) for Intracranial Vessel Wall Characterization. *Journal of Magnetic Resonance Imaging*. 2022;56(3):944-955. doi:10.1002/jmri.28087

5. Sanchez S, Raghuram A, Fakih R, et al. 3D Enhancement Color Maps in the Characterization of Intracranial Atherosclerotic Plaques. *American Journal of Neuroradiology*. August 2022. doi:10.3174/ajnr.A7605

6. HashemizadehKolowri S, Akcicek EY, Akcicek H, et al. Efficient and Accurate 3D Thickness Measurement in Vessel Wall Imaging: Overcoming Limitations of 2D Approaches Using the Laplacian Method. *JCDD*. 2024;11(8):249. doi:10.3390/jcdd11080249

Images/Tables

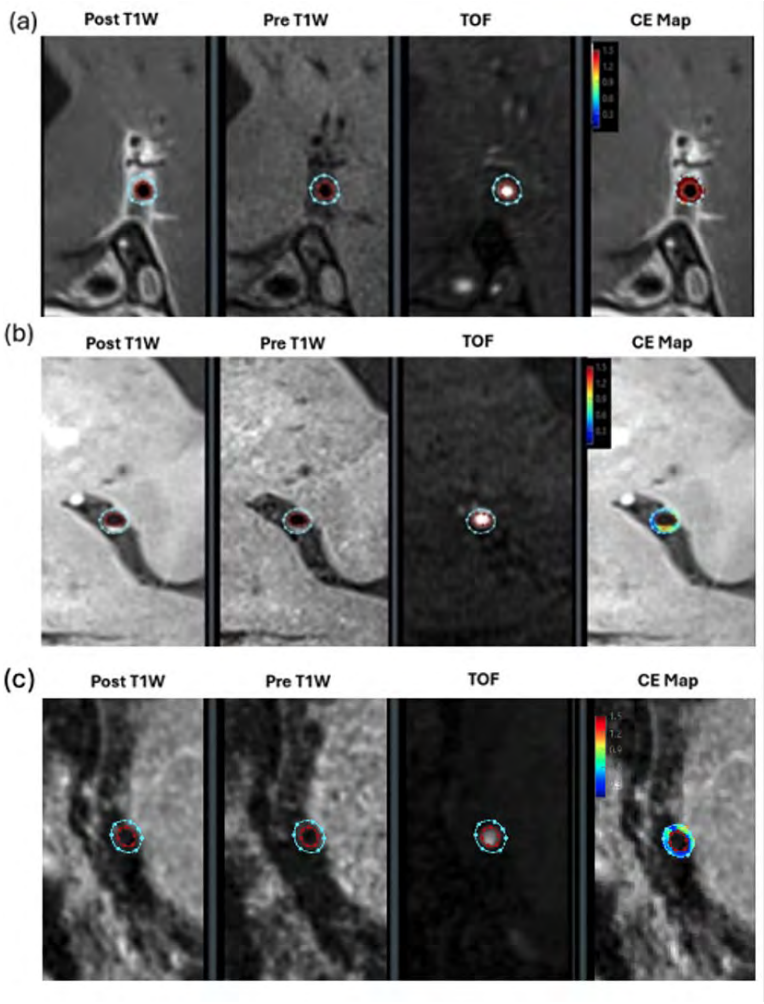

---

354 **Bayesian Derived Multiparametric MRI Model Predicts Development of Parenchymal Hematoma in Acute Stroke Following Reperfusion**

Mona Asghariahmadabad MD[1], Ameera Ismail MD[2], Mehmet Kurt PhD[3], Mersedeh Bahr-Hosseini MD[2], Viktor Szeder MD[2], Jeffrey Saver MD[2], Wade S Smith MD, PhD[1], Nerissa Ko MD[1], Kazim Narsinh MD[1], Luis E Savastano MD, PhD[1], Ethan Winkler MD, PhD[1], Daniel L Cooke MD[1], Steven W Hetts MD[1], Matthew R Amans MD[1], S. Andrew Josephson MD[1], Christopher P Hess MD, PhD[1], David S Liebeskind MD, MBA[2], Kambiz Nael MD[1]
[1]UCSF, San Francisco, CA, USA. [2]UCLA, Los Angeles, CA, USA. [3]UW, Seattle, WA, USA

Purpose

Parenchymal hemorrhage (PH) is a feared complication of reperfusion therapy in acute ischemic stroke (AIS), closely linked to neurological deterioration and poor functional outcomes[1,2]. We evaluated whether pretreatment MRI biomarkers derived from dynamic susceptibility contrast (DSC) perfusion, together with diffusion MRI, predict PH among AIS patients with anterior-circulation large-vessel occlusion undergoing endovascular therapy.

Materials & Methods

In this retrospective single-center cohort (2015–2020), patients were included if they underwent baseline diffusion-weighted imaging (DWI) and DSC MRI prior to reperfusion and had follow-up MRI within 48 hours to assess PH. Using a Bayesian vascular-modeling framework[3,4], we generated parametric maps of cerebral blood flow (CBF), cerebral blood volume (CBV), capillary transit-time heterogeneity (CTH), blood-brain barrier leakage, oxygen extraction fraction (OEF), and cerebral metabolic rate of oxygen ($CMRO_2$). Ischemic core masks were defined on apparent diffusion coefficient (ADC) maps using a threshold ≤ 620×10^{-6} mm^2/s, refined by a board-certified neuroradiologist, and rigidly coregistered to perfusion maps. Voxel values within the core were normalized to contralateral white matter to obtain relative metrics (rCBF, rCBV, rCTH, r-leakage, rOEF, $rCMRO_2$); ADC was analyzed as absolute values. For each variable, the median, 5th, and 95th percentiles were extracted. Univariate analysis identified candidates for multivariable logistic regression with backward AIC selection. A prediction model was then trained using a histogram-based gradient boosting classifier with 5-fold stratified cross-validation and interpreted with SHAP. External validation was performed in an independent cohort (n=20) meeting identical criterion.

Results

Of 166 screened patients,124 met inclusion criteria; 35 (28%) developed PH (PH1 n=13; PH2 n=22). Groups did not differ in age, sex, baseline NIHSS, last-known-well time, occlusion site, reperfusion grade, or core/penumbra volumes. Voxel-level analyses showed lower ADC, rCBF, rCBV, and $rCMRO_2$ and higher r-leakage, rCTH, and rOEF among PH patients (all P<0.001). Multivariable modeling identified three independent predictors: 95th-percentile r-leakage (odds ratio [OR] 1.31; 95% CI 1.10–1.63; P=0.006), 95th-percentile rCTH (OR 2.67; 95% CI 1.55–5.52; P=0.002), and 5th-percentile ADC (OR 0.97; 95% CI 0.96–0.99; P<0.001). The cross-validated three-variable model achieved mean AUC 0.84±0.05, sensitivity 0.91, specificity 0.78, and accuracy 84.5%. SHAP ranked 95th-percentile r-leakage as the dominant contributor, followed by 5th-percentile ADC and 95th-percentile rCTH. In external validation (n=20; PH 10/20), the model identified 80% of PH with 90% specificity and 85% accuracy.

Conclusion

Extreme distribution-tail abnormalities within the baseline ischemic core, markedly elevated leakage and capillary flow heterogeneity together with profoundly reduced diffusion were independently associated with PH after reperfusion. A concise multiparametric framework integrating 95th-percentile r-leakage, 95th-percentile rCTH, and 5th-percentile ADC demonstrated strong internal performance and preserved discrimination in an external cohort. Incorporating advanced DSC-derived microvascular metrics alongside diffusion into periprocedural workflows may enable more precise hemorrhage risk stratification and support individualized treatment decisions in AIS. Although rCBV and rCBF were lower in PH, they were not independent after adjustment, highlighting the added value of leakage, CTH, and ADC. Prospective multicenter work with standardized acquisition and harmonized postprocessing should validate these thresholds and assess real-time use in clinical decision-making.

References

1. Jovin TG, Nogueira RG, Lansberg MG, et al. Thrombectomy for anterior circulation stroke beyond 6 h from time last known well (AURORA): a systematic review and individual patient data meta-analysis. *Lancet*. Jan 15 2022;399(10321):249-258. doi:10.1016/s0140-6736(21)01341-6
2. Olivot J-M, Finitsis S, Lapergue B, et al. Parenchymal Hemorrhage Rate Is Associated with Time to Reperfusion and Outcome. *Annals of Neurology*. 2022;92(5):882-887. doi:https://doi.org/10.1002/ana.26478
3. Mouridsen K, Friston K, Hjort N, Gyldensted L, Østergaard L, Kiebel S. Bayesian estimation of cerebral perfusion using a physiological model of microvasculature. *Neuroimage*. Nov 1 2006;33(2):570-9. doi:10.1016/j.neuroimage.2006.06.015
4. Mouridsen K, Hansen MB, Østergaard L, Jespersen SN. Reliable estimation of capillary transit time distributions using DSC-MRI. *J Cereb Blood Flow Metab*. Sep 2014;34(9):1511-21. doi:10.1038/jcbfm.2014.111

Images/Tables

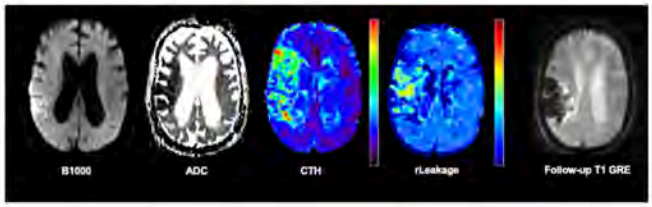

Figure. Example baseline imaging including ADC, CTH and leakage in a patient who developed PH.

Patients with right MCA ischemic stroke who underwent TICI2C reperfusion. B1000 and ADC from baseline diffusion-weighted imaging demonstrate reduced diffusion associated with ischemic core. note heterogenous increased in CTH and leakage values within the ischemic bed. Elevation of $95^{th\%}$-rCTH (5.5) indicative of microvascular dysfunction and elevation of $95^{th\%}$-rleakage (11.4) indicative of sever blood brain disruption in this patient who developed a parenchymal hematoma (PH).

---

368 Deterioration of microvascular hemodynamics following successful reperfusion in acute ischemic stroke predicts infarct growth

YANNAN YU MD[1], Mona Asghariahmadabad MD[1], Keon Mahmoudi MD[2], Michael Thomas MD[1], Ammera Ismail MD[2], Mersedeh Bahr-Hosseini MD[2], Jeffrey L Saver MD[2], David Liebeskind MD, MBA[2], S. Andrew Josephson MD[1], Christopher P Hess MD, PhD[1], Kambiz Nael MD[1]

[1]University of California, San Francisco, San Francisco, CA, USA. [2]University of California, Los Angeles, Los Angeles, CA, USA

Purpose

The no-reflow phenomenon after successful thrombectomy in acute ischemic stroke (AIS) is associated with worse functional outcome. Microvascular hemodynamic deterioration is a promising theory of the no-reflow phenomenon and is a potential target for new treatment development (1). Previous studies have shown that relative heterogeneity of transit time (RTH) is a promising biomarker of microvascular hemodynamics (2). We aim to investigate whether RTH is a predictor of infarct progression after successful thrombectomy.

Materials & Methods

In this retrospective single institutional study, AIS patients were included if they had successful thrombectomy (defined as TICI 2C or 3), and MRI including diffusion weighted imaging (DWI) and perfusion-weighted imaging at baseline (pretreatment), immediate post-thrombectomy, and another follow up with 24-48h hours from the thrombectomy time. All MR images were registered and normalized to MNI space. Penumbra was defined on baseline MRI using volume of Interest (VOI) encompassing brain tissue with Tmax≥6s (Figure). From immediate post-thrombectomy MRIs (PT-MRI), perfusion parameters including Tmax, mean transit time (MTT) and capillary transit heterogeneity (CTH) were obtained and voxel-based values from penumbral mask were extracted. In addition, penumbral RTH defined as CTH/MTT were calculated for each patient. The volume of infarct growth was calculated by subtracting the volume of infraction on final MRI from volume of infarct on PT-MRI (Figure). Infraction growth of ≥ 10 ml was defined as substantial infarct progression. T-test and logistic regression analysis were performed.

Results

Fourty-five patients were included in the analysis (28 Females, age 72±13). 19 (42%) patients demonstrated significant infarct growth. Penumbral-RTH (mean ± SD) was significantly (P=0.005) higher in patients with substantial infarct growth (0.90±0.07) vs. those without infarct growth (0.66±0.05). After adjusting for age, the RTH is an independent predictor of significant infarct progression (OR 61, 95%CI 3.2-1180.4, p=0.006) with a ROC-AUC of 0.84 (95%CI 0.73-0.96).

Conclusion

Increased RTH on immediate post-thrombectomy MR predicts substantial infarct growth in AIS patients despite achieving excellent reperfusion. In theory, RTH is associated with capillary constriction (2), a critical phase before capillary occlusion. This study provides insight on how quantitative assessment of microvascular hemodynamics immediate post-thrombectomy may play an important role in infarct progression despite successful reperfusion.

References

1. Zhang Y, Jiang M, Gao Y, Zhao W, Wu C, Li C, et al. "No-reflow" phenomenon in acute ischemic stroke. J Cereb Blood Flow Metab. 2024;44(1):19-37.
2. Engedal TS, Hjort N, Hougaard KD, Simonsen CZ, Andersen G, Mikkelsen IK, et al. Transit time homogenization in ischemic stroke - A novel biomarker of penumbral microvascular failure? J Cereb Blood Flow Metab. 2018;38(11):2006-20.

Images/Tables

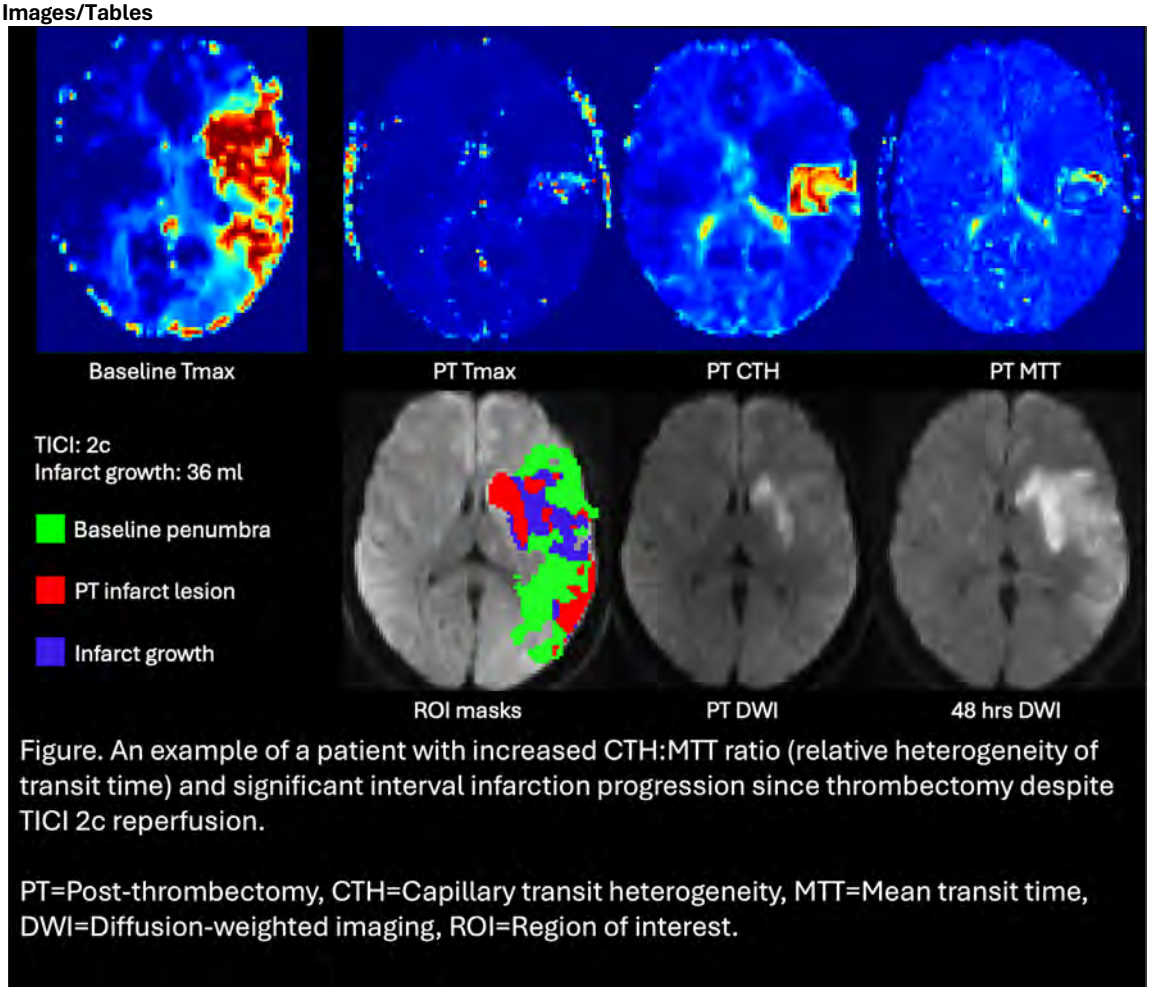

Figure. An example of a patient with increased CTH:MTT ratio (relative heterogeneity of transit time) and significant interval infarction progression since thrombectomy despite TICI 2c reperfusion.

PT=Post-thrombectomy, CTH=Capillary transit heterogeneity, MTT=Mean transit time, DWI=Diffusion-weighted imaging, ROI=Region of interest.

---

390 **Mean Transit Time (MTT)-Derived Venous Transit Delay is Associated with Poor Outcomes in Successfully Reperfused Stroke Patients with Large Vessel Occlusion: A Bayesian-Based Approach**

Matthew Halber BS[1], Mona Asghariahmadabad MD[1], Charlie Wang MD[1], Michael Thomas MD[1], Ameera Ismail MD[2], Mersedeh Bahr-Hosseini MD[2], David S Liebeskind MD, MBA[2], Anthony Kim MD[1], Nerissa Ko MD[1], Kazim Narsinh MD[1], Luis E Savastano MD, PhD[1], Daniel L Cooke MD[1], Steven W Hetts MD[1], Matthew R Amans MD[1], S. Andrew Josephson MD[1], Christopher P Hess MD, PhD[1], Kambiz Nael MD[1]
[1]University of California, San Francisco, San Francisco, California, USA. [2]David Geffen School of Medicine, Los Angeles, California, USA

Purpose

Venous transit delay (VTD) as a marker of poor venous outflow has been successfully measured on CTP using time-to-maximum (Tmax) maps and is associated with unfavorable outcomes in patients with acute ischemic stroke (AIS) caused by large vessel occlusion (LVO)[1,2]. Mean transit time (MTT) is a perfusion parameter that encompasses both arterial input and venous outflow with potential for a more robust representation of cerebral arteriovenous transit time in comparison to Tmax which is heavily arterially weighted. In this study, using a Bayesian framework, we aimed to compare the association of VTD calculated from MTT and arterial delay (Tmax equivalent in Bayesian) with poor clinical outcomes after reperfusion in AIS-LVO patients.

Materials & Methods

This retrospective study included AIS patients with large vessel occlusion stroke who had baseline CTP and follow-up MRI from two comprehensive stroke centers. CTPs were processed with the Bayesian method[3] using an FDA approved software (Olea Medical) to generate MTT and arterial delay maps (Tmax equivalent in Bayesian). VTD was measured in the transverse sinuses on both the ischemic and normal (contralateral) side and the posterior aspect of the superior sagittal sinus (SSS) in each patient using both MTT and AD maps. Two outcome measures were included: Infarct growth (poor: ≥ 10 mL) and functional outcome defined by 90-day modified Rankin Scale score (mRS) (poor: ≥3).

Results

A total of 80 patients were included, of which 51% had infarct growth ≥ 10 mL and 34% had poor functional outcome (90d-mRS ≥ 3). MTT-derived VTD from the transvers sinus ipsilateral to the ischemic hemisphere was significantly longer in patients with substantial infarct growth (p=0.0007) and poor functional outcome (p=0.001). Similarly, MTT-derived VTD from the SSS was significantly longer in patients with substantial infarct growth (p=0.003) and poor functional outcome (p=0.012). However, AD-derived VTDs from the transverse sinus and SSS were not significantly different (p>0.05) for either outcome measures (infarct growth and 90-day mRS). The difference between VTDs measured on MTT and AD (ΔVTD_{MTT}- ΔVTD_{AD})

was significantly higher in patients with substantial infarct growth (p<0.0001 for transverse sinus and p=0.0002 for SSS) and in those with poor functional outcomes (p=0.0002 for transverse sinus and p=0.0307 for SSS).

Conclusion

Results showed that MTT-derived VTD measured in the transverse sinus and SSS was significantly different between patients with poor and favorable outcomes. This association was not reflected in VTDs measured on arterially weighted AD maps. This signifies the potential for MTT to be a superior parameter for VTD measurements and predictor of outcomes in AIS patients.

References

1. Yedavalli, V. S., Koneru, M., Hoseinyazdi, M., et al. Prolonged venous transit on perfusion imaging is associated with higher odds of mortality in successfully reperfused patients with large vessel occlusion stroke. *J NeuroIntervent Surg. 2024*; *17*(3): 321–326. https://doi.org/10.1136/jnis-2024-021488

2. Mei, J., Salim, H. A., Lakhani, D. A., et al. Prolonged venous transit is associated with worse neurological recovery in successfully reperfused large vessel strokes. *Ann Clin Transl Neurol. 2024*; *12*(1): 26–33. https://doi.org/10.1002/acn3.52243

3. Boutelier, T., Kudo, K., Pautot, F., & Sasaki, M. Bayesian hemodynamic parameter estimation by bolus tracking perfusion weighted imaging. *IEEE Trans Med Imaging*. 2012; *31*(7): 1381–1395. https://doi.org/10.1109/tmi.2012.2189890

Images/Tables

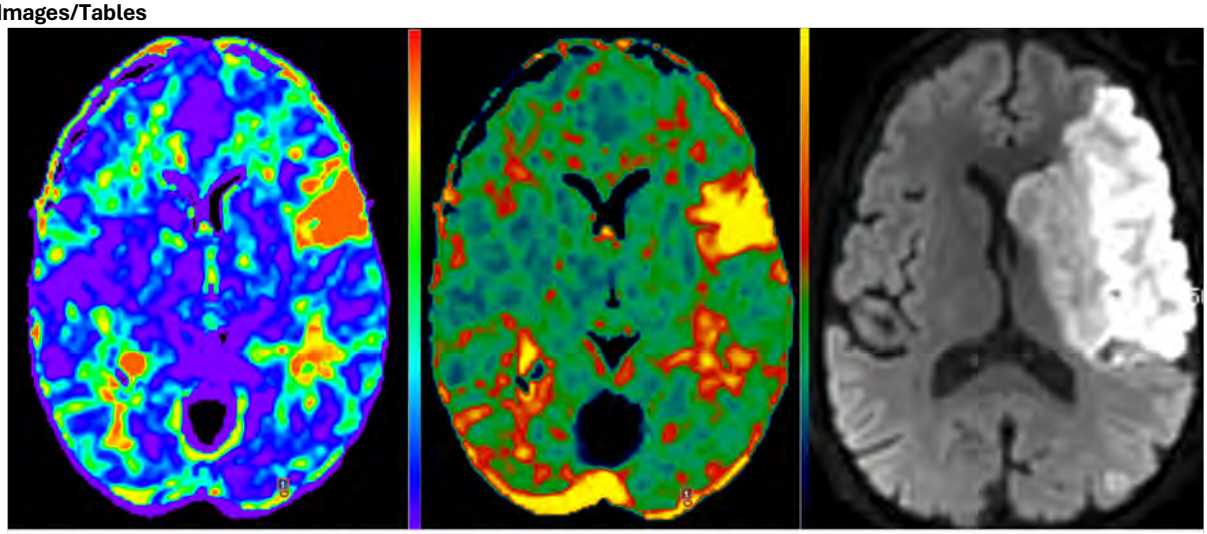

Figure 1 CTP parametric maps including arterial delay (left) and mean transit time (middle) are shown demonstrating baseline perfusion deficit in this patient with left MCA occlusion. Region of interest drawn on the left (ipsilateral) transverse sinus shows a prolonged venous transit delay (VTD) of 17 seconds on MTT and 3.5 seconds on arterial delay (AD) map. This patient had a significant infarct growth (follow up MRI, B1000 shown) despite undergoing TICI-2C reperfusion.

1057 Vessel Wall Remodeling Index and Pathologic Plaque Burden as Quantitative Markers to Differentiate Intracranial Arterial Pathologies in High-Resolution Vessel Wall MRI

David Timaran MD[1], Mario E Mahecha MD[1], Santiago Aristizabal-Ortiz MD[1], Laura Ocasio MD, MSc[1], Elham Tavakkol MD[2], Andres F Rodriguez MD[1], Stephanie Assimonye MD[1], Abdulla A Alhashmi MD[1], Preston Weaver MD[1], Konstanze Guggenberger MD[3], Andres F Mejia MD[4], Juan C Ricardo MD[5], Roy F Riascos MD, MBA, FACR[1]

[1]University of Texas Health Science Center at Houston, Houston, Texas, USA. [2]UC Davis Health, Sacramento, California, USA. [3]University of Wuerzburg Bestätigte, Wurzburg, Bavaria, Germany. [4]Fundación CardioInfantil- Instituto de Cardiología, Bogota, Bogota, Colombia. [5]Universidad del Rosario, Bogota, Bogota, Colombia

Purpose

High-resolution vessel wall MRI (HR-VWI) provides detailed visualization of arterial wall pathology beyond luminal imaging. The purpose of this study was to assess quantitative parameters, specifically vessel wall remodeling and pathological wall burden, across major intracranial vasculopathies, and determine whether these parameters can help differentiate diseases that often appear similar on conventional luminal angiographic techniques such as CTA, MRA, or DSA.

Materials & Methods

A retrospective single-center study included 339 patients who underwent HR-VWI over seven years. After excluding suboptimal images, 179 patients (52.8%) were analyzed, and 84 (46.9%) were randomly selected for quantitative evaluation. Imaging was performed on 3T MRI scanners using pre- and post-contrast 3D turbo spin-echo sequences with isotropic 1 mm voxels. Curved multiplanar reconstructions were used to measure vessel and lumen areas at stenotic and reference sites. The remodeling index (RI) was defined as the ratio of stenotic to reference vessel area (positive >1.05, negative <0.95, absent 0.95–1.05). Pathologic wall burden was calculated as (stenotic wall area/stenotic vessel area) × 100. Two neuroradiologists, blinded to clinical information, reviewed qualitative features including enhancement, morphology, and mural hemorrhage. Statistical analyses used ANOVA, Kruskal-Wallis, and multivariate logistic regression to identify independent diagnostic predictors.

Results

Final diagnoses included intracranial atherosclerotic disease (ICAD, n=40), dissection (n=14), vasculitis (n=8), vasospasm (n=4), normal controls (n=10), and others (n=8). Positive remodeling occurred in 55% of ICAD, 86% of dissections, and 38% of vasculitis cases, while negative remodeling predominated in vasospasm (75%) and controls (80%) (p<0.01). Mean pathological wall burden was 71.9% ±20.8 in ICAD, 84% ±20.9 in dissection, 75.6% ±16.3 in vasculitis, and 30% ±20.7 in vasospasm (p<0.01). Wall enhancement occurred in 47.5% of ICAD (mostly eccentric) and 87.5% of

vasculitis (concentric). Mural hemorrhage was present in 92.9% of dissections (p<0.001). Multivariate logistic regression identified plaque burden (OR 1.04; 95% CI 1.02–1.07; p<0.001) and mural hemorrhage (OR 0.04; 95% CI 0.01–0.20; p<0.001) as independent predictors of ICAD (AUC=0.82). For dissection, mural hemorrhage was the strongest predictor (OR 471.8; 95% CI 10.1–>999.9; AUC=0.94).

Conclusion

Quantitative HR-VWI parameters, particularly remodeling index and wall burden, effectively distinguish intracranial vascular pathologies. Distinct signatures were observed: positive remodeling and high burden in dissection, variable remodeling in ICAD, mixed remodeling with concentric enhancement in vasculitis, and low burden with absent remodeling in vasospasm. Combining these quantitative indices with qualitative features such as enhancement and mural hemorrhage increases diagnostic specificity and supports HR-VWI as a precision imaging tool for intracranial vascular disease evaluation.

References

1. Mandell DM, Mossa-Basha M, Qiao Y, Hess CP, Hui F, Matouk C, et al. Intracranial vessel wall MRI: principles and expert consensus recommendations of the American Society of Neuroradiology. *AJNR Am J Neuroradiol*. 2017;38(2):218-29.
2. Tritanon O, Mataeng S, Apirakkan M, Panyaping T. Utility of high-resolution magnetic resonance vessel wall imaging in differentiating between atherosclerotic plaques, vasculitis, and arterial dissection. *Neuroradiology*. 2023;65(3):441-51.
3. Song JW, Pavlou A, Xiao J, Kasner SE, Fan Z, Messé SR. Vessel wall MRI biomarkers of symptomatic intracranial atherosclerosis: a meta-analysis. *Stroke*. 2021;52(1):193-202.
4. Obusez EC, Hui F, Hajj-Ali RA, Calabrese LH, Hammad T, et al. High-resolution MRI vessel wall imaging: spatial and temporal patterns of reversible cerebral vasoconstriction syndrome and CNS vasculitis. *AJNR Am J Neuroradiol*. 2014;35(8):1527-32.
5. Yuan W, Liu X, Yan Z, Wu B, Lu B, Chen B, et al. Association between high-resolution magnetic resonance vessel wall imaging characteristics and recurrent stroke. *Int J Stroke*. 2024;19(5):569-76.

Images/Tables

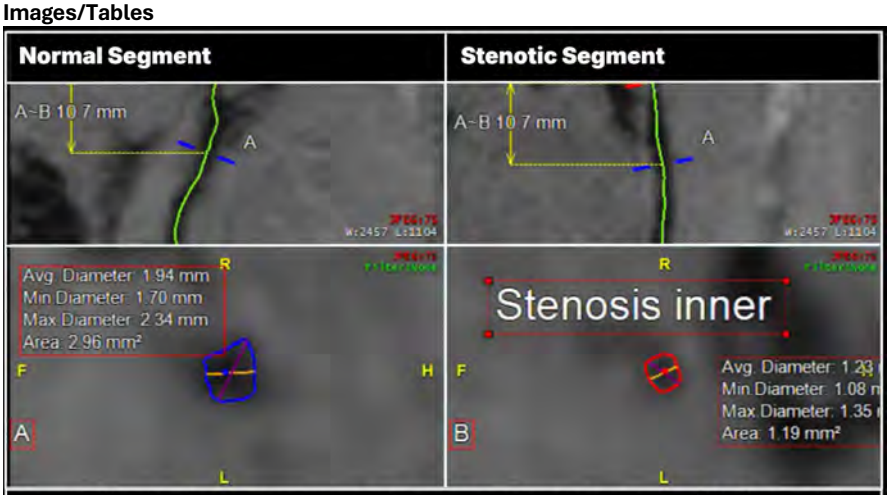

Figure 1. Quantitative measurement of the left posterior cerebral artery (PCA) in a patient with vasospasm - The blue contour delineates a normal reference segment, and the red contour delineates the stenotic segment. Vessel and lumen areas were obtained using curved multiplanar reconstruction on high-resolution vessel wall MRI for calculation of the remodeling index and pathologic wall burden.

---

465 Diagnostic Test Accuracy of DWI-FLAIR Mismatch for the Identification of Patients with Hyperacute Ischemic Stroke: A Systematic Review and Meta-analysis

Mahmoud Omar MD[1], Hussain Alkhars BS[2], Dottie Yu BS[3], Mohammed Almarkhan BS[2], Paul Wang MD, PhD[1], Michael DeGeorgia MD[1], Wassim Malak MD[1]

[1]University Hospitals Cleveland Medical Center, Cleveland, Ohio, USA. [2]George Washington School of Medicine and Health Sciences, Washington, District of Columbia, USA. [3]Cleveland Clinic Lerner College of Medicine, Cleveland, Ohio, USA

Purpose

Accurate estimation of stroke onset is critical in wake-up stroke protocols, as inappropriate thrombolysis may lead to catastrophic hemorrhage. DWI/FLAIR mismatch is widely used to approximate onset timing, however, substantial variability exists in how subtle FLAIR hyperintensity is interpreted. Some studies classify faint FLAIR signal as a positive mismatch (liberal threshold), whereas others regard it as negative (conservative threshold). To address this inconsistency, we conducted a clustering meta-analysis comparing the diagnostic performance of these two visual thresholds for identifying stroke onset within 4.5 hours.

Materials & Methods

This systematic review and meta-analysis was prospectively registered (PROSPERO: CRD420251107468). PubMed, Embase, and Scopus were searched for studies published between 2000 and 2025. Studies were required to include patients with known time from symptom onset (reference standard). Two independent reviewers performed screening and data extraction. Sensitivity and specificity were pooled using a random-effects model with 95% CIs.

Results

Of 1,387 unique references, 28 studies met inclusion criteria. For identifying stroke onset <4.5 hours using the conservative FLAIR threshold, pooled sensitivity was 0.55 (95% CI, 0.47–0.64) and specificity was 0.84 (95% CI, 0.79–0.88) (15 studies; n=2,756). Using the liberal threshold, sensitivity increased to 0.74 (95% CI, 0.67–0.81) with a corresponding decrease in specificity to 0.71 (95% CI, 0.56–0.82) (8 studies; n=1,165).

Conclusion

Compared with the conservative approach, the liberal FLAIR threshold demonstrated higher sensitivity with slightly lower specificity in identifying patients likely to be within the therapeutic window. These defined data can provide a framework for clinicians to optimize patient selection for reperfusion therapy in wake-up stroke protocols.

References

1. Thomalla G, Cheng B, Ebinger M, et al. DWI-FLAIR mismatch for the identification of patients with acute ischaemic stroke within 4·5 h of symptom onset (PRE-FLAIR): a multicentre observational study. Lancet Neurol. 2011;10(11):978-986. doi:10.1016/S1474-4422(11)70192-2
2. Legge J, Graham A, Male S, et al. Fluid-Attenuated Inversion Recovery (FLAIR) Signal Intensity Can Identify Stroke Within 6 and 8 Hours. J Stroke Cerebrovasc Dis. 2017;26(7):1582-1587. doi:10.1016/j.jstrokecerebrovasdis.2017.02.030

Images/Tables

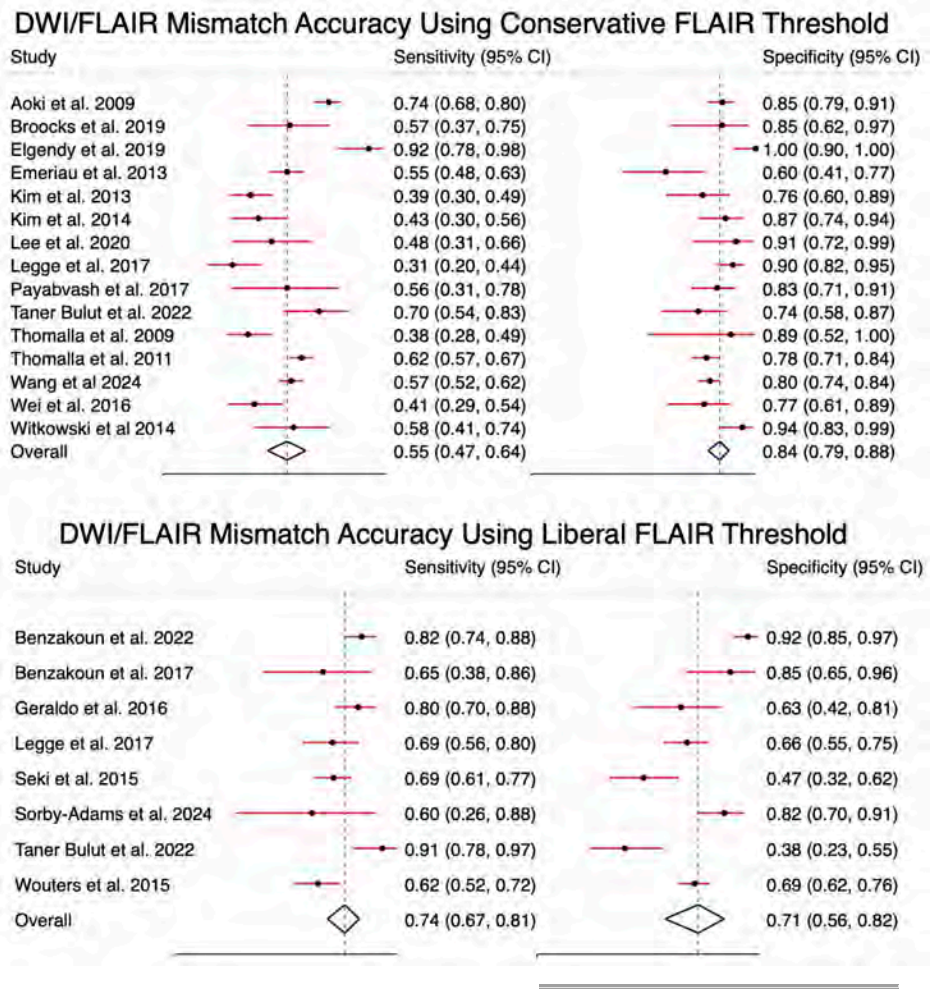

1025 Added Value of Vessel Wall MRI in Distinguishing Large-Artery Atherosclerosis and Cardioembolic Stroke.

Cristina Sanchez-Vizcaino MD[1], Daniel S. Hippe MSc[2], Ahmed A. Safwat MD[1], Mona Kharaji MD[1], Maoxue Wang MD[1], Dan Cheng MD[1], Gador Canton PhD[1], Kristi D. Pimentel[1], Lauren Klein-Murrey[3], Thomas S. Hatsukami MD[4], Chun Yuan PhD[1], Nazem W. Akoum MD[5], Niranjan Balu PhD[1], David L. Tirschwell MD[3], Mahmud Mossa-Basha MD[1]

[1]Department of Radiology, University of Washington, Seattle, Washington, USA. [2]Clinical Research Division, Fred Hutchinson Cancer Center, Seattle, Washington, USA. [3]Department of Neurology, University of Washington, Seattle, Washington, USA. [4]Department of Surgery, Division of Vascular Surgery, Seattle, Washington, USA. [5]Department of Cardiology, University of Washington, Seattle, Washington, USA

Purpose

To assess the ability of vessel wall MRI (vwMRI) based high-risk plaque features[1] to differentiate large-artery atherosclerosis (LAA) from cardioembolic (CE) strokes and their added value beyond CTA, to improve embolic stroke of undetermined source (ESUS) reclassification[2]

Materials & Methods

We retrospectively reviewed consecutive patients evaluated for acute ischemic stroke at a comprehensive stroke center between June 2022 and April 2024. Patients who underwent both neck and head CTA and intracranial and extracranial vwMRI during routine institutional diagnostic work-up and had a single-territory stroke with an LAA or CE etiology according to TOAST criteria[3] were included. The single-territory criterion allowed reliable attribution of the upstream arterial segment potentially related to the stroke mechanism, as the analysis focused on its atherosclerotic imaging features.

Three radiologists independently extracted imaging variables, including intraplaque hemorrhage (IPH) and plaque enhancement on vwMRI (each assessed from the carotid bifurcation level upward), and non-calcified stenosis >30% on CTA. The 30% stenosis threshold was chosen based on results from a prior study where CTA was used as part of a model to reclassify ESUS (when stenosis is <50% by definition) into LAA or CE strokes[4]. Clinical and demographic variables were also collected.

Logistic regression was used to assess associations between imaging features and stroke mechanism (LAA vs CE). Model performance was summarized with the area under the curve (AUC) statistic.

Results

The cohort included 212 single-territory acute ischemic stroke patients. Most were male (59%) with a median age of 69 years (IQR=60-77) and a median NIHSS of 8 (IQR=2-17). Stroke mechanisms were LAA in 108 patients (51%) and CE in 104 (49%).

In univariable analyses, LAA patients had a greater percentage of vessel segments upstream from the stroke with non-calcified stenoses>30% than CE patients on CTA (odds ratio [OR] = 2.8 per 1-standard deviation [SD] increase, 95% CI = 1.8-5.1, p < 0.001). On vwMRI, LAA patients also had a larger percentage of enhancing upstream intracranial plaques (OR = 2.2 per 1-SD increase, 95% CI=1.6-3.1, p < 0.001) and were more likely to have upstream extracranial IPH (OR = 4.0, 95% CI=1.5-12.8, p=0.008).

When CTA- and vwMRI-based evaluations were combined into a single multivariable model, both the percentage of upstream enhancing intracranial plaques (adjusted OR [aOR] = 2.3 per 1-SD increase, 95% CI=1.5-3.5, p<0.001) and upstream extracranial IPH (aOR = 6.2 per 1-SD increase, 95% CI=2.2-20.7, p=0.001) on vwMRI remained significantly associated with LAA vs. CE stroke classification. The AUC of the CTA+vwMRI model was improved compared to CTA-based alone (AUC = 0.80 vs. 0.63, p<0.001) (**Figure**).

Conclusion

Upstream atherosclerotic markers on CTA and vwMRI, not captured by current diagnostic criteria, differed significantly between LAA and CE strokes, reinforcing their potential to improve etiologic classification. Notably, vwMRI features provided superior predictive value over the non-calcified stenosis >30% CTA-based marker alone, reflecting the added benefit of more detailed plaque characterization, as these high-risk features are not captured by CTA. These results suggest that evaluating vessel wall pathology proximal to the infarct may strengthen multimodal models for ESUS reclassification and help refine future secondary prevention strategies.

References

1. Saba L, Yuan C, HatsukamiTS, et al.; Vessel Wall Imaging Study Group of the American Society of Neuroradiology. Carotid Artery Wall Imaging: Perspective and Guidelines from the ASNR Vessel Wall Imaging Study Group and Expert Consensus Recommendations of the American Society of Neuroradiology. *AJNR Am J Neuroradiol* 2018 Feb;39(2):E9-E31. DOI: https://doi.org/10.3174/ajnr.A5488
2. SannananjaB, Zhu C, Mossa-Basha M. Vessel Wall Imaging in Cryptogenic Stroke. *RadiolClin North Am* 2023 May;61(3):491-500. DOI: https://doi.org/10.1016/j.rcl.2023.01.006
3. Adams HP Jr, Bendixen BH, KappelleLJ, et al. Classification of subtype of acute ischemic stroke. Definitions for use in a multicenter clinical trial. TOAST. Trial of Org 10172 in Acute Stroke Treatment. *Stroke* 1993 Jan;24(1):35-41. DOI: https://doi.org/10.1161/01.STR.24.1.35
4. Klein-Murrey L,Tirschwell DL, Hippe DS, et al. Using clinical data to reclassify ESUS patients to large artery atherosclerotic or cardioembolic stroke mechanisms. *J Neurol* 2024 Dec 21;272(1):87. DOI: https://doi.org/10.1007/s00415-024-12848-6

Images/Tables

Figure. Receiver operating characteristic (ROC) curves comparing logistic regression models for large artery atherosclerosis (LAA) vs. cardioembolic (CE) stroke classification based on features from CTA alone vs. CTA + vessel wall MRI (vwMRI).

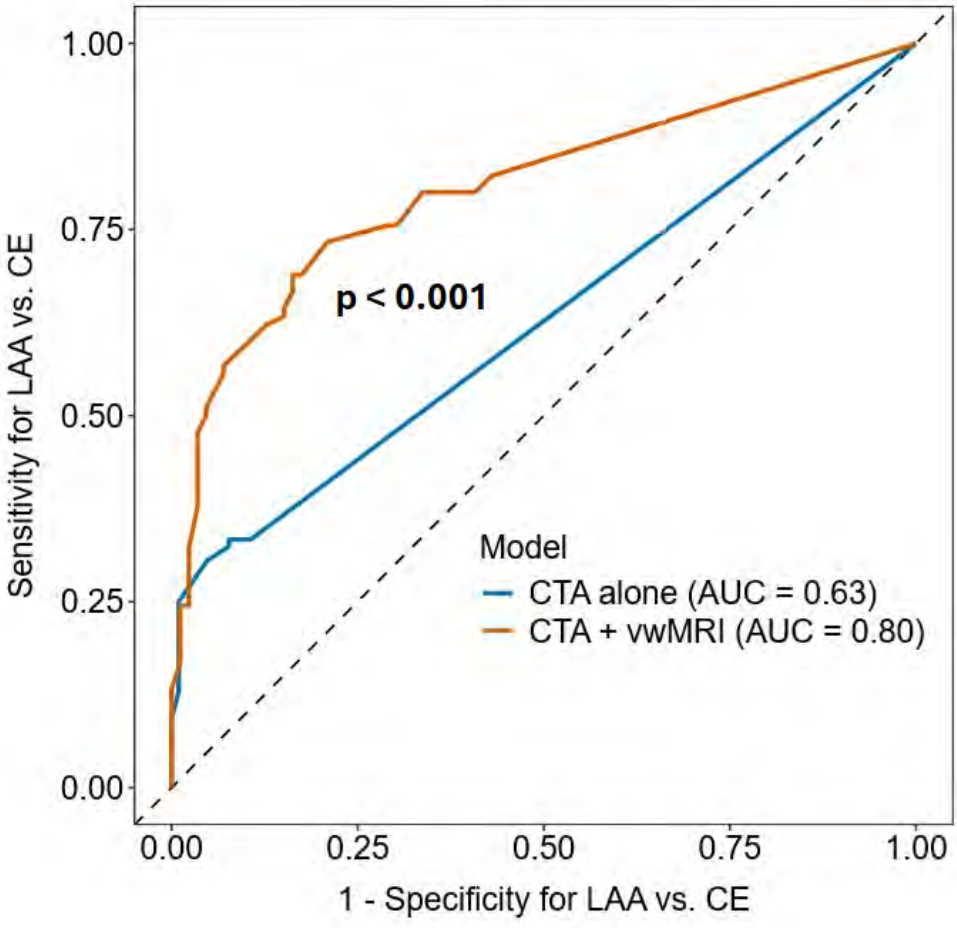

364 Presence of Intracranial Atherosclerotic Plaque in Patients with Embolic Stroke of Undetermined Source

Logan Lee MD[1], Aaron Shoskes DO[1], Sinead Culleton MBBChBAO, FRCR, FFR(RCSI)[1], Greg Stoddard[1], Scott McNally MD, PhD[1], Hediyeh Baradaran MD, MS[2]

[1]University of Utah, Salt Lake City, UT, USA. [2]Columbia University, New York, NY, USA

Purpose

Embolic strokes of undetermined source (ESUS) describe non-lacunar ischemic infarcts without an identifiable cause after a thorough diagnostic workup [1]. Under the current etiologic framework, a stroke is only attributed to large artery atherosclerosis when atherosclerotic plaque causes ≥50% luminal stenosis [2]. Underdiagnosed non-stenosing intracranial atherosclerotic plaque may result in undertreatment of vascular risk factors, with an annual stroke recurrence rate of 5% [3]. Intracranial vessel wall MR (vwMR) is an imaging modality that can identify non-stenosing atherosclerotic plaques without angiographically significant luminal narrowing but that may contribute to ischemic infarcts. We sought to evaluate if patients with ESUS were more likely to have findings of enhancing atherosclerotic plaque on intracranial vwMR compared to those with infarcts of other etiologies.

Materials & Methods

We conducted a single-center retrospective study of all patients with intracranial vwMR from July 2017 to June 2023 at our institution. A board-certified vascular neurologist determined stroke etiology based on TOAST criteria for each patient with a vwMR [2]. Of the 266 vwMRs, 52 exams were in patients with ESUS with infarcts in a single vascular territory. We compared this group against a control group of patients with stroke secondary to either small vessel disease or cardioembolic source (n=30). Each vwMR was assessed by board-certified neuroradiologists to evaluate presence and location of intracranial atherosclerotic plaque with vessel wall enhancement.

Results

Analysis of our patient demographics between the two cohorts showed no significant difference in sex, age, race, statin or anti-platelet use, and multiple stroke risk factors (Table 1). We found that in patients with ESUS, vwMR demonstrated intracranial vessel wall enhancement in 19 of 52 patients (36.5%) compared to 5 of 30 patients (16.7%) in our control group (RR = 2.19; p = 0.050). Further, in those with ESUS, 12 of 52 (23.1%) had vessel wall enhancement in the vascular territory of their acute infarct compared to 2 of 30 (6.7%) in the control group (RR = 3.46; p = 0.043).

Conclusion

Overall, our findings demonstrate that those with ESUS are more likely to have enhancing intracranial atherosclerotic plaque supplying the vascular territory of their acute infarct compared to those without ESUS. This confirms that vwMR can be a useful tool in the diagnostic workup of those with ESUS by helping to identify enhancing intracranial atherosclerosis as a potential stroke etiology, thus guiding therapeutic management to reduce stroke recurrence.

References

1. Ntaios G. Embolic Stroke of Undetermined Source: JACC Review Topic of the Week. *JACC* 2020;75(3):333-340. DOI: https://doi.org/10.1016/j.jacc.2019.11.024

2. Adams Jr HP, Bendixen BH, Kappelle LJ, et al. Classification of subtype of acute ischemic stroke. Definitions for use in a multicenter clinical trial. TOAST. Trial of Org 10172 in acute stroke treatment. *Stroke* 1993;24:35-41. DOI: https://doi.org/10.1161/01.str.24.1.35

3. Hart RG, Diener H-C, Coutts SB, et al. Embolic strokes of undetermined source: the case for a new clinical construct. *Lancet Neurol* 2014;13(4):429-38. DOI: https://doi.org/10.1016/s1474-4422(13)70310-7

Images/Tables

Table 1. Patient Demographics

	ESUS [n = 52]	Control [n = 30]	P Value
Sex, n (%)			0.20
Female	23 (44)	9 (30)	
Male	29 (56)	21 (70)	
Age, years, mean±SD	53±15	52±16	0.63
Smoker Status, n (%)			0.42
never smoker	31 (60)	15 (50)	
past smoker	12 (23)	11 (37)	
current smoker	9 (17)	4 (13)	
Hypertension, n (%)	27 (52)	18 (60)	0.48
Hyperlipidemia, n (%)	27 (52)	18 (60)	0.48
Diabetes Mellitus Type 2, n (%)	15 (29)	9 (30)	0.91
Race, n (%)			0.93
Nonwhite	10 (19)	6 (20)	
White	42 (81)	24 (80)	
Statin use, n (%)	17 (33)	6 (20)	0.22
Antiplatelet use, n (%)	14 (27)	7 (23)	0.72

Scientific Abstract Power Pitches & Luminary Speaker: Pediatric

11:00am - 12:00pm Monday, 18th May, 2026

934 Hybrid Diffusion (HYDI) Imaging of the Cervical-Thoracic Pediatric Spinal Cord: Measurement and Analysis of NODDI, DKI and DTI metrics

Zahra Sadeghi Adl M.S.[1], Devon Middleton PhD[2], Laura Krisa PhD[3], Sara Naghizadehkashani MD[3], Mahdi Alizadeh PhD[2], Slimane Tounekti PhD[4], Scott H Faro MD[2], Adam Flanders MD[2], Jürgen Finsterbusch PhD[5], Julien Cohen-Adad PhD[6], Feroze Mohamed PhD[2]

[1]Temple University, Philadelphia, PA, USA. [2]Jefferson Integrated Magnetic Resonance Imaging Center, Department of Radiology, Thomas Jefferson University, Philadelphia, PA, USA. [3]Department of Occupational Therapy, Thomas Jefferson University, Philadelphia, PA, USA. [4]Center for Advanced Metabolic Imaging in Precision Medicine, Philadelphia, PA, USA. [5]Department of Systems Neuroscience, University Medical Center Hamburg-Eppendorf, Hamburg, Hamburg, Germany. [6]NeuroPoly Lab, Institute of Biomedical Engineering, Polytechnique Montreal, Montreal, QC, Canada

Purpose

Normative diffusion metrics enable quantitative comparison, age-adjusted interpretation, and outlier detection for disease-related microstructural changes in the spinal cord. Multi-shell diffusion MRI improves sensitivity beyond the tensor model. Diffusion kurtosis imaging (DKI) captures non-Gaussian diffusion, and neurite orientation dispersion and density imaging (NODDI) offers greater specificity than diffusion tensor imaging (DTI). Most cord studies emphasize adults, use modest cohorts, and rely on single-shell DTI; pediatric references are scarce and DTI-based. Hybrid Diffusion Imaging (HYDI) efficiently acquires multiple shells in one protocol, enabling simultaneous DTI, DKI, and NODDI. We build tissue-specific (white and gray matter) normative references for DTI, DKI, and NODDI across cervical and thoracic levels in typically developing children and quantify age-related change.

Materials & Methods

Ninety-nine typically developing participants (ages 6–17 years) were recruited. Each underwent high-resolution T2-weighted imaging and two multi-shell HYDI slabs (b=0, 800, 2000 s/mm^2) covering the cervical and thoracic cord. Processing included MP-PCA denoising, motion correction and vertebral labeling with the Spinal Cord Toolbox (SCT), and cord segmentation. For model-specific fitting, the b=800 shell was used for DTI, while b=800 and 2000 were combined for NODDI and DKI. T2-weighted images were segmented and levels labeled from C1–T12. All diffusion maps were co-registered to T2 and normalized to the PAM50 template via SCT. Tissue masks for white matter (WM), gray matter (GM), and whole cord were applied for quantitative extraction. Ten biomarkers were derived: fractional anisotropy (FA), mean diffusivity (MD), axial diffusivity (AD), and radial diffusivity (RD) from DTI; mean kurtosis (MK), axial kurtosis (AK), and radial kurtosis (RK) from DKI; and neurite density index (NDI), orientation dispersion index (ODI), and isotropic volume fraction (FISO) from NODDI. For each subject, metrics were averaged within WM, GM, and whole cord at each vertebral level. Tissue-specific normative values (mean, SD) were generated per level (C1–T12). Cohort-level references were computed, and age associations were tested with linear models on subject-wise regional means (cervical, thoracic) with false-discovery-rate control.

Results

Tissue-specific references were generated for all ten biomarkers across C1–T12. WM exceeded GM for FA and NDI (FA ≈0.62 vs 0.58; NDI ≈0.67 vs 0.57). Profiles were structured: FA peaked in upper cervical levels and declined caudally; MD and AD rose into mid-thoracic levels then decreased; ODI increased caudally (WM ODI ≈0.16 at C2 vs ≈0.30 at T12). Age effects were significant: FA increased with age in WM and whole cord; MD decreased in WM and whole cord; NDI increased in GM and whole cord with a WM trend. All DKI metrics increased with age; MK, RK, and AK were significant across tissues.

Conclusion

We provide a comprehensive normative diffusion database of the pediatric spinal cord, with reference values for ten biomarkers from multi-shell DTI, DKI, and NODDI. Age-related increases in FA, MK, RK, AK, and NDI, together with decreasing MD, quantify maturation through late childhood and adolescence. These references enable z-score–based outlier detection and age-adjusted interpretation in clinical and research settings, including pediatric spinal cord injury and transverse myelitis, where distinguishing development from pathology is essential.

References

1. Chagawa, K., et al., Normal values of diffusion tensor magnetic resonance imaging parameters in the cervical spinal cord. Asian spine journal, 2015. 9(4): p. 541.
2. Grussu, F., et al., Neurite orientation dispersion and density imaging of the healthy cervical spinal cord in vivo. Neuroimage, 2015. 111: p. 590-601.
3. Conklin, C.J., et al., Spatially selective 2D RF inner field of view (iFOV) diffusion kurtosis imaging (DKI) of the pediatric spinal cord. NeuroImage: Clinical, 2016. 11: p. 61-67.
4. Shahrampour, S., et al., Atlas-based quantification of DTI measures in a typically developing pediatric spinal cord. American Journal of Neuroradiology, 2021. 42(9): p. 1727-1734.
5. De Leener, B., et al., SCT: Spinal Cord Toolbox, an open-source software for processing spinal cord MRI data. Neuroimage, 2017. 145: p. 24-43.

Images/Tables

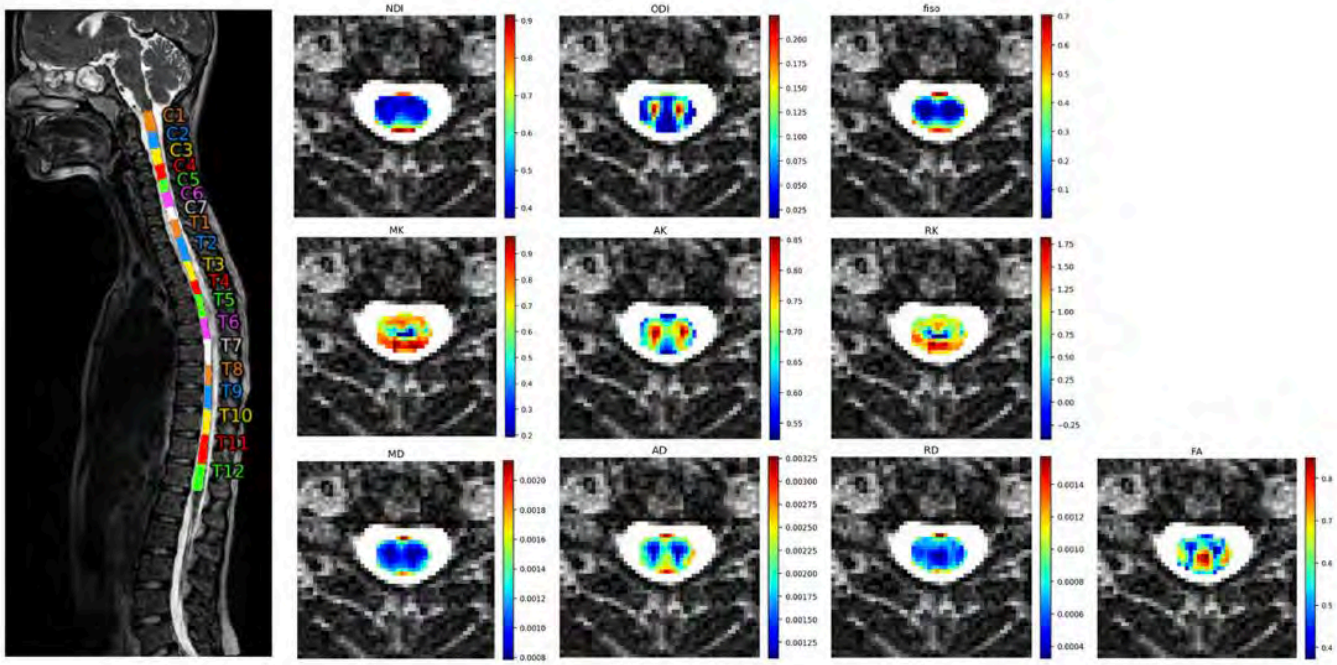

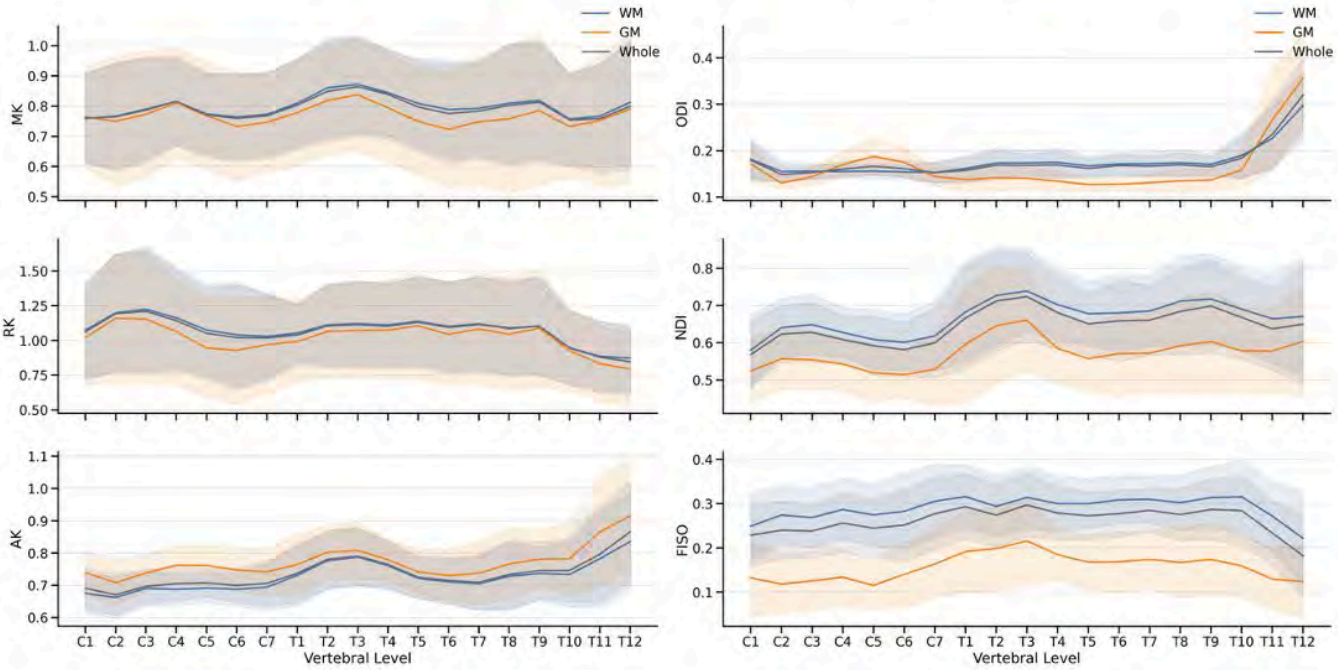

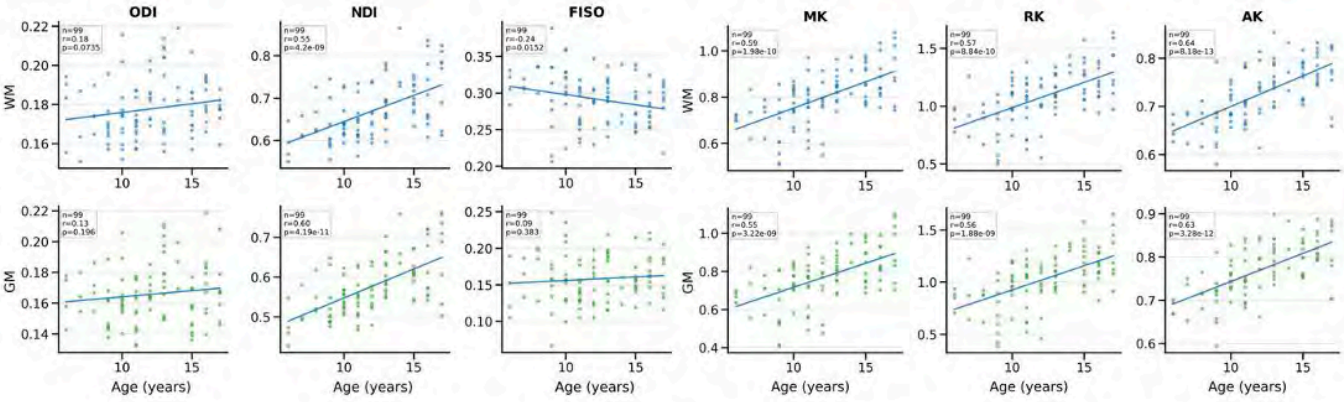

580 Simplified Gyral Pattern in Children: Quantitative Morphometric Assessment on Brain MRI and Correlation with Clinical Outcome

Stefanie Chambers MD[1], Mateus A. Esmeraldo MD[2], Yanniklas Kravutske MD[1], Lukas Haider MD[1], Gregor Kasprian MD[1], Ana F Geraldo MD[2], Bruno P Soares MD[2]

[1]Medical University of Vienna, Vienna, Vienna, Austria. [2]Stanford University, Stanford, CA, USA

Purpose

Simplified gyral pattern (SGP) represents an often subtle radiological feature of malformations of cortical development. Its recognition on MRI requires extensive neuropediatric expertise and discerning which radiological features predict clinical outcome remains challenging. Existing MRI-based classification schemes(1) rely on subjective visual assessment and have not been quantitatively linked to clinical outcomes. Our goal is to apply a quantitative, morphometric approach to disentangle cortical simplification from microcephaly-related effects and to correlate MRI-derived features with clinical outcome.

Materials & Methods

We retrospectively identified 34 patients with isolated SGP on clinical MRI. Cases were verified in consensus by two expert pediatric neuroradiologists. Inclusion criteria include follow-up period >1 year. Exclusion criteria comprised cortical malformations secondary to hemorrhagic or ischemic injury and additional complex corticalmalformations. Clinical data including history of epilepsy, neurodevelopmental delay, head-circumference z-scores, and genetic findings were extracted from records.

FreeSurfer v8.1.0 (or Infant FreeSurfer for <4 years) was used to derive global and lobar measures of gray-matter volume (GMV), WMV, cortical thickness, surface area, sulcal depth, curvature, and local gyrification index (LGI) from 3D T1-weighted images. GMV and WMV were normalized to intracranial volume (ICV).

Statistical analyses (Python) included group comparisons (t-test or Mann–Whitney U, FDR-corrected), ANCOVA controlling for age, sex, and ICV, and robust allometric scaling to model relationships of volume to area. Principal component analysis (PCA) identified imaging phenotypes, which were related to clinical variables using Kendall's τ correlations, and logistic regression.

Results

Following availability of data and validation of correct segmentation, eighteen patients with SGP (mean age 7.1±6.5 years) and nineteen matched controls were included. Three cases showed mild, and ten showedsevere microcephaly. 83% presented with neurodevelopmental delay, and 44% had a history of epilepsy. Due to their high overlap, these were analyzed as a combined clinical outcome.

After ICV normalization, patients showed significantly reduced WMV (~17%), surface area (~50%), and LGI (~19%), while cortical thickness was increased by ~17% compared to controls ($q<0.005$), frontal and parietal lobes were most affected. Allometric scaling confirmed that surface area loss exceeded what would be expected from reduced ICV alone.

PCA identified three morphometric subtypes differing mainly along a thickness-curvature axis, separating controls from patients and stratifying clinical severity. Both deaths occurred in the most severely affected cluster. Correlating these findings to clinical outcome using Kendall's τ correlations and logistic regression, reduced area, WMV, LGI, and higher cortical thickness were most strongly associated with epilepsy or developmental delay ($q<0.02$).

Conclusion

We found that patients with SGP exhibited marked reductions in surface area and WMV, exceeding what would be expected from total volume loss. Although LGI was significantly decreased, values remained within the expected variance accounting for reduced brain volume in allometric scaling. Cortical thickness was increased, but remained within measures typically considered normal in literature(2). These features were predictive for the development of delay and epilepsy in logistic regression, highlighting the importance of assessing outer area surface and potentially refining cortical thickness thresholds. Given the limited cohort size, these findings should be considered exploratory and require validation in larger samples.

References

1. Vermeulen RJ, Wilke M, Horber V, Krägeloh-Mann I. Microcephaly with simplified gyral pattern: MRI classification. Neurology. 2010 Feb 2;74(5):386–91.

2. Severino M, Geraldo AF, Utz N, Tortora D, Pogledic I, Klonowski W, et al. Definitions and classification of malformations of cortical development: practical guidelines. Brain. 2020 Aug 10;143(10):2874–94.

Images/Tables

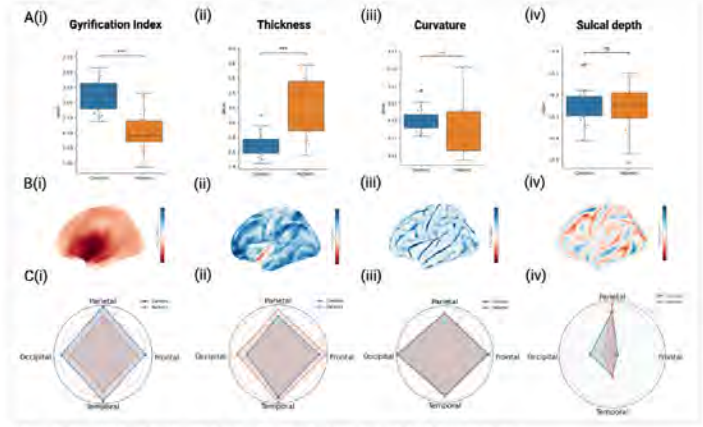

Figure: Patients with SGP (orange) show distinct patterns in surface-based metrics.
A Boxplots, **B** overlay on brain surface (= mean values patients – mean value controls), red indicating decreased, and blue increased values, compared to controls and **C** radar plots indicating lobar distribution.
(i) LGI shows homogeneous decrease over all lobes in SGP, particularly in insular regions.
(ii) Thickness is significantly increased over all lobes in SGP (mean=3.17mm vs. 2.7mm in controls, q=0.002).
(iii) Curvature shows no significant group differences, patients with SGP. Radar plots demonstrate almost complete overlap in both groups.
(iv) Whilst total sulcal depth shows no group differences, lobar analyses reveal that patients show shallower sulci in frontal and occipital regions, conversely parietal lobes show accentuated sulci.

1065 Comparing Automated and Manual Fractional Anisotropy Measurements in Pediatric Neonatal Brachial Plexus Injury: Validation of the Spinal Cord Toolbox

Jocelyn Yang MD, Jason Talbott MD, PhD, Laura Deering MD, Jonathan Strober MD, Nalin Gupta MD, PhD, Cynthia Chin MD, Yi Li MD
University of California, San Francisco, San Francisco, CA, USA

Purpose

Neonatal brachial plexus injury (NBPI) affects 0.4-3 per 1,000 births, causing varying upper extremity dysfunction (1). While MRI is the primary non-invasive evaluation method, diffusion tensor imaging (DTI) with post-processed fractional anisotropy (FA) offers quantitative microstructural assessment of nerve roots and spinal cord organization in brachial plexus injuries (2).

FA measurements within cervical spinal cord may reveal microstructural organization differences between injured and normal sides. Manual region of interest (ROI) calculation of FA values, however, is time-consuming, requires specialized expertise, and demonstrates considerable interobserver variability (3,4).

The Spinal Cord Toolbox (SCT) provides automated processing capabilities for spinal cord and nerve tissue analysis, including FA analysis (5). SCT is primarily validated in adults; to date, no studies have systematically compared automated FA measurement of the spinal cord with manual methods in children, especially in those <1 year of age. This study compares the correlation and interrater reliability of manual ROI with automated SCT-derived FA measurements in the cervical cord of children with NBPI.

Materials & Methods

Seventeen children (median age 6 months, IQR 4-9 months) with NBPI underwent MRI of the brachial plexus, including DTI of bilateral plexus and the cervical cord. A single reader manually calculated FA values of the cervical cord at C5-C8 levels, obtaining values at each level for the whole cord, and right and left hemicords. The same DTI datasets were processed using the SCT automated pipeline for spinal cord segmentation, FA quantification and metric extraction. FA values for the same regions as the manual ROI measurements were used. Correlation analysis was performed between manual and automated FA measurements at each cervical level using Pearson correlation. Bland-Altman analysis was performed to assess systematic bias and limits of agreement between the two measurement methods.

Results

For each subject, manual and SCT-derived FA values for twelve cord regions (whole cord, right hemicord and left hemicord per level for four levels: C5-C8) were available. SCT measurements demonstrated strong positive correlation with manual FA calculations across all cervical levels, with a mean correlation coefficient of $r = 0.64$ (median $r = 0.61$, range 0.43-0.87). Statistical significance ($p < 0.05$) was achieved in 11 of 12 regions (91.7%), with 7 regions (58.3%) demonstrating strong correlations ($r \geq 0.60$). The mean coefficient of determination was $R^2 = 0.4353$, indicating that automated measurements captured 43.5% of the variance in manual FA values. Bland-Altman analysis confirms good agreement with minimal systematic bias (mean difference = +0.025) and tight 95% limits of agreement (±0.12 to ±0.28). C7 showed the best overall agreement with the smallest variability (SD = 0.06-0.08), while C8 had the largest bias (+0.05 to +0.07).

Conclusion

Automated FA measurement derived using SCT demonstrates strong correlation with manual ROI measurements in the pediatric spinal cord, achieving statistically significant correlation in > 90% of studied regions, strong correlation in almost 60% of regions, and with overall good agreement and minimal systematic bias. These findings support the use of SCT as a reliable tool for quantitative DTI analysis in the pediatric spinal cord in children less than 1 year.

References

1. Van der Looven R, Le Roy L, Tanghe E, et al. Risk factors for neonatal brachial plexus palsy: a systematic review and meta-analysis. Dev Med Child Neurol. 2020;62(6):673-683.
2. Shah V, Coroneos CJ, Ng E. The evaluation and management of neonatal brachial plexus palsy. Paediatr Child Health. 2021;26(8):493-497.
3. Wade RG, Tanner SF, Teh I, et al. MRI for detecting root avulsions in traumatic adult brachial plexus injuries: a systematic review and meta-analysis of diagnostic accuracy. Radiology. 2019;293(1):125-133.
4. Vargas MI, Viallon M, Nguyen D, et al. Diffusion tensor imaging (DTI) and tractography of the brachial plexus: feasibility and initial experience in neoplastic conditions. Neuroradiology. 2010;52(3):237-245.
5. De Leener B, Lévy S, Dupont SM, et al. SCT: Spinal Cord Toolbox, an open-source software for processing spinal cord MRI data. Neuroimage. 2017;145(Pt A):24-43.

Images/Tables

Figure 1: Example of Pearson correlation between manual ROI and SCT-derived ROI FA values at the C7 level for whole cord FA value. r=0.86 signifies strong correlation (p=0.0001).

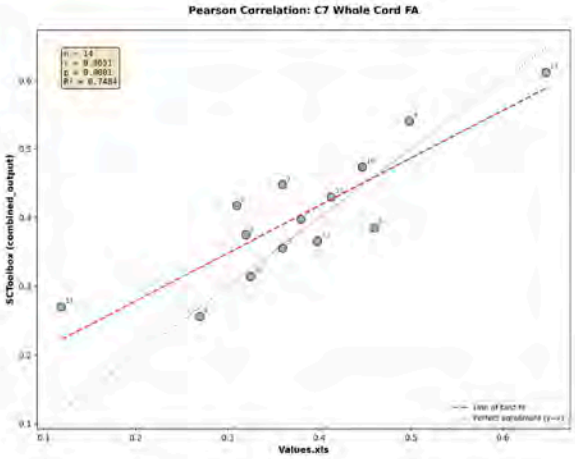

Figure 2: Example of Bland-Altman interrater agreement analysis between SCT-derived and manual ROI FA values at the C7 level for whole cord. SCT-derived FA measurements are on average 0.02 higher than manual ROI, and the SD of differences is 0.06.

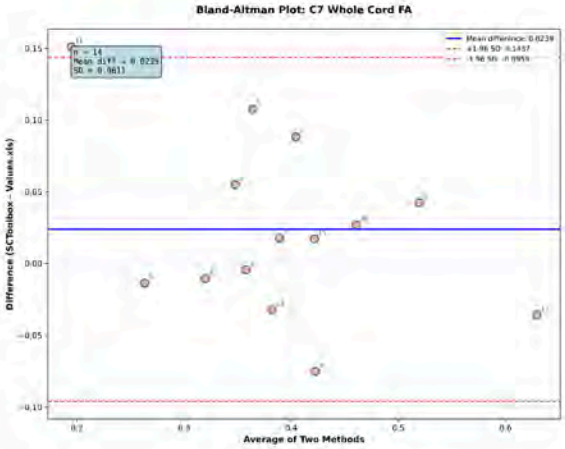

---

373 Towards Standardized Imaging in Sturge–Weber Syndrome: Development and Validation of a Multiparametric MRI Score Integrating Vascular and Parenchymal Characteristics

Ajay Kumar MD, PhD[1], Aimee Luat MD[2], Michael E Behen PhD[2], Csaba Juhasz MD, PhD[2]

[1]University of Pennsylvania, Philadelphia, PA, USA. [2]Detroit Medical Center Wayne State University, Detroit, MI, USA

Purpose

Sturge–Weber syndrome (SWS) is a sporadic neurocutaneous disorder marked by leptomeningeal angiomatosis and progressive neurological dysfunction. While MRI is essential for diagnosis and monitoring, existing imaging assessments lack standardized, quantitative approaches to characterize overall disease burden. Purpose of this study was to design and validate a reproducible MRI-based scoring system that comprehensively captures both vascular and parenchymal brain abnormalities in SWS and to evaluate its clinical relevance by correlating imaging findings with seizure severity, motor function, and cognitive outcomes.

Materials & Methods

Twenty-five children (mean age 9.5 years) with unilateral SWS underwent high-resolution 3T MRI using standardized protocols including susceptibility weighted imaging (SWI) and formal neuro-cognitive evaluation, prospectively. Six imaging features (Figure-top row)—pial enhancement, enlarged medullary veins, choroid plexus enlargement, absence of the internal cerebral and basal veins, cortical atrophy, and parenchymal calcification—were scored across lobes using a structured 3-point ordinal scale. Interrater reliability was assessed using intra-class correlation (ICC), and correlations with clinical data were analyzed using non-parametric statistics.

Results

Both the total MRI score and each sub-score demonstrated excellent interrater reliability (ICC range: 0.913–0.995). Motor function (Grooved Pegboard T-score) showed strong negative correlations with the total MRI score ($\rho = -0.82$, $p < 0.0001$) (Figure-bottom row), as well as with specific

features including pial enhancement, atrophy, and calcification. Verbal IQ and full-scale IQ were moderately correlated with calcification and atrophy (ρ = –0.45 to –0.55, p <0.05), while non-verbal IQ showed a trend-level association with atrophy and total score (p = 0.06). Seizure frequency correlated modestly with pial enhancement and choroid plexus scores but showed no association with the total MRI score. No significant relationships were found between imaging scores and patient age, age of seizure onset, or epilepsy duration. A comparison with an established asymmetry-based MRI score showed that the new multiparametric score offered superior sensitivity to cognitive outcomes and seizure-related variables.

Conclusion

This study introduces a reliable, user-friendly MRI scoring system that integrates vascular and parenchymal features relevant to SWS pathophysiology and provides a comprehensive measure of disease burden. Its simplicity, reproducibility, and reliance on routine MRI sequences make it highly suitable for longitudinal clinical monitoring, prognostication, and standardized outcome assessment in multicenter research and therapeutic trials.

References

1. Gupta SS, Joslyn KE, McKenney KD, Comi AM. Biomarker development in Sturge-Weber syndrome. J Neurodev Disord. 2025 Aug 25;17(1):50.
2. Lo W, Marchuk DA, Ball KL, Juhász C, Jordan LC, Ewen JB, Comi A; Brain Vascular Malformation Consortium National Sturge-Weber Syndrome Workgroup. Updates and future horizons on the understanding, diagnosis, and treatment of Sturge-Weber syndrome brain involvement. Dev Med Child Neurol. 2012 Mar;54(3):214-23.
3. Albazron FM, Haacke EM, Kumar A, Buch S, Xuan Y, Jeong JW, Luat AF, Behen ME, Gjolaj N, Juhász C. Absence of Deep and Basal Veins Is Common and Clinically Relevant in Sturge-Weber Syndrome. Pediatr Neurol. 2025 Oct;171:63-71.
4. Juhász C, Luat AF, Behen ME, Gjolaj N, Jeong JW, Chugani HT, Kumar A. Deep Venous Remodeling in Unilateral Sturge-Weber Syndrome: Robust Hemispheric Differences and Clinical Correlates. Pediatr Neurol. 2023 Feb;139:49-58.

Images/Tables

Relevant MRI sequences used for MRI scoring, showing venous vascular and parenchymal abnormalities

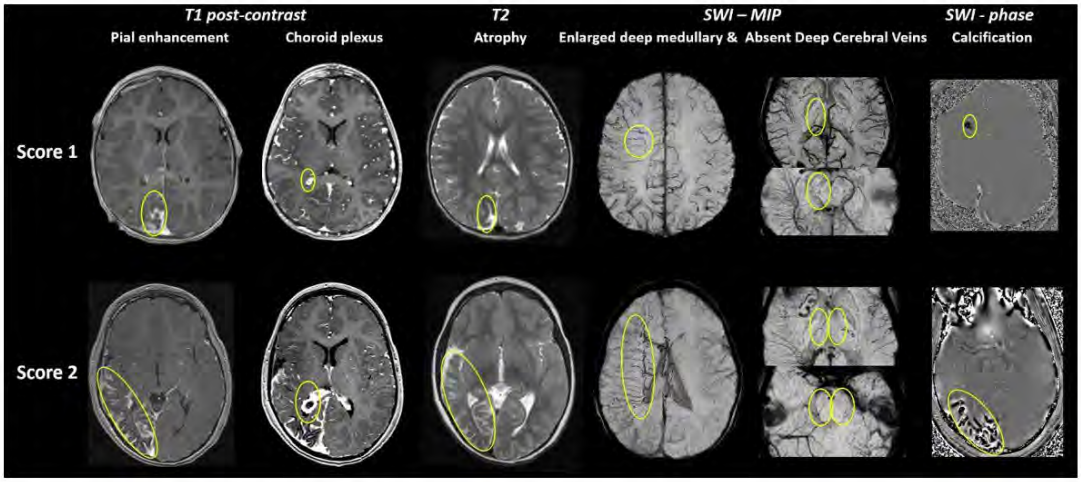

Correlation of total MRI score with motor T-score*

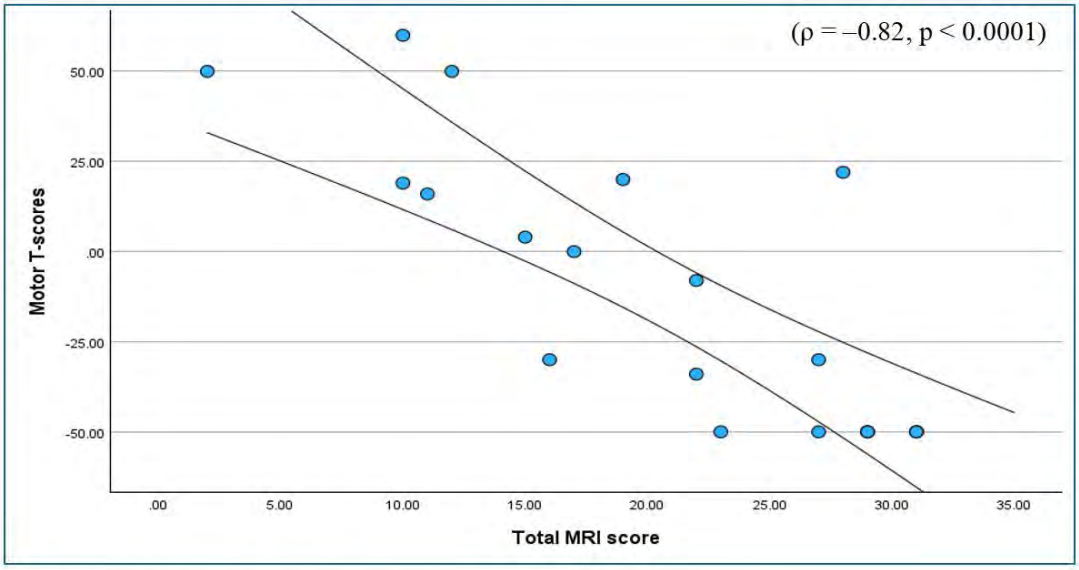

*Only 17 data points, as a few patients had overlapping scores

64 Ultra High Field 7 Tesla MRI for Assessing Small Artery Structure and Hemodynamic Flow: Initial Feasibility in Children

Ioana Pinzaru BSc[1], Anthony N Price PhD[1], Maria Zuluaga PhD[2], Philip Benjamin MD, PhD, FRCR[3], Jon O Cleary MD-PhD, FRCR[1]
[1]King's College London/Guy's and St. Thomas' NHS Foundation Trust, London, London, United Kingdom. [2]EURECOM/King's College London, Biot, Alpes-Maritimes, France. [3]St. George's University Hospitals NHS Foundation Trust, London, London, United Kingdom

Purpose

Several pediatric conditions, including sickle cell disease, radiation-induced vasculopathy, perinatal infections, mineralising microangiopathies, and interferonopathies, affect small brain arteries. Limited visualization of these vessels on conventional (1.5/3T) MRI may underestimate microvascular disease burden[1].

Ultra-high-field 7T MRI, with superior signal-to-noise ratio and spatial resolution, enables depiction of small perforating arteries such as the lenticulostriates (LSAs)[2]. Although 7T imaging of LSAs yielded novel insights into adult small vessel disease, its potential in children remains largely unexplored[3].

This study aims to develop and test a protocol for small-vessel angiography and flow quantification in a preliminary cohort of four healthy children.

Materials & Methods

We used a 7T MAGNETOM Terra.X (Siemens) and 32-channel/8-channel Rx/Tx head-coil (Nova Medical). Four healthy children were scanned with IRB-approved parental consent (7–14 years; 2 males).

Optimised protocol included:

- Compressed-Sensing (CS) Time-of-Flight (TOF) angiography - covering ~4cm from the base of the CoW, encompassing LSA origins to the caudate nuclei;
- Phase-Contrast (PC)-M1-MCA and LSAs to quantify flow; with peripheral pulse unit (PPU) cardiac gating.
- High-resolution anatomical imaging: 0.2mm-in-plane deep-learning-enhanced (Deep Resolve Boost) T2-weighted Turbo Spin Echo (TSE) and 0.55mm isotropic prototype parallel-transmit(pTx) T2 SPACE(perivascular space assessment);
- Multi-echo gradient-echo(GRE) (0.7mm isotropic) for venography.

Pulsatility and resistive indices were calculated: $PI=(v_{max}-v_{min})/v_{mean}$ and $RI=(v_{max}-v_{min})/v_{max}$

Results

LSAs were visualised in all children with our optimised protocol. CS allowed TOF acquisition of 5min38sec.

Figure1: 7-year-old female: (a),(c) - coronal/sagittal 3D MIPs of 0.55mm T2 pTx SPACE showing LSAs' perivascular spaces (blue arrows)
(b),(d) coronal/sagittal MIPs of TOFs showing LSAs(red arrows) and thalamic perforating arteries(yellow arrows)

Figure2: 14-year-old male: LSAs within perivascular spaces and adjacent veins
(a) coronal TOF MIP showing acquisition plane (green line) of axial images shown in (b)
(b) axial 0.2mm in-plane DL-T2-TSE and enlargement (d) showing perivascular spaces (blue arrows)
(c) axial TOF shows LSAs (red arrows); visible on (d) as dark flow voids
(e) axial multi-echo GRE MinIP and enlargement (f) showing basal ganglia veins (green arrows) draining into internal cerebral veins

Figure3: 14-year-old male: Flow in a LSA and the left M1-MCA
(c),(f) coronal TOF MIPs used to plan phase-contrast perpendicular to the LSA/MCA;
(b),(e) phase and magnitude images showing flow in 3 LSAs/MCA (red arrows);
(a),(d) blood flow in an LSA/MCA

Mean LSA-flow in the 4 children was 9.5±3.1cm/s(range 8–15.3cm/s) with PI=0.7,comparable to adults[4]. LSA diameters ranged 200-700µm. Mean MCA-flow was 45.6±8cm/s(range 31.7–58.5cm/s), consistent with transcranial Doppler[5].

Conclusion

The optimised protocol visualized LSAs, perivascular spaces and small veins, and quantified LSA/MCA flow and resistance metrics. The combination of TOF, phase-contrast, and high-resolution anatomical imaging provides an integrated assessment of cerebral microvasculature.

This preliminary study demonstrates feasibility of characterising small artery anatomy and flow in children using Ultra-High-Field MRI – which may give new insights into pediatric vasculopathies, to improve clinical management.

References

1. Osuafor C et al. (2022). Visualisation of lenticulostriate arteries using contrast-enhanced time-of-flight magnetic resonance angiography at 7 Tesla. Scientific Reports. 12. doi:10.1038/s41598-022-24832-z.
2. Marinkovic S, Gibo H, Milisavljevic M, & Cetkovic M. (2001). Anatomic and clinical correlations of the lenticulostriate arteries. Clin. Anat., 14(3), 190–195. https://doi.org/10.1002/ca.1032
3. Valencia S, Machado-Rivas F, Cortes-Albornoz MC, et al. 7 Tesla Time-of-Flight MRA in Adolescents. American Journal of Neuroradiology Jul 2025, ajnr.A8908; doi:10.3174/ajnr.A8908
4. van den Kerkhof, M, Jansen JFA, van Oostenbrugge RJ, Backes WH, 1D versus 3D blood flow velocity and pulsatility measurements of lenticulostriate arteries at 7T MRI, 2023 Magnetic Resonance Imaging, Volume 96, 144-150, https://doi.org/10.1016/j.mri.2022.12.005.
5. Lovett ME, O'Brien NF. Transcranial Doppler Ultrasound, a Review for the Pediatric Intensivist. Children (Basel). 2022 May 16;9(5):727. doi: 10.3390/children9050727.

Images/Tables

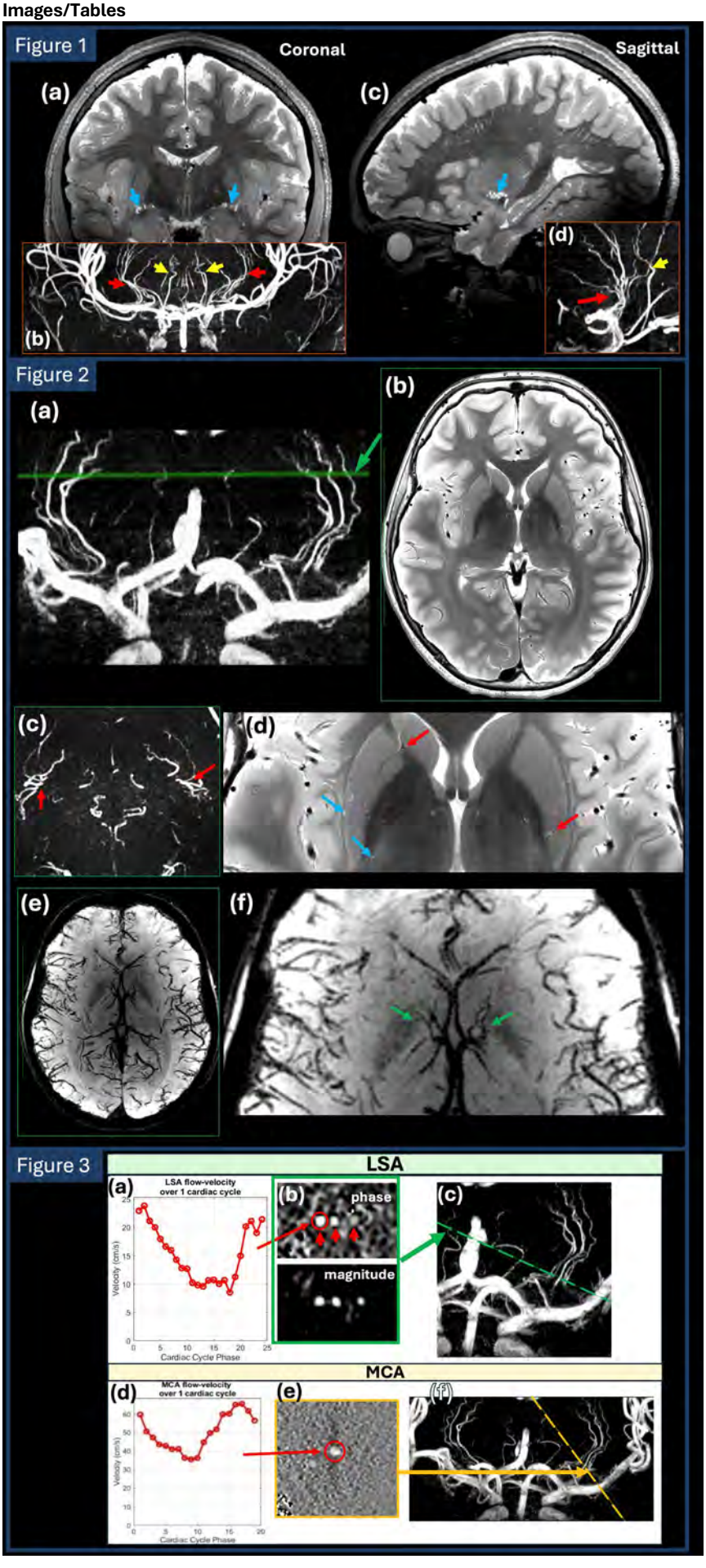

1114 Brain Growth and Neurodevelopment of Infants with Myelomeningocele: Impact of Hydrocephalus and Surgical Outcomes

Marcia H Yoshikawa MD[1], Mingzhao Yu PhD[2], Julia Tatz[2], Sofia Sandoval[1], Maria Elena Dominguez Villasenor[1], Jason Sutin PhD[1], P. Ellen Grant MD, MSc[1], Benjamin Warf MD[1], Jennifer T. Queally PhD[1], Pei-Yi Lin PhD[1]

[1]Boston Children's Hospital, Boston, MA, USA. [2]Boston Children's Hospital, Boston, Massachusetts, USA

Purpose

Myelomeningocele (MM) is a neural tube defect frequently associated with ventriculomegaly, hydrocephalus, and neurological deficits. Clinical management of hydrocephalus relies on longitudinal assessment of ventricular size to determine treatment success. Although the ultimate goal of hydrocephalus treatment is to promote healthy brain growth, data on the impact of hydrocephalus surgery on the brain development of infants with MM remain limited. Therefore, this study aims to assess the brain growth trajectories in MM patients with different hydrocephalus outcomes (no surgery required, surgical success, and surgical failure) and to compare their neurocognitive scores at two years of age.

Materials & Methods

Patients with a brain MRI within the first 30 days of life and at least one follow-up MRI within the first two years were included. Clinical and surgical data were collected from medical records. Neurodevelopment at two years was assessed using the *Bayley Scales of Infant and Toddler Development (BSID)* as part of clinical care. BPV and cerebrospinal fluid volume (CSFV) were obtained through intracranial segmentation performed by a deep-learning model based on an encoder–decoder convolutional neural network architecture. All segmentations were reviewed and corrected as needed. Age- and sex-adjusted Z-scores were generated from normative growth curves [1]. Normal BPV was defined as BPV z-score greater than -2. Surgical failure was defined as progressive ventricular expansion requiring reoperation.

Results

Thirty-nine patients were included (Table 1). Eleven did not require hydrocephalus-related surgery. Among those who required surgery, all underwent endoscopic third ventriculostomy with choroid plexus cauterization (ETV/CPC) at a median [IQR] corrected age of 14.5 [18.5] days. Sixteen (57.1%) experienced surgical failure, most occurring within six months postoperatively (n=11, 68.7%).

At neonatal MRI, there was a significant group difference in BPV Z-score (p=0.03) that no-surgery patients had a significantly lower BPV Z-scores at baseline in the post-hoc analysis. CSFV Z-scores (p=0.03) also showed a group difference that surgical-failure patients had higher CSFV Z-scores in the first month of life. There were no significant between-group differences in BPV or CSFV Z-scores at 6, 12 and 24 months of age (Figure 1). Across all timepoints, most patients had normal BPV: 89.7% (35/39) in neonates, 96.3% (26/27) at 6 and 12 months, and 95.6% (22/23) at 24 months. Cognitive (p=0.02) and motor (p=0.03) BSID scores at two years differed significantly among hydrocephalus outcome groups, with surgical-failure patients demonstrating lower scores compared with surgical-success and no-surgery patients (Figure 2).

Conclusion

MM patients who did not require hydrocephalus treatment had lower BPV Z-scores at birth compared to those requiring surgical intervention. At two years of age, patients with MM had similar BPV regardless of the surgical interventions undergone. However, those with persistent ventricular enlargement demanding additional surgeries exhibited poorer neurocognitive outcomes at two years when compared to surgical-success and no-surgery groups.

References

[1] Peterson MR, Cherukuri V, Paulson JN, et al. Normal childhood brain growth and a universal sex and anthropomorphic relationship to cerebrospinal fluid. *J Neurosurg Pediatr.* 2021 Jul 9;28(4):458-468.

Images/Tables

Table 1. Baseline characteristics of study population. BPV: brain parenchymal volume. *Chi-square or Kruskal-Wallis test.

	Overall	No Surgery	Surgical Success	Surgical Failure	p-value*
Total	39 (100)	11 (100)	12 (100)	16 (100)	
Females	16 (41)	4 (36.3)	5 (41.6)	7 (43.7)	0.92
Premature	8 (20.5)	6 (54.5)	2 (16.6)	0 (0)	**0.002**
Birth weight, g	3050 [650]	2640 [865]	3065 [845]	3226 [488]	**0.02**
Prenatal closure	7 (17.9)	6 (54.5)	1 (8.3)	0 (0)	**0.001**
Lesion level					0.41
Thoracic	1 (2.5)	0 (0)	0 (0)	1 (6.2)	
High lumbar	3 (7.7)	0 (0)	2 (16.6)	1 (6.2)	
Mid lumbar	16 (41)	3 (27.2)	4 (33.3)	9 (56.2)	
Low lumbar	17 (43.6)	7 (63.3)	5 (41.6)	5 (31.2)	
Sacral	2 (5.1)	1 (9)	1 (8.3)	0 (0)	
Normal BPV	35 (89.7)	8 (72.7)	12 (100)	16 (100)	**0.01**

Figure 1. Brain Parenchymal Volume z-score and Cerebrospinal Fluid (CSF) Volume z-score at different ages. Data grouped by hydrocephalus surgical outcome. P-values from Kruskal-Wallis test.

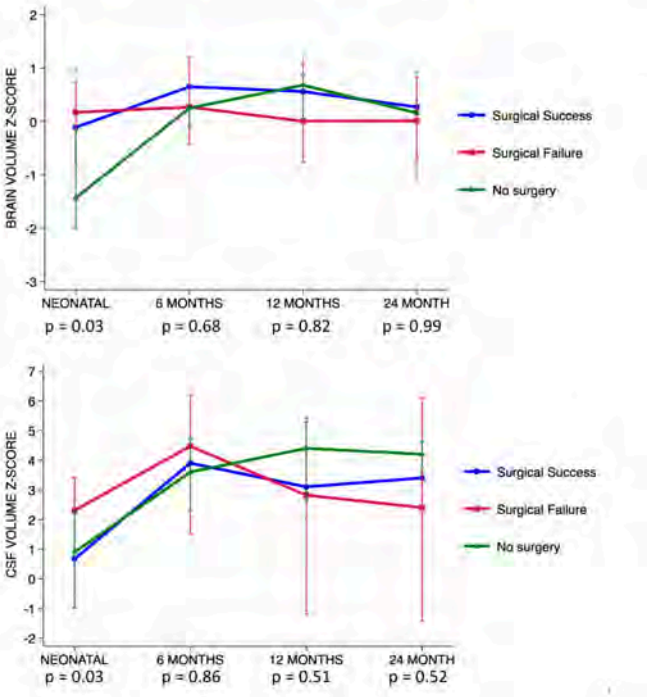

Figure 2. Bayley Scales of Infant and Toddler Development (BSID) Composite Scores at two years of age. Data grouped by hydrocephalus surgical outcome. *P-values from Kruskal-Wallis test.

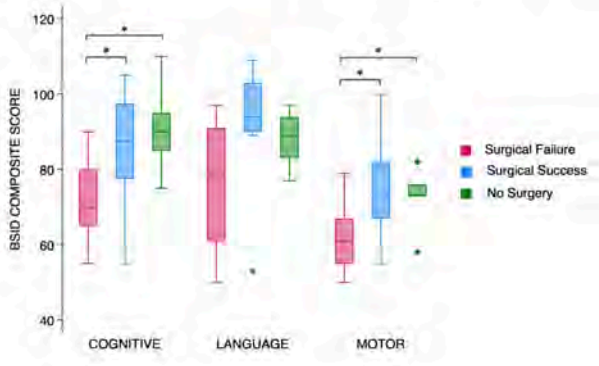

333 Optimizing Pediatric Head CT: Comparative Phantom Analysis of Photon-Counting and Energy-Integrating Detector Systems

Laura Valentina Klüner Dr. Dr. med.[1], Sebastian Zensen PD Dr. med.[1], Hannah Peuster[2], Raya Ocker-Serger Dr. med.[1], Marcel Drews Dr. med.[1], Denise Bos PD Dr. med.[1], Cornelius Deuschl PD Dr. med.[1], Lale Umutlu Prof. Dr. med.[1], Michael Forsting Prof. Dr. med.[1], Johannes Haubold Prof. Dr. med.[1], Marcel Opitz PD Dr. med.[1]

[1]Institute of Diagnostic and Interventional Radiology and Neuroradiology, University Hospital Essen, Essen, NRW, Germany. [2]University Duisburg-Essen, Essen, NRW, Germany

Purpose

To evaluate how image quality levels (IQLs) influence radiation exposure and signal-to-noise ratio (SNR) in pediatric head CT using photon-counting CT (PCCT) compared with conventional energy-integrating detector CT (EID-CT). The objective was to characterize dose efficiency and image quality across different pediatric age groups.

Materials & Methods

Three age-specific anthropomorphic phantoms (representing 1-, 5-, and 10-year-old patients) were scanned using standard pediatric head protocols on both an EID-CT (SOMATOM X.ceed) and a PCCT system (NAEOTOM Alpha, Siemens Healthineers, Germany). IQL values were varied across a clinically relevant range (1-300). For each scan, volume CT dose index ($CTDI_{vol}$) and dose-length product (DLP) were recorded. Organ-specific doses were estimated using Monte Carlo simulation software. Image quality was quantified by measuring signal and noise within brain parenchyma and bone-equivalent regions of interest, from which SNR was calculated. Paired statistical analyses (Wilcoxon signed-rank test) were performed with significance defined as $p<0.05$.

Results

Across all phantom sizes, PCCT required significantly higher tube current-time products than EID-CT ($p<0.05$) but achieved lower radiation exposure in terms of $CTDI_{vol}$ ($p<0.05$). Within the clinical IQL-range (200-300), PCCT reduced $CTDI_{vol}$ by up to 9% in the 10-year-old phantom, while the smallest reduction (0.4%) was seen in the 1-year-old phantom. Organ dose analysis revealed the highest values for red bone marrow and skin in the 1-year-old phantom, with no significant intersystem differences.

SNR performance was consistently superior with PCCT. For brain parenchyma, SNR was significantly higher across all phantoms ($p<0.02$), averaging 45% greater than EID-CT over the full IQL-range (1-300). Bone SNR gains were even more pronounced, averaging 73% higher with PCCT ($p=0.012$). The relationship between IQL and radiation dose was linear for both systems, whereas SNR exhibited nonlinear saturation behavior at higher IQLs, indicating diminishing image quality benefits with further radiation dose escalation.

Conclusion

PCCT demonstrated superior image quality for both soft tissue and bone while maintaining or reducing radiation dose in pediatric head imaging. These improvements are attributed to PCCT's single-step photon-to-signal conversion and elimination of electronic integration noise, which enhance dose efficiency and SNR compared with conventional detectors [1]. The magnitude of radiation dose reduction increased with phantom size, suggesting greater efficiency for older children. The nonlinear radiation dose – SNR relationship emphasizes the need for tailored protocol optimization to balance image quality and radiation safety. PCCT thus provides a promising pathway for advancing pediatric neuroimaging by improving diagnostic reliability without increasing radiation exposure.

References

[1] M. J. Willemink, M. Persson, A. Pourmorteza, N. J. Pelc, and D. Fleischmann, "Photon-counting CT: Technical principles and clinical prospects," *Radiology*, vol. 289, no. 2, pp. 293–312, 2018, doi: 10.1148/radiol.2018172656.

---

735 Saving the Brain: Contrast-Enhanced Ultrasound Evaluation of Brain Perfusion in a Piglet Model of Venoarterial Extracorporeal Membrane Oxygenation

Colbey W Freeman MD[1], Misun Hwang MD, MSTR, MBA[2]

[1]University of Pennsylvania, Philadelphia, PA, USA. [2]Children's Hospital of Philadelphia, Philadelphia, PA, USA

Purpose

To evaluate the relationship between parameters of brain contrast-enhanced ultrasound (CEUS) and a biochemical marker of hypoxia/anoxia, lactate-pyruvate ratio, in a piglet model of infant venoarterial extracorporeal membrane oxygenation (VA-ECMO).

Materials & Methods

After anesthesia with mechanical ventilation, VA-ECMO catheters were placed in five female 7-week old piglets weighing approximately 10 kg. Ventricular fibrillation was induced via transcutaneous electric induction, and VA-ECMO was maintained (at flow rates of 55, 70, 80, or 90 mL/kg/min, with one piglet experiencing contrast-induced anaphylaxis and being placed on varying flow rates of 80-122) for eight hours or until expiration. CEUS coronal cine clips were acquired from contrast injection to wash-out via a dural window at the level of the thalami after 0.2 mL boluses of microbubble contrast. Clips were acquired at the start of ECMO and every two hours to eight hours or to expiration. Time-intensity curves were generated for the segmented whole-brain slice and peak enhancement (PE), time-to-peak (TTP), mean transit time (MTT), rise time (RT), fall time (FT), area under the curve (AUC), wash-in rate (WI), and wash-out rate (WO) were calculated. Concomitantly, a burr hole was drilled into the calvarium opposite the dural window and a microdialysis catheter inserted into the brain parenchyma. Microdialysis samples were acquired with each CEUS clip acquisition, and lactate-pyruvate ratios (LPR) were calculated. A mixed-effects model was used to analyze the relationships between the CEUS measurements and LPR.

Results

Of five piglets, four survived eight hours on ECMO, while the 70-flow rate piglet became hemodynamically unstable and expired at five hours. Overall, the mixed-effects model integrating all CEUS parameters resulted in an R^2 of 0.94. Of the calculated CEUS parameters, only MTT ($p=0.025$) had a significant effect on LPR. AUC ($p=0.77$), FT ($p=0.066$), TTP ($p=0.90$), RT ($p=0.34$), PE (0.063), WI ($p=0.36$), and WO ($p=0.29$) had no significant effect. Similarly, neither the time of CEUS clip acquisition (2 hours $p=0.58$, 4 hours $p=0.30$, 6 hours $p=0.85$, 8 hours $p=0.70$ with 0 hour as reference) nor the ECMO flow rate (rate 55 $p=0.64$, rate 70 $p=0.96$, rate 80 $p=0.67$, anaphylactic pig $p=0.97$ with rate 90 as the reference) had a significant effect. Images from the 55-flow rate piglet are presented in the figure and demonstrate progressive decline in brain contrast enhancement with time.

Conclusion

While VA-ECMO supports infants with cardiac and/or respiratory failure, it is associated with long-term functional deficits[1]. Under current practice, evaluation of brain perfusion during ECMO indirectly depends on systemic measures of perfusion. Off-label use of CEUS allows characterization of

microcirculation cerebral blood flow at the bedside[2]. Here, we demonstrate that MTT calculated from CEUS is statistically significantly associated with a biochemical measure of hypoxic-ischemic injury in the brain, LPR. Our technique here, combined with our piglet model, can help develop imaging biomarkers of brain ischemia while potentially identifying targets for clinical practice optimization in VA-ECMO.

References

1. Boyle K, Felling R, Yiu A, et al. Neurologic outcomes after extracorporeal membrane oxygenation: a systematic review. Pediatr Crit Care Med 2018;19(8):760-6.
2. Hwang M. Introduction to contrast-enhanced ultrasound of the brain in neonates and infants: current understanding and future potential. Pediatr Radiol 2019;49(2):254-62.

Images/Tables

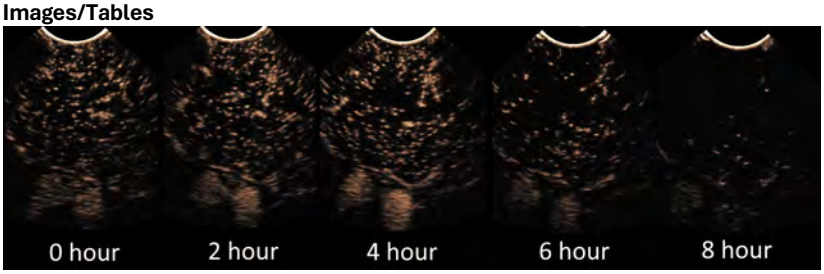

---

235 Structural Alterations in Cortical Thickness and Volume in ADHD: A Surface-Based Morphometric Study

Amanda Kettman BS[1], Mario Murakami MD[2]
[1]Alabama College of Osteopathic Medicine, Dothan, AL, USA. [2]Massachusetts General Hospital, Harvard Medical School, Boston, MA, USA

Purpose

This study investigates significant clusters of structural alterations across cortical regions between individuals with attention deficit hyperactivity disorder and healthy controls and explores their potential functional implications.

Materials & Methods

A comparative analysis of cortical thickness and volume in the left and right hemispheres was conducted using FreeSurfer on a structural MRI dataset comprising attention deficit hyperactivity disorder and control participants. Surface-based morphometric data were analyzed with a minimum z-score threshold of 1.3, and cluster-wise correction with a cluster-wise P value (CWP) ≤ 0.05 was applied to account for multiple comparisons. Clusters showing significant differences were mapped to anatomical regions, and their functional relevance was interpreted.

Results

Reduced cortical thickness was observed in the right superior frontal gyrus and increased in the left postcentral gyrus. The right and left hemispheres both demonstrated various clusters with a significant (CWP ≤ 0.0002) increase or decrease in volume compared to the control. An increased volume was observed in the right pre- and post-central, lingual, and fusiform gyri, and the left postcentral gyrus, lateral occipital gyrus, inferior parietal cortex, and rostral middle frontal cortex. A decreased volume was observed in the right superior frontal and left supramarginal gyri. Bidirectional volume changes were observed in the right lateral occipital gyrus and rostral middle frontal cortex.

Conclusion

Significant structural differences in cortical thickness and volume highlight attention deficit hyperactivity disorder-related alterations in executive, motor, and sensory processing regions.

References

Booth JR, Burman DD, Gitelman DR, Lytle MN, Mesulam MM, Meyer JR Jr, Parrish TR, Trommer B. Response inhibition and selective attention in adults and children with and without ADHD. *OpenNeuro* [dataset]. 2021. doi:10.18112/openneuro.ds003500.v1.2.0

Images/Tables

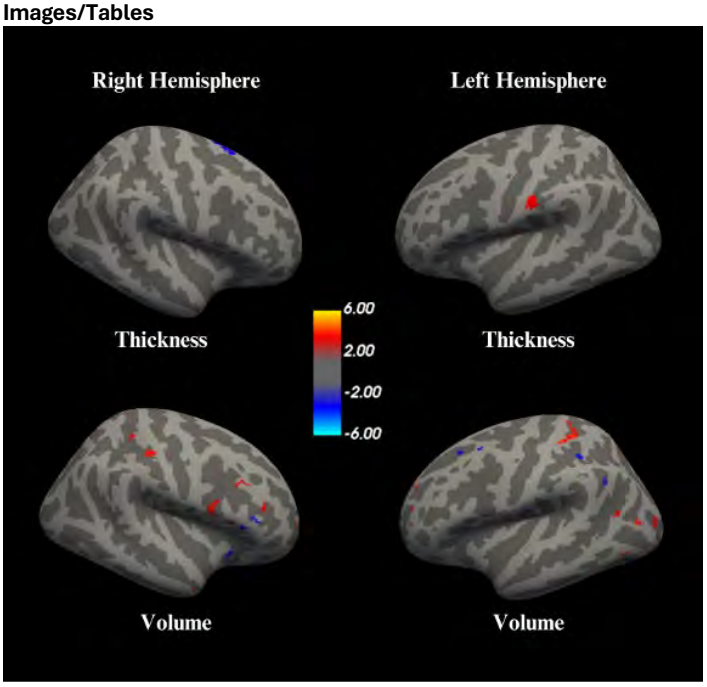

Head and Neck Emergencies

1:00 - 2:00pm Monday, 18th May, 2026

138 Risk of ipsilateral and recurrent stroke over 5-years in patients with non-stenotic carotid disease: A retrospective imaging-based population level study from Manitoba

Kamran Zahid BSc[1], Michael A Salas BSc[1], Ala Ghrooda BSc[1], Areej Zahid BSc[1], Elliot Kinnear BSc[1], Wafa Kammouni PhD[1], Ankur Wadhwa MD[1], Claudia C Radu MD[1], Babawale Arabambi MD[1], Esseddeeg Ghrooda MD[1], Naveed Akhtar MD[1], Anurag Trivedi MD[1], Mohammed Suheel Abdul Salam MD[2], Jai J Shankar MD[3], Aravind Ganesh MD[4], Nima Kashani MD[3], Nishita Singh MD[1]

[1]Department of Medicine (Neurology Division), Rady Faculty of Health Sciences, University of Manitoba, Winnipeg, Manitoba, Canada. [2]Department of Neurosurgery, Rady Faculty of Health Sciences, University of Manitoba, Winnipeg, Manitoba, Canada. [3]Department of Radiology, Rady Faculty of Health Sciences, University of Manitoba, Winnipeg, Manitoba, Canada. [4]Department of Clinical Neurosciences, Cumming School of Medicine, University of Calgary, Calgary, Alberta, Canada

Purpose

Symptomatic Non-stenotic Carotid (SyNC) disease is an increasingly recognized etiology in ischemic stroke, particularly in the presence of certain high-risk plaque features. The aim of this population level clinical-imaging study was to examine the risk of ipsilateral and recurrent stroke in patients with SyNC with 5-year follow-up. In addition, we aimed to identify plaque features that predict higher risk of ipsilateral and recurrent stroke in this population.

Materials & Methods

All patients presenting with stroke or transient ischemic attack (TIA) in fiscal year 2019/20 were identified using administrative data. All baseline and follow up imaging within 5-years of presentation was analyzed. CT Angiograms were assessed for plaque features such as degree of stenosis, plaque thickness, calcification, plaque irregularity, ulceration, positive rim sign, and focal vessel caliber increase. Parenchymal imaging was reviewed for infarct presence on the same side as carotid disease (concordant stroke). Analyses were performed at the patient and carotid level comparing 1-50% stenosis versus no stenosis using unadjusted and adjusted (for age and sex) logistic regression analysis. Predicted probabilities were also plotted to visualize the relationship between plaque thickness and stenosis grade with concordant and recurrent concordant stroke.

Results

Among 1249 patients presenting with stroke or TIA, 658 (52.7%) patients had 0-50% stenosis. Of the total 658 patients included, 153 (23.3%) had concordant stroke and 76 (11.6%) had recurrent stroke. Of the 76 patients that developed recurrence, 49 (7.5%) patients had SyNC on the ipsilateral side. In adjusted analyses, there was significantly increased odds of concordant stroke at index presentation with 1-50% stenosis [aOR 3.56, 95% CI 2.99 – 4.25] and increasing plaque thickness (per mm) [aOR 1.19, 95% CI 1.03 – 1.38]. Similarly, adjusted analysis showed significant increase in odds of recurrent concordant stroke with 1-50% stenosis [aOR 2.39, 95% CI 1.94 – 2.95], plaque thickness [aOR 1.32, 95% CI 1.05 – 1.67], and plaque ulceration [aOR 3.86, 95% CI 1.31 – 11.35]. For every 1mm increase in plaque thickness, there was 2% higher odds of concordant stroke and 3% increase in odds of recurrent concordant stroke. In addition, for every 10% increase in stenosis grade, there was approximately 2% higher odds of concordant stroke.

Conclusion

This retrospective population-level study demonstrates that non-stenotic carotid disease carries a significant risk of ipsilateral and recurrent stroke, particularly with degree of stenosis, increasing plaque thickness, and ulceration. These findings suggest that current risk stratification may underemphasize non-stenotic plaques, warranting further prospective validation to guide monitoring and treatment strategies.

References

Singh N, Marko M, Ospel JM, Goyal M, Almekhlafi M. The Risk of Stroke and TIA in Nonstenotic Carotid Plaques: A Systematic Review and Meta-Analysis. *American Journal of Neuroradiology*. 2020;41(8):1453-1459. doi:10.3174/ajnr.A6613

Ospel JM, Marko M, Singh N, Goyal M, Almekhlafi MA. Prevalence of Non-Stenotic (<50%) Carotid Plaques in Acute Ischemic Stroke and Transient Ischemic Attack: A Systematic Review and Meta-Analysis. *Journal of Stroke and Cerebrovascular Diseases*. 2020;29(10). doi:10.1016/j.jstrokecerebrovasdis.2020.105117

Ospel JM, Singh N, Marko M, et al. Prevalence of Ipsilateral Nonstenotic Carotid Plaques on Computed Tomography Angiography in Embolic Stroke of Undetermined Source. *Stroke*. 2020;51(6):1743-1749. doi:10.1161/STROKEAHA.120.029404

Singh N, Ospel J, Mayank A, et al. Nonstenotic Carotid Plaques in Ischemic Stroke: Analysis of the STRATIS Registry. *American Journal of Neuroradiology*. 2021;42(9):1645-1652. doi:10.3174/ajnr.A7218

Kamtchum-Tatuene J, Wilman A, Saqqur M, Shuaib A, Jickling GC. Carotid Plaque With High-Risk Features in Embolic Stroke of Undetermined Source. *Stroke*. 2020;51(1):311-314. doi:10.1161/STROKEAHA.119.027272

Images/Tables

Table 3: Carotid level analysis: Plaque features in patients with concordant vs. non-concordant stroke

Plaque feature	Concordant stroke (n = 306)	Non-concordant stroke (n = 1010)	Unadjusted OR (95% CI)	Adjusted OR (95% CI)
Degree of stenosis (NASCET) *(median %, IQR)*	20.0% (7.93 – 33.13)	15.8% (5.42 – 27.99)	3.53 (2.94–4.25)*	3.56 (2.99 - 4.25)*
Plaque features				
Irregularity *(%, n / total)*	7.94% (22 / 277)	7.96% (36 / 452)	1.00 (0.55 - 1.80)	0.98 (0.57-1.66)
Ulceration *(%, n / total)*	5.42% (15 / 277)	2.88% (13 / 452)	1.93 (0.89 – 4.20)	1.93 (0.97 - 01.02)
Positive Rim Sign *(%, n / total)*	5.78% (16 / 277)	3.10% (14 / 452)	1.92 (0.87 – 4.21)	1.89 (0.85 - 4.22)
Plaque thickness *(median, mm, IQR))*	2.5 (1.95 – 3.33)	2.32 (1.81 – 2.98)	1.19 (1.00 – 1.41)*	1.19 (1.03 - 1.38)*
Focal vessel caliber increase / dolichoectasia *(%, n / total)*	0.65% (2 / 306)	0.4% (4 / 1010)	1.65 (0.17 – 16.6)	1.71 (0.21 - 13.81)
Calcification				
Purely hypodense plaque *(%, n / total)*	8.66% (24 / 277)	8.4% (38 / 452)	REFERENCE	REFERENCE
Microcalcificaton *(%, n / total)*	27.1% (75 / 277)	32.3% (146 / 452)	0.81 (0.45 – 1.47)	0.79 (0.44 - 1.41)
Predominantly non-calcified *(%, n / total)*	18.8% (52 / 277)	13.9% (63 / 452)	1.31 (0.67 – 2.54)	1.30 (0.70 - 2.40)
Predominantly calcified *(%, n / total)*	45.5% (126 / 277)	45.1% (204 / 452)	0.98 (0.54 – 1.77)	0.97 (0.55 - 1.69)
Purely calcific plaque *(%, n / total)*	0.00% (0 / 277)	0.22% (1 / 452)	--	--

*Statistically significant

Table 4: Carotid level analysis: Plaque features in patients with recurrent concordant stroke vs. without recurrent concordant stroke

Plaque feature	Recurrent concordant stroke YES (n = 90)	Recurrent concordant stroke NO (n = 639)	Unadjusted OR (95% CI)	Adjusted OR (95% CI)
Degree of stenosis (NASCET) *(median %, IQR)*	18.9% (7.90 – 29.8)	17.4% (5.70– 29.5)	3.53 (2.94 – 4.25) *	2.39 (1.94 – 2.95) *
Plaque features				
Irregularity *(%, n / total)*	4.44% (4 / 90)	8.45% (54 / 639)	0.50 (0.14 – 1.76)	0.47 (0.13 – 1.73)
Ulceration *(%, n / total)*	10.0% (9 / 90)	2.97% (19 / 639)	3.63 (1.53 – 8.62)*	3.86 (1.31 – 11.35)*
Positive Rim Sign *(%, n / total)*	6.67% (6 / 90)	3.76% (24 / 639)	1.83 (0.71 – 4.57)	1.89 (0.85 – 4.22)
Plaque thickness *(median, mm, IQR))*	2.47 (2.03 – 3.36)	2.36 (1.83 – 3.05)	1.30 (1.05 – 1.60) *	1.32 (1.05 – 1.67) *
Focal vessel caliber increase / dolichoectasia *(% n / total)*	0% (0 / 98)	0.49% (6 / 1218)	--	--
Calcification				
Purely hypodense plaque *(%, n / total)*	3.33% (3 / 90)	9.23% (59 / 639)	REFERENCE	REFERENCE
Microcalcification *(%, n / total)*	25.6% (23 / 90)	31.0% (198 / 639)	2.28 (0.65 – 8.09)	2.32 (0.66 – 8.19)
Predominantly non-calcified *(%, n / total)*	15.8% (14 / 90)	15.8% (101 / 639)	2.73 (0.74 – 10.09)	2.79 (0.75 – 10.40)
Predominantly calcified *(%, n / total)*	55.6% (50 / 90)	43.8% (280 / 639)	3.51 (1.08 – 11.42)*	3.60 (1.12 – 11.56)*
Purely calcific plaque *(%, n / total)*	0.00% (0 / 90)	0.16% (1 / 639)	--	--

*Statistically significant

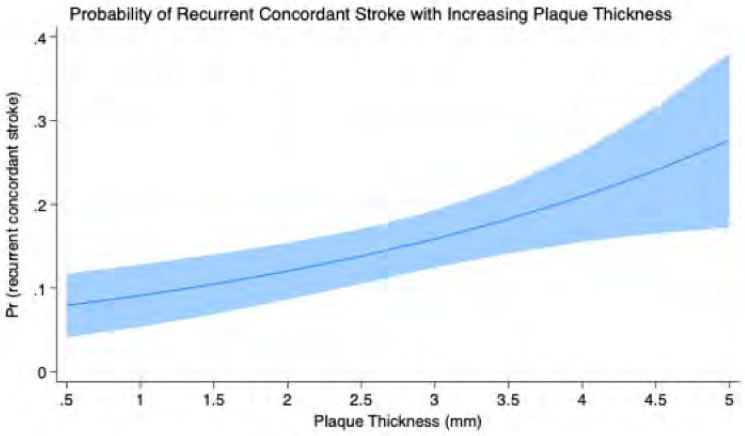

Scientific Abstract Power Pitches & Luminary Speaker: Imaging Biomarkers and Molecular Correlates in Adult Gliomas

1:00 - 2:00pm Monday, 18th May, 2026

1067 Fasting-Induced Metabolic Reprogramming in Glioma: Multinuclear MR Spectroscopic Imaging Demonstrates In Vivo Changes in Ketone Utilization and Cellular Energy Homeostasis

Seyma Alcicek[1], Iris Divé[2], Dennis C Thomas[1], Vincent Prinz[3], Katharina J Weber[4], Joachim Steinbach[2], Michael W Ronellenfitsch[2], Elke Hattingen[1], Ulrich Pilatus[1], Katharina J Wenger[1]

[1]Goethe University Frankfurt, Institute of Neuroradiology and Cooperative Brain Imaging Center - CoBIC, Frankfurt, Hesse, Germany. [2]Dr. Senckenberg Institute of Neurooncology, University Hospital Frankfurt, Goethe University, Frankfurt, Hesse, Germany. [3]Department of Neurosurgery, University Hospital Frankfurt, Goethe University, Frankfurt, Hesse, Germany. [4]Institute of Neurology (Edinger-Institute), University Hospital Frankfurt, Goethe University, Frankfurt, Hesse, Germany

Purpose

Nutritional interventions such as fasting and ketogenic diets have been explored as anticancer strategies for several decades. However, the metabolic consequences of glucose restriction in glioma remain uncertain. Gliomas encompass multiple molecular subtypes and display pronounced intratumoral heterogeneity, including regions of variable hypoxia, all of which can drive distinct and sometimes opposing metabolic adaptations.[1–4] This study aimed to noninvasively monitor fasting-induced metabolic alterations in glioma tissue using a previously published, multinuclear MR spectroscopic imaging (MRSI) protocol optimized for the detection of ketone bodies, lactate, energy metabolites, and intracellular pH, and to assess the metabolic flexibility of gliomas during a 72-hour fasting intervention.[5]

Materials & Methods

Patients with MRI-suspected glioma scheduled for biopsy or resection were prospectively enrolled and examined on a clinical 3T MRI system at baseline and after a 72-hour fasting period. Alongside anatomical imaging, 2D proton MRSI using an sLASER sequence at a long echo time (TE = 144 ms) was acquired to quantify lactate, β-hydroxybutyrate (β-OHB), acetoacetate, acetone, and standard brain metabolites including choline-containing compounds. The long TE enabled suppression of macromolecular background and inversion of J-coupled lactate and β-OHB resonances, improving quantification reliability. 2D proton CSI without water suppression and B1 mapping was used for absolute metabolite quantification. Complementary 3D phosphorus CSI data provided information on ATP, phosphocreatine, phosphomonoesters, phosphodiesters, and intracellular pH.

Twenty-one patients were examined; datasets from temporal lobe tumors affected by B0 inhomogeneity and patients who did not complete fasting were excluded. MRSI data from 13 patients were analyzed. Proton spectra were quantified using LCModel with a sequence-matched basis set, and phosphorus spectra were analyzed using AMARES. Fully automated multiparametric tumor segmentation was performed using the BraTS toolkit and volumes of tumor subregions were calculated. Statistical analysis used paired non-parametric testing.

Results

Following fasting, tumor tissue displayed a significant increase in ketone body concentrations, particularly β-OHB and acetoacetate, with the highest levels observed in necrotic and contrast-enhancing tumor regions. Lactate concentrations decreased significantly in tumor tissue after fasting, consistent with reduced glycolytic flux under limited glucose availability. Choline levels, initially elevated in tumor tissue relative to contralateral white matter, decreased following fasting, suggesting reduced membrane turnover or altered phospholipid metabolism. Phosphorus spectroscopy revealed preserved ATP/phosphocreatine ratios after fasting, indicating maintained energy homeostasis, while intracellular pH decreased, suggesting disrupted buffering capacity.

Conclusion

This multinuclear MRSI approach enables comprehensive, noninvasive monitoring of metabolic reprogramming in gliomas during nutrient restriction. Despite reduced glucose availability, gliomas maintained energy homeostasis while accumulating ketone bodies and exhibiting a shift in membrane metabolism and intracellular pH regulation. These findings suggest that gliomas exhibit substantial metabolic flexibility during fasting, and highlight the importance of integrating metabolic imaging with molecular tumor characterization to guide future nutritional or metabolic therapeutic strategies.

References

1. Sperry J, Condro MC, Guo L, Braas D, Vanderveer-Harris N, Kim KKO, Pope WB, Divakaruni AS, Lai A, Christofk H, Castro MG, Lowenstein PR, Le Belle JE, Kornblum HI. Glioblastoma Utilizes Fatty Acids and Ketone Bodies for Growth Allowing Progression during Ketogenic Diet Therapy. iScience. 13. August 2020;23(9):101453.

2. De Feyter HM, Behar KL, Rao JU, Madden-Hennessey K, Ip KL, Hyder F, Drewes LR, Geschwind JF, de Graaf RA, Rothman DL. A ketogenic diet increases transport and oxidation of ketone bodies in RG2 and 9L gliomas without affecting tumor growth. Neuro-Oncol. August 2016;18(8):1079–87.

3. Agnihotri S, Zadeh G. Metabolic reprogramming in glioblastoma: the influence of cancer metabolism on epigenetics and unanswered questions. Neuro-Oncol. Februar 2016;18(2):160–72.

4. Kim J whan, Tchernyshyov I, Semenza GL, Dang CV. HIF-1-mediated expression of pyruvate dehydrogenase kinase: a metabolic switch required for cellular adaptation to hypoxia. Cell Metab. März 2006;3(3):177–85.

5. Alcicek S, Dive I, Thomas D, Prinz V, Forster MT, Czabanka M, Weber K, Steinbach J, Ronellenfitsch M, Hattingen E, Pilatus U, Wenger K. 2D 1H sLASER long-TE and 3D 31P chemical shift imaging at 3T MRI for monitoring fasting-induced changes in brain tumor tissue. J Magn Reson Imaging. April 2024;

Images/Tables

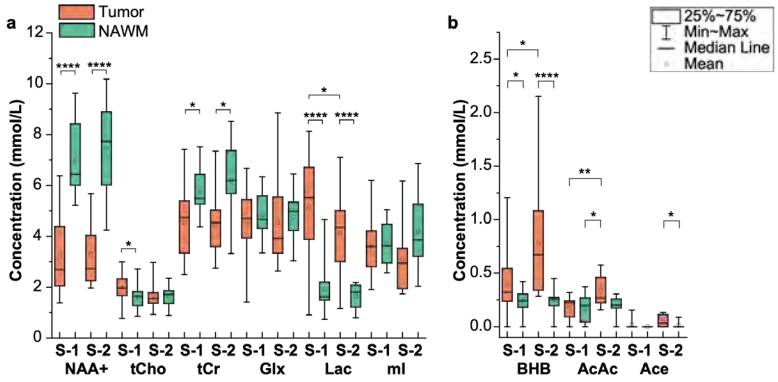

Figure 1. Box plots of metabolite concentrations from the tumor and NAWM at baseline (S-1) and after 72 hours of fasting (S-2). For statistical analysis, a Wilcoxon signed-rank test as a paired, non-parametric statistical hypothesis test was used. Results were considered significant at *P < 0.05; **P < 0.01; ***P < 0.001; ****P < 0.001. Following fasting, tumor tissue displayed a significant increase in ketone body concentrations, particularly β-OHB and acetoacetate. Lactate concentrations, on the other hand, decreased significantly in tumor tissue after fasting, consistent with reduced glycolytic flux under limited glucose availability. Choline levels, initially elevated in tumor tissue relative to contralateral white matter, decreased following fasting, suggesting reduced membrane turnover or altered phospholipid metabolism. Box-and-whisker plots are presented with minimum, maximum, interquartile ranges (25th and 75th percentiles), and median. NAA = N-Acetyl-Aspartate; tCho = total Choline; tCr = total Creatinine; Lac = Lactate, mI = myo-Inositol; BHB = Beta-Hydroxy-Butyrate; AcAc = Acetoacetate; Ace = Acetone.

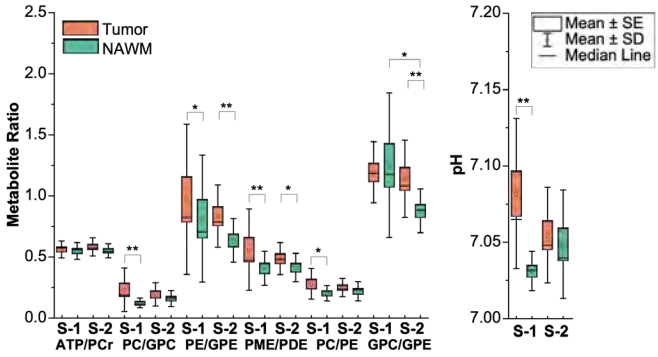

Figure 2. Box plots of AMARES estimated metabolite ratios from the tumor and NAWM at baseline (S-1) and after 72 hours of fasting (S-2). Phosphorus spectroscopy revealed preserved ATP/phosphocreatine ratios after fasting, indicating maintained energy homeostasis, while intracellular pH decreased, suggesting disrupted buffering capacity. Box-and-whisker plots are presented with minimum, maximum, interquartile ranges (25th and 75th percentiles), and median. PCr = phosphocreatine; PC = phosphocholine; PE = phosphoethanolamine; GPE = glycerophosphoethanolamine; GPC = glycerophosphocholine; ATP = adenosine triphosphate; Pi = inorganic phosphate.

---

411 Diagnostic Value of [18F]-Fluciclovine PET for Differentiating Tumor Progression from Treatment-Related Changes in IDH-Mutant Glioma

Kellen Vo Vu[1], Valentina Marulanda Corzo[1], Fabio Iwamoto[2], Peter Pan[2], Mary Welch MD[2], Benjamin Liechty[1], David J Pisapia[1], Joseph R Osborne[1], Ali Nabavizadeh MD[3], Ramon F Barajas[4], Jana Ivanidze[1]

[1]Weill Cornell Medicine, New York, NY, USA. [2]Columbia University, New York, NY, USA. [3]University of Pennsylvania, Philadelphia, PA, USA. [4]Oregon Health & Science University, Portland, OR, USA

Purpose

Differentiating true tumor progression from treatment-related changes (TRC) in the post-chemoradiotherapy setting is a persistent challenge in glioma imaging.[1] Although advanced MRI techniques such as perfusion, diffusion, and spectroscopy improve diagnostic accuracy, the overlap between progression and TRC remains a challenge for clinical decision-making.[2]

Amino acid PET provides complementary metabolic information that can clarify equivocal post-treatment findings.[3] Its diagnostic performance varies by tumor biology; for example, established tracers such as [18F]-FET demonstrate reduced accuracy in isocitrate dehydrogenase (IDH)-mutant gliomas compared to IDH-wildtype glioblastomas, possibly reflecting reduced and heterogenous amino acid metabolism in IDH-mutant tumors.[4] [18F]-Fluciclovine, a synthetic amino acid analog transported by upregulated amino acid transporters in glioma, offers high tumor-to-background contrast and correlates with both glioma grade and IDH mutation status on PET/MRI.[5] We aimed to assess the diagnostic accuracy of [18F]-Fluciclovine PET for distinguishing tumor progression from TRC among patients with IDH-mutant glioma in a real-world clinical setting.

Materials & Methods

In this retrospective IRB-approved study, we included biopsy-confirmed IDH-mutant glioma patients who underwent radiotherapy followed by [18F]-Fluciclovine PET/MRI or PET/CT for suspected recurrence. For PET/MRI, lesions were identified on post-contrast T1-weighted MRI acquired concurrently. For PET/CT, scans were fused to MRI obtained within one month. The maximum standardized uptake value (SUV_{max}) was measured within the enhancing lesion. Pathology served as the reference standard when available; otherwise, MRI follow-up determined progression of disease (PD) or TRC. Receiver operating characteristic (ROC) analysis evaluated SUV_{max} for differentiating PD from TRC, and the optimal cutoff was determined using Youden's index. Mean SUV_{max} was compared between PD and TRC groups using an independent t-test.

Results

Thirteen IDH-mutant glioma patients (54% female; mean age 43.6 ± 7.7 years), including four WHO 2, five WHO 3, and four WHO 4 tumors, underwent radiotherapy followed by [18F]-Fluciclovine PET (77% PET/MR, 23% PET/CT). Outcomes were determined by pathology (23%) or MRI (77%) a median of 51 days later. Across all grades, SUV_{max} showed good discrimination (AUC = 0.76) with an optimal SUV_{max} cutoff of 3.5 yielding 100% sensitivity and 50% specificity. Mean SUV_{max} was higher in PD than TRC (5.3 vs. 3.4, p = 0.11). In WHO 3–4 tumors only (n = 9), the diagnostic accuracy improved (AUC = 0.85) with an optimal SUV_{max} cutoff of 6.0 yielding 60% sensitivity and 100% specificity. Mean SUV_{max} was higher in PD than TRC (6.3 vs. 3.4, p = 0.05), supporting stronger discriminative performance in higher-grade disease.

Conclusion

[18F]-Fluciclovine PET demonstrated good overall diagnostic performance and excellent specificity within WHO grade 3–4 IDH-mutant gliomas for distinguishing PD from TRC. The observed AUCs (0.76 overall and 0.85 in high-grade disease) compare favorably with prior amino acid PET studies, where pooled AUCs for FET-, MET-, and DOPA-PET ranged from 0.80–0.90.[3] These results support further prospective validation of [18F]-Fluciclovine PET, particularly in hybrid PET/MRI workflows, to refine post-treatment response assessment and improve clinical confidence in IDH-mutant glioma management.

References

1. Abbasi AW, Westerlaan HE, Holtman GA, et al. Incidence of Tumour Progression and Pseudoprogression in High-Grade Gliomas: a Systematic Review and Meta-Analysis. *Clin Neuroradiol* 2018;28:401–11.
2. van Dijken BRJ, van Laar PJ, Holtman GA, et al. Diagnostic accuracy of magnetic resonance imaging techniques for treatment response evaluation in patients with high-grade glioma, a systematic review and meta-analysis. *Eur Radiol* 2017;27:4129–44.
3. Cui M, Zorrilla-Veloz RI, Hu J, et al. Diagnostic Accuracy of PET for Differentiating True Glioma Progression From Post Treatment-Related Changes: A Systematic Review and Meta-Analysis. *Front Neurol* 2021;12.
4. Maurer GD, Brucker DP, Stoffels G, et al. 18F-FET PET Imaging in Differentiating Glioma Progression from Treatment-Related Changes: A Single-Center Experience. *J Nucl Med* 2020;61:505–11.
5. Karlberg A, Pedersen LK, Vindstad BE, et al. Diagnostic accuracy of anti-3-[18F]-FACBC PET/MRI in gliomas. *Eur J Nucl Med Mol Imaging* 2024;51:496–509.

Images/Tables

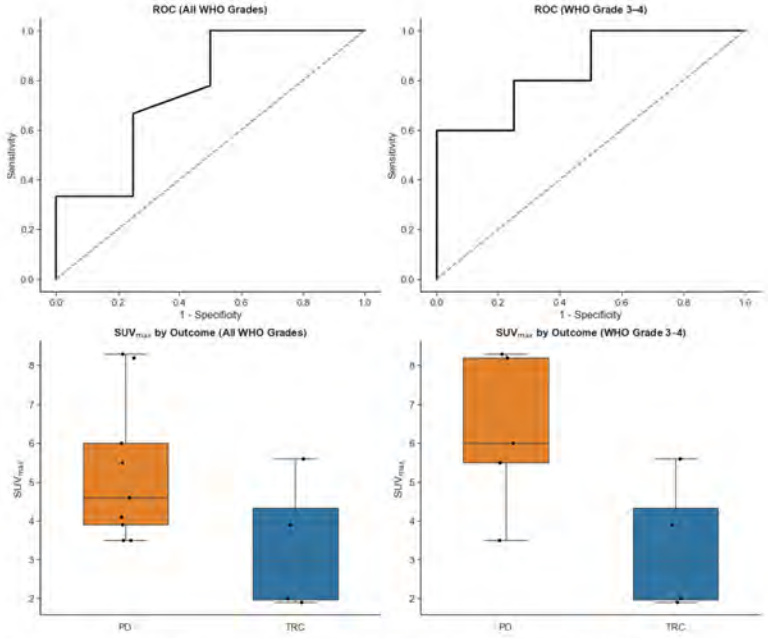

Figure 1. Receiver operating characteristic (ROC) curves and boxplots of [18F]-Fluciclovine PET performance for differentiating progression of disease (PD) from treatment-related changes (TRC) in IDH-mutant glioma. Top Row: ROC curves for all WHO grades (left) and for WHO grade 3–4 tumors only (right). Bottom Row: Corresponding distributions of lesion SUV_{max} by outcome.

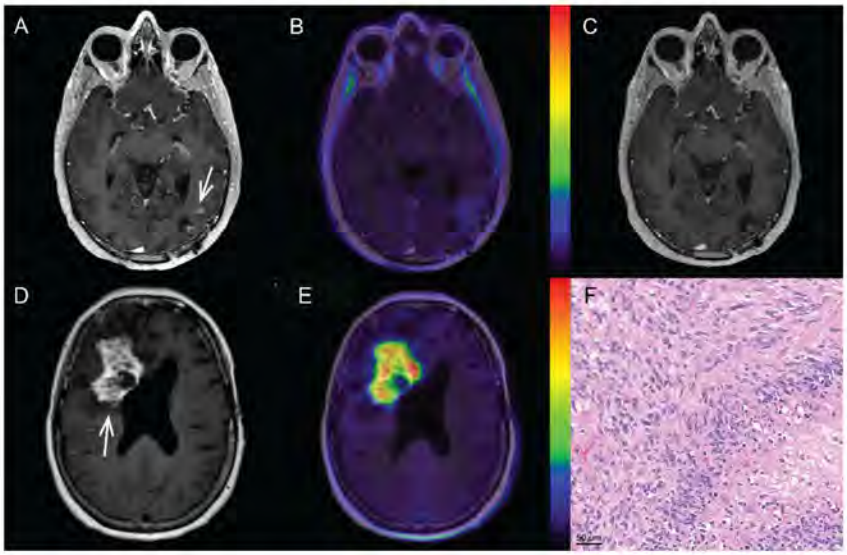

Figure 2. Representative [18F]-Fluciclovine PET/MRI and histopathology findings. (A–C) 48-year-old man with IDH-mutant WHO grade 4 astrocytoma following resection, proton radiotherapy, and temozolomide. Post-gadolinium T1-weighted MRI (A) shows increased nodular enhancement along the inferior margin of the left parietal resection cavity (arrow). Fused [18F]-Fluciclovine PET/MRI (B) demonstrates low-level uptake (SUV 1.9) consistent with treatment-related changes, with follow-up MRI 4 months later (C) showing near-complete resolution. (D–F) 51-year-old woman with recurrent IDH-mutant astrocytoma previously treated with chemoradiation and repeat resection demonstrating treatment-related changes, now on IDH inhibitor therapy. Post-gadolinium T1-weighted MRI (D) shows new heterogeneous enhancement along the right frontal resection cavity (arrow). Fused [18F]-Fluciclovine PET/MRI (E) demonstrates intense circumscribed uptake (SUV 8.3) consistent with viable tumor. Subsequent H&E-stained section (F) demonstrates a highly cellular population of atypical spindled tumor cells, mitotic figures, and palisading necrosis consistent with WHO grade 4 histological features (scale bar = 50 µm). Color bar indicates SUV windowing (0–15).

1007 Quantitative Arterial Spin-Labeling MRI Distinguishes Brain Tumor Reporting and Data System (BT-RADS) 3a from 4 in Treated High-Grade Gliomas

Alexander L Lindqwister MD[1], Sarkis Garo Bouladian[1], Brent Weinberg MD[2], Gordon Li MD[1], Patrick Wen MD[3], Michael Iv MD[1], Abdelkader Mahammedi MD[1]

[1]Stanford University, Palo Alto, CA, USA. [2]Emory University, Atlanta, GA, USA. [3]Harvard Cancer Center, Boston, MA, USA

Purpose

Differentiating viable tumor from treatment-related effects in patients with treated high-grade gliomas remains a major clinical challenge. We hypothesized that quantitative arterial spin-labeling (ASL) perfusion MRI can distinguish Tumor Reporting and Data System (BT-RADS) 3a lesions (treatment-related effects) from BT-RADS 4 lesions (recurrent or progressive tumor) in treated glioblastomas.

Materials & Methods

In this retrospective study, we evaluated patients with treated high-grade gliomas who underwent MRI with DSC and ASL perfusion after surgical resection, radiotherapy plus concomitant and adjuvant temozolomide between 2015–2024. Serial perfusion MRI served as the reference standard for determining recurrence versus treatment effect. Quantitative ASL-derived cerebral blood flow (CBF) images were analyzed by placing regions of interest (ROIs) on target lesions and the cerebellum for normalization, yielding absolute and normalized maximum CBF values. Target lesions were segmented on co-registered ASL and DSC images, with ROIs placed over the highest-perfusion focus (focal ROI), the entire hyperperfusing lesion (total ROI), and the contralateral cerebellum. For each lesion, mean normalized and standardized relative CBV and fractional tumor burden (FTB) were calculated, using rCBV thresholds of 1.0 and 1.75 to define low and high FTB. BT-RADS 3a and 4 lesions were compared using Mann–Whitney U tests. Receiver operating characteristic (ROC) analysis was performed for all continuous metrics, with optimal thresholds determined by Youden's J statistic. Longitudinal follow-up on serial MR perfusion examinations was used to determine stability (3a to 3a and 4 to 4), progression (3a to 4), or regression (4 to 3a).

Results

Out of 231 patients in the cohort (98 BT-RADS 3a and 133 BT-RADS 4), both absolute and normalized ASL-CBF showed highly significant separation between BT-RADS 3a and 4 lesions ($p < 0.001$). Normalized focal CBF values were most discriminative. Normalized maximum focal CBF values averaged 0.96 ± 0.60 (standard deviation) for BT-RADS 3a and 2.63 ± 1.49 for BT-RADS 4, yielding the highest area under the ROC curve (AUC = 0.91; 95% CI, 0.87-0.95). A threshold of 1.49 provided an accuracy of 0.85, sensitivity of 0.80, and specificity of 0.91. Absolute maximum focal CBF and normalized maximum total CBF values also demonstrated strong performance (0.87, 95% CI: 0.82-0.91, and 0.89, 95% CI: 0.85-0.93, respectively). Quantitative high FTB values had a positive correlation with both normalized maximum focal and total CBF lesions ($r = 0.49$ and $r = 0.50$, respectively, $P < 0.001$).

Conclusion

Quantitative ASL perfusion MRI effectively distinguishes BT-RADS 3a from BT-RADS 4 lesions in treated high-grade gliomas. These findings support incorporating ASL into routine glioma surveillance protocols and potentially into the BT-RADS and the Response Assessment in Neuro-Oncology (RANO) classification systems.

References

Falk Delgado, A., De Luca, F., van Westen, D., & Falk Delgado, A. (2018). Arterial spin labeling MR imaging for differentiation between high- and low-grade glioma—A meta-analysis. *Neuro-Oncology*, *20*(11), 1450–1461. https://doi.org/10.1093/neuonc/noy095

Ye, J., Bhagat, S. K., Li, H., Luo, X., Wang, B., Liu, L., & Yang, G. (2016). Differentiation between recurrent gliomas and radiation necrosis using arterial spin labeling perfusion imaging. *Experimental and Therapeutic Medicine*, *11*(6), 2432–2436. https://doi.org/10.3892/etm.2016.3225

Images/Tables

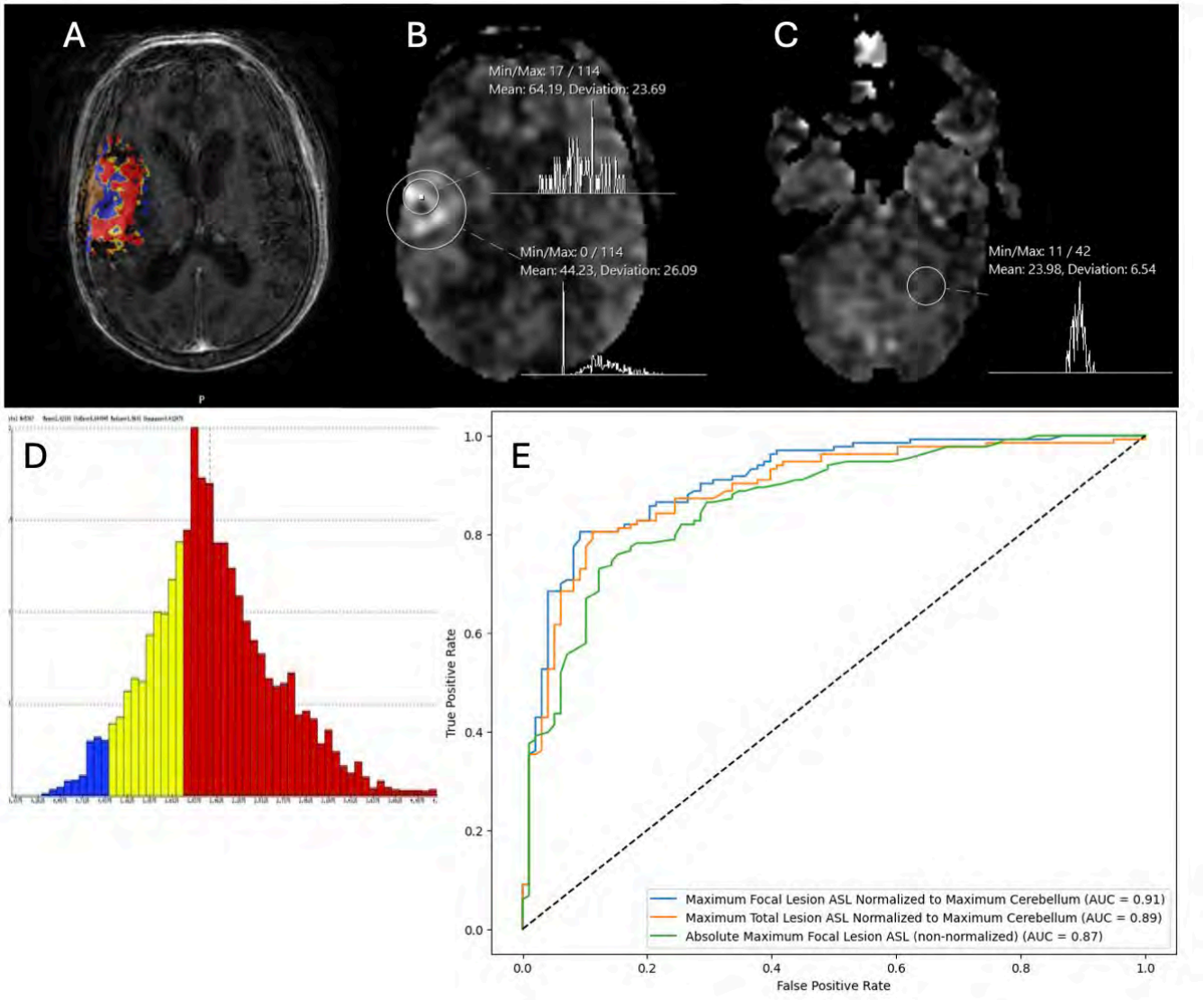

438 **Tumor Growth Rate (TGR) Analysis Predicts Survival in a Multicenter Phase II Study of the PARP Inhibitor Pamiparib (BGB-290) with Temozolomide in Recurrent IDH-Mutant Gliomas (ABTC-1801)**

Benjamin M Ellingson[1], Timothy F Cloughesy[1], Xiaobu Ye[2], Ashley Teraishi[1], Catalina Raymond[1], Sonoko Oshima[1], Francesco Sanvito[1], Patrick Y Wen[3], Tobias Walbert[4], Jian L Campian[5], Burt Nabors[6], Arati Desai[7], Antonio Omuro[8], Serena Desideri[2], Stuart Grossman[2], Ranjit S Bindra[8], David Schiff[9]
[1]University of California Los Angeles, Los Angeles, CA, USA. [2]Johns Hopkins University, Baltimore, MD, USA. [3]Dana-Farber Cancer Institute, Boston, MA, USA. [4]Hermelin Brain Tumor Center, Henry Ford Health, Detroit, MI, USA. [5]Washington University School of Medicine, St. Louis, MO, USA. [6]University of Alabama at Birmingham, Birmingham, AB, USA. [7]University of Pennsylvania Perelman School of Medicine, Philadelphia, PA, USA. [8]Yale School of Medicine, New Haven, CT, USA. [9]University of Virginia School of Medicine, Charlottesville, VA, USA

Purpose

Mutations in isocitrate dehydrogenase (IDH) leads to production of the oncometabolite 2-hydroxygluterate (2-HG), which suppresses homologous recombination and confer poly (ADP-ribose) polymerase (PARP) inhibitor sensitivity. Pre-clinical studies demonstrate that IDH-mutant gliomas are sensitive to PARP inhibitors. Tumor growth rate (TGR) assessment offers a novel approach to evaluate treatment effects beyond traditional response criteria, particularly relevant for cytostatic therapies. Here, we report the change in TGR in a multicenter phase Ib/II study of the PARP inhibitor pamiparib with low-dose temozolomide in recurrent IDH-mutant gliomas.

Materials & Methods

In this Adult Brain Tumor Consortium multicenter phase Ib/II clinical trial (ABTC-1801; ClinicalTrials.gov #NCT03914742), patients with recurrent IDH-mutant gliomas were enrolled in three cohorts: Arm A (grade 2-3, failed ≥2 alkylators), Arm B (grade 2-3, failed single alkylator ≥12 months prior), and an exploratory cohort of grade 4 IDH-mutant patients. All patients received pamiparib 60 mg twice daily with temozolomide 20 mg daily. Tumor growth rates were assessed using serial MRI FLAIR measurements before and during treatment. Growth rate inhibition was defined as a decrease in TGR after treatment compared to pre-treatment growth rate.

Results

Among evaluable patients in the dose expansion cohorts enrolled between February 2020 and March 2022, 5/11 (45.5%) in Arm A, 6/20 (30%) in Arm B, and 3/10 (30%) in the grade 4 arm demonstrated a decrease in TGR during treatment relative to pre-treatment TGRs. Cox regression analysis showed that higher post-treatment TGR (All patients, *HR=1.0065 [95%CI:1.0031-1.01], P=0.0002*; Arms A-B, *HR=1.0068 [95%CI:1.0027-1.011],*

P=0.0012) and an increase in TGR after treatment were significantly associated with shorter survival for all patients as well as when only including grades 2-3 gliomas in Arms A-B (All patients, *HR=1.007 [95%CI:1.0032-1.0107], P=0.0003*; Arms A-B, *HR=1.008 [95%CI:1.0034-1.0126], P=0.0006*). Pre-treatment TGRs were not prognostic for survival. Patients with TGR change <+25 mL/6 months had significantly improved survival compared to those with TGR >+25 mL/6 months (All patients, *HR=4.946, P=0.0044*; Arms A-B, *HR=3.210, P=0.0108*).

Conclusion

Despite limited radiographic response rates in the primary study, many patients demonstrated growth rate inhibition. TGR changes were significantly associated with survival outcomes, suggesting that growth stabilization may be an important metric for assessing treatment benefit in IDH-mutant gliomas.

References

Schiff D, Ye X, Li J, Ellingson BM, Wen PY, Walbert T, Campian J, Burt Nabors L, Ozer BH, Desai A, Omuro A, Desideri S, Danda N, Grossman S, Bindra RS. Phase I/II and Window-of-Opportunity Study of Pamiparib and Metronomic Temozolomide for Recurrent IDH Mutant Gliomas. Neuro Oncol. 2025 Oct 16:noaf246. doi: 10.1093/neuonc/noaf246. Epub ahead of print. PMID: 41099363.

Images/Tables

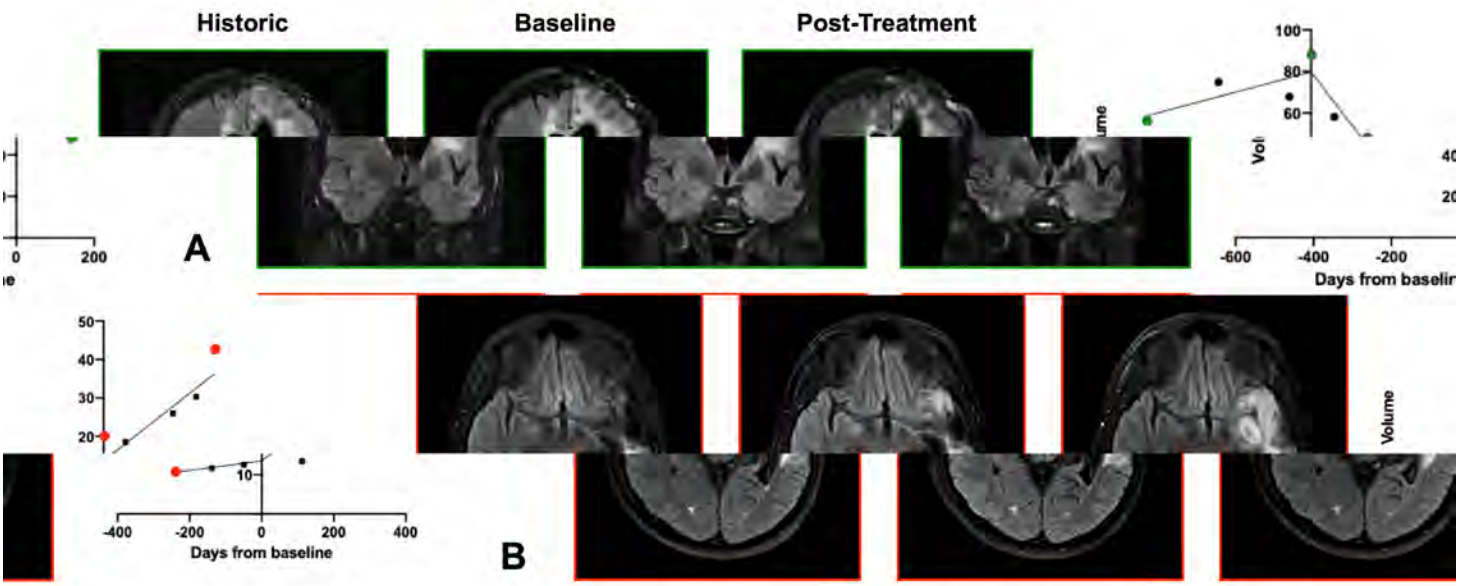

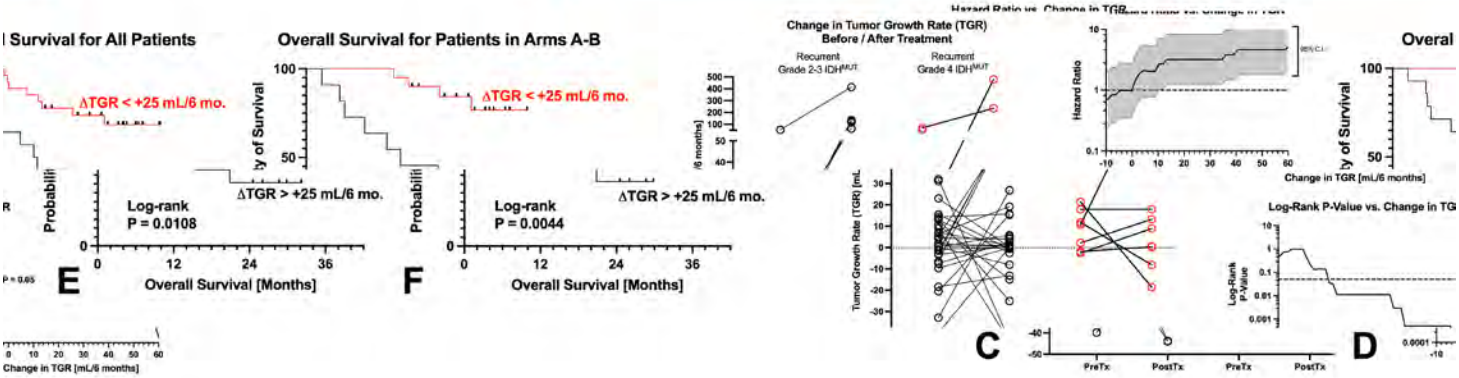

1060 Association of T2-FLAIR Mismatch Volumetrics with Survival in IDH-Mutant Gliomas: Preliminary Results

Aman Jaiswal MD, Andres F Rodriguez MD, David E Timaran MD, Santiago Aristizabal-Ortiz MD, Mario E Mahecha MD, Laura Ocasio MD, Roy F Riascos MD

University of Texas Health Science Center at Houston, Houston, Texas, USA

Purpose

The T2-FLAIR mismatch sign has been described as a characteristic imaging feature of IDH-mutant, 1p/19q-intact astrocytomas, with proposed diagnostic and prognostic implications (1,2). However, evidence regarding its relationship to clinical outcomes remains limited and heterogeneous [3]. This study aimed to evaluate whether the presence or volumetric extent of the T2-FLAIR mismatch correlates with survival or recurrence outcomes in patients with IDH-mutant gliomas.

Materials & Methods

We retrospectively analyzed a cohort of 20 patients with histologically confirmed IDH-mutant gliomas who underwent preoperative MRI. Lesion volumes were segmented on T2-weighted and FLAIR sequences to derive a quantitative measure of mismatch extent. Clinical data, including seizure presentation and Ki-67 proliferation index, were recorded. Overall survival (OS) and recurrence-free survival (RFS) were assessed using Kaplan–Meier analysis, and differences between mismatch-positive and mismatch-negative groups were compared with log-rank tests. Correlations between volumetric and clinical variables were evaluated using Pearson and Spearman coefficients, with statistical significance set at $p < 0.05$. Follow-up extended to a maximum of 135 months.

Results

Twenty patients were included (X male, Y female; mean age Z years). Twelve (60%) demonstrated the T2-FLAIR mismatch sign. Mean T2 lesion volume was 36.8 ± 35.0 cm^3, mean FLAIR volume 17.6 ± 22.6 cm^3, and mean mismatch extent 19.1 ± 42.8 cm^3. Mismatch volume strongly correlated with T2 lesion size ($r = 0.85$, $p < 0.001$) and inversely with FLAIR volume ($r = –0.58$, $p = 0.008$).

Clinically, mismatch was more common among patients presenting with seizures (66.7% vs 50%), though not statistically significant ($p = 0.50$) Kaplan–Meier analysis revealed no significant difference in OS between mismatch-positive and mismatch-negative tumors (mean 94.5 vs 45.0 months, log-rank $p = 0.78$). RFS similarly showed no difference (mean 44.0 vs 57.0 months, $p = 0.98$). Neither the presence nor volumetric extent of mismatch correlated with OS or RFS ($p > 0.05$).

Taken together, volumetric, clinical, and survival analyses demonstrated no statistically significant associations between the T2-FLAIR mismatch and outcomes in this exploratory sample. A non-significant trend toward longer survival in mismatch-positive cases may warrant confirmation in larger, prospective studies.

Conclusion

In this preliminary cohort of IDH-mutant gliomas, the T2-FLAIR mismatch sign extent differences were not associated with overall or recurrence-free survival. While these findings do not support the mismatch as an independent prognostic biomarker, the consistent imaging-volume relationships suggest biological coherence of the measure. Further studies with larger, molecularly stratified datasets are needed to clarify the clinical relevance of this imaging phenotype.

References

(1) Broen MPG, et al. The T2-FLAIR mismatch sign as an imaging marker for non-enhancing lower-grade glioma. Neuro Oncol. 2018;20(2):295-302.
(2) Deguchi S, et al. Clinicopathological analysis of T2-FLAIR mismatch sign in lower-grade gliomas. Sci Rep. 2020;10:10113.
(3) Pinto C, et al. T2-FLAIR mismatch sign: a roadmap of pearls and pitfalls. Eur Radiol. 2021;31(2):1048-1058.
(4) Van Garderen KA, et al. Longitudinal characteristics of T2-FLAIR mismatch in IDH-mutant gliomas. Neuro-Oncol Adv. 2023;5(1):vdad149.
(5) Ozono I, et al. Super T2-FLAIR mismatch sign: a prognostic imaging biomarker for non-enhancing astrocytoma, IDH-mutant. J Neuro-Oncol. 2024;169:571-579.

Images/Tables

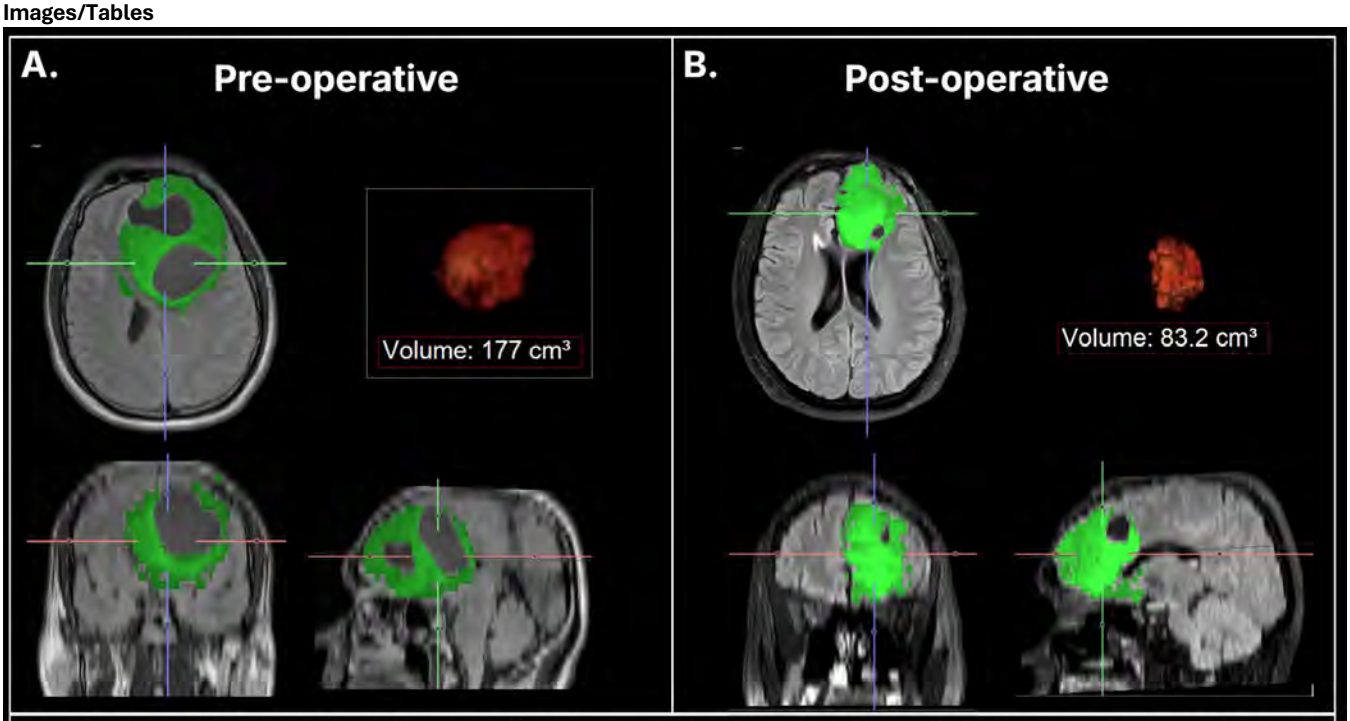

Figure 1. Preoperative and postoperative volumetric assessment of an IDH-mutant glioma. Axial, coronal, and sagittal FLAIR images with 3D segmentations (green) demonstrate the tumor burden before and after surgical resection (panel A). The preoperative tumor volume measured 177 cm^3, which decreased to 83.2 cm^3 following surgery (panel B). The 3D reconstructions (red) illustrate the spatial extent of the lesion and confirm a substantial reduction in tumor volume postoperatively. These volumetric estimates were used to evaluate residual disease burden in the study cohort.

1124 Spatial Heterogeneity of Cellular Composition and Stem Cell Markers Across MRI-Defined Tumor Regions in Glioblastoma

Benjamin Chao BS, Fitzgerald Kyereme BS, Savannah R Duenweg PhD, Aleksandra Winiarz BS, Allison K Lowman BS, Daniel Kim BS, Hope M Reecher BS, Mrina Mtenga BS, Adam Lahrache BS, Michael Barrett, Jennifer Connelly MD, Max Krucoff MD, Jennifer Tuscher PhD, Rupen Desai MD, Samuel A Bobholz PhD, Peter S LaViolette PhD
Medical College of Wisconsin, Milwaukee, WI, USA

Purpose

Glioblastoma (GBM) is an aggressive malignant tumor with a median survival of less than 18 months.[1] GBM is pathologically heterogenous and spatially diffuse, adding to the clinical challenge of assessing the fullest extent of tumor burden using T1-weighted images post contrast.[2] These challenges are further compounded by the effect of radiation and antiangiogenic therapy, which often impacts clinician's ability to assess tumor extent or recurrence on clinical imaging via T1-weighted contrast enhancing margins.[3] We hypothesize that contrast enhancing (CE), FLAIR

hyperintense (FH), and MR-Negative (MR-N) regions harbor distinct cellular compositions of known tumor associated markers which can be quantified using MRI-aligned, segmented digital immunohistochemical histology.

Materials & Methods

This study used data from our neuro-oncology brain bank to evaluate for potential relationships between post-treatment imaging and pathological findings, using autopsy tissue aligned to MRI as ground truth. Retrospective analyses were completed for 60 primary GBM patients with clinical MR images, segmented into CE, FH, and MR-N regions. Large tissue sections were sliced and collected at autopsy, paraffin-embedded, and stained for H&E (cell morphometry), SOX2 (pluripotency), Ki67 (mitotic activity), and CD68 (immune cells). Slides were then digitized at 40x and computationally segmented for cellularity, SOX2 positivity ratio, Ki67 positivity ratio, CD68 positivity ratio, and nuclear eccentricity. Tissue information was then aligned to the last MRI obtained prior to death using custom in-house software that uses control points to define a non-linear transform to account for tissue shrinkage during formalin fixation. Tissue data was then averaged per subject across aligned samples within CE, FH, and MR-N regions. Pairwise repeated measures t-tests were used to compare pathological features within MRI regions of interest.

Results

Cell density within CE and FLAIR was higher than MR-N (CE: t=+2.88, p<0.01, FH: t=+2.14, p=0.04), with CE also showing increased cellularity relative to FLAIR (t=+2.22, p=0.03). SOX2 positivity was higher in the CE region relative to the MR-N region (t=+2.43, p=0.02), and Ki67 positivity was higher in FH relative to MR-N (t=+2.49, p=0.02).

Conclusion

This study assessed pathological characteristics of common MR-defined regions of interest at autopsy, elucidating the microenvironmental landscape of late-term post-treatment GBM. A reduction in cellularity was observed in regions further from CE, following the expected trend of decreasing infiltration further from the primary tumor mass. SOX2 and Ki67 showed differences between CE/FLAIR and MR negative regions but did not show differences between CE and FLAIR themselves, perhaps indicating features more sensitive to non-enhancing tumor presence extend beyond the angiogenic margin. Future studies investigating transcriptomic and multiplex immunohistochemical tissue samples aligned to MRI could allow for single-cell characterization of the true tumor landscape and may provide novel therapeutic targets for GBM.

References

1. Price M, Ballard C, Benedetti J, et al. CBTRUS statistical report: primary brain and other central nervous system tumors diagnosed in the United States in 2017–2021. *Neuro Oncol* 2024;26(suppl 6):vi1–vi85 CrossRef Medline

2. Lasocki A, Gaillard F. Non-contrast-enhancing tumor: a new frontier in glioblastoma research. *AJNR Am J Neuroradiol* 2019;40:758–65 CrossRef Medline

3. Autry A, Phillips JJ, Maleschlijski S, et al. Characterization of metabolic, diffusion, and perfusion properties in GBM: contrast-enhancing versus non-enhancing tumor. *Transl Oncol* 2017;10:895–903 CrossRef Medline

Images/Tables

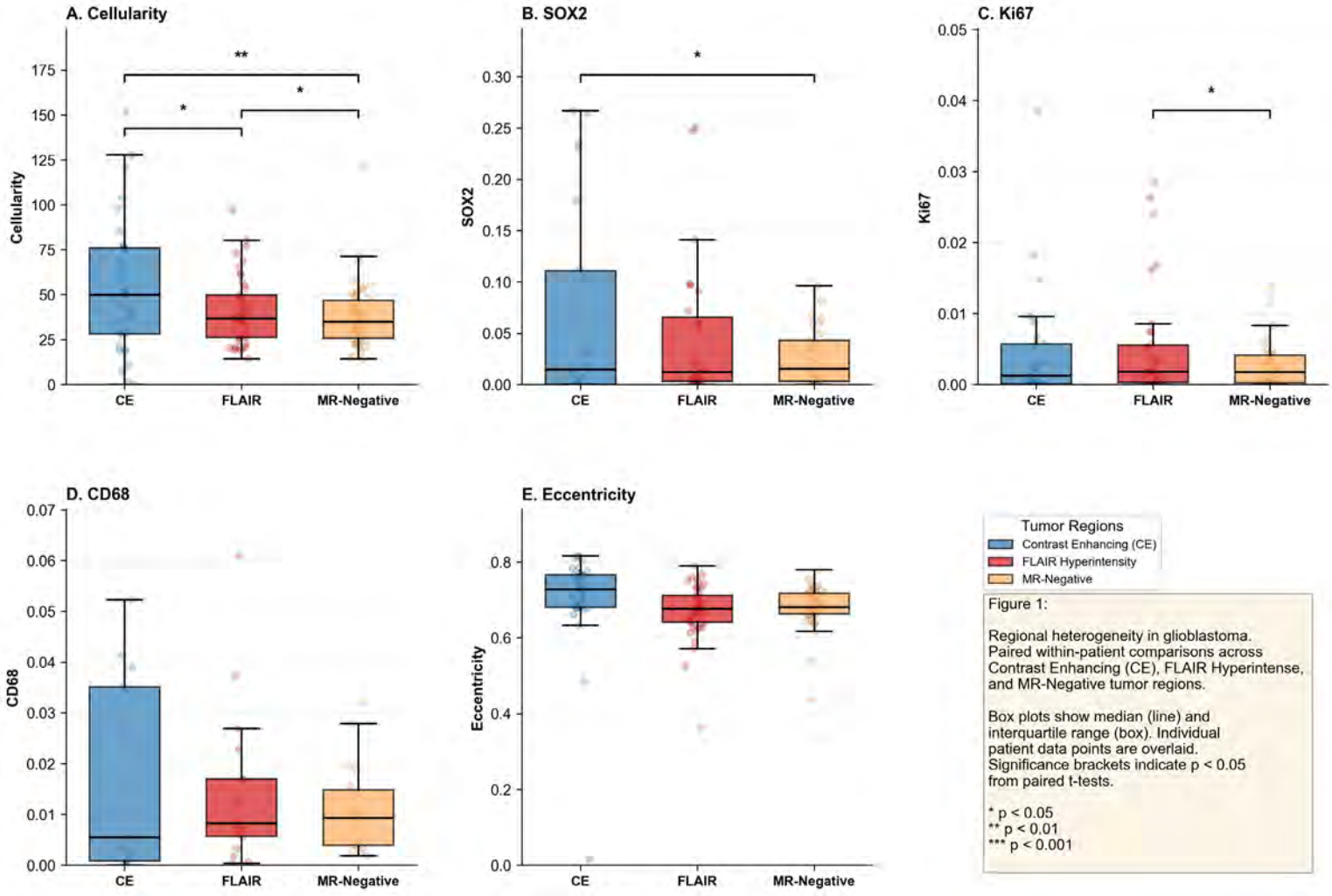

289 Perfusion parameters at the first post-radiotherapy scans correlate with survival in patients with newly diagnosed glioblastoma.

Michael Zhao MD[1], Melissa A Prah BS[2], Zhou Lan PHD[1], Kathleen M Schmainda PHD[2], Raymond Y Huang MD, PHD[1]
[1]Mass General Brigham, Boston, MA, USA. [2]Medical College of Wisconsin, Milwaukee, WI, USA

Purpose

In evaluation of glioblastoma (GBM), dynamic susceptibility contrast (DSC) perfusion-weighted magnetic resonance imaging (pMRI) has shown promise in its ability to differentiate between disease progression and pseudoprogression, and parameters have been shown to correlate with overall survival and progression-free survival. However, how DSC can be incorporated into response assessment in neuro-oncology (RANO) 2.0 criteria and its prognostic value in this context is less clear. Our purpose was to evaluate the added prognostic value of DSC perfusion parameters on survival in a large cohort with newly diagnosed GBM stratified based on RANO 2.0 criteria for progressed or not-progressed disease.

Materials & Methods

We retrospectively analyzed patients with newly diagnosed GBM treated with standard resection and chemoradiation. Patients were identified who had standard MRI and gradient or spin echo single-dose DSC pMRI performed at two timepoints: a baseline scan <8 weeks after radiation therapy (T1), and a follow-up scan at ≤16 weeks after radiation therapy (T2). Patients were divided into progressed and not-progressed groups based on the percentage change in enhancing tissue volume between time point 1 (T1) and time point 2 (T2) using RANO 2.0 thresholds for progression (≥40% and <40% increase from T1 to T2). For each group, the perfusion parameters fractional tumor burden (FTB), percentage signal recovery (PSR), standardized leakage parameter (sK2), and average standardized relative cerebral blood volume (srCBV) were calculated for the T1 and T2 scans. The prognostic value of each parameter for overall survival was assessed by time-dependent AUC.

Results

A total of 148 patients were divided into progressed (N=35) and not-progressed groups (N=113). Our preliminary analysis demonstrates that both FTB and PSR have predictive ability for survival. At T1 scans, FTB and PSR were correlated with worse survival in the not-progressed group. In contrast, in the progressed group, no statistically significant association was found between perfusion parameters and survival. Final statistical analysis and results for additional subgroups will be presented.

Conclusion

We find that perfusion parameters from the first post-radiation MRI (RANO 2.0 baseline) provide prognostic information. Specifically, the parameters FTB and PSR, appear to be markers for survival at the baseline scan post-radiation in patients who do not progress at follow-up, whereas no perfusion parameter was found to predict survival in patients who do progress at follow-up. This may have practical applications for the interpretation of pMRI in the context of RANO 2.0 in the early post-radiation setting and potentially allow for improved prognostication and earlier intervention.

References

Wen PY, Bindra RS, de Groot JF, et al. Updated Response Assessment in Neuro-Oncology (RANO 2.0) Criteria for High-Grade Glioma: A Report From the RANO 2.0 Working Group. *J Clin Oncol* 2023;41:4578–89. DOI: https://doi.org/10.1200/JCO.23.01059
Zhang J, Lei Y, Ma X, et al. Perfusion magnetic resonance imaging in the differentiation between glioma recurrence and pseudoprogression: a systematic review, meta-analysis and meta-regression. *Quant Imaging Med Surg* 2022;12:4805–22. DOI: https://doi.org/10.21037/qims-22-32
Qi D, Li J, Quarles CC, et al. Assessment and prediction of glioblastoma therapy response: challenges and opportunities. *Brain* 2023;146:1281–98. DOI: https://doi.org/10.1093/brain/awac450

Images/Tables

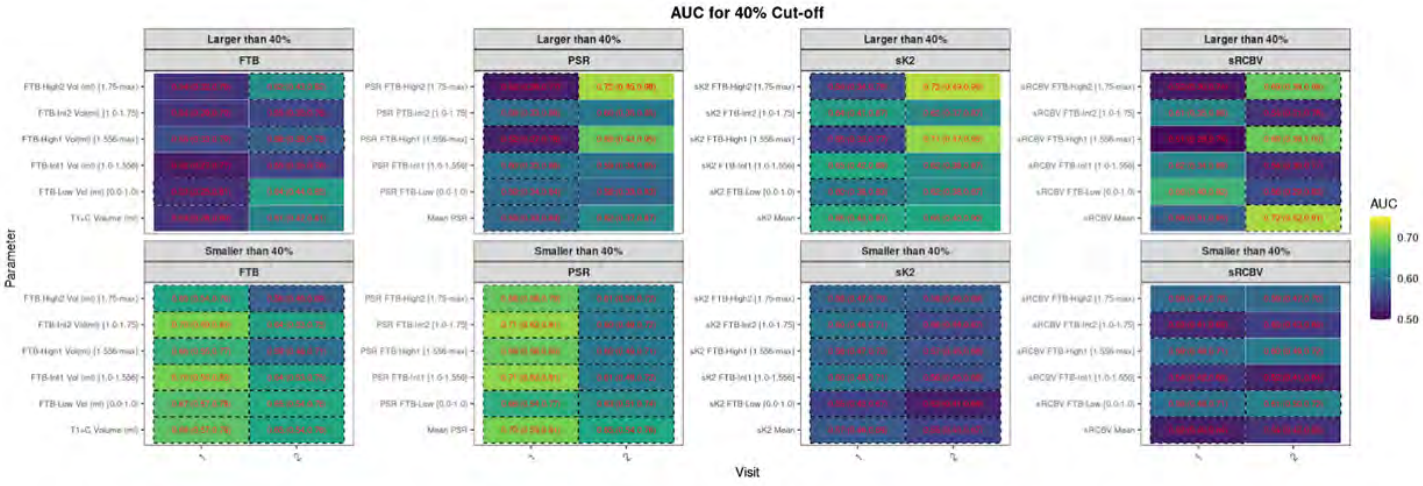

The value in each cell is the time-dependent AUC for overall survival of each parameter (95% confidence interval in brackets). Dashed cell borders indicate correlation with death and no cell borders indicate correlation with survival.
Larger than 40% group (progressed group): patients with ≥40% increase in enhancing tissue volume between visit 1 (T1) and visit 2 (T2); Smaller than 40% group (not-progressed group): patients with <40% increase in enhancing tissue between T1 and T2.
FTB: fractional tumor burden [srCBV low cutoff - srCBV high cutoff]; T1+C: Enhancing tissue volume on T1 postcontrast sequences; PSR: percentage signal recovery within each FTB group; sK2: leakage parameters within FTB group; srCBV: mean standardized relative cerebral blood volume within each FTB group.

725 Effect of deep learning reconstruction on quantitative analysis in brain tumors with diffusion-weighted imaging and dynamic susceptibility contrast imaging

E-Nae Cheong PhD[1], Geunu Jeong MD[2], Celina Nahyun Jo MD[3], Ho Sung Kim MD, PhD[1], Ji Eun Park MD, PhD[3]

[1]Asan Medical Center, Seoul, Seoul, Korea, Republic of. [2]AIRS Medical Inc., Seoul, Seoul, Korea, Republic of. [3]Johns Hopkins University, Baltimore, Maryland, USA

Purpose

The impact of deep learning reconstruction (DLR) on quantitative metrics from physiologic MRI, including diffusion-weighted imaging (DWI) and dynamic susceptibility contrast (DSC), remains uncertain. The purpose of this study was to evaluate the impact of DLR on quantitative parameters derived from DWI and DSC in patients with brain tumors.

Materials & Methods

This retrospective study included 113 MRI examinations from 62 patients with brain metastases (61.1 years; 53.2% male) undergoing stereotactic radiosurgery with two consecutive scans including DWI and DSC perfusion imaging. DWI and DSC images were reconstructed at three DLR levels (high, medium, and low using a commercially available software). The mean ADC and rCBV were extracted from the tumor mask of each of the four maps (original, low, medium, and high DLR) for each acquisition. For DWI, the b = 0 and b = 1000 signal intensity were also extracted from the three DLR images, while time-series data were extracted from the corresponding DSC images. Agreement on apparent diffusion coefficient (ADC) and rcerebral blood volume (CBV) values between original and DLR images was tested using limits of agreement, repeatability coefficient (RC), and concordance correlation coefficient (CCC). For DSC time-series, signal-to-noise ratio (SNR), root mean square error (RMSE), mean absolute error (MAE), and normalized cross-correlation (NCC) were computed within tumor masks. DWI comparisons used mean signal intensity at b = 0 and b = 1000.

Results

ADC and CBV values showed no significant differences between original and DLR images ($p > .05$). RCs demonstrated high reproducibility across DLR levels for ADC (38.6, 38.4, and 38.2) and for CBV (0.89, 0.93, and 1.09). On DWI, b=1000 signals were more reproducible than b=0. DSC analysis showed the best noise reduction with high-level DLR (lowest RMSE and MAE of DSC) without affecting CBV quantification. The SNR was highest in the original images (146.6 ± 73.7), followed by the low (139.7 ± 65.1), medium (139.1 ± 65.0), and high level (138.8 ± 65.0) DLR.

Conclusion

DLR effectively reduced noise in DWI and DSC while preserving quantitative values. DLR may enable robust physiologic imaging and faster acquisitions in brain tumor MRI.

References

1. Jeong G, Kim H, Yang J, Jang K, Kim J. All-in-one deep learning framework for mr image reconstruction. arXiv preprint arXiv:240503684 2024.

2. Choi Y, Ko JS, Park JE, et al. Beyond the Conventional Structural MRI: Clinical Application of Deep Learning Image Reconstruction and Synthetic MRI of the Brain. Invest Radiol 2025;60(1):27–42.

3. Hanamatsu S, Murayama K, Ohno Y, Yamamoto K, Yui M, Toyama H. Deep learning reconstruction for brain diffusion-weighted imaging: efficacy for image quality improvement, apparent diffusion coefficient assessment, and intravoxel incoherent motion evaluation in in vitro and in vivo studies. Diagn Interv Radiol 2023;29(5):664–673.

Images/Tables

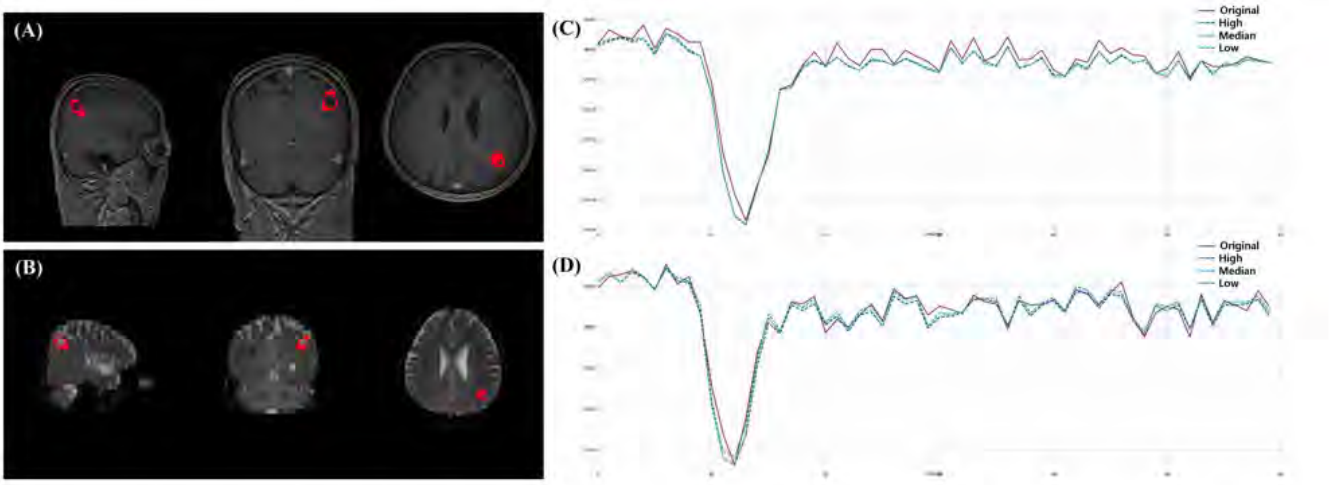

Representative examples of DSC time-series curves from original and DLR reconstructed images.

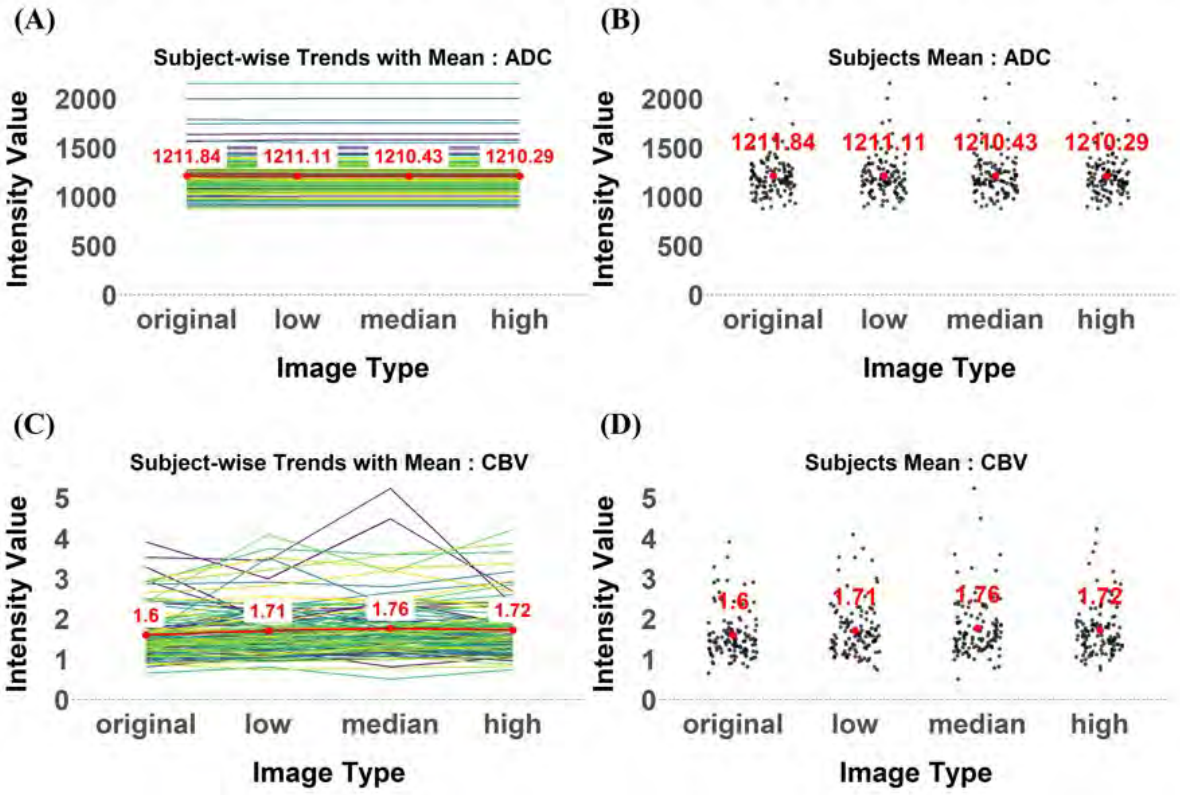

Comparison of ADC and CBV between original images and low, medium, and high levels of deep learning r econstruction (DLR). Subject-wise trends show individual intensity values for ADC (A) and CBV (C) across original, low, median, and high DLR images. The bold red numbers represent the mean intensity values across all subjects for each image type. Scatter plots of individual subject intensity values for ADC (B) and CBV (D) display the distribution and variation between image types. Mean values are annotated in red above each group. These results illustrate how different levels of DLR denoising affect the intensity values of ADC and CBV.

Scientific Abstract Power Pitches & Luminary Speaker: Neuroimaging: Innovations in AI & Biomarkers

1:00 - 2:00pm Monday, 18th May, 2026

1208 Fetal Endovascular Management of Vein of Galen Malformation: A Systematic Review and Technical Overview

Ali Mortezaei MD[1], Abhishek Saha[2], Sai Sanikommu MD[3], Amirhossein Zare MD[4], Ahmed Abdelsalam MD[3], Khaled Taghlabi[5], Bardia Hajikarimloo MD[6], Ibrahim Mohammadzadeh[4], Adam A. Dmytriw MD[7], Amir H. Faraji MD[5], Samer K. Elbabaa[8], Redi Rahmani[9], Robert M. Starke MD[3]

[1]Gonabad University of Medical Scieneses, Gonabad, Khorasan Razavi, Iran, Islamic Republic of. [2]University of Oxford, Oxford, Oxford, United Kingdom. [3]University of Miami, Miami, Florida, USA. [4]Tehran University of Medical Scieneses, Tehran, Tehran, Iran, Islamic Republic of. [5]Houston Methodist, Houston, Texas, USA. [6]University of Virginia, Charlottesville, Virginia, USA. [7]Massachusetts General Hospital & Brigham and Women's Hospital, Boston, Massachusetts, USA. [8]Arnold Palmer Hospital for Children, Orlando, Florida, USA. [9]University of Louisville, Louisville, Kentucky, USA

Purpose

To evaluate the feasibility, safety, and outcomes of prenatal in-utero embolization (IUE) for fetal Vein of Galen malformation through a systematic review of reported cases.

Materials & Methods

A systematic literature review was conducted following PRISMA guidelines using PubMed/MEDLINE, Scopus, Web of Science, and Google Scholar databases. Eligible reports included cases of fetal VOGM treated with IUE with documentation of maternal, fetal, perinatal, and postnatal outcomes. Data extraction was performed by two independent reviewers, with discrepancies resolved by a third reviewer. Quantitative variables were descriptively pooled.

Results

Across identified cases, the mean maternal age was 29.7 years and BMI 31.4. Diagnosis occurred at an average gestational age of 33 3/7 weeks, and intervention was performed at 34 2/7 weeks. The mean VOGM diameter was 26.4 mm. Following embolization, the falcine sinus diameter decreased from 10.3 mm to 8.7 mm, and fetal cardiac output dropped from 2745.4 to 1811.5 mL/min (mean reduction 35.5%). No procedure-related distal embolization occurred. Despite technical success, 37.5% (3/8) required neonatal embolization. Post-IUE fetal MRI showed hemorrhage in 25% and cerebral edema in 12.5%, without ischemic injury. At last follow-up, 60% demonstrated normal cardiac function and 80% were neurologically intact, while overall mortality was 44.4%. Greater reductions in cardiac output (≥40%) and falcine sinus size (≥20%) were associated with improved survival, whereas lack of neonatal embolization and unscheduled delivery correlated with poorer outcomes.

Conclusion

Fetal in-utero embolization for VOGM appears technically achievable and provides measurable improvements in intrauterine hemodynamics. Nonetheless, perinatal risk remains considerable, and most patients still require postnatal endovascular treatment. Given that reported experiences originate from highly specialized centers and lack comparator groups, these findings should be viewed as preliminary. Broader multicenter collaborations and prospective comparative studies are warranted to validate the safety, reproducibility, and long-term efficacy of this emerging prenatal intervention.

References

Orbach DB, Shamshirsaz AA, Wilkins-Haug L, et al. In Utero Embolization for Fetal Vein of Galen Malformation. *JAMA*. 2025;334(10):878-885. doi:10.1001/jama.2025.12363

Ruano R, Abdelsalam A, Harris S, et al. Ultrasound-guided transuterine coil embolization of a Vein of Galen malformation. *Clin Neurol Neurosurg*. 2025;249:108682. doi:10.1016/j.clineuro.2024.108682

Cruz-Martinez R, Mendez A, Lara-Avila L, Monroy A, Coronel F, Cruz-Martinez M. P20.08: Percutaneous fetal intracranial venous embolization in a case with vein of Galen aneurysmal malformation and hydrops. *Ultrasound in Obstetrics & Gynecology*. 2014;44(S1):306-306. doi:10.1002/uog.14401

Gowda M, Krishnaraj A, Ambalakkuthan M, Chinta N, Selvan T. Reversal of Fetal Compromise Following In Utero Treatment of Vein of Galen Malformation Using Glue. *Prenat Diagn*. 2024;44(11):1367-1371. doi:10.1002/pd.6662

Naggara O, Stirnemann J, Boulouis G, et al. Prenatal treatment of a vein of Galen malformation by embolization and 1-year follow-up. *Am J Obstet Gynecol*. 2024;230(3):372-374. doi:10.1016/j.ajog.2023.11.1248

Images/Tables

Table 3. Anatomical, surgical, obstetric details of the included studies	
Outcomes	Value
VOGM, mm	26.4 (11.5)
Falcine sinus diameter, mm	
Before embolization	10.3 (4.1, 7-14)
After embolization	8.7 (1.35, 7-11)
Cardiac output, mL/min	
Before embolization	2745.4 (699.5, 2137-4341)
After embolization	1811.5 (326, 1385-1942)
Reduction, %	35.5 (13.4, 16-46)
Distal embolization	0% (0/9)
Neonatal embolization	37.5% (3/8)
Intervention to delivery, day	16.3 (12.3, 7-37)
Gestational age at delivery, week	36 2/7 (35 3/7 - 39)
Delivery scheduling	
Scheduled	62.5% (5/8)
Unscheduled	37.5% (3/8)
Delivery mode	
Vaginal	50% (4/8)
Cesarean	50% (4/8)
Fetal MRI pathology after embolization	
Ischemic brain injury	0% (0/8)
Intracranial hemorrhage or hematoma	25% (2/8)
Edema	12.5% (1/8)
Clinical outcome at last follow-up	
Normal cardiac function	60% (3/5)
Neurodevelopmental intact	80% (4/5)
Neurodevelopmental delay	20% (1/5)
Sepsis	11.1% (1/9)
Mortality	44.4% (4/9)
VOGM, Vein of Galen Malformation; Continuous variables are reported as mean (SD, range), and categorical variables are reported as % (n/N)	

1085 Long-Term Angiographic Outcomes and Complications of Flow Diverters in Intracranial Aneurysm Treatment

Theodore Liu MS3[1], Ammar Alam DCS[1], Rebecca Thornhill PhD[1], Richard Aviv PhD[2], Wassim Elmasry MD[1], Ahsas Nagee MD[1], Victoria Smyth BSc[3], Logan Milne BSc[3], Rajiv Hira MD MPH[1], Thorsteinn Gunnarsson MD MSc PhD[4], Paula Klurfan MD MSc[5], Robert Fahed MD MSc[1], Brian Drake MD FRCSC[1], Marlise P dos Santos MD FRCPC MSc MPH[1]

[1]University of Ottawa, Ottawa, ON, Canada. [2]The Ottowa Hospital, Ottowa, ON, Canada. [3]OHRI, Ottawa, ON, Canada. [4]Queen Silvia Children's Hospital, Gothenburg, Sweden, Sweden. [5]Sahlgrenska University Hospital, Gothenburg, Sweden, Sweden

Purpose

To evaluate long-term angiographic outcomes and complications after flow diverter treatment, and to determine clinical, anatomical, and device-related factors associated with safety and efficacy.

Materials & Methods

We performed a retrospective cohort study of patients treated with flow diverters between January 2012 and October 2024 at a single tertiary neurovascular center. Clinical, demographic, and imaging data were obtained from EPIC EMR and PACS. Variables included age, sex, body mass index (BMI), aneurysm rupture status, clinical presentation, circulation territory, smoking status, prior stroke,rupture status, family history of SAH, antiplatelet therapy, and flow diverter type.

Primary outcomes include immediate (before discharge) and late complications (following discharge), recurrence, and mortality due to treatment. Secondary outcomes included long-term occlusion status and functional status assessed using the modified Rankin Scale (mRS).

Group comparisons were performed using Mann-Whitney U orKruskal Wallis tests for continuous variables and Chi-squared/Fisher's exact tests for categorical variables.

Results

Patients with immediate complications or mortality were notably older, with median ages of 67 and 66 years, respectively, compared to 58 years among those without such events ($P = 0.003$). Increasing age also predicted poor functional recovery (mRS 3–6, $P < 0.001$).

The median BMI of patients who developed late complications was 20.4 kg/m^2 (IQR 19.2–23.9), significantly lower than the 27.8 kg/m^2 (IQR 24.1–32.2) in those without complications (P = 0.008).
These patients exhibited markedly higher immediate complication rates (41.7% vs. 8.0%, P < 0.01), recurrence rates (16.0% vs. 4.9%, P = 0.05), and mortality rates (24.0% vs. 6.0%, P = 0.01). Functional independence was less frequently achieved among those with previous stroke (76% vs 92.3%), with significantly increased mortality (P = 0.019).
Never smokers more frequently showed residual neck filling (Raymond-Roy Class 2). In contrast, current smokers exhibited more complete occlusion (Class 2) and fewer cases of incomplete filling (Class 3) compared to former smokers (P = 0.04).
Patients presenting with ruptured aneurysms or complications such as subarachnoid hemorrhage (17.8% vs 2.9%, P = 0.03), seizures (21.4% vs 2.9%, P = 0.02), or mass effect (15.8% vs 2.9%, P = 0.04) experienced higher mortality and worse functional results. Conversely, incidental aneurysms were associated with more favourable outcomes, with 94.7% attaining good recovery (mRS 0–2) compared to 81.2% in the SAH group (P = 0.03).
Procedures involving the internal carotid artery (ICA) had fewer immediate complications (7.3%) compared to the anterior cerebral artery (30.0%, P = 0.01) and vertebrobasilar sites (20.7%, P = 0.04). Mortality was also lowest for ICA aneurysms (4.6%) relative to interventions in the posterior cerebral artery (33.3%, P = 0.01).
Pipeline use resulted in statistically fewer adverse events than both Silk (P = 0.03) and LEO (P = 0.02). Similarly, Surpass devices demonstrated a lower complication rate versus LEO (P = 0.04).

Conclusion

Overall complication, recurrence, and mortality rates aligned with prior reports, but subgroup analyses revealed distinct risk patterns. Poorer outcomes were associated with older age, history of stroke, low body mass index, and ruptured or symptomatic aneurysm presentations.

References

1. Al-Mufti F, Amuluru K, Gandhi CD, Prestigiacomo CJ. Flow Diversion for Intracranial Aneurysm Management: A New Standard of Care. Neurotherapeutics. 2016 Jul;13(3):582-9. doi: 10.1007/s13311-016-0436-4.
2. Shehata MA, Ibrahim MK, Ghozy S, et al Long-term outcomes of flow diversion for unruptured intracranial aneurysms: a systematic review and meta-analysis. J Neurointerv Surg. 2023 Sep;15(9):898-902. doi: 10.1136/jnis-2022-019240.

Images/Tables

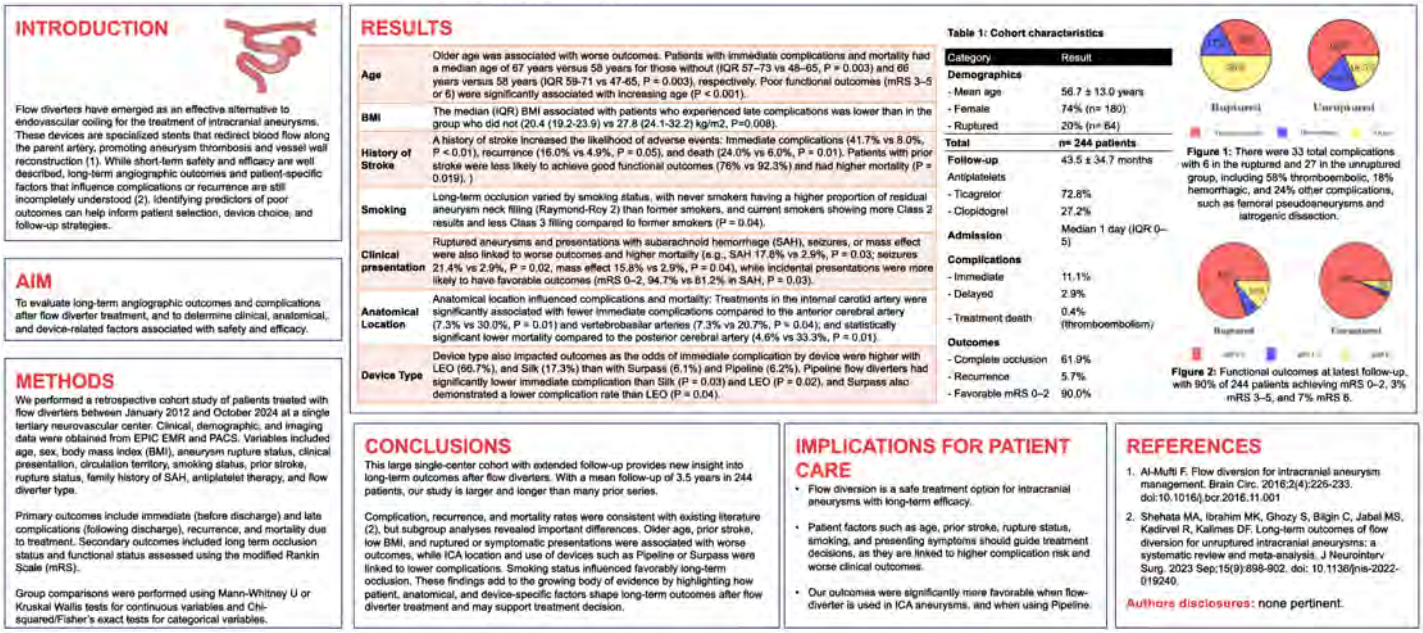

---

97 Middle Meningeal Artery Embolization With vs Without Surgery for Non-Acute Subdural Hematoma

Huanwen Chen MD[1], Jay kakadiya MD[2], Hamza Salim MD[3], Muhammed Amir Essibayi MD[4], Vivek Yedavalli MD[2], Adam Dmytriw MD[5], David Altschul MD[4], Marco Colasurdo MD[6], Ajay Malhotra MD[7], Dheeraj Gandhi MD[1], Dhairya A Lakhani MD[8]
[1]University of Maryland, Baltimore, MD, USA. [2]Johns Hopkins, Baltimore, MD, USA. [3]MD Anderson, Houston, TX, USA. [4]Montefiore, Bronx, NY, USA. [5]University of Oxford, London, London, United Kingdom. [6]OHSU, Oregon, Portland, USA. [7]Yale, New Haven, CT, USA. [8]West Virginia University, Morgantown, WV, USA

Purpose

Middle meningeal artery embolization (MMAE) is an effective treatment for non-acute subdural hematoma (NASDH) patients, and it is increasingly being adopted into routine clinical practice as standard of care. This study aims to determine whether additional surgery is effective in preventing treatment failure for NASDH patients treated with MMAE.

Materials & Methods

We conducted a retrospective cohort study using the 2016–2022 Nationwide Readmissions Database. NASDH patients were stratified into standalone MMAE vs. combined MMAE+surgery groups. Propensity score matching (PSM) accounted for presenting symptoms and discharge functional status. The Elixhauser Comorbidity Index (ECI) quantified comorbidity burden. The primary outcome was treatment failure, defined as NASDH-related death, readmission, or surgical evacuation within 180 days post-discharge.

Results

Among 3,213 NASDH patients who underwent MMAE, 1,669 received no surgery, and 1,544 received surgery; 1,108 patients remained in each group after PSM. Overall, 86% of patients had no mental status changes, and 76.7% were discharged home. Overall, surgery was not significantly associated with a lower risk of treatment failure (5.3% vs. 7.5% within 180 days, HR 0.67 [95%CI 0.371.21], p=0.19), with treatment effects varying by ECI (p-interaction=0.002). For patients with low comorbidity burden (ECI<5, n=631), surgery was associated with a significantly lower risk of treatment failure (3.3% vs. 9.6% within 180 days, HR 0.29 [95%CI 0.11-0.78], p=0.014). For patients with medium (ECI 5–14, n=996) or high (ECI≥15, n=589) comorbidity burden, no significant differences were observed (p=0.56 and 0.43, respectively).

Conclusion

In neurologically stable NASDH patients who underwent MMAE, higher baseline comorbidity burden significantly blunted the benefit of additional surgery, and additional surgery was not associated with different rates of treatment failure for patients with medium to high comorbidity burdens. These findings suggest that standalone MMAE may be a viable alternative to surgical evacuation for neurologically stable NASDH with medium to high baseline comorbidity burdens.

References

1. Chen H, Colasurdo M, Bodanapally UK, Malhotra A, Gandhi D. Chronic Subdural Hematoma. Neurol Clin Pract. 2025;15(4). doi:10.1212/CPJ.0000000000200501

2. Rai AT, Link PS, Lakhani DA. Rising tide of middle meningeal artery embolization for chronic subdural hematomas: current volumes and future growth compared with cerebral aneurysm and stroke interventions. J Neurointerv Surg. Published online February 25, 2025:jnis-2025-023109. doi:10.1136/jnis-2025-023109

3. Chen H, Colasurdo M, Kan P. Middle Meningeal Artery Embolization for Subdural Hematoma. Neurosurg Clin N Am. 2025;36(1):73-82. doi:10.1016/j.nec.2024.08.006

4. Chen H, Colasurdo M, Kan PT. Middle meningeal artery embolization as standalone treatment versus combined with surgical evacuation for chronic subdural hematomas: systematic review and meta-analysis. J Neurosurg. doi:10.3171/2023.7.JNS231262 Published online September 1, 2023:1-7.

5. Lakhani DA, Balar AB, Boo S, Bhatia S, Rai AT. Middle meningeal artery embolization with surgical evacuation improves outcomes in chronic subdural hematoma: a multi-institutional and multinational database study. J Neurointerv Surg. 2025 Jan 16:jnis-2024-022932. doi: 10.1136/jnis-2024-022932. Epub ahead of print. PMID: 39824597.

Images/Tables

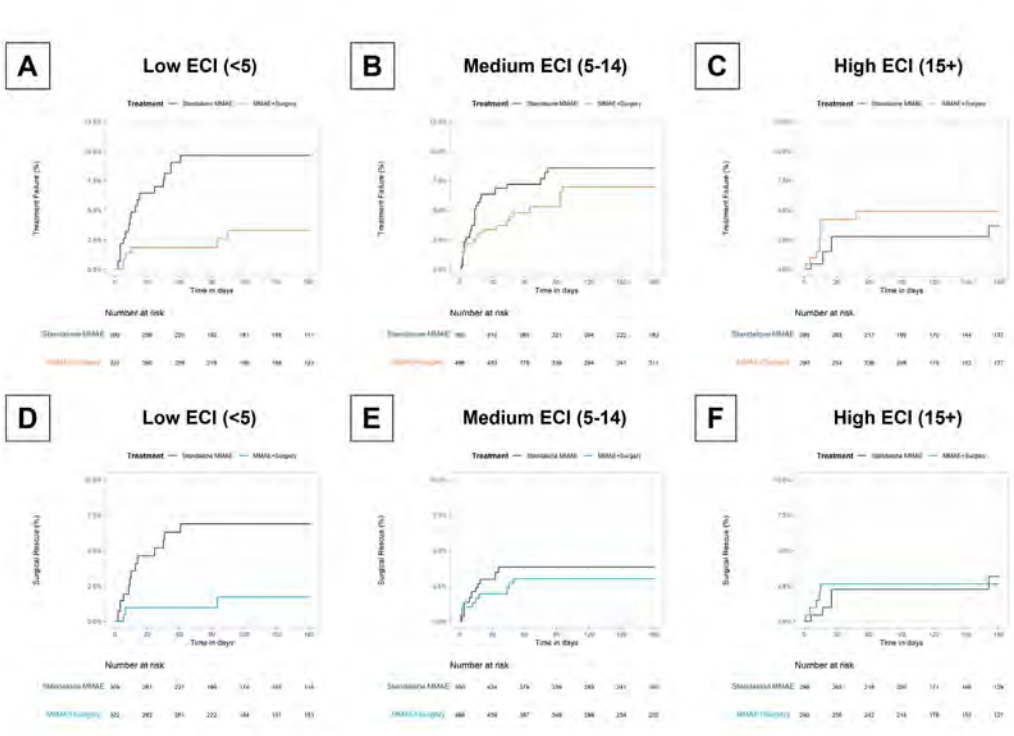

Figure : Outcomes of middle meningeal artery embolization (MMAE) with versus without surgical evacuation for patients with NASDH after propensity score matching, stratified by Elixhauser comorbidity index (ECI). Panels A, B, and C shows time to treatment failure for patients with low, medium, and high ECI, respectively; Panels D, E, and F shows the same for surgical rescue.

---

367 Comparative Outcomes of Intrasaccular Flow Disruptors versus Traditional Coiling Techniques in Wide-Neck Intracranial Aneurysms: A Systematic Review and Meta-Analysis

Mitesh Gupta, sanket dash
nims, jaipur, rajasthan, India

Purpose

Background: Wide-neck intracranial aneurysms (WNIAs) remain technically challenging for endovascular management. Intrasaccular flow disruptors (IFDs), particularly the Woven EndoBridge (WEB) device, have emerged as an alternative to traditional coiling techniques. This study systematically compares the procedural, angiographic, and clinical outcomes of IFDs versus conventional coiling techniques, including primary (PC), stent-assisted (SAC), and balloon-assisted (BAC) coiling.

Materials & Methods

Methods: A systematic literature search was conducted in PubMed, Scopus, and Cochrane CENTRAL databases up to May 2025. Eligible cohort studies were assessed using the Joanna Briggs Institute (JBI) critical appraisal checklist. Meta-analysis was performed using Review Manager 5.4 software with pooled mean difference (MD) or odds ratio (OR) and 95% confidence intervals (CI).

Results

Results: Nineteen studies involving 2,088 patients met inclusion criteria (841 WEB, 482 PC, 658 SAC, 107 BAC). Compared to coiling, WEB significantly reduced procedural (MD = –22.77 [95% CI, –29.68 to –15.86]) and fluoroscopy times (MD = –26.25 [95% CI, –37.08 to –15.42]). Although immediate complete occlusion rates were lower with WEB, follow-up results demonstrated comparable complete occlusion (OR = 1.08 [95% CI, 0.83–1.41]) and higher adequate occlusion (OR = 1.37 [95% CI, 0.97–1.93]). Retreatment rates were lower in the WEB group (OR = 0.94 [95% CI, 0.55–1.59]). Favorable functional outcomes were more frequent after WEB treatment both immediately (OR = 1.54 [95% CI, 1.13–2.10]) and at follow-up (OR = 1.51 [95% CI, 1.10–2.28]). Complication rates were significantly lower in the WEB group (OR = 0.56 [95% CI, 0.41–0.77]), while mortality remained similar (OR = 1.06 [95% CI, 0.54–2.09]).

Conclusion

Conclusion: Intrasaccular flow disruptors, particularly the WEB device, demonstrate superior procedural efficiency, reduced radiation exposure, lower complication rates, and comparable long-term angiographic and clinical outcomes compared with conventional coiling. These findings support the expanding role of WEB devices as a safe and effective alternative in the management of wide-neck intracranial aneurysms.

References

[1] A. M. Jersey and D. M. Foster, "Cerebral Aneurysm," *PubMed*, Apr. 03, 2023. https://www.ncbi.nlm.nih.gov/books/NBK507902/
[2] L. B. Hindenes *et al.*, "Anatomical variations in the circle of Willis are associated with increased odds of intracranial aneurysms: The Tromsø study," *Journal of the Neurological Sciences*, vol. 452, p. 120740, Sep. 2023, doi: https://doi.org/10.1016/j.jns.2023.120740.
[3] L.-H. Johnsen *et al.*, "Prevalence of unruptured intracranial aneurysms: impact of different definitions – the Tromsø Study," *Journal of Neurology, Neurosurgery & Psychiatry*, vol. 93, no. 8, pp. 902–907, Jun. 2022, doi: https://doi.org/10.1136/jnnp-2022-329270.
[4] N. K. Rooij, B. K. Velthuis, A. Algra, and G. J. E. Rinkel, "Configuration of the circle of Willis, direction of flow, and shape of the aneurysm as risk factors for rupture of intracranial aneurysms," *Journal of Neurology*, vol. 256, no. 1, pp. 45–50, Jan. 2009, doi: https://doi.org/10.1007/s00415-009-0028-x.
[5] M. H. Vlak, A. Algra, R. Brandenburg, and G. J. Rinkel, "Prevalence of unruptured intracranial aneurysms, with emphasis on sex, age, comorbidity, country, and time period: a systematic review and meta-analysis," *The Lancet. Neurology*, vol. 10, no. 7, pp. 626–36, 2011, doi: https://doi.org/10.1016/S1474-4422(11)70109-0.

---

812 Endolectomy using the pRELAX device for cerebral vasospasm: a novel treatment method

Ali Khanafer Dr, Hans Henkes
Klinikum Stuttgart, Stuttgart, Baden Wüttenberg, Germany

Purpose

Cerebral vasospasm remains a major cause of delayed ischemic neurological deficits after aneurysmal subarachnoid hemorrhage (SAH). Endovascular management is typically limited to intra-arterial vasodilators and balloon angioplasty, while the off-label use of stent retrievers has demonstrated temporary efficacy. The *pRELAX* device was developed as the first dedicated temporary implant for the treatment of cerebral vasospasm, aiming to combine controlled radial expansion with atraumatic vessel wall interaction.

Materials & Methods

A retrospective, multicenter analysis was conducted including 48 patients (HH 3, Fisher 3) treated with *pRELAX* for severe cerebral vasospasm across four neurointerventional centers. A total of 124 vessel segments were treated (MCA/ICA = 90; ACA/PCA = 34).

Results

Successful angiographic improvement was achieved in 119/124 vessels (95.9%). Only two vessels required retreatment within the same session. Ischemia despite treatment occurred in 1/40 patients (2.5%). Median mRS improved from 5 during vasospasm to 4 at discharge and 1 at 3–6 months, with 72.9% achieving mRS 0–2. Minor complications included two instances of clot formation without clinical consequence.

Conclusion

The endolectomy using *pRELAX* device demonstrated a high rate of angiographic and clinical success with good safety in patients with cerebral vasospasm following SAH.

References

Khanafer A, von Gottberg P, Albiña-Palmarola P, Liebig T, Forsting M, Ganslandt O, Henkes H. Is Stent Retraction to ReLieve Arterial Cerebral VaSospasm Caused by SAH (Stent-ReLACSS) Using PRELAX the Long-awaited Solution for Treatment of Posthemorrhagic Cerebral Vasospasm? Treatment of Posthemorrhagic Cerebral Vasospasm with PRESET and PRELAX: Technical Aspects, Efficacy, and Safety Margins in a Case Series. **Clin Neuroradiol.** 2024;34:649–662.

---

106 Prolonged Venous Transit is Associated with Unfavorable Functional Outcomes in Anterior Circulation Distal Medium Vessel Occlusion Strokes

Hamza A Salim MD[1], Dhairya A Lakhani MD[2], Jay Kakadiya MD[3], Cynthia Greene MD, PhD[3], Argye E Hillis MD, PhD[4], Kambiz Nael MD[5], Jeremy J Heit MD, PhD[6], Adam A Dmytriw MD, MPH, MSc[7], Tyler McGaughey PhD[2], Tobias D Faizy MD[8], Max Wintermark MD[1], Vivek S Yedavalli MD, MS, FAHA[3]
[1]Department of Neuroradiology, MD Anderson Medical Center, Houston, TX, USA. [2]Department of Neuroradiology, West Virginia University, Morgantown, WV, USA. [3]The Russell H. Morgan Department of Radiology and Radiological Science, Johns Hopkins University School of Medicine, Baltimore, MD, USA. [4]Department of Neurology, Johns Hopkins University School of Medicine, Baltimore, MD, USA. [5]Radiology and Biomedical Imaging, University California, San Francisco, CA, USA. [6]Department of Radiology, Division of Neuroradiology and Neurointervention, Stanford University, Stanford, CA, USA. [7]Neuroendovascular Program, Massachusetts General Hospital & Brigham and Women's Hospital, Harvard Medical School, Boston, MA, USA. [8]Department of Radiology, Neuroendovascular Division, University Medical Center Münster, Münster, Münster, Germany

Purpose

Distal medium-vessel occlusion (DMVO) strokes represent a significant proportion of acute ischemic stroke cases, yet optimal management remains unclear. Prolonged venous transit (PVT), a marker of poor venous outflow, has been associated with worse outcomes in large-vessel occlusion strokes, but its role in DMVO is unknown.

Materials & Methods

In a retrospective study, consecutive patients with anterior-circulation DMVO undergoing multimodal CT imaging and clinical evaluation were analyzed. PVT status was determined on pretreatment time-to-maximum perfusion maps by identifying ≥10-second delays in either the posterior superior sagittal sinus or the torcula. Baseline characteristics, imaging findings, and interventions were collected. The primary outcome was 90-day modified Rankin Scale (mRS) score 0–2.

Results

Among 77 patients (median age 70 years, 56% female), 18 (23%) had PVT. Median admission NIHSS scores were 11 (IQR, 7–15), and intravenous thrombolysis was administered to 35% of patients. Patients with PVT+ were less likely to achieve mRS 0–2 at 90 days (adjusted odds ratio, 0.14; 95% CI, 0.02–0.85; P=0.046). There were no significant differences in rates of hemorrhagic transformation or mortality.

Conclusion

PVT is independently associated with unfavorable functional outcomes in anteriorcirculation DMVO. These findings suggest PVT may serve as a prognostic indicator and could inform treatment decisions in this challenging stroke subtype.

References

1. Yedavalli VS, Koneru M, Hoseinyazdi M, Greene C, Lakhani DA, Xu R, Luna LP, Caplan JM, Dmytriw AA, Guenego A, Heit JJ, Albers GW, Wintermark M, Gonzalez LF, Urrutia VC, Huang J, Nael K, Leigh R, Marsh EB, Hillis AE, Llinas RH. Prolonged venous transit on perfusion imaging is associated with higher odds of mortality in successfully reperfused patients with large vessel occlusion stroke. J Neurointerv Surg. 2025 Feb 14;17(3):321-326. doi: 10.1136/jnis-2024-021488. PMID: 38471762.
2. Yedavalli V, Salim HA, Mei J, Lakhani DA, Balar A, Musmar B, Adeeb N, Hoseinyazdi M, Luna L, Deng F, Hyson NZ, Dmytriw AA, Guenego A, Faizy TD, Heit JJ, Albers GW, Lu H, Urrutia VC, Nael K, Marsh EB, Hillis AE, Llinas R. Decreased Quantitative Cerebral Blood Volume Is Associated With Poor Outcomes in Large Core Patients. Stroke. 2024 Oct;55(10):2409-2419. doi: 10.1161/STROKEAHA.124.047483. Epub 2024 Aug 26. PMID: 39185560.
3. Lakhani DA, Balar AB, Koneru M, Wen S, Ozkara BB, Caplan J, Dmytriw AA, Wang R, Lu H, Hoseinyazdi M, Nabi M, Mazumdar I, Cho A, Chen K, Sepehri S, Hyson N, Xu R, Urrutia V, Luna LP, Hillis A, Heit JJ, Albers GW, Rai AT, Faizy T, Wintermark M, Nael K, Yedavalli VS. Perfusion-Based Relative Cerebral Blood Volume Is Associated With Functional Dependence in Large-Vessel Occlusion Ischemic Stroke. J Am Heart Assoc. 2024 Dec 3;13(23):e034242. doi: 10.1161/JAHA.124.034242. Epub 2024 Nov 22. PMID: 39575711; PMCID: PMC11681566.
4. Lakhani DA, Balar AB, Koneru M, Hoseinyazdi M, Hyson N, Cho A, Greene C, Xu R, Luna L, Caplan J, Dmytriw A, Guenego A, Wintermark M, Gonzalez F, Urrutia V, Huang J, Nael K, Rai AT, Albers GW, Heit JJ, Yedavalli V. Pretreatment CT perfusion collateral parameters correlate with penumbra salvage in middle cerebral artery occlusion. J Neuroimaging. 2024 Jan-Feb;34(1):44-49. doi: 10.1111/jon.13178. Epub 2023 Dec 6. PMID: 38057941.
5. Lakhani DA, Salim H, Balar AB, Ali S, Wen S, Mei J, Hillis AE, Urrutia VC, Xu R, Broocks G, Fiehler J, Kniep HC, Stracke P, Krähling H, Albers GW, Lansberg M, Wintermark M, Heit JJ, Faizy TD, Yedavalli VS. The Cortical Vein Opacification Score (COVES) is independently associated with good and excellent functional outcomes at 90-days in minor stroke patients with anterior circulation large vessel occlusion: A Multicenter Study. AJNR Am J Neuroradiol. 2025 May 19:ajnr.A8739. doi: 10.3174/ajnr.A8739. Epub ahead of print. PMID: 40389269.

---

96 Sex Differences in Surgical Treatment and Middle Meningeal Artery Utilization and Outcomes in Chronic Subdural Hematoma: A Multi-institutional Database Study

Huanwen Chen MD[1], Jay Kakadiya, MD[2], Hamza Salim MD[3], Muhammed Amir Essibayi MD[4], David Altschul MD[5], Vivek Yedavalli MD[2], Adam Dmytriw MD[6], Marco Colasurdo MD[7], Ajay Malhotra MD[8], Dheeraj Gandhi MD[1], Dhairya Lakhani MD[9]

[1]University of Maryland, Baltimore, MD, USA. [2]Johns Hopkins, Baltimore, MD, USA. [3]MD Anderson, Houston, TX, USA. [4]Montefiore Medical Center,, Bronx, NY, USA. [5]Montefiore, Bronx, NY, USA. [6]University of Oxford, London, London, United Kingdom. [7]OHSU, Portland, OR, USA. [8]Yale, New Haven, CT, USA. [9]West Virginia University, Morgantown, WV, USA

Purpose

Non-acute subdural hematoma (NASDH) represents a significant cause of morbidity and mortality, yet sex-specific differences in presentation, treatment patterns, and outcomes remain poorly understood. In this study, we investigated sex disparities in SDH management and outcomes using two large multicenter databases.

Materials & Methods

This was a retrospective analysis using the TriNetX and 2016-2022 Nationwide Readmissions Databases. In Cohort 1 (TriNetX), patients with newly-diagnosed NASDH were identified, and rates of surgical treatment within 6 months were compared between sexes. In Cohort 2 (NRD), patients who underwent surgical NASDH drainage were identified, and functional independence at the time of hospital discharge was compared between sexes. Finally, MMAE utilization rates among patients who underwent percutaneous drainage (Burr-hole or twist drill trephination within Cohort 2) were assessed, and differences MMAE's effectiveness between sexes in terms of preventing NASDH recurrence were compared using interaction analysis. Propensity score matching (PSM) was performed to adjust for confounders.

Results

Among 44,659 newly-diagnosed NASDH patients (Cohort 1), 15,043 (33.6%) were female. Female patients had fewer vascular risk factors but higher rates of dementia, psychiatric comorbidities, and headaches. Compared to PSM male controls, female patients were significantly less likely to undergo surgery within 6 months (11.6% vs. 15.7%, p<0.001). Among 35,148 surgically treated patients (Cohort 2), 9,287 (28.6%) were female, and female patients were younger but had higher rates of moderate to severe mental status compromise. Compared to PSM male controls, female patients had lower rates of functional independence (40.4% vs. 47.1%, p<0.001). MMAE utilization was also lower in women (4.5% vs. 5.7%, p=0.014); patient sex did not modulate the effectiveness of MMAE (interaction p=0.45).

Conclusion

Significant sex differences exist in NASDH presentation, treatment utilization, and outcomes. Future work is needed to better understand potential pathophysiological explanations for sex-specific differences and to better characterize disparities in NASDH treatments.

References

1. Chen H, Colasurdo M, Bodanapally UK, Malhotra A, Gandhi D. Chronic Subdural Hematoma. Neurol Clin Pract. 2025;15(4). doi:10.1212/CPJ.0000000000200501

2. Rai AT, Link PS, Lakhani DA. Rising tide of middle meningeal artery embolization for chronic subdural hematomas: current volumes and future growth compared with cerebral aneurysm and stroke interventions. J Neurointerv Surg. Published online February 25, 2025:jnis-2025-023109. doi:10.1136/jnis-2025-023109

3. Lakhani DA, Balar AB, Bhatia S, Rai AT. Standalone Middle Meningeal Artery Embolization Versus Medical Management for Chronic Subdural Hematomas: A Multi-Institutional and Multinational Database Study. World Neurosurg. 2025;201:124275. doi:10.1016/j.wneu.2025.124275

4. Chen H, Colasurdo M, Kan PT. Middle meningeal artery embolization as standalone treatment versus combined with surgical evacuation for chronic subdural hematomas: systematic review and meta-analysis. J Neurosurg. Published online September 1, 2023:1-7. doi:10.3171/2023.7.JNS231262

5. Kan P, Fiorella D, Dabus G, et al. ARISE I Consensus Statement on the Management of Chronic Subdural Hematoma. Stroke. 2024;55(5):1438-1448. doi:10.1161/STROKEAHA.123.044129

Images/Tables

Table 1: MMAE outcomes among patients who underwent percutaneous drainage for NASDH stratified by sex

	Kaplan Meier Analysis		Cox Proportional Hazards		
Outcomes and cohorts	MMAE	No MMAE	HR [95%CI]	p-value	p-int
180-day NASDH recurrence					
Total PSM cohort	4.1% [2.1% to 6.1%]	7.4% [5.7% to 9.1%]	0.53 [0.29 to 0.95]	0.033	-
Male patients	5.0% [2.5% to 7.4%]	8.2% [6.2% to 10.2%]	0.57 [0.33 to 0.99]	0.046	0.45
Female patients	1.2% [0.0% to 3.6%]	4.6% [1.6% to 7.6%]	0.29 [0.04 to 2.02]	0.21	
180-day repeat NASDH surgery					
Total PSM cohort	2.6% [1.0% to 4.1%]	5.3% [3.8% to 6.8%]	0.46 [0.23 to 0.93]	0.032	-
Male patients	3.0% [1.0% to 4.9%]	6.0% [4.2% to 7.8%]	0.46 [0.23 to 0.90]	0.023	0.91
Female patients	1.2% [0.0% to 3.6%]	2.8% [0.6% to 5.0%]	0.50 [0.07 to 3.62]	0.49	

Table 2: Hospitalization and follow-up outcomes for male vs. female patients following NASDH surgery (Cohort 2)

	Unmatched cohorts			PSM cohorts		
	Male	Female		Male	Female	
Outcomes^	N = 25,861	N = 9,287	p-value	N = 9,267	N = 9,210	p-value
Functional independence	47.8% (12,355)	40.3% (3,746)	<0.001	47.1% (4,369)	40.4% (3,720)	<0.001
In-hospital mortality	0.9% (221)	0.6% (60)	0.20	1.1% (99)	0.7% (60)	0.041
Length of stay	8.5 (8.7)	8.9 (8.6)	<0.001	9.3 (10.1)	8.8 (8.0)	0.44
180-day NASDH recurrence*	6.8% [6.3% to 7.3%]	4.5% [3.8% to 5.1%]	0.014	5.7% [5.0% to 6.4%]	4.5% [3.8% to 5.2%]	0.014
180-day repeat NASDH surgery*	4.6% [4.2% to 5.0%]	2.4% [2.0% to 2.9%]	<0.001	3.8% [3.2% to 4.4%]	2.5% [2.0% to 2.9%]	0.001

^data repesented as % (n), mean (SD), or event probability [95%CI]; statistical comparisons were performed using chi-squared, wilcoxon rank-sum, and log-rank tests, respectively. *23,454 male and 8,477 female patients in the unmatched cohorts and 8,431 male and 8,406 female patients in the PSM cohorts were eligible for follow-up.

---

877 Does AI-Based 3D Volumetry Improve Detection of Aneurysm Growth Compared to 2D Diameter Measurements?

Attill Saemann MD, Géraud Forestier MD PhD, Vanessa Chan MSc, Nicole Cancelliere MSc, Vitor Pereira MD MSc
St. Michaels Hospital, Toronto, Ontario, Canada

Purpose

To compare an AI-assisted three-dimensional aneurysm analysis solution (RapidAI Aneurysm, “RAPID”) with conventional two-dimensional linear measurements for longitudinal assessment of intracranial aneurysms on serial CTA and MRA at St. Michael’s Hospital. The primary outcome is agreement for detecting interval morphological change or growth. Secondary outcomes are detection performance, correspondence between diameter and volumetric or surface-area metrics, effects on a hypothetical treatment recommendation, reader confidence, and technical quality of the AI output.

Materials & Methods

This single-center, crossover reader study utilizes a curated cohort of 596 intracranial aneurysms from patients evaluated and counseled for aneurysm management at St. Michael’s Hospital. The cohort includes treated and untreated aneurysms, each with at least two CTA and/or MRA time points. Two independent readers, a neurosurgeon and a neuroradiologist, interpreted each case in opposite order with a one-month washout: one started with the AI-assisted 3D analysis and then performed conventional 2D measurements; the other did the reverse. Readers were blinded to each other’s assessments. For each time pair, we recorded the presence of morphological change using descriptors, including 2D maximum diameter, AI-derived volume and surface area, location and side, irregularity, lobulation, parent vessel disease, and de novo formation. Readers answered “Would you treat?” and rated confidence on a 1–5 scale. Tool performance included per-aneurysm detections, misses, and extras, overlay quality (0 = good; 1 = poor due to tool; 2 = poor due to voxel size mismatch), and correctness of the automated neck plane.

Results

Data assembly is complete for 596 aneurysms with serial CTA and/or MRA. The AI software produced volumetric segmentations and neck-plane overlays for the included studies, enabling direct comparison with conventional measurements. Cross-over readings are underway, adhering to the washout schedule and the standardized training protocol. Quality control indicates that mixed-modality pairs can be evaluated within the same framework by scoring overlay quality and documenting neck-plane adjustments when required. The final analysis will report per-method growth calls, agreement statistics with confidence intervals, correlations between diameter and volumetrics, Bland–Altman bias and limits of agreement for change measurements, AI detection sensitivity and positive predictive value against the curated reference list, and the frequency with which the hypothetical treatment recommendation differs between methods, with clustering by patient.

Conclusion

Using real-world aneurysm clinic data, this cross-over study provides a rigorous head-to-head comparison of AI-assisted 3D analysis and conventional 2D measurement for longitudinal aneurysm surveillance across CTA and MRA. The design aims to determine whether 3D volumetrics capture clinically meaningful changes beyond diameter and to define how AI outputs can be incorporated into routine decision-making.

References

- **Journal Article**
  Liu X, Haraldsson H, Wang Y, et al. A volumetric metric for monitoring intracranial aneurysms: repeatability and growth criteria in a longitudinal MR imaging study. *AJNR Am J Neuroradiol* 2021;42:1591-1597. DOI: https://doi.org/10.3174/ajnr.A7190.
- **Journal Article**
  Timmins KM, Kuijf HJ, Vergouwen MDI, et al. Reliability and agreement of 2D and 3D measurements on MRAs for growth assessment of unruptured intracranial aneurysms. *AJNR Am J Neuroradiol* 2021;42:1598-1603. DOI: https://doi.org/10.3174/ajnr.A7186.
- **Journal Article**
  Sahlein DH, Gibson D, Scott JA, et al. Artificial intelligence aneurysm measurement tool finds growth in all aneurysms that ruptured during conservative management. *J Neurointerv Surg* 2023;15:766-770. DOI: https://doi.org/10.1136/jnis-2022-019339.

Images/Tables

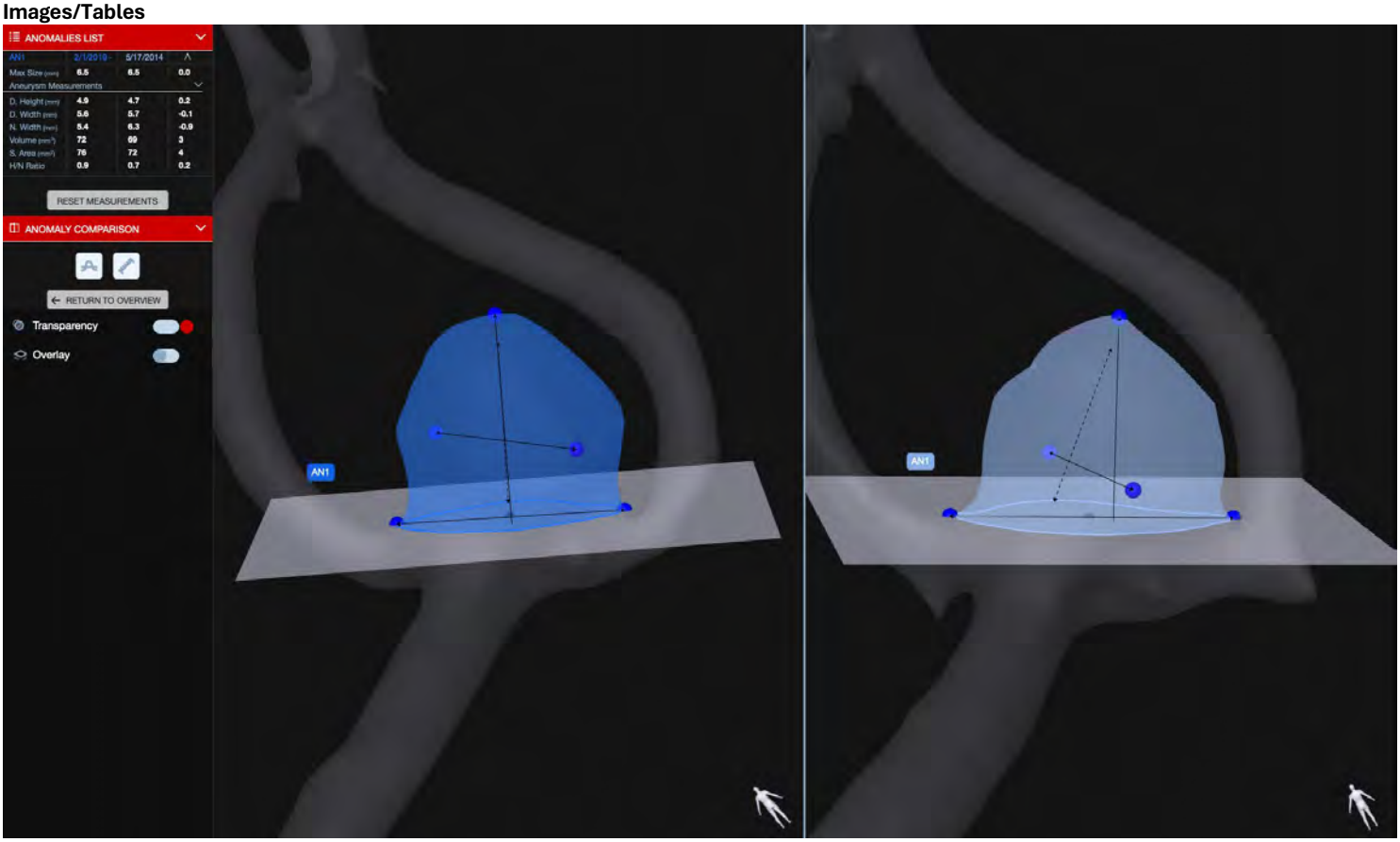

1149 Analysis of Long-term Clinical and Angiographic Outcomes of Intracranial Parent Artery Occlusion in a Large Canadian Academic Center

Ammar Alam BSc[1], Mahad Siddiqi MS4[2], Theodore Liu MS3[2], Richard Aviv PhD[3], Matthew Bilson BSc[1], Logan Milne BSc[1], Wassim Elmasry MD[2], Ahsas Nagee MD[2], Rebecca Thornhill PhD[2], Rajiv Hira MD MPH[2], Satya N Patro MD[4], Robert K Moreland MD FRCPC MSc[5], Robert Fahed MD MSc[2], Brian Drake MD FRCSC[2], Paula Klurfan MD MSc[6], Thorsteinn Gunnarsson MD MSc PhD[7], Marlise P dos Santos MD FRCPC MSc MPH[2]

[1]OHRI, Ottawa, ON, Canada. [2]University of Ottawa, Ottawa, ON, Canada. [3]The Ottowa Hospital, Ottowa, ON, Canada. [4]University of Arkansas for Medical Sciences, Little Rock, AR, USA. [5]University of Toronto, Toronto, ON, Canada. [6]SahlgrenskaUniversity Hospital, Gothenburg, Sweden, Sweden. [7]Queen Silvia Children's Hospital, Gothenburg, Sweden, Sweden

Purpose

Parent artery occlusion (PAO) remains an essential and durable treatment strategy for complex intracranial aneurysms that are not amenable to reconstructive endovascular or microsurgical techniques. Despite the increasing use of flow diversion, PAO remains a critical treatment option in carefully selected cases. This study evaluated the long-term clinical and angiographic outcomes following PAO, with subgroup analysis based on aneurysm morphology, size, location, rupture status, and clinical presentation.

Materials & Methods

We retrospectively reviewed all patients who underwent PAO for intracranial aneurysms at a single tertiary center between March 2005 and December 2024. Clinical outcomes were evaluated using the modified Rankin Scale (mRS). Angiographic and morphological data were collected from procedural and follow-up imaging. Pearson's chi-square tests and Cox proportional hazards models were applied to identify predictors of poor functional outcome (mRS ≥ 3), late complications, and mortality.

Results

Fifty-six patients (mean age, 53.7 years; range, 7–79 years) with 57 aneurysms were included, with a mean follow-up period of 26.2 months. Thirty-two (48.5%) aneurysms were ruptured, and 12 (21.4%) demonstrated fusiform morphology. Complete baseline occlusion was achieved in 83% of cases, with recurrence occurring in 3 patients (5.3%). No post-procedural ruptures were observed. Nine patients (15.8%) died during follow-up, including three peri-procedural deaths. In multivariable analysis, baseline mRS was the only independent predictor of poor long-term outcome (HR, 1.80; 95% CI, 1.19–2.73; p = 0.005). Rupture status, older age, and smaller aneurysm size were associated with poorer outcomes in unadjusted analyses. Patients who underwent balloon test occlusion (n = 20) had no ischemic complications, confirming adequate collateral flow.

Conclusion

PAO offers a safe and effective long-term treatment for select complex intracranial aneurysms, providing durable occlusion with low recurrence and hemorrhagic risk. Functional outcome is most strongly influenced by pre-treatment neurological status, underscoring the importance of patient selection and multidisciplinary planning.

References

1. Akimoto T, Ito Y, Akutagawa K, et al. Perioperative and long-term complications following therapeutic internal carotid artery occlusion. Interv Neuroradiol. 2023 Aug;29(4):426-433. doi: 10.1177/15910199221095786.
2. Elhammady MS, Wolfe SQ, Farhat H, et al. Carotid artery sacrifice for unclippable and uncoilable aneurysms: endovascular occlusion vs common carotid artery ligation. Neurosurgery. 2010 Nov;67(5):1431-6; discussion 1437. doi: 10.1227/NEU.0b013e3181f076ac.

Scientific Abstract Power Pitches & Luminary Speaker: Advanced Neuroimaging in Cerebrovascular Disease and Neurotrauma

3:20 - 4:20pm Monday, 18th May, 2026

362 Cumulative Blast Exposure and Intracranial Aneurysms in Special Operations Forces: A Retrospective MRI Analysis

Sara De Giorgi[1], Andrea Diociasi[2], Rehab Naeem Khalid[1], Quirin Strotzer[3], Phoebe Degn[4], Katelyn Rand[4], Seba Gabali[4], Ronald Hirschberg[4], Scott Sorg[4], Michael Lev[1], Rajiv Gupta[1]

[1]Department of Radiology, Massachusetts General Hospital, Harvard Medical School, Boston, MA, USA. [2]Department of Internal Medicine (DiMI), University of Genoa, Genoa, IT, Italy. [3]Institute of Radiology, University of Regensburg Medical Center, Regensburg, Germany, Germany. [4]Home Base Program, Massachusetts General Hospital, Boston, ma, USA

Purpose

Special Operations Forces (SOF) personnel are frequently exposed to blast forces; however, the structural MRI correlates and vascular effects of cumulative blast exposure remain poorly defined. This study aimed to determine the prevalence of structural brain MRI abnormalities in SOF personnel and to examine their association with cumulative blast exposure, quantified using the Generalized Blast Exposure Value (GBEV).

Materials & Methods

This retrospective study included 564 SOF participants (evaluated from 2021 to 2024) enrolled in the ComBHaT program. All participants underwent 3T brain MRI with TOF-MRA. Imaging findings were extracted from structured neuroradiology reports. Cumulative blast exposure was modeled as $\log_{10}$ (GBEV + 1) and referred to as logGBEV. Associations between blast exposure and MRI findings were evaluated using Mann-Whitney U tests, Fisher's exact tests, and multivariable logistic regression.

Results

A total of 564 participants (mean age, 43 years ± 9; 563 men) were evaluated. The most prevalent MRI finding was white matter hyperintensities (215/564, 38.1%), followed by low-lying cerebellar tonsils (84/564, 14.9%) and intracranial aneurysms (33/564, 5.9%). Using a median split (cutoff = 6.549), aneurysm presence was associated with higher logGBEV (p = .012). Aneurysm prevalence was significantly greater in the high-exposure group (21/220, 9.5%) compared to the low-exposure group (6/220, 2.7%) (p = .005; OR = 3.76, 95% CI: 1.49–9.51; RR = 3.52, 95% CI: 1.44–8.51). In multivariable regression (n = 293), logGBEV remained an independent predictor of aneurysm presence (OR = 1.81, 95% CI: 1.09–3.03; p = .023).

Conclusion

In this large military cohort, intracranial aneurysms - but not other structural MRI findings - were independently associated with greater cumulative blast exposure suggesting a possible vascular effect of repeated blast forces. These findings support consideration of vascular imaging surveillance in highly exposed military personnel and require confirmation in longitudinal studies.

References

1. Edlow BL, Bodien YG, Baxter T, et al. Long-term effects of repeated blast exposure in United States Special Operations Forces personnel: a pilot study protocol. *J Neurotrauma* 2022;39(19–20):1391–1407; doi:10.1089/neu.2022.0030
2. Belding JN, Englert RM, Fitzmaurice S, et al. Potential health and performance effects of high-level and low-level blast: a scoping review of two decades of research. *Front Neurol* 2021;12:628782; doi:10.3389/fneur.2021.628782
3. Riedy G, Senseney JS, Liu W, et al. Findings from structural MR imaging in military traumatic brain injury. *Radiology* 2016;279(1):207–215; doi:10.1148/radiol.2015150438
4. Patel JB, Wilson SH, Oakes TR, et al. Structural and volumetric brain MRI findings in mild traumatic brain injury. *AJNR Am J Neuroradiol* 2020;41(1):92–99; doi:10.3174/ajnr.A6346
5. Modica LCM, Egnoto MJ, Statz JK, et al. Development of a blast exposure estimator from a Department of Defense–wide survey study on military service members. *J Neurotrauma* 2021;38(12):1654–1661; doi:10.1089/neu.2020.7405

Images/Tables

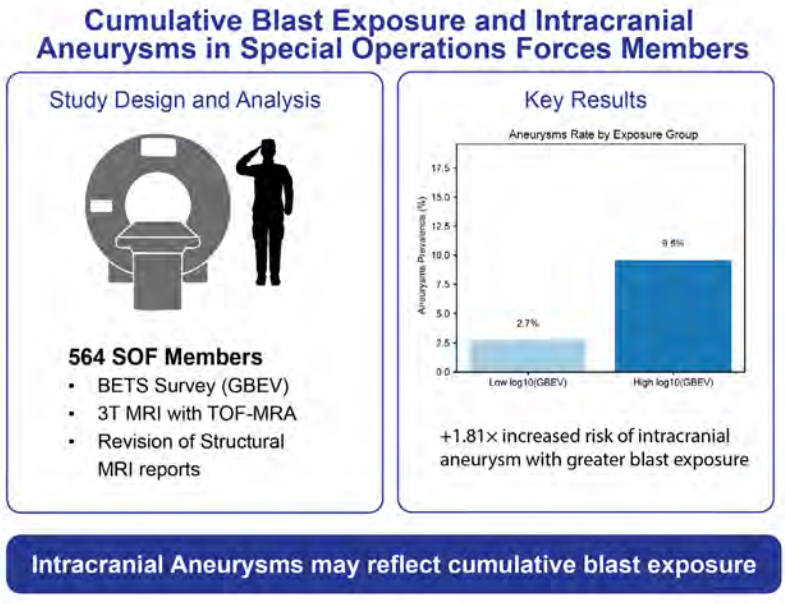

482 Early Prediction of Alzheimer's Conversion Among Patients with MCI Using Temporal and Limbic Predominant Volumetric Analysis

Michael A Thomas MD, Mona Asghariahmadabad MD, Luke Bonham MD, Kambiz Nael MD
University of California, San Francisco, San Francisco, CA, USA

Purpose

Among patients with mild cognitive impairment (MCI), the timeline for conversion to Alzheimer's disease (AD) is variable. However, predicting this conversion is increasingly important now that anti-amyloid treatments which slow the rate of disease progression are available. Commercially available software allows for automated volumetric analysis of the brain with generation of structure-specific normative percentiles. Using automated volumetric measurements of MRI, we aimed to generate a predictive model for early detection of conversion from MCI to AD.

Materials & Methods

In this retrospective analysis, we used imaging and clinical data obtained from the Alzheimer's Disease Neuroimaging Initiative (ADNI) to identify MCI patients who 1) converted to AD at least 24 months after initial study enrollment and 2) did not convert to AD at any point in study enrollment with at least 24 months of follow-up.

For all patients, baseline MRIs were analyzed using Cortechs.ai NeuroQuant® (software version 5.2.0), generating structure-specific normative percentiles. Univariate analysis was used to assess the associations between MRI normative percentile values among patients with AD conversion (converters) and those without (non-converters). Independent predictors of early AD conversion were identified using a multivariate stepwise logistic regression model and discrimination was evaluated by ROC analysis (AUC).

Results

So far, a total of 65 patients have been included (Converted, n=51; non-converted, n=14). In univariate analysis, lower normative percentiles across the temporal and limbic regions were associated with higher odds of AD conversion including the amygdala (OR= 0.952, 95% CI 0.925-0.981, p=0.002), temporal cortex (OR= 0.953, 95% CI 0.924-0.983, p=0.002), fusiform cortex (OR= 0.958, 95% CI 0.930-0.986, p=0.004), entorhinal cortex (OR= 0.967, 95% CI 0.945-0.990, p= 0.005), hippocampal occupancy score (OR= 0.975, 95% CI 0.954-0.996, p=0.02) and hippocampus (OR= 0.966, 95%CI 0.938-0.996, p=0.03). Multivariate logistic regression analysis revealed normative percentiles of the amygdala (OR= 0.966, 95% CI 0.935-0.998, p=0.04) and fusiform cortex (OR= 0.965, 95% CI 0.933-0.998, p=0.04) as the only independent predictors. The final combined model achieved an AUC of 0.83 (95% CI 0.68-0.94). Using this model, if the normative percentile values of amygdala <0.83 and fusiform cortex < 0.76, this model predicts AD conversion with an overall accuracy of 75% (sensitivity 71%, specificity 93%).

Conclusion

Preliminary results showed that our combined model using automated volumetric analysis of the amygdala and fusiform cortex can predict conversion from MCI to AD up to two years prior to diagnosis. These findings may be useful in risk stratification of patients and aid identification of those most at risk of AD conversion for more targeted assessment. We plan to increase the number of participants to 100 in each cohort (converters and non-converters) by the time of ASNR.

Funding for ADNI has been provided by the National Institute on Aging (NIA), the National Institute of Biomedical Imaging and Bioengineering (NIBIB), the Food and Drug Administration (FDA), private pharmaceutical companies and non-profit organizations.

References

1. Luo W, Airriess C, Albright J. The NeuroQuant normative database comparing individual brain structures. CorTechs Labs; 2015.
2. Braak H, Alafuzoff I, Arzberger T, Kretzschmar H, Del Tredici K. Staging of Alzheimer disease–associated neurofibrillary pathology using paraffin sections and immunocytochemistry. *Acta Neuropathol* 2006;112:389–404.
3. Klöppel S, Peter J, Ludl A, et al. Applying automated MR-based diagnostic methods to the memory clinic: a prospective study. *J Alzheimers Dis* 2015;47:939–954.

615 Initial Intracranial MR Angiography Findings in the Large Cohort TwinsUK Imaging Study

Jon O. Cleary MD-PhD, FRCR[1], Liane S Canas[2], Maria Zuluaga PhD[3], Anthony N Price PhD[1], Marc Modat PhD[2]
[1]King's College London/Guy's and St. Thomas' NHS Foundation Trust, London, London, United Kingdom. [2]King's College London, London, London, United Kingdom. [3]EURECOM/King's College London, Biot, Alpes-Maritimes, France

Purpose

The TwinsUK Imaging Study is creating a ~2,500 monozygotic (MZ) and dizygotic (DZ) twin repository, which, in combination with extensive longitudinal, non-imaging TwinsUK data, aims to identify key biomarkers of ageing and disease; and determine genetic, lifestyle and environmental influences.

A comprehensive multi-organ imaging protocol includes the whole neuro-axis, with time-of-flight (ToF) intracranial MR angiography (MRA)[1], potentially allowing identification of genetic influences on cerebrovascular phenotype.

While there have been previous large-scale population studies examining intracranial anatomy[2,3], MRA studies in twins have been very limited[4]. These studies also typically perform visual assessment of circle of Willis variants in each dataset.

Given the high numbers in the TwinsUK study, there is need for a more automated approach to analysis, which could allow a more detailed assessment of arterial tree features.

We performed a preliminary assessment of differences in arterial morphology between MZ and DZ pairs in an initial, unique twin MRA dataset, using automated methodology.

Materials & Methods

In this IRB-approved study, 728 individual twins (278 DZs/450 MZs, median age 67 years, IQR: [58; 73], Males: 95) underwent 3T intracranial ToF (Siemens MAGNETOM Vida, 64-channel Head/Neck Coil, 0.3x0.3x0.6mm, compressed-sensing ToF MRA, TR/TE/FA=22ms/3.4/18deg, acquisition time:3min13sec) as part of a comprehensive multiorgan imaging protocol[1].

MRA vessel segmentation used a deep learning model (nnUNet v2)[5]. Vessel segments were extracted and metrics (vessel count, total length, bifurcations, volume, curvature, and tortuosity) computed using graph-analysis (metrics overview given in Figure1).

Metrics were aggregated by vascular region after standardization to a vascular territory atlas and summarized for each twin (Figure1). We calculated absolute differences within pairs for each feature and region and assessed differences between MZ and DZs using Mann-Whitney U testing (two-sided, p<0.05 deemed significant).

Results

Summarized in Table1, overall median twin-pair differences in vessel metrics were typically smaller in MZ compared to DZ twins. In particular, differences were significant in: component number, vessel length, volume, and bifurcation root-mean-square curvature (a tortuosity measure).

Figure2: Example rigid-registered raw MRA volume-renderings from the most similar MZ twin pair (based on lowest differences in an aggregate of imaging metrics), shows the degree of marked overlap of the vessel tree overall.

Comparing differences between MZ and DZ pairs regionally, these were significant in:

- Posterior tree *components* (basilar, cerebellar regions)
- *Total length* of anterior cerebral (ACA) and middle cerebral (MCA) artery regions (frontal, parietal, insula)
- *Tortuosity* in frontal MCA regions

This is shown graphically for total vessel length in Figure3, with generally greater length differences in DZ compared to MZ twins in the frontal regions (warmer colors, normalized to maximum population length difference for that region).

Conclusion

Initial findings of our analysis of 728 individuals – the largest twin MRA dataset so far – suggest genetic factors may strongly influence cerebrovascular variation, particularly vessel length, volume, and tortuosity given the smaller differences observed between MZ vs. DZ twins in these metrics.

Recruitment is ongoing and we continue to add additional participants to our analysis.

Future inclusion of non-imaging data may help disentangle genetic and environmental factors affecting phenotypic differences within pairs.

References

1. Thornley R, Ning Z, Canas LS et al The TwinsUK MR Imaging study protocol: Brain and spine at 3T and cardiac plus whole-body at 0.55T Proc. ISMRM 2025 #1649 2025

2. Hindenes LB, Håberg AK, Johnsen LH et al. . Variations in the Circle of Willis in a large population sample using 3D TOF angiography: The Tromsø StudyPLoS ONE 15(11): e0241373, https://doi.org/10.1371/journal.pone.024137

3. Qiu C, Zhang Y, Xue C et al. MRA Study on Variation of the Circle of Willis in Healthy Chinese Male AdultsBiomed Res Int. 2015 Jan 5;2015:976340. https://doi.org/10.1155/2015/976340

4. Forgo B, Tarnoki AD, Tarnoki DL, et al. Are the Variants of the Circle of Willis Determined by Genetic or Environmental Factors? Results of a Twin Study and Review of the Literature Twin Research and Human Genetics, 21 Number 5 pp. 384–393 https://doi.org/10.1017/thg.2018.50

5. Galati F, Falcetta D, Cortese R, et al. Multi-Domain Brain Vessel Segmentation Through Feature Disentanglement Machine Learning for Biomedical Imaging 2025 477-495https://doi.org/10.59275/j.melba.2025-4582

Images/Tables

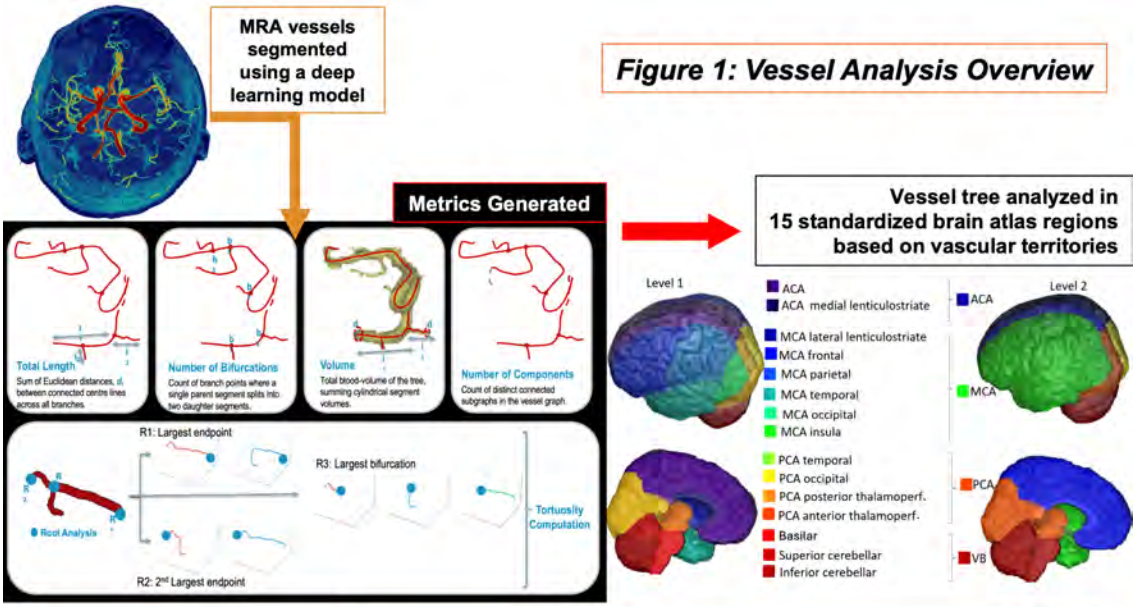

Figure 1: Vessel Analysis Overview

Table 1

MZ and DZ Global Twin Pair Differences	Median DZ (n=278)	IQR DZ	Median MZ (n=450)	IQR MZ	*p-value*
Number of Components	33	14; 64	30	12.00; 59.00	$4.8x10^{-5}$
Total Length (mm)	175	80; 335	150	67; 291	$1.21x10^{-11}$
Number of Bifurcations	11	4; 26	11	4; 24	*0.03*
Volume (mm^3)	2544	1149; 5034	2172	932.10; 4294	$7.65x10^{-13}$
Largest Bifurcation Root-Mean-Square Curvature (~Tortuosity)	3.1	1.2; 6.7	2.9	1.1; 6.4	*0.04*

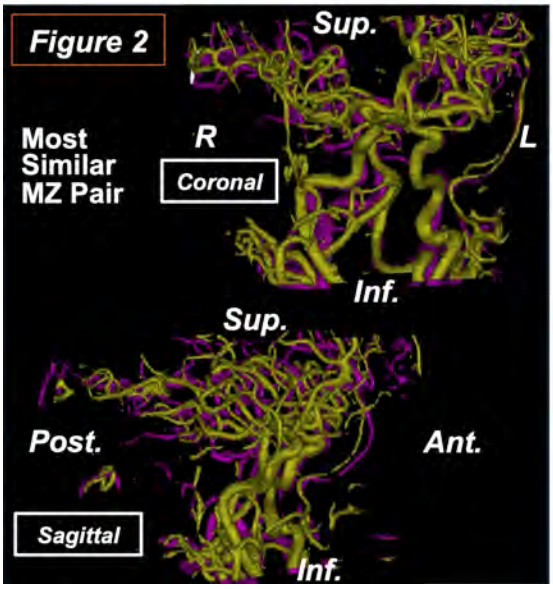

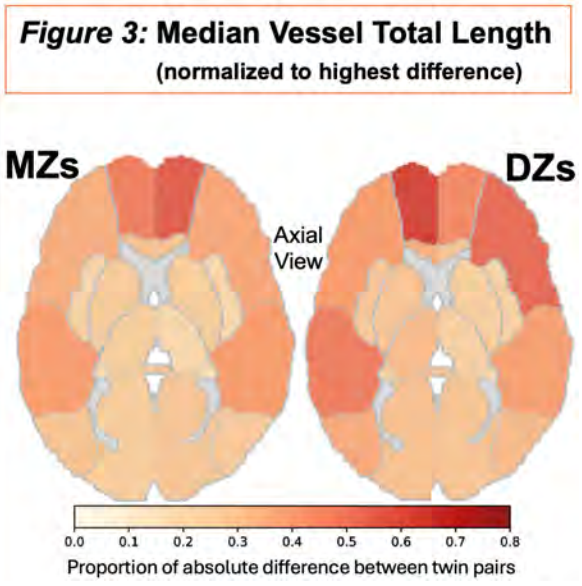

692 **CHANTER Syndrome and Related Pathologies: a Spectrum of MR Brain Imaging Findings in Acute Toxic Disorders**

Kevin Peng MD, Adonay Castillo MD, Ivan Ivanov DO, Mehruba Parris MD, Esther A. Nimchinsky MD, PhD
Rutgers New Jersey Medical School, Newark, NJ, USA

Purpose

Cerebellar, hippocampal, and basal nuclei transient edema with restricted diffusion (CHANTER) syndrome is a disease entity defined by unique imaging findings, recently described in patients presenting in acutely unresponsive states following exposure to illicit drugs. It is most frequently encountered in opioid use,[1] though it has also been reported in the setting of cocaine toxicity.[3] As its name suggests, CHANTER syndrome is characterized by otherwise unexplained edema and diffusion restriction in three characteristic brain regions of the cerebellum, hippocampi, and basal

ganglia, and can frequently lead to significant morbidity and mortality related to development of acute obstructive hydrocephalus and herniation[1,2]. Despite the severity of this disease entity, there has been no large case series investigating CHANTER syndrome and related neuroimaging findings in the setting of various toxic exposures.

Materials & Methods

A retrospective review of imaging and clinical records of 107 patients with toxic or metabolic exposures who underwent MR brain imaging at our tertiary care center over the past 7 years was performed with IRB approval. The clinical records were reviewed for neurologic findings and toxic exposures, including but not limited to urine drug screen at presentation. Advanced toxicology screening was also performed in some, but not all, cases. MR imaging was screened for characteristic signal changes of CHANTER syndrome in the cerebellum, hippocampi, and basal ganglia.

Results

Five cases of the typical MR brain imaging findings of CHANTER syndrome were identified (mean age 41.4 years, 60% female), with diffusion restriction in all three structures (cerebellum, hippocampi, and basal nuclei). Of these typical CHANTER syndrome cases, 2 (40%) had urine drug screens positive only for opiates, 2 (40%) were positive only for cocaine, and 1 (20%) was positive for both. Other cases demonstrated diffusion restriction in 2 out of the typical triad of brain regions, sparing the third, including 5 cases without hippocampal involvement, 2 without basal ganglia involvement, and 1 without cerebellar involvement. Of these 8 "incomplete" or *forme fruste* CHANTER syndromes, none had urine drug screens positive for opiates only, 2 (25%) were positive for opiates and cocaine, 4 (50%) were positive for only cocaine, and 2 had other toxic exposures to ethylene glycol and hydrogen sulfide respectively. One case was identified with T2/FLAIR signal abnormalities in all three brain regions without diffusion restriction.

Conclusion

Typical neuroimaging findings of CHANTER syndrome were seen in cases of both opioid and cocaine positive drug screens, indicating that contrary to the predominant pattern of previously described literature, this disease pattern is not relatively specific for opioid use. A subset sample showed partial but potentially related neuroimaging findings involving only 2 regions of the typical triad, most commonly sparing the hippocampus, all of which were less commonly associated with opioid toxicity. An instance of edema without diffusion restriction involving the cerebellum, hippocampi, and basal ganglia, may suggest a possible subacute or evolving form of the syndrome. These observations may support the reconceptualization of CHANTER syndrome as a spectrum of disease potentially seen in the context of varying toxic exposures rather than uniquely opioids.

References

1. Jasne AS, Alsherbini KH, Smith MS, Pandhi A, Vagal A, Kanter D. Cerebellar Hippocampal and Basal Nuclei Transient Edema with Restricted diffusion (CHANTER) Syndrome. Neurocrit Care. 2019 Oct;31(2):288-296. doi: 10.1007/s12028-018-00666-4. PMID: 30788708; PMCID: PMC6757017.
2. Mallikarjun KS, Parsons MS, Nigogosyan Z, Goyal MS, Eldaya RW. Neuroimaging Findings in CHANTER Syndrome: A Case Series. AJNR Am J Neuroradiol. 2022 Aug;43(8):1136-1141. doi: 10.3174/ajnr.A7569. Epub 2022 Jul 7. PMID: 35798385; PMCID: PMC9575414.
3. Meadow M, Tsai M, Carter S. CHANTER syndrome in a cocaine positive patient. Radiol Case Rep. 2025 May 30;20(8):4123-4127. doi: 10.1016/j.radcr.2025.05.013. PMID: 40519849; PMCID: PMC12164012.

Images/Tables

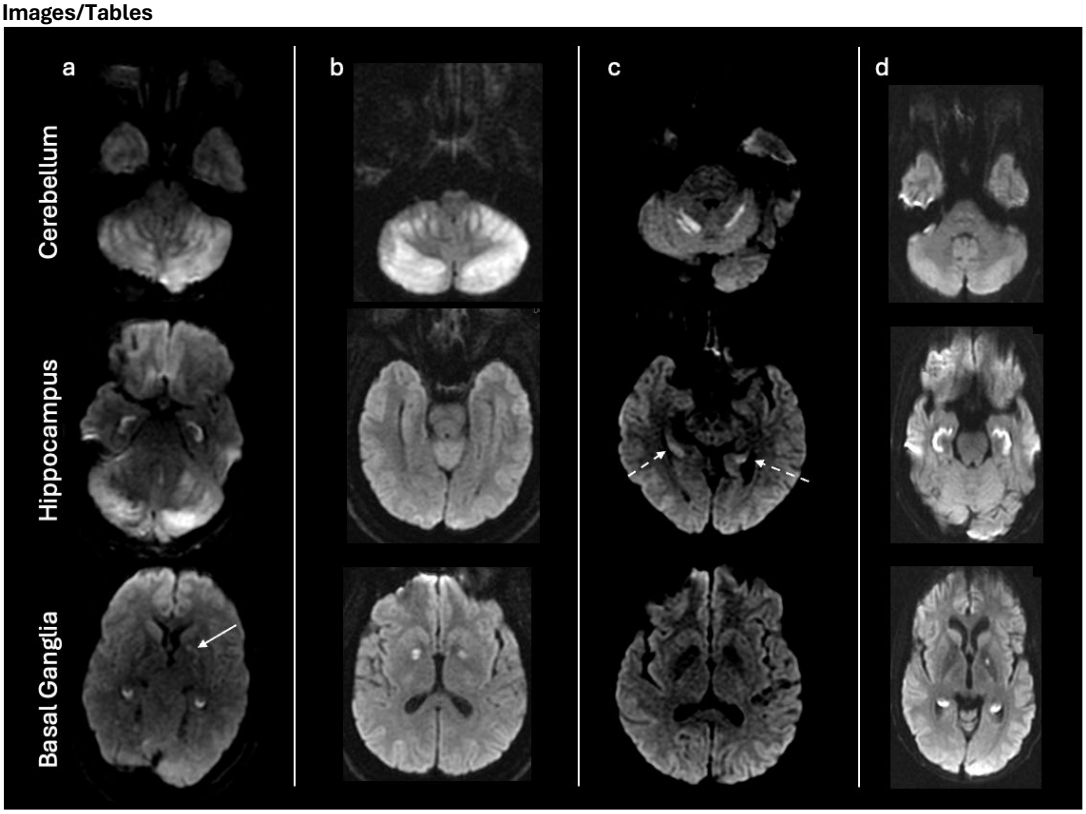

Fig. 1 Diffusion-weighted magnetic resonance imaging by patient and brain regions, demonstrating variable involvement of the cerebellum, hippocampus, and cerebellum. A typical example of CHANTER syndrome (a) demonstrates diffusion restriction in the cerebellum, hippocampus, and subtle diffusion restriction in the left globus pallidus (white solid arrow). "Incomplete" forms of CHANTER syndrome involve two out of these three brain regions, with examples shown here which spare the hippocampus (b), basal ganglia (c) (subtle symmetric diffusion restriction in the hippocampi shown by the dashed white arrows), and cerebellum (d).

310 Latent Class Symptom Profiles and White Matter Injury Trajectories in Mild Traumatic Brain Injury

Sohae Chung PhD[1], Seon-Hi Shin PhD[1], Alaleh Alivar PhD[1], Jed N McGiffin PhD[2], Santiago Coelho PhD[1], Joseph F Rath PhD[3], Els Fieremans PhD[1], Dmitry S Novikov PhD[1], Prin X Amorapanth MD[3], Steven R Flanagan MD[3], Yvonne W Lui MD[1]

[1]Department of Radiology, NYU Grossman School of Medicine, New York, NY, USA. [2]Department of Rehabilitation Medicine, University of Washington School of Medicine, Seattle, WA, USA. [3]Department of Rehabilitation Medicine, NYU Grossman School of Medicine, New York, NY, USA

Purpose

Heterogeneity in symptom profiles after mild traumatic brain injury (MTBI) hampers discovery of robust imaging biomarkers. We used latent class analysis (LCA) of Rivermead Post-concussive Questionnaire (RPQ) [1] symptoms to define data-driven phenotypes and tested whether white matter (WM) microstructural changes evolve differently over time to inform risk stratification and clinical decision making.

Materials & Methods

3T multi-shell diffusion MRI was obtained in 54 MTBI patients within 1 month of injury; a subset (n=24) returned for 6 months. Thirty-one neurologically normal controls were scanned once. RPQ symptoms were grouped into 9 clinically informed domains (RPQ-3, somatic, irritability, depression, frustration, poor memory, poor concentration, mental slowing, restlessness). LCA of binarized RPQ items (0-1 = absent; 2-4 = present) defined symptom-based phenotypes. Diffusion data were processed using in-house pipelines [2, 3]. ROI analyses used MANCOVA across 11 diffusion metrics (see Table), comparing MTBI phenotypes with controls while adjusting for age.

Results

LCA identified three phenotypes (Fig.1): Less symptomatic, Cognitively symptomatic, and Globally symptomatic. Abnormality burden scaled with symptom severity (Fig.2). At baseline (<1 month), the Less symptomatic group showed focal involvement of the genu of the corpus callosum (CC) (decreased MD/AD/RD/D_a/$D_e^{\parallel}$/$D_e^{\perp}$; increased MK). The Cognitively symptomatic group demonstrated broader abnormalities involving the internal capsule, corona radiata, and patches of the superior longitudinal fasciculus (SLF) (decreased FA/AK; increased D_a/$D_e^{\parallel}$). The Globally symptomatic group exhibited the most widespread patterns, spanning the genu/body of the CC, internal capsule, corona radiata, and SLF (decreased FA/MK/AK/RK; increased MD/AD/RD/D_a). At 6 months, the Less symptomatic group (n=3) was underpowered and is not shown; Cognitively and Globally symptomatic groups displayed persistent abnormalities, most notably within callosal, capsular, and posterior projection/associated pathways (decreased MD/AD/RD/D_a/$D_e^{\parallel}$/$D_e^{\perp}$; increased MK/AK/RK). Aggregate analyses of All MTBI recapitulated but diluted phenotype-specific effects.

Conclusion

Symptom-informed stratification reveals distinct, phenotype-linked WM injury patterns, from focal to widespread with increasing symptom severity. By 6 months, cognitively and globally symptomatic groups retained abnormal microstructural signatures, whereas the overall pattern converged toward that of the less symptomatic baseline phenotype, suggesting partial recovery and phenotype-dependent trajectories. These findings highlight the value of longitudinal, symptom-anchored imaging biomarkers for individualized prognosis and monitoring recovery after MTBI.

References

1. Potter S., et al. The Rivermead Post Concussion Symptoms Questionnaire: a confirmatory factor analysis. J Neurol 253:1603-1614, 2006.
2. Novikov D, et al. Quantifying brain microstructure with diffusion MRI: Theory and parameter estimation.
NMR Biomed 32:e3998, 2019.
3. Coelho S, Baete SH, Lemberskiy G, et al. Reproducibility of the Standard Model of diffusion in white matter on clinical MRI systems. *Neuroimage* 2022;257:119290

Images/Tables

Table: Study design and MRI parameters

Subjects	**54 MTBI patients** (35±13 years old; RPQ total scores, 25±15) **31 normal controls** (34±11 years old; RPQ total scores, 3±3)
Symptom measures	Rivermead Post-concussion symptoms Questionnaire (**RPQ**) [1]; 1) RPQ-3 (headaches, dizziness, nausea/vomiting); 2) somatic (phonophobia, sleep disturbance, fatigue, blurred vision, photophobia, double vision); 3) irritability; 4) depression; 5) frustration; 6) poor memory; 7) poor concentration; 8) mental slowing; and 9) restlessness.
Multi-shell diffusion MRI	5 b-values = 0.25, 1, 1.5, 2, 2.5 ms/μm² with total 137 diffusion-encoding directions, 2.5 mm-isotropic resolution, FOV = 220 × 220 mm², slices = 56, TR/TE = 4.9s/95ms, GRAPPA factor = 2
11 diffusion metrics	DTI: fractional anisotropy (**FA**), mean/axial/radial diffusivities (**MD/AD/RD**) DKI: mean/axial/radial kurtosis (**MK/AK/RK**) SMI [3,4]: axonal water fraction (***f***), intra-axonal diffusivity ($\mathbf{D_a}$), extra-axonal axial diffusivity ($\mathbf{D_e^{\parallel}}$), extra-axonal radial diffusivity ($\mathbf{D_e^{\perp}}$)
WM ROIs	25 major white matter ROIs from JHU-ICBM-DTI-81 WM atlas

References:

1. Potter S., et al. The Rivermead Post Concussion Symptoms Questionnaire: a confirmatory factor analysis. J Neurol 253:1603-1614, 2006.
2. Novikov D, et al. Quantifying brain microstructure with diffusion MRI: Theory and parameter estimation. NMR Biomed 32:e3998, 2019.
3. Coelho S, Baete SH, Lemberskiy G, et al. Reproducibility of the Standard Model of diffusion in white matter on clinical MRI systems. *Neuroimage* 2022;257:119290

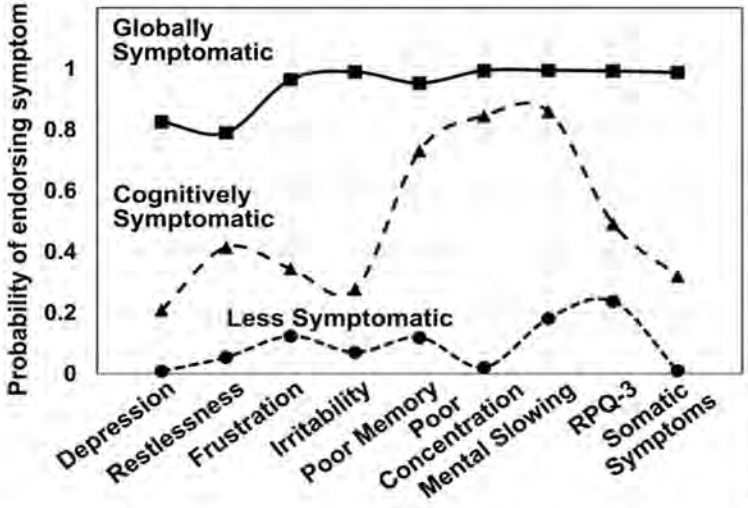

Figure 1. RPQ symptom-endorsement probabilities across three LCA-derived subgroups. 1) Less symptomatic: uniformly low endorsement across domains. 2) Cognitively symptomatic: selectively elevated endorsement for memory, concentration, and mental slowing with comparatively fewer somatic complaints. 3) Globally symptomatic: high endorsement across nearly all domains, reflecting the broadest symptom burden. RPQ-3 denotes the triad of headaches, dizziness, and nausea; and somatic symptoms include phonophobia, sleep disturbance, fatigue, blurred vision, photophobia, and double vision.

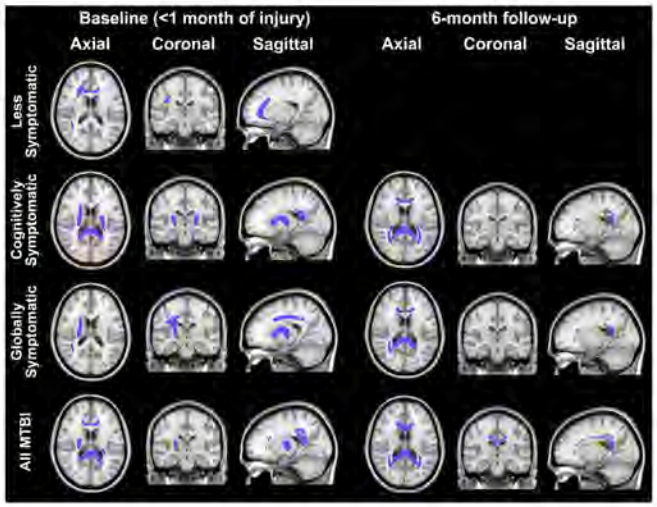

Figure 2. Summary composite maps comparing MTBI and health controls with respective to 11 diffusion metrics reveal significant diffusion differences (purple) at baseline (<1 month) and 6-month follow-up, stratified by LCA phenotypes (Less, Cognitive, Global) and All MTBI. The Less-symptomatic group is shown as baseline only (6-month omitted; n=3). Abnormality burden scales with symptom severity–focal callosal changes in Less symptomatic; broader internal capsule/corona radiata/SLF in Cognitive/Global with persistence at 6 months.

---

535 **Photon-Counting Spectral Integration Improves Head CT Gray-White CNR/SNR Beyond Any Single VMI**

Yu Sakai MD[1], Lori Huang[2], Konstanze V Guggenberger MD[3], Fengling Hu PhD[2], Courteney Wiredu[2], Colbey W Freeman MD[1], Ada Bozikov[4], Martin Rybertt[1], Peter B Noël PhD[1], Jae W Song MD, MS[1]

[1]Department of Radiology, University of Pennsylvania, Philadelphia, PA, USA. [2]Perelman School of Medicine, University of Pennsylvania, Philadelphia, PA, USA. [3]Department of Radiology, University of Wuerzburg, Wuerzburg, Bavaria, Germany. [4]Mary Baldwin University, Staunton, VA, USA

Purpose

Photon-counting CT (PCCT) enables virtual monoenergetic imaging (VMI), which allows reconstruction of images at different energy levels to optimize tissue contrast and reduce noise or beam-hardening artifacts. However, adoption remains limited because optimal keV selection varies by tissue, and reviewing multiple VMIs is impractical in clinical workflows. To address this, we developed a voxel-wise spectral area-under-the-curve (AUC) map that integrates attenuation across all energy levels into a single image. By combining information from the full spectral range, we hypothesize this approach would enhance signal averaging and reduce noise variation, yielding higher signal-to-noise (SNR) and contrast-to-noise ratios (CNR) than any single-energy VMI for noncontrast head PCCT exams.

Materials & Methods

In this retrospective single-center study (August 2022–December 2024), adults who underwent noncontrast head PCCT and brain MRI within 4 days were included if the bifrontal cortex, centrum semiovale, caudate, pons, medulla, and cerebellum demonstrated no acute/subacute infarction on DWI/ADC. The goal was to assess parenchymal signal variance across VMIs without confounding by underlying pathology. PCCT, DWI, and ADC images were reviewed to confirm the absence of infarcts; FLAIR was not reviewed, which may have limited detection of chronic microvascular changes.

Eleven virtual monoenergetic images (40-140 keV) were reconstructed, and voxel-wise spectral area-under-the-curve (AUC) maps were generated using trapezoidal integration of attenuation-energy curves. Circular ROIs (5 mm) were bilaterally placed using 3D Slicer in the centrum semiovale, cortical gray matter, caudate head, cerebellar gray matter, and cerebellar white matter (**Figure 1**); VMIs are by default co-registered and ROIs were propagated to all VMIs. A 30-mm ROI was centered on the pontine region between the petrous bones using a prior method[1], and a 10-mm ROI on the medulla. Gray/white matter differentiation was quantified by analyzing mean Hounsfield Units (HU) from the ROIs and calculating CNR defined as $CNR = |HU_{GM} - HU_{WM}| / \sqrt{(SD_{GM}^2 + SD_{WM}^2)}$, SNR defined as SNR = Mean/SD; image noise was measured by SD. Supratentorial analysis compared the bifrontal cortical gray matter and centrum semiovale, while infratentorial analysis compared cerebellar gray/white matter pairs. Pons, medulla, and

caudate were analyzed separately. Paired comparisons of AUC maps versus clinically-equivalent 70 keV VMIs from the same PCCT exam were performed using the Wilcoxon signed-rank test.

Results

Nine patients (mean age, 67 years; 5 men) were included. The spectral AUC map demonstrated the highest supratentorial and infratentorial gray/white matter CNR and also the highest SNR across all anatomic regions (**Figure 2**). Compared with the clinically-equivalent VMI image at 70 keV, noise (SD) was significantly lower across all brain regions (median 31% reduction; all $p < 0.01$), SNR was higher across all regions (median 42% increase; all $p < 0.01$), and gray/white matter CNR was higher for both the supratentorial (5.9 vs 4.4) and infratentorial (4.7 vs 3.1; both $p < 0.01$) brain.

Conclusion

Spectral AUC maps consistently showed higher supratentorial/infratentorial gray/white differentiation and higher SNR regardless of anatomical location. AUC maps outperformed all other single VMIs, including clinical equivalent (70keV).

References

1. van Ommen F, Kauw F, Bennink E, Heit JJ, Wolman DN, Dankbaar JW, de Jong HWAM, Wintermark M. Image Quality of Virtual Monochromatic Reconstructions of Noncontrast CT on a Dual-Source CT Scanner in Adult Patients. Acad Radiol. 2021 Oct;28(10):e323-e330. doi: 10.1016/j.acra.2020.05.038. Epub 2020 Jun 30. PMID: 32616420.

Images/Tables

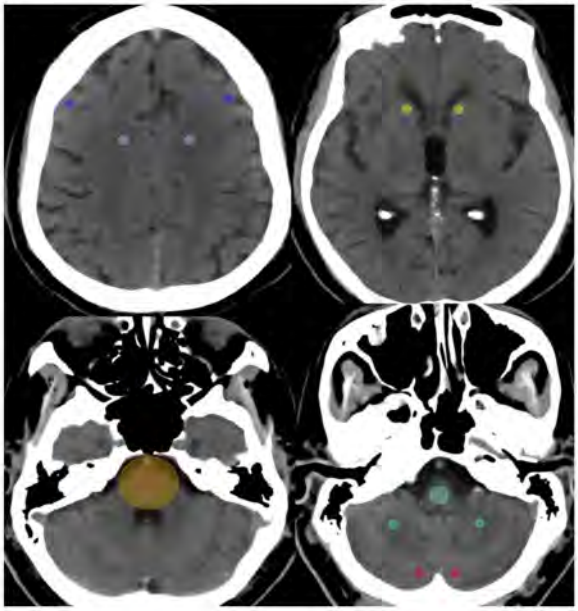

Figure 1. Sample ROIs obtained on 3D Slicer; 5 mm ROIs at centrum semiovale (lavendar), bifrontal cortical gray (blue), caudate (yellow), cerebellar gray/white (red and green). 30 mm ROI at pontine region (brown) between petrous bones. 10 mm ROI at medulla (light blue).

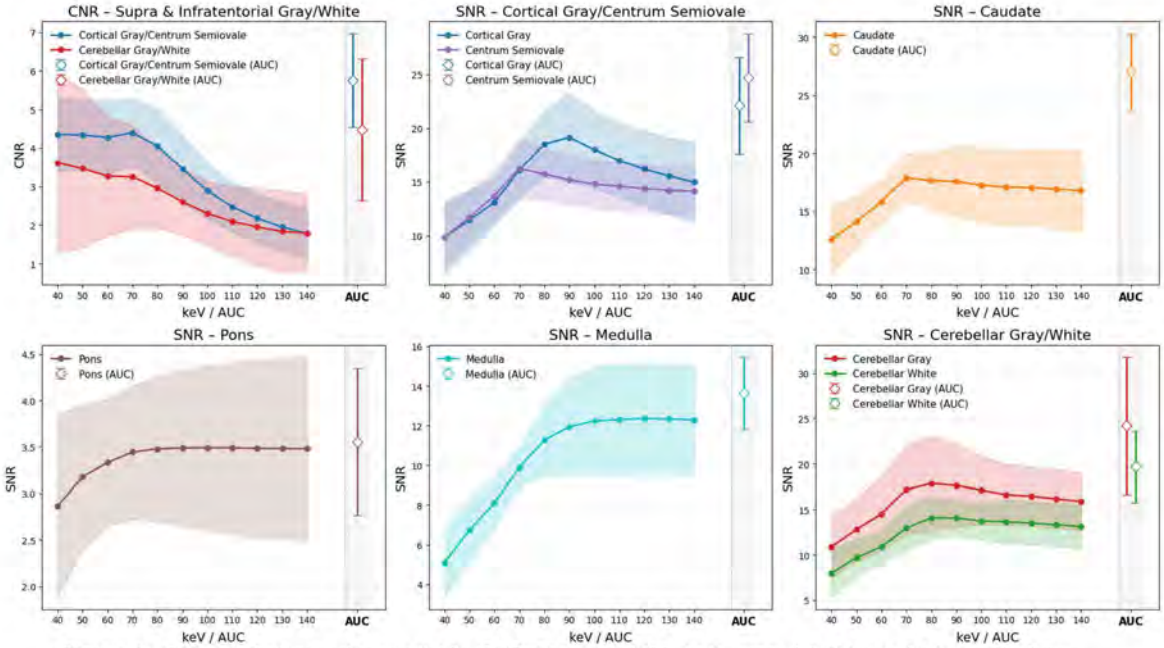

Figure 2. AUC map has superior gray/white CNR than any VMI in both supra & infratentorial (top left). Other panels show AUC maps have superior SNR than any other VMI in all assessed anatomical locations.

551 Cerebrovascular Outcomes in Reversible Cerebral Vasoconstriction Syndrome With and Without Posterior Reversible Encephalopathy Syndrome

Hamza A Salim MD[1], Orabi Hajjeh MD[1], Marco Colasurdo MD[2], Dheeraj Gandhi MD[3], Ajay Malhotra MD[4], Vivek Yedavalli MD[5], Max Wintermark[6], Dhairya A, Lakhani MD[7]

[1]MD Andersonc Cancer Cener, Houston, TX, USA. [2]Department of Interventional Radiology, Oregon Health and Science University, Portland, OR, USA. [3]Division of Neurointerventional Surgery, Department of Neurosurgery University of Maryland Medical Center, Baltimore, MD, USA. [4]Department of Radiology Yale New Haven Hospital New Haven CT, New Haven, CT, USA. [5]Department of Radiology, Division of Neuroradiology, Johns Hopkins Medical Center, Baltimore, Maryland, USA. [6]Department of Neuroradiology, MD Anderson Medical Center, Houston, TX, USA. [7]Department of Neuroradiology, Rockefeller Neuroscience Institute, West Virginia University, Morgantown, WV, USA

Purpose

The prognostic significance of posterior reversible encephalopathy syndrome (PRES) among patients with reversible cerebral vasoconstriction syndrome (RCVS) is uncertain.

Materials & Methods

We performed a retrospective cohort study in TriNetX. Adults with an index diagnosis of RCVS were stratified by concomitant PRES. Patients with prior stroke, hemorrhage, or cerebral edema were excluded. Propensity-score matching (1:1) balanced covariates. Primary outcomes at 1 and 5 years were ischemic stroke, subarachnoid hemorrhage, intracerebral hemorrhage, cerebral edema, and a composite of these events; secondary outcomes were inpatient readmission and emergency department visits. Odds ratios (ORs) with 95% confidence intervals (CIs) were estimated.

Results

Of 162 RCVS+PRES and 3295 RCVS-only patients, 161 matched pairs were created (standardized differences <0.10). At 1 year, ischemic stroke occurred more often with RCVS+PRES than RCVS alone (31.7% vs. 18.6%; HZ, 1.536; 95% CI, 1.070-2.206) and inpatient readmissions were higher (47.2% vs. 29.8%; OR, 1.970; 95% CI, 1.370-2.833); rates of subarachnoid or intracerebral hemorrhage were not significantly different. At 5 years (156 matched pairs), RCVS+PRES was associated with higher risks of ischemic stroke (44.9% vs. 32.7%; HR, 1.536; 95% CI, 1.536-2.206), subarachnoid hemorrhage (32.1% vs. 21.2%; HR, 1.585 ; 95% CI, 1.21-2.461), cerebral edema (28.2% vs. 10.9%; HR, 2.775; 95% CI, 1.585-4.858), and the composite outcome (71.2% vs. 49.4%; HR, 1.694; 95% CI, 1.265-2.269).

Conclusion

Among patients with RCVS, concomitant PRES identifies a high-risk subgroup with excess ischemic events at 1 year and sustained, broader cerebrovascular complications through 5 years, supporting closer monitoring and risk-factor management.

References

Ribas MZ, Paticcié GF, de Medeiros SDP, et al. Reversible cerebral vasoconstriction syndrome: literature review. *Egypt J Neurol Psychiatr Neurosurg* 2023;59:5.

569 Membranous Chronic Subdural Hematomas Show Superior Resolution and Lower Recurrence After Surgical Evacuation with Adjunctive MMAE

Hamza A Salim MD[1], Dhairya A. Lakhani MD[2], Muhammed Amir Essibayi MD, MS[3], Vivek Yedavalli MD[4], Max Wintermark MD[1], David J Altschul MD[3], Adam A. Dmytriw MD MPH MSc[5]

[1]Department of Neuroradiology, MD Anderson Medical Center, Houston, TX, USA. [2]Department of Neuroradiology, Rockefeller Neuroscience Institute, West Virginia University, Morgantown, WV, USA. [3]Department of Neurological Surgery, Montefiore-Einstein Cerebrovascular Research Lab, Montefiore Medical Center, Albert Einstein College of Medicine, Bronx, NY, USA. [4]Department of Radiology, Division of Neuroradiology, Johns Hopkins Medical Center, Baltimore, Maryland, USA. [5]Neuroendovascular Program, Massachusetts General Hospital & Brigham and Women's Hospital, Harvard Medical School, Boston, MA, USA

Purpose

Chronic subdural hematoma (cSDH) is a common neurosurgical condition with high recurrence rates following surgical evacuation, largely due to persistent inflammation and neovascularized membrane formation. Middle meningeal artery embolization (MMAE) is a minimally invasive adjunctive therapy that targets membrane vascularity to reduce re-bleeding and promote hematoma resolution. However, the effect of membrane presence on outcomes following MMAE remains unclear. This study aimed to assess whether membrane presence on pre-procedural imaging is associated with improved hematoma resolution, reduced recurrence, and decreased need for repeat surgical evacuation in patients undergoing combined surgical evacuation and adjunctive MMAE.

Materials & Methods

In this retrospective cohort study, 691 patients (849 cSDHs) from the international MESH registry underwent surgery plus MMAE between January 2018 and December 2024. Membranous hematomas were identified on CT by neuroradiologists blinded to outcomes. Primary outcomes included hematoma resolution (>60% and >80% reduction in thickness), recurrence, and repeat surgical evacuation. Multivariable logistic regression adjusted for clinical and imaging variables.

Results

Of 849 hematomas, 460 were membranous and 389 non-membranous. Membranous cSDHs were initially thicker but showed greater resolution (>60%: 71% vs. 59%, p<.001; >80%: 51% vs. 41%, p=.004) and lower recurrence (1.8% vs. 4%, p=.05). Repeat evacuation was less frequent in the membranous group (4.9% vs. 7.4%, p=.18). Membrane presence independently predicted higher resolution (aOR 1.54; 95% CI: 1.25-1.89; p<.001) and lower recurrence (aOR 0.50; 95% CI: 0.31-0.81; p=.005).

Conclusion

Membrane presence on imaging is associated with improved radiographic outcomes and reduced recurrence following surgery with adjunctive MMAE. A non-significant trend toward fewer repeat surgeries was also observed, suggesting membrane status may serve as a prognostic imaging biomarker in cSDH management.

References

Wang X, Hung A, Das O, et al. Membrane presence in chronic subdural hematomas is associated with a reduced rate of resolution following middle meningeal artery embolization. *Clin Neurol Neurosurg*. 2025;255:108977. doi:10.1016/j.clineuro.2025.108977

Images/Tables

Table 3. Unadjusted and Adjusted Odds Ratios for Key Clinical and Radiographic Outcomes Comparing Membranous vs. Non-Membranous Hematomas

Characteristic	Unadjusted		Adjusted*	
	OR (95% CI)[1]	p-value	OR (95% CI)[1]	p-value
Recurrence	0.51 (0.33 to 0.77)	**0.002**	0.50 (0.31 to 0.81)	**0.005**
SDH resolution (>60%)	1.35 (1.13 to 1.60)	**<0.001**	1.54 (1.25 to 1.89)	**<0.001**
SDH resolution (>80%)	1.24 (1.04 to 1.47)	**0.015**	1.45 (1.18 to 1.77)	**<0.001**
Repeat surgical evacuation	0.78 (0.51 to 1.18)	0.24	0.72 (0.45 to 1.14)	0.16

[1] **OR = Odds Ratio, CI = Confidence Interval**

* ***All estimates were adjusted for the following covariates: age, sex, alcohol use, hematoma type on admission, presence of brain atrophy, presentation subdural hematoma (SDH) thickness, general anesthesia (GA) use and last follow-up time.***

---

644 **Increased Relative Risk of Delayed Hemorrhage in Patients Taking Oral Anticoagulant/Antiplatelet Medications with Concurrent Aspirin Therapy: 10 Year Retrospective Analysis with Updated Clinical Recommendations**

Chang Warren MD, MBA[1], Raven Spencer MD[1], Li Charles MD[1], Laura Eisenmenger MD[2], Michael F Goldberg MD, MPH[1]
[1]Allegheny Health Network, Pittsburgh, PA, USA. [2]University of Wisconsin, Madison, WI, USA

Purpose

The risk of delayed posttraumatic intracranial hemorrhage (DH) in patients on anticoagulant (AC) and antiplatelet (AP) medications is not well established, with studies reporting between 1-10% risk of DH and 0-3% mortality. There are few studies that examine patients taking AC and AP medications along with concurrent aspirin therapy. Management of these patients is difficult due to the risk of potentially catastrophic DH after discharge, while also considering increased time in the emergency department (ED) or observation units if follow-up imaging is performed. We report our eight-year results and networkwide changes in patient management based on updated data.

Materials & Methods

2310 patients (1139 male, 1171 female, average age 77.4 years) taking AP/AC medication as documented in the electronic medical record (EMR) presenting to network EDs with head trauma between 2018 and 2025 were included. The EMR was searched to identify which patients were also taking concurrent aspirin. Repeat CT was typically performed within 24 hours (average follow-up time was 21 hours; 99% were within 3 days). Average time to DH was 20 hours. Patients were included in the study if the initial examination was interpreted as negative and there were no additional instances of trauma between the examinations. All positive studies were reviewed by two board certified neuroradiologists. Patients were excluded if hemorrhage was retrospectively identified on the initial CT. Cases were positive for DH if the initial CT was negative and the follow-up CT demonstrated new hemorrhage. The study was performed under the supervision of the local institutional review board.

Results

Overall, there was 1.9% incidence (44 patients) of DH and 0.2% overall mortality (9 patients). The group of patients taking AP/AC medications with concurrent aspirin had significantly higher risk of DH (34/44, 3.5% vs 0.7%, RR 5.0) and mortality (8/9, 0.8% vs <0.1%) when compared to those taking AP/AC medications alone. The patients taking warfarin or AP medications without aspirin had higher risk of DH when compared to those taking DOAC medications (1.4% vs 0.3%, RR 4.7).

Patients taking DOACs with aspirin also had significantly higher risk of DH than those not taking aspirin (1.9% vs 0.3%, RR 6.3).

Conclusion

Patients taking AP/AC medications with concurrent aspirin had higher risk of DH and mortality than those taking AP/AC medications without aspirin. Based on these results, we updated our EMR to automatically display the AC/AP medications that patients are taking, recommend repeat head CTs on patients taking AP/AC medications with aspirin and administer reversal agents if hemorrhage is detected.

Patients taking warfarin or AP medications without aspirin had higher risk of DH compared to those taking DOACs alone. We now recommend repeat head CTs on patients taking AC/AP medications with aspirin or warfarin or AP agents without aspirin, and reverse the medications when hemorrhage is detected.

Due to consistent data showing a low risk of delayed hemorrhage in patients taking DOACs without aspirin, repeat examinations are deferred unless clinically indicated due to dangerous injury mechanism or lack of social support.

References

Chang W, Yin JD, Li CQ,et al. Increased Relative Risk of Delayed Hemorrhage in Patients Taking Anticoagulant/Antiplatelet Medications with Concurrent Aspirin Therapy: Implications for Clinical Practice Based on Three year Retrospective Analysis in a Large Health System. Emergency Radiology. November, 2021

Nishijima DK, Offerman SR, Ballard DW, et al. Risk of traumatic intracranial hemorrhage in patients with head injury and preinjury warfarin or clopidogrel use.Acad Emerg Med. 2013;20(2):140-145.

Valiuddin H, Alam A, Calice M, et al. Utility of INR For Prediction of DH Among Warfarin Users with Head Injury.J Emerg Med. 2020;58(2):183-190.

Chan N, Sobieraj-Teague M, and Eikelboom JW. Direct oral anticoagulants: evidence and unresolved issues. Lancet. 2020;396(10264):1767-1776.

Mann N, Welch K, Martin A, Subichin M, Wietecha K, Birmingham LE, Marchand TD, George RL. DH in elderly anticoagulated patients sustaining a minor fall. BMC Emerg Med. 2018 Aug 24;18(1):27

Images/Tables

Medication	Total Patients	Negative	Positive	% Positive	Deaths	% Death	Aspirin	Positive w/ aspirin
Apixiban (Eliquis)	760	757	3	0.04%	0	0	335	3
Warfarin (Coumadin)	603	583	20	3.31%	6	1.0%	221	14
Rivaroxaban (Xarelto)	360	352	8	2.22%	0	0	115	7
Clopidogrel (Plavix)	398	385	13	3.26%	3	0.8%	200	11
Other	189	189	0	0	0	0	88	0
Total	2310	2266	44	1.90%	9	0.2%	959	34

All Patients

	DH	No DH
Aspirin	34 (3.5%)	925
No Aspirin	10 (0.7%)	1341

$p < 0.0001$, RR = 5.0

DOACs

	DH	No DH
Aspirin	9 (1.9%)	476
No Aspirin	2 (0.3%)	720

$p < 0.01$, RR = 6.3

Warfarin + AP

	DH	No DH
Aspirin	25 (5.9%)	396
No Aspirin	8 (1.4%)	572

$p < 0.001$, RR = 4.2

Figure 1: a) Patients taking AP/AC medications, and number of patients taking aspirin. **b)** Number of patients with DH taking AP/AC medications with and without aspirin therapy.

Scientific Abstract Power Pitches & Luminary Speaker: Head and Neck/Neurovascular Imaging

3:20 - 4:20pm Monday, 18th May, 2026

826 Maintaining Diagnostic Quality While Cutting Contrast Dose and Cost in Head and Neck CTA

Branten Page D.O.[1], William Faunce B.S.[2], Dereje Negatu Ph.D.[1], Parampreet Kaur M.D.[1], Kavin Mistry M.D.[1], Pallav Shah M.D.[1]
[1]St. Luke's University Health Network, Bethlehem, PA, USA. [2]Temple/St. Luke's School of Medicine, Bethlehem, PA, USA

Purpose

Dual-energy CT angiography (DECTA) improves iodine conspicuity at low-energy virtual monoenergetic reconstructions and affords an opportunity to lower iodinated contrast dose while maintaining diagnostic quality. We evaluated whether a 50 mL Omnipaque 350 protocol maintains image quality compared with 65 mL and 75 mL protocols and its impact on diagnostic quality and quantify the potential cost savings.

Materials & Methods

We retrospectively reviewed 102 adult head and neck DECTA examinations performed on a dual-energy CT platform. Patients received 75 mL, 65 mL, or 50 mL of Omnipaque 350 (n = 34 per group), with all other technical parameters held constant. Quantitative analysis assessed vascular attenuation, signal-to-noise ratio (SNR), contrast-to-noise ratio (CNR), and noise using low-keV monoenergetic (55 keV) and blended reconstructions (120 kVp-like blended reconstruction, which is quantitatively equivalent to ~74 keV). Differences across dose groups were evaluated using the Kruskal-Wallis test with Dunn post-hoc comparisons and Holm adjustment. Two blinded fellowship-trained neuroradiologists with more than 40 years of combined clinical experience evaluated diagnostic image quality and graded artifact and noise severity using standardized Likert-type scales. An internal cost analysis estimated per-exam and annual savings based on Omnipaque pricing and the number of head and neck CTA examinations performed over the previous fiscal year.

Results

All three contrast-dose protocols achieved diagnostic intravascular enhancement based on a ≥200 HU threshold across major head and neck arterial levels.[1-3] Despite contrast volume reduction, the median enhancement values remained well above the diagnostic threshold of 200 HU throughout the craniocervical vasculature.

Qualitative assessments demonstrated no statistically significant differences in image quality, artifact, or noise between cohorts. Regardless of the contrast volume, all examinations with the reduced contrast volume (i.e. at 50 mL and 65 mL) remained diagnostically acceptable and did not demonstrate non-inferiority when compared to full dose (75 mL) studies.

The 33% reduction in contrast volume directly cuts overhead cost, particularly when bulk pricing calculations are utilized. Applied to the 9,073 head and neck CTA studies performed within our health system over the previous fiscal year, this reduction corresponds to an estimated annual savings of approximately 36,000 dollars while maintaining diagnostic performance.

Conclusion

A 50 mL DECTA protocol maintains diagnostic subjective and objective image quality while lowering iodine exposure, which may be particularly beneficial for patients at increased risk for contrast-associated complications. This approach is adaptable across dual-energy CT systems capable of virtual monoenergetic reconstruction and supports broader resource stewardship and value-based care in neurovascular imaging. Reducing iodinated contrast volume from the commonly used 75 mL protocol to 50 mL decreases contrast utilization by 33 percent per exam. Given the large volume of head and neck CTA examinations typically performed in clinical practice, even modest per-study reductions can scale to substantial institutional cost savings.

References

1. Martins J, dos Santos DP, Caramella D, et al. Carotid CT angiography: optimization of luminal enhancement and image quality. J Neuroradiol 2020;47:345-52. DOI: https://doi.org/10.1016/j.neurad.2019.09.004
2. Capps EF, Smith TR, Gupta R, et al. Dual-energy CT angiography for cervical carotid stenosis: diagnostic performance and image quality. AJNR Am J Neuroradiol 2019;40:1402-8. DOI: https://doi.org/10.3174/ajnr.A6123
3. Zhang H, Qian W, Li S, et al. Reduced-iodine contrast protocols in head and neck CT angiography: impact on arterial enhancement and diagnostic quality. Clin Imaging 2021;74:37-43. DOI: https://doi.org/10.1016/j.clinimag.2020.12.017

Images/Tables

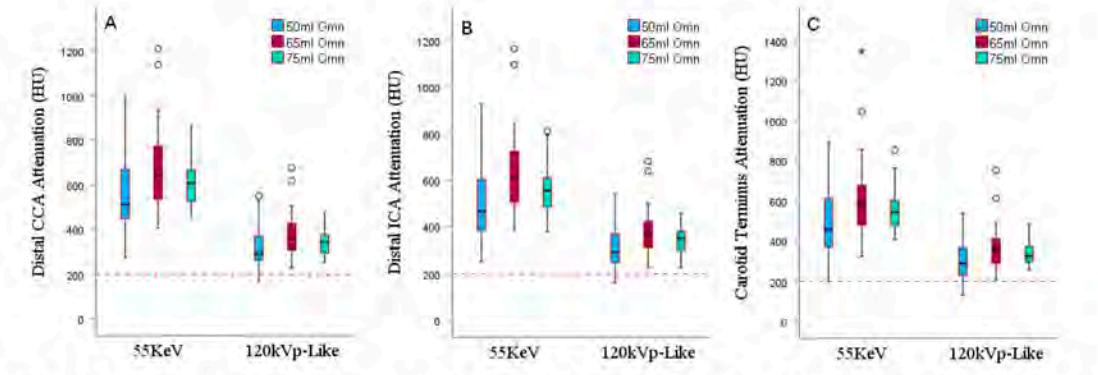

FIG 1. Box plot comparing attenuation values at 55 keV and 120 kVp-like reconstructions among the 50 mL, 65 mL and 75 mL Omnipaque (Omn) contrast groups. Each group consists of 34 images. The plot illustrates the median, interquartile range, and outliers for each group. The dashed red line at 200 HU indicates the acceptable threshold for attenuation values

860 The Interplay of Germline SDHx Mutations and Anatomical Phenotype in Head and Neck Paragangliomas: Implications for Radiologic Surveillance and Genetic Screening

Jay R Argue MD[1], Richard Wiggins MD[2]
[1]University of Utah, Salt Lake, Utah, USA. [2]University of Utah, Salt Lake, utah, USA

Purpose

To quantify the relationship between anatomic phenotype (location and multiplicity) and germline SDHx mutation status in head and neck paragangliomas (HNPGLs), and to translate these correlations into a practical, risk-stratified approach to genetic counseling and radiologic surveillance.

Materials & Methods

We conducted a single-institution retrospective study of 244 HNPGL patients (2015–2025). Collected variables included age at diagnosis, sex, predominant anatomic phenotype [jugulotympanic (JT), carotid body (CB), vagal, or multiple], and germline testing for SDHA/B/C/D and SDHAF2. SDHx positivity was defined as a pathogenic or likely pathogenic variant. Descriptive statistics summarized demographics. Associations between phenotype and SDHx status were assessed.

Results

Mean age at diagnosis was 52 years (range 12–89) with female predominance (69%). Overall, 55.9% of tested patients harbored a germline SDHx mutation. Phenotype distribution was JT (n=99), CB (n=82), vagal (n=16), and multiple tumors (n=39). SDHx yields differed markedly by phenotype: multiple 94.9%, CB 70.9%, vagal 66.7%, and JT 27.4%. Age at presentation inversely tracked with genetic burden: multiple and CB tumors presented younger (36 and 42 years, respectively) than JT tumors (54.5 years). Although JT tumors were the most common solitary phenotype, they carried the lowest SDHx yield and the strongest female predilection. In contrast, multifocality was nearly pathognomonic for an SDHx mutation.

Conclusion

Anatomical phenotype and multiplicity strongly predict germline SDHx status in HNPGLs. Multifocal disease (~95% SDHx+) and CB/vagal tumors (~70% SDHx+) should trigger immediate genetic counseling and systemic functional imaging—preferably somatostatin-receptor PET/CT (e.g., 68Ga-DOTATATE)—to detect synchronous or extra-adrenal disease and guide lifelong surveillance. Solitary JT tumors, typically older at presentation and with a lower genetic yield, can generally be followed with focused local MRI/CT, reserving systemic imaging for high-risk features (rapid growth, biochemical secretion, or confirmed SDHB). Age <45 years at diagnosis should lower the threshold for comprehensive genetic evaluation regardless of site. These data support a phenotype-driven, risk-stratified imaging pathway to align genetic risk with surveillance intensity in HNPGLs.

References

1. Richter S, Pacak K, Kunst HPM, Januszewicz A, Nölting S, Remde H, Robledo M, Eisenhofer G, Timmers HJLM, Pamporaki C. Management and follow-up strategies for patients with head and neck paraganglioma. Eur J Endocrinol. 2024 Sep 30;191(4):389-398. doi: 10.1093/ejendo/lvae113. PMID: 39303070; PMCID: PMC11443905.
2. Taïeb D, Nölting S, Perrier ND, Fassnacht M, Carrasquillo JA, Grossman AB, Clifton-Bligh R, Wanna GB, Schwam ZG, Amar L, Bourdeau I, Casey RT, Crona J, Deal CL, Del Rivero J, Duh QY, Eisenhofer G, Fojo T, Ghayee HK, Gimenez-Roqueplo AP, Gill AJ, Hicks R, Imperiale A, Jha A, Kerstens MN, de Krijger RR, Lacroix A, Lazurova I, Lin FI, Lussey-Lepoutre C, Maher ER, Mete O, Naruse M, Nilubol N, Robledo M, Sebag F, Shah NS, Tanabe A, Thompson GB, Timmers HJLM, Widimsky J, Young WJ Jr, Meuter L, Lenders JWM, Pacak K. Management of phaeochromocytoma and paraganglioma in patients with germline SDHB pathogenic variants: an international expert Consensus statement. Nat Rev Endocrinol. 2024 Mar;20(3):168-184. doi: 10.1038/s41574-023-00926-0. Epub 2023 Dec 14. PMID: 38097671.

---

515 Improved Image Quality and Reduced Radiation Dose with Photon-Counting CT in 4D Parathyroid Imaging

Elly Arizono MD, PhD, Karen Buch MD, Hillary R Kelly MD, Osamu Sakai MD, PhD
Massachusetts General Hospital, Boston, MA, USA

Purpose

4DCT is an established method for localizing hyperfunctioning parathyroid glands, but typically requires at least three imaging phases (non-contrast, arterial, venous), resulting in high radiation exposure. Imaging the neck is further complicated by its complex anatomy and frequent artifacts, which can limit image quality. Photon-counting CT (PCCT) offers higher spatial resolution and improved dose efficiency compared to conventional energy-integrating detector CT (EID CT). In this study, we compared radiation dose and image quality of a 4DCT parathyroid protocol performed on PCCT versus EID CT.

Materials & Methods

This retrospective, IRB-approved study included 96 patients with hyperparathyroidism who underwent 4DCT for preoperative localization of parathyroid lesions. 32 patients were scanned with PCCT and 64 with conventional EID CT. Each examination included non-contrast (NC), arterial (AP), and venous phases. Radiation exposure was assessed using the volume CT dose index ($CTDI_{vol}$) and dose length product (DLP). Image quality was evaluated quantitatively via signal-to-noise ratio (SNR) and contrast-to-noise ratio (CNR). ROIs were placed in the background (NC and AP) and at five muscle locations in all patients: right sternocleidomastoid muscle (SCM) at the upper thyroid level (NC and AP) and anterior scalene muscles at the lower thyroid level (right on NC, bilateral on AP). Bilateral measurement in the arterial phase was performed to account for potential differences in arterial enhancement between the injection and non-injection sides at the lower thyroid level. Mean attenuation and standard deviation (SD) were measured within each ROI. SNR and CNR were calculated using air as background noise to minimize variation between levels and phases. All statistical analyses were performed using unpaired t-tests, with $P < 0.05$ considered significant.

Results

Patient demographics, including age, sex, body mass index, injection side, and parathyroid hormone levels, showed no differences between groups (all $P > 0.05$). The total radiation dose across all phases was significantly lower with PCCT ($CTDI_{vol}$: 30.6 ± 3.3 vs. 60.8 ± 15.7 mGy; DLP: 860 ± 180 vs. 1520 ± 520 mGy·cm; both $P < 0.001$). PCCT exhibited significantly higher SNR and CNR across all evaluated regions (right SCM at the upper thyroid level and anterior scalene muscles at the lower thyroid level; $P < 0.05$). Compared to EID CT, mean attenuation was significantly higher in the right SCM on both NC and AP images and in the right anterior scalene muscle on NC, with a similar non-significant trend on AP. Background SD was significantly reduced in both phases. These factors contributed to the observed improvements in SNR and CNR with PCCT.

Conclusion

Photon-counting CT provides higher image quality at lower radiation doses than EID CT when using a 4DCT protocol for preoperative localization of parathyroid lesions.

References

1. Rodgers SE, Hunter GJ, Hamberg LM, et al. Improved preoperative planning for directed parathyroidectomy with 4-dimensional computed tomography. *Surgery*. 2006;140:932–941.
2. Mahajan A, Starker LF, Ghita M, et al. Parathyroid four-dimensional computed tomography: evaluation of radiation dose exposure during preoperative localization of parathyroid tumors in primary hyperparathyroidism. *World J Surg*. 2012;36:1335–1339.
3. Symons R, Pourmorteza A, Sandfort V, et al. Feasibility of dose-reduced chest CT with photon-counting detectors: initial results in humans. *Radiology*. 2017;285:980–989.

---

880 Comparison of Ultrasonography and Diffusion-Weighted Magnetic Resonance Imaging in Differentiating Benign and Malignant Thyroid Nodules

Abhishek Jagdishchander Arora MD, FRCR, Mohit Kapoor MBBS
AIIMS, Bibinagar, Hyderabad, Telangana, India

Purpose

There are very few studies evaluating the role of MRI in Thyroid nodules, and even lesser comparing two modalities. Therefore, the purpose of our study was to evaluate the diagnostic performance of Ultrasonography (USG) and Magnetic Resonance Imaging(MRI) in differentiating benign from malignant thyroid nodules, using fine-needle aspiration cytology (FNAC) or histopathology as the reference standard.

Materials & Methods

In this prospective study, 56 patients with thyroid nodules underwent both USG and 3T MRI within one week of their diagnosis. USG features were assessed using the ACR TI-RADS system. MRI scan included all regular sequences, with addition of diffusion-weighted sequences (b = 50–1200 s/mm^2) and quantitative ADC mapping. ADC values were measured using restricted region-of-interest (ROI) from the 1) most diffusion-limited area of the lesion, 2) large ROI from the bulk of the lesion, and 3) contralateral normal thyroid lobe tissue. Diagnostic metrics—sensitivity, specificity, positive predictive value (PPV), negative predictive value (NPV), accuracy—and receiver operating characteristic (ROC) analysis were calculated.

Results

Among 56 nodules, 32 (57.1%) were benign and 24 (42.9%) malignant as per final FNAC/Histopathology reports. USG with TI-RADS achieved high sensitivity (96.7%) but low specificity (37.0%), with overall accuracy of 78.2% in differentiating benign from malignant lesions ADC values were significantly lower in malignant nodules as compared to benign nodules across all ROI strategies ($p < 0.001$). A restricted ROI ADC cutoff of $<1.002 \times 10^{-3}$ mm^2/s yielded sensitivity of 87.5%, specificity of 90.6%, and accuracy of 89.3% (AUC = 0.878). Large ROI cutoff $<1.16 \times 10^{-3}$ mm^2/s achieved 100% specificity but reduced sensitivity (70.8%). Contralateral thyroid ADC comparison showed moderate discriminatory value (accuracy 69.6%). In nodules classified indeterminate by USG or FNAC, ADC mapping correctly reclassified over 80% of the nodules, reducing diagnostic uncertainty.

Conclusion

USG remains a sensitive first-line tool for thyroid nodule evaluation, but ADC mapping on diffusion-weighted MRI provides robust quantitative marker, that substantially enhances specificity and classify indeterminate cases. Incorporating ADC into the diagnostic pathway helps in better stratification, improves reporting confidence and eventually clinical decision-making.

References

Haugen BR, Alexander EK, Bible KC, Doherty GM, Mandel SJ, Nikiforov YE, Pacini F, Randolph GW, Sawka AM, Schlumberger M, Schuff KG, Sherman SI, Sosa JA, Steward DL, Tuttle RM, Wartofsky L. 2015 American Thyroid Association Management Guidelines for Adult Patients with Thyroid Nodules and Differentiated Thyroid Cancer: The American Thyroid Association Guidelines Task Force on Thyroid Nodules and Differentiated Thyroid Cancer. Thyroid. 2016 Jan;26(1):1-133. doi: 10.1089/thy.2015.0020. PMID: 26462967; PMCID: PMC4739132.
Bitar R, Leung G, Perng R, Tadros S, Moody AR, Sarrazin J, McGregor C, Christakis M, Symons S, Nelson A, Roberts TP. MR pulse sequences: what every radiologist wants to know but is afraid to ask. Radiographics. 2006 Mar-Apr;26(2):513-37. doi: 10.1148/rg.262055063. PMID: 16549614.
Boers T, Braak SJ, Rikken NET, Versluis M, Manohar S. Ultrasound imaging in thyroid nodule diagnosis, therapy, and follow-up: Current status and future trends. J Clin Ultrasound. 2023 Jul-Aug;51(6):1087-1100. doi: 10.1002/jcu.23430. Epub 2023 Jan 19. PMID: 36655705.

Images/Tables

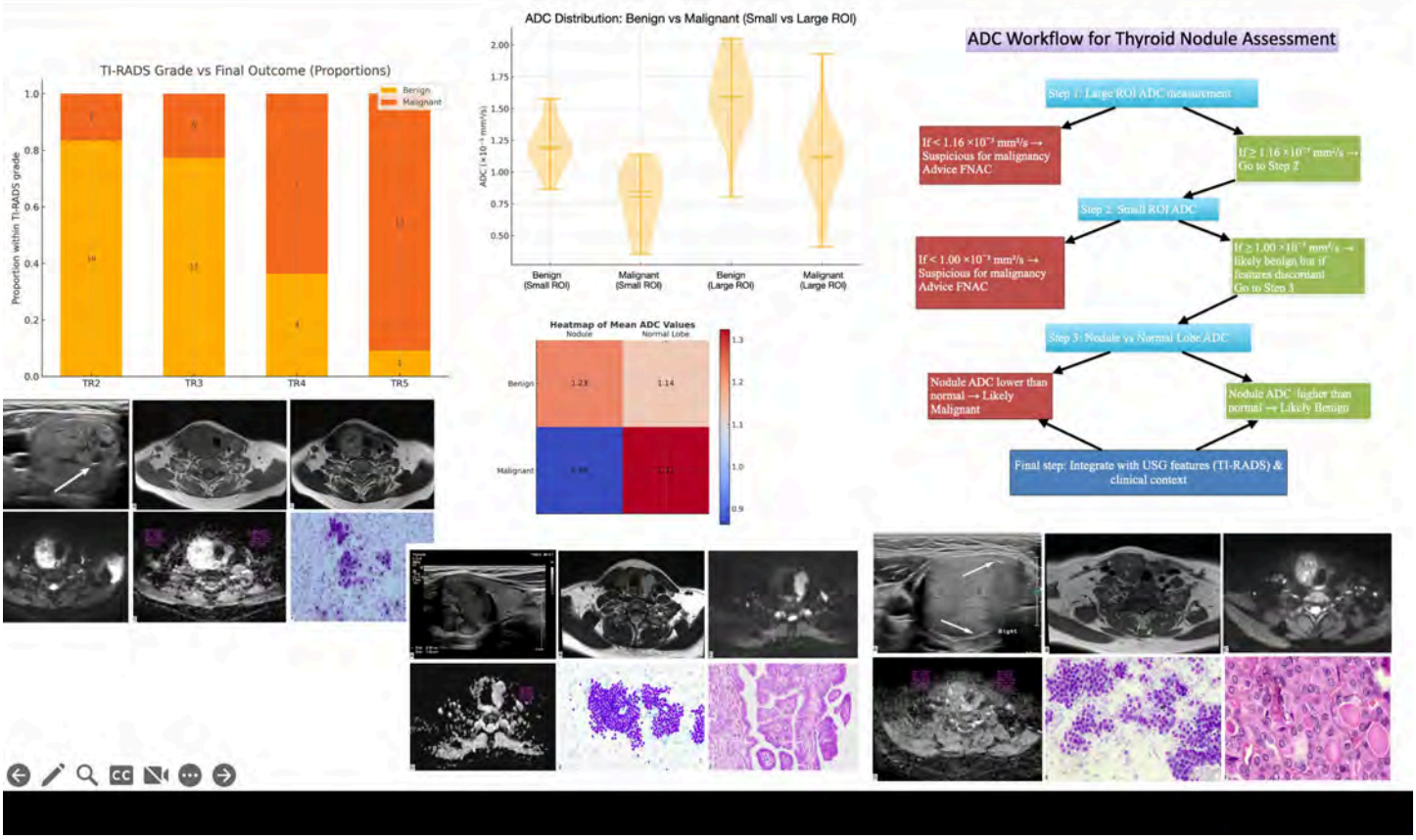

767 **Perineural Tumor Spread Along the Cervical Plexus**

Heba Al Qudah, Noah N. Chasen, Melissa M. Chen, Rami W. Eldaya, Diana Kaya, Ahmed Msherghi, Sahar Alizada, Max Wintermark, Lawrence Ginsberg, Kim Learned
Houston, Tx, USA

Purpose

Perineural Tumor Spread (PNS) in head and neck cancer is often associated with a poor prognosis and represents a diagnostic challenge for neuroradiologists who may be unfamiliar with the neural anatomy. Although much of the literature emphasizes anatomy and PNS along the cranial nerves, there has been relatively little focus on the cervical plexus, due to lack of knowledge of the complex plexus anatomy or recognition that PNS can occur on spinal nerves, and consequent under-diagnosis of this disease entity.

Materials & Methods

We reviewed 27 patients with PNS along the cervical plexus. Age at the time of PNS, sex, clinical symptoms, primary tumor pathology and location. Different imaging modalities were evaluated for the presence of nodular thickening along the expected anatomical location of the cervical plexuses and/or cervical nerve roots and neural foramina and the presence of corresponding muscular denervation.

Results

The majority (92.6%) of cases presented with symptoms related to PNS along the cervical plexus, rather than symptoms of the primary tumor. The most common symptoms were ear numbness and pain (44.4%). Cutaneous squamous cell carcinoma accounted for most of the primary tumors, representing 66.7% of cases.

The cervical plexus is formed by the ventral rami of C1-C4, and then divided into cutaneous and muscular branches. The cutaneous branches of the cervical plexus emerge from a common point posterior to the sternocleidomastoid muscle at the midway point between the origin and insertion of the muscle, named punctum nervosum, or Erb's point.

PNS along the great auricular nerve was detected as a tubular structure running from the Erb's point in a vertical course over the sternocleidomastoid muscle to parotid gland and external ear. PNS along the supraclavicular nerves was detected as a tubular structure running from the Erb's point to branch into three branches in the posterior triangle of the neck. PNS along the transverse cutaneous nerve was detected as a linear or cord-like structure at the Erb's point with a small branch, running in a horizontal and anterior course over the sternocleidomastoid muscle. PNS along the lesser occipital nerve was detected as a cord-like structure running from the Erb's point superiorly toward the occiput.

Phrenic nerve denervation was identified as an elevated diaphragm with PNS along the ipsilateral C3-C5 cervical roots to neuroforamina.

Conclusion

PNS along the cervical plexus is an under-recognized entity in head and neck malignancies and can significantly impact treatment decisions and outcome. The keys to radiological diagnosis of PNS encompass a thorough understanding of the complex and function of the plexus, including relevant landmarks such as Erb's point and the neural foramina, as well as its relationships with cranial nerves and carotid sheath

References

1. Front Matter. In: Surgical Anatomy of the Cervical Plexus and its Branches. Elsevier; 2022:iii.

2. Kikuta S, Jenkins S, Kusukawa J, et al. Ansa cervicalis: a comprehensive review of its anatomy, variations, pathology, and surgical applications. Anat Cell Biol 2019;52:221.
3. Pei M, Wiefels M, Harris D, et al. Perineural Invasion in Head and Neck Cutaneous Squamous Cell Carcinoma. Cancers 2024;16:3695.
4. Paes FM, Singer AD, Checkver AN, et al. Perineural Spread in Head and Neck Malignancies: Clinical Significance and Evaluation with ^{18}F-FDG PET/CT. RadioGraphics 2013;33:1717–36.
5. Ginsberg LE, Eicher SA. Great Auricular Nerve: Anatomy and Imaging in a Case of Perineural Tumor Spread. Am J Neuroradiol 2000;21:568.

Images/Tables

Figure 1A. The CP is formed from the anterior primary rami of the C1, C2, C3, and C4 spinal nerves. The ventral rami, except C1, from the C2, C3, and C4 levels divides into two branches, superior and inferior, superior branch of C2 with C1, inferior branch of C2 with superior branch of C3, inferior branch of C3 with superior branch of C4 to form three communicating loops which forms the CP. The plexus divides into anterior muscular and posterior cutaneous branches.

Figure 1B. The cutaneous branches—the GAN (C2–C3), LOS (C2–C3), TCN (C2–C3), and SCN (C3–C4)—emerge from a common point located posterior to the sternocleidomastoid muscle (SCM), approximately midway between the muscle's origin and insertion, at the level of the hyoid bone or the C5 vertebrae. This anatomical landmark is known as the punctus nervosum, or Erb's point.

Figure 1C. Sagittal enhanced neck CT, of a 45-year-old male with a history of recurrent multifocal cutaneous carcinoma of the left neck demonstrates nodular enhancing tumor (arrows) at Erb's point.

Figure 2. Axial (A) and sagittal (B) contrast- enhanced neck CT for the same 72 –year-old male patient with recurrent cutaneous SCC of the left supraorbital region and a metastatic mass anterior to the left parotid (star), demonstrates a necrotic nodal metastasis within the left parotid gland (arrowhead), and a cord-like structure extending inferiorly from the parotid region (arrow) over the oblique sternocleidomastoid muscle representing PNS along the GAS.

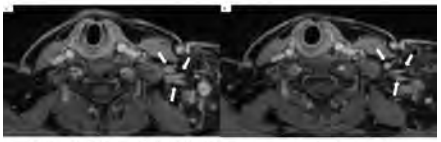

Figure 3. Axial neck MRI with contrast of a 71-year-old female patient presenting with left anterior shoulder pain and discovered to have a nodular cord-like enhancing structure is seen in the left posterior triangle (arrow) , giving rise to three enhancing branches. These findings are consistent with perineural tumor spread along the supraclavicular nerves, involving its three distal branches: the medial, intermediate and lateral supraclavicular nerve.

Figure 4. Axial (A) and coronal enhanced neck CT (B) of a 67-year-old male patient presenting with left neck pain demonstrates a left neck thickened, enhancing structure seen at the left Erb's point (thick arrow) with a small horizontal branch (thin arrow) extending anterior to the left sternocleidomastoid muscle, consistent with perineural tumor spread along the transverse cutaneous branch of the superficial cervical plexus.

Figure 5. Axial (A) , sagittal (B) enhanced Neck CT of a 56-year-old man a history of multiply excised right scalp SCC treated with adjuvant radiation and multiple lines of chemotherapy, presenting with right sided scalp pain radiating down his neck, demonstrates cord-like enhancing structure , running from the right suboccipital region representing perineural tumor spread along the LOS (thick arrows).

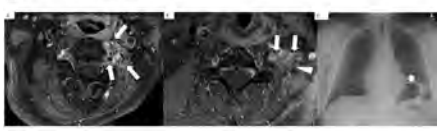

Figure 6. Axial post contrast –fat saturated neck MRI (A-B) and chest X-ray (C) of a 45-year-old male with a history of recurrent multifocal cutaneous carcinoma of the left neck demonstrates nodular enhancing tumor (arrows) at the Erb's point, retrograde along C3-C5 spinal nerves to the sternothyroid and adjacent scalene muscles, affecting the phrenic nerve (C3-C5) causing elevation of the left hemidiaphragm on chest X-ray (star).

1106 Visualization of Extra-Foraminal Accessory Nerve in Cadavers Using Submilimetric CISS MRI

Shruti Kumari MD, Mridhula Muthukumar MS, Ari Blitz MD
University Hospitals, Case Western Reserve University, Cleveland, Ohio, USA

Purpose

The Spinal Accessory Nerve (Eleventh cranial nerve or CN XI) is a motor nerve responsible for innervation of the sternocleidomastoid and trapezius muscles. Injury to CN XI can lead to dysfunction of the trapezius. The superficial course of the spinal accessory nerve in the posterior cervical triangle makes it susceptible to injury. Iatrogenic injury to the nerve after a surgical procedure is one of the most common causes of trapezius palsy. Preoperative imaging of CN XI does not routinely take place prior to surgery and current clinical MRI does not allow for the visualization of the extraforaminal segment of CN XI. The aim of our study is to determine the visibility of CN XI in cadavers using 0.5-0.6 mm CISS in different segments throughout its course to assess its feasibility for routine clinical use in living subjects.

Materials & Methods

54 cadavers were scanned using CISS MRI sequences at isotropic resolutions of 0.6 and 0.5 mm. The visibility of extraforaminal CN XI was evaluated independently by 2 using a qualitative scale of 0-3 with 3 being the best. For the purposes of this work, we divided the extraforaminal segment of CN XI into 4 subsegments: anterior triangle (from the skull base to the anterior border of the sternocleidomastoid), intramuscular (sternocleidomastoid), posterior triangle (from the origin of CN XI from the sternocleidomastoid to the border of the trapezius), and intramuscular (trapezius). These subsegments are rated separately. The MRI slices demarcating transitions between sub-segments were set prospectively.

Results

Portions of extraforaminal CN XI in the neck can be consistently well visualized on CISS MRI. Table 1 summarizes the sub-segmental CISS MRI visibility scores (0–3 scale) assigned independently by both raters. A linear mixed model with pairwise comparisons between segments and Tukey-adjusted p-values was used to compare the differences between the visibility scores of each sub-segment. The **anterior triangle subsegment** had the best visualization with a score of **2.75 ± 0.27**. The **intramuscular (Sternocleidomastoid) subsegment (2.66 ± 0.13)** has a similarly high visibility rating. On the other hand, CN XI is less visible in the **posterior triangle subsegment (1.47 ± 0.23)**. The **intramuscular (trapezius) subsegment** has the lowest score of **0.25 ± 0.12**.

There are no differences between the visualization of the left versus the right CN XI except in the posterior triangle subsegment where the left CN XI was better visualized than the right. The ICC for rater reliability was 0.4, indicating that there was fair agreement between the two raters.

Conclusion

Submilimetric CISS MRI allows for the visualization of portions of extraforaminal sub-segments with excellent visualization of CN XI in the anterior triangle segment and its innervation of the sternocleidomastoid muscle. Future integration of CISS in living subjects, with reasonable acquisition times and motion compensation techniques, holds promise for its incorporation into routine preoperative and diagnostic imaging protocols to prevent iatrogenic nerve injury during procedures and pathologic assessment.

References

- Wiater JM, Bigliani LU. Spinal accessory nerve injury. Clinical Orthopaedics and Related Research (1976-2007). 1999 Nov 1;368:5-16.
- Kim DH, Cho YJ, Tiel RL, Kline DG. Surgical outcomes of 111 spinal accessory nerve injuries. Neurosurgery. 2003 Nov 1;53(5):1106-13.
- Wen J, Desai NS, Jeffery D, Aygun N, Blitz A. High-resolution isotropic three-dimensional MR imaging of the extraforaminal segments of the cranial nerves. Magnetic Resonance Imaging Clinics. 2018 Feb 1;26(1):101-19.

Images/Tables

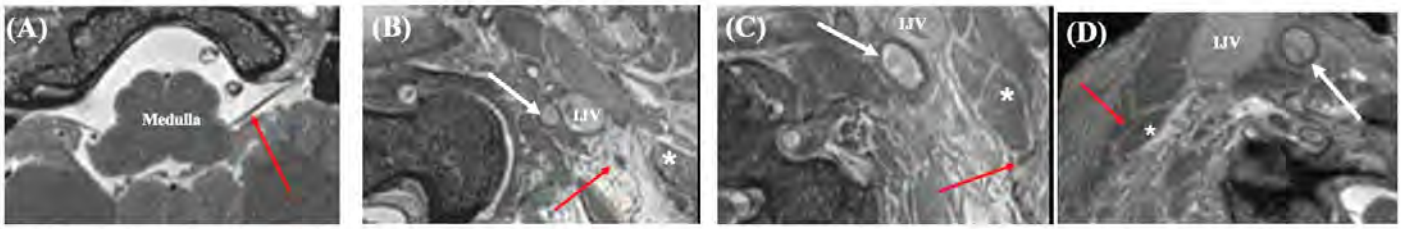

Fig. 1: (A) Axially reformatted 0.5mm CISS MRI of the cisternal segment of left CN X-XI complex (red arrow) as it originates from the posterolateral sulcus of medulla oblongata; (B) Axially reformatted 0.5mm CISS MRI of left CN XI in the anterior triangle segment as it travels laterally in the neck to supply the sternocleidomastoid muscle (*); (C) Axially reformatted 0.5mm CISS MRI of the intramuscular segment of left CN XI as it emerges after piercing the sternocleidomastoid muscle; common carotid artery (white arrow); (D) Axially reformatted 0.5mm CISS MRI of the intramuscular segment of right CN XI as it pierces the sternocleidomastoid muscle;

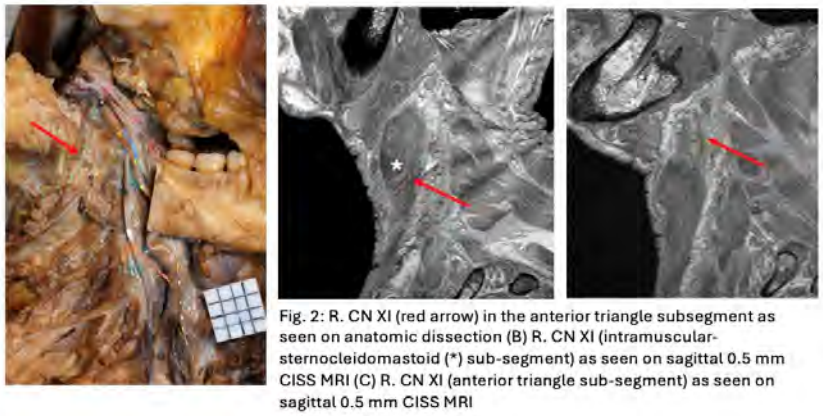

Fig. 2: R. CN XI (red arrow) in the anterior triangle subsegment as seen on anatomic dissection (B) R. CN XI (intramuscular-sternocleidomastoid (*) sub-segment) as seen on sagittal 0.5 mm CISS MRI (C) R. CN XI (anterior triangle sub-segment) as seen on sagittal 0.5 mm CISS MRI

Table 1: Mean Visibility Scores of the CN XI in Each Sub-segment

Average ± SD	Anterior triangle	Intramuscular (Sternocleidomastoid)	Posterior triangle	Intramuscular (Trapezius)
Combined Average ± SD	2.75 ± 0.27	2.66 ± 0.13	1.47 ± 0.23	0.25 ± 0.12
Average ± SD R. CN X	2.69 ± 0.26	2.5 ± 0.00	1.27 ± 0.19	0.30 ± 0.29
Average ± SD L. CN X	2.8 ± 0.28	2.82 ± 0.25	1.68 ± 0.27	0.20 ± 0.05

Note: Data shows the average visibility scores of CN XI in each sub-segment and the visibility of the left and right CN XI in each sub-segment in the axial plane on CISS MRI.

409 Prospective MR Evaluation of Endolymphatic Hydrops Using Half-dose Gadopiclenol

Rafail C Christodoulou MD[1], Nancy Fischbein MD[1], Nikolas Blevins MD[2], Sachin Malik MD[1], Lukas D. Landegger MD[2], Fanrui Fu[2], Nancy Pham MD[1]
[1]Department of Radiology, Stanford University School of Medicine, Stanford, CA, Stanford, California, USA. [2]Department of Otolaryngology - Head & Neck Surgery, Stanford University School of Medicine, Stanford, CA, Stanford, California, USA

Purpose

Gadopiclenol is a next-generation macrocyclic GBCA distinguished by its high T1 relaxivity and kinetic stability. It was developed to address the clinical need for reduced gadolinium dosing while maintaining high diagnostic accuracy, thereby minimizing potential long-term risks associated with gadolinium retention. Although various neuroradiology applications have been explored, the potential benefits of gadopiclenol's increased T1 relaxivity have not been investigated for the purpose of evaluating endolymphatic hydrops (EH) using delayed contrast- enhanced inner ear imaging.

Materials & Methods

We prospectively enrolled 26 consecutive patients at our institution's Otology clinic based on the 2015 American Academy of Otolaryngology- Head and Neck Surgery criteria for MD, including acute or fluctuating symptoms of vertigo, hearing loss, tinnitus, or aural fullness. Each patient underwent 4-hour delayed contrast-enhanced inner ear imaging at 3T with half-dose (0.05 mmol/kg) GBCA administration using gadopiclenol. The contrast-to-noise ratio (CNR) and signal-to-noise ratio (SNR) were determined. Assessment of blood-labyrinthine barrier (BLB) permeability, utricle-saccule discrimination, and endolymphatic hydrops was performed by two head and neck neuroradiologists. Image quality, SNR, and CNR was compared to previously published data that utilized the same technical parameters with a contrast dose of 0.1 mmol/kg.

Results

Fifty-one ears were analyzed. One ear was excluded based on a prior history of left labyrinthectomy after failed medical management of MD. There were 31 symptomatic and 20 asymptomatic ears determined by clinical and hearing evaluation. Delayed contrast-enhanced inner ear imaging with gadopiclenol at 0.05 mmol/kg is similar in CNR and similar in SNR to gadobenate dimeglumine at 0.1 mmol/kg ($P > 0.05$). There was excellent interobserver agreement for the grading EH ($\kappa > 0.80$).

Conclusion

Our study demonstrates that 3D-FLAIR inner ear imaging using gadopiclenol at 0.05 mmol/kg is a reliable method for detecting clinically concordant EH and that image quality, based on qualitative and quantitative metrics, is comparable to a previously published study using gadobenate dimeglumine at a single-dose of 0.1 mmol/kg.

References

1. Ravin ED, Quimby AE, Bartellas M, et al. An Update on the Epidemiology and Clinicodemographic Features of Meniere's Disease. The Laryngoscope. 2024;134(7):3310-3315. doi:10.1002/lary.31282
2. Mohseni-Dargah M, Falahati Z, Pastras C, et al. Meniere's disease: Pathogenesis, treatments, and emerging approaches for an idiopathic bioenvironmental disorder. Environ Res. 2023;238(Pt 1):116972. doi:10.1016/j.envres.2023.116972
3. Lopez-Escamez JA, Carey J, Chung WH, et al. Diagnostic criteria for Meniere's disease. J Vestib Res Equilib Orientat. 2015;25(1):1-7. doi:10.3233/VES-150549
4. Zanetti D, Conte G, Scola E, Casale S, Lilli G, Berardino FD. Advanced Imaging of the Vestibular Endolymphatic Space in Ménière's Disease. Front Surg. 2021;8:700271. doi:10.3389/fsurg.2021.700271
5. Hoskin JL. Ménière's disease: new guidelines, subtypes, imaging, and more. Curr Opin Neurol. 2022;35(1):90-97. doi:10.1097/WCO.0000000000001021

Images/Tables

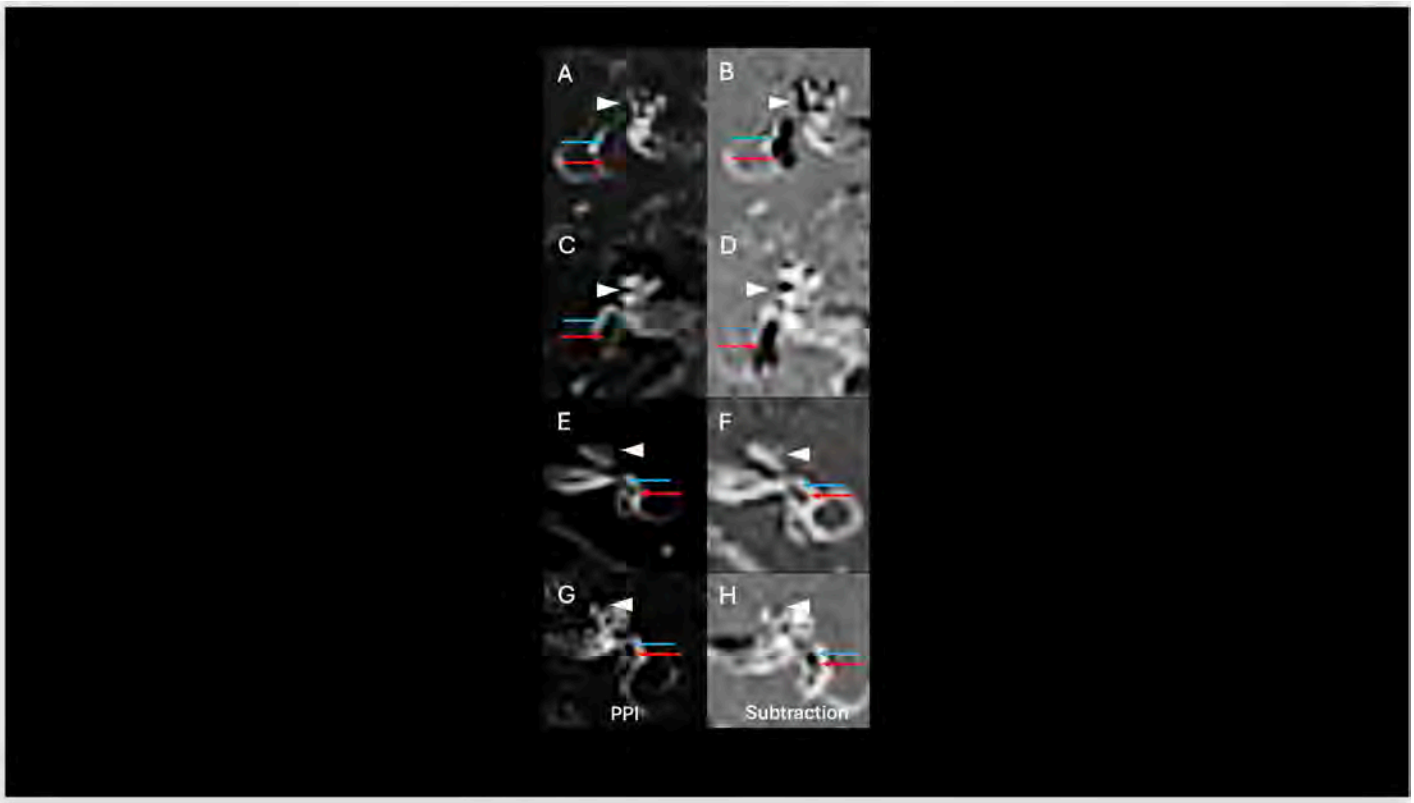

Figure 1. Various grades of cochlear and vestibular endolymphatic hydrops on 3D-FLAIR image (left panel; A, C, E, G) and corresponding post-processed grey-value subtraction image (B, D, F, H). (A, B) Patient 1 demonstrates right grade 2 cochlear and grade 3 vestibular hydrops. (C, D) Patient 2 demonstrates right grade 2 cochlear and grade 3 vestibular hydrops. (E F) Patient 3 demonstrates left grade 0 cochlear and grade 1 vestibular hydrops. (G, H) Patient 4 demonstrates left grade 1 and 2 vestibular hydrops. Cochlear duct (white arrowhead), saccule (blue arrow), and utricle (red arrow). PPI, positive perilymphatic image.

---

501 Contrast Dynamics on Multiphase CT Angiography in Carotid Webs and Their Association with Ischemic Stroke

Shenghua Zhu MD PhD[1], Chelsea Scott[2], Baris Alten MD[3], Brooks Applewhite MD[1], Saurabh Rohatgi MD[1], Jeremy Ford MD[1], Scott Kasner MD[3], Javier Romero MD[1]

[1]Mass General Hospital, Boston, MA, USA. [2]University of Virginia School of Medicine, Charlottesville, VA, USA. [3]University of Pennsylvania, Philadelphia, PA, USA

Purpose

Carotid webs (CWs) are shelf-like fibrous intimal projections in the internal carotid artery that perturb laminar flow, promote local stasis, and predispose to embolic stroke. While morphology correlates with events, in-vivo hemodynamic markers of stasis are lacking. This study evaluated whether multiphase CT angiography (mCTA) quantifies contrast persistence and whether impaired wash-out is associated with stroke/transient ischemic attack (TIA).

Materials & Methods

This is a single-center retrospective study (January 2021 to June 2024) of consecutive adults with CTA-confirmed CWs. Among 190 patients (206 webs), 42 presented with stroke/TIA; a multidisciplinary team adjudicated the web as the sole culprit in 14. mCTA (arterial and delayed phases) was available for 7 of these 14 forming the symptomatic cohort. Seven age- and sex-matched asymptomatic patients with incidental webs served as controls. Using Visage, Hounsfield-unit (HU) densities were sampled in the posterior recess of the web and in reference segments (proximal common and internal carotid arteries) on both phases. Two indices were derived: contrast-washout ratio (CWR) = $(A_{web} - D_{web})/(A_{ref} - D_{ref})$; contrast-pooling index (CPI) = $(D_{web}/D_{ref}) - (A_{web}/A_{ref})$. Continuous variables were compared with independent t-test or Mann-Whitney U test as appropriate and categorical variables with Fisher exact tests.

Results

Baseline demographics, vascular risk factors, and CW morphology did not differ between cohorts. CWR was lower in symptomatic patients than controls (median [IQR] 0.672 [0.652-0.920] vs. 0.918 [0.819-1.076]; $p = 0.038$), indicating reduced wash-out. CPI was higher in symptomatic patients (median [IQR] 0.098 [0.074-0.212] vs. -0.009 [-0.169-0.060]; $p = 0.038$), consistent with contrast persistence and blood stasis.

Conclusion

mCTA reveals impaired contrast clearance within CWs associated with ipsilateral stroke/TIA, independent of baseline characteristics and morphology. Quantitative mCTA metrics offer a feasible, noninvasive biomarker for thromboembolic risk stratification and warrant prospective validation.

References

Table 1. Baseline morphologic features of symptomatic vs. asymptomatic carotid webs.

Figure 1. 3D reconstruction (a) and multiphase CTA examples of carotid web. Proximal CCA (Green) and ICA (Purple) reference ROIs are labeled in circles on the arterial phase representative image (b). The Sagittal plane CTA imaging slice on which the carotid web appears the longest protrusion coming from the carotid wall was used for all the measurements. Axial plane demonstrates web recess (arrow) with persistent hyperattenuation from arterial (d) to delayed phase (e) in the symptomatic case. CCA, common carotid artery; ICA, internal carotid artery; ROI, region of interest.

Figure 2. Box-and-whisker plots of **CWR** and **CPI** comparing symptomatic vs asymptomatic cohorts. CWR is lower in symptomatic patients (p = 0.038); CPI is higher in symptomatic patients (p = 0.038).

1. Choi PM, Singh D, Trivedi A, Qazi E, George D, Wong J, Demchuk AM, Goyal M, Hill MD, Menon BK. Carotid Webs and Recurrent Ischemic Strokes in the Era of CT Angiography. *AJNR Am J Neuroradiol*. 2015;36:2134-2139. doi: 10.3174/ajnr.A4431

2. Sajedi PI, Gonzalez JN, Cronin CA, Kouo T, Steven A, Zhuo J, Thompson O, Castellani R, Kittner SJ, Gandhi D, et al. Carotid Bulb Webs as a Cause of "Cryptogenic" Ischemic Stroke. *AJNR Am J Neuroradiol*. 2017;38:1399-1404. doi: 10.3174/ajnr.A5208

Images/Tables

Table 1

Feature	Symptomatic (n=7)	Asymptomatic (n=7)	*p*
Length (mm)	2.40 (2.30-4.15)	2.30 (2.10-2.65)	0.271
Thickness (mm)	1.20 (1.10-1.55)	1.15 (1.10-1.40)	0.731
Base width (mm)	1.75 (1.65-2.40)	1.70 (1.55-2.25)	0.398
Angle to vessel wall	70.0 (51.5-82.9)	70.5 (57.5-87.5)	0.559
Distance to bifurcation (mm)	3.50 (0.75-4.05)	1.60 (0.40-4.60)	0.921
Web-to-bulb ratio (ECST)	39.1 (31.8-45.2)	39.5 (31.7-43.0)	1.0
Percent stenosis (NASCET)	3.8 (0.0-9.3)	1.22 (0.0-9.3)	0.831
Concurrent calcification	1 (14.3%)	0 (0%)	1.0
Coexistence of a non-stenotic carotid plaque	0 (0%)	0 (0%)	1.0

Figure 1

Figure 2

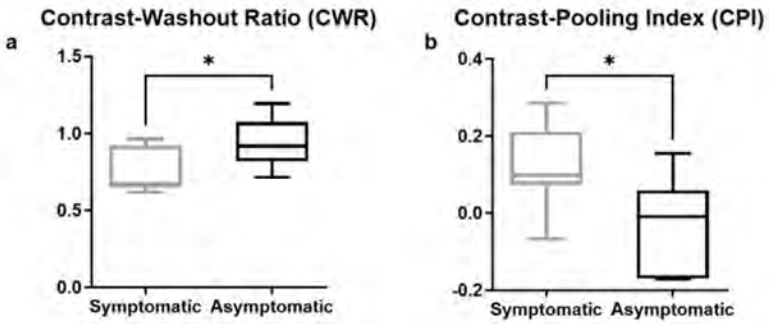

Scientific Abstract Power Pitches & Luminary Speaker: Biomarker and Neuroimaging Correlates of Alzheimer's Disease and Anti-Amyloid Immunotherapy

9:55 - 10:55am Tuesday, 19th May, 2026

702 Association Between Amyloid PET Centiloid Values and Amyloid-Related Imaging Abnormalities in Patients Treated With Lecanemab

Thomas Dowling MD, Shenghua Zhu, Odette Ganem Chagui, Saurabh Rohatgi, Jeremy Ford, Javier Romero
Massachusetts General Hospital, Boston, MA, USA

Purpose

Advances in anti-amyloid immunotherapies (AAIs), including lecanemab, represent the first FDA-approved disease-modifying treatments for Alzheimer disease (AD). However, these agents have been associated with Amyloid-Related Imaging Abnormalities (ARIA) in up to 22% of treated patients, presenting with a range of clinical symptoms from mild to severe. Identifying risk factors among eligible patients is essential for individualized risk assessment before therapy. With the increasing use of amyloid PET-CT, Centiloid scoring has become a validated and standardized method for quantifying baseline amyloid burden. Prior studies evaluating the role of baseline amyloid burden (Centiloids) have shown inconsistent results across analyses of patients on AAIs. This study aimed to examine the relationship between baseline amyloid burden (Centiloids) and the development of ARIA in patients with AD treated with lecanemab.

Materials & Methods

We retrospectively identified 25 patients with AD who received lecanemab therapy and developed ARIA between April 18, 2024, and July 12, 2025, and who had undergone Florbetaben (Neuraceq) PET-CT within 12 months before treatment initiation. A control cohort of 25 patients who completed at least 14 infusions without evidence of ARIA was matched for age, sex, and APOE ε4 carrier status. PET studies were processed using MIM Neuro software to obtain Centiloid scores by a fellowship-trained neuroradiologist blinded to ARIA outcomes. Mean Centiloid scores were compared between groups using a two-tailed independent t-test.

Results

Amyloid PET scans from 50 patients were analyzed. Three were excluded due to segmentation or registration errors identified while still blinded to ARIA status, leaving 47 patients included in the analysis (23 ARIA-positive, 24 ARIA-negative). Baseline characteristics were similar between groups in age (75.0 vs 75.1 years), sex (57% vs 54% female), and APOE ε4 carrier status (78% vs 75%). Data were normally distributed in both groups by the Shapiro–Wilk test ($p = .72$ and $p = .90$). Patients who developed ARIA had significantly higher baseline Centiloid scores than those who did not (82.4 ± 36.8 vs 57.2 ± 33.5; $p = .033$).

Conclusion

Our results demonstrate that a higher baseline amyloid burden on PET scans (Centiloids) correlates with an increased risk of ARIA during lecanemab treatment. These findings imply that greater amyloid burden may serve as an independent risk factor for ARIA development in patients receiving lecanemab.

References

1. van Dyck CH, Swanson CJ, Aisen P, Bateman RJ, Chen C, Gee M, Kanekiyo M, Li D, Reyderman L, Cohen S, Froelich L, Katayama S, Sabbagh M, Vellas B, Watson D, Dhadda S, Irizarry M, Kramer LD, Iwatsubo T; for the Clarity-AD Study Group. Lecanemab in Early Alzheimer's Disease. N Engl J Med. 2023 Jan 5;388(1):9-21. doi:10.1056/NEJMoa2212948.
2. Klunk WE, Koeppe RA, Price JC, Benzinger TL, Devous MD Sr, Jagust WJ, Johnson KA, Mathis CA, Minhas HS, Pontecorvo MJ, Rowe CC, Skovronsky DM, Mintun MA. The Centiloid Project: Standardizing Quantitative Amyloid Plaque Estimation by PET. AJNR Am J Neuroradiol. 2015;36(7):1200-5. doi:10.3174/ajnr.A4117.
3. Collij LE, Vans IJ, Verfaillie S, Teunissen CE, Barkhof F, van der Flier WM, Scheltens P, Visser PJ, van Berckel BNM, Ossenkoppele R. Centiloid cut-off values for optimal agreement between PET and CSF biomarkers. AJNR Am J Neuroradiol. 2019;40(12):1981-1987. doi:10.3174/ajnr.A6260.
4. Swanson CJ, van Dyck CH, Irizarry MC, et al; CLARITY-AD Study Group. Impact of Clinical Subgroup and Baseline Amyloid PET Centiloid Level on ARIA Occurrence in Lecanemab-Treated Patients. Presented at: American Academy of Neurology Annual Meeting; April 13–18, 2024; Denver, CO. Abstract 9-007. Available at: https://www.aan.com/msa/Public/Events/AbstractDetails/55647. Accessed November 3, 2025.
5. Mintun MA, Wessels AM, Andrews RD, et al. Amyloid-Related Imaging Abnormalities With Donanemab in Early Symptomatic Alzheimer Disease. JAMA Neurol. 2024;81(7):673-683. doi:10.1001/jamaneurol.2024.1128.

Images/Tables

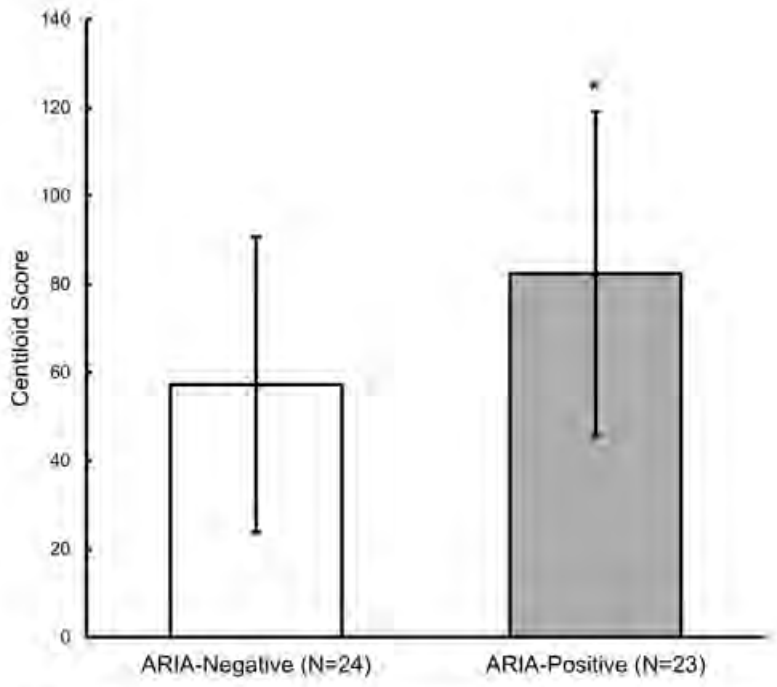

Figure 1: Mean Centiloid scores in ARIA-positive and ARIA-negative groups ($p = .033$).

---

807 **Correlation of Cerebrospinal Fluid and Plasma Biomarkers of Alzheimer's Disease with Amyloid PET: A Retrospective Large Cohort Study**

Maryam Fotouhi MD, Nasim Sheikh-Bahaei MD, PhD

Department of Radiology, Keck School of Medicine, University of Southern California, Los Angeles, CA, USA

Purpose

This study utilized a quantitative, threshold independent approach based on positron emission tomography (PET) to evaluate the correlations between global amyloid PET Centiloid values and plasma amyloid and tau biomarkers, in comparison to the relationships identified for cerebrospinal fluid (CSF) amyloid beta 42 (Aβ42).

Materials & Methods

Data were obtained from the Alzheimer's Disease Neuroimaging Initiative (ADNI), including two amyloid PET indexed cohorts: amyloid Florbetaben and Florbetapir PET paired with CSF Aβ42 (n = 2,081 matched visits) and amyloid PET paired with plasma amyloid and tau biomarkers. Plasma biomarkers were assayed for Aβ42, Aβ40, and the Aβ42/40 ratio, pTau217, and pTau181 (C2N Diagnostics, Fujirebio Diagnostics, Quanterix, Roche Diagnostics). Primary outcomes were global Centiloid values. Predictor variables comprised native-scale biomarker concentrations without thresholding. Covariates included age, sex, apolipoprotein E ε4 (APOE4) carrier status, and the interval between PET and sample collection. Partial Spearman correlations were estimated between each biomarker and PET Centiloid, adjusting for covariates. Incremental model fit was evaluated by ordinary least squares regression, comparing covariate-only models (M0) with biomarker-augmented models (M1) through changes in R-squared and Cohen's f^2, with additional assessment by Akaike information criterion (AIC). Predictive performance was evaluated using 5-fold cross-validation, aggregating root mean squared error (RMSE) and mean absolute error (MAE).

Results

Plasma tau demonstrated the strongest alignment with amyloid PET. The pTau217 ratio to non-pTau217 (C2N assay) exhibited a high positive correlation with amyloid-PET centiloids ($\rho = 0.73$, $p < .00001$, N = 1,170) and increased explained variance from 14.4% (model with covariates) to 55.6% ($\Delta R^2 = 0.41$; $f^2 = 0.92$) with a concurrent improvement in RMSE (from 41.80 to 30.02) and MAE (from 32.47 to 21.03) differences. Single-analyte assays of pTau217 were slightly lower but highly correlated with PET data ($\rho = 0.69$, $\Delta R^2 = 0.24$). CSF Aβ42 was, as expected, moderately inversely correlated with centiloids ($\rho = -0.55$, $p < .00001$, N = 2,081) and increased model fit from 0.22 to 0.41 ($\Delta R^2 = 0.19$) with RMSE improvement (from 42.7 to 37) and MAE (from 33.2 to 29) differences. Similar improvements occurred for FBB ($\rho = -0.52$, $\Delta R^2 = 0.14$) and FBP ($\rho = -0.55$, $\Delta R^2 = 0.21$). By contrast, plasma amyloid was clearly lower in performance variables. Aβ42/40 ratio (C2N assay) was best in amyloid plasma markers while weaker compared to pTau217 ($\rho = -0.35$, $p<.00001$), and plasma Aβ40 contributed negligibly ($\Delta R^2 \leq 0.005$).

Conclusion

In this analysis of the ADNI cohort within a covariate-adjusted PET framework, plasma pTau217, specifically its ratio, was more closely related to amyloid PET than all plasma amyloid measures combined and explained more variance than CSF Aβ42. However, CSF Aβ42 remained a consistent and biologically valid PET amyloid burden. Plasma Aβ42/40 provided a substantially inferior correlation, and plasma Aβ40 alone had a negligible contribution. In conclusion, our results indicate that, within this data set and analysis framework, pTau217 in plasma exhibits greater concordance as a diagnostic marker for amyloid PET than plasma amyloid measures.

References

1. Royse SK, Minhas DS, Lopresti BJ, et al. Validation of amyloid PET positivity thresholds in centiloids: a multisite PET study approach. Alzheimer's Res Ther. 2021;13(1):99. DOI: https://doi.org/10.1186/s13195-021-00836-1
2. Cogswell PM, Wiste HJ, Weigand SD, et al. Plasma Alzheimer's disease biomarker relationships with incident abnormal amyloid PET. Alzheimer's Dement. 2025; 21:e14629. DOI: https://doi.org/10.1002/alz.14629
3. Jack CR, Wiste HJ, Algeciras-Schimnich A, et al. Comparison of plasma biomarkers and amyloid PET for predicting memory decline in cognitively unimpaired individuals. Alzheimer's Dement. 2024; 20: 2143–2154. DOI: https://doi.org/10.1002/alz.13651
4. Blennow K, Shaw LM, Stomrud E, et al. Predicting clinical decline and conversion to Alzheimer's disease or dementia using novel Elecsys Aβ(1–42), pTau and tTau CSF immunoassays. Sci Rep. 2019;9(1):19024. DOI: https://doi.org/10.1038/s41598-019-54204-z

Images/Tables

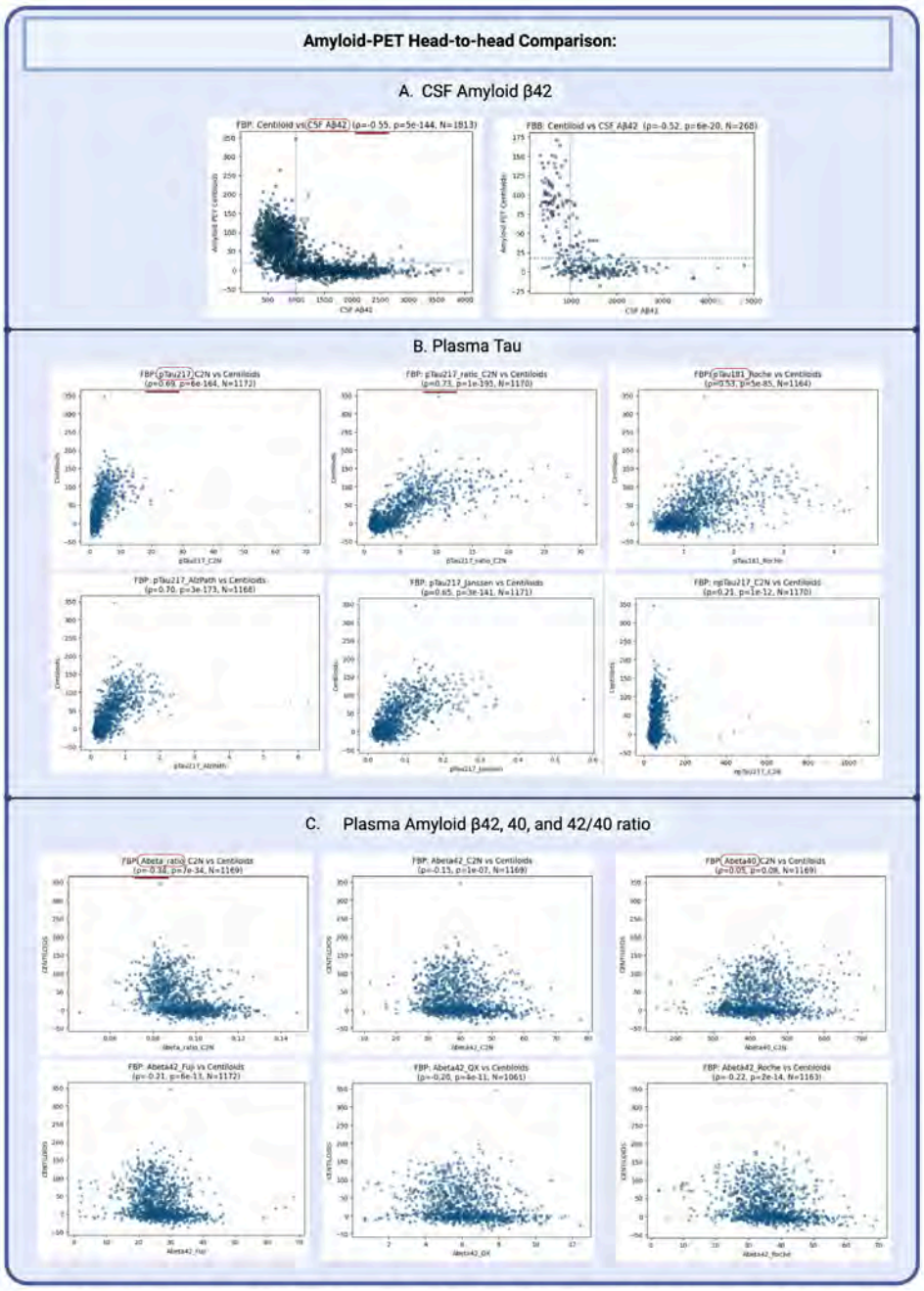

Figure. Covariate-adjusted correlations between Amyloid-PET centiloid and fluid biomarkers: CSF and plasma (correlation coefficient, p, N shown on each panel)

* PET: Positron emission tomography, CSF: Cerebrospinal fluid, FBB: Florbetaben amyloid PET, FBP: Florbetapir amyloid PET

** Correlations between global amyloid PET Centiloid:

(A) CSF amyloid β42 measured on the Roche assay.

(B) plasma tau biomarkers (pTau217, phosphorylated to non-phosphorylated Tau217 ratio, pTau181, npTau217) measured on assays from C2N Diagnostics, Fujirebio Diagnostics, Quanterix/Janssen, and Roche Diagnostics.

(C) plasma amyloid biomarkers (Aβ42, Aβ40, and Aβ42/40 ratio) measured on assays from C2N Diagnostics, Fujirebio Diagnostics, Quanterix, and Roche Diagnostics.

All models were covariate-adjusted for age, sex, APOE4 carrier status, and PET to sample collection interval. For the CSF cohort, amyloid-PET was available with both Florbetaben (FBB) and Florbetapir (FBP); for the plasma cohort, only FBP was available. The figure highlights the stronger correspondence of plasma pTau217 with amyloid PET compared with plasma amyloid measures, and the expected moderate inverse relationship between CSF Aβ42 and PET centiloid.

808 Association of Tau PET with CSF and Plasma Tau Biomarkers in a Large Alzheimer's Disease Study

Maryam Fotouhi MD, Nasim Sheikh-Bahaei Md, PhD
Department of Radiology, Keck School of Medicine, University of Southern California, Los Angeles, CA, USA

Purpose

This study utilized a positron emission tomography (PET) anchored, with no threshold method, with the aim of measuring the relationships between regional tau PET standardized uptake value ratio (SUVR) and plasma tau biomarkers against the corresponding relationships between cerebrospinal fluid (CSF) phosphorylated tau-181 and regional tau PET SUVR, conducted on paired PET-plasma and PET-CSF data in the entorhinal and meta-temporal composite brain regions.

Materials & Methods

Data were obtained from the Alzheimer's Disease Neuroimaging Initiative (ADNI), which included two tau PET indexed cohorts: Flortaucipir tau-PET with CSF pTau-181 (n = 578) and tau-PET with plasma tau biomarkers (n = 364). Plasma biomarkers were assayed for pTau217 (C2N Diagnostics, Fujirebio Diagnostics, Quanterix Janssen Laboratories), pTau181 (Roche Diagnostics, Quanterix), and non-pTau217 (C2N Diagnostics). The primary outcomes were the SUVRs within the entorhinal and meta-temporal regions. Predictor variables comprised native-scale assay-specific biomarker concentrations without thresholding. Covariates included age, sex, apolipoprotein E ε4 (APOE4) carrier status, and the interval between PET imaging and plasma/CSF sample collection. Partial Spearman correlations were calculated between biomarkers and SUVRs while adjusting for covariates. The incremental fit of the model was evaluated with ordinary least squares regression analysis by comparing models with covariates only (M0 models) to models with biomarkers added (M1 models), via change in R-squared and f2 values, with Akaike information criterion in model fit evaluation. The predictive fit was done with 5-fold cross-validation, aggregated root mean squared error (RMSE) and mean absolute error (MAE) values. All tests were two-tailed.

Results

Adjusted correlations between CSF pTau181 and tau-PET SUVR were moderate (entorhinal $\rho = 0.498$, $p < 0.0001$; meta-temporal $\rho = 0.456$, $p < 0.0001$). The addition of CSF pTau181 to the covariate model increased the variance explained from 15.0% to 35.3% in the entorhinal cortex and from 8.9% to 29.0% in the meta-temporal cortex, with corresponding substantial effect sizes (Cohen's $f^2 = 0.314$ and 0.283, respectively). Cross-validated prediction errors decreased significantly upon inclusion of CSF biomarkers. Plasma pTau217, particularly the C2N assay, exhibited the strongest alignment with tau-PET measures, surpassing CSF pTau-181 in variance explained and predictive accuracy (entorhinal $\rho = 0.512$, $\Delta R^2 = 0.327$, $f^2 = 0.575$; meta-temporal $\rho = 0.524$, $\Delta R^2 = 0.577$, $f^2 = 1.516$). Other plasma assays (pTau181 Roche, Quanterix Simoa; npTau217 C2N) showed weaker associations. Predictive improvements were consistently greater in the meta-temporal region.

Conclusion

Plasma pTau217 and C2N specifically offer a useful proxy for tau pathology in the regions studied, outperforming pTau181 in CSF, even with respect to tau PET imaging in meta-temporal and entorhinal regions. These data support the use of plasma pTau217 as a sensitive biomarker in therapeutic trials and prospective studies in which assessment can be simplified while preserving signal to tau imaging biomarkers.

References

1. Jagust WJ, Koeppe RA, Rabinovici GD, et al. The ADNI PET Core at 20. Alzheimer's Dement. 2024; 20: 7340–7349. DOI: https://doi.org/10.1002/alz.14165
2. Insel PS, Mattsson-Carlgren N, Langford O, et al. Concurrent Changes in Plasma Phosphorylated Tau 217, Tau PET, and Cognition in Preclinical Alzheimer Disease. JAMA Neurol. 2025;82(10):985–993. DOI: https://doi.org/10.1001/jamaneurol.2025.2974
3. Blennow K, Shaw LM, Stomrud E, et al. Predicting clinical decline and conversion to Alzheimer's disease or dementia using novel Elecsys Aβ(1–42), pTau and tTau CSF immunoassays. Sci Rep. 2019;9(1):19024. DOI: https://doi.org/10.1038/s41598-019-54204-z
4. Montoliu-Gaya, L., Salvadó, G., Therriault, J. et al. Plasma tau biomarkers for biological staging of Alzheimer's disease. Nat Aging (2025). DOI: https://doi.org/10.1038/s43587-025-00951-w

Images/Tables

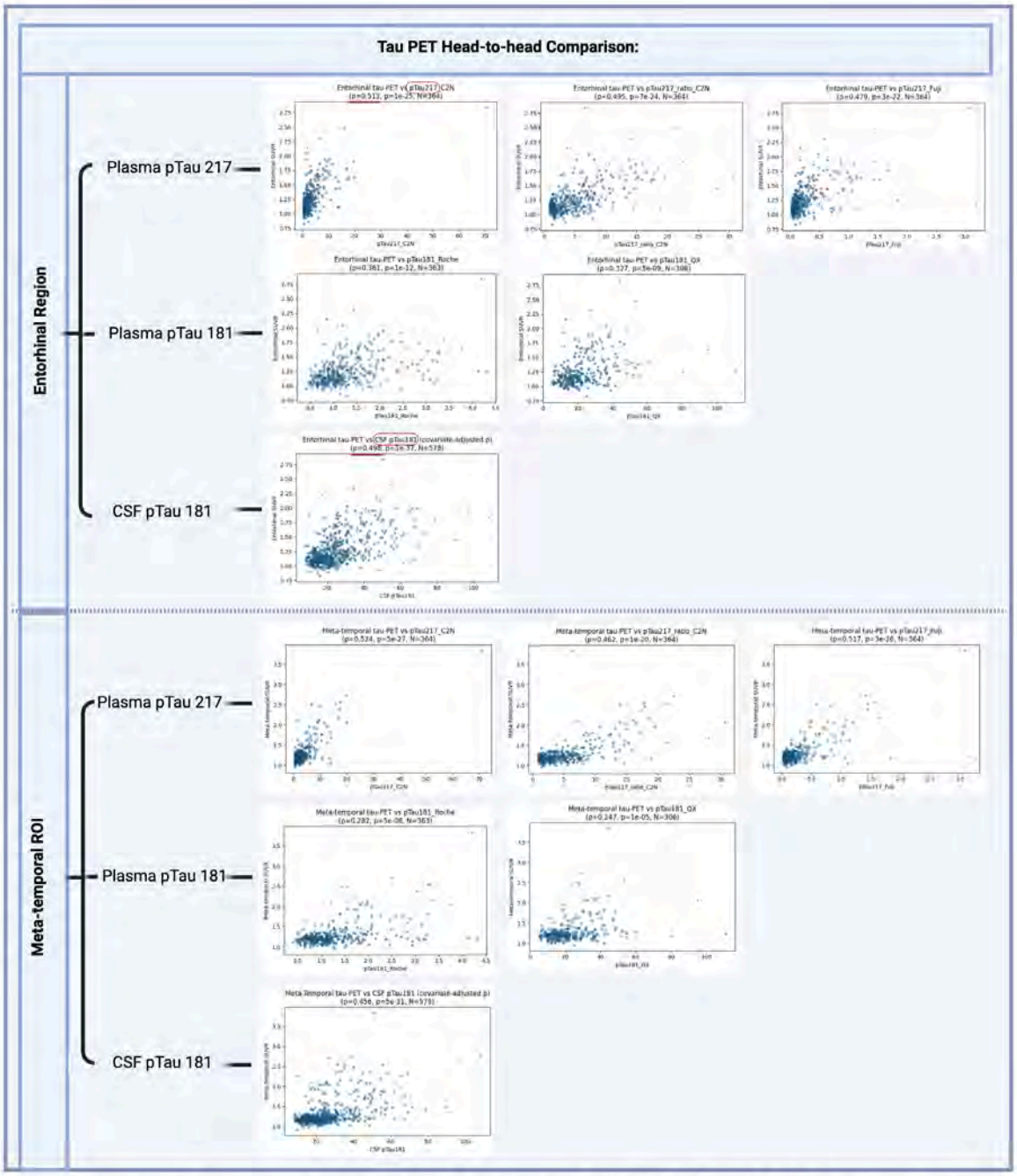

Figure. Covariate-adjusted correlations between Flortaucipir Tau-PET SUVR and Tau fluid biomarkers: CSF and plasma (correlation coefficient, p, N shown on each panel)
* PET: Positron emission tomography, CSF: Cerebrospinal fluid, SUVR: Standardized uptake value ratio

** Correlations between regional Tau-PET SUVR:
(A) Plasma pTau217 biomarker (pTau217, phosphorylated to non-phosphorylated Tau217 ratio) measured on assays from C2N Diagnostics, Fujirebio Diagnostics, Quanterix/Janssen, and Roche Diagnostics.
(B) Plasma pTau181 biomarker measured on assays from Quanterix, and Roche Diagnostics.
(C) CSF pTau181 measured on the Roche assay.

All models were covariate-adjusted for age, sex, APOE4 carrier status, and PET to sample collection interval.
Regional SUVR has been analysed in two regions: Entorhinal and Meta-temporal ROI (entorhinal, amygdala, fusiform, inferior temporal, middle temporal)
The figure highlights the stronger correspondence of plasma pTau217 with Tau PET, and the expected moderate correlation between CSF pTau181 and PET SUVR.

193 Multimodal Neuroimaging Approach for Cognitive Impairment in Alzheimer's Disease

Marlon Gonzales BHS[1], Xiaojian Kang PhD[2], Maheen M Adamson PhD[3], Steven Z Chao MD, PhD[3], Byung C Yoon MD, PhD[3]
[1]Meharry Medical College, Nashville, TN, USA. [2]VA Palo Alto, Palo Alto, CA, USA. [3]VA Palo Alto/Stanford, Palo Alto, CA, USA

Purpose

Positron emission tomography (PET), such as [^{18}F]florbetapir (FBP) and [^{18}F]flortaucipir (FTP) studies, and magnetic resonance imaging (MRI) are increasingly utilized for the diagnostic work-up of patients suspected of Alzheimer's disease (AD)(1). However, there is still limited understanding of how FBP and FTP are associated with regional brain atrophy and to what extent each neuroimaging modality is correlated with cognitive impairment in AD. This study aimed to determine whether a multimodality neuroimaging approach combining PET and MRI is superior to a single modality for predicting cognitive impairment.

Materials & Methods

Data from 381 Alzheimer's Disease Neuroimaging Initiative 3 participants were retrospectively analyzed. FBP/FTP results were correlated with brain cortical thickness and gray matter (GM) volumes and measures of cognitive impairment, including Mini-Mental State Examination (MMSE) and the Montreal Cognitive Assessment (MoCA). Statistical analyses, including linear and logistical regression analyses, were performed using Matlab2024b and RStudio 4.4.3.

Results

The cohort (n = 381; 200 females, 181 males) was divided into four groups: FBP+/FTP+ (n = 38), FBP+/FTP- (n = 133), FBP-/FTP+ (n = 5), and FBP-/FTP- (n = 205). Double positivity in PET (i.e. FBP+/FTP+) was associated with the greatest cortical thickness and GM atrophy, particularly in the temporal and parietal lobes (Figure 1). FBP+/FTP- and FBP-/FTP+ demonstrated more atrophy than FBP-/FTP- but less than FBP+/FTP+ (Figure 1). FBP+/FTP+ also showed stronger associations with cognitive impairment with odds ratios (OR) of 10.3 for MMSE ≤ 26 ($p < 0.001$) and 5.7 for MoCA < 26 ($p < 0.001$). In comparison, FBP+/FTP- demonstrated a lower ORs of 4.7 for MMSE ($p < 0.001$) and 1.78 for MoCA ($p = 0.017$). Among FBP/FTP groups, the inclusion of cortical thickness, temporal gray matter, or parietal lobe gray matter atrophy conferred the strongest associations with cognitive impairment. Among the FBP+/FTP+ cohort, for instance, those positive for a substantial mean cortical thickness loss had an OR of 28.89 for MMSE ≤ 26 ($p < 0.001$), compared to those negative for mean cortical thickness loss (OR 8.04, $p < 0.001$).

Conclusion

FBP, FTP, and regional brain atrophy were independently associated with cognitive impairment. A combination of all three modalities showed the strongest correlations with cognitive impairment, underscoring the value of a multimodality approach.

References

1. Jack Jr. CR, Andrews JS, Beach TG, et al. Revised criteria for diagnosis and staging of Alzheimer's disease: Alzheimer's Association Workgroup. *Alzheimer's Dement* 2024; 20: 5143–5169. doi: 10.1002/alz.13859.

Images/Tables

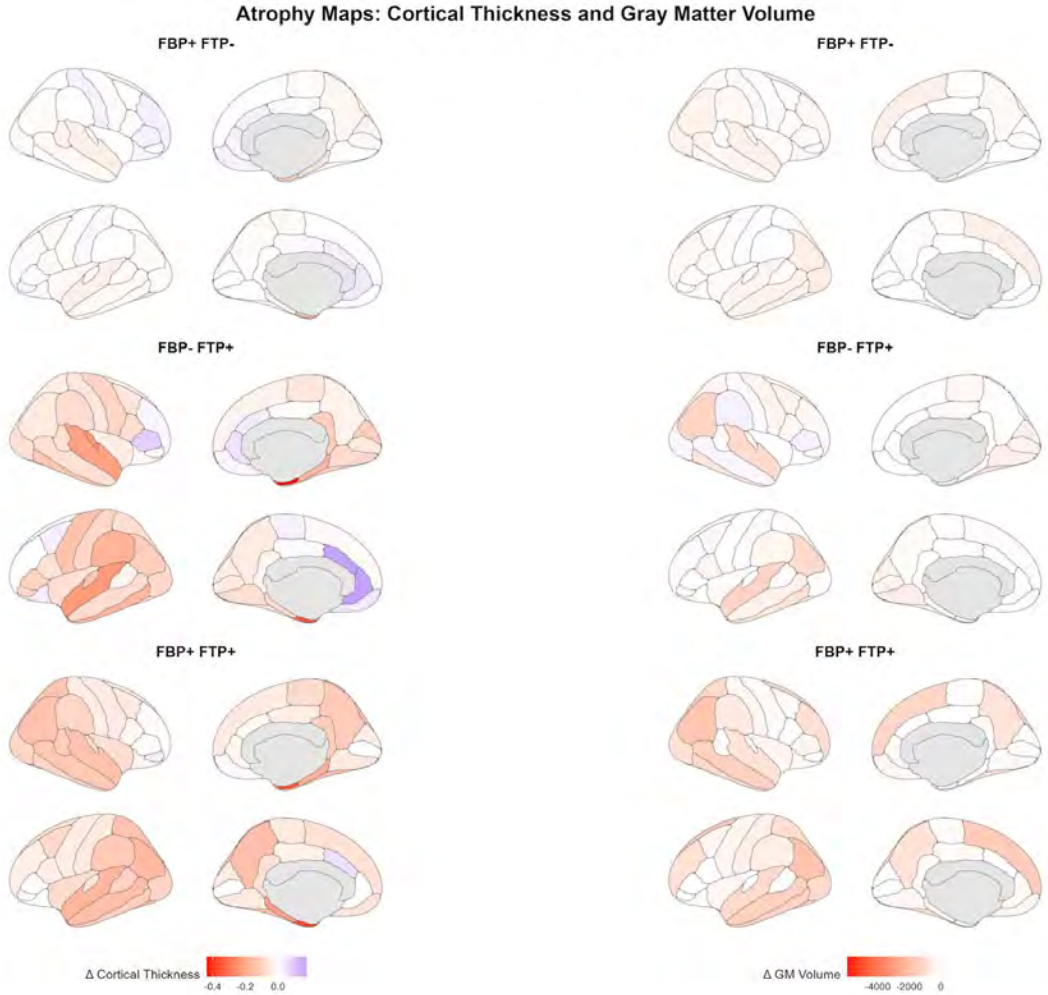

330 Characterization of microstructural white matter changes associated with PET in Alzheimer's disease

Marlon Gonzales BHS[1], Xiaojian Kang PhD[2], Christian Cort MD[3], Maheen M Adamson PhD[2], Steven Z Chao MD, PhD[2], Byung C Yoon MD, PhD[2]
[1]Meharry Medical College, Nashville, TN, USA. [2]VA Palo Alto Healthcare System, Palo Alto, CA, USA. [3]United States Navy, Port Hueneme, CA, USA

Purpose

Alzheimer's disease (AD) is associated with regional brain atrophy as well as elevated positron emission tomography (PET) markers of amyloid-beta (e.g. [^{18}F]florbetapir (FBP)) and tau protein (e.g. [^{18}F]flortaucipir (FTP))(1). White matter microstructures have also been shown to be affected in AD (2), but less is known about their specific associations with FBP or FTP. Herein, we used diffusion tensor imaging (DTI) to characterize microstructural white matter changes in Alzheimer's disease neuroimaging initiative (ADNI) participants who underwent FBP and FTP PET.

Materials & Methods

A retrospective study was performed using the data from 381 ADNI-3 participants (F:M = 200:181). FBP and FTP results were correlated with DTI metrics, including the apparent fiber density (AFD), complexity (CX), functional anisotropy (FA), fixel number (FN), and mean diffusivity (MD). For PET, Standardized Uptake Value Ratio (SUVR) and binary classifications (positive vs negative) were both used. DTI image analysis was performed using Mrtrix3 (2). Linear regression analysis was adjusted for age, sex, and education. Statistical analyses were performed using Matlab2024b and RStudio 4.4.3.

Results

Negative correlations were observed between FBP SUVR and CX, FN, and FA, but not AFD and MD. FN showed the highest degree of correlations (beta coefficients of -0.37 to -0.27 vs -0.06 to -0.03 for CX and FA) with significant correlations (P<0.05) seen in the forceps minor, left uncinate fasciculus, and bilateral anterior thalamic radiations, inferior fronto-occipital fasciculi, inferior longitudinal fasciculi, and cingulum-cingulate gyri. No significant correlation was observed between DTI measures and FTP SUVR, independently. However, combined PET positivity (FBP+/FTP+) showed the greatest reductions in CX, FN, and FA of various tracts, compared to single PET-positive or PET-negative groups (Table 1). Among single PET-positive groups, FBP+/FTP- generally showed more reduction in CX, FN, and FA than FBP-/FTP+. For instance, FA of the forceps major was the lowest at 0.3030 for FBP+/FTP+, followed by FBP+/FTP- (0.3219), FBP-/FTP+ (0.3338), and FBP-/FTP- (0.3427, P=0.0100).

Conclusion

DTI metrics such as CX, FN, and FA were negatively correlated with FBP levels but not with FTP. Double PET positivity (FBP+/FTP+) generally showed the greatest reduction. These results suggest that there may be specific patterns of microstructural changes associated with elevated amyloid and tau proteins in AD.

References

1. Jack Jr. CR, Andrews JS, Beach TG, et al. Revised criteria for diagnosis and staging of Alzheimer's disease: Alzheimer's Association Workgroup. *Alzheimer's Dement* 2024; 20: 5143–5169.
2. Chen Y, Wang Y, Song Z, et al. Abnormal white matter changes in Alzheimer's disease based on diffusion tensor imaging: a systematic review. Ageing Res Rev. 2023; 87.
3. Kang X, Yoon BC, Shah S, et al. Fixel-based analysis of the diffusion properties of the patients with brain injury and chronic health symptoms. *Neurosci Res*. 2023;192:63-76.

Images/Tables

Metric	Fiber Tract	FBP- FTP- (n = 206)	FBP+ FTP- (n = 132)	FBP- FTP+ (n = 5)	FBP+ FTP+ (n = 38)	P-value (P<0.0125)
Complexity	ATRL	0.5764	0.5466	0.6114	0.5321	0.0081
	CCF	0.5503	0.5230	0.5672	0.4999	0.0092
	CSTR	0.4659	0.4443	0.5020	0.4187	0.0115
Fixel Number	ILFL	2.9814	2.8025	2.9448	2.6360	0.0099
	SLFBL	3.0653	2.8728	2.9432	2.6931	0.0113
	ATRL	2.8983	2.7267	2.9634	2.5757	0.0113
Fractional Anisotropy	CgLR	0.2678	0.2447	0.2406	0.2204	0.0005
	ATRR	0.3026	0.2779	0.2514	0.2709	0.0007
	CSTR	0.4085	0.3819	0.3938	0.3756	0.0008
	IFOR	0.3439	0.3190	0.3180	0.3114	0.0022
	CSTL	0.4151	0.3898	0.4006	0.3851	0.0033
	ILFR	0.3400	0.3186	0.3236	0.3048	0.0042
	ATRL	0.3141	0.2922	0.2946	0.2774	0.0047
	IFOL	0.3465	0.3234	0.3288	0.3151	0.0048
	SLFBR	0.3117	0.2905	0.3016	0.2804	0.0090
	CCO	0.3427	0.3219	0.3338	0.3030	0.0100

ATRL: left anterior thalamic radiations, ATRR: right anterior thalamic radiations, CCF: corpus callosum – forceps minor, CCO: corpus callosum – forceps major, CgLR: right cingulum – hippocampus, CSTL: left corticospinal tract, CSTR: right corticospinal tract, IFOL: left inferior fronto-occipital fasciculus, IFOR: right inferior fronto-occipital fasciculus, ILFR: left inferior longitudinal fasciculus, ILFR: right inferior fronto-occipital fasciculus, SLFBL: left superior longitudinal fasciculus frontal – temporal, SLFBR: left superior longitudinal fasciculus frontal – temporal.

608 Longitudinal Evaluation of β-Amyloid Plaque Burden and Brain Volume Changes in Patients Receiving Anti-Amyloid Immunotherapy

Nelson H Gil MD, PhD, Suely Fazio Ferraciolli MD, PhD, Jeremy Ford MD, MS, MBA
Massachusetts General Hospital, Harvard Medical School, Boston, MA, USA

Purpose

Brain volume loss incurred during anti-amyloid treatment has been called amyloid-removal-related pseudoatrophy, and may predominantly involve expansion of the lateral ventricles, hypothesized as being driven by cerebrospinal fluid shifts [1, 2]. Still, dose-response relationships between amyloid removal and volume loss are unclear, and repeated-measures data tracking changes longitudinally in patients are lacking. The purpose of this work is to quantitatively evaluate the relationship between immunotherapy-mediated β-amyloid plaque removal and changes in brain volume over time in a clinical population undergoing anti-amyloid treatment.

Materials & Methods

Adults on anti-amyloid treatment at our institution who had undergone two F-18 β-amyloid brain PET scans (APETs) from any date up to September 2025 were retrospectively included. For each patient, the two APETs defined a “first” and “second” timepoint. Brain MRI examinations including a 3D T1-weighted sequence performed in closest proximity to the APETs were also identified. Therefore, both timepoints had an APET-MRI pair for each patient. All scans were manually inspected to be free of major structural abnormalities.

Using petBrain [3] on APET-MRI pairs yielded centiloid scores, Hippocampal Amygdalo-Ventricular Atrophy scores (HAVAs) [4], lateral ventricle volumes (excluding the inferior lateral ventricles used in HAVAs), hippocampus volumes, and total brain volumes. The distributions of these measures across the patients were compared between the first and second timepoints. Percent differences were normalized by the years between the first and second timepoints. The yearly percent differences of HAVAs and lateral ventricle/hippocampus/total brain volumes were correlated with the yearly percent difference in centiloid scores.

Results

45 patients (15 female, 73.4±6.8 years old at first timepoint) were included (Fig. A), with a mean interval between timepoints of 1.65±1.37 years. Centiloid scores significantly decreased between the timepoints (Fig. B; mean -42.078 points [56%], $p<0.001$). Volumetric measures demonstrated small statistically significant changes (Fig. C): HAVAs scores increased (mean +0.081 [10%], $p<0.001$), lateral ventricle volume increased (mean +7.432 cc [12%], $p<0.001$), hippocampus volume decreased (mean -0.238 cc [3.8%], $p<0.001$) and total brain volume decreased (mean -18.918 cc [1.7%], $p<0.001$).

There was no significant difference in the yearly percent changes of HAVAs and lateral ventricle volume (mean difference 0.036, $p=0.361$) (Fig. D(i)). Additionally, there was no significant correlation between percent changes per year in centiloid scores and HAVAs ($R^2=0.0255$, $p=0.295$), lateral ventricle volume ($R^2=0.0097$, $p=0.520$), hippocampus volume ($R^2=0.008$, $p=0.559$), and total brain volume ($R^2=0.0447$, $p=0.164$) (Fig. D(ii)).

Conclusion

While amyloid burden decreases substantially during anti-amyloid treatment, small changes in HAVAs and ventricular/hippocampus/total brain volume are not correlated with the degree of amyloid reduction, suggesting that volume loss is not directly driven by amyloid clearance. Specifically, that the lateral ventricular volume did not change significantly differently from the HAVAs score argues against the cerebrospinal-fluid-shift mechanism for volume loss in our dataset. Additionally, symmetric global decreases in hippocampus volume argue against focal neurodegeneration in this dataset. Our study complements recent evidence that degree of amyloid plaque removal does not correlate with cognitive outcomes [5]. Ultimately, our results suggest that removal of amyloid plaque is not a direct causal contributor to volume loss.

References

[1] Belder CRS, Boche D, Nicoll JAR, et al. Brain volume change following anti-amyloid beta immunotherapy for Alzheimer's disease: amyloid-removal-related pseudo-atrophy. Lancet Neurol. 2024;23:1025-34.

[2] Alves F, Kalinowski P, Ayton S. Accelerated Brain Volume Loss Caused by Anti-beta-Amyloid Drugs: A Systematic Review and Meta-analysis. Neurology. 2023;100:e2114-e24.

[3] Coupe P, Mansencal B, Morandat F, et al. petBrain: a new pipeline for amyloid, Tau tangles and neurodegeneration quantification using PET and MRI. Alzheimers Res Ther. 2025;17:209.

[4] Coupe P, Manjon JV, Mansencal B, et al. Hippocampal-amygdalo-ventricular atrophy score: Alzheimer disease detection using normative and pathological lifespan models. Hum Brain Mapp. 2022;43:3270-82.

[5] Biel D, Steward A, Dewenter A, et al. A systematic comparison of ATN biomarkers for monitoring longitudinal cognitive changes in Alzheimer's disease. Alzheimers Dement. 2025;21:e70783.

Images/Tables

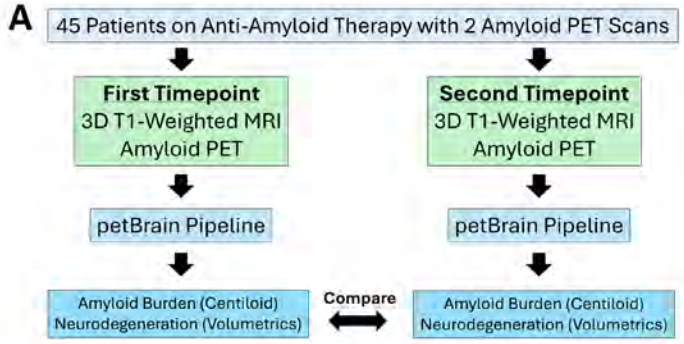

Figure A. Outline of the present study. 45 patients on anti-amyloid immunotherapy Treatment and who had two F-18 beta amyloid PETs (APETs) were retrospectively identified. The APETs defined first and second timepoints and were paired with clinical 3D T1-weighted brain MRIs that were closest in date to the timepoints. The APETs and MRIs for the two timepoints were input into the petBrain pipeline, which returned measures of amyloid burden (centiloid score) and neurodegeneration (brain volumetrics). These measures were compared between the timepoints.

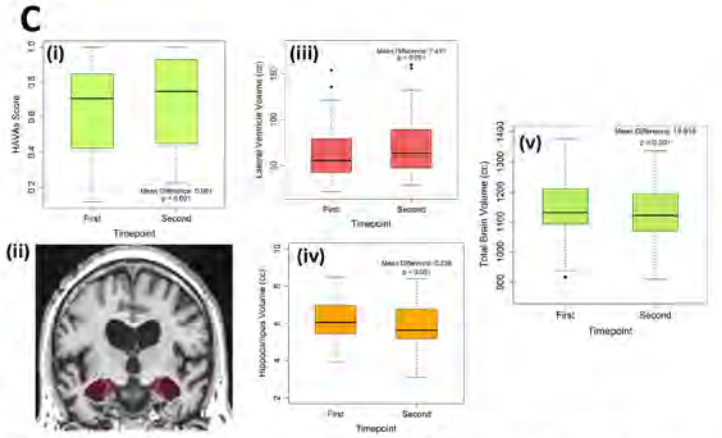

Figure C. Changes in neurodegeneration measures from the first to second timepoints. (i) Comparison in Hippocampal Amygdalo-Ventricular Atrophy score (HAVAs), demonstrating a small statistically significant increase from the first to second timepoint. (ii) Example coronal MRI of a patient with a high HAVAs score, illustrating hippocampal atrophy (red). Small statistically significant changes are also seen for the lateral ventricle volume (iii, increase), hippocampus volume (iv, decrease), and the total brain volume (v, decrease).

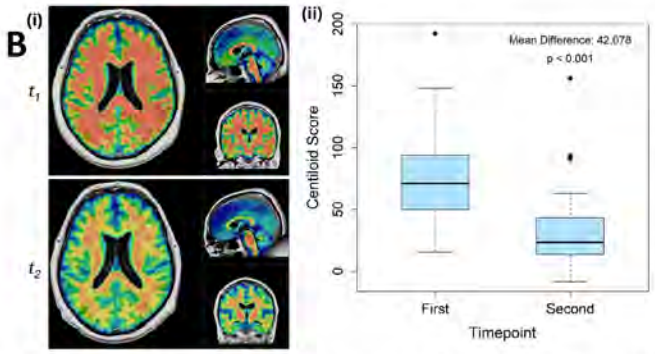

Figure B. Changes in beta amyloid plaque burden between the first (t_1) and second (t_2) timepoints at which F-18 beta amyloid PETs (APETs) were obtained. (i) Example of axial, sagittal, and coronal APETs overlaid on the corresponding 3D T1-weighted MRI at timepoints t_1 (top) and t_2 (bottom) for a single patient. There is qualitatively marked decrease in uptake throughout the brain, as shown by the decrease in red coloring from t_1 to t_2. (ii) Quantitative comparison of centiloid scores for the 45 patients in the study. There is a statistically significant decrease in centiloid score from the first to second timepoint, with a mean decrease of 42.078 points (56.1%).

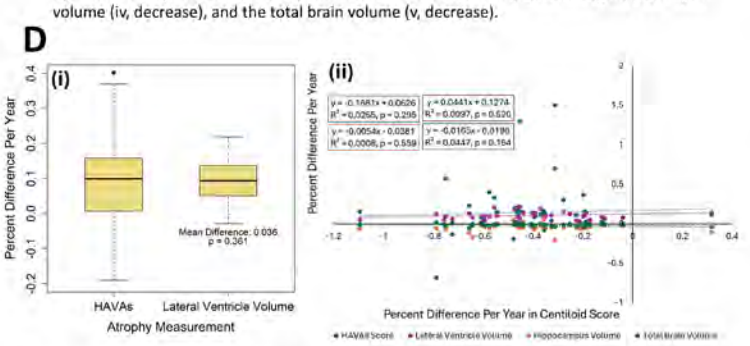

Figure D. (i) Comparison of percent changes per year in Hippocampal Amygdalo-Ventricular Atrophy score (HAVAs) and lateral ventricular volume from the first to second timepoint, showing no significant differences. (ii) Correlation plot showing the linear regressions between the percent difference per year in centiloid score and the HAVAs score (blue), lateral ventricle volume (purple), hippocampus volume (orange), and total brain volume (green). Regression line equations, R^2 values, and associated p-values are shown in correspondingly colored boxes. There is no correlation between the change in centiloid score and the neurodegeneration measures.

---

652 **Perivascular Diffusivity Predicts Amyloid Clearance Rate in Patients Treated with Lecanemab**

Rafael E Martinez Imbett MD[1], Nelson H Gil MD,PhD[1], Saurabh Rohatgi MD[1], Hana Farzaneh MD[1], Christina M Younan[1], Marvin Relerford[1], Odette Ganem[1], Javier M Romero MD[1], Jeremy N Ford MD[2]

[1]MGH, BOSTON, MASSACHUSETTS, USA. [2]MGH, BOSTON, Massachusetts, USA

Purpose

To determine whether perivascular diffusivity, quantified by the ALPS-index, predicts amyloid clearance rate in patients undergoing lecanemab therapy.

Materials & Methods

Patients were included if they received lecanemab for ≥6 months, had at least two florbetaben PET scans, and underwent baseline diffusion MRI as part of the anti-amyloid protocol. Twenty-five of forty-five eligible participants had DTI-quality diffusion data. Diffusion-weighted images were preprocessed using EDDY correction, GQI reconstruction, and QSDR normalization. Diffusivity along orthogonal fiber axes was extracted to compute the ALPS-index (Taoka et al., 2017). The outcome variable was amyloid clearance rate, defined as monthly change in centiloid units between baseline and follow-up PET. Linear and multiple regression models examined associations between baseline ALPS-index and amyloid clearance, with and without adjustment for baseline centiloid values.

Results

Baseline ALPS-index predicted amyloid clearance rate (β = −6.98, p = 0.022, R^2 = 0.23). After adjusting for baseline centiloid, both ALPS-index (β = −4.79, p = 0.027) and baseline centiloid (β = −0.0288, p < 0.001) remained independent predictors, improving model fit (R^2 = 0.64). Higher ALPS-indices and greater baseline amyloid burden were associated with faster declines in centiloid values.

Conclusion

The observed association between higher ALPS-index and faster amyloid clearance suggests that perivascular diffusivity contributes to treatment variability in lecanemab. Further longitudinal and multimodal studies are warranted to confirm the ALPS-index as a marker of glymphatic function and predictor of clinical outcomes in anti-amyloid treated patients.

References

Taoka T, Masutani Y, Kawai H, Nakane T, Matsuoka K, Yasuno F, Kishimoto T, Naganawa S. Evaluation of glymphatic system activity with the diffusion MR technique: diffusion tensor image analysis along the perivascular space (DTI-ALPS) in Alzheimer's disease cases. Jpn J Radiol. 2017 Apr;35(4):172-178. doi: 10.1007/s11604-017-0617-z. Epub 2017 Feb 14. PMID: 28197821.

Images/Tables

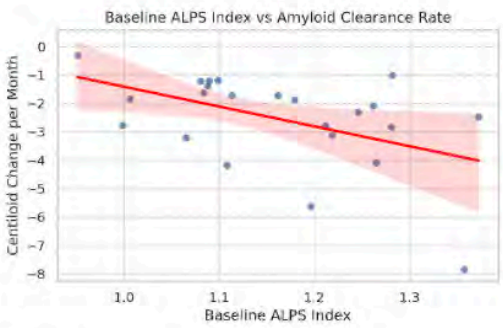

Figure 1. Linear regression Baseline ALPS Index vs Amyloid Clearance Rate. Higher ALPS associated with faster amyloid clearance.

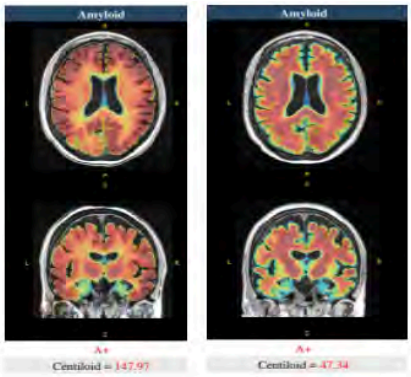

Figure 2. Baseline centiloid value (left) and 12 months follow up (right). Baseline ALPS-index 1.35.

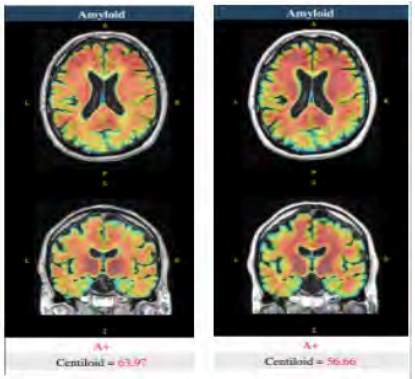

Figure 3. Baseline centiloid value (left) and 12 months follow up (right). Baseline ALPS-index 1.08.

295 **Hippocampal subfield geometry-based analysis and TDP-43 in primary age-related tauopathy**

Hossam Youssef M.B., B.Ch., Rodolfo G. Gatto M.D., Ph.D., Ronald C. Petersen M.D., Ph.D., R. Ross Reichard M.D., Clifford R. Jack M.D., Jennifer L. Whitwell Ph.D., Keith A. Josephs MD, MST, MSc
Mayo Clinic, Rochester, MN, USA

Purpose

We aimed to examine shape deformation of the presubiculum, subiculum, CA1, and CA2/3 hippocampal subfields in relation to the presence of the Transactive Response DNA-Binding Protein of 43 kDa (TDP-43) in primary age-related tauopathy (PART).

Materials & Methods

We identified 80 cases that fulfilled the criteria for PART[1] from a cohort of 1,720 autopsy-confirmed cases sourced from the Mayo Clinic Alzheimer's Disease Research Center (ADRC), the Mayo Clinic Study of Aging (MCSA), and the Neurodegenerative Research Group (NRG). Each case had one antemortem GE 3T MRI brain scan and postmortem brain examination conducted between January 1, 1999, and December 31, 2022. TDP-43 status was determined based on presence of TDP-43 in the amygdala. In addition, we identified 16 healthy control individuals from the MCSA who also underwent 3T MRI, were negative for amyloid-β deposition on positron emission tomography (PET) and were aged 50 years or younger at the time of scan.

All MRI hippocampal subfields were segmented using FreeSurfer 8.0.0, followed by the application of a geometry-based algorithm designed to produce a parametric shape representation of the hippocampus and its subfields[2, 3]. This algorithm creates a mesh, enabling the calculation of various statistics, including Gaussian curvature and thickness of the segmented subfields, and the generation of raw mesh vertex data in a grid-based sampling format. Thickness and curvature analyses were performed using two statistical methods: the spatial x-axis-specific t-test and the point-wise cluster-based permutation test.

Of the 80 cases, 66 successfully underwent bilateral hippocampal segmentation and shape analysis, alongside 14 controls, resulting in three distinct groups: PART(TDP-) (n=47), PART(TDP+) (n=19), and controls (n=14), which were subsequently included in the statistical analyses. Data analysis, comparison, and visualization were conducted using Python 3.13.3.

Results

The subfields that demonstrated significant group differences in thickness and curvature were represented in a mesh format in **figure 1.**

PART(TDP-) vs Controls

Thickness analyses showed that PART (TDP-) cases had reduced thickness of bilateral presubiculum and subiculum with reduction being more extensive in the right hemisphere. Curvature analysis showed greater curvature changes in bilateral subiculum and right presubiculum and CA1 in PART (TDP-) cases.

PART(TDP+) vs Controls

Thickness analyses showed that PART (TDP+) cases had reduced thickness in bilateral presubiculum and subiculum. Curvature changes were more pronounced in right presubiculum and subiculum.

PART(TDP+) vs PART(TDP-)

Thickness analyses showed that PART (TDP+) cases had reduced thickness in left subiculum and CA1 compared to PART (TDP-) cases. Curvature changes differed between groups in CA1 and CA2/3.

Conclusion

Geometry-based analysis identified distinct patterns of hippocampal thinning and curvature differences in PART cases compared to controls and in those with and without TDP-43. This suggests that thickness and curvature occur in PART with some changes related to the presence of TDP-43.

References

1. Crary JF, Trojanowski JQ, Schneider JA, et al. Primary age-related tauopathy (PART): a common pathology associated with human aging. *Acta Neuropathol* 2014;128:755-766

2. Diers K, Baumeister H, Jessen F, et al. An automated, geometry-based method for hippocampal shape and thickness analysis. *Neuroimage* 2023;276:120182

3. Fischbach L, Bauer T, Diers K, et al. A novel geometry-based analysis of hippocampal morphometry in mesial temporal lobe epilepsy. *Hum Brain Mapp* 2023;44:4467-4479

Images/Tables

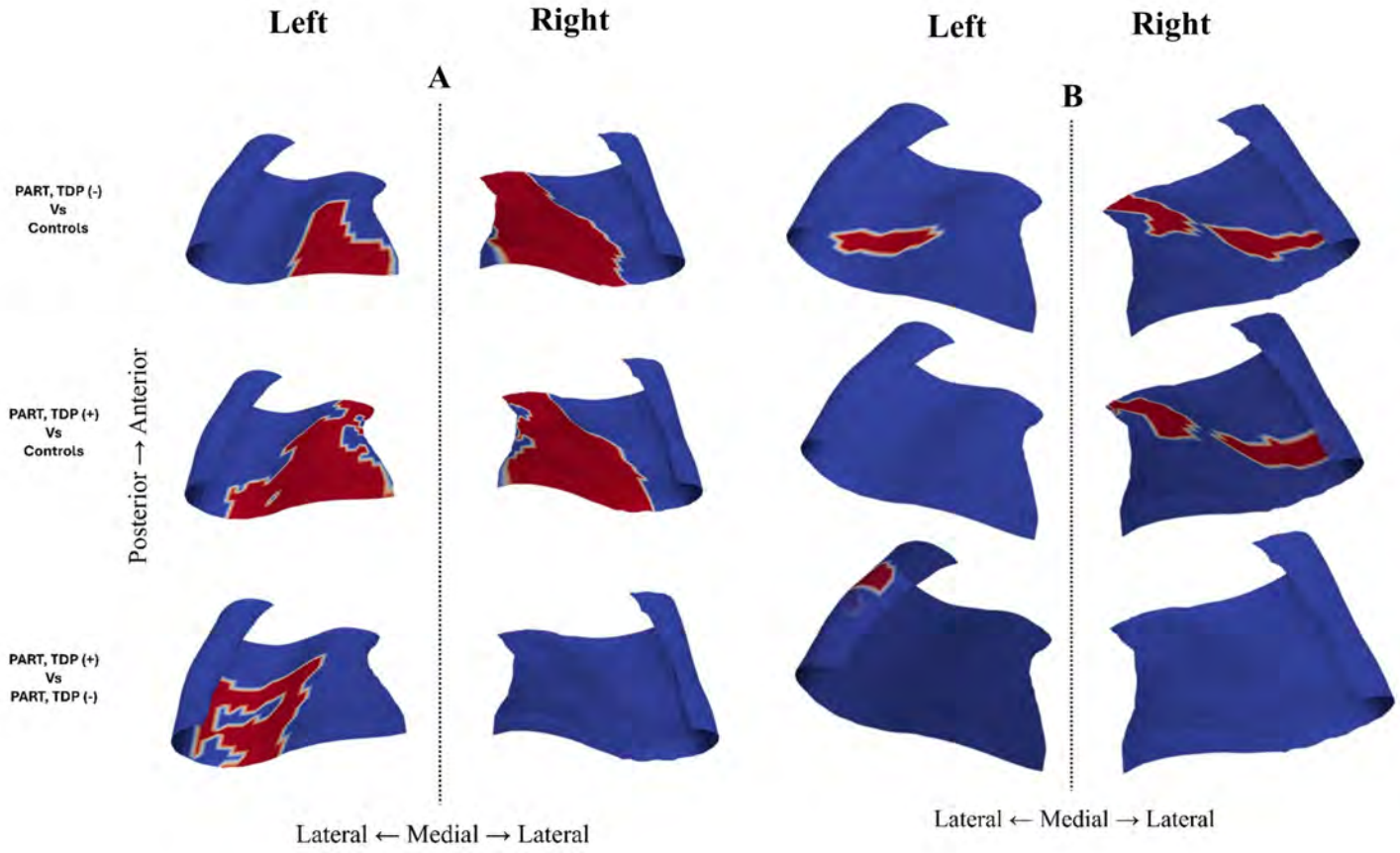

---

505 **Biomarker pattern of Amyloid-Related Imaging Abnormalities in Lecanemab-Treated Alzheimer's Disease**

Shenghua Zhu MD, PhD, Saurabh Rohatgi MD, Odette Ganem Chagui, Esteban Calle Cadavid MD, Rafael Eduardo Martinez MD, Thomas Dowling MD, Hana Farzaneh MD, Christina Younan, Nima Omid-Fard MD, Jeremy Ford MD, Javier Romero MD
Mass General Hospital, Boston, MA, USA

Purpose

Amyloid-related imaging abnormalities (ARIA) are a major concern during anti-amyloid therapy. While APOE ε4 carriers are at higher risk, additional baseline biomarkers to refine risk stratification are needed. To evaluate whether ARIA observed in lecanemab was associated with specific biomarker patterns.

Materials & Methods

We conducted a retrospective cohort study of patients with early Alzheimer's disease initiating lecanemab at a single academic center (November 2023–January 2025). Baseline clinical variables, APOE genotype, and CSF biomarkers (Aβ42, total tau [t-tau], phosphorylated tau [p-tau], p-tau/Aβ42, and integrated tau-associated index [ATI]) were obtained prior to therapy. ARIA was detected on MRI surveillance and neuroradiology review.

Results

Among 108 patients, 28 developed ARIA and 80 did not. Groups did not differ by age, sex, cognition, or metabolic profiles (all p>0.05). APOE ε4 carriage was more frequent in ARIA-positive patients (82.1% vs 48.8%, p=0.002). Baseline CSF t-tau was lower in ARIA-positive patients (mean 376.2 ± 41.97 pg/mL) versus ARIA-negative (567.5 ± 45.48 pg/mL; p=0.0199). In univariate analyses, lower t-tau was associated with higher ARIA risk (OR 0.998 per pg/mL, 95% CI 0.995–0.999; p=0.0058; AUC 0.671, p=0.0073). In multivariable models including age, sex, cognition, microbleed count, Aβ42, t-tau, p-tau, and APOE ε4, lower t-tau and ε4 carriage independently predicted ARIA (model AUC 0.814; 95% CI 0.712–0.916; p<0.0001). Other CSF measures were not associated with ARIA (all p>0.05).

Conclusion

Lower baseline CSF t-tau independent from APOE ε4 identifies patients at increased risk for ARIA during lecanemab therapy, beyond cognition or metabolic factors. These data support biomarker-guided risk stratification and motivate prospective validation of models combining genotype, CSF t-tau, and cerebrovascular markers to optimize monitoring and safety.

References

Legends:

Figure 1. Diagram illustration of the workflow of patient selection.

Figure 2. Median and range of baseline CSF biomarkers between ARIA-positive and ARIA-negative patients treated with Lecanemab. (* $p < 0.05$; ** $p < 0.01$). [The box notes values between 25th percentile and 75th percentile. Midline marks the median and the whiskers extend to 1.5 times the height of the box].

Figure 3. Univariate logistic regression analyses modeled each CSF biomarkers predicting ARIA in AD patients treated with lecanemab. (* $p < 0.05$; ** $p < 0.01$).

Table 1. Multivariate logistic regression analysis with models predicting ARIA in AD patients treated with lecanemab with age, sex, MoCA score, APOE ε4 status, CSF Aβ42, t-tau and p-tau as independent variables. (* $p < 0.05$; ** $p < 0.01$).

Reference:

1. van Dyck CH, Swanson CJ, Aisen P, et al. Lecanemab in Early Alzheimer's Disease. N Engl J Med 2023; 388:9-21
2. Cummings J, Osse AML, Cammann D, Powell J, Chen J. Anti-Amyloid Monoclonal Antibodies for the Treatment of Alzheimer's Disease. BioDrugs 2024; 38:5-22
3. Roytman M, Mashriqi F, Al-Tawil K, et al. Amyloid-Related Imaging Abnormalities: An Update. AJR Am J Roentgenol 2023; 220:562-574
4. Doran SJ, Sawyer RP. Risk factors in developing amyloid related imaging abnormalities (ARIA) and clinical implications. Front Neurosci 2024; 18:1326784

Images/Tables

Figure 1

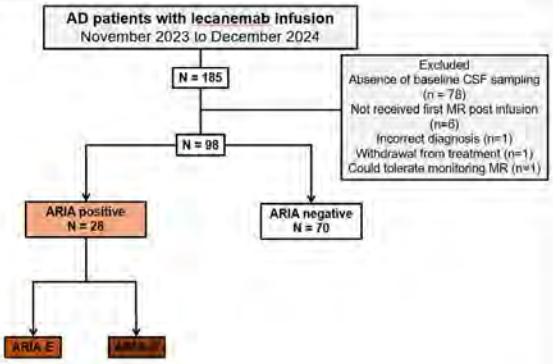

Figure 2

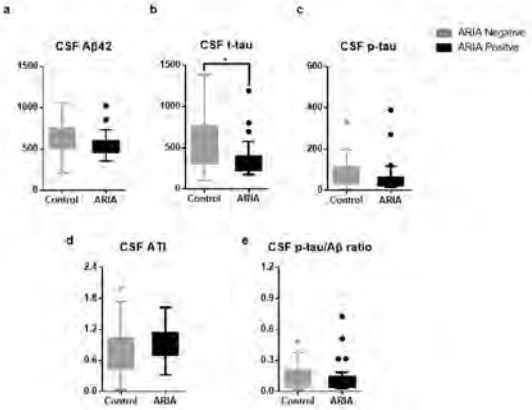

Figure 3

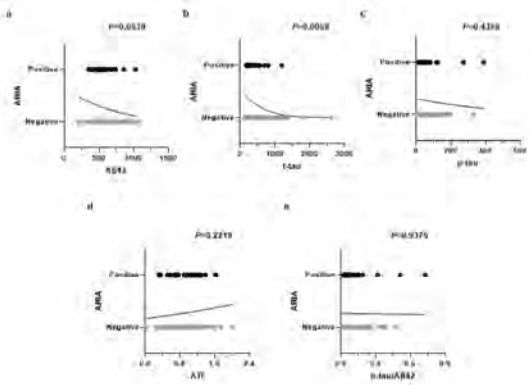

Table 1

Variable	Odds ratios	95% CI	*P* values
Age	1.026	0.950-1.111	0.523
Sex	0.776	0.228-2.555	0.677
MoCA	0.928	0.779-1.095	0.380
CSF Aβ42	0.997	0.993-1.000	0.107
CSF t-tau	0.992	0.985-0.998	0.032*
CSF p-tau	1.035	1.004-1.077	0.064
APOE ε4	6.501	1.762-31.16	0.0091**

Scientific Abstract Power Pitches & Luminary Speaker: Spine

9:55 - 10:55am Tuesday, 19th May, 2026

790 Successful streamlined photon-counting CT myelography protocol for detection of CSF-venous fistulas in busy practice settings

Fides R Schwartz MD[1], Raymond Y Huang MD[1], Jason R Lauer MD[2], Matthew N DeSalvo MD[1], Shuhan Zhu MD[1], Rose Wach BS[1], Aaron D Sodickson MD[1], Neel Madan MD[3]

[1]Brigham and Women's Hospital, Boston, MA, USA. [2]Mass General Hospital, Boston, MA, USA. [3]Tufts Medicine, Boston, MA, USA

Purpose

CSF leaks are difficult to detect with energy-integrating (EID) CT myelography due to its limitation in spatial resolution. The purpose of this study was to develop a streamlined protocol for entire-spine-evaluation for CSF leaks in patients with spontaneous intracranial hypotension using photon-counting CT (PCCT).

Materials & Methods

In this IRB-approved study, 35 patients (25 women, mean age: 51.6±15.6 years) with prior inconclusive spine imaging for CSF-leak detection received PCCT myelographic imaging. Contrast was injected utilizing digital subtraction myelography, and the patient was transported to the PCCT scanner in decubitus positioning. PCCT was performed with a protocol minimizing patients' time in the scanner to 15 minutes, while acquiring full spine images at 0.2x0.1 mm resolution in three breathing phases: resistive inspiration, end inspiration and Valsalva (six series total). All but two patients had imaging performed on two consecutive days, once for each decubitus position.

The number of CT/MRI investigations and blood patches prior to the PCCT were documented for each patient. One neuroradiologist with subspecialty training in spinal interventions assessed each PCCT to define whether a CSF leak was identified. Three separate readers assessed best breathing phase for leak detection. Treatment was considered a success if patients received an intervention that provided symptom relief.

Results

Patients had received 4.6±5.0 prior CTs (range: 0-26) and 4.0±3.0 prior MRIs (range: 1-13); this had led to a mean of 2.1±1.3 prior blood/fibrin glue patches (range: 1-6) without lasting symptom relief.

A CSF leak was definitively identified in 12/35 (34%) patients; an additional 8/35 (23%) patients had potential CSF leak sites. Following PCCT imaging, four patients received surgical treatment, eight received percutaneous embolization and 17 received blood/fibrin glue patches. Resistive inspiration was most frequently considered the best phase for leak detection. Of patients who underwent treatment, it was considered a success in 18/29 (62%) patients, 5/29 (17%) had no relief, 6/29 (21%) had incomplete relief and seven patients had not been treated at the time of last follow-up.

Conclusion

Using a streamlined PCCT protocol for CSF leak detection is feasible and provides targeted treatment options for patients whose prior imaging was inconclusive.

References

1. Kranz PG, Gray L, Malinzak MD, Houk JL, Kim DK, Amrhein TJ. CSF-Venous Fistulas: Anatomy and Diagnostic Imaging. AJR Am J Roentgenol. 2021;217(6):1418–1429. doi: 10.2214/AJR.21.26182.

2. Callen AL, Jones LC, Timpone VM, et al. Factors Predictive of Treatment Success in CT-Guided Fibrin Occlusion of CSF-Venous Fistulas: A Multicenter Retrospective Cross-Sectional Study. American Journal of Neuroradiology. American Journal of Neuroradiology; 2023;44(11):1332–1338. doi: 10.3174/ajnr.A8005.

3. Mamlouk MD. Image-guided Epidural Blood Patching and Fibrin Glue Occlusion of Cerebrospinal Fluid Leaks and Venous Fistulas. Neuroimaging Clinics. Elsevier; 2025;35(1):143–154. doi: 10.1016/j.nic.2024.08.006.

4. Shlobin NA, Shah VN, Chin CT, Dillon WP, Tan LA. Cerebrospinal Fluid-Venous Fistulas: A Systematic Review and Examination of Individual Patient Data. Neurosurgery. 2021;88(5):931–941. doi: 10.1093/neuros/nyaa558.

5. Madhavan AA, Brinjikji W, Cutsforth-Gregory JK, et al. Myelographic Techniques for the Localization of CSF-Venous Fistulas: Updates in 2024. American Journal of Neuroradiology. American Journal of Neuroradiology; 2024;45(10):1403–1412. doi: 10.3174/ajnr.A8299

Images/Tables

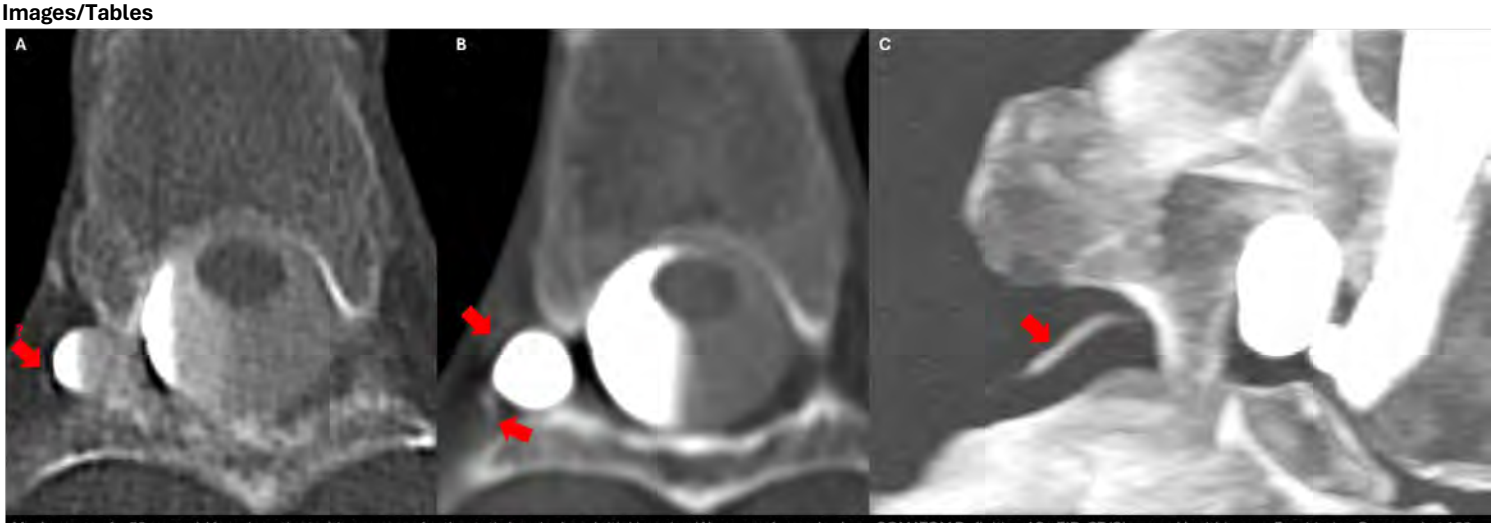

Myelograms of a 59-year-old female patient with one year of orthostatic headaches. Initial imaging (A) was performed using a SOMATOM Definition AS+ EID-CT (Siemens Healthineers, Forchheim, Germany) at 120 kVp and reconstructed with a Br38f kernel, iterative reconstruction strength of 2 and slice thickness and interval of 0.6x0.3 mm; $CTDI_{vol}$ was 28.8 mGy and time in scanner was **62 minutes**. The same-level axial image from the PCCT (B) shows a definitive CSF-venous fistula (red arrows), with the maximum intensity projection (C) showing the course of the fistula at the right T7 level. PCCT was acquired at 140 kVp and reconstructed with a Br48u kernel with an iterative reconstruction strength of 3 and slice thickness and interval of 0.2x0.1 mm. $CTDI_{vol}$ was 8.12 mGy and time in scanner was **12 minutes**.

313 Spinal Cord Ischemia Secondary to Fibrocartilaginous Embolism: A Systematic Review of reported cases

Jay Kakadiya MD[1], Dhairya A. Lakhani MD[2], Siddhartha Gaddamanugu MD[1], Lydia Marcus MD[3], Fabricio G. Goncalves MD[4], Alexander J Mullen MD[1]
[1]The University of Alabama at Birmingham, Birmingham, AL, USA. [2]West Virginia University, Morgantown, WV, USA. [3]Department of Pediatric Neurology, Children's Hospital of Alabama, Birmingham, AL, USA. [4]Department of Radiology, Children's Hospital of Alabama, Birmingham, AL, USA

Purpose

Fibrocartilaginous embolism (FCE) represents a rare, underrecognized cause of spinal cord ischemia (SCI) characterized by embolic migration of nucleus pulposus material into spinal vasculature, leading to ischemic myelopathy. Although histopathologic confirmation remains uncommon, characteristic clinical and radiologic features support a presumptive diagnosis. This systematic review aims to synthesize the demographic, clinical, imaging, and cerebrospinal fluid (CSF) characteristics of reported SCI cases attributable to FCE to enhance diagnostic recognition and inform management strategies.

Materials & Methods

A comprehensive literature search was conducted across three electronic databases (PubMed, Embase, and Scopus) to identify all published cases of SCI secondary to FCE from database inception to May 2025. All retrieved reports were screened, and duplicates removed using Covidence. Inclusion criteria encompassed original case reports and case series with sufficient clinical or radiologic evidence supporting a diagnosis of FCE-related SCI. Data were extracted on demographics, triggering events, lesion characteristics, CSF findings, and outcomes. A total of 67 reports encompassing 88 individual cases met inclusion criteria. Descriptive statistics were used to summarize findings.

Results

Among the 88 identified cases, the median age was 24 years (range: 8 months–78 years), with a mean age of 32.1 years (95% CI 27.6–36.6). A bimodal age distribution was observed, with peaks in adolescence and late adulthood. Pediatric patients (≤18 years) comprised 42% of cases, adults aged 19–54 years 35.2%, and those ≥55 years 22.8%. A female predominance was noted (56.8% vs. 43.2% male).

An identifiable trigger such as heavy lifting (13.6%), falls (6.8%), bending (5.6%), or gymnastics (4.5%) was reported in 75% of cases, whereas no preceding event was noted in 25%. Clinically, neck or back pain was the most common presenting symptom (67.1%), followed by paraplegia (46.8%), quadriparesis (22.8%), and bowel/bladder dysfunction (20.2%).

Lesions most frequently involved the thoracic spinal cord (69.3%), followed by cervical (53.4%) and lumbosacral (21.6%) segments. On MRI, the hallmark finding was linear T2-weighted hyperintensity often with diffusion restriction. Schmorl's nodes were observed in 26.7%, and intervertebral disc disease or herniation in 40.8% of cases, supporting a mechanical pathogenesis.

CSF analysis was normal in 70.4% of patients, while elevated protein was seen in 24%. Myelin basic protein and oligoclonal bands were rarely detected (4.2% and 1.4%, respectively). Histopathologic confirmation was obtained in only a minority of older reports.

Treatment strategies varied widely, with most patients receiving empirical corticosteroids and intensive rehabilitation. Anticoagulation or fibrinolytic therapy was inconsistently applied. Overall prognosis was variable but generally guarded, though select pediatric cases demonstrated substantial recovery.

Conclusion

This systematic review consolidates the summary of FCE-related SCI, encompassing 88 cases from 67 reports. FCE should be considered in patients presenting with acute myelopathy and characteristic MRI features—particularly longitudinal ventral cord T2 hyperintensity and disc pathology—in the absence of inflammatory or compressive etiologies. While diagnosis remains presumptive in most cases, early recognition and supportive management, including corticosteroids and physical rehabilitation, may improve functional outcomes. Standardized diagnostic criteria and prospective reporting are needed to clarify the natural history and optimize management of this rare vascular phenomenon.

References

1. Han, J. J., Massagli, T. L. & Jaffe, K. M. Fibrocartilaginous embolism--an uncommon cause of spinal cord infarction: a case report and review of the literature. *Arch. Phys. Med. Rehabil.* **85**, 153–157 (2004).
2. Cuello, J. P. *et al.* Acute cervical myelopathy due to presumed fibrocartilaginous embolism: a case report and systematic review of the literature. *J. Spinal Disord. Tech.* **27**, E276-281 (2014).
3. Ke, W. *et al.* Clinically suspected fibrocartilaginous embolism: a case report and literature review. *Int. J. Neurosci.* **132**, 378–383 (2022).
4. Ahluwalia, R., Hayes, L., Chandra, T. & Maugans, T. A. Pediatric fibrocartilaginous embolism inducing paralysis. *Childs Nerv. Syst. ChNS Off. J. Int. Soc. Pediatr. Neurosurg.* **36**, 441–446 (2020).

Images/Tables

Age		
	Mean Age (95% CI)	32.06 (27.58 – 36.55)
	Median Age (95% CI)	24 (17 – 31.1)
	≤18 years	37/88 (42%)
	19 - 54 years	31/88 (35.2%)
	≥ 55 ψεαρσ	20/88 (22.8%)
Gender		
	Male	38/88 (43.2%)
	Female	50/88 (56.8%)
Triggers		
	Weight/Heavy lifting	12/88 (13.6%)
	Fall down	6/88 (6.8%)
	Bending Down	5/88 (5.6%)
	Gymnastics	4/88 (4.5%)
	No Trigger	22/88 (25%)
Lesion Location		
	Thoracic spine	61/88 (69.3%)
	Cervical spine	47/88 (53.4%)
	Lumbo-sacral spine	19/88 (21.6%)
CSF findings		
	- Protein	17/71 (24%)
	- Myelin basic protein	3/71 (4.2%)
	- Oligoclonal band	1/71 (1.4%)
	Normal	50/71 (70.4%)
Schmoral's Node		
	Present	19/71 (26.7%)
	Absent	52/71 (73.3%)
Intervertebral disc disease		
	Present	29/71 (40.8%)
	Absent	42/71 (59.2%)
Presenting Complain		
	Neck/Back Pain	53/79 (67.1%)
	Quadriparesis/weakness	18/79 (22.8%)
	Paraplegia/weakness	37/79 (46.8%)
	Bowel/Bladder dysfunction	16/79 (20.2%)

Table 1: Summary findings from literature of SCI attributable to FCE

758 Photon-Counting Detector vs. Energy-Integrating Detector CT Myelography for Detecting CSF-Venous Fistulas in Spontaneous Intracranial Hypotension: Substantially Lower Radiation Dose

Soren Christensen BS[1], Peter G Kranz MD[2], Michael D Malinzak MD, PhD[2], Ajay A Madhavan MD[3], Ehsan Abadi PhD[2], Jay Willhite MD[2], Linda Gray MD[2], Daphne Zhu BS[1], Timothy J Amrhein MD[2]

[1]Duke University School of Medicine, Durham, NC, USA. [2]Duke University Medical Center, Department of Radiology, Durham, NC, USA. [3]Mayo Clinic, Department of Radiology, Rochester, MN, USA

Purpose

Spontaneous intracranial hypotension (SIH) is a debilitating condition caused by a spinal CSF leak or CSF-venous fistula (CVF). CVFs are often difficult to detect, commonly requiring repeat, multi-acquisition CT myelography (CTM), driving cumulative radiation exposure.[1] Although photon-counting detector CT myelography (PCD-CTM) improves CVF conspicuity compared with energy-integrating detector CT myelography (EID-CTM), the radiation and cancer-risk consequences of choosing PCD versus EID remain unclear.[2] The primary objective was to compare exam-level radiation dose for PCD-CTM versus EID-CTM in SIH. A secondary objective was to report modeled BEIR VII-based lifetime cancer risk.

Materials & Methods

This was a retrospective cohort study of consecutive patients meeting ICHD-3 criteria for SIH who underwent CTM for detecting the causative CVF at a single institution from March 2023 to August 2025.[3] For each exam, we recorded session dose-length product (DLP, mGy·cm; sum across acquisitions), sex, and $CTDI_{vol}$ (mGy) of the most diagnostic series when applicable. Effective dose E (mSv) was estimated as $E = k \times DLP$ with $k = 0.015$ mSv/(mGy·cm) for thoracoabdominal coverage.[4] Modeled lifetime attributable risk (LAR) for all-solid cancers (incidence, mortality) was derived from BEIR VII sex-specific 0.1-Gy coefficients.[5] Group comparisons used Welch's t-tests.

Results

We analyzed 162 exams (42 PCD, 120 EID). Mean session DLP was considerably lower for PCD: 2101 mGy·cm for PCD and 6073 mGy·cm for EID, a 3972 mGy·cm difference corresponding to 65.4% reduction; $p<0.001$. In the CVF-positive subset (33 PCD, 103 EID), diagnostic-series $CTDI_{vol}$ was 7.6 vs 36.3 mGy, corresponding to 79.2% reduction; $p<0.001$. Secondary, model-based analyses showed lower BEIR VII LAR with PCD: all-solid cancer incidence 0.34% vs 1.00% and mortality 0.17% vs 0.48% (PCD vs EID; both $p<0.001$).

Conclusion

The use of PCD in CT myelography for the detection of CVFs in SIH patients reduced session DLP by ~65% compared with EID-CTM. In CVF-positive exams, diagnostic-series $CTDI_{vol}$ was ~79% lower. Together, these results show a substantially lower patient radiation burden with PCD. BEIR VII modeling indicated lower LAR with PCD. When available and clinically appropriate, PCD should be considered, especially for patients requiring repeat imaging.

References

1. Habibi P, Verdoorn JT, Madhavan AA, et al. The Diagnostic Burden of Spontaneous Intracranial Hypotension: Imaging Volume and Specialists Involvement Prior to Diagnosis. *AJNR Am J Neuroradiol*. Published online September 18, 2025:ajnr.A9012. doi:10.3174/ajnr.A9012

2. Schwartz FR, Kranz PG, Malinzak MD, et al. Myelography Using Energy-Integrating Detector CT Versus Photon-Counting Detector CT for Detection of CSF-Venous Fistulas in Patients With Spontaneous Intracranial Hypotension. *AJR Am J Roentgenol*. 2024;222(4):e2330673. doi:10.2214/AJR.23.30673

3. Headache Classification Committee of the International Headache Society (IHS) The International Classification of Headache Disorders, 3rd edition. *Cephalalgia*. 2018;38(1):1-211. doi:10.1177/0333102417738202

4. Deak PD, Smal Y, Kalender WA. Multisection CT Protocols: Sex- and Age-specific Conversion Factors Used to Determine Effective Dose from Dose-Length Product. *Radiology*. 2010;257(1):158-166. doi:10.1148/radiol.10100047

5. *Health Risks from Exposure to Low Levels of Ionizing Radiation: BEIR VII Phase 2*. National Academies Press; 2006:11340. doi:10.17226/11340

Images/Tables

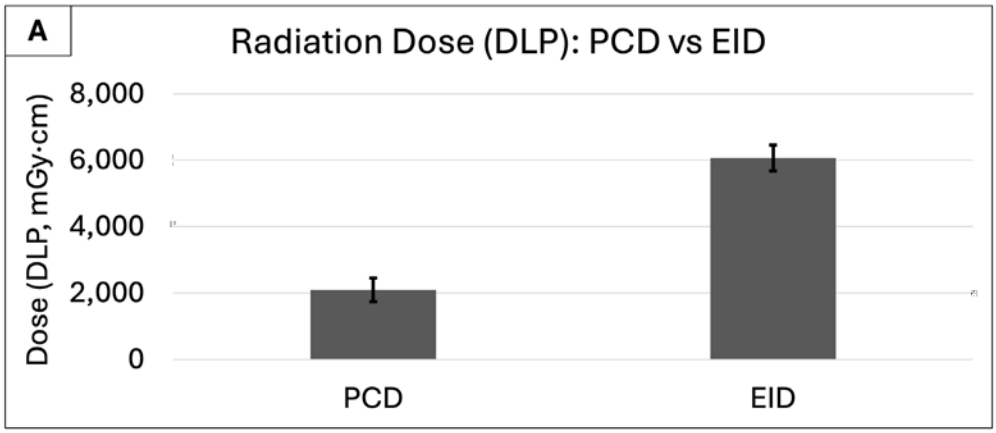

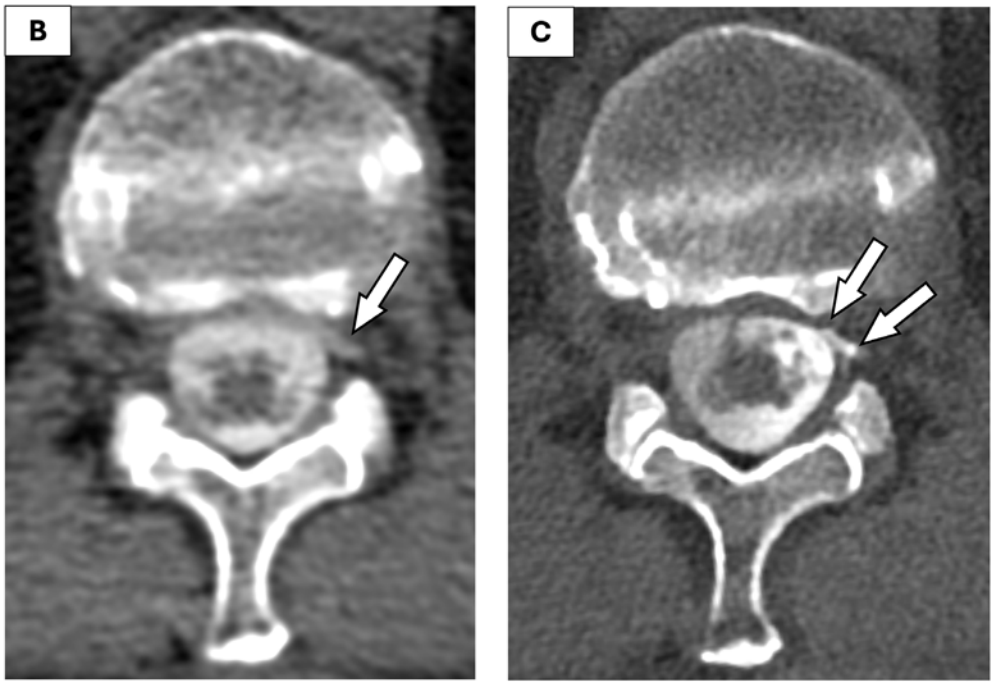

Exam-level radiation dose reduction with photon-counting detector vs energy-integrating CT myelography with representative CVF myelograms. A, Exam-level dose-length product (DLP, mGy·cm; summed across acquisitions) by detector type; bars show mean with 95% CI. PCD demonstrates ~65% lower dose than EID (21101 vs 6073 mGy·cm; n = 42 vs 120). **B,** EID-CTM: Axial image demonstrating a subtle possible left T12 CVF (white arrow). **C,** PCD-CTM: Axial image confirming a definite left T12 CVF in the same patient CVF with drainage into the internal vertebral venous plexus (white arrows).

---

991 **Synthetic STIR Sequences Show Equivalent Tissue Contrast to Standard-of-Care Acquisitions**

Thomas Campbell Arnold PhD, Long Wang MS, Ajit Shankaranarayanan PhD
Subtle Medical, Menlo Park, CA, USA

Purpose

Spine MRI protocols typically include time-consuming STIR sequences. Synthetic imaging could reduce scan times, but the performance of synthetic STIR for tissue visualization is not established.[1-3] We previously developed a deep-learning algorithm to synthesize spinal STIR images from sagittal T1-weighted (T1w) and T2-weighted (T2w) inputs.[1] This study quantitatively compares the relative tissue contrasts between standard-of-care acquired STIR and synthetic STIR images.

Materials & Methods

We retrospectively analyzed sagittal 2D T1w, 2D T2w, and 2D STIR spine MRI data from 80 participants. Four regions-of-interest (ROIs) were manually drawn on acquired STIR images in five normal-appearing tissue types (**Figure 1A**: vertebrae, disc, spinal cord, CSF, fat). Synthetic STIR sequences were generated using our deep-learning algorithm and coregistered to the acquired STIR images. We extracted normalized mean intensity values from all ROIs to calculate relative tissue contrasts. We then assessed cosine similarity between contrast measures and evaluated for measurement bias using Bland-Altman plots.

Results

Analysis of 80 participants demonstrated similar tissue contrast between acquired STIR and synthetic STIR images with cosine similarity values for all tissue pairs ranging from 0.81-0.96 (with 1 being perfect similarity) (**Figure 1B**). Bland-Altman analysis revealed no significant bias between synthetic and acquired STIR sequences across all five tissues (Figure 1C), with 95% confidence intervals well-centered around zero (Bone: -0.011 [-0.087,0.065], Disc: -0.001 [-0.100,0.098], CSF: 0.015 [-0.097,0.127], Spinal Cord: 0.025 [-0.074,0.124], Fat: 0.042 [-0.065,0.148]).

Conclusion

Our deep-learning model generates synthetic STIR images that preserve the quantitative appearance and contrast of individual tissue types. The lack of significant bias in tissue contrast suggests synthetic STIR sequences are an acceptable approximation of acquired sequences. This approach could potentially accelerate spine MRI protocols by replacing the time-consuming STIR acquisition, thereby increasing scanner throughput.

References

1. Tanenbaum, L. N., et al. "Deep Learning–Generated Synthetic MR Imaging STIR Spine Images Are Superior in Image Quality and Diagnostically Equivalent to Conventional STIR: A Multicenter, Multireader Trial." American Journal of Neuroradiology 44.8 (2023): 987-993. DOI: 10.3174/ajnr.A7920
2. Kim, Sewon, et al. "Deep-learned short tau inversion recovery imaging using multi-contrast MR images." Magnetic Resonance in Medicine 84.6 (2020): 2994-3008. DOI: 10.1002/mrm.28327
3. Haubold, Johannes, et al. "Generating virtual short tau inversion recovery (STIR) images from T1-and T2-weighted images using a conditional generative adversarial network in spine imaging." Diagnostics 11.9 (2021): 1542. DOI: 10.3390/diagnostics11091542

Images/Tables

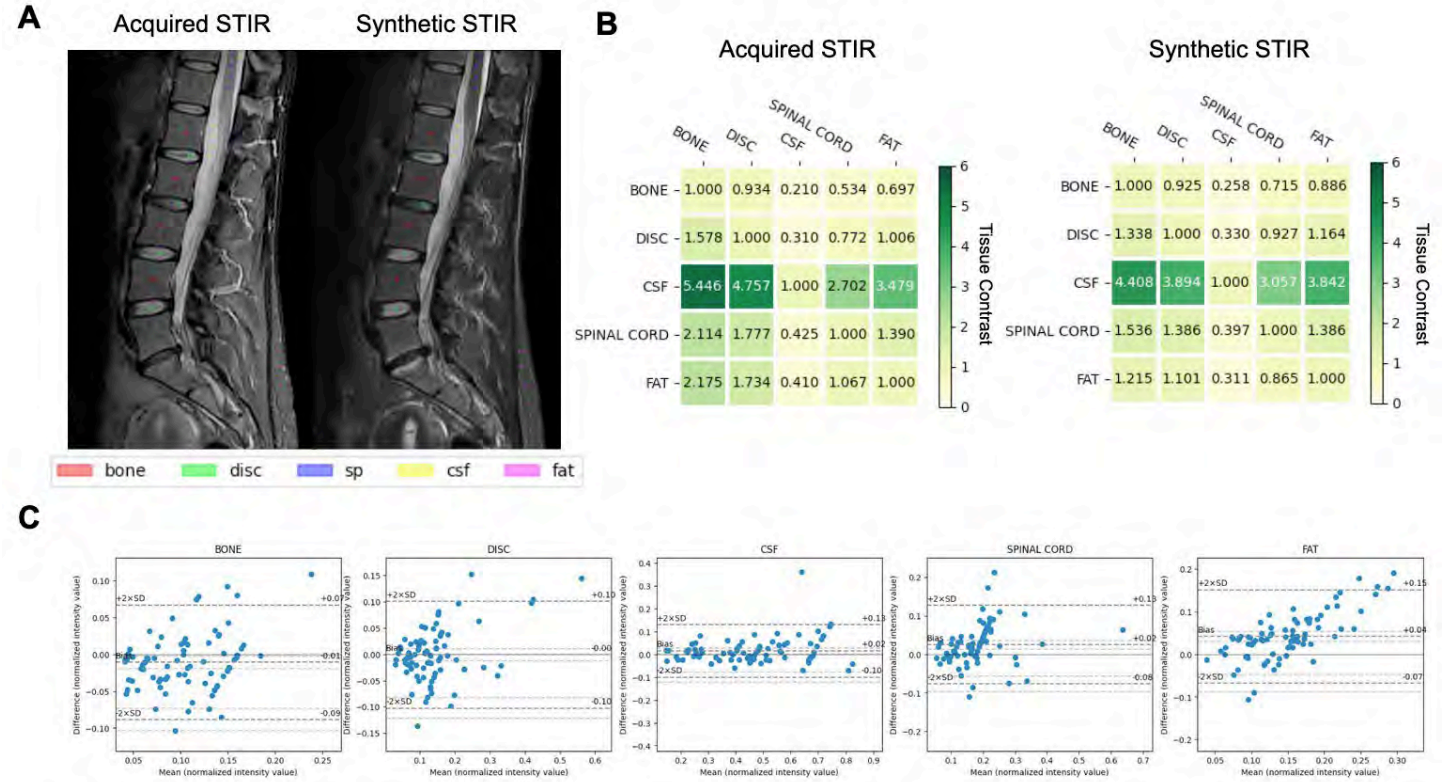

Figure 1. A) Examples of tissue segmentations on acquired STIR (left) and coregistered synthetic STIR (right) sequences, with four separate regions-of-interest drawn in each of five tissue types(bone, disc, spinal cord, CSF, and posterior fat. **B)** A comparison of tissue contrasts between acquired STIR and synthetic STIR sequences. **C)** Bland-Altman plots show no bias when comparing tissue measurements made on acquired versus synthetic STIR sequences.

---

752 **Clinical Validation of Deep Learning Accelerated Sagittal Cervical Spine MRI with VORTEX acquisition: A Prospective Multi-Rater Comparison**

Atefeh Zeinoddini MD[1], Thomas Dowling MD[1], Samuel Cartmell MD[1], Min Lang MD[1], Eugene Milshteyn PHD[2], Ajeetkumar Gaddipati[3], Anand Venkatachari[4], Mary Thomas[2], Rory Cochran[1], Susie Huang MD-PHD[1], Ivan Jambor MD-PHD[1]

[1]Massachusetts General Hospital, Boston, MA, USA. [2]GE HealthCare, Boston, MA, USA. [3]GE HealthCare, Waukesha, WI, USA. [4]GE HealthCare, Rochester, MN, USA

Purpose

Deep learning (DL) reconstruction combined with novel acquisition methods holds promise for a significant reduction in MRI scan time, with the potential for minimizing motion-related artifacts due to shorter scan time [1]. However, evaluation of the impact of these new acquisition and reconstruction methods on diagnostic image quality requires rigorous, clinically-oriented validation. The aim of this study was to provide a comprehensive, multi-rater comparison of a novel acquisition technique for fast-spin echo imaging (FSE), VORTEX (VERSE SAR reduction, Optimized RF waveform, Refocus flip angle modulation, Tuned Hyper Echoes, External volume suppression, X-factor spin efficiency), with standard cervical spine MRI.

Materials & Methods

Thirty-one consecutive patients requiring clinical cervical spine MRI were included. Sagittal T1-weighted and T2-weighted images were acquired using three different sequences (scan time): standard FSE with cartesian read-out (141s for T1; 115s for T2), VORTEX with cartesian read-out (141 for T1; 53s for T2) and VORTEX with radial (PROPELLER) read-out (65s for T1; 58s for T2). Sagittal STIR images were acquired (scan time) with VORTEX with cartesian read-out (172s) and VORTEX with radial (PROPELLER) read-out (73s). A commercially available DL reconstruction algorithm (AIRTM Recon DL, GE HealthCare, Waukesha, WI), which is based on a Convolutional Neural Network (CNN) trained to remove ringing, reduce noise, and increase sharpness, was applied to all acquisitions [2, 3]. Five board-certified radiologists independently evaluated all sequences for four metrics (Image Quality, Noise, Sharpness, and Artifacts) on a 5-point scale (1=non-diagnostic, 5=excellent). Inter-rater reliability (IRR) was quantified using intraclass correlation coefficients (ICC). Diagnostic performance was analyzed using Cumulative Link Mixed Models (CLMM).

Results

IRR for average-rater measures was excellent across all metrics (ICC[2,k]=0.94 for Image Quality, ICC[2,k]=0.92 for Artifacts, ICC[2,k]=0.85 for Noise, and ICC[2,k]=0.83 for Sharpness).

Both sagittal T2-weighted VORTEX with cartesian read-out (54% scan time reduction) and PROPELLER read-out (50% scan time reduction) significantly outperformed standard FSE with cartesian read-out across all four metrics (all $p<0.01$). The T2-weighted VORTEX with PROPELLER read-out showed significantly superior image quality and fewer artifacts compared to VORTEX with cartesian read-out ($p<0.05$).

Sagittal T1-weighted VORTEX with cartesian read-out (60% scan time reduction) showed comparable results to the FSE with cartesian read-out for overall image quality, sharpness, and artifacts ($p>0.12$), but offered significantly improved noise ratings (OR=3.21, $p<0.001$). However, sagittal T1-weigthted VORTEX with PROPELLER read-out (54% scan time reduction) resulted in significant degradation across multiple metrics, including Image Quality (OR=0.17, $p<0.001$), Sharpness (OR=0.13, $p<0.001$), and Noise (OR=0.17, $p<0.001$).

No statistically significant difference was found between the sagittal STIR VORTEX with cartesian read-out versus VORTEX with PROPELLER read-out (all $p>0.24$).

Conclusion

Our study demonstrates that accelerated acquisition of sagittal cervical spine imaging using VORTEX can outperform standard FSE acquisition when DL reconstruction is applied. The impact of the read-out method was variable across sagittal T2-, T1- and STIR images, potentially stressing the need for tailored acquisition methods for different sequences. Our findings underscore the need for selective, evidence-based deployment rather than universal application across all sequences.

References

1. Ichikawa H, Yasaka K, Akai H, et al. Clinical impact of deep learning reconstruction in MRI. Radiographics 2022;42:E152-53. DOI: https://doi.org/10.1148/rg.220133

2. Ahn SJ, Kim GU, Kim JH, et al. Deep learning-based reconstruction of highly accelerated 3D MRI. arXiv 2022 Mar 9. [Preprint] DOI: https://doi.org/10.48550/arXiv.2203.04674

3. Desai, A. D., Gunel, B., Ozturkler, B. M., Beg, H., Vasanawala, S., Hargreaves, B. A., ... & Chaudhari, A. S. (2021). VORTEX: Physics-Driven Data Augmentations Using Consistency Training for Robust Accelerated MRI Reconstruction. *arXiv preprint arXiv:2111.02549*.

Images/Tables

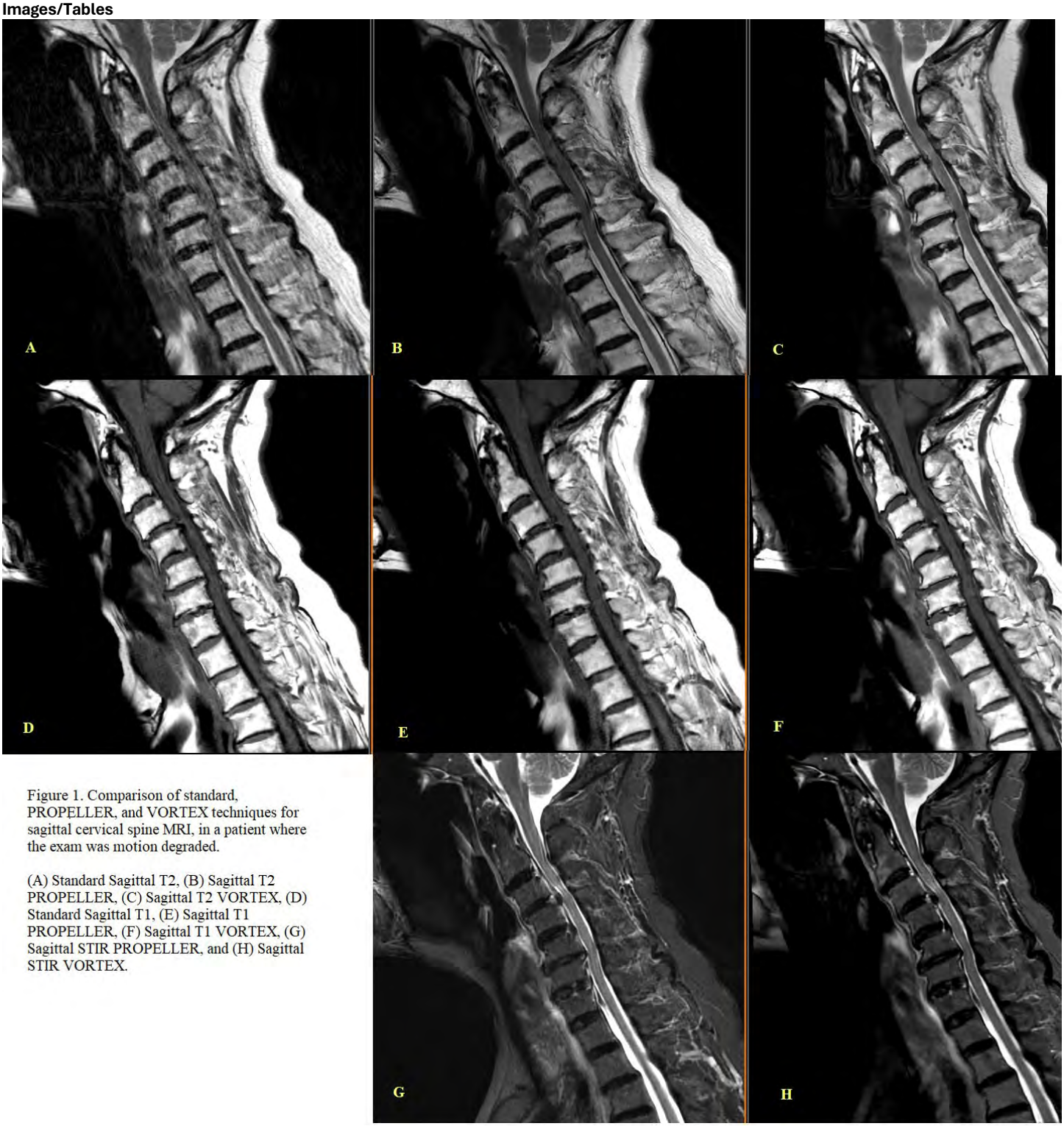

Figure 1. Comparison of standard, PROPELLER, and VORTEX techniques for sagittal cervical spine MRI, in a patient where the exam was motion degraded.

(A) Standard Sagittal T2, (B) Sagittal T2 PROPELLER, (C) Sagittal T2 VORTEX, (D) Standard Sagittal T1, (E) Sagittal T1 PROPELLER, (F) Sagittal T1 VORTEX, (G) Sagittal STIR PROPELLER, and (H) Sagittal STIR VORTEX.

1116 Bone-RADS MRI Algorithm has Excellent Negative Predictive Value for Spine Lesions with "Fair" Inter-Reader Reliability

Emil J Barkovich MD[1], Will A Mehan MD[2], Karen Buch MD[2]

[1]UC San Francisco, San Francisco, CA, USA. [2]Massachusetts General Hospital, Boston, MA, USA

Purpose

To evaluate the Society of Skeletal Radiology Bone-RADS [1] MRI algorithm performance and inter-reader reliability for challenging spine lesions.

Materials & Methods

In this IRB-approved retrospective study, we reviewed 538 exams with spine lesions reported as "indeterminate." Studies were excluded if targeted MRI protocols lacked pre-contrast T1 and T2-weighted images or if there was known history of spine metastases.

Lesion follow-up outcomes were collected from our multi-institution PACS and EMR. Subsequent imaging was reviewed including non-spine MR and CT studies performed for other indications. Lesions were categorized as: stable, no follow-up, incomplete follow-up, typically benign or degenerative on CT or follow-up MR or malignant. Minimum interval of 24 months was required for stability per Bone-RADS [1], incomplete follow-up was defined as 2-24 months and <2 months was considered no follow-up. Lesions were also classified as stable if a CT performed >2 years from the initial MRI

demonstrated no change or no detectable abnormality. Malignancy history was categorized as (1) none known, (2) active or prior malignancy without known metastatic disease and (3) known metastatic disease.
Two attending neuroradiologists independently reviewed the images and used the Bone-RADS MRI algorithm to assign each lesion a score of 1 (likely benign), 2/3 (incompletely assessed or indeterminate) or 4 (suspicious). Of note, they did not apply Bone-RADS clinical criteria and cases with multiple lesions were not excluded. The radiologists also recorded whether they would recommend imaging follow-up separate from Bone-RADS.

Results

282 spine lesions met inclusion criteria of which 59% had subsequent diagnosis or imaging follow-up of ≥2 months. 66% of patients with follow-up had no malignancy history, 28% had a non-bone primary malignancy without metastatic disease and 9% had metastatic disease without bone involvement. There were 4 cases of new bone metastases and two cases of multiple myeloma. The negative predictive value of at least one Bone-RADS 1 score was 100% (n = 84). The positive predictive value (PPV) for at least one score of 4 was 25%. PPV for consensus indeterminate 2/3 lesions was 5.1%; when clinical Bone-RADS criteria were applied this dropped to 0%. Cohen's kappa test for inter-reader reliability was 0.24 for Bone-RADS and 0.22 for follow-up recommendations.

Conclusion

A Bone-RADS 1 score showed excellent negative predictive value for spine lesions reported as "indeterminate." Lesions scored as 2/3 had low rate of malignancy which dropped to 0% when exclusionary clinical criteria were applied. Bone-RADS MRI algorithm has only "fair" inter-reader reliability when applied to challenging cases. Given low inter-reader reliability and the increased prevalence of both benign and metastatic vertebral lesions relative to primary bone tumors, a spine specific algorithm would be helpful.

References

1. Chang CY, Garner HW, Ahlawat S, Amini B, Bucknor MD, Flug JA, Khodarahmi I, Mulligan ME, Peterson JJ, Riley GM, Samim M, Lozano-Calderon SA, Wu JS (2022) Society of Skeletal Radiology- white paper. Guidelines for the diagnostic management of incidental solitary bone lesions on CT and MRI in adults: bone reporting and data system (Bone-RADS). Skeletal Radiol 51:1743-1764.

---

263 Examining the Current Image-Guided Biopsy Paradigm for Suspected Spondylodiscitis

Frederick W. Ott MD[1], Caleb D. Hoover MD, MS[1], Jordan A. Helmer MD[2], Tanner L. Nordseth BS[2], Kevin Ehlers DO[1], Russell Pluhm DO[1], Kerem Ozturk MD[1], Mark Folkertsma MD[1], Jeffrey B. Rykken MD[1]
[1]University of Minnesota Department of Radiology, Minneapolis, MN, USA. [2]University of Minnesota Medical School, Minneapolis, MN, USA

Purpose

This study aimed to identify factors associated with successful pathogen isolation via percutaneous image-guided biopsy (IGB) in suspected spondylodiscitis, compare diagnostic value between fluoroscopy- and CT-guided IGB, and assess the influence of IGB results on patient treatment and outcomes.

Materials & Methods

This retrospective study examined 81 IGBs (62 CT-guided, 19 fluoroscopy-guided) performed for suspected spondylodiscitis between March 2014 and February 2025. Retrospective diagnosis was determined using biopsy microbiology, clinical criteria, and radiologic findings. Primary analyses included IGB culture yield, sensitivity, specificity, and diagnostic accuracy. Subgroup analyses included biopsy modality and prior antibiotic administration.

Results

Overall culture yield was 37.0%, with sensitivity of 44.4% and specificity of 88.9%. Yield among patients receiving antibiotics before biopsy was 36.4%, compared to 37.8% in those who did not (p=0.890). CT-guided IGB had a yield of 38.7%, compared to 31.6% in fluoroscopic IGB (p=0.586). Excluding tuberculosis cases, 99% of cultured organisms were susceptible to the empiric antibiotic regimen.

Conclusion

In suspected spondylodiscitis, IGB demonstrates low sensitivity and rarely alters patient care. Although its high specificity may help narrow antibiotics in positive cultures, the infrequency of positive cultures suggests empiric therapy should not await biopsy when there is strong clinical or MRI evidence of infection. Furthermore, culture yield was not significantly decreased by prior antibiotic administration. IGB may be best reserved for patients without clinical improvement or with MRI evidence of progression after empiric treatment. These findings suggest reevaluation of current Infectious Diseases Society of America guidelines for IGB is warranted.

References

1. Gouliouris T, Aliyu SH, Brown NM. Spondylodiscitis: update on diagnosis and management. *J Antimicrob Chemother*. 2010;65 Suppl 3:iii11-iii24. doi:10.1093/jac/dkq303
2. Mylona E, Samarkos M, Kakalou E, Fanourgiakis P, Skoutelis A. Pyogenic vertebral osteomyelitis: a systematic review of clinical characteristics. *Semin Arthritis Rheum*. 2009;39(1):10-17. doi:10.1016/j.semarthrit.2008.03.002
3. Michel SC, Pfirrmann CW, Boos N, Hodler J. CT-guided core biopsy of subchondral bone and intervertebral space in suspected spondylodiskitis. *AJR Am J Roentgenol*. 2006;186(4):977-980. doi:10.2214/AJR.05.0109
4. Cheung WY, Luk KD. Pyogenic spondylitis. *Int Orthop*. 2012;36(2):397-404. doi:10.1007/s00264-011-1384-6
5. Prodi E, Grassi R, Iacobellis F, Cianfoni A. Imaging in Spondylodiskitis. *Magn Reson Imaging Clin N Am*. 2016;24(3):581-600. doi:10.1016/j.mric.2016.04.005

Images/Tables

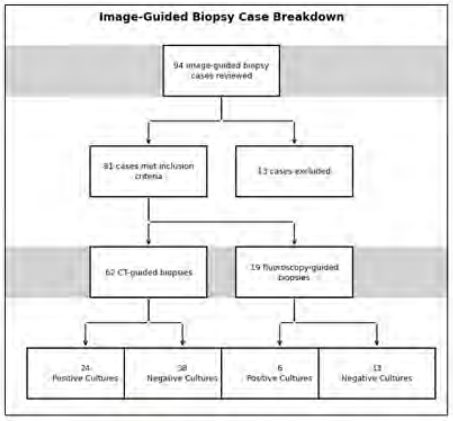

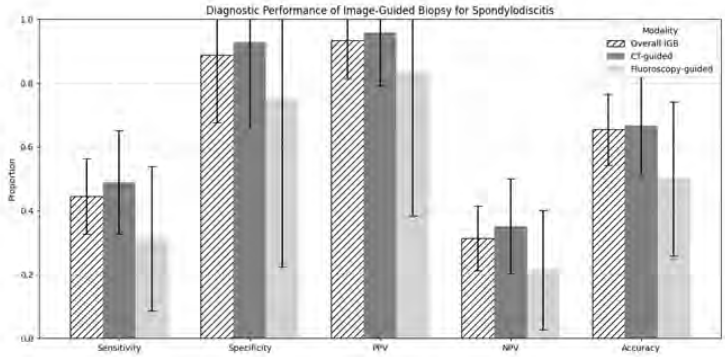

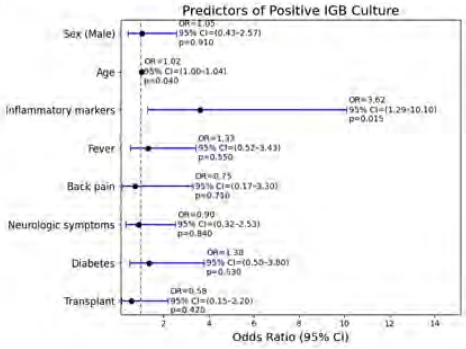

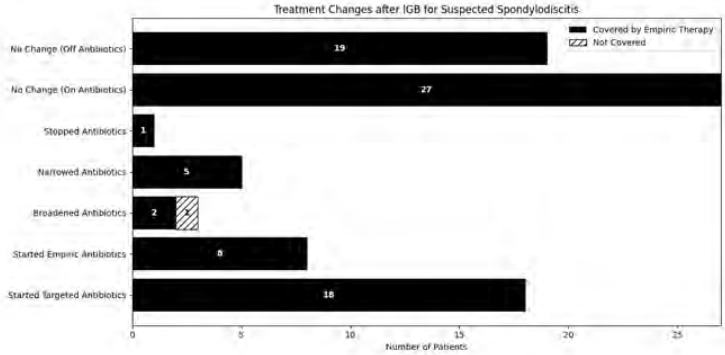

1101 Long-term effectiveness and feasibility of CT-guided cryoablation as a novel treatment option for symptomatic lumbar synovial cysts

Manraj K.S. Heran MD FRCPC[1], Marlise P dos Santos MD FRCPC MSc MPH[2], Emmanuel K.Y. Jackson MD[1], Nerses Nersesyan MD[2], Michael G Craig MD FRCSC[1], Charles G Fisher MD FRCSC[1]

[1]University of British Columbia, Vancouver, BC, Canada. [2]University of Ottawa, Ottawa, ON, Canada

Purpose

To present a case series with a long-term follow-up of CT-guided cryoablation procedure for the minimally invasive treatment of symptomatic lumbar facet synovial cyst with a mean follow-up of 38 months (range, 15–55).

Materials & Methods

We present a retrospective, uncontrolled clinical case series from a single institution on patients treated with CT-guided cryoablation for symptomatic lumbar facet joint synovial cysts that are refractory to or not suitable for imaging-guided rupture procedures. In two cases, patients underwent cryoablation and cyst rupture within 2 weeks. Outcome measures included post-procedural radiologic studies and clinical examinations, which continued up to the end of the follow-up period. Selected patients underwent post-procedural clinical and imaging studies, including CT and MRI, which were reviewed up to the conclusion of follow-up. All patients were clinically assessed and evaluated by the spine surgery team. Technical success was the complete resolution of the patients' symptoms.

Results

We treated three females and three males (mean age 64 years). Four patients had cysts located at L4–L5, and the remaining two at L5–S1. We used two cryoprobes in five patients, and three in one. Clinical and/or technical success was documented in all cases (mean follow-up, 38 months [range,15–55]). We found no major complications related to the cryoablation itself.

Conclusion

Our initial experience with CT-guided cryoablation for symptomatic lumbar facet synovial cysts describes a less invasive alternative treatment option to surgery for the management of such lesions. Our long-term outcome experience showed low recurrence and complication rates. CT-guided cryoablation may be a reasonable alternative approach for treating lumbar synovial cysts that are refractory to or contraindicated for rupture procedures and where surgical management is unfeasible.

References

1. Heran MKS, Jackson EKY, Nersesyan N, et al. Long-term effectiveness and feasibility of CT-guided cryoablation as a novel treatment option for symptomatic lumbar synovial cysts. Skeletal Radiol. 2025 May;54(5):1101-1108. doi: 10.1007/s00256-024-04808-y.

Images/Tables

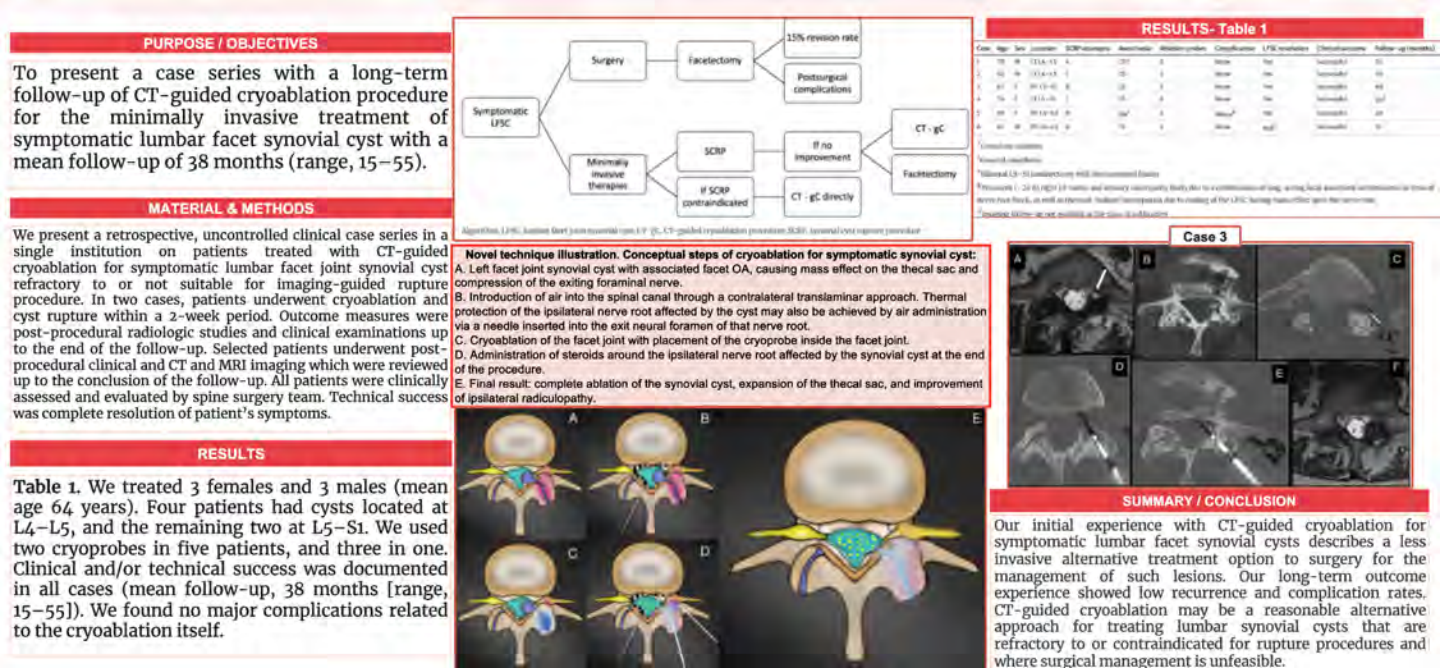

798 Deep learning enhancement in 3D fast spin-echo with fat and blood suppression for brachial plexus imaging

Daehyun Yoon Ph.D.[1], David D. Shin[2], Nathan T. Rober[3], Cynthia T. Chin M.D.[1], Vinil N. Shah M.D.[1]
[1]University of California San Francisco, San Francisco, California, USA. [2]GE Healthcare, Menlo Park, California, USA. [3]GE Healthcare, Waukesha, Wisconsin, USA

Purpose

We have recently presented a 3D nerve imaging fast spin-echo (FSE) sequence with fast triple-echo Dixon fat-water separation and blood flow signal suppression by motion-sensitized driven-equilibrium preparation[1] for robust brachial plexus imaging. Fast triple-echo Dixon facilitates reliable fat-water separation despite strong off-resonance in the brachial plexus without increasing scan time. However, it requires a high readout bandwidth (±200 kHz), which, along with 1mm isotropic resolution, reduces the signal-to-noise ratio (SNR) to the acceptable minimum. A prototype of the deep learning (DL) reconstruction algorithm (AIR™ Recon DL, GE Healthcare)[2] was released to improve the SNR and sharpness for our sequence. In this study, we evaluated the DL enhancement in the image qualities of our 3D sequence for the brachial plexus.

Materials & Methods

We retrieved raw data of our 3D coronal nerve imaging FSE sequence from 21 clinical 3T MRI exams of the brachial plexus in our clinics. For each case, we generated four sets of raw data by retrospectively truncating 0%, 10%, 20%, and 30% of slice-directional high-frequency raw data, corresponding to 0%, 10%, 20%, and 30% scan time acceleration, respectively. However, this also causes proportional SNR reduction and slice-directional blurring with standard non-DL reconstruction. We conducted two evaluation studies as follows.

Study A: Evaluation of non-DL and DL reconstruction images.

Study B: Evaluation of DL-reconstruction images with 0%, 10%, 20%, and 30% raw data truncation.

For Study A, two radiologists graded the water images for apparent SNR, nerve visualization, diagnostic confidence, and overall image quality on a 5-point scale (1 = worst, 5 = best). For Study B, they graded the water images for apparent SNR, nerve visualization of the original coronal images, and nerve visualization of the axial reformats on the same scale. We used the axial reformat because slice-directional blurring due to data truncation can be more apparent on the axial reformat. We conducted the two-sided Wilcoxon signed-rank test to compare grades in Study A) and the one-way repeated measures ANOVA to compare grades in Study B) with a significance level of 5%.

Results

Tables 1 and 2 show the grades from Study A and Study B. Images with DL reconstruction achieved significantly higher grades in all categories (p-value < 0.01). It suggests that DL reconstruction contributed to improved nerve visibility with a SNR boost and image sharpening, leading to increased diagnostic confidence. There was no significant difference between DL-reconstructed images with different rates of data truncation in any of the compared categories. It suggests that the DL construction also helped alleviate the expected SNR drop and blurring artifacts due to data truncation. Figure 1 shows superior visualization of supraclavicular and infraclavicular nerves (arrows) in the DL-reconstructed image (1A) compared to the original image (1B). Figure 2 shows comparable reformat image quality between DL-reconstructed images with different data truncation rates (2A: 0%, 2B: 10%, 2C: 20%, 2D: 30%).

Conclusion

In 21 brachial plexus MRI exams, our DL-reconstruction algorithm enhanced the image qualities of our 3D nerve imaging FSE sequence and mitigated significant SNR decrease and blurring due to data truncation.

References

1. Yoon D, Antil N, Biswal S, et al. A robust 3D fast spin-echo technique for fast examination of the brachial plexus. *Skeletal Radiol* 2022;51:1865–1872
2. Lebel R. Performance characterization of a novel deep learning-based MR image reconstruction pipeline. 2020. http://arxiv.org/abs/2008.06559

Images/Tables

Table 1.	Apparent SNR	Nerve visualization	Diagnostic confidence	Overall image quality
Non-DL reconstruction	2.8 ± 0.8	3.5 ± 0.8	3.4 ± 0.8	3.3 ± 0.8
DL reconstruction	3.5 ± 0.8	4.0 ± 0.7	3.9 ± 0.7	3.9 ± 0.7
p-value	< 0.01	< 0.01	< 0.01	< 0.01

Table 2.	Apparent SNR	Nerve visualization on the original coronal plane	Nerve visualization on the axial reformat
0% slice-directional high-frequency raw data truncation	3.52 ± 0.76	4.0 ± 0.69	4.02 ± 0.64
10% slice-directional high-frequency raw data truncation	3.52 ± 0.76	3.98 ± 0.67	3.98 ± 0.67
20% slice-directional high-frequency raw data truncation	3.5 ± 0.76	3.98 ± 0.67	3.98 ± 0.67
30% slice-directional high-frequency raw data truncation	3.48 ± 0.79	3.98 ± 0.67	4.0 ± 0.65
p-value	0.47	0.8	0.19

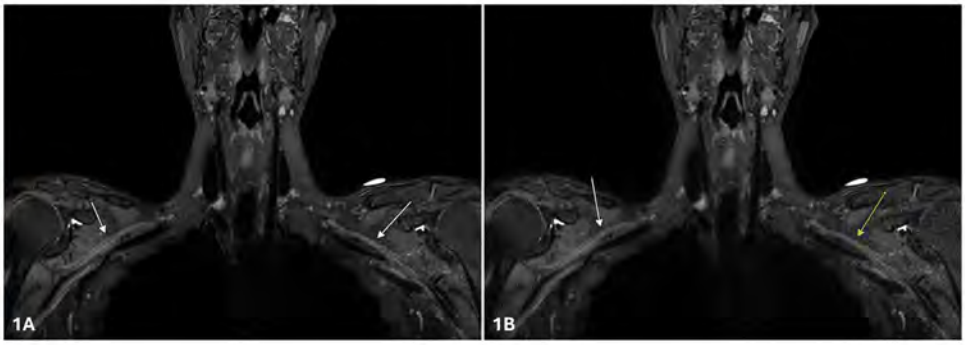

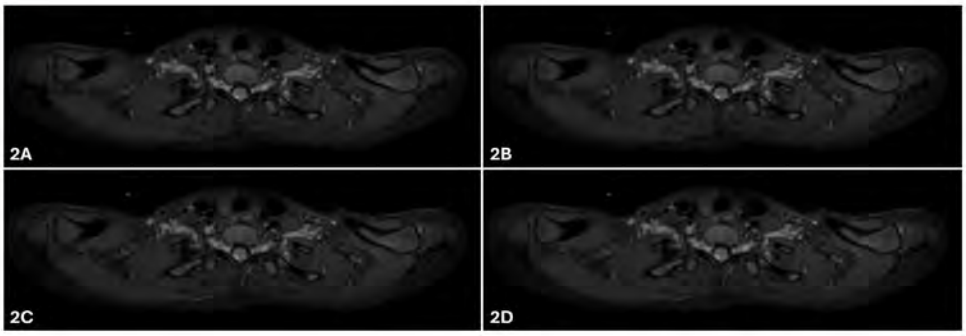

Scientific Abstract Power Pitches & Luminary Speaker: Translational Neuroimaging: Innovations in Vascular, Traumatic, and Degenerative Pathologies

11:00am - 12:00pm Tuesday, 19th May, 2026

666 Hepatic Fat Is Linked with Neuroinflammation, Reduced Cerebral Blood Flow, and Cortical Atrophy: Multimodal Advanced Neuroimaging Insights

Soheil Mohammadi[1], Mahsa Dolatshahi[1], Claude B. Sirlin[2], Paul K. Commean[1], Farzaneh Rahmani[1], LaKisha Lloyd[1], Mahshid Naghashzadeh[1], Mobina Amanollahi[1], Mona Mirbeyk[1], Bettina Mittendorfer[3], Tammie L.S. Benzinger[1], Joseph E. Ippolito[1], John C. Morris[4], Cyrus A. Raji[1]

[1]Mallinckrodt Institute of Radiology, Washington University in St. Louis, St. Louis, MO, USA. [2]Liver Imaging Group, Department of Radiology, University of California-San Diego, San Diego, CA, USA. [3]Departments of Medicine and Nutrition & Exercise Physiology, University of Missouri, School of Medicine,, Columbia, MO, USA. [4]Department of Neurology, Washington University in St. Louis, St. Louis, MO, USA

Purpose

Hepatic fat as a measure of body composition has been associated with increased systemic inflammation and cognitive decline, while neurodegeneration in AD is partly driven by reduced cerebral perfusion. This study investigates the relationship between MRI-derived Proton Density Fat Fraction (PDFF) and brain microstructure, as assessed by Diffusion Basis Spectrum Imaging (DBSI), brain structure, including volumetric and cortical thickness measures, and brain perfusion assessed using arterial spin labeling (ASL) in cognitively healthy midlife adults.

Materials & Methods

A total of 96 cognitively normal middle-aged participants (average age: 49.83 years, female: 65.6%, obesity: 54.2%, BMI: 32.43 kg/m2) underwent both brain and abdominal MRI scans, along with metabolic assessments (Table 1). Hepatic PDFF maps were generated from liver chemical shift encoded MR images, followed by segmentation using a CNN model. DBSI maps, including fractional anisotropy (overall integrity), axial diffusivity (axonal injury), radial diffusivity (myelin loss), restricted fraction (inflammation and cellularity), hindered fraction (extracellular edema), and fiber fraction (axonal density), were computed using an in-house MATLAB script after preprocessing (eddy current and motion correction). Voxel-wise analyses were performed using the TBSS pipeline[1], contrasting PDFF with age and sex as covariates. Automatic segmentation of cortical and subcortical brain regions was performed using FreeSurfer 7.1.1, accompanied by visual inspection, quality control, and manual adjustments as needed. Cerebral blood flow was measured using 3D pseudo-continuous arterial spin labeling (pCASL) with a 1.5 s labeling duration and 2.025 s post-labeling delay. Absolute CBF (aCBF) maps were generated in SPM12 (MATLAB) by subtracting label and control images, dividing by the M0 image, and preprocessing (co-registration, normalization to MNI space, skull stripping, and 6 mm smoothing). A multiple linear regression model was implemented to study the link between PDFF and volumetric and cortical thickness measurements in the regions of interest of AD, as well as aCBF in the whole brain and region specific aCBF, with age and sex as covariates. Analyses were corrected for multiple comparisons using false discovery rate (FDR) adjustment method.

Results

TBSS analysis revealed significant positive associations between PDFF and restricted fraction in widespread regions the corpus callosum, bilateral anterior and superior corona radiata, posterior limb of the internal capsule, and superior longitudinal fasciculus, cingulum bundle, inferior fronto-occipital fasciculus (IFOF), forceps minor and forceps major (Figure 1). Higher PDFF was linked with lower left hemisphere temporal pole thickness (B = -8.60, p = 0.007) and lower aCBF in the whole brain and multiple regions of interest, including bilateral amygdala, hippocampus, parahippocampal gyrus, calcarine cortex, middle temporal gyrus, posterior cingulate, and precuneus (Table 2).

Conclusion

This study demonstrates that increased liver fat is associated with elevated cellularity in white matter, suggesting early, potentially reversible neuroinflammatory changes in the absence of axonal injury or demyelination. Moreover, the observed widespread reduction in cerebral blood flow and decreased temporal pole thickness further support a mechanistic link between hepatic fat accumulation and AD–related vulnerability in midlife. Together, these results underscore the potential of PDFF as an opportunistic, non-invasive screening biomarker for identifying individuals at risk for AD during a critical window for intervention.

References

1. Bach M, Laun FB, Leemans A, et al. Methodological considerations on tract-based spatial statistics (TBSS). *Neuroimage*. 2014; **100**: 358-369.

Images/Tables

Table 1. Characteristics of study participants
Participants were divided into Low and High PDFF groups using the median PDFF value as the cutoff.

		Overall	Low PDFF	High PDFF	P-value
N		96	48	48	
Age (mean (SD))		49.83 (6.41)	49.21 (6.11)	50.46 (6.69)	0.3
Sex (%)	Male	33 (34.4)	12 (25.0)	21 (43.8)	0.08
	Female	63 (65.6)	36 (75.0)	27 (56.2)	
Race (%)	White	62 (64.6)	33 (68.8)	29 (60.4)	0.1
	African America n	22 (22.9)	10 (20.8)	12 (25.0)	
	Asian	3 (3.1)	1 (2.1)	2 (4.2)	
	Other	9 (9.4)	4 (8.3)	5 (10.4)	
Years of education (mean (SD))		15.52 (2.28)	15.71 (2.15)	15.32 (2.43)	0.4
Left handedness (%)		4 (4.2)	1 (2.1)	3 (6.2)	0.08
Mean PDFF (mean (SD))		6.53 (6.48)	2.34 (1.34)	10.73 (6.87)	**<0.001**
BMI (mean (SD))		32.43 (7.54)	29.17 (6.46)	35.99 (7.06)	**<0.001**
Obesity (%)		52 (54.2)	18 (37.5)	34 (70.8)	**<0.001**
SAT (mean (SD))		2958.54 (1366.61)	2580.72 (1279.19)	3344.39 (1357.74)	**0.006**
		1063.19		1412.68	
VAT (mean (SD))		(600.49)	720.99 (373.68)	(589.23)	**<0.001**
VAT to SAT ratio (mean (SD))		0.40 (0.26)	0.32 (0.16)	0.49 (0.30)	**0.001**
Waist circumference (cm) (mean (SD))		104.08 (83.67)	86.60 (11.81)	122.52 (116.86)	**0.03**
Cholesterol (mean (SD))		184.15 (35.92)	181.87 (36.16)	186.71 (35.92)	0.5
Triglycerides (mean (SD))		105.52 (54.58)	79.29 (31.51)	132.89 (60.16)	**<0.001**
HDL (mean (SD))		104.00 (19.22)	98.93 (15.79)	109.30 (21.14)	**0.008**
LDL (mean (SD))		107.24 (31.41)	102.98 (30.29)	112.07 (32.31)	**0.1**
Non-HDL cholesterol (mean (SD))		127.49 (34.52)	117.96 (31.81)	138.20 (34.66)	**0.006**
Chol to HDL ratio (mean (SD))		3.48 (1.19)	3.00 (0.92)	4.02 (1.23)	**<0.001**
HbA1c (mean (SD))		5.69 (0.72)	5.47 (0.53)	5.94 (0.82)	**0.002**
HOMAJR (mean (SD))		1.57 (1.16)	1.05 (0.70)	2.12 (1.30)	**<0.001**
MoCA (mean (SD))		25.86 (3.30)	26.26 (2.95)	25.30 (3.72)	0.2
CRP (mean (SD))		4.26 (5.83)	2.92 (3.12)	5.63 (7.49)	0.05
IL_6 (mean (SD))		3.34 (10.50)	4.35 (14.80)	2.34 (1.55)	0.4
IL_10 (mean (SD))		2.40 (2.66)	2.13 (2.29)	2.71 (3.03)	0.3
TNF alpha (mean (SD))		2.46 (1.44)	2.24 (1.14)	2.70 (1.71)	0.2
Amyloid positivity (%)		5 (5.2)	3 (6.2)	2 (4.2)	0.3
Centiloids (mean (SD))		-1.61 (8.94)	-2.43 (8.70)	-0.64 (9.25)	0.3

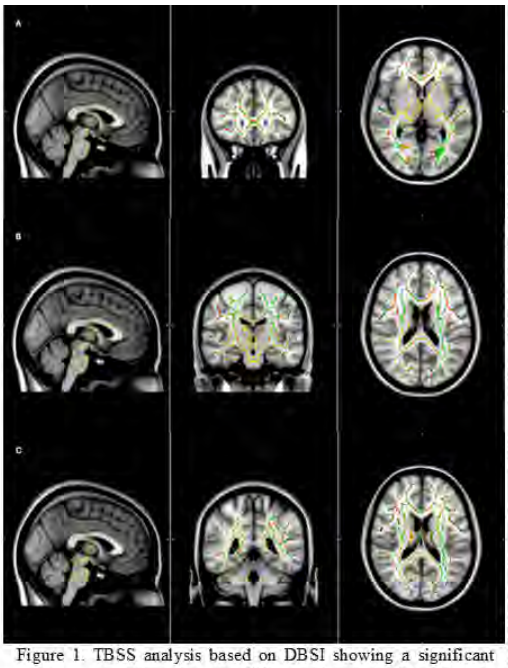

Figure 1. TBSS analysis based on DBSI showing a significant positive association between PDFF and restricted fraction in widespread regions at TFCE of 0.95. Green color represents the normal white matter skeleton, whereas yellow to red color shows the white matter tract showing a positive association with PDFF. TBSS, tract-based spatial statistics; DBSI, diffusion basis spectrum imaging; TFCE, threshold-free cluster enhancement; PDFF, Positron Density Fat Fraction.

Table 2. Results of multiple linear regression analysis studying the association between PDFF and aCBF in the whole brain and regions of interest of AD with age and sex as covariates.

Variable	B Weight	FDR-adjusted p-value
Left Amygdala	-3.0	**0.003**
Right Amygdala	-2.9	**0.005**
Left CalcarineL	-1.6	**0.01**
Right Calcarine	-2.6	**0.002**
Left HippoL	-2.9	**0.004**
Right Hippo	-3.6	**0.002**
LeftMidTempL	-2.1	**0.005**
Right MidTemp	-2.4	**0.003**
Left Medial Orbitofrontal Cortex	-1.6	**0.01**
Right Medial Orbitofrontal Cortex	-1.6	**0.01**
Left Parahippocampal	-2.9	**0.004**
Right Parahippocampal	-3.0	**0.003**
Left PostCingulate	-1.7	**0.005**
PostCingulate	-2.3	**0.003**
Left Precuneus	-1.7	**0.006**
Right Precuneus	-2.2	**0.003**
Whole Brain	-3.5	**0.002**

782 Two-minute Susceptibility Weighted Imaging using 3D Echo Planar Imaging: A Practical Approach for Evaluating the Novel Diagnostic Biomarkers for Multiple Sclerosis

Sreekanth Madhusoodhanan Nair Ph.D[1], Yin-Chen Hsu MD[2], Lixia Wang MD[2], Joshua D Lee MD, Ph.D[3], Jin Jin Ph.D[4], Chang Gao Ph.D[5], Abdul Jaber Tayem MD[6], Angel Liu BS[1], Nader Binesh Ph.D[7], Yibin Xie Ph.D[2], Debiao Li Ph.D[2], Paula Barreras MD[3], Marwa Kaisey MD[3], Omar Al-Louzi Ph.D[6], Nancy L Sicotte MD[3], Daniel Ontaneda MD[8], Pascal Sati Ph.D[1]

[1]Neuroimaging Program, Department of Neurology, Cedars-Sinai Medical Center, Los Angeles, CA, USA. [2]Biomedical Imaging Research Institute, Cedars-Sinai Medical Center, Los Angeles, CA, USA. [3]Department of Neurology, Cedars-Sinai Medical Center, Los Angeles, CA, USA. [4]Siemens Healthineers, Brisbane, Queensland, Australia. [5]Siemens Healthineers, Los Angeles, CA, USA. [6]Visual Outcomes Laboratory, Department of Neurology, Cedars-Sinai Medical Center, Los Angeles, CA, USA. [7]Department of Imaging, Cedars-Sinai Medical Center, Los Angeles, CA, USA. [8]Mellen Center for Multiple Sclerosis and Research, Department of Neurology, Cleveland Clinic Foundation, Cleveland, OH, USA

Purpose

The 2024 revised McDonald criteria for multiple sclerosis (MS)[1] incorporate two novel imaging biomarkers: the central vein sign (CVS)[2] and paramagnetic rim lesions (PRL)[3]. Due to their paramagnetic properties, CVS and PRL can be detected using susceptibility-weighted imaging (SWI).[4] However, standard SWI is not optimized for CVS imaging and relies on a gradient-echo (GRE) sequence which significantly limits its scanning speed. In this study, we propose a fast 2-minute SWI optimized for simultaneous detection of CVS and PRL using 3D echo-planar-imaging (EPI).

Materials & Methods

Twenty subjects being evaluated for suspected MS were scanned on a 3T MRI scanner (MAGNETOM Skyra, Siemens Healthineers, Forchheim, Germany). MS clinical diagnosis was confirmed using 2024 McDonald criteria. Two different brain SWI protocols with the same spatial resolution (0.6 × 0.6 × 2 mm) and coverage were compared: (1) standard SWI-GRE (TE /TR = 20/27 ms, FA = 15°, GRAPPA = 2, TA = 4 minutes); and (2) fast optimized SWI-EPI (TE/TR=35/60 ms, FA = 5°, EPI factor = 9, TA = 2 minutes). Selection of the EPI factor (9 echoes per shot) was guided to reduce scan time, enabling 50% faster scan time without parallel imaging. Two trained raters independently reviewed CVS and PRLs using SWI magnitude and filtered phase images. A third expert rater adjudicated any discrepancies. The confidence level in CVS classification (high confidence or low confidence) was recorded for each CVS+ lesion. Subjects were subsequently classified as CVS+ or CVS- using the new Select-6 criterion (>6 CVS+ lesions or >50% CVS+ lesions if fewer than 10 total brain lesions). Subjects were also classified as PRL+ or PRL- based on the presence of at least one PRL. Agreement in PRL detection was assessed using the intraclass correlation coefficient (ICC), and a sign test was used to compare lesion-wise CVS classifications between SWI-GRE and SWI-EPI.

Results

Optimized SWI-EPI (TA = 2 minutes) demonstrated higher CVS detection than standard SWI-GRE (TA=4 minutes), identifying 135 CVS+ lesions versus 85 CVS+ lesions (63% increase, <0.001). High-confidence CVS classification increased from 50 CVS+ lesions using SWI-GRE to 115 CVS+ lesions using SWI-EPI (~2-fold increase). The number of CVS+ subjects increased from 8 with SWI-GRE to 16 with SWI-EPI. Both SWI-GRE and SWI-EPI showed perfect agreement (ICC = 1) for PRL classification at the subject level. Using 2024 McDonald criteria, 17 out of 20 subjects fulfilled criteria for MS diagnosis. CVS diagnostic sensitivity increased from 47% (8/17 MS) on SWI-GRE to 94% (16/17 MS) on SWI-EPI. PRL diagnostic sensitivity was 50% on both sequences. All CVS+ or PRL+ subjects fulfilled the 2024 McDonald criteria, thus resulting in 100% specificity.

Conclusion

This study demonstrates that a 2-minute optimized SWI-EPI protocol outperforms standard SWI-GRE for CVS and PRL detection with 50% faster acquisition time, thus offering a practical solution for routine diagnostic evaluation of MS using the 2024 revised McDonald criteria.

References

1. Montalban X, Lebrun-Frenay C, Oh J, Arrambide G, Moccia M, Amato MP, Amezcua L, Banwell B, Bar-Or A, Barkhof F. Diagnosis of multiple sclerosis: 2024 revisions of the McDonald criteria. The Lancet Neurology. 2025.
2. Sati P, Oh J, Constable RT, Evangelou N, Guttmann CR, Henry RG, Klawiter EC, Mainero C, Massacesi L, McFarland H. The central vein sign and its clinical evaluation for the diagnosis of multiple sclerosis: a consensus statement from the North American Imaging in Multiple Sclerosis Cooperative. Nature Reviews Neurology. 2016;12(12):714-22.
3. Bagnato F, Sati P, Hemond CC, Elliott C, Gauthier SA, Harrison DM, Mainero C, Oh J, Pitt D, Shinohara RT. Imaging chronic active lesions in multiple sclerosis: a consensus statement. Brain. 2024:awae013.
4. Barkhof F, Reich DS, Oh J, Rocca MA, Li DK, Sati P, Azevedo CJ, Bagnato F, Calabresi PA, Ciccarelli O. 2024 MAGNIMS–CMSC–NAIMS consensus recommendations on the use of MRI for the diagnosis of multiple sclerosis. The Lancet Neurology. 2025;24(10):866-79.

Images/Tables

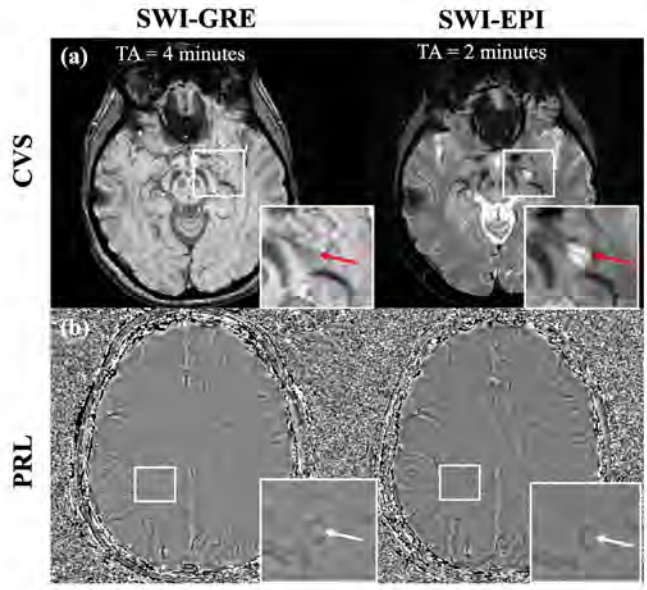

Figure 1: Head-to-head comparison of standard SWI-GRE (left) and optimized SWI-EPI (right) acquired at 3T on the same MS patient. (a) MS lesion is invisible on standard SWI-GRE whereas lesion appears hyperintense on optimized SWI-EPI, enabling the detection of the Central Vein Sign (CVS) (red arrows). (b) Filtered phase image from SWI-EPI exhibits similar contrast as SWI-GRE, enabling the detection of Paramagnetic Rim Lesions (PRL) (white arrows).

---

714 Prevalence of Possible and Probable LATE among patients undergoing clinical Amyloid PET Scans

Suely Fazio Ferraciolli MD, PhD, David Alvarez, Jeremy N Ford MD, MS, MBA
MGH - Harvard, Boston, MA, USA

Purpose

Limbic-predominant age-related TDP-43 encephalopathy (LATE) is increasingly recognized as a key contributor to cognitive impairment in older adults. While definitive diagnosis remains post-mortem, recent criteria integrating age, hippocampal atrophy, and amyloid status enable in vivo identification. The 25th percentile hippocampal threshold, as operationalized by Mundada et al., has emerged as a robust measure of medial temporal vulnerability. Here, we modeled the prevalence of Possible and Probable LATE using structural MRI and florbetaben PET in patients with memory loss.

Materials & Methods

We retrospectively analyzed 258 participants (mean age: 73.4 ± 7.8 years; 136 female /122 male) who underwent 3T T1-weighted MRI and florbetaben amyloid-PET. Total hippocampal volumes, normalized to intracranial volume (ICV), were used to compute the 25th percentile cutoff (3.12 cm^3 in our cohort). Following Mundada et al. and Wolk et al., we classified participants aged > 75 with hippocampal volume below the threshold and amyloid presence as **Possible LATE**, and with amyloid absence as **Probable LATE**. Four subgroups were evaluated: amyloid-positive (+) non-LATE (n = 155), amyloid-positive (+) Possible LATE (n = 28), amyloid-negative (–) non-LATE (n = 65), and amyloid-negative (–) Probable LATE (n = 10). ANCOVA was performed to adjust regional volume differences for age and sex.

Results

Among 258 participants:

- 10.9% (n = 28) met criteria for **Possible LATE**
- 3.9% (n = 10) met criteria for **Probable LATE**

Combined, 14.7% of the cohort showed LATE-like patterns, increasing to 28.6% in those older than 75.

Morphologic Findings (Age- and Sex-Adjusted):

Participants in LATE-like subgroups had significantly reduced hippocampal ($F = 24.7$, $p < 0.001$), amygdalar ($F = 13.3$, $p < 0.001$), and entorhinal

cortex volumes (F = 6.5, p = 0.000) compared to non-LATE cases. Precuneus and posterior cingulate volumes did not differ significantly between groups (p > 0.10).

Conclusion

Approximately 1 in 7 individuals undergoing amyloid-PET and MRI for memory loss exhibited LATE-like features, defined by disproportionate medial temporal atrophy and advanced age. This highlights the need to include LATE in differential diagnoses of late-life amnestic syndromes, even in amyloid-positive cases.

References

Wolk DA, Nelson PT, Apostolova L, Arfanakis K, Boyle PA, Carlsson CM, Corriveau-Lecavalier N, Dacks P, Dickerson BC, Domoto-Reilly K, Dugger BN, Edelmayer R, Fardo DW, Grothe MJ, Hohman TJ, Irwin DJ, Jicha GA, Jones DT, Kawas CH, Lee EB, Lincoln K, Maestre GE, Mormino EC, Onyike CU, Petersen RC, Rabinovici GD, Rademakers R, Raman R, Rascovsky K, Rissman RA, Rogalski E, Scheltens P, Sperling RA, Yang HS, Yu L, Zetterberg H, Schneider JA. Clinical criteria for limbic-predominant age-related TDP-43 encephalopathy. Alzheimers Dement. 2025 Jan;21(1):e14202. doi: 10.1002/alz.14202. Epub 2025 Jan 14. PMID: 39807681; PMCID: PMC11772733.

Images/Tables

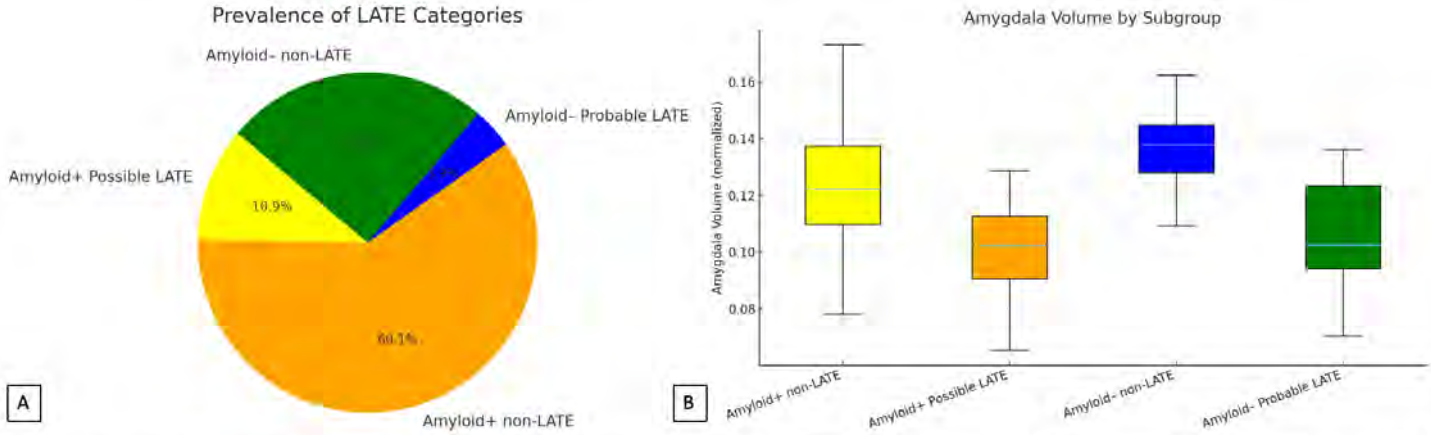

Figure. *Prevalence and imaging features of LATE spectrum subgroups and Probable LATE case example.*

(A) Prevalence of LATE-defined subgroups in the total cohort (N = 258), categorized by age and hippocampal volume percentile thresholds.

(B) Boxplot of ICV-normalized amygdala volume across the four subgroups, highlighting reduced amygdala volumes in LATE-like participants.

(C & D) Coronal T1-weighted MRI (C) and quantitative amyloid PET (D) in a 78-year-old woman show marked bilateral hippocampal atrophy with a negative amyloid PET scan (centiloid value = 13.13). This combination of severe medial temporal atrophy, age > 75 years, hippocampal volume below the 25th percentile, and negative amyloid PET uptake is consistent with **Probable LATE**, based on proposed in vivo diagnostic criteria.

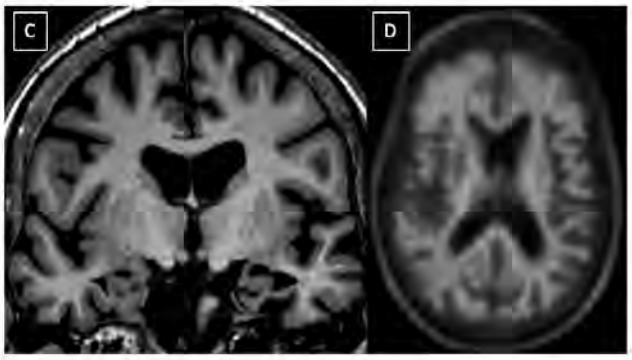

---

976 The Role of Pro-Inflammatory to Anti-Inflammatory Cytokine Balance in Brain Structure: IL-6:IL-10 Ratio Association with Regional Brain Atrophy in Middle-Aged Adults at Risk for Alzheimer's Disease

Mobina Amanollahi[1], Soheil Mohammadi[1], Mahsa Dolatshahi[1], Mona Mirbeyk[1], Paul K Commean[1], Farzaneh Rahmani[1], LaKisha Lloyd[1], Mahshid Naghashzadeh[1], Bettina Mittendorfer[2], Claude Sirlin[3], Tammie L.S Benzinger[1], Joseph E. Ippolito[1], John C Morris[4], Cyrus A Raji[1]
[1]Mallinckrodt Institute of Radiology, Washington University in St. Louis, St. Louis, Missouri, USA. [2]Missouri University School of Medicine, Columbia, Missouri, USA. [3]University of California, San Diego, San Diego, California, USA. [4]Knight Alzheimer Disease Research Center, St. Louis, Missouri, USA

Purpose

Systemic inflammation has been implicated in Alzheimer's disease (AD) pathogenesis and cognitive function. This study aims to examine whether the IL-6:IL-10 ratio is associated with cortical thickness and volume in AD-vulnerable brain regions.

Materials & Methods

Seventy-four cognitively normal adults underwent 3T MRI and peripheral blood cytokine assessment. The IL-6:IL-10 ratio was log-transformed to account for non-normal distribution. The studied brain regions (n=23) included autosomal dominant AD and late-onset AD cortical signature regions. FreeSurfer 7.1.1 was used for cortical segmentation with quality control. Multiple linear regression models, controlling for age and sex, examined associations between log(IL-6:IL-10 ratio) and regional cortical thickness and volume. Multiple comparison correction was performed using the false discovery rate (FDR).

Results

Seventy-four cognitively normal adults (mean age 49.92 (6.09) years; 53 (71.6%) females; mean BMI: 32.45 (7.68); mean MMSE: 29.16 (1.06)) were included in the final analysis. We observed significant associations between higher IL-6:IL-10 ratio and reduced cortical thickness in nine regions after FDR correction ($p < 0.05$), including left transverse temporal (β = -0.050, p = .006), right superior temporal (β = -0.034, p = .006), left banks of superior temporal sulcus (β = -0.031, p = .047), left middle temporal (β = -0.041, p = .047), right supramarginal (β = -0.022, p = .0498), right fusiform (β = -0.028, p = .0498), right lateral occipital (β = -0.029, p = .0498), left superior temporal (β = -0.026, p = .0498), and right superior parietal (β = -0.022, p = .0498) **(Figure 1)**. There were no significant associations for ROI volumes after FDR correction ($p > 0.05$). To verify that the ratio finding was not driven by a single cytokine, we studied the association of IL-6 and IL-10 separately on cortical thickness. Only one region survived FDR correction for each

cytokine: IL-6 with the right posterior cingulate cortex thickness and IL-10 with the right entorhinal cortex thickness (p = 0.006 for IL-6 and p = 0.003 for IL-10).

Conclusion

Our findings show that a higher IL-6:IL-10 ratio, reflecting greater pro-inflammatory activity, is associated with cortical thinning, but not volume loss. This implies that inflammatory imbalance may disturb cortical microarchitecture before overt tissue loss occurs because cortical thickness is more sensitive to early microstructural changes and inflammation-related neurotoxicity. This pro- to anti-inflammatory ratio may represent a shared pathway linking high BMI to AD risk, relevant given our predominantly obese sample. Future studies should evaluate how metabolic factors such as obesity, waist circumference, and insulin resistance integrate with systemic inflammation to accelerate neurobiological vulnerability. Also, because the IL-6:IL-10 balance, but not either cytokine alone, was associated with cortical thickness changes across several regions, this suggests that pro- vs anti-inflammatory balance might better track neuroanatomical differences than absolute cytokine concentrations. These results point to the potential need for developing targeted interventions aimed at modulating inflammatory balance in the preclinical stage.

References

Xie J, Van Hoecke L, Vandenbroucke RE. The impact of systemic inflammation on Alzheimer's disease pathology. *Front Immunol* 2022;12:796867. DOI: https://doi.org/10.3389/fimmu.2021.796867

Ellulu MS, Patimah I, Khaza'ai H, et al. Obesity and inflammation: the linking mechanism and the complications. *Arch Med Sci* 2017;13:851-63. DOI: https://doi.org/10.5114/aoms.2016.58928

Images/Tables

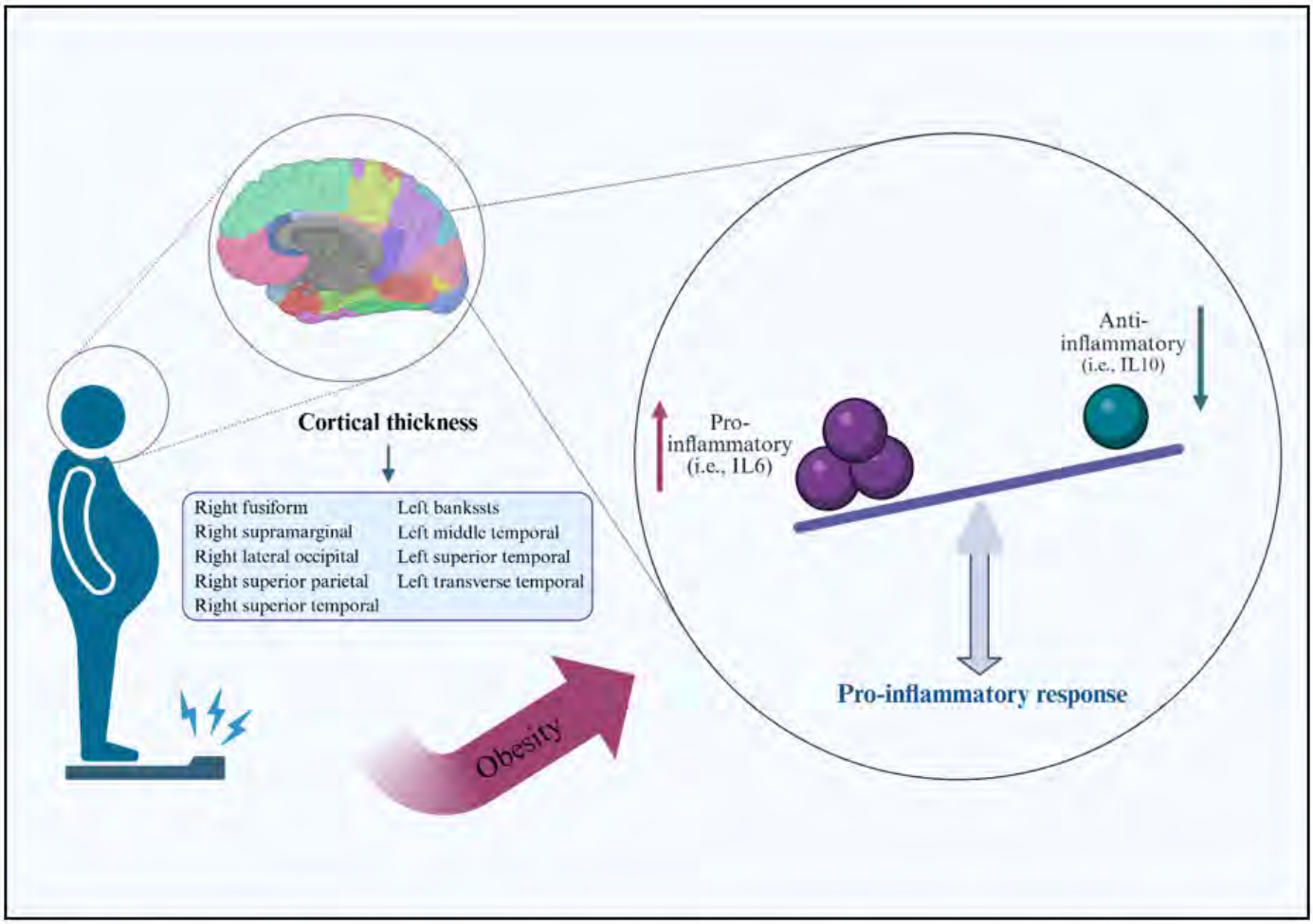

Figure 1. IL-6:IL-10 Ratio and Cortical Thinning: Systemic pro- to anti-inflammatory cytokine imbalance (IL-6:IL-10 ratio) is associated with early cortical thinning in AD-vulnerable regions among midlife adults with obesity.

---

385 Scalloping of the Petrous Apex on CT: A Novel Imaging Marker for Idiopathic Intracranial Hypertension

Rishi D Patel MD, Alex Jeon DO, Carson S Potts BS, Ashley Pankey BS, Mia Cirrincione, Dara Adams MD, Burce Ozgen MD
University of Illinois in Chicago, Chicago, IL, USA

Purpose

Dilation of Meckel's cave on MRI has been associated with idiopathic intracranial hypertension (IIH), but no comparable marker has been described on computed tomography (CT). This study aimed to evaluate scalloping of the petrous apex (PA) as a potential CT marker of IIH, particularly in cases with otherwise subtle imaging findings.

Materials & Methods

In this retrospective case-control study, 51 patients with confirmed IIH and 51 age- and sex-matched controls who underwent non-contrast CT head or temporal bone imaging were reviewed. The presence of PA scalloping—defined as cortical resorption or concavity of the PA on at least one side—

was recorded. Secondary analyses assessed the degree of PA resorption and the presence of established CT and MRI signs of IIH, including empty or partially empty sella and arachnoid pits.

Results

Scalloping of the PA was identified in 48 of 51 IIH patients (94.1%) compared with 27 of 51 controls (52.9%, $p<0.01$). The mean depth of PA resorption was significantly greater in IIH patients (2.3 mm vs. 0.73 mm, $p<0.01$). Additional imaging signs of IIH were present in 90.2% of IIH patients versus 29.4% of controls ($p<0.01$). Notably, most studies (83.3%) were standard head CTs, indicating that PA scalloping can be recognized on routine imaging.

Conclusion

Scalloping of the petrous apex on CT is significantly associated with IIH and may represent a novel, readily identifiable imaging marker. Because it can be detected on routine non-contrast head CT, recognizing this feature may facilitate earlier diagnosis and prompt further evaluation in patients with suspected IIH.

References

Aaron GP, Illing E, Lambertsen Z, et al. Enlargement of Meckel's cave in patients with spontaneous cerebrospinal fluid leaks. Int Forum Allergy Rhinol. 2017;7(4):421-424. doi:10.1002/alr.21891

Eggerstedt M, Dua SG, Varelas AN, Bhabad SH, Batra PS, Tajudeen BA. Enlargement of Dorello's Canal as a Novel Radiographic Marker of Idiopathic Intracranial Hypertension. J Neurol Surg B Skull Base. 2020;81(3):232-236. doi:10.1055/s-0039-1688783

Kamali A, Sullivan KC, Rahmani F, et al. Indentation and Transverse Diameter of the Meckel Cave: Imaging Markers to Diagnose Idiopathic Intracranial Hypertension. AJNR Am J Neuroradiol. 2020;41(8):1487-1494. doi:10.3174/ajnr.A6682

Images/Tables

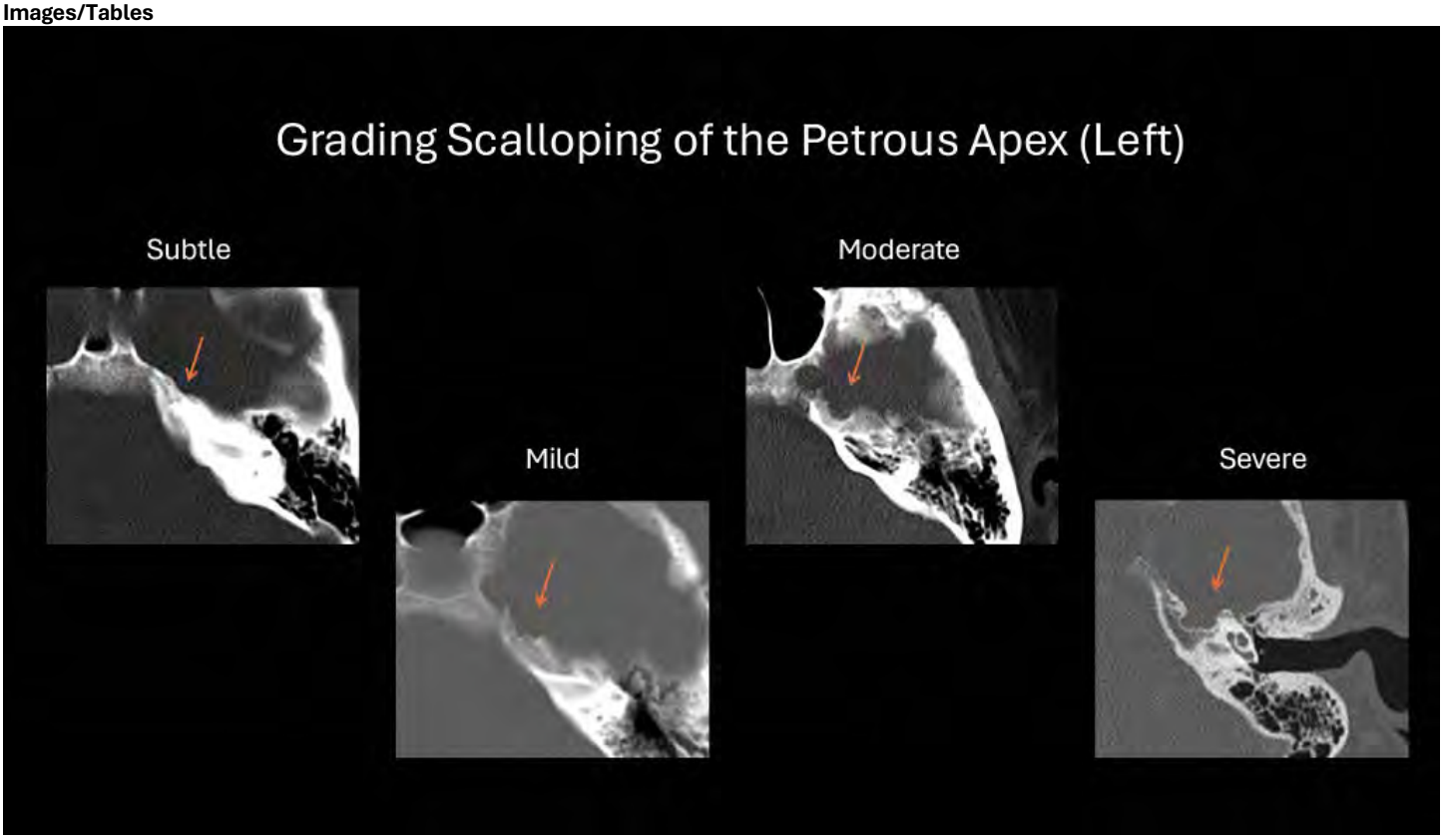

891 Elevated blood pressure is causally associated with larger subcortical gray matter structure through perivascular clearance routes

Jing Sun Dr., Han Lv Dr.

Department of Radiology, Beijing Friendship Hospital, Capital Medical University, Beijing, Beijing, China

Purpose

Subcortical gray matter structures have been considered primary regions vulnerable to hypertension-induced brain damage; however, evidence about the relationship between their morphological characteristics and elevated blood pressure (BP) remains limited. This study aimed to investigate the associations between elevated BP and subcortical gray matter structures, and to further elucidate the potential causal relationships and underlying neuroradiological mechanisms.

Materials & Methods

This study enrolled 1,012 community-dwelling participants from a population-based cohort study in China. Generalized linear models were used to evaluate the associations between different degrees of BP and subcortical gray matter volumes. Mendelian randomization analysis based on genome-wide data was performed to investigate the causal relationships. We further conducted mediation analysis to analyze whether the associations were mediated by dysfunctional brain clearance.

Results

Compared with the lowest group of systolic BP (SBP) < 120 mmHg and diastolic BP (DBP) < 80 mmHg, elevated BP was associated with larger subcortical gray matter volumes, including caudate volumes (SBP/DBP 130/80-140/90 mmHg: beta = 0.19, 95% CI 0.01 to 0.37), putamen volumes

(SBP/DBP 130/80-140/90 mmHg: beta = 0.27, 95% CI 0.08 to 0.46; SBP/DBP ≥ 140/90 mmHg: beta = 0.31, 95% CI 0.13 to 0.49), and pallidum volumes (SBP/DBP 120/80-130/80 mmHg: beta = 0.25, 95% CI 0.02 to 0.48; SBP/DBP 130/80-140/90 mmHg: beta = 0.28, 95% CI 0.08 to 0.48; SBP/DBP ≥ 140/90 mmHg: beta = 0.25, 95% CI 0.06 to 0.45). Genetically determined hypertension was causally associated with increased volumes of subcortical gray matter (left caudate: beta = 1.59, 95% CI 1.07 to 2.10; right caudate: beta = 1.42, 95% CI 0.82 to 2.03; left putamen: beta = 0.84, 95% CI 0.36 to 1.31; right putamen: beta = 0.69, 95% CI 0.25 to 1.14; left pallidum: beta = 0.59, 95% CI 0.09 to 1.08). It was the number of enlarged perivascular spaces in the basal ganglia (BG-EPVS) that mediated the relationship between elevated BP and larger volumes of subcortical gray matter.

Conclusion

Elevated BP is causally associated with larger subcortical gray matter volumes, mediated by the heightened burden of BG-EPVS. Our study establishes a pathophysiological relationship between elevated BP, perivascular clearance routes, and disrupted subcortical gray matter structures.

References

1. Whelton PK, Carey RM, Aronow WS, Casey DE, Jr., Collins KJ, Dennison Himmelfarb C, DePalma SM, Gidding S, Jamerson KA, Jones DW *et al*: **2017 ACC/AHA/AAPA/ABC/ACPM/AGS/APhA/ASH/ASPC/NMA/PCNA Guideline for the Prevention, Detection, Evaluation, and Management of High Blood Pressure in Adults: A Report of the American College of Cardiology/American Heart Association Task Force on Clinical Practice Guidelines**. *Hypertension* 2018, **71**(6):e13-e115.

2. Sun J, Zeng N, Hui Y, Li J, Liu W, Zhao X, Zhao P, Chen S, Wu S, Wang Z *et al*: **Association of variability in body size with neuroimaging metrics of brain health: a population-based cohort study**. *Lancet Reg Health West Pac* 2024, **44**:101015.

3. Beauchet O, Celle S, Roche F, Bartha R, Montero-Odasso M, Allali G, Annweiler C: **Blood pressure levels and brain volume reduction: a systematic review and meta-analysis**. *J Hypertens* 2013, **31**(8):1502-1516.

4. Shi H, Cui L, Hui Y, Wu S, Li X, Shu R, Song H, Wang J, Yu P, Chen S *et al*: **Enlarged Perivascular Spaces in Relation to Cumulative Blood Pressure Exposure and Cognitive Impairment**. *Hypertension* 2023, **80**(10):2088-2098.

5. Florio TM, Scarnati E, Rosa I, Di Censo D, Ranieri B, Cimini A, Galante A, Alecci M: **The Basal Ganglia: More than just a switching device**. *CNS Neurosci Ther* 2018, **24**(8):677-684.

Images/Tables

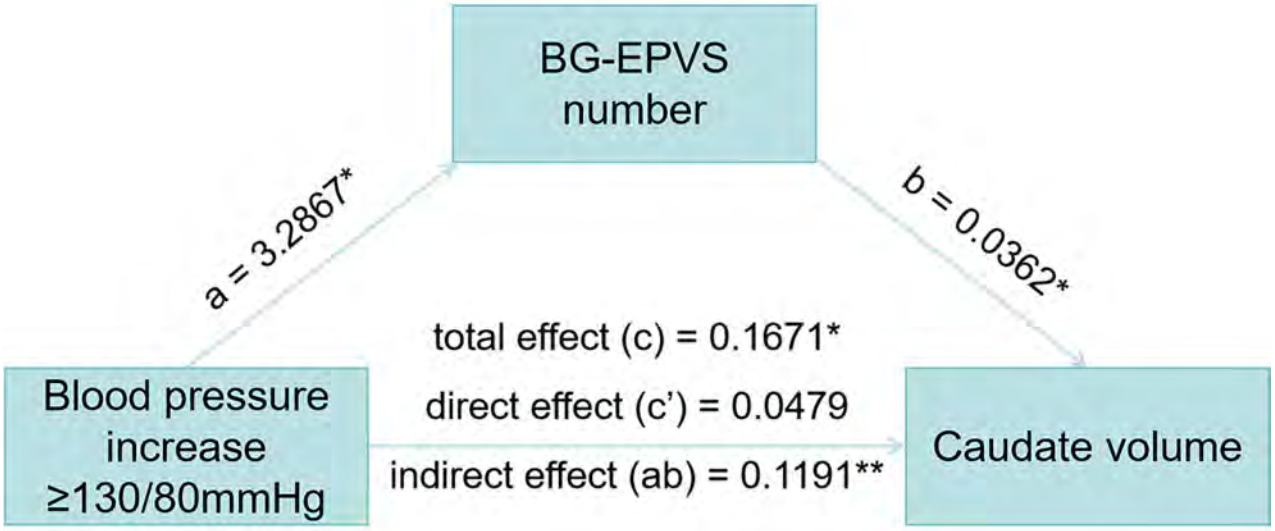

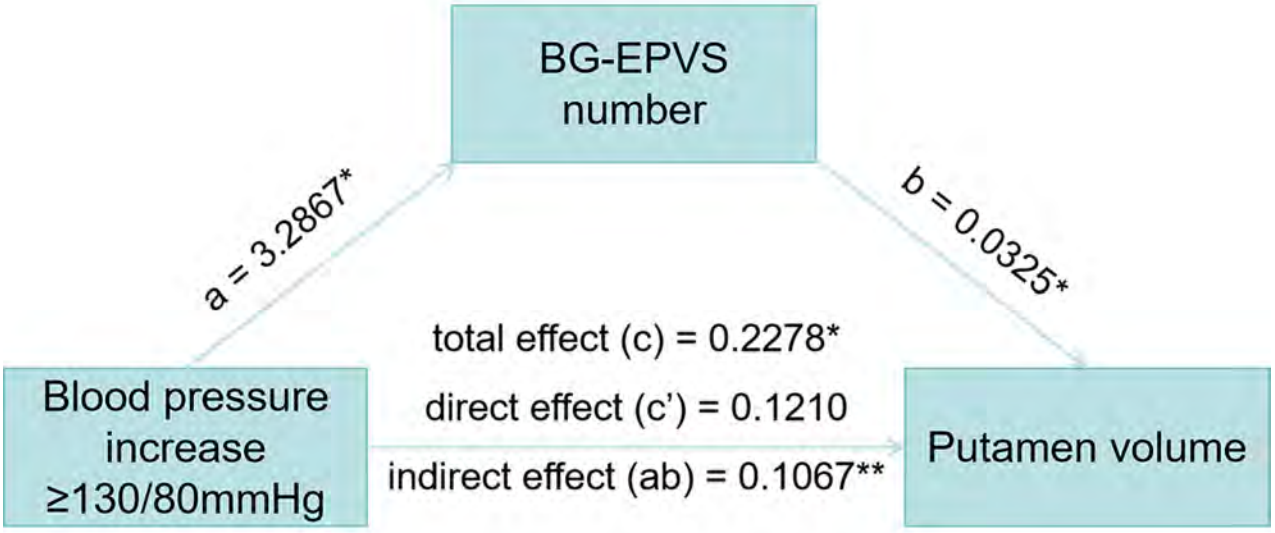

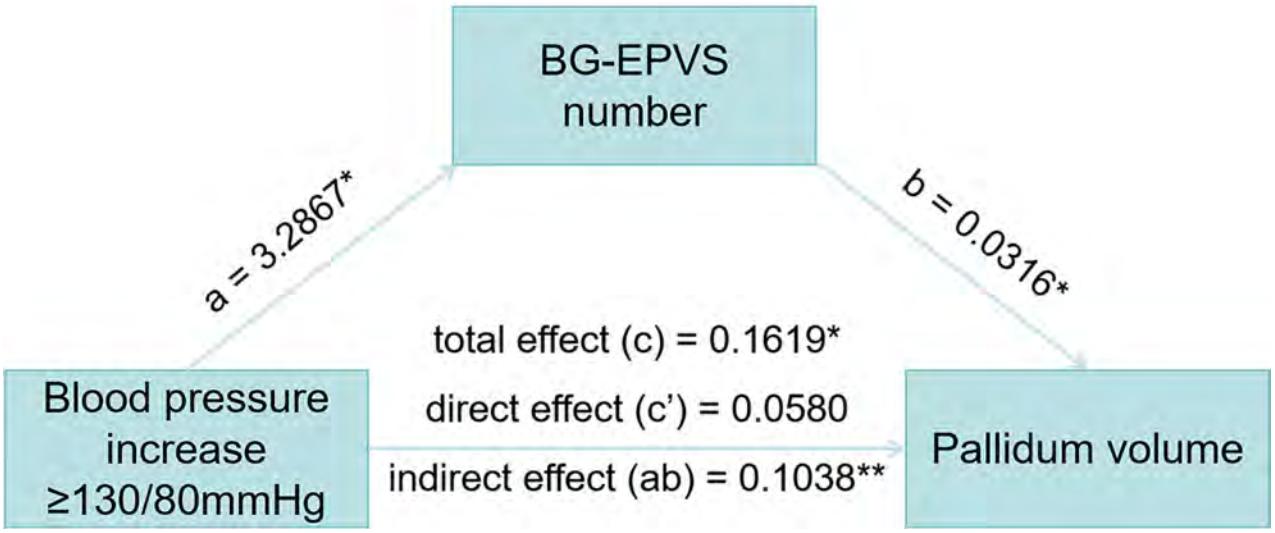

901 Evaluation of the central vein sign (CVS) in white matter T2 hyperintense lesions in patients with Multiple Sclerosis using 3D-T2*-weighted Echo-Planar Imaging.

Kamaljeet Singh MBBS, MD, DNB, Santanu Chakraborty MBBS, MRCP, DMRD, FRCR, FRCPC
The University of Ottawa, Ottawa, Ontario, Canada

Purpose

Determine if the high-resolution T2*-weighted brain MRI sequence improves diagnostic information for suspected Multiple Sclerosis patients.

Materials & Methods

This is a prospective study with 40 participants. Individuals over the age of 18 who have a clinical diagnosis of multiple sclerosis and provide consent are eligible to participate in the study.

Participants are grouped into two groups: Group 1 with a confirmed MS diagnosis and Group 2 with not yet been diagnosed or MS has not been confirmed. These groups are then further categorized based on the number of lesions with a Positive CVS sign and the percentage of T2 lesions showing CVS.

For statistical analysis, the specificity and sensitivity of the 3D T2*-weighted sequence in detecting CVS will be compared with those without the 3D T2*-weighted sequence. Additionally, measures of agreement using Fleiss Kappa statistics were conducted to achieve the secondary objective. The comparative image quality between the high-resolution 3D T2*-weighted sequence (0.6 mm isotropic) and the clinical reference images was assessed using a non-inferiority test.

Results

Analysis of the number of T2 lesions revealed a statistically significant difference between patients of Group 1 and Group 2. Similar differences were seen in the number of CVS lesions and the percentage of T2 lesions showing CVS. No correlation between the number of T2 lesions and the number of years of disease activity in MS patients. ROC curve analysis revealed high sensitivity and specificity of the number of lesions with central vein sign in patients with MS, with an area under the curve being 0.896. It was also observed that the best subset of images to visualise the central vein sign is the magnitude images of the 3D EPI sequence.

Conclusion

CVS represents a significant advance in the imaging-based diagnosis of MS, offering high specificity and the potential to reduce misdiagnosis. 3D EPI, with its improved visualization of CVS, is an important breakthrough. While its integration into routine clinical practice is promising, there is a need to standardize imaging protocols, validate diagnostic thresholds, and confirm its utility across diverse patient populations

References

1. Montalban X, Lebrun-Frénay C, Diagnosis of multiple sclerosis: 2024 revisions of the McDonald criteria. Lancet Neurol. 2025 Oct;24(10):850-865. doi: 10.1016/S1474-4422(25)00270-4. PMID: 40975101.
2. Tenembaum et al . Multiple sclerosis: advances and challenges in diagnosis. Current Opinion in Neurology 38(3):p 197-204, June 2025.
3. Martin ML et al Reliability of Central Vein Sign Imaging With 3T FLAIR* in a Multicenter Study. J Neuroimaging. 2025 Jan-Feb;35(1):e70011.
4. Cagol A et al MAGNIMS Study Group. Diagnostic Performance of Cortical Lesions and the Central Vein Sign in Multiple Sclerosis. JAMA Neurol. 2024 Feb 1;81(2):143-153.
5. Sinnecker T et al Evaluation of the Central Vein Sign as a Diagnostic Imaging Biomarker in Multiple Sclerosis. JAMA Neurol. 2019;76(12):1446–1456.

Images/Tables

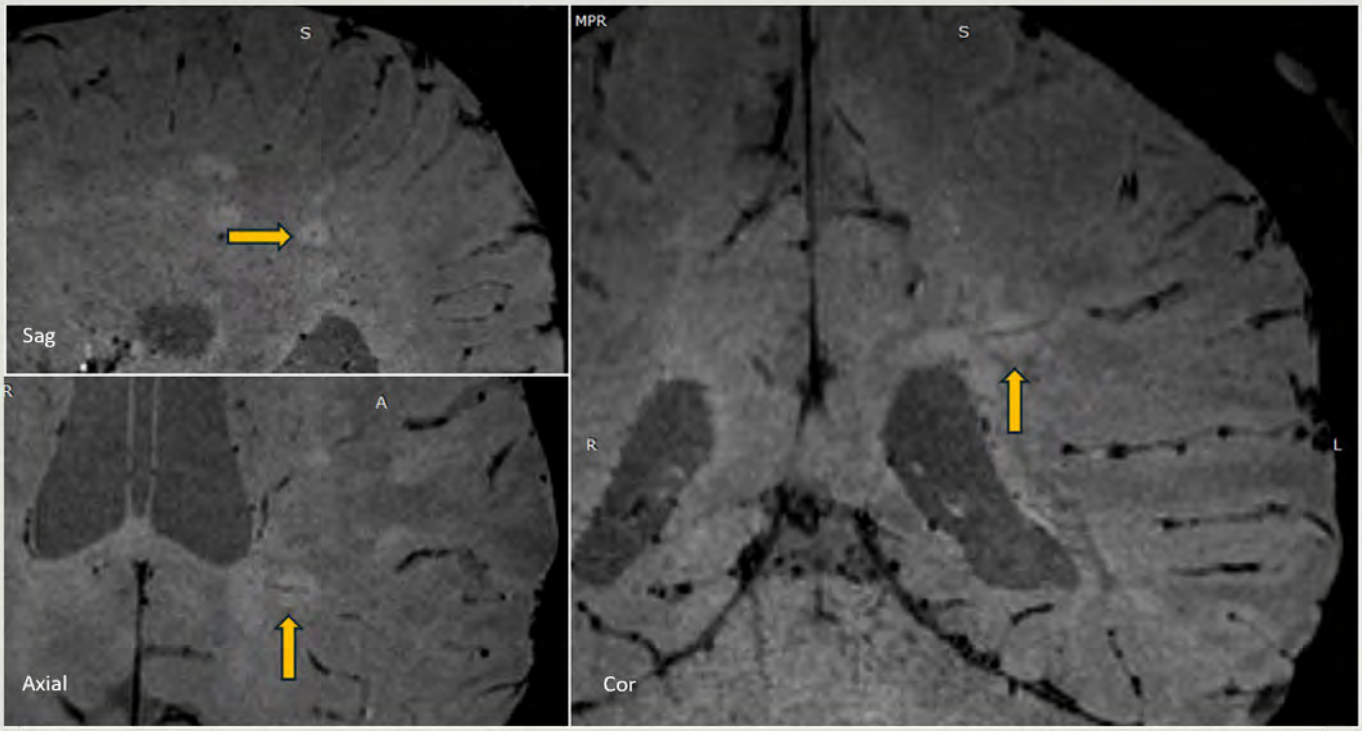

Figure 1. Multiplanar 3D EPI Mag sequence showing hypointense central vein in white matter lesion.

922 Generalizable DIR-like Image Synthesis Across Multisite MRI Data for Improved Multiple Sclerosis Lesion Assessment

Long Wang[1], Campbell Arnold[1], Zechen Zhou[1], Lei Xiang[1], Ajit Shankaranarayanan[1], Suzie Bash[2], Lawrence Tanenbaum[3]
[1]Subtle Medical, Menlo Park, CA, USA. [2]RadNet, Los Angeles, CA, USA. [3]Los Angeles, CA, USA

Purpose

Double inversion recovery (DIR) MRI provides superior gray–white matter differentiation and lesion visibility in multiple sclerosis (MS), but is rarely acquired in routine practice due to long scan times. We repurposed a synthesis model originally developed for STIR[1] and applied it to multiple brain MS datasets to evaluate its cross-domain generalization. Despite being trained in a different anatomical setting, the model demonstrates strong performance in generating DIR-like (SynDIR) images, with consistent improvements across multisite MS datasets.

Materials & Methods

The model was directly applied to T1-weighted and T2-FLAIR brain scans to generate DIR-like images without additional training. Two external MS datasets were analyzed: open_ms_data[2] and MSLesSeg[3]. The open_ms_data cohort comprises 30 patients with both cross-sectional and longitudinal MRI scans of multiple sclerosis (MS) patients, whereas the MSLesSeg cohort includes 75 patients and 115 MRI scans acquired on 1.5 T and 3 T scanners from multiple vendors. The T1 and T2 FLAIR are registered using SimpleITK[4], and then fed into the synthesis network.
Evaluation included (i) structural fidelity, assessed using SSIM and Dice overlap in brain-volume segmentation Freesurfer[5]; (ii) tissue contrast enhancement, quantified by gray-to-white-matter and lesion-to-white-matter ratios; (iii) multisite consistency, comparing results across multiple sites and vendors; and (iv) longitudinal stability, testing reproducibility of the SynDIR contrast over repeated scans using the Wilcoxon signed-rank test.

Results

Figure 1A illustrates representative T2 FLAIR and SynDIR images alongside their corresponding raw inputs and tissue segmentation masks. Quantitatively, T2 FLAIR and SynDIR demonstrated strong structural fidelity across sites (mean SSIM = 0.8719 ± 0.0217), with Dice scores exceeding 0.85 for all major brain regions.
Figure 1B shows an example subject from the MSLesSeg dataset scanned at two time points. The Wilcoxon signed-rank test revealed no significant longitudinal difference ($p = 0.1478$) among the cases. Similarly, the t-test on the ratio of gray-to-white-matter ratio to lesion-to-white-matter between the two cohorts showed no significant difference, indicating consistent performance across sites.
As shown in Figure 1C, SynDIR showed substantially enhanced tissue and lesion contrast relative to T2 FLAIR. The gray-to-white-matter ratio increased from 1.2688 ± 0.0617 to 1.6134 ± 0.1946, while the lesion-to-white-matter ratio rose from 1.4035 ± 0.1309 to 1.9335 ± 0.3833 ($p < 0.001$), indicating markedly improved delineation of both normal and pathological structures.

Conclusion

A spine-trained synthesis model generalized effectively to multiple MS cohorts, producing DIR-like images that enhanced lesion visibility and showed consistent performance across sites and timepoints. This repurposed approach enables advanced contrasts for MS studies without acquiring the DIR series.

References

1. Tanenbaum, L. N., Bash, S. C., Zaharchuk, G., Shankaranarayanan, A., Chamberlain, R., Wintermark, M., ... & Wang, L. (2023). Deep learning–generated synthetic MR imaging STIR spine images are superior in image quality and diagnostically equivalent to conventional STIR: a multicenter, multireader trial. American Journal of Neuroradiology, 44(8), 987-993.
2. Lesjak, Žiga, et al. "A novel public MR image dataset of multiple sclerosis patients with lesion segmentations based on multi-rater consensus." Neuroinformatics 16 (2018): 51-63.
3. Guarnera, F., Rondinella, A., Crispino, E., Russo, G., Di Lorenzo, C., Maimone, D., ... & Battiato, S. (2025). MSLesSeg: baseline and benchmarking of a new Multiple Sclerosis Lesion Segmentation dataset. Scientific Data, 12(1), 920.
4. Beare, Richard, Bradley Lowekamp, and Ziv Yaniv. "Image segmentation, registration and characterization in R with SimpleITK." Journal of statistical software 86 (2018).
5. Fischl, B. (2012). FreeSurfer. Neuroimage, 62(2), 774-781.

Images/Tables

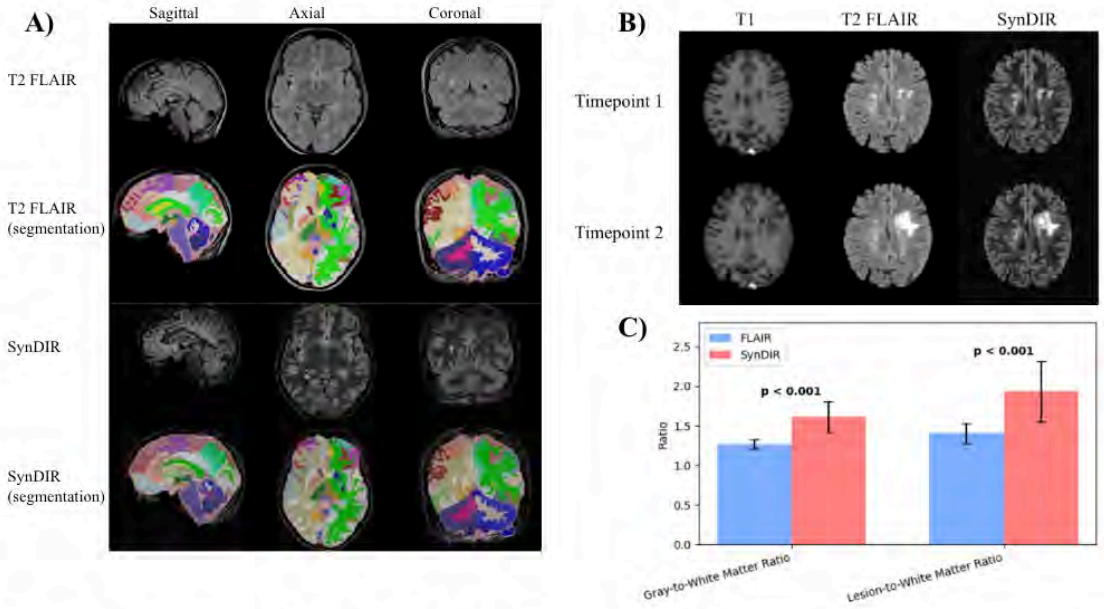

Figure 1. Comparison of FLAIR and SynDIR images across tissues, time points, and quantitative metrics. **(A)** Representative examples of T2 FLAIR and SynDIR images, each shown with their corresponding raw inputs and tissue segmentation masks. The top two rows display FLAIR images, and the bottom two rows show SynDIR results. Columns (left → right) correspond to sagittal, axial, and coronal views. **(B)** Longitudinal example from a subject in the *MSLesSeg* dataset imaged at two time points (top row = baseline; bottom row = follow-up). Each row shows T1-weighted, T2 FLAIR, and SynDIR images (left → right). **(C)** Quantitative comparison of tissue and lesion contrast between FLAIR (blue) and SynDIR (pink). Bars represent mean ± SD of gray-to-white-matter ratio and lesion-to-white-matter ratio across subjects. SynDIR demonstrates significantly higher contrast in both metrics ($p < 0.001$).

1193 **Superior Cervical Ganglion Enlargement Reflects CSF Opening Pressure in Idiopathic Intracranial Hypertension: Evidence for a Novel MRI Biomarker**

Mohamed S Muneer[1], Elfatih A Hasabo[2], Tarik F Massoud[1]

[1]Stanford University School of Medicine, Stanford, CA, USA. [2]Royal College of Surgeons in Ireland (RCSI) University of Medicine and Health Sciences, Dublin, Dublin, Ireland

Purpose

The etiology of idiopathic intracranial hypertension (IIH) remains unclear, though obesity in women of childbearing age is a well-recognized association. Recent work suggests that capillary damage, blood–brain barrier disruption, and astrogliosis may impair intracranial compliance and elevate intracranial pressure (ICP). Elevated ICP in turn acts as a physiological stressor that increases central sympathetic outflow, even at modest pressure elevations; whereas chronic sympathetic activation is also associated with migraine, present in ~80% of IIH patients. Thus, sympathetic overactivity appears closely linked to raised ICP in IIH. We therefore hypothesize that an easily obtainable orthogonal MRI-based morphometric of superior cervical ganglion (SCG) size (volume) may serve as a novel surrogate biomarker of sympathetic activity and IIH. A secondary aim is to test whether SCG size tracks with CSF opening pressure (OP) as a marker of IIH severity.

Materials & Methods

This IRB-approved retrospective case-control study included patients who underwent lumbar puncture (LP) for suspected IIH over a 6-year period and who had a brain MRI with a volumetric (1-mm isotropic) FLAIR sequence within six weeks of LP. We excluded patients without reported OP or non-IIH diagnoses. Healthy controls (HCs) comprised age- and BMI-matched subjects with normal brain 3D FLAIR-MRI. We adjusted for patient BMI because, similar to adrenal glands, SCG size likely scales with adiposity. We obtained digital measurements for bilateral FLAIR-hyperintense SCGs in orthogonal planes. We computed descriptive statistics and compared demographics, morphometrics, and OPs between IIH patients and HCs using Mann–Whitney U test, independent t-test, and Fisher's exact test; and performed unadjusted and age-adjusted logistic regression modeling for associations between SGC size and OP. Significance was set at $P<0.05$.

Results

We studied 36 IIH patients and 36 healthy controls (HCs) (mean ages, 36 and 43 years; 76% female). In IIH, median OP was 24.5cmH_2O (Q1–Q3, 17.10–34). The median right SCG size was significantly larger in IIH than HCs (281 vs. 208mm^3, P=0.038), and this difference remained after BMI correction (11 vs. 6.3mm^3/kg/cm^2, P=0.032). Left SCG size showed no significant group difference, with or without BMI adjustment. However, combined (right+left) SCG size was greater in IIH (631 vs. 381mm^3, P=0.030), and this also remained significant after BMI correction (21 vs. 13mm^3/kg/cm^2, P=0.026). Logistic regression identified an optimal right SCG size cutoff of ≥442mm^3 for predicting elevated OP (AUC=0.713). Right SCG enlargement at this threshold was associated with higher OP (OR 12.11, 95% CI 2.38–21.83; P=0.016) and remained significant after age adjustment (OR 14.04, 95% CI 3.12–24.95; P=0.013), though with moderate precision.

Conclusion

Volumes of right and bilateral SCGs are elevated in IIH. A cross-validated right-sided cutoff of ≥442mm^3 identifies a high-volume SCG phenotype associated with higher OP, independent of age and robust to BMI adjustment. These findings support SCG volume as a promising, noninvasive MRI biomarker that reflects ICP, may assist in IIH diagnosis and phenotyping, and could potentially reduce the frequency of non-therapeutic LPs. Larger prospective studies are needed to validate threshold values and further clarify the basis of lateralized SCG involvement.

References

Yokota H, Mukai H, Hattori S, et al. MR imaging of the superior cervical ganglion and inferior ganglion of the vagus nerve: structures that can mimic pathologic retropharyngeal lymph nodes. *AJNR Am J Neuroradiol* 2018;39:170–76.

Loke SC, Karandikar A, Ravanelli M, et al. Superior cervical ganglion mimicking retropharyngeal adenopathy in head and neck cancer patients: MRI features with anatomic, histologic, and surgical correlation. *Neuroradiology* 2016;58:45–50.

Fazliogullari Z, Kilic C, Karabulut AK, et al. A morphometric analysis of the superior cervical ganglion and its surrounding structures. *Surg Radiol Anat* 2016;38:299–302.

Eide PK, Hansson HA. A new perspective on the pathophysiology of idiopathic intracranial hypertension: role of the glia-neuro-vascular interface. *Front Mol Neurosci* 2022;15:900057.

Schmidt EA, Despas F, Pavy-Le Traon A, et al. Intracranial pressure is a determinant of sympathetic activity. *Front Physiol* 2018;9:11.

Scientific Abstract Power Pitches & Luminary Speaker: Neuroimaging: AI, Biomarkers, and Therapeutics

11:00am - 12:00pm Tuesday, 19th May, 2026

101 Post Treatment Follow-up MRI Imaging Biomarkers of Collateral Status Are Associated with Short-Term Outcomes in Large Vessel Acute Ischemic Stroke (LVO-AIS)

Hamza A Salim MD[1], Dhairya A Lakhani MD[2], Jay Kakadiya MD[3], Cynthia Greene MD, PhD[3], Argye E Hillis MD, PhD[4], Kambiz Nael MD[5], Adam A Dmytriw MD, MPH, MSc[6], Tyler Tyler McGaughey PhD[7], Jeremy J Heit MD, PhD[8], Max Wintermark MD[1], Tobias D Faizy MD[9], Vivek S Yedavalli MD, MS, FAHA[3]

[1]Department of Neuroradiology, MD Anderson Medical Center, Houston, TX, USA. [2]Department of Neuroradiology, West Virginia University,, Morgantown, WV, USA. [3]The Russell H. Morgan Department of Radiology and Radiological Science, Johns Hopkins University School of Medicine, Baltimore, MD, USA. [4]Department of Neurology, Johns Hopkins University School of Medicine, Baltimore, MD, USA. [5]Radiology and Biomedical Imaging, University California, San Francisco, CA, USA. [6]Neuroendovascular Program, Massachusetts General Hospital & Brigham and Women's Hospital, Harvard Medical School, Boston, MA, USA. [7]Department of Neuroradiology, West Virginia University, Morgantown, WV, USA. [8]Department of Radiology, Division of Neuroradiology and Neurointervention, Stanford University, Stanford, CA, USA. [9]Department of Radiology, Neuroendovascular Division, University Medical Center Münster, Münster, Münster, Germany

Purpose

FLAIR hyperintense vessels (FHV), quantified using the NIH-FHV score (NFS), and the SWI brush sign (SBS) are MRI markers associated with hemodynamic impairment in acute ischemic stroke (AIS). We aimed to evaluate the prognostic significance of post-treatment NFS and SBS in patients with anterior circulation large vessel occlusion (AIS-LVO), including those with successful reperfusion.

Materials & Methods

We retrospectively analyzed 215 AIS-LVO patients with in-hospital follow-up MRI. NFS and SBS were evaluated and correlated with clinical outcomes including NIHSS shift (≥4-point improvement) and hemorrhagic transformation (HT). Spearman correlation and logistic regression were performed, adjusting for clinical covariates. Analyses were repeated in the successfully reperfused subgroup (mTICI ≥2b).

Results

FHV and SBS were observed post-treatment in 38% and 20% of patients, respectively. NFS and SBS were positively correlated ($\rho = 0.57$, $p < .01$). NFS inversely correlated with NIHSS shift ($\rho = -0.26$, $p < .01$) and reperfusion grade (mTICI; $\rho = 0.25$, $p < .01$). NFS was independently associated with worse NIHSS shift (OR 0.60, $p < .01$) and reduced odds of HT (OR 0.78, $p = .04$). Among 154 patients with successful reperfusion, 24% of mTICI 3 cases showed FHV. In this subgroup, NFS remained predictive of poor NIHSS shift (OR 0.58, $p = .03$). SBS alone was not independently associated with outcomes.

Conclusion

NFS on post-treatment MRI is a robust imaging biomarker of persistent perfusion deficits and early neurological outcome, even after successful reperfusion. SBS may reflect complementary collateral dynamics but showed limited independent prognostic utility.

References

1. Yedavalli VS, Koneru M, Hoseinyazdi M, Greene C, Lakhani DA, Xu R, Luna LP, Caplan JM, Dmytriw AA, Guenego A, Heit JJ, Albers GW, Wintermark M, Gonzalez LF, Urrutia VC, Huang J, Nael K, Leigh R, Marsh EB, Hillis AE, Llinas RH. Prolonged venous transit on perfusion imaging is associated with higher odds of mortality in successfully reperfused patients with large vessel occlusion stroke. J Neurointerv Surg. 2025 Feb 14;17(3):321-326. doi: 10.1136/jnis-2024-021488. PMID: 38471762.
2. Yedavalli V, Salim HA, Mei J, Lakhani DA, Balar A, Musmar B, Adeeb N, Hoseinyazdi M, Luna L, Deng F, Hyson NZ, Dmytriw AA, Guenego A, Faizy TD, Heit JJ, Albers GW, Lu H, Urrutia VC, Nael K, Marsh EB, Hillis AE, Llinas R. Decreased Quantitative Cerebral Blood Volume Is Associated With Poor Outcomes in Large Core Patients. Stroke. 2024 Oct;55(10):2409-2419. doi: 10.1161/STROKEAHA.124.047483. Epub 2024 Aug 26. PMID: 39185560.
3. Lakhani DA, Balar AB, Koneru M, Wen S, Ozkara BB, Caplan J, Dmytriw AA, Wang R, Lu H, Hoseinyazdi M, Nabi M, Mazumdar I, Cho A, Chen K, Sepehri S, Hyson N, Xu R, Urrutia V, Luna LP, Hillis A, Heit JJ, Albers GW, Rai AT, Faizy T, Wintermark M, Nael K, Yedavalli VS. Perfusion-Based Relative Cerebral Blood Volume Is Associated With Functional Dependence in Large-Vessel Occlusion Ischemic Stroke. J Am Heart Assoc. 2024 Dec 3;13(23):e034242. doi: 10.1161/JAHA.124.034242. Epub 2024 Nov 22. PMID: 39575711; PMCID: PMC11681566.
4. Lakhani DA, Balar AB, Koneru M, Hoseinyazdi M, Hyson N, Cho A, Greene C, Xu R, Luna L, Caplan J, Dmytriw A, Guenego A, Wintermark M, Gonzalez F, Urrutia V, Huang J, Nael K, Rai AT, Albers GW, Heit JJ, Yedavalli V. Pretreatment CT perfusion collateral parameters correlate with penumbra salvage in middle cerebral artery occlusion. J Neuroimaging. 2024 Jan-Feb;34(1):44-49. doi: 10.1111/jon.13178. Epub 2023 Dec 6. PMID: 38057941.
5. Lakhani DA, Salim H, Balar AB, Ali S, Wen S, Mei J, Hillis AE, Urrutia VC, Xu R, Broocks G, Fiehler J, Kniep HC, Stracke P, Krähling H, Albers GW, Lansberg M, Wintermark M, Heit JJ, Faizy TD, Yedavalli VS. The Cortical Vein Opacification Score (COVES) is independently associated with good and excellent functional outcomes at 90-days in minor stroke patients with anterior circulation large vessel occlusion: A Multicenter Study. AJNR Am J Neuroradiol. 2025 May 19:ajnr.A8739. doi: 10.3174/ajnr.A8739. Epub ahead of print. PMID: 40389269.

Images/Tables

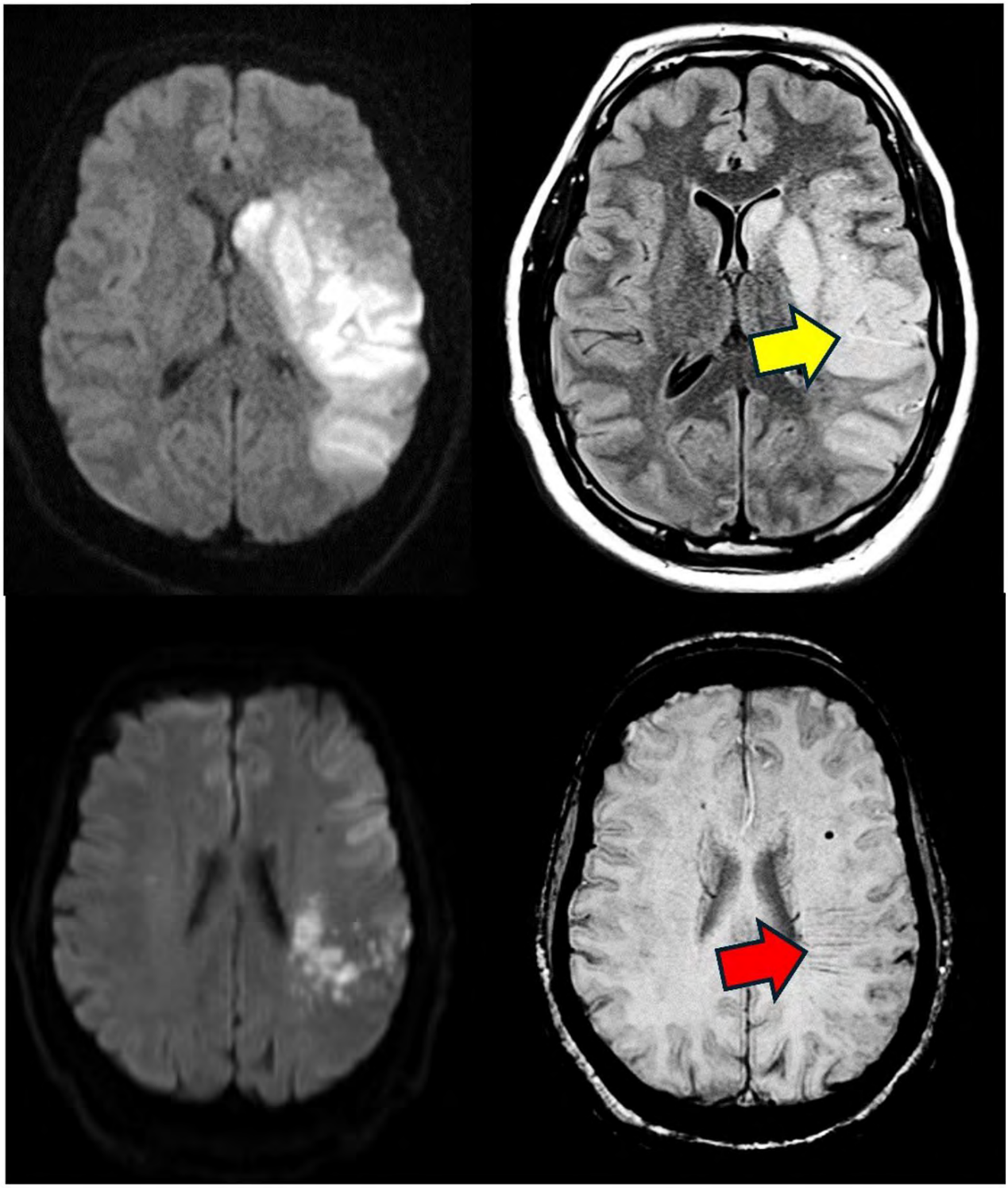

102 Gradation of prolonged venous transit highlights the impact of deep venous drainage impairment in successfully reperfused anterior circulation large vessel occlusion stroke

Hamza A Salim MD[1], Dhairya A Lakhani MD[2], Jay Kakadiya MD[3], Cynthia Greene MD, PhD[3], Argye E Hillis MD, PhD[4], Tyler McGaughey PhD[2], Adam A Dmytriw MD, MPH, MSc[5], Kambiz Nael MD[6], Jeremy J Heit MD, PhD[7], Max Wintermark MD[8], Tobias D Faizy MD[9], Vivek S Yedavalli MD, MS, FAHA[3]
[1]Department of Neuroradiology, MD Anderson Medical Center,, Houston, TX, USA. [2]Department of Neuroradiology, West Virginia University, Morgantown, WV, USA. [3]The Russell H. Morgan Department of Radiology and Radiological Science, Johns Hopkins University School of Medicine, Baltimore, MD, USA. [4]Department of Neurology, Johns Hopkins University School of Medicine, Baltimore, MD, USA. [5]Neuroendovascular Program, Massachusetts General Hospital & Brigham and Women's Hospital, Harvard Medical School, Boston, MA, USA. [6]Department of Radiology and Biomedical Imaging, University of California, San Francisco, CA, USA. [7]Department of Radiology, Division of Neuroradiology and Neurointervention, Stanford University, Stanford, CA, USA. [8]Department of Neuroradiology, MD Anderson Medical Center, Houston, TX, USA. [9]Department of Radiology, Neuroendovascular Division, University Medical Center Münster, Münster, Münster, Germany

Purpose

Prolonged venous transit (PVT), derived from CT perfusion (CTP) imaging, serves as a surrogate for venous outflow (VO) impairment and has been associated with worse outcomes in acute ischemic stroke due to large vessel occlusion (AIS-LVO). However, the differential impact of superficial versus deep venous drainage impairment on functional outcomes remains unclear.

Materials & Methods

We retrospectively analyzed 128 AIS-LVO patients from a prospective registry who underwent successful mechanical thrombectomy [modified treatment in cerebral infarction (mTICI) 2b/2c/3] with available baseline CTP and 90-day modified Rankin Scale (mRS) scores. PVT- was defined as the absence of Tmax ≥10 s in the posterior superior sagittal sinus (SSS) or torcula (no VO impairment). PVT1 was defined as the presence of Tmax ≥10 s in the posterior SSS only (superficial VO impairment), and PVT2 as the presence of Tmax ≥10 s at the torcula with or without posterior SSS involvement (deep VO impairment). Multivariable logistic regression assessed the association between PVT gradation and 90-day mRS score.

Results

The proportion of patients achieving favorable outcomes (mRS≤2) declined stepwise across PVT gradation: 60.9% in PVT-, 42.1% in PVT1, and 22.7 % in PVT2. After adjusting for age, admission NIHSS score, hypertension, hemorrhagic transformation, intravenous thrombolysis, and mTICI score, PVT gradation remained independently associated with reduced odds of favorable outcome. This association was primarily driven by the PVT2 group, with an adjusted odds ratio of 0.230 (95% CI, 0.068–0.780) compared to PVT- group.

Conclusion

PVT gradation based on Tmax ≥10 s timing in distinct venous territories provides prognostic insight into the differential contributions of superficial versus deep venous drainage dysfunction, supporting the use of PVT as a meaningful VO imaging biomarker. Deep VO impairment, as reflected by PVT2, is the primary driver of worse functional outcomes despite successful reperfusion in AIS-LVO, indicating its stronger negative prognostic impact compared to superficial VO impairment.

References

1. Yedavalli VS, Koneru M, Hoseinyazdi M, Greene C, Lakhani DA, Xu R, Luna LP, Caplan JM, Dmytriw AA, Guenego A, Heit JJ, Albers GW, Wintermark M, Gonzalez LF, Urrutia VC, Huang J, Nael K, Leigh R, Marsh EB, Hillis AE, Llinas RH. Prolonged venous transit on perfusion imaging is associated with higher odds of mortality in successfully reperfused patients with large vessel occlusion stroke. J Neurointerv Surg. 2025 Feb 14;17(3):321-326. doi: 10.1136/jnis-2024-021488. PMID: 38471762.
2. Yedavalli V, Salim HA, Mei J, Lakhani DA, Balar A, Musmar B, Adeeb N, Hoseinyazdi M, Luna L, Deng F, Hyson NZ, Dmytriw AA, Guenego A, Faizy TD, Heit JJ, Albers GW, Lu H, Urrutia VC, Nael K, Marsh EB, Hillis AE, Llinas R. Decreased Quantitative Cerebral Blood Volume Is Associated With Poor Outcomes in Large Core Patients. Stroke. 2024 Oct;55(10):2409-2419. doi: 10.1161/STROKEAHA.124.047483. Epub 2024 Aug 26. PMID: 39185560.
3. Lakhani DA, Balar AB, Koneru M, Wen S, Ozkara BB, Caplan J, Dmytriw AA, Wang R, Lu H, Hoseinyazdi M, Nabi M, Mazumdar I, Cho A, Chen K, Sepehri S, Hyson N, Xu R, Urrutia V, Luna LP, Hillis A, Heit JJ, Albers GW, Rai AT, Faizy T, Wintermark M, Nael K, Yedavalli VS. Perfusion-Based Relative Cerebral Blood Volume Is Associated With Functional Dependence in Large-Vessel Occlusion Ischemic Stroke. J Am Heart Assoc. 2024 Dec 3;13(23):e034242. doi: 10.1161/JAHA.124.034242. Epub 2024 Nov 22. PMID: 39575711; PMCID: PMC11681566.
4. Lakhani DA, Balar AB, Koneru M, Hoseinyazdi M, Hyson N, Cho A, Greene C, Xu R, Luna L, Caplan J, Dmytriw A, Guenego A, Wintermark M, Gonzalez F, Urrutia V, Huang J, Nael K, Rai AT, Albers GW, Heit JJ, Yedavalli V. Pretreatment CT perfusion collateral parameters correlate with penumbra salvage in middle cerebral artery occlusion. J Neuroimaging. 2024 Jan-Feb;34(1):44-49. doi: 10.1111/jon.13178. Epub 2023 Dec 6. PMID: 38057941.
5. Lakhani DA, Salim H, Balar AB, Ali S, Wen S, Mei J, Hillis AE, Urrutia VC, Xu R, Broocks G, Fiehler J, Kniep HC, Stracke P, Krähling H, Albers GW, Lansberg M, Wintermark M, Heit JJ, Faizy TD, Yedavalli VS. The Cortical Vein Opacification Score (COVES) is independently associated with good and excellent functional outcomes at 90-days in minor stroke patients with anterior circulation large vessel occlusion: A Multicenter Study. AJNR Am J Neuroradiol. 2025 May 19:ajnr.A8739. doi: 10.3174/ajnr.A8739. Epub ahead of print. PMID: 40389269.

Images/Tables

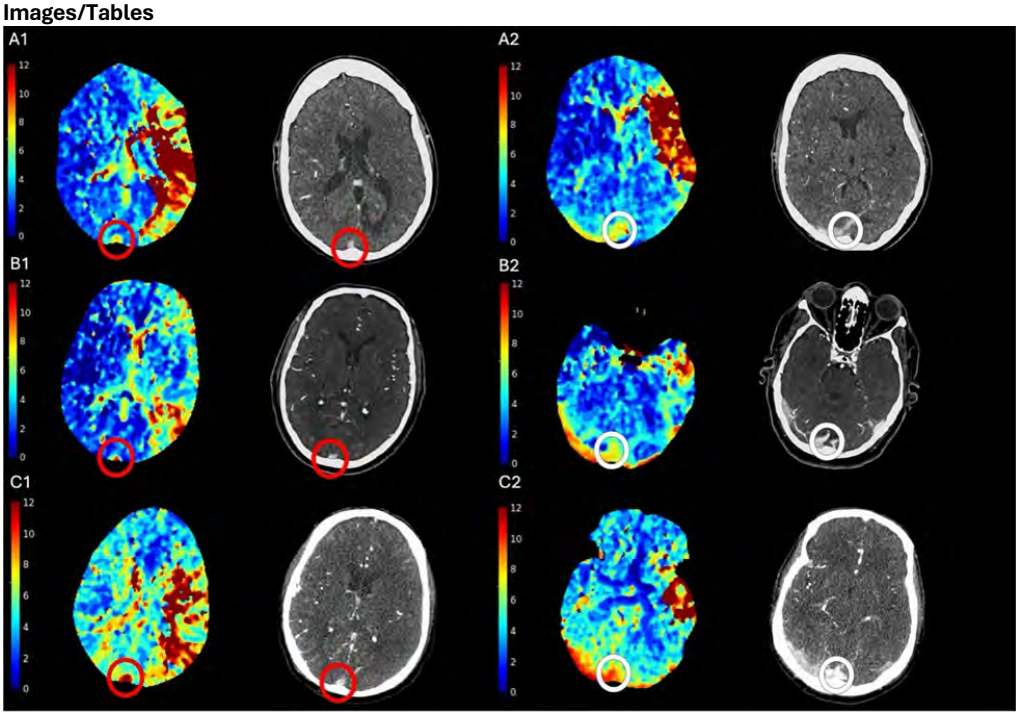

109 Redefining ischemic core, penumbra, and target mismatch on CT perfusion in acute anterior distal medium vessel occlusion

Hamza A Salim MD[1], Dhairya A Lakhani MD[2], Jay Kakadiya MD[3], Cynthia Greene MD, PhD[3], Argye E Hillis MD, PhD[4], Kambiz Nael MD[5], Jeremy J Heit MD, PhD[6], Adam A Dmytriw MD, MPH, MSc[7], Tyler McGaughey PhD[2], Max Wintermark MD[1], Tobias D Faizy MD[8], Vivek S Yedavalli MD, MS, FAHA[3]
[1]Department of Neuroradiology, MD Anderson Medical Center, Houston, TX, USA. [2]Department of Neuroradiology, West Virginia University, Morgantown, WV, USA. [3]The Russell H. Morgan Department of Radiology and Radiological Science, Johns Hopkins University School of Medicine, Baltimore, MD, USA. [4]Department of Neurology, Johns Hopkins University School of Medicine, Baltimore, MD, USA. [5]Radiology and Biomedical Imaging, University California, San Francisco, CA, USA. [6]Department of Radiology, Division of Neuroradiology and Neurointervention, Stanford University, Stanford, CA, USA. [7]Neuroendovascular Program, Massachusetts General Hospital & Brigham and Women's Hospital, Harvard Medical School, Boston, MA, USA. [8]Department of Radiology, Neuroendovascular Division, University Medical Center Münster, Münster, Münster, Germany

Purpose

Recent trials of endovascular thrombectomy (EVT) for acute distal medium vessel occlusions (DMVOs) were negative but also used inconsistent imaging-based inclusion criteria, whereas many successful large vessel occlusion (LVO) EVT trials used empirically validated CT perfusion-based target mismatch (TMM) criteria: an ischemic penumbra (time-to-maximum [Tmax] >6s) to core (relative cerebral blood flow [rCBF] <30%) mismatch ratio (MMR) ≥1.8 and volume (MMV) ≥15mL. We aimed to determine optimal corresponding definitions in DMVOs to improve patient selection for EVT.

Materials & Methods

We retrospectively analyzed patients with acute anterior DMVOs from prospectively collected databases at four comprehensive stroke centers. To assess core, we evaluated how well pretreatment rCBF <20%, <30%, <34%, and <38% volumes correlated with MRI-based posttreatment follow-up volumes (FIVs) in successfully recanalized patients. To evaluate penumbra, we assessed how well pretreatment Tmax >4s, >6s, >8s, and >10s volumes correlated with FIVs in unrecanalized patients. Then, we evaluated whether these improved parameters for core and penumbra better quantified LVO TMM and identified an optimal DMVO TMM definition.

Results

In 122 core patients, rCBF <38% most strongly correlated with FIVs (concordance correlation coefficient [CCC] 0.30 [95% CI, 0.15-0.48]), outperforming rCBF <30% (CCC 0.21 [0.10-0.35]) ($p < 0.001$). In 70 penumbra patients, Tmax >8s most strongly correlated with FIVs (CCC 0.49 [0.25-0.77]), outperforming Tmax >6s (CCC 0.39 [0.17-0.68]) ($p < 0.001$). In 180 patients undergoing EVT with Tmax >6s to rCBF <30% MMR ≥1.8 and MMV ≥15mL, recomputing MMR and MMV using Tmax >8s and rCBF <38% further separated those with favorable outcomes ($p = 0.007$). In the same cohort, Tmax >8s to rCBF <38% MMR ≥2.2 and MMV ≥10mL maximized the number of patients benefitted ($p < 0.001$, absolute risk reduction 26%).

Conclusion

In acute anterior DMVOs, rCBF <38% and Tmax >8s best correspond to ischemic core and penumbra, respectively; more favorably quantify LVO TMM; and reveal optimal TMM criteria. These results should be prospectively investigated as inclusion criteria for EVT in this population and suggest recent negative DMVO EVT trials may have been confounded by suboptimal patient selection.

References

1. Yedavalli VS, Koneru M, Hoseinyazdi M, Greene C, Lakhani DA, Xu R, Luna LP, Caplan JM, Dmytriw AA, Guenego A, Heit JJ, Albers GW, Wintermark M, Gonzalez LF, Urrutia VC, Huang J, Nael K, Leigh R, Marsh EB, Hillis AE, Llinas RH. Prolonged venous transit on perfusion imaging is associated with higher odds of mortality in successfully reperfused patients with large vessel occlusion stroke. J Neurointerv Surg. 2025 Feb 14;17(3):321-326. doi: 10.1136/jnis-2024-021488. PMID: 38471762.
2. Yedavalli V, Salim HA, Mei J, Lakhani DA, Balar A, Musmar B, Adeeb N, Hoseinyazdi M, Luna L, Deng F, Hyson NZ, Dmytriw AA, Guenego A, Faizy TD, Heit JJ, Albers GW, Lu H, Urrutia VC, Nael K, Marsh EB, Hillis AE, Llinas R. Decreased Quantitative Cerebral Blood Volume Is Associated With Poor Outcomes in Large Core Patients. Stroke. 2024 Oct;55(10):2409-2419. doi: 10.1161/STROKEAHA.124.047483. Epub 2024 Aug 26. PMID: 39185560.
3. Lakhani DA, Balar AB, Koneru M, Wen S, Ozkara BB, Caplan J, Dmytriw AA, Wang R, Lu H, Hoseinyazdi M, Nabi M, Mazumdar I, Cho A, Chen K, Sepehri S, Hyson N, Xu R, Urrutia V, Luna LP, Hillis A, Heit JJ, Albers GW, Rai AT, Faizy T, Wintermark M, Nael K, Yedavalli VS. Perfusion-Based Relative Cerebral Blood Volume Is Associated With Functional Dependence in Large-Vessel Occlusion Ischemic Stroke. J Am Heart Assoc. 2024 Dec 3;13(23):e034242. doi: 10.1161/JAHA.124.034242. Epub 2024 Nov 22. PMID: 39575711; PMCID: PMC11681566.
4. Lakhani DA, Balar AB, Koneru M, Hoseinyazdi M, Hyson N, Cho A, Greene C, Xu R, Luna L, Caplan J, Dmytriw A, Guenego A, Wintermark M, Gonzalez F, Urrutia V, Huang J, Nael K, Rai AT, Albers GW, Heit JJ, Yedavalli V. Pretreatment CT perfusion collateral parameters correlate with penumbra salvage in middle cerebral artery occlusion. J Neuroimaging. 2024 Jan-Feb;34(1):44-49. doi: 10.1111/jon.13178. Epub 2023 Dec 6. PMID: 38057941.
5. Lakhani DA, Salim H, Balar AB, Ali S, Wen S, Mei J, Hillis AE, Urrutia VC, Xu R, Broocks G, Fiehler J, Kniep HC, Stracke P, Krähling H, Albers GW, Lansberg M, Wintermark M, Heit JJ, Faizy TD, Yedavalli VS. The Cortical Vein Opacification Score (COVES) is independently associated with good and excellent functional outcomes at 90-days in minor stroke patients with anterior circulation large vessel occlusion: A Multicenter Study. AJNR Am J Neuroradiol. 2025 May 19:ajnr.A8739. doi: 10.3174/ajnr.A8739. Epub ahead of print. PMID: 40389269.

1013 Early (≤6h) vs Late (>6h – 24h) Window Thrombectomy for Acute Ischemic Stroke: A Pooled Analysis of 28,075 Patients

Ahmed Naeem[1], Omar A Mohamed[2], Sarah m Mesbah[3], Omar Rageh[4], Abdelrahman M Abdelwahab[5], Islam Nadim[6], Khaled M Hamam[7], Mai S Mohamed[5], Rahma A Ibrahim[6], Lobna A Mohamed[5], Mohamed M Wahdan[2], Max Wintermark[1]
[1]Neuroradiology Department, The University of Texas MD Anderson Cancer Center, Houston, Texas, USA. [2]Faculty of Medicine, Ain Shams University, Cairo, CAI, Egypt. [3]Faculty of Medicine, Mansoura University, Mansoura, MAN, Egypt. [4]Faculty of Medicine, Tanta University, Tanta, TAN, Egypt. [5]Faculty of Medicine, Alexandria University, Alexandria, ALEX, Egypt. [6]Faculty of Medicine, KafrElsheikh University, KafrElsheikh, KS, Egypt. [7]College of Health and Human Sciences, North Dakota State University, Fargo, North Dakota, USA

Purpose

The clinical benefit of mechanical thrombectomy (MT) for acute ischemic stroke (AIS) caused by large vessel occlusion has been well established through recent clinical trials. While the recommended time window is within six hours from symptoms onset, pushing the edges towards the

extension beyond six hours carries a potential to increase the number of eligible patients. Comparing the outcomes of late window MT with those of early window intervention remains a matter of clinical importance [1-2].

Materials & Methods

A systematic literature review and meta-analysis was conducted including studies comparing late (>6h - 24h) versus early (≤ 6h) MT for AIS patient. Outcomes analyzed were functional independence (modified Rankin Scale [mRS] 0–2), successful recanalization (defined as a score of 2b or higher on the Thrombolysis in Cerebral Infarction (TICI) scale), 90-day mortality, and symptomatic ICH (sICH). Pooled odds ratios (ORs) with 95% confidence intervals (CIs) were calculated using fixed- or random-effects models according to heterogeneity.

Results

Seventeen studies with a total of 28,075 patients, were included in our analysis. Compared to early window MT, late window was significantly associated with lower odds of achieving functional independence (OR, 0.81; 95%CI [0.77, 0.86]; P=0.00; I^2= 36.8%) (Figure A). However, we found no significant differences between either groups in sICH (OR, 1.01; 95%CI [0.91, 1.13]; P=0.80; I^2= 16.5%) (Figure B), 90-day mortality (OR, 1.00; 95%CI [0.93, 1.08]; P=0.95; I^2= 22.1%) (Figure C), and successful recanalization (OR, 0.91; 95%CI [0.66, 1.25]; P=0.55; I^2= 92.8%) (Figure D).

Conclusion

Although patients treated with MT in the late window (6–24h) achieve less favorable functional outcomes compared with early intervention, late thrombectomy does not increase mortality or hemorrhagic complications, underscoring its safety in carefully selected patients. These findings highlight that while earlier treatment maximizes recovery potential, future research on late window thrombectomy remains highly warranted.

References

1. Nogueira RG, Jadhav AP, Haussen DC, et al., DAWN Trial Investigators. Thrombectomy 6 to 24 Hours after Stroke with a Mismatch between Deficit and Infarct. N Engl J Med. 2018 Jan 4;378(1):11-21. doi: 10.1056/NEJMoa1706442.
2. Albers GW, Marks MP, Kemp S, et al., Thrombectomy for Stroke at 6 to 16 Hours with Selection by Perfusion Imaging. N Engl J Med. 2018 Feb 22;378(8):708-718. doi: 10.1056/NEJMoa1713973

Images/Tables

A)

Study	Late Window [>6h–24h] Events	Late Window [>6h–24h] Total	Early Window [<6h] Events	Early Window [<6h] Total	OR	95%–CI	P–value
Motyer 2017	32	74	130	281	0.88	[0.53; 1.48]	0.6427
Asdaghi 2023	954	2742	2040	5260	0.84	[0.76; 0.93]	0.0005
Bhan 2020	27	82	55	82	0.24	[0.13; 0.46]	< 0.0001
Castillo 2023	115	241	126	280	1.12	[0.79; 1.58]	0.5351
Huang 2021	22	64	85	230	0.89	[0.50; 1.60]	0.7043
Jahan 2019	134	691	1091	4643	0.78	[0.64; 0.96]	0.0169
Peretz 2019	21	81	71	218	0.72	[0.41; 1.28]	0.2698
Hendrix 2021	38	112	51	112	0.61	[0.36; 1.05]	0.0767
Nogueira 2021	129	256	406	705	0.75	[0.56; 1.00]	0.0474
Sadeler 2024	593	1580	2511	5936	0.82	[0.73; 0.92]	0.0006
Wali 2024	911	2437	2900	6876	0.82	[0.74; 0.90]	< 0.0001
T. Mierzwa 2024	60	189	74	216	0.89	[0.59; 1.35]	0.5918
Elawady 2024	16	84	12	84	1.41	[0.62; 3.20]	0.4090
Coutinho 2024	19	45	45	110	1.06	[0.52; 2.13]	0.8802
Meinel 2019	135	393	463	1068	0.68	[0.54; 0.87]	0.0020
Shi 2025	55	131	56	111	0.71	[0.43; 1.18]	0.1884
Fixed effects model (p = 0.00)		**9202**		**26212**	**0.81**	**[0.77; 0.86]**	

Heterogeneity: $I^2 = 36.8\%$, $\tau^2 < 0.0001$, $p = 0.0697$

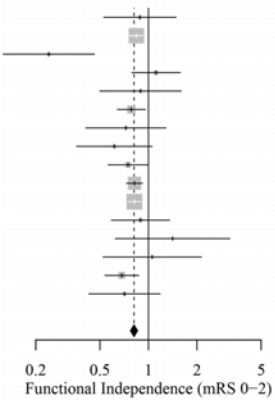

B)

Study	Late Window [>6h–24h] Events	Late Window [>6h–24h] Total	Early Window [<6h] Events	Early Window [<6h] Total	OR	95%–CI	P–value
Motyer 2017	6	74	16	281	1.46	[0.55; 3.88]	0.4458
Asdaghi 2023	132	2742	274	5260	0.92	[0.74; 1.14]	0.4448
Castillo 2023	10	268	16	311	0.71	[0.32; 1.60]	0.4148
Huang 2021	5	67	16	238	1.12	[0.39; 3.17]	0.8327
Jahan 2019	71	845	378	5905	1.34	[1.03; 1.75]	0.0295
Hendrix 2021	7	112	6	112	1.18	[0.38; 3.62]	0.7753
Nogueira 2021	2	257	12	709	0.46	[0.10; 2.05]	0.3055
Sadeler 2024	106	1589	369	5936	1.08	[0.86; 1.35]	0.5082
Wali 2024	113	2437	301	6876	1.06	[0.85; 1.33]	0.5936
T. Mierzwa 2024	10	189	15	216	0.75	[0.33; 1.71]	0.4916
Elawady 2024	9	84	19	84	0.41	[0.17; 0.97]	0.0424
Coutinho 2024	3	45	11	110	0.64	[0.17; 2.42]	0.5139
Meinel 2019	21	393	73	1068	0.77	[0.47; 1.27]	0.3040
Fixed effects model (p = 0.80)		**9102**		**27106**	**1.01**	**[0.91; 1.13]**	

Heterogeneity: $I^2 = 16.5\%$, $\tau^2 = 0.0106$, $p = 0.2774$

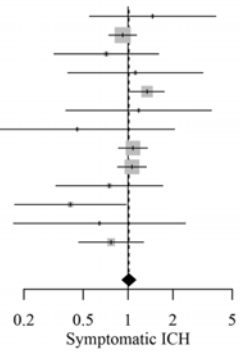

C)

Study	Late Window [>6h–24h] Events	Late Window [>6h–24h] Total	Early Window [<6h] Events	Early Window [<6h] Total	OR	95%–CI	P–value
Motyer 2017	13	74	65	281	0.71	[0.37; 1.37]	0.3054
Castillo 2023	47	268	44	311	1.29	[0.82; 2.02]	0.2646
Jahan 2019	164	851	1162	5905	0.97	[0.81; 1.17]	0.7800
Hendrix 2021	19	112	29	112	0.58	[0.31; 1.12]	0.1055
Nogueira 2021	27	256	68	705	1.10	[0.69; 1.77]	0.6790
Sadeler 2024	268	1580	958	5936	1.06	[0.91; 1.23]	0.4313
Wali 2024	514	2437	1442	6876	1.01	[0.90; 1.13]	0.9005
Elawady 2024	33	84	39	84	0.75	[0.40; 1.38]	0.3500
Coutinho 2024	4	45	21	110	0.41	[0.13; 1.28]	0.1260
Meinel 2019	84	393	209	1068	1.12	[0.84; 1.49]	0.4450
Shi 2025	13	131	20	111	0.50	[0.24; 1.06]	0.0711
Fixed effects model (p = 0.95)		**6231**		**21499**	**1.00**	**[0.93; 1.08]**	

Heterogeneity: $I^2 = 22.1\%$, $\tau^2 < 0.0001$, $p = 0.2327$

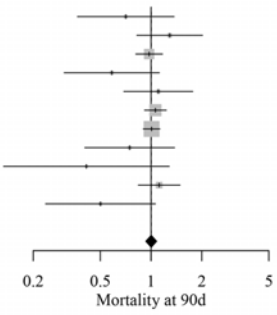

C)

Study	Late Window [>6h–24h] Events	Late Window [>6h–24h] Total	Early Window [<6h] Events	Early Window [<6h] Total	OR	95%–CI	P–value
Motyer 2017	57	74	228	281	0.78	[0.42; 1.45]	0.4298
Bhan 2020	68	88	124	147	0.63	[0.32; 1.23]	0.1763
Castillo 2023	230	268	275	311	0.79	[0.49; 1.29]	0.3502
Huang 2021	55	67	202	238	0.82	[0.40; 1.67]	0.5808
Jahan 2019	684	791	3426	5533	3.93	[3.18; 4.85]	< 0.0001
Maslias 2021	178	193	432	465	0.91	[0.48; 1.71]	0.7618
Peretz 2019	51	81	155	218	0.69	[0.40; 1.18]	0.1778
Hendrix 2021	104	112	106	112	0.74	[0.25; 2.19]	0.5821
Nogueira 2021	246	257	654	709	1.88	[0.97; 3.65]	0.0621
Sadeler 2024	745	1580	2878	5936	0.95	[0.85; 1.06]	0.3464
T. Mierzwa 2024	149	189	180	216	0.74	[0.45; 1.23]	0.2484
Elawady 2024	67	84	65	84	1.15	[0.55; 2.41]	0.7070
Coutinho 2024	36	45	91	110	0.84	[0.35; 2.02]	0.6890
Meinel 2019	316	393	961	1068	0.46	[0.33; 0.63]	< 0.0001
Shi 2025	119	131	107	111	0.37	[0.12; 1.18]	0.0940
Random effects model (p = 0.55)		**4353**		**15539**	**0.91**	**[0.66; 1.25]**	

Heterogeneity: $I^2 = 92.8\%$, $\tau^2 = 0.2935$, $p < 0.0001$

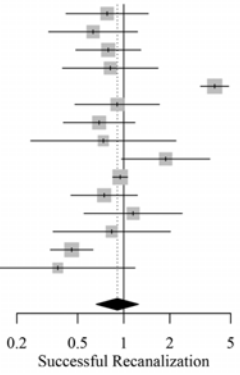

761 Hyperattenuating Clot Length Modifies First Pass Effect in Mechanical Thrombectomy for Large Vessel Occlusive Acute Ischemic Stroke

Miranda R Gonzales B.S.[1], Revyn Kim B.S.[1], Gnaneswari Karayi B.A.[1], David S Hong B.A.[1], Lulu Bi B.S.[1], Krisztina Moldovan M.D.[2], Radmehr Torabi M.D.[2], Elias Shaaya M.D.[2], Grayson Baird Ph.D.[2], Mahesh V Jayaraman M.D.[2], Dylan N Wolman M.D.[2]

[1]The Warren Alpert Medical School of Brown University, Providence, Rhode Island, USA. [2]Brown University Health, Providence, Rhode Island, USA

Purpose

Non-contrast CT (NCCT) is the most common initial imaging in the triage of acute ischemic stroke (AIS), and approximately ⅔ of large vessel occlusions (LVO) are hyperattenuating and measurable on NCCT. Mechanical thrombectomy (MT) is the standard of care AIS-LVO treatment, but disagreement on the most effective first-line thrombectomy technique remains, typically either aspiration (ADAPT) or combined stent-retriever/aspiration (CAPTIVE).[1,2] We hypothesize that increasing clot length will modify first pass efficacy (FPE) and neurologic outcomes as a function of initial thrombectomy technique.

Materials & Methods

We performed a retrospective cohort analysis of consecutive patients who underwent MT for AIS-LVO from 2022-2024 at our comprehensive stroke center. Inclusion criteria were anterior or posterior circulation LVO (ICA terminus, M1 MCA, proximal dominant M2 MCA, and basilar artery occlusions) with hyperattenuating target thrombi visible on initial NCCT. Preprocedural NCCTs were manually reviewed for the presence of hyperattenuating thrombi, and clot length and attenuation values were measured. Patients were excluded if they had no visible hyperattenuating thrombus on NCCT, or if initial NCCT was technically inadequate or follow-up data was unavailable. The primary outcome measure was FPE, defined as achieving modified Thrombolysis in Cerebral Infarction (mTICI) ≥2c reperfusion after a single pass. Secondary outcome measures included 90-day modified Rankin scale (mRS) scores and safety metrics, such as symptomatic intracranial hemorrhage (sICH). Generalized linear modeling was used to examine outcomes with binary (1/0) and Poisson (number of passes) distributions as a main effect and interaction effect (when appropriate).

Results

Eight-hundred forty-eight patients were screened, with 512 included. Patient demographics are summarized in Table 1. There was no evidence of a relationship between the likelihood of achieving FPE when using CAPTIVE as the first line technique (OR 1.009, 95%CI 0.976-1.042; p>0.05), however, there was a significant negative association between increasing clot length and likelihood of FPE with ADAPT (OR 0.935, 95%CI 0.889-0.984; p<0.05), with an inflection toward lower FPE likelihood at approximately 16 mm (Figure 1). For every 1 mm increase in clot length, the probability of achieving FPE with ADAPT decreased by 6.5%. Beyond the approximate threshold length, the use of CAPTIVE had a higher likelihood of FPE than ADAPT (p=0.014). Accordingly, ADAPT correlated with lower 90-day median mRS (3 [IQR 6-1], p=<0.001) for patients with shorter clots, while the use of CAPTIVE correlated with lower mRS scores for patients with longer clots (Figure 2).

Conclusion

For AIS-LVO patients with hyperattenuating thrombi on initial NCCT, increasing visible clot length was correlated with a lower likelihood of FPE with ADAPT while FPE was not significantly modified by clot length when CAPTIVE was selected as the first line technique. Below a threshold value of approximately 16 mm, ADAPT was associated with superior 90d neurologic outcomes, while CAPTIVE was associated with superior outcomes above the threshold value. Optimal first-line MT technique choice may be informed by clot length.

References

1. Munoz A, Jabre R, Orenday-Barraza JM, et al. A review of mechanical thrombectomy techniques for acute ischemic stroke. Interv Neuroradiol. 2023;29(4):450-458. doi:10.1177/15910199221084481

2. McTaggart RA, Tung EL, Yaghi S, et al. Continuous aspiration prior to intracranial vascular embolectomy (CAPTIVE): A technique which improves outcomes. J Neurointervent Surg. 2017;9(12):1154-1159. doi:10.1136/neurintsurg-2016-012838

Images/Tables

	ADAPT	CAPTIVE
Mean Age ± SD (years)	69.4±15.13	73.23±13.44
% Female	89/203 (43.84%)	155/309 (50.16 %)
ICA Occlusions	29/203 (14.29%)	68/309 (22.01%)
M1 Occlusions	96/203 (47.29%)	186/309 (60.19%)
M2 Occlusions	48/309 (23.65%)	46/309 (14.89%)
Basilar Occlusions	30/203 (14.78%)	9/309 (2.91%)
Initial NIHSS (Median [IQR])	15 (IQR 9-21.5)	17 (IQR 12-22)
Mean Clot Length ± SD (mm)	10.72±6.09	13.17±6.85
Mean Clot NCCT HU ± SD	52.86±14.25	54.83±30.06
# of Passes (Median [IQR])	2 (IQR 1-3)	1 (IQR 1-2)
sICH	16/203 (7.88%)	33/309 (10.68%)
Prior Stroke	53/203 (25.62%)	81/309 (26.21%)
Diabetes	74/203 (36.45%)	88/309 (28.48%)
HTN	164/203 (80.79%)	257/309 (83.17%)
Hyperlipdemia	164/203 (80.79%)	250/309 (80.91%)
CAD	38/203 (18.72%)	93/309 (30.1%)
Atrial Fibrillation	92/203 (45.32%)	137/309 (44.34%)
Smoking (within past year)	41/203 (20.2%)	55/309 (17.8%)
Cancer	36/203 (17.73%)	86/309 (27.83%)

Table 1

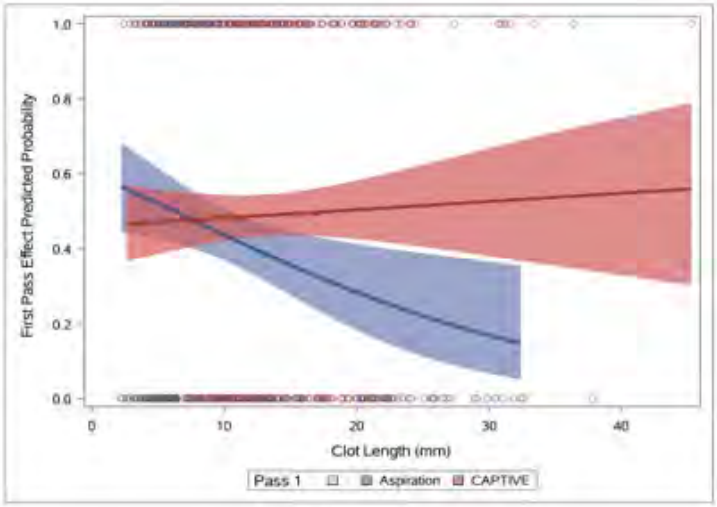

Figure 1

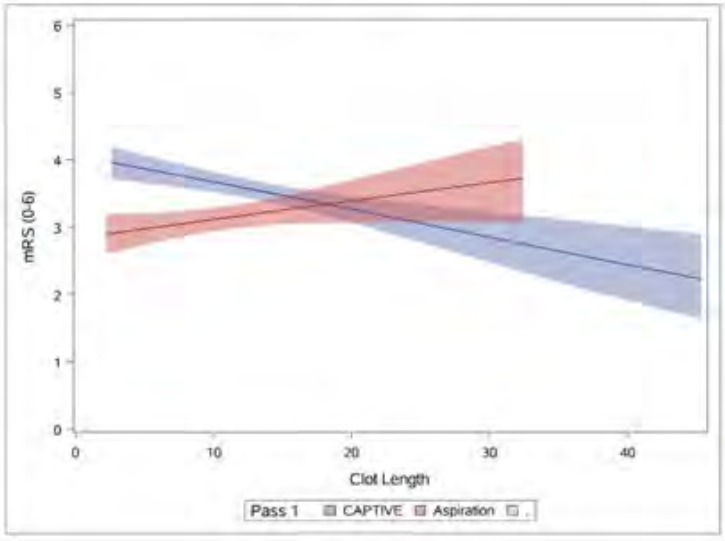

Figure 2

108 Ischemic Lesion Net Water Uptake Outperforms ASPECTS and CBF<30% in Predicting Futile Recanalization After Mechanical Thrombectomy

Hamza A Salim MD[1], Dhairya A Lakhani MD[2], Jay Kakadiya MD[3], Cynthia Greene MD, PhD[3], Argye E Hillis MD, PhD[4], Kambiz Nael MD[5], Jeremy J Heit MD, PhD[6], Adam A Dmytriw MD, MPH, MSc[7], Tyler McGaughey PhD[2], Max Wintermark MD[1], Vivek S Yedavalli MD, MS, FAHA[3], Tobias D Faizy MD[8]
[1]Department of Neuroradiology, MD Anderson Medical Center, Houston, TX, USA. [2]Department of Neuroradiology, West Virginia University, Morgantown, WV, USA. [3]The Russell H. Morgan Department of Radiology and Radiological Science, Johns Hopkins University School of Medicine, Baltimore, MD, USA. [4]Department of Neurology, Johns Hopkins University School of Medicine, Baltimore, MD, USA. [5]Radiology and Biomedical Imaging, University California, San Francisco, CA, USA. [6]Department of Radiology, Division of Neuroradiology and Neurointervention, Stanford University, Stanford, CA, USA. [7]Neuroendovascular Program, Massachusetts General Hospital & Brigham and Women's Hospital, Harvard Medical School, Boston, MA, USA. [8]Department of Radiology, Neuroendovascular Division, University Medical Center Münster, Münster, Münster, Germany

Purpose

Ischemic lesion net water uptake (NWU), a biomarker of cerebral edema, has been associated with poor outcomes in acute ischemic stroke due to large vessel occlusion (AIS-LVO). This study evaluates whether NWU more accurately predicts futile recanalization (FR)—defined as poor functional outcome despite successful endovascular thrombectomy (EVT)—compared to other biomarkers of ischemic injury, including the Alberta Stroke Program Early CT Score (ASPECTS) and CT perfusion (CTP)-derived ischemic core volume.

Materials & Methods

We conducted a retrospective analysis of AIS-LVO patients who achieved successful recanalization via EVT at two comprehensive stroke centers. NWU and ASPECTS were measured on admission CT head; ischemic core volume was quantified as relative cerebral blood flow <30% (rCBF<30%) on CTP. Futile recanalization (FR) was defined as a 90-day modified Rankin Scale (mRS) score of 3–6. Logistic regression and receiver operating characteristic (ROC) curve analyses were performed.

Results

A total of 530 patients were included. NWU and rCBF<30% were significantly higher in patients with FR compared to those with good outcomes (median NWU: 7.77% vs. 2.75%; p<0.001; rCBF<30%: 17.0 mL vs. 3.0 mL; p<0.001). NWU (adjusted OR 1.72, 95% CI: 1.53–1.94, p<0.001), rCBF<30% (adjusted OR 1.01, 95% CI: 1.00–1.02, p<0.01), and ASPECTS (adjusted OR 0.79, 95% CI: 0.69–0.90, p<0.001) were independently associated with FR. NWU demonstrated significantly superior predictive performance (AUC=0.89) compared to rCBF<30% (AUC=0.66) and ASPECTS (AUC=0.65).

Conclusion

NWU is a strong, non-invasive biomarker of futile recanalization, outperforming rCBF<30% and ASPECTS in AIS-LVO.

References

1. Yedavalli VS, Koneru M, Hoseinyazdi M, Greene C, Lakhani DA, Xu R, Luna LP, Caplan JM, Dmytriw AA, Guenego A, Heit JJ, Albers GW, Wintermark M, Gonzalez LF, Urrutia VC, Huang J, Nael K, Leigh R, Marsh EB, Hillis AE, Llinas RH. Prolonged venous transit on perfusion imaging is associated with higher odds of mortality in successfully reperfused patients with large vessel occlusion stroke. J Neurointerv Surg. 2025 Feb 14;17(3):321-326. doi: 10.1136/jnis-2024-021488. PMID: 38471762.
2. Yedavalli V, Salim HA, Mei J, Lakhani DA, Balar A, Musmar B, Adeeb N, Hoseinyazdi M, Luna L, Deng F, Hyson NZ, Dmytriw AA, Guenego A, Faizy TD, Heit JJ, Albers GW, Lu H, Urrutia VC, Nael K, Marsh EB, Hillis AE, Llinas R. Decreased Quantitative Cerebral Blood Volume Is Associated With Poor Outcomes in Large Core Patients. Stroke. 2024 Oct;55(10):2409-2419. doi: 10.1161/STROKEAHA.124.047483. Epub 2024 Aug 26. PMID: 39185560.
3. Lakhani DA, Balar AB, Koneru M, Wen S, Ozkara BB, Caplan J, Dmytriw AA, Wang R, Lu H, Hoseinyazdi M, Nabi M, Mazumdar I, Cho A, Chen K, Sepehri S, Hyson N, Xu R, Urrutia V, Luna LP, Hillis A, Heit JJ, Albers GW, Rai AT, Faizy T, Wintermark M, Nael K, Yedavalli VS. Perfusion-Based Relative Cerebral Blood Volume Is Associated With Functional Dependence in Large-Vessel Occlusion Ischemic Stroke. J Am Heart Assoc. 2024 Dec 3;13(23):e034242. doi: 10.1161/JAHA.124.034242. Epub 2024 Nov 22. PMID: 39575711; PMCID: PMC11681566.
4. Lakhani DA, Balar AB, Koneru M, Hoseinyazdi M, Hyson N, Cho A, Greene C, Xu R, Luna L, Caplan J, Dmytriw A, Guenego A, Wintermark M, Gonzalez F, Urrutia V, Huang J, Nael K, Rai AT, Albers GW, Heit JJ, Yedavalli V. Pretreatment CT perfusion collateral parameters correlate with penumbra salvage in middle cerebral artery occlusion. J Neuroimaging. 2024 Jan-Feb;34(1):44-49. doi: 10.1111/jon.13178. Epub 2023 Dec 6. PMID: 38057941.
5. Lakhani DA, Salim H, Balar AB, Ali S, Wen S, Mei J, Hillis AE, Urrutia VC, Xu R, Broocks G, Fiehler J, Kniep HC, Stracke P, Krähling H, Albers GW, Lansberg M, Wintermark M, Heit JJ, Faizy TD, Yedavalli VS. The Cortical Vein Opacification Score (COVES) is independently associated with good and excellent functional outcomes at 90-days in minor stroke patients with anterior circulation large vessel occlusion: A Multicenter Study. AJNR Am J Neuroradiol. 2025 May 19:ajnr.A8739. doi: 10.3174/ajnr.A8739. Epub ahead of print. PMID: 40389269.

Images/Tables

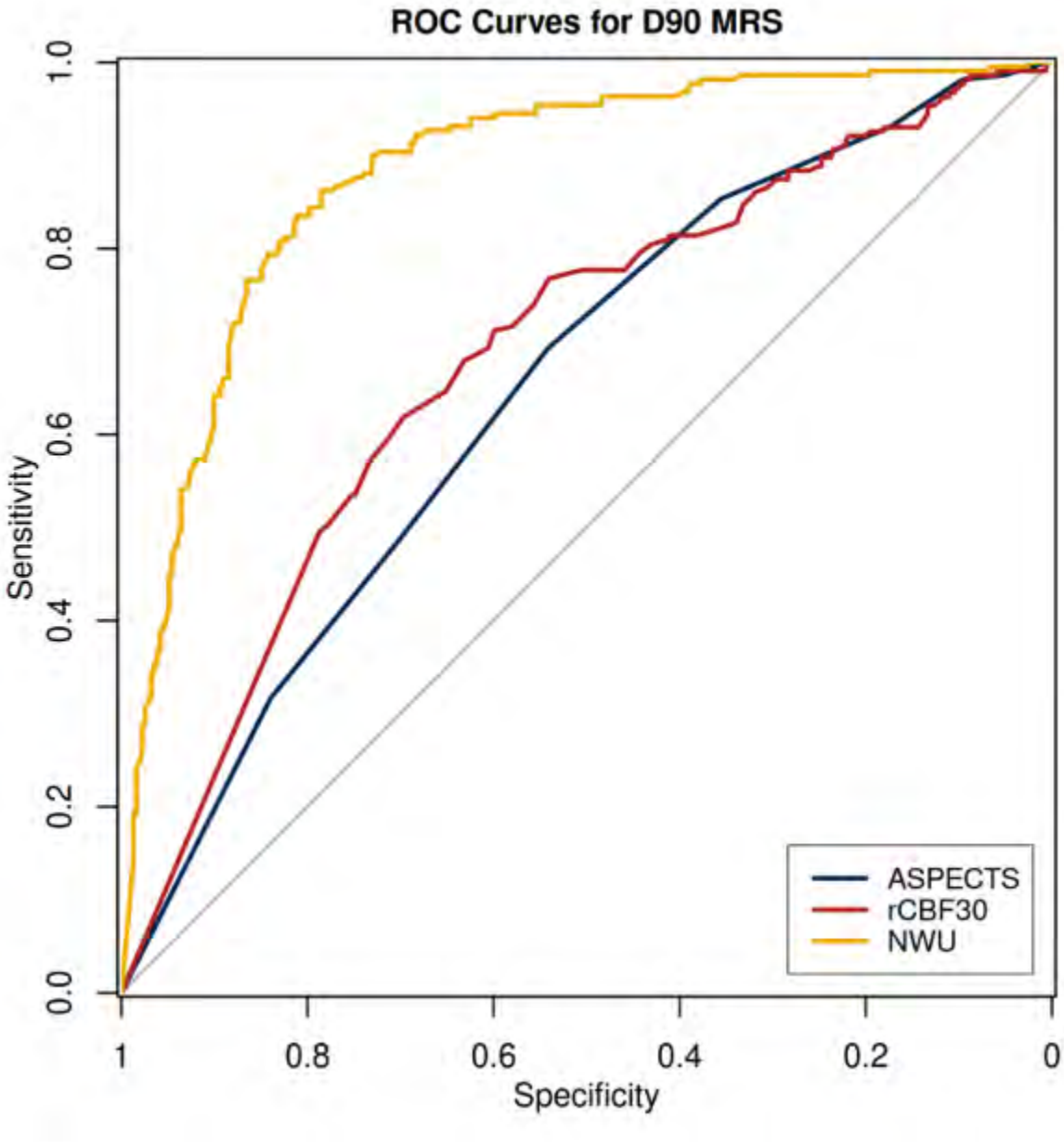

99 Prolonged Venous Transit Is Associated with Unfavorable Functional Outcomes in Large Core Stroke

Hamza A Salim MD[1], Dhairya A Lakhani MD[2], Jay Kakadiya MD[3], Argye E Hillis MD, PhD[4], Kambiz Nael MD[5], Tyler McGaughey PhD[2], Adam A Dmytriw MD, MPH, MSc[6], Jeremy J Heit MD, PhD[7], Tobias D Faizy MD[8], Max Wintermark MD[1], Vivek S Yedavalli MD, MS, FAHA[3]

[1]Department of Neuroradiology, MD Anderson Medical Center, Houston, TX, USA. [2]Department of Neuroradiology, West Virginia University, Morgantown, WV, USA. [3]The Russell H. Morgan Department of Radiology and Radiological Science, Johns Hopkins University School of Medicine, Baltimore, MD, USA. [4]Department of Neurology, Johns Hopkins University School of Medicine, Baltimore, MD, USA. [5]Radiology and Biomedical Imaging, University California, San Francisco, CA, USA. [6]Neuroendovascular Program, Massachusetts General Hospital & Brigham and Women's Hospital, Harvard Medical School, Boston, MA, USA. [7]Department of Radiology, Division of Neuroradiology and Neurointervention, Stanford University, Stanford, CA, USA. [8]Department of Radiology, Neuroendovascular Division, University Medical Center Münster, Munster, Munster, Germany

Purpose

Large core acute ischemic stroke (AIS) caused by large vessel occlusion (LVO) is associated with high rates of disability despite mechanical thrombectomy (MT) treatment. Recent studies suggest that prolonged venous transit (PVT) may indicate impaired venous drainage, influencing functional outcomes. However, its prognostic value in large core AIS-LVO patients remains unclear.

Materials & Methods

We conducted a retrospective cohort study using data from consecutive patients with AIS-LVO and large ischemic core volumes (ASPECTS <6 or relative cerebral blood flow < 30% volume ≥50 mL; per SELECT-2 trial definition) between September 1, 2016 and September 2, 2024. The primary outcome was unfavorable functional recovery at 83 90 days, defined as a modified Rankin Scale (mRS) score of 4-6.

Results

100 patients met inclusion criteria, and 41 (41%) had PVT. Unfavorable functional outcomes were more frequent in the PVT+ group (59% vs. 37%, p=0.036). Multivariable analysis confirmed that PVT was independently associated with unfavorable outcomes (adjusted OR 4.07, 95% CI 1.15-14.4, p=0.03), even after accounting for penumbra size (Tmax >6s) and large core volumes (rCBF <30%). Other predictors included older age (adjusted OR

1.07, 95% CI 1.02 to 1.11, P=0.003), higher admission NIHSS (adjusted OR 1.16, 95% 89 CI 1.05 to 1.29, P=0.005), and larger rCBF <30% volume (adjusted OR 1.02, 95% CI 1.00 to 1.04, P=0.032).

Conclusion

PVT is independently associated with unfavorable outcomes in patients with large core AIS-LVO.These findings suggest PVT may serve as a prognostic marker, warranting further investigation in larger prospective studies to guide treatment decisions in this high-risk population.

References

1. Yedavalli VS, Koneru M, Hoseinyazdi M, Greene C, Lakhani DA, Xu R, Luna LP, Caplan JM, Dmytriw AA, Guenego A, Heit JJ, Albers GW, Wintermark M, Gonzalez LF, Urrutia VC, Huang J, Nael K, Leigh R, Marsh EB, Hillis AE, Llinas RH. Prolonged venous transit on perfusion imaging is associated with higher odds of mortality in successfully reperfused patients with large vessel occlusion stroke. J Neurointerv Surg. 2025 Feb 14;17(3):321-326. doi: 10.1136/jnis-2024-021488. PMID: 38471762.
2. Yedavalli V, Salim HA, Mei J, Lakhani DA, Balar A, Musmar B, Adeeb N, Hoseinyazdi M, Luna L, Deng F, Hyson NZ, Dmytriw AA, Guenego A, Faizy TD, Heit JJ, Albers GW, Lu H, Urrutia VC, Nael K, Marsh EB, Hillis AE, Llinas R. Decreased Quantitative Cerebral Blood Volume Is Associated With Poor Outcomes in Large Core Patients. Stroke. 2024 Oct;55(10):2409-2419. doi: 10.1161/STROKEAHA.124.047483. Epub 2024 Aug 26. PMID: 39185560.
3. Lakhani DA, Balar AB, Koneru M, Wen S, Ozkara BB, Caplan J, Dmytriw AA, Wang R, Lu H, Hoseinyazdi M, Nabi M, Mazumdar I, Cho A, Chen K, Sepehri S, Hyson N, Xu R, Urrutia V, Luna LP, Hillis A, Heit JJ, Albers GW, Rai AT, Faizy T, Wintermark M, Nael K, Yedavalli VS. Perfusion-Based Relative Cerebral Blood Volume Is Associated With Functional Dependence in Large-Vessel Occlusion Ischemic Stroke. J Am Heart Assoc. 2024 Dec 3;13(23):e034242. doi: 10.1161/JAHA.124.034242. Epub 2024 Nov 22. PMID: 39575711; PMCID: PMC11681566.
4. Lakhani DA, Balar AB, Koneru M, Hoseinyazdi M, Hyson N, Cho A, Greene C, Xu R, Luna L, Caplan J, Dmytriw A, Guenego A, Wintermark M, Gonzalez F, Urrutia V, Huang J, Nael K, Rai AT, Albers GW, Heit JJ, Yedavalli V. Pretreatment CT perfusion collateral parameters correlate with penumbra salvage in middle cerebral artery occlusion. J Neuroimaging. 2024 Jan-Feb;34(1):44-49. doi: 10.1111/jon.13178. Epub 2023 Dec 6. PMID: 38057941.
5. Lakhani DA, Salim H, Balar AB, Ali S, Wen S, Mei J, Hillis AE, Urrutia VC, Xu R, Broocks G, Fiehler J, Kniep HC, Stracke P, Krähling H, Albers GW, Lansberg M, Wintermark M, Heit JJ, Faizy TD, Yedavalli VS. The Cortical Vein Opacification Score (COVES) is independently associated with good and excellent functional outcomes at 90-days in minor stroke patients with anterior circulation large vessel occlusion: A Multicenter Study. AJNR Am J Neuroradiol. 2025 May 19:ajnr.A8739. doi: 10.3174/ajnr.A8739. Epub ahead of print. PMID: 40389269.

Images/Tables

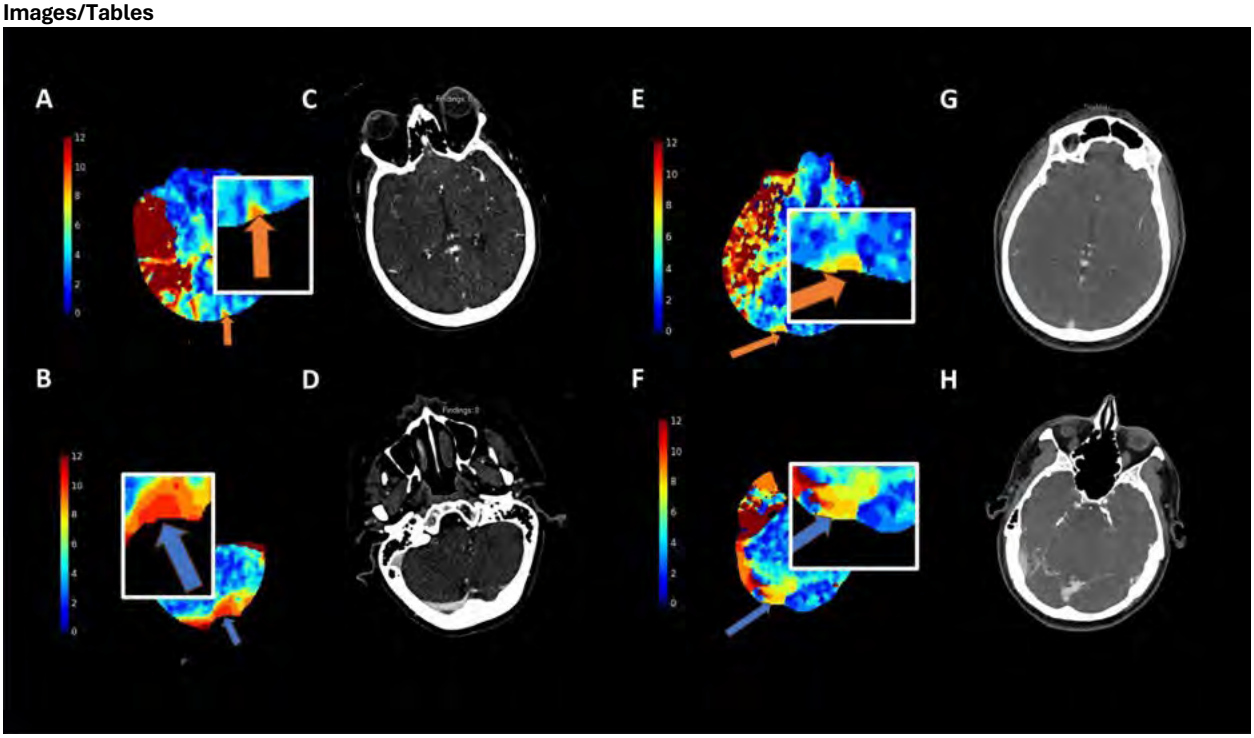

---

306 Association of evolving thrombectomy device and technique selection on angiographic reperfusion at a single, large-volume stroke center over 10-years

David S. Hong BA[1], Revyn Kim BS[1], Gnaneswari Karayi BA[1], Lulu Bi BS[1], Miranda Gonzales BS[1], Joshua Feler MD MS[2], Krisztina Moldovan MD[2], Radmehr Torabi MD[2], Elias Shaaya MD[2], Vivek Yedavalli MD[3], Mahesh Jayaraman MD[2], Dylan N. Wolman MD[2]

[1]The Warren Alpert Medical School of Brown University, Providence, RI, USA. [2]Brown University Health, Providence, RI, USA. [3]Johns Hopkins School of Medicine, Baltimore, MD, USA

Purpose

Contact aspiration (ADAPT) and combined stent-retriever and aspiration (CAPTIVE) are common mechanical thrombectomy (MT) techniques for treatment of large-vessel occlusive acute ischemic stroke (LVO-AIS), but optimal first-line technique and equipment choices remain subjects of debate.[1–3] This study evaluates technical effectiveness over a decade of evolving MT practice at a single center to evaluate performance differences among progressive generations of aspiration catheters for both ADAPT and CAPTIVE. We hypothesized that newer-generation catheters would achieve superior first-pass efficacy, and that technique switching after an unsuccessful first-pass would be more likely to achieve excellent final reperfusion.

Materials & Methods

We performed a retrospective review of a prospectively maintained thrombectomy registry at a single, high-volume comprehensive stroke center from February 2015 to July 2025. Consecutive patients with LVO-AIS involving the ICA terminus, M1 and proximal M2 segments of the middle cerebral artery, basilar artery, or P1 segment of the posterior cerebral artery were included. We excluded cases with insufficient procedural or outcome data and tandem cervical-anterior occlusions or distal occlusions. Equipment choice and first-pass technique were at the discretion of the operating neurointerventionalist**,** of which 7 were included. Aspiration catheters were included only if used >10 times, and were defined as "large" if 6-French equivalent, or "small" if 5-French equivalent. Aspiration catheter, technique choice, and resultant mTICI were collected for each pass.

The primary outcome measure was First-Pass Effect (FPE), defined as achieving mTICI 2c or 3 on the first pass. Secondary outcomes included modified FPE (mFPE) (defined as mTICI 2b-3 on first pass), adequate final reperfusion (final mTICI 2b-3), excellent final reperfusion (final mTICI 2c-3), total number of passes, crossover to alternative techniques, and 90-day modified Rankin Scale (mRS). All modeling was conducted using SAS Software 9.4 (Cary, NC). All modeling was accomplished with the GLIMMIX procedure using generalized estimating equations where observations were nested within radiologist assuming a binary or Poisson distribution with classic sandwich estimation. Alpha was established a priori at the 0.05 level and all interval estimates were calculated for 95% confidence.

Results

Among 3,669 MT cases, 1,926 were included (mean age: 72.0±14.8, 51.5% female). Among large aspiration catheters (n=1,330), FPE was not significantly more likely for first-pass CAPTIVE technique compared to ADAPT (p=0.184). However, mFPE was significantly more likely when using CAPTIVE as the first-line technique (p=0.026). Among large aspiration catheters, irrespective of first-line technique, the 6F-Sofia outperformed previous generation and contemporary catheters in achieving FPE (OR 1.46, 95%CI [1.19, 1.79]; p=0.002). Furthermore, the 6F-Sofia was associated with increased odds of achieving excellent final reperfusion (OR 4.38, 95%CI [3.38, 5.67]; p<0.001). Crossover from first-pass ADAPT to second-pass CAPTIVE demonstrated improved likelihood of achieving excellent reperfusion on the second pass (p=0.002). While 90d-mRS was not significantly different by technique or equipment selection, it remained relatively flat despite more inclusive selection criteria over time (slope = 0.044, mean = 3.47).

Conclusion

Within our 10-year cohort, we found that more deliverable catheters and use of CAPTIVE was associated with an increased likelihood of FPE.

References

1. Lapergue B, Blanc R, Gory B, et al. Effect of Endovascular Contact Aspiration vs Stent Retriever on Revascularization in Patients With Acute Ischemic Stroke and Large Vessel Occlusion: The ASTER Randomized Clinical Trial. *JAMA*. 2017;318(5):443-452. doi:10.1001/jama.2017.9644

2. Turk AS, Siddiqui A, Fifi JT, et al. Aspiration thrombectomy versus stent retriever thrombectomy as first-line approach for large vessel occlusion (COMPASS): a multicentre, randomised, open label, blinded outcome, non-inferiority trial. *Lancet*. 2019;393(10175):998-1008. doi:10.1016/S0140-6736(19)30297-1

3. Lapergue B, Blanc R, Costalat V, et al. Effect of Thrombectomy With Combined Contact Aspiration and Stent Retriever vs Stent Retriever Alone on Revascularization in Patients With Acute Ischemic Stroke and Large Vessel Occlusion: The ASTER2 Randomized Clinical Trial. *JAMA*. 2021;326(12):1158-1169. doi:10.1001/jama.2021.13827

Images/Tables

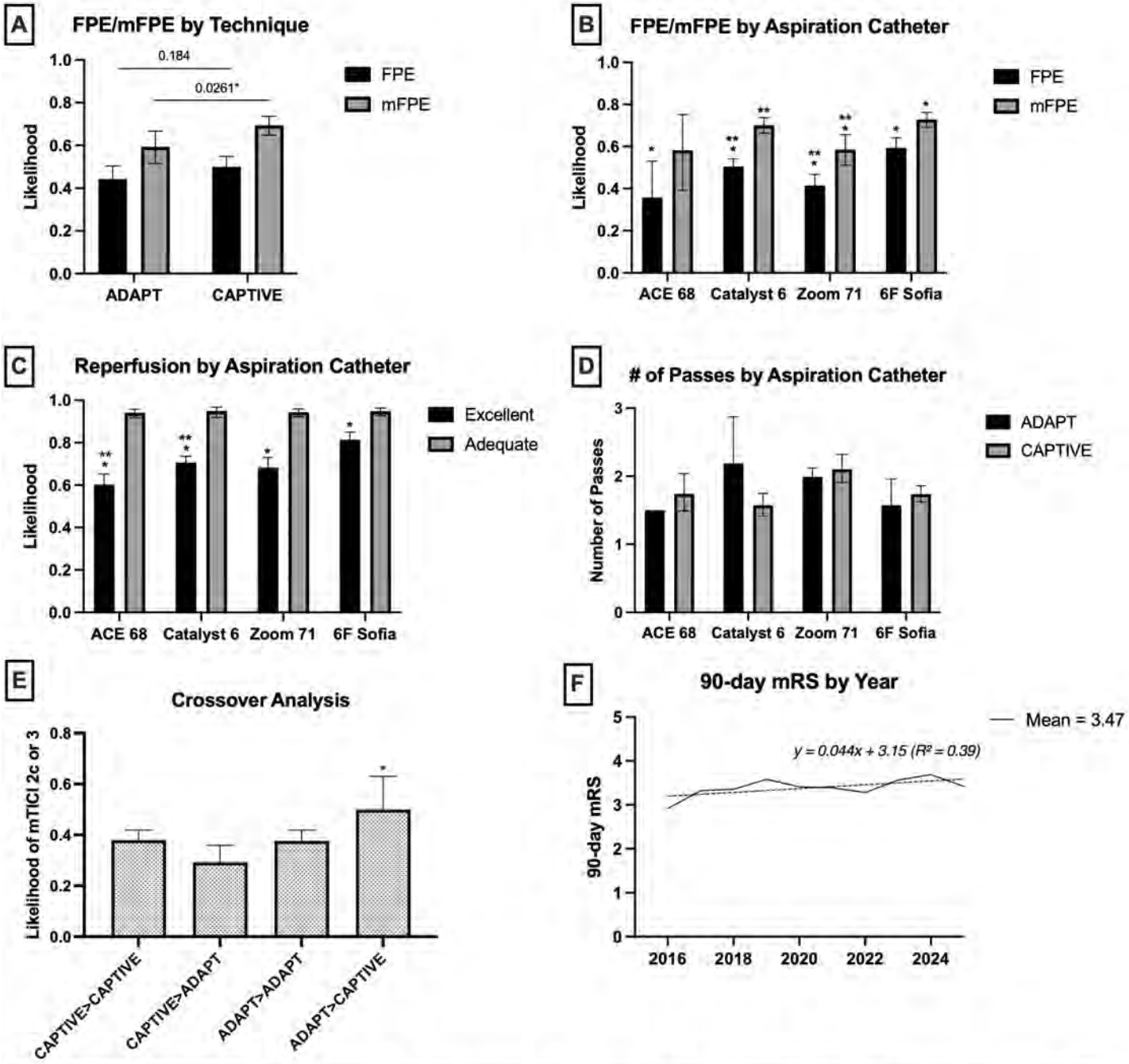

Figure 1: Procedural variables (**A**, First-pass technique. **B**, FPE/mFPE by first-pass large aspiration catheter. **C**, Final reperfusion by large aspiration catheter. **D**, Number of passes by large aspiration catheter. **E**, Crossover analysis for second pass reperfusion. **F**, 90-day mRS by year for large aspiration catheters.) **B** and **C**, * and ** indicate significant pair-wise comparison with 6F Sofia and Catalyst 6, respectively. Error bars represent standard error of the mean.

---

257 **Impact of balloon guide catheter use and operator experience on mechanical thrombectomy outcomes at a single large-volume stroke center**

Gnaneswari Karayi B.A.[1], Revyn Kim B.S.[1], Lulu Bi B.S.[1], David S Hong B.S.[1], Miranda Gonzales B.S.[1], Joshua Feler M.D.[2], Radmehr Torabi M.D.[2], Elias Shaaya M.D.[2], Krisztina Moldovan M.D.[2], Mahesh Jayaraman M.D.[2], Dylan N. Wolman M.D.[2]

[1]Warren Alpert Medical School of Brown University, Providence, Rhode Island, USA. [2]Brown University Health, Providence, Rhode Island, USA

Purpose

Use of balloon-guide catheters (BGC) during mechanical thrombectomy (MT) for acute ischemic stroke (AIS) has been associated with improved procedural efficacy and clinical outcomes.[1,2] We sought to determine the extent to which operator experience with BGCs influences technical

efficacy when using BGCs or standard guide sheaths (GS) for MT. We present a retrospective analysis of a single high-volume comprehensive stroke center comparing the use of BGC versus GS to examine if BGC use improves the efficacy of MT for anterior circulation AIS, and whether this effect persists after controlling for operators and operator level of experience.

Materials & Methods

We performed a retrospective review of all patients who underwent MT for AIS due to anterior circulation large-vessel occlusion (LVO) from 2015 to 2025 at our single comprehensive stroke center. Inclusion criteria were age >18 with an occlusion of the ICA terminus, M1, or M2 segment of the middle cerebral artery. Patients with missing procedural and neurointerventionalist data were excluded. Thrombectomy candidacy, procedural approach and equipment was decided by the attending neurointerventionalist with 7 separate operators included.

We performed an operator-dependent analysis by stratifying neurointerventionalists into low (Group A), medium (Group B), and high BGC-use (Group C) groups by their historical practice patterns, and compared associated procedural and neurologic outcomes. The primary outcome measure was the rate of achieving first pass effect (FPE), defined as achieving excellent or good reperfusion with a single pass (mTICI 2c-3). Secondary outcome measures included time from access-to-reperfusion, access-to-first device deployment, and 90-day neurologic outcomes by modified Rankin scale. Matched-pair analyses and mixed-effects sensitivity models were performed. Wilcoxon rank-sum tests, two-sample t-tests, and Fisher's exact tests were used for statistical comparisons.

Results

A total of 3,587 patients were screened, with 2,290 included. 811 (35%) underwent BGC-MT on the first pass. The mean age was 72±15 years, and 51% were female. Matched-pair analysis showed that BGC use significantly increased rates of FPE (p=0.00755) and increased rates of mFPE (p=0.0077), reduced puncture-to-first deployment time (p<0.0001), recanalization time (p=0.0001). Mixed-effects sensitivity analyses controlling for operators found that BGC use remained associated with significantly decreased recanalization time (p=0.031397), puncture-to-first deployment time (p=0.007304). Neurointerventionalists were then grouped according to mean BGC usage rates: Group A (26%), Group B (49%), and Group C (71%). FPE rates were also significantly higher with BGC use only for Group C. BGC use in Groups A and B did not significantly reduce procedural times, while Group C showed significantly faster times associated with BGC use and the lowest overall procedural times (Table 1). BGC use significantly improved NIHSS at discharge in Group C, but did not affect 90-day mRS within any group.

Conclusion

Our results show that BGC use improves procedural metrics regardless of operator. However, when stratified by operator group, only high-frequency BGC users showed significant improvements in procedural time and efficacy. Infrequent users saw no such benefit, suggesting that the effectiveness of balloon guides depends on regular use and operator familiarity.

References

1. Zaidat, O. O. et al. Impact of Balloon Guide Catheter Use on Clinical and Angiographic Outcomes in the STRATIS Stroke Thrombectomy Registry. *Stroke* 50, 697–704 (2019).

2. Pederson, J. M. *et al.* Comparison of Balloon Guide Catheters and Standard Guide Catheters for Acute Ischemic Stroke: An Updated Systematic Review and Meta-analysis. *World Neurosurg.* 185, 26–44 (2024)

Images/Tables

Operator Group	First Pass BGC Used?	Mean Puncture to First Deployment (min)	p values	SD Puncture to Deployment (min)	Mean Recanalization (min)	p values2	SD Recanalization (min)	Median 90-day mRS	p values3	IQR mRS	Median NIHSS Shift at Discharge	p values4	IQR NIHSS Shift at Discharge	FPE Rate	p values5	n
Group A (26% BGC)	No	16.9	0.327545	11.6	27.4	0.409799	21.9	4	0.954199	2–6	-10	0.12381	-15–3	48.40%	1	252
Group A	Yes	18.1		9.5	29.2		16.8	4		3–6	-10		-15.75–3.25	47.80%		90
Group B (49% BGC)	No	19.5	0.411845	12.7	30.8	0.981609	21.6	4	0.04945 *	3–6	-9	0.261046	-15–4	43.30%	0.186804	231
Group B	Yes	18.6		11.5	30.7		22	4		2–6	-11		-16–5	49.80%		221
Group C (72% BGC)	No	19.5	0.0000608 *	18.7	32.7	0.00000365 *	26.5	4	0.03956 *	3–6	-8	0.035708 *	-14–3	40.10%	0.002093 *	142
Group C	Yes	12.7		9	21.2		18.2	4		2–6	-9.5		-14–4	55.80%		364

Table 1: Summary statistics across operators, grouped according to frequency of usage. p values indicate statistical tests comparing outcome variables between BGC use and GS use within each group. A star (*) indicates statistical significance (p < 0.05).

Scientific Abstract Power Pitches & Luminary Speaker: Socioeconomics/Health Policy

1:00 - 2:00pm Tuesday, 19th May, 2026

412 No Rest Since DAWN? Decade of Unrelenting CTA Growth in the Emergency Department

Yu Sakai MD[1], Alvand Hassankhani MD[1], Shawn Lyo MD[1], Arun Venkataraman MD, PhD[1], Manav Jha[1], Andrea Pogozelski MPH, RT, CT, MR[1], James DeMasi CFA[1], Gregory Lewis BSN, RN, CEN[2], Lisa Ferretti MBA[3], David Thomas MBA[1], David Waters MBA, RT[1], Suyash Mohan MD, PDCC[1]
[1]Department of Radiology, University of Pennsylvania, Philadelphia, PA, USA. [2]Department of Emergency Medicine, Hospital of University of Pennsylvania, Philadelphia, PA, USA. [3]Department of Emergency Medicine, University of Pennsylvania, Philadelphia, PA, USA

Purpose

Neuroradiologists working in the emergency department (ED) increasingly report an overwhelming surge in CTA Head and Neck volumes[1]. Although CT perfusion (CTP) drew attention following the 2018 DAWN and DEFUSE-3 trials[2,3], the relative contributions of CTA and CTP to overall neuro-ED imaging growth—and how CTA compares with routine studies such as noncontrast head and cervical spine CT—have not been systematically quantified. We sought to characterize decade-long neuro-ED imaging trends, with emphasis on CTA and CTP, and to contextualize growth relative to conventional CT.

Materials & Methods

Retrospective cross-sectional study of all neuroradiological ED imaging (CT/MRI) from fiscal years (FY) 2016–2025 (July–June) across two emergency departments in a single tertiary academic health system (Hospital of the University of Pennsylvania and Penn Presbyterian Medical Center). Analysis was focused on CTA Head, CTA Neck, CTP, and routine neuro-ED CT exam comparators (noncontrast Head, Cervical spine, Maxillofacial CT, and contrast-enhanced Neck CT). Annual metrics included absolute exam volumes and CTA Head-and-Neck-to-CTP ratios. Compound annual growth rate (CAGR) of different exam types were calculated for post DAWN/DEFUSE-3 era, from FY18 until FY25.

Results

Among 293,715 neuro-ED exams, CTA Head and Neck volumes increased nearly 850%, from ~750 in FY2016 to >6,300 in FY2025 (**Fig. 1A**). Increase in CTA Head and Neck were disproportionate to routine neuro-ED CT exams, with CAGR tripling the rate of noncontrast head CT (>15% vs. 4.9%), while CT perfusion lagged (**Figure 1B**).

CTA Head-and-Neck-to-CTP ratio more than doubled (4.2 to 9.9) between 2018 and 2025, confirming disproportionate angiographic utilization (**Fig. 1C**).

Conclusion

This decade-long analysis quantitatively confirms what many neuroradiologists observe daily: CTA Head and Neck volumes in the ED have risen explosively, far outpacing CT perfusion and conventional CT growth. The disproportionate rise in CTA highlights a fundamental shift in stroke triage with important implications for workflow burden, staffing models, and strategic planning for future neuroimaging resource allocation.

References

1. Tu LH, Malhotra A, Venkatesh AK, Taylor RA, Sheth KN, Forman HP, Yaesoubi R. Head and Neck CTA Utilization: Analysis of Ordering Frequency and Nonroutine Results Communication, With Focus on the 50 Most Common Emergency Department Clinical Presentations. AJR Am J Roentgenol. 2022 Mar;218(3):544-551. doi: 10.2214/AJR.21.26543. Epub 2021 Sep 29. PMID: 34585611.
2. Nogueira RG, et al. Thrombectomy 6 to 24 Hours after Stroke with a Mismatch between Deficit and Infarct (DAWN Trial). N Engl J Med. 2018;378:11–21. doi:10.1056/NEJMoa1706442.
3. Albers GW, et al. Thrombectomy for Stroke at 6 to 16 Hours with Selection by Perfusion Imaging (DEFUSE-3). N Engl J Med. 2018;378:708–718. doi:10.1056/NEJMoa1713973.

Images/Tables

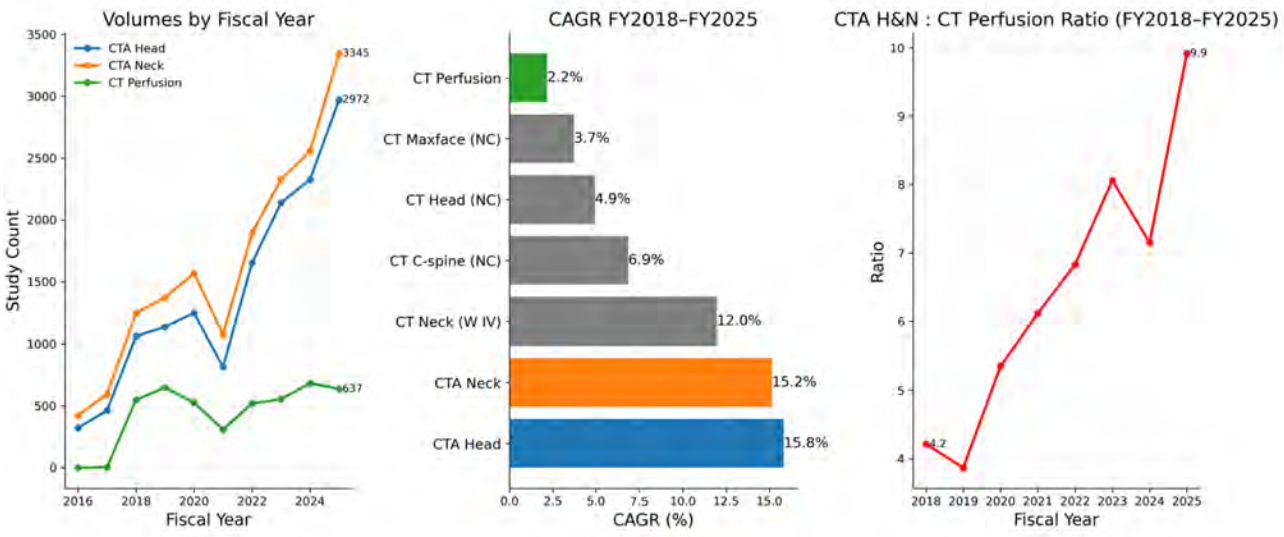

Figure 1. CTA H&N and CTP imaging trends. A. Annual CTA Head, CTA Neck, and CT Perfusion (CTP) volumes in the ED. **B.** CAGR in post DAWN/DEFUSE-3 era (FY18-25) of CTA, CTP, and routine neuro-ED CT exams. **C.** CTA Head & Neck-to-CTP ratio.

1121 Sustaining the Neuroradiology Workforce: The Role of International Medical Graduates

Keervani Kandala MS[1], Raj Moily MBBS, PhD, MBA[1], Dhairya A. Lakhani MD[2], Ajay Malhotra MD[1]
[1]Department of Radiology and Biomedical Imaging, Yale School of Medicine, New Haven, Connecticut, USA. [2]Department of Radiology, West Virginia University, Morgantown, West Virginia, USA

Purpose

We evaluated national trends in the practicing neuroradiology workforce from 2017 to 2021. Our goal was to examine differences between U.S. medical graduates (USMGs) and international medical graduates (IMGs) to better understand factors influencing workforce composition and equity.

Materials & Methods

We conducted a retrospective cross-sectional study analyzing Medicare payments to neuroradiologists from 2017–2021 using the Centers for Medicare & Medicaid Services (CMS) Medicare Part B provider utilization and payment dataset. Physicians with a specialty listed as Diagnostic Radiology and a U.S. practice location were included. We identified neuroradiologists using the Neiman Imaging Types of Services (NITOS) code system, classifying those performing more than 50% of their work relative value units (wRVUs) in brain, head/neck, or spine procedures. Physician characteristics, including years in practice, group type, academic affiliation, and rurality, were obtained from the CMS National Plan and Provider Enumeration System (NPPES). We defined IMGs as physicians whose medical school was listed as "OTHER" in NPPES, whereas USMGs included U.S. allopathic and osteopathic physicians. Financial data were inflation-adjusted to 2021 U.S. dollars. Academic status was defined using the Neiman Academic Radiology Practices database, and rurality was assigned using the University of Washington Rural-Urban Commuting Area (RUCA) Codes. We excluded providers with fewer than 150 NITOS-classified wRVUs during the 5-year span and those without radiology relevant credentials (e.g., DDM, DC, MNT). Statistical comparisons were done using t-tests and Wilcoxon tests, and multivariable linear regression was performed adjusting for years in practice, region, academic status, and rurality.

Results

We identified 2,312 neuroradiologists: 1,648 (71.3%) USMGs and 664 (28.7%) IMGs. The proportion of IMGs remained stable from 2017 to 2021. Most neuroradiologists were male (80.0%) and practiced in urban areas (87.0%). Academic affiliation was present in 34.6% of IMGs and 31.7% of USMGs. Female representation was higher among IMGs (25.6%) than USMGs (17.8%). Among academic neuroradiologists, 277 (34.6%) were IMGs and 523 (65.4%) were USMGs. Median years in practice did not differ significantly between groups (20 vs 19 years, P = 0.25). IMGs received lower unadjusted mean annual Medicare payments than USMGs ($274,088 vs $321,947, P = 0.0001), but differences were not significant after multivariable adjustment. IMG status was not independently associated with payment per service or productivity measures. IMGs were widely distributed across the United States, with the higher concentrations in New York, California, Pennsylvania, Texas, and Florida.

Conclusion

Our findings show that IMGs represent a substantial and stable component of the U.S. neuroradiology workforce, contributing significantly to nationwide access and continuity of specialized imaging care. Despite comparable productivity and compensation to U.S.-trained physicians, IMGs continue to face barriers such as restrictive visa policies. The national radiologist shortage is further exacerbated by the limited expansion of fellowship opportunities and the uneven regional distribution of training programs, trends that will likely intensify without targeted policy intervention. Expanding fellowship positions, strengthening IMG recruitment and retention, and enacting thoughtful immigration reforms are essential to sustain a diverse, equitable, and geographically balanced neuroradiology workforce capable of meeting future patient care demands.

References

1. Centers for Medicare & Medicaid Services (CMS). *Medicare Provider Utilization and Payment Data: Physician and Other Supplier Public Use File (2017–2021)*. U.S. Department of Health and Human Services. Available at: https://data.cms.gov/provider-summary-by-type-of-service/medicare-physician-other-practitioners. Accessed November 1, 2025.
2. Rosman DA, Duszak R Jr, Wang W, Hughes DR, Rosenkrantz AB. Changing utilization of noninvasive diagnostic imaging over 2 decades: an examination of Medicare claims using the Neiman Imaging Types of Service categorization system. *AJR Am J Roentgenol.* 2018;210(2):364-368. doi:10.2214/AJR.17.18292
3. United States Department of Health and Human Services. *National Plan & Provider Enumeration System (NPPES) NPI Registry*. Available at: https://npiregistry.cms.hhs.gov/search. Accessed November 1, 2025.
4. Harvey L. Neiman Health Policy Institute. *Neiman Imaging Types of Service (NITOS) Classification System*. Available at: https://www.neimanhpi.org/nitos/. Accessed November 1, 2025.
5. WWAMI Rural Health Research Center. *Rural-Urban Commuting Area Codes (RUCAs)*. Available at: https://depts.washington.edu/uwruca/index.php. Accessed November 1, 2025.

1164 Nine-Year Trajectory of Head and Neck CTA Utilization: Pandemic Effects and Long-Term Growth Patterns in Commercially Insured Populations

Nagaraja S Moily MBBS,PhD, MBA,MAM[1], Keervani Kandala[1], Max Wintermark MD,MS, MBA[2], Ajay Malhotra MD, MMM[1]
[1]Department of Radiology and Biomedical Imaging, Yale School of Medicine, New Haven, CT, USA. [2]Chair, Department of Neuroradiology, The University of Texas MD Anderson Cancer Center, Houston, TX, USA

Purpose

Head and neck computed tomography angiography (CTA) is indispensable for diagnosing cerebrovascular emergencies, trauma, and complex vascular disorders. While previous analyses relied primarily on Medicare data, most U.S. neurovascular imaging now occurs in commercially insured populations. This study characterizes nine-year national trajectories in head and neck CTA, quantifying pandemic-related inflection points and identifying structural and operational drivers—including billing separability and protocol standardization—that have shaped modern imaging practice. Recent institutional and system-level studies indicate persistent growth in CT angiography (CTA) and a diminishing diagnostic yield in emergency contexts (1-3), highlighting the necessity for revised multi-payer benchmarks.

Materials & Methods

We performed a longitudinal cohort analysis of 1,991,194 head and neck CTA procedures performed between 2016 and 2024 using the IBM MarketScan® Commercial and Medicare Supplemental databases, encompassing >40 million covered lives annually across 350 health plans and 100 major employers. A validated multi-stage analytic pipeline was used to harmonize inpatient, outpatient, and facility claims. Procedure verification

leveraged the PROCTYP field to isolate true CPT-4 codes (70496, 70498) with >97 % specificity. Cross-table reconciliation and deterministic encounter linkage reduced redundancy to <10 %, yielding 833,128 encounters representing 701,815 unique patients. Clinical indications were mapped via hierarchical ICD-9/10 prefix groupings (>95 % mapping success). Analyses were stratified into pre-COVID (2016–2019), acute pandemic (2020–2021), and recovery (2022–2024) phases. Temporal trends were evaluated using compound annual growth rates (CAGR) and seasonal decomposition to model longitudinal utilization trajectories.

Results

CTA volume increased from 130,080 (2016) to 310,745 (2023) (CAGR 8.4 %). The COVID-19 pandemic produced a –6.5 % dip followed by strong recovery (mean 263,782 procedures/year, 2022–2024). **S**ame-encounter head and neck imaging rose from 54.9 % to 79.8 %, reflecting consolidation toward standardized "head-through-arch" protocols. Regional growth was consistent, led by the South (38.2 % of volume; CAGR 9.6 %) and Midwest (30.6 %; CAGR 7.2 %). Adults 45–64 accounted for 48 % of patients; pediatric imaging < 2 %. Seasonal cyclicity persisted with December troughs. The verified overall emergency-department (ED) share was 22.7 % (annual rates under validation), consistent with reports identifying the ED as the predominant source of neurovascular CTA growth and increasing use in acute stroke and neurologic presentations (1-3).

Conclusion

Over nine years, head and neck CTA utilization in commercially insured populations has doubled, revealing sustained growth and pandemic-related acceleration of comprehensive imaging practices. The convergence of evolving stroke-protocol coverage ("head-through-arch"), operational efficiencies, and structural incentives from separate CPT codes (70496 for head, 70498 for neck) contributed to this trend. These findings highlight how workflow design and reimbursement architecture have aligned, fostering consolidation of imaging encounters and greater per-episode complexity. Using a rigorously validated, multi-level analytic framework integrating CPT verification, cross-table deduplication, and ICD-based mapping, this study establishes the first reproducible national benchmark for CTA utilization beyond the Medicare population. The framework enables future system-level monitoring of imaging growth, capacity forecasting, and evaluation of post-pandemic care dynamics.

References

1. Tu LH, Krupinski EA, Heilbrun ME, et al. Head and neck CT angiography utilization: analysis of ordering frequency and nonroutine results communication. *AJR Am J Roentgenol.* 2022;218(3):544–551. doi:10.2214/AJR.21.26543
2. Rigney GH, Romano AM, Carhuapoma JR, et al. Trends in nonfocal neurological chief complaints and CT angiography utilization among adults in the emergency department. *Intern Emerg Med.* 2024;19(4):785–793. doi:10.1007/s11739-024-03569-9
3. Mullins ME, Lev MH, Doshi AH, et al. CT and CT angiography utilization trends for suspected stroke and TIA in emergency departments. *Emerg Radiol.* 2019;26(4):399–406. doi:10.1007/s10140-019-01672-5

1073 Sex-Related Differences in Fetal Brain Volume and Early Neurodevelopmental Outcomes: A Developing Human Connectome Project Analysis

Siddharthasiva Anbu Rajan MD, MS, Duan Xu PhD, Orit A Glenn MD, Andreas M Rauschecker MD, PhD, Elizabeth George MBBS
University of California, San Francisco, San Francisco, CA, USA

Purpose

Early childhood neurodevelopment is affected by many factors, including brain structure, genetics, and environmental factors. Standardized public datasets such as the Developing Human Connectome Project (dHCP)[1] provide rigorously collected and curated neuroimaging data to investigate early brain development in the normal population. This work examines the interplay of sex and brain structure, specifically fetal brain volumes, on early neurodevelopmental outcomes in the dHCP cohort.

Materials & Methods

We used fetal brain MRI data from the latest dHCP data release [1]. We included 273 fetuses with reconstructed 3D volumetric images and standardized segmentation masks. The labels from the masks were extracted to calculate total parenchymal brain volume (TBV), white matter volume (WM), and deep gray matter volume (DGM). The subjects who underwent neurodevelopmental assessment using the Bayley-III Scales of Infant Development (BSID-III) questionnaire at 18 months of age were included in the analysis.[2]

The volumes were adjusted for gestational age (GA) using quadratic fits for TBV and DGM, and a linear fit for WM. From these fits, we calculated predicted volumes and subsequently residual volumes (actual volume – predicted volume) for each subject. Residual volumes were compared against the composite scores for cognition, language, and motor domains in males and females, using linear regression.

Results

A total of 182 participants had fetal MRI brain volumes and neurological examination as an infant in the dataset. This was comprised of 92 males and 90 females. The median gestational age of the cohort was 29 weeks 1 day (IQR=26w-32w). The mean GA in males was 29w2d (±3w5d), and in females was 29w2d (±4w1d). The cohort had a median TBV of 147.13 cc (IQR=94.12-202.29 cc), median WM of 78.52 cc (IQR=52.66-102.63 cc), and a median DGM of 12.22 cc (IQR=8.53-16.23 cc). The GA-adjusted residual volumes for all three regions were significantly higher in males ($p<0.0001$). The median composite cognitive, language, and motor scores were 105 (IQR=95-111.25), 106 (IQR=100-115), and 103 (IQR=97-110), respectively. Language score was higher in females than males ($p=0.04$), but the other scores were not significantly different between sexes. On comparison of residual brain volumes against scores, there were positive correlation trends in males and negative correlation trends in females. Of note, motor scores were positively correlated with residual WM volume in males ($p=0.02$, $r=0.24$), while they were negatively correlated with residual TBV ($p=0.02$, $r=-0.24$), and residual WM ($p=0.03$, $r=-0.22$), and residual DGM ($p=0.05$, $r=-0.20$) in females. The results of this comparison are shown in Figure 1.

Conclusion

This study explores sex-related variability in brain growth in the fetal period and compares its neurodevelopmental outcomes in the cognitive, linguistic, and motor domains. The results show variability in the associations of age-adjusted regional volumes and motor scores. This broadens our understanding of sex-related differences in fetal brain growth.

References

[1] Edwards AD, Rueckert D, Smith SM, et al. The Developing Human Connectome Project Neonatal Data Release. *Front Neurosci*. 2022;16:886772. Published 2022 May 23. doi:10.3389/fnins.2022.886772

[2] Weiner IB, Craighead WE. Bayley Scales of Infant and Toddler Development. In: The Corsini Encyclopedia of Psychology. John Wiley & Sons, Ltd. https://doi.org/10.1002/9780470479216. Accessed October 29, 2025.

Images/Tables

	Males			Females		
	Cognitive Scores	Language Scores	Motor Scores	Cognitive Scores	Language Scores	Motor Scores
Residual Total Brain Volume	R=0.181 (p=0.08)	R=0.152 (p=0.15)	R=0.160 (p=0.13)	R=-0.197 (p=0.06)	R=-0.178 (p=0.09)	R=-0.239 (p=0.02)
Residual White Matter Volume	R=0.163 (p=0.12)	R=0.129 (p=0.22)	R=0.242 (p=0.02)	R=-0.177 (p=0.09)	R=-0.147 (p=0.17)	R=-0.224 (p=0.03)
Residual Deep Gray Matter Volume	R=0.154 (p=0.14)	R=0.183 (p=0.08)	R=0.125 (p=0.23)	R=-0.077 (p=0.47)	R=-0.107 (p=0.32)	R=-0.205 (p=0.05)

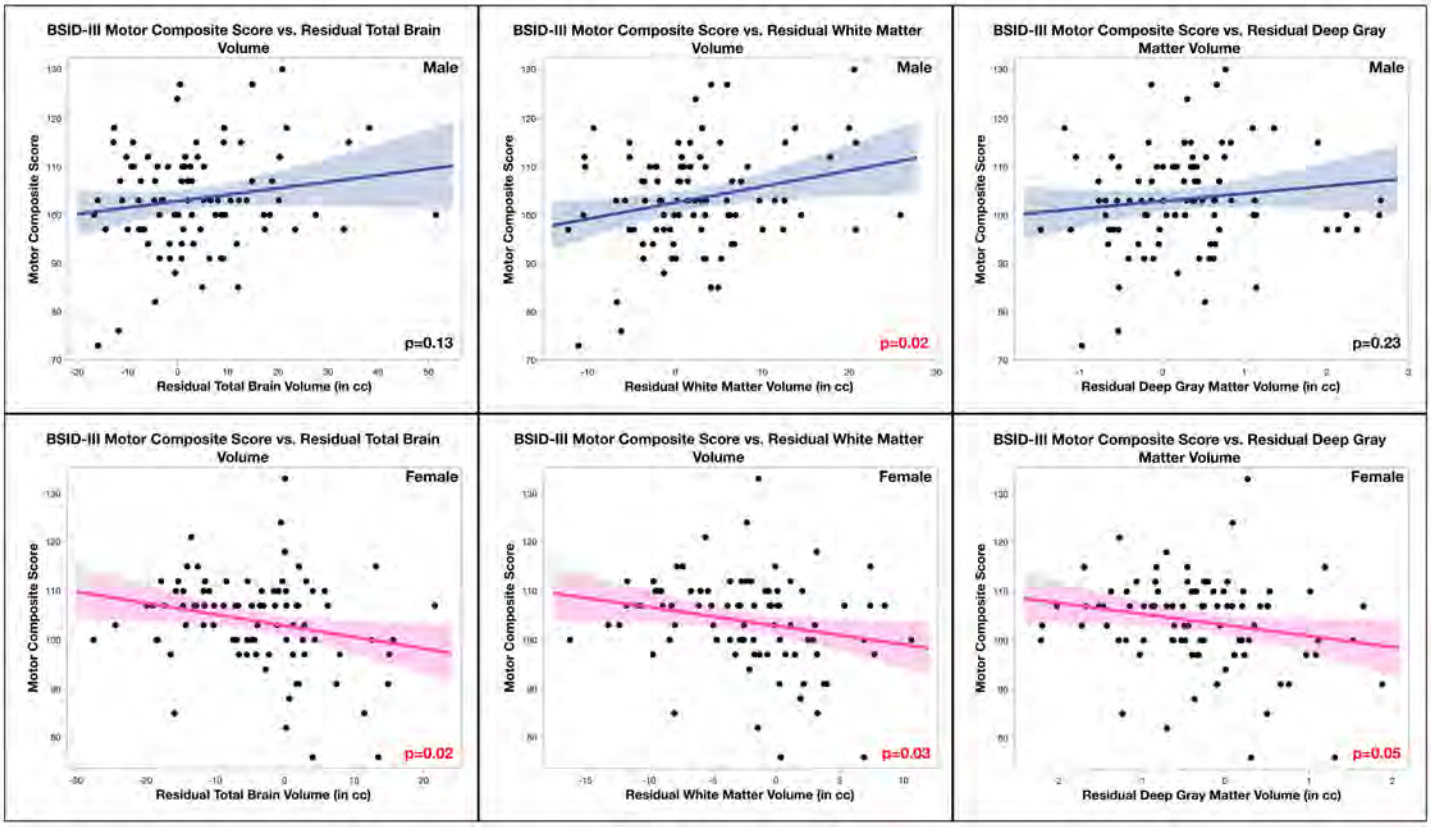

398 ED Imaging Surge and Neuroradiology: A 10-Year Analysis at a Tertiary Care Teaching Hospital

Arun Venkataraman MD, PhD, Alvand Hassankhani MD, Yu Sakai MD, Andrea Pogozelski MPH, RT, James Demasi CFA, David Waters MBA, RT, Suyash Mohan MD

Hospital of the University of Pennsylvania, Philadelphia, PA, USA

Purpose

Diagnostic imaging is a cornerstone of emergency medicine and serves an important role in initial diagnosis and triage. ED Imaging volumes have increased dramatically over the past decade[1] with an increase in the associated radiation exposure to patients[2]. As part of this, neuroradiology has seen a large increase in the number of imaging studies ordered. For radiologists, this increasing volume has been found to contribute to fatigue,

cognitive errors, and burnout[3]. In this study, we aimed to quantify growth in ED imaging utilization over the past decade, with a focus on neuroradiology.

Materials & Methods

All ordered imaging from the Hospital of the University of Pennsylvania (HUP) ED in the 2016-2025 fiscal years (July 1st – June 30th) was tabulated via the electronic health record. Data included the study modality and anatomy imaged.

Imaging volume was further segregated by individual radiology sub-specialty and analyses were completed with a focus on cross-sectional studies (i.e., non-radiographic studies). Metrics included absolute imaging volume, relative growth compared to 2016, and subspecialty share of total imaging. Combined annual growth rate (CAGR) was calculated to quantify exponential volume growth by specialty.

Results

There were 601,892 imaging orders over the 10-year period. There were increases in all subspecialty imaging over the 10-year study period (Figure 1). Neuroradiology showed the greatest growth with 159% in the 10-year period (7,736 in 2016 to 20,067 in 2024). In fact, throughout the 10-year period analyzed, neuroradiologic studies routinely comprised approximately half of all cross-sectional ED studies (Figure 1, right panel and Table 1). When considering all ordered ED imaging studies, CAGR was highest for neuroradiology, with an annual growth rate of 0.11 (Table 2).

Conclusion

We found an increasing trend in ED imaging orders over the past decade. When considering all ordered cross-sectional imaging, neuroradiology experienced the greatest increase in ED studies and routinely comprised half of all ordered ED cross-sectional imaging. Future work will focus on understanding if there are individual studies (e.g., CTA head and neck) that disproportionately contribute to this increase in ordering and further analyze how turnaround times for reports are affected by increasing volume. In addition, the impact of increasing volume on report quality can also be analyzed, such as looking at the rate of addended reports over the 10-year period. Understanding these factors is essential in developing strategies to reduce physician burnout and medical errors.

References

1. Poyiadji, Neo, et al. "Diagnostic imaging utilization in the emergency department: recent trends in volume and radiology work relative value units." Journal of the American College of Radiology 20.12 (2023): 1207-1214.
2. Smith-Bindman, Rebecca, et al. "Use of diagnostic imaging studies and associated radiation exposure for patients enrolled in large integrated health care systems, 1996-2010." Jama 307.22 (2012): 2400-2409.
3. Aggarwal, Abhimanyu, et al. "Maximizing value while volumes are increasing." Current problems in diagnostic radiology 50.4 (2021): 451-453.

Images/Tables

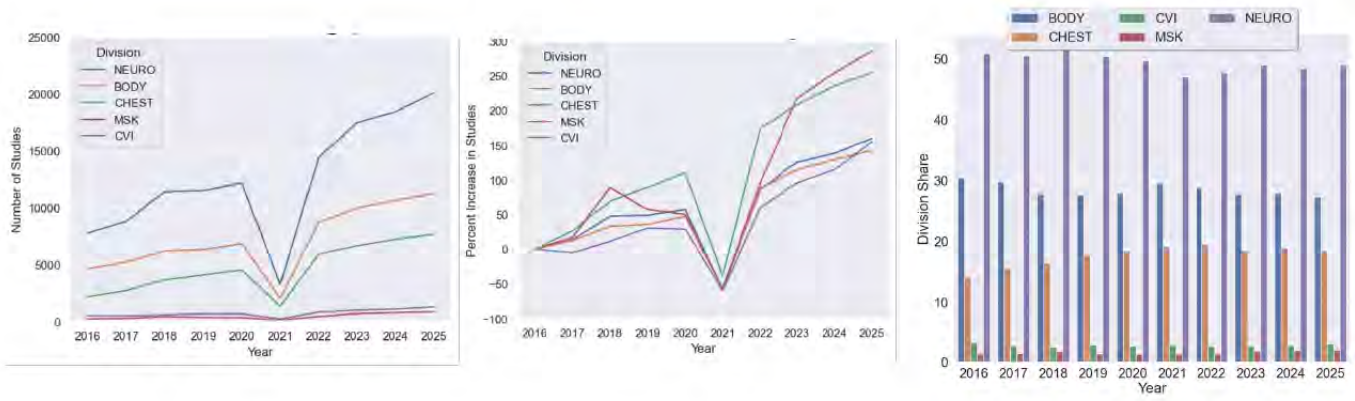

Figure 1 – Absolute (left panel) and relative (middle panel) cross-sectional ED volumes by division (line colors). Division share of ED cross-sectional imaging (right panel)

Division	2016	2017	2018	2019	2020	2021	2022	2023	2024	2025
BODY	30.43764	29.8764	27.84381	27.54462	27.8921	29.61622	28.85189	27.85421	27.91315	27.39763
CHEST	14.12801	15.57344	16.41434	17.81783	18.49635	19.17451	19.52311	18.59381	18.94961	18.61487
CVI	3.226442	2.673182	2.463054	2.811034	2.599	2.853005	2.603303	2.695569	2.767921	3.050417
MSK	1.373374	1.402702	1.78063	1.438407	1.283102	1.274439	1.356371	1.861627	1.945167	1.966909
NEURO	50.83454	50.47427	51.49817	50.38811	49.72944	47.08182	47.66532	48.99478	48.42415	48.97018

Table 1 – Tabular representation of right panel of Figure 1, representing division share of ED cross-sectional imaging.

Division	NEURO	BODY	CHEST	MSK	CVI
CAGR	0.111722	0.091159	0.056761	0.077524	0.10941

Table 2 – Compound annual growth rate (CAGR) from fiscal year 2016-2025 by division.

1130 Trends in Neuroradiology Fellowship Positions and Match Outcomes in the United States, 2009–2025

Keervani Kandala MS[1], Raj Moily MBBS, PhD, MBA[1], Dhairya A Lakhani MD[2], Ajay Malhotra MD[3]
[1]Department of Radiology and Biomedical Imaging, Yale School of Medicine, New Haven, Connecticut, USA. [2]Department of Radiology, West Virginia University, Morgantown, West Virginia, USA. [3]Department of Radiology and Biomedical Imaging and Neurosurgery, Yale School of Medicine, New Haven, Connecticut, USA

Purpose

To evaluate national trends, match outcomes, and geographic distribution of neuroradiology fellowship positions in the United States from 2009 to 2025, to better understand changes in training capacity and workforce patterns.

Materials & Methods

We used publicly available data from the JAMA Graduate Medical Education Reports (2009–2024) and the National Resident Matching Program (NRMP) Specialties Matching Service (2009–2025). The number of Accreditation Council for Graduate Medical Education (ACGME)-accredited neuroradiology fellowship programs, positions offered, and positions filled through the Match were obtained for each year. Applicant composition by training background (U.S. MDs, DOs, international medical graduates [IMGs], and Canadian graduates) was analyzed. State-level distribution of 2025 programs and positions was obtained from NRMP and AMA FREIDA databases. Descriptive statistics were applied to summarize longitudinal and geographic trends.

Results

Between 2009 and 2025, ACGME-accredited neuroradiology programs increased from 86 to 94 (+9%), and fellows in training rose from 250 to 262 (+5%). NRMP fellowship positions expanded from 190 to 316 (+66%), while positions filled rose from 127 to 287 (+126%), thereby improving the overall fill rate from 66.8% to 90.8% over the years. U.S. MDs comprised the majority of matched fellows (69–80% annually), while DO participation grew from 4% to 15% and IMGs from 19 to 54 matches (19% in 2025). Canadian graduates consistently accounted for ≤2% of matches. In 2025, 94 ACGME-accredited programs across 33 states and D.C. offered 385 total positions, of which 316 were offered through the NRMP Match. Despite national growth, programs demonstrated geographic disparities, remaining concentrated in a few states. California (10 programs, 48 positions), New York (10 programs, 35 positions), Massachusetts (5 programs, 28 positions), and Texas (6 programs, 16 positions) together accounted for one-third of all programs and positions whereas eleven states (e.g., Maine, Idaho, North Dakota, and South Dakota) lacked accredited fellowships, and several states (e.g., Iowa, Nebraska, Oklahoma, and New Hampshire) maintained accredited programs but did not participate in the NRMP Match, suggesting that positions were filled outside the Match.

Conclusion

While neuroradiology fellowship positions have expanded over time, the number of active fellows has not kept pace with training capacity. The rising participation of DOs and IMGs reflects diversification of the training pipeline; however, persistent geographic concentration of programs underscores regional inequities that may exacerbate workforce shortages. Policies aimed at expanding graduate medical education (GME) funding, incentivizing program development in underserved regions, and strengthening pathways for international and osteopathic physicians are essential to achieving a more balanced and sustainable neuroradiology workforce amid increasing imaging demand and ongoing radiologist attrition.

References

1. Andrews JS, Mathews C. US Graduate Medical Education, 2023–2024. JAMA. 2024;332(24):2127-2153.
2. National Resident Matching Program (NRMP). Results and Data: Specialties Matching Service, 2025 Appointment Year. Available at: https://www.nrmp.org/match-data/2025/02/results-and-data-specialties-matching-service-2025-appointment-year/. Accessed October 27, 2025.
3. American Medical Association (AMA). The AMA Residency & Fellowship Database (FREIDA). Available at: https://freida.ama-assn.org/search/list?spec=43296&fromHeader=true. Accessed October 27, 2025.
4. Prajapati P, Wu X, Bajaj S, Gandhi D, Wintermark M, Malhotra A. Trends of diversity in neuroradiology trainees in the United States, 2015–2022. AJNR Am J Neuroradiol. 2023;44(9):1009-1011.
5. Futela D, Malhotra S, Payabvash S, et al. Recent trends in diagnostic radiology application and match rates. J Am Coll Radiol. 2025.

1201 Representation of Women on Neuroradiology Journal Editorial Boards: Recent trends

Ajay Malhotra, Bhumija Grandhe
Yale, New Haven, CT, USA

Purpose

Women have historically been under-represented in radiology/ neuroradiology, including in leadership positions. Several steps have been taken at the national level to increase representation of women for greater diversity. We examined female representation on editorial boards of four prominent neuroradiology journals in the last 7 years.

Materials & Methods

We collected data on the gender of the Editorial board members as listed on the mastheads of four prominent neuroradiology journals-*American Journal of Neuroradiology (AJNR), Journal of Neuroradiology, Journal of Neuroimaging and Diagnostic and Interventional Imaging*. The proportion of women on the Editorial Boards was collected for the years 2018, 2022 and 2025 to assess trends over time.

Results

The proportion of women on the *AJNR* Editorial Board increased from 21.6% in 2018 to 34.4% in 2025. *Journal of Neuroradiology* saw the increase in proportion of women from 14% in 2018 to 28% in 2025. The proportion of women on editorial board of *Journal of Neuroimaging* increased from 16% in 2018 to 20% in 2025. *Diagnostic and Interventional Imaging* saw the proportion of women increase from 19% in 2018 to 27% in 2025.

Conclusion

Our study results show that the proportion of women on Editorial Boards of prominent neuroradiology journals have increased over time. Women constitute approximately 20% of practicing neuroradiologists in the US national workforce.[1] There is a higher proportion of women in academic neuroradiology relative to non-academic radiology practices.[1] Increasing proportion of women on the Editorial Boards represents success of some of the initiatives for broader diversity and hopefully will lead to improvement in women representation in the overall workforce.[2,3]

References
1. Malhotra A, Lee C, Khunte M, et al. Gender Differences in Medicare Practice and Payment of Neuroradiologists. *AJNR Am J Neuroradiol*. 2025;46(6):1093-1099.
2. Wu X, Bajaj S, Khunte M, et al. Diversity in Radiology: Current Status and Trends Over the Past Decade. *Radiology*. 2022;305(3):640-647.
3. Prajapati P, Wu X, Bajaj S, Gandhi D, Wintermark M, Malhotra A. Trends of Diversity in Neuroradiology Trainees in United States 2015-2022. *AJNR Am J Neuroradiol*. 2023;44(9):1009-1011.

---

542 Altered Brain Connectome in Children with Blast-induced Traumatic Brain Injury

Hyuk Jin Yun PhD[1], Ramya Varadarajan MD[2], Stephen Kralik MD[3], Zili David Chu PhD[4], Joshua Rotenberg MD[5], Avner Meoded MD[1]
[1]Children's Mercy Hospital, University of Missouri-Kansas City School of Medicine, Kansas City, MO, USA. [2]Texas A&M University Health Science Center, Bryan, TX, USA. [3]Texas Children's Hospital, Houston, TX, USA. [4]Baylor College of Medicine, Houston, TX, USA. [5]Houston Specialty Clinic, Houston, TX, USA

Purpose

Blast-induced traumatic brain injury (TBI) presents unique neuropathological challenges, particularly in pediatric populations, where ongoing neurodevelopment may exacerbate vulnerability to injury[1]. Despite increasing civilian exposure to blast events, the long-term effects on pediatric brain connectivity remain poorly understood. In January 2020, a local industrial explosion resulted in 3 deaths, 18 non-fatal injuries, and damage to over 200 nearby buildings. Among those affected were children who later exhibited behavioral and neurological symptoms. Despite being presented with anxiety, executive dysfunction, and persistent headaches, there were no notable abnormalities found on conventional MRI scan.
This study aimed to investigate alterations in white matter connectivity in children exposed to blast-induced TBI using Diffusion Tensor Imaging (DTI)-based connectome analysis. DTI offers a sensitive modality to detect microstructural white matter changes that are often missed by conventional imaging. We hypothesized that pediatric patients would exhibit significant disruptions in both global and regional brain connectome measures compared to healthy controls.

Materials & Methods

We retrospectively included five pediatric patients (ages 7–13) exposed to the 2020 Houston explosion and seven age- and sex-matched healthy controls. From T1-weighted MRI scans, we used FreeSurfer and ACAPULCO to segment 91 cortical, subcortical, and cerebellar regions as predefined nodes for connectivity analysis[2,3]. For DTI scans, motion and eddy current-induced distortions were corrected to minimize artifacts using FMRIB Software Library (FSL)[4]. Then, we performed streamline tractography using DSI Studio for the artifacts-corrected DTI scans. To model the structural brain connectivity, we generated a matrix for each subject describing a collection of nodes and their connections[5]. Then, topology analysis was applied to obtain global and local network metrics such as efficiency, clustering coefficient, and betweenness centrality.
For the metrics, statistical comparisons were performed to evaluate differences in the network measures between patients and controls using general linear models, controlling for age, sex, and scanner type.

Results

Significant reductions were observed in global network metrics among patients, including network density ($p=0.030$), global efficiency ($p=0.030$), and rich club coefficients at $k=5$ ($p=0.005$) and $k=15$ ($p=0.039$). Regionally, patients demonstrated decreased degree, strength, clustering coefficient, local efficiency, and betweenness centrality across cortical and subcortical regions. Subcortical regions such as amygdala, pallidum, caudate showed consistently lower degree, local efficiency, and betweenness centrality in patients. Temporal and parietal regions showed smaller strength, clustering coefficient, and local efficiency in patients compared to controls. Notably, increased clustering coefficient and local efficiency were found in the right cuneus, and elevated betweenness centrality was observed in the superior parietal gyrus.

Conclusion

This study demonstrates that pediatric patients exposed to blast-induced TBI exhibit significant disruptions in both global and regional white matter connectivity. The observed reductions in network density, global efficiency, and rich club organization suggest impaired integration across brain networks. Regional alterations, including both decreased and compensatory increases in local connectivity metrics, highlight the heterogeneous impact of blast injury on the developing brain. These findings indicate that DTI-based connectome analysis can detect subtle but clinically relevant changes in pediatric blast-induced TBI and may inform future diagnostic and therapeutic strategies.

References
1. Tovar MA, Pilkington RA, Goodwin T, et al. Pediatric Blast Trauma: A Systematic Review and Meta-Analysis of Factors Associated with Mortality and Description of Injury Profiles. *Prehospital and Disaster Medicine* 2022;37:492–501.
2. Desikan RS, Ségonne F, Fischl B, et al. An automated labeling system for subdividing the human cerebral cortex on MRI scans into gyral based regions of interest. *NeuroImage* 2006;31:968–80.
3. Han S, Carass A, He Y, et al. Automatic cerebellum anatomical parcellation using U-Net with locally constrained optimization. *NeuroImage* 2020;218:116819.
4. Andersson JLR, Sotiropoulos SN. An integrated approach to correction for off-resonance effects and subject movement in diffusion MR imaging. *NeuroImage* 2016;125:1063–78.
5. Yeh F-C, Badre D, Verstynen T. Connectometry: A statistical approach harnessing the analytical potential of the local connectome. *Neuroimage* 2016;125:162–71.

---

933 Data-Driven Multivariate Decision-Tree Age–Sex Stratification for Pediatric Spinal Cord MR Imaging

Zahra Sadeghi Adl M.S.[1], Devon Middleton PhD[2], Laura Krisa PhD[3], Sara Naghizadehkashani MD[2], Mary Jane Mulcahey PhD[3], Feroze Mohamed PhD[2]
[1]Temple University, Philadelphia, PA, USA. [2]Jefferson Integrated Magnetic Resonance Imaging Center, Department of Radiology, Philadelphia, PA, USA. [3]Department of Occupational Therapy, Thomas Jefferson University, Philadelphia, PA, USA

Purpose

Pediatric spinal cord MRI lacks a consistent approach to age–sex handling, despite clear developmental changes in morphometry and microstructure. Prior work shows age-related trajectories in cervical cross-sectional area (CSA), related morphometrics, and diffusion indices. In practice, studies use broad age bins or continuous age; sex is inconsistently modeled or ignored despite reported effects. Research shows ad-hoc age binning discards

information, inflates residual variance, and weakens power. A transparent, data-driven stratification aligned to anatomical change points could standardize cohorts and demonstrably lower within-group variability versus conventional bins.

Materials & Methods

High-resolution isotropic T2-weighted MRI of the cervical spine was acquired in 170 typically developing children (6-17 y) on a 3T scanner. Data were processed using the Spinal Cord Toolbox (SCT) for cord segmentation and vertebral labeling. At each cervical (C) level from C2-C8, we extracted CSA, anterior-posterior (AP), and right-left (RL) widths. To identify demographic boundaries that minimize morphometric variability, we fit a multivariate decision-tree regression model using age and sex as predictors and the stacked multilevel morphometric matrix (CSA, AP, RL across C2-C8) as the response. Splits were minimized using within-group sum of squares (SSW) across all measures, and cost-complexity pruning with 10-fold cross-validation controlled overfitting. We compared the learned grouping to common baselines: Age-2 (6-12 vs 12-18 y), Age-4 (6-9, 9-12, 12-15, 15-18 y), Age-2×Sex (four classes), and Age-4×Sex (eight classes). For each strategy, we quantified pooled within-group variability, between-group separation (η^2), and a cross-validated reconstruction Root Mean Square Error (RMSE) obtained by predicting held-out subjects from group means.

Results

The decision tree identified five clusters: <9 y, 9-13 y (females), 9-13 y (males), 13-16 y, and ≥16 y. The only sex-specific split occurred within 9-13 y. Compared with conventional schemes, the data-driven grouping achieved the lowest within-group variability and highest between-group separability across CSA, AP, and RL at C2-C8. It explained 13.7% of total variance (η^2 = 0.137; median 0.134, IQR 0.089-0.197), yielded the lowest pooled SSW = 3081.7, and the smallest cross-validated RMSE = 4.54. Among baselines, Age-4×Sex (8 classes) produced a slightly higher total η^2 (0.158) but required more, uneven, and undersized subgroups, resulting in higher RMSE = 4.63 and greater internal variability. Age-4 (η^2 = 0.117) and Age-2×Sex (η^2 = 0.073) showed moderate separability, whereas Age-2 (η^2 = 0.058) had the weakest discrimination and SSW > 3300. The learned strata achieved 20-40% lower within-group variability and 5-13% lower cross-validated error than conventional bins, while producing stable, biologically meaningful clusters corresponding to pre-adolescent, adolescent, and mature stages. The largest morphometric contrasts were localized to C4-C6, driven primarily by CSA and RL differences.

Conclusion

A data-driven decision-tree framework identified five reproducible demographic stages, requiring sex stratification only at 9–13 years. By optimizing within-group homogeneity and between-group separation, it matched or outperformed conventional age/sex bins while avoiding undersized, uneven subgroups and minimizing cross-validated error. These rules provide an objective basis for normalizing pediatric spinal cord measures, improving sensitivity in developmental and clinical studies, and standardizing reference categories for multicenter work.

References

1. Reynolds, B., et al., *Quantification of DTI in the pediatric spinal cord: application to clinical evaluation in a healthy patient population.* American Journal of Neuroradiology, 2019. **40**(7): p. 1236-1241.
2. Alizadeh, M., et al., *Age related diffusion and tractography changes in typically developing pediatric cervical and thoracic spinal cord. Neuroimage Clin. 2018; 18: 784–92*.
3. Papinutto, N., et al., *MRI measurement of upper cervical spinal cord cross-sectional area in children.* Journal of Neuroimaging, 2020. **30**(5): p. 598-602.
4. Saksena, S., et al., *Diffusion tensor imaging of the normal cervical and thoracic pediatric spinal cord.* American Journal of Neuroradiology, 2016. **37**(11): p. 2150-2157.
5. De Leener, B., et al., *SCT: Spinal Cord Toolbox, an open-source software for processing spinal cord MRI data.*Neuroimage, 2017. **145**: p. 24-43.

Images/Tables

Summary of Demographic Grouping Rules

Group	Rule	Description	n
Group 1	Age < 9	Early childhood	21
Group 2	9 ≤ Age < 13 and Sex = Female	Pre-adolescent females	41
Group 3	9 ≤ Age < 13 and Sex = Male	Pre-adolescent males	25
Group 4	13 ≤ Age < 16	Adolescence	52
Group 5	Age ≥ 16	Late adolescence / mature	31

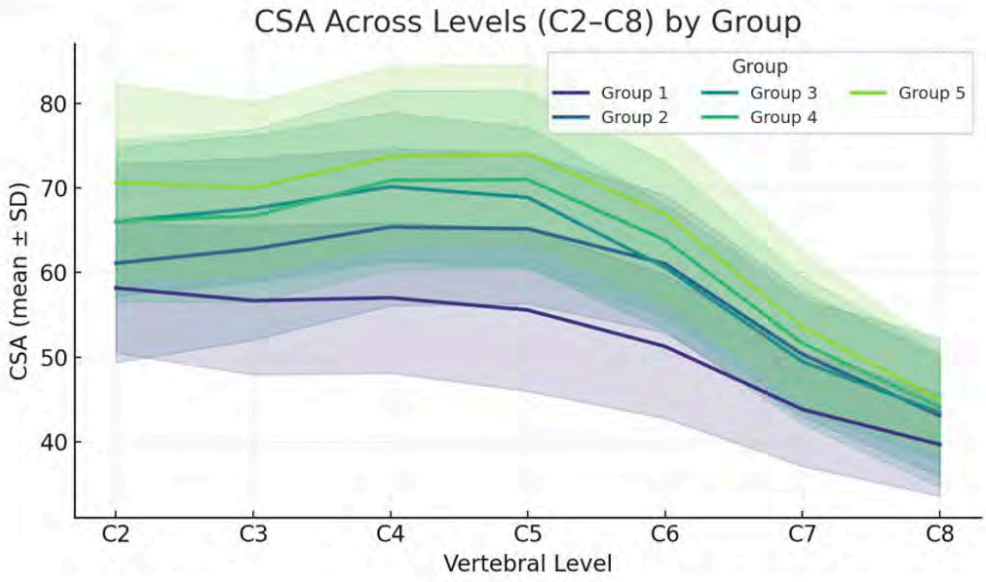

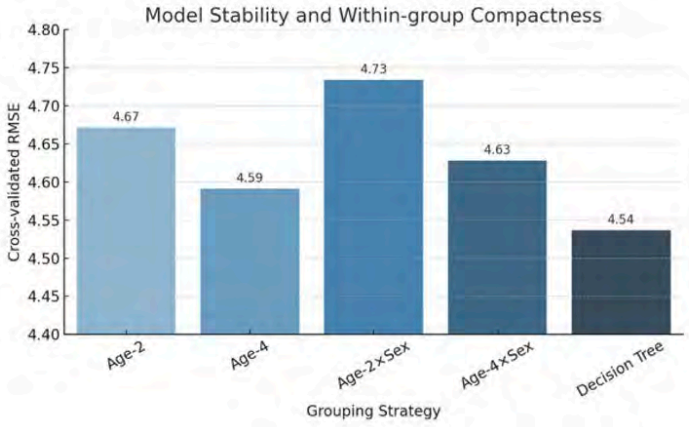

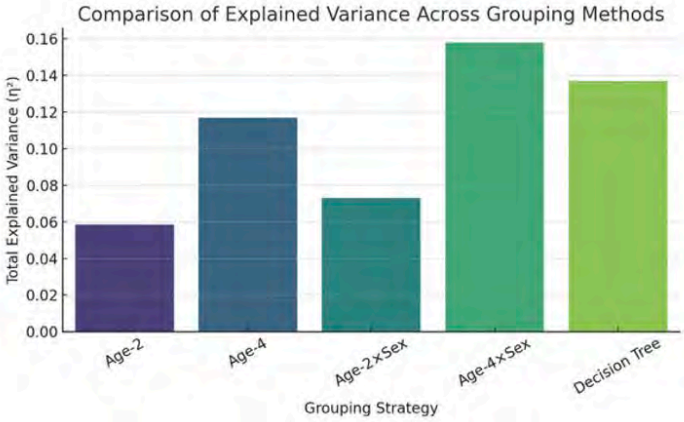

Scientific Abstract Power Pitches & Luminary Speaker: Functional/Advanced Imaging/Interventional

1:00 - 2:00pm Tuesday, 19th May, 2026

1043 300 patients: Our Experience in Magnetic Resonance Guided Focused Ultrasound Thalamothomy (MRgFUS) for Essential Tremor and Parkinson's Disease Tremor.

Antonio Innocenzi Dr[1], Federico Bruno Dr[1], Alessia Catalucci Dr[2], Patrizia Sucapane Dr[3], Francesca Pistoia Prof[1], Ernesto Di Cesare Prof[1], Alessandra Splendiani Prof[1]

[1]University of L'Aquila, L'Aquila, Italy, Italy. [2]Neuroradiology Unit, San Salvatore Hospital, L'Aquila, Italy, Italy. [3]Neurology Unit, San Salvatore Hospital, L'Aquila, Italy, Italy

Purpose

Magnetic resonance-guided focused ultrasound (MRgFUS) has emerged as a promising, minimally invasive treatment, enabling precise targeting of the ventral intermediate nucleus (VIM) of the thalamus to disrupt the dentato-rubro-thalamic tract (DRTT) and effectively reduce tremor in Essential Tremor (ET) and Parkinson's disease (PD).

Materials & Methods

Between 2018 and 2024, 300 patients (240 men, 60 women; mean age 69.1; mean disease duration 13.2 years; 169 ET, 125 PD) were treated at San Salvatore Hospital, L'Aquila. Patients underwent clinical evaluations before and after treatment using the Fahn-Tolosa-Marin scale (ET) and UPDRS III (PD). 3T MRI scans and clinical evaluation were performed before treatment and at 1 day, 1 month, 6 months and yearly up to 5 years after the procedure. We evaluated the lesions volume on FLAIR, T2w, T1w, DWI and SWI sequences .

Results

Tremor resolution was achieved in 90% of patients. ET patients improved on FTM scores (baseline: 5 ± 2; 5-year: 1 ± 1), while PD patients showed reductions in both FTM (6 ± 2 to 2 ± 1) and UPDRS-III scores. Nine patients experienced early tremor recurrence; ten underwent retreatment; ten received bilateral ablations (4 PD, 6 ET). Severe but reversible adverse effects occurred in <2% of cases. Mean lesion volume on T2w was 216 mm^3 at 24h and 31 mm^3 at 1 year. Lesion size remained stable in 67% of patients and showed minimal enlargement in 33% (mean: 34 mm^3) up to 5 years. Similar trends were observed on FLAIR and T1w. No cytotoxic edema was evident on DWI at 6 months, while lesions remained visible on SWI in all cases during the entire follow-up.

Conclusion

This represents the longest clinical and radiological follow-up reported to date. MRgFUS targeting the VIM appears to be a safe, effective, and durable treatment for ET and PD, with sustained clinical and radiological outcomes at 5 years.

References

Bruno F, Catalucci A, Arrigoni F, et al. An experience-based review of HIFU in functional interventional neuroradiology: transcranial MRgFUS thalamotomy for treatment of tremor. Radiol Med (Torino). 2020 Sept;125(9):877–86.

565 Magnetization Transfer Ratio Detects and Quantifies Lower Extremity Peripheral Nerve Involvement in Relapsing-Remitting Multiple Sclerosis

Kira Goeldner MD[1], Andrea Viehoever MD[2], Markus Weiler MD[2], Brigitte Wildemann MD[2], John M. Hayes BA[3], Sabine Heiland PhD[2], Martin Bendszus MD[2], Jennifer C. Hayes MD, PhD[3]

[1]Klinikum Darmstadt, Darmstadt, Hessen, Germany. [2]University Hospital Heidelberg, Heidelberg, Baden-Wuerttemberg, Germany. [3]University of Michigan, Ann Arbor, MI, USA

Purpose

Multiple sclerosis (MS) is conventionally thought to be restricted to the central nervous system (CNS) and manifests with a relapsing-remitting (RRMS) course in up to 90% of cases. Over the last century, involvement of the peripheral nervous system (PNS) has been controversially discussed. Recent studies utilizing high-resolution magnetic resonance neurography (MRN) have detected PNS involvement [1-4]. Conventional MRI sequences used in these studies primarily detect free water molecules but fail to generate contrast derived from macromolecular-bound protons. Magnetization transfer contrast (MTC) imaging overcomes these limitations and provides information on the density of protons in macromolecules such as myelin. MTC imaging has been successfully applied in CNS evaluations of MS patients, where the magnetization transfer ratio (MTR) correlates with areas of demyelination. Here, we aim to characterize and quantify lower extremity peripheral nerve involvement in RRMS by MTC imaging, in correlation with demographic, clinical, and electrophysiologic data.

Materials & Methods

Sixty RRMS patients and 60 age- and sex-matched healthy controls prospectively underwent MTC imaging using a 3.0 Tesla MR scanner. Two axial, three-dimensional gradient-echo sequences, with and without an off-resonance saturation rapid frequency pulse (Gaussian envelope, duration 9984 µs, frequency offset 1200 Hz), were conducted at the right mid-to-distal thigh. Sciatic nerve regions of interest were manually delineated on ten consecutive axial slices, with subsequent evaluation of the sciatic nerve MTR. Detailed neurologic and electrophysiologic examinations were conducted in all RRMS patients. Statistical analyses included evaluation of differences in MTR between RRMS patients and controls using a t-test with Welch's correction, as well as correlation analyses between MRN parameters and demographic, clinical, and nerve conduction study (NCS) results by calculating Pearson's correlation coefficients.

Results

All 60 RRMS patients fulfilled the revised 2017 McDonald criteria. Results from NCS were all within physiologic ranges, without evidence of peripheral neuropathy. Sciatic nerve MTR was lower in RRMS patients (27.2 ± 0.5%) than in controls (29.5 ± 0.4%; $p = 0.0002$) and inversely correlated with the duration of symptoms ($r = -0.2715$; $p = 0.0358$), the Expanded Disability Status Scale ($r = -0.3091$; $p = 0.0182$), and the distal motor latency of the tibial nerve ($r = -0.3285$; $p = 0.0174$) in RRMS patients, as well as with age and body mass index in controls.

Conclusion

Our study provides further evidence of peripheral nerve involvement in RRMS by showing a decrease in the sciatic nerve MTR in RRMS patients compared to healthy controls, supporting the hypothesis of peripheral co-demyelination. Additionally, the strong correlations between MTR and disease severity, as depicted by the Expanded Disability Status Scale, as well as with the duration of symptoms and tibial nerve distal motor latency, suggest that MTR is not only a sensitive marker, but also clinically relevant. MTR holds potential for inclusion in future diagnostic evaluations of MS patients while contributing to a better understanding of the pathophysiology involved in the evolution and progression of RRMS. Further longitudinal investigations are required to analyze implications for future patient management and imaging-based disease monitoring.

References

1. Jende JME, Hauck GH, Diem R, et al. Peripheral nerve involvement in multiple sclerosis: Demonstration by magnetic resonance neurography. Ann Neurol 2017; 82(5): 676-685. DOI: https://doi.org/10.1002/ana.25068

2. Pietsch AM, Viehoever A, Diem R, et al. Quantification and Proximal-to-Distal Distribution Pattern of Tibial Nerve Lesions in Relapsing-Remitting Multiple Sclerosis: Assessment by MR Neurography. Clin Neuroradiol 2023; 33(2):383-392. DOI: https://doi.org/10.1007/s00062-022-01219-1

3. Foesleitner O, Sturm V, Hayes J, et al. Microstructural changes of peripheral nerves in early multiple sclerosis: A prospective magnetic resonance neurography study. Eur J Neurol 2024; 31(2):e16126. DOI: https://doi.org/10.1111/ene.16126

4. Foesleitner O, Hayes JC, Weiler M. Evolution of peripheral nerve changes in early multiple sclerosis-a longitudinal MR neurography study. Front Neurol 2024;15:1335408. DOI: https://doi.org/10.3389/fneur.2024.1335408

Images/Tables

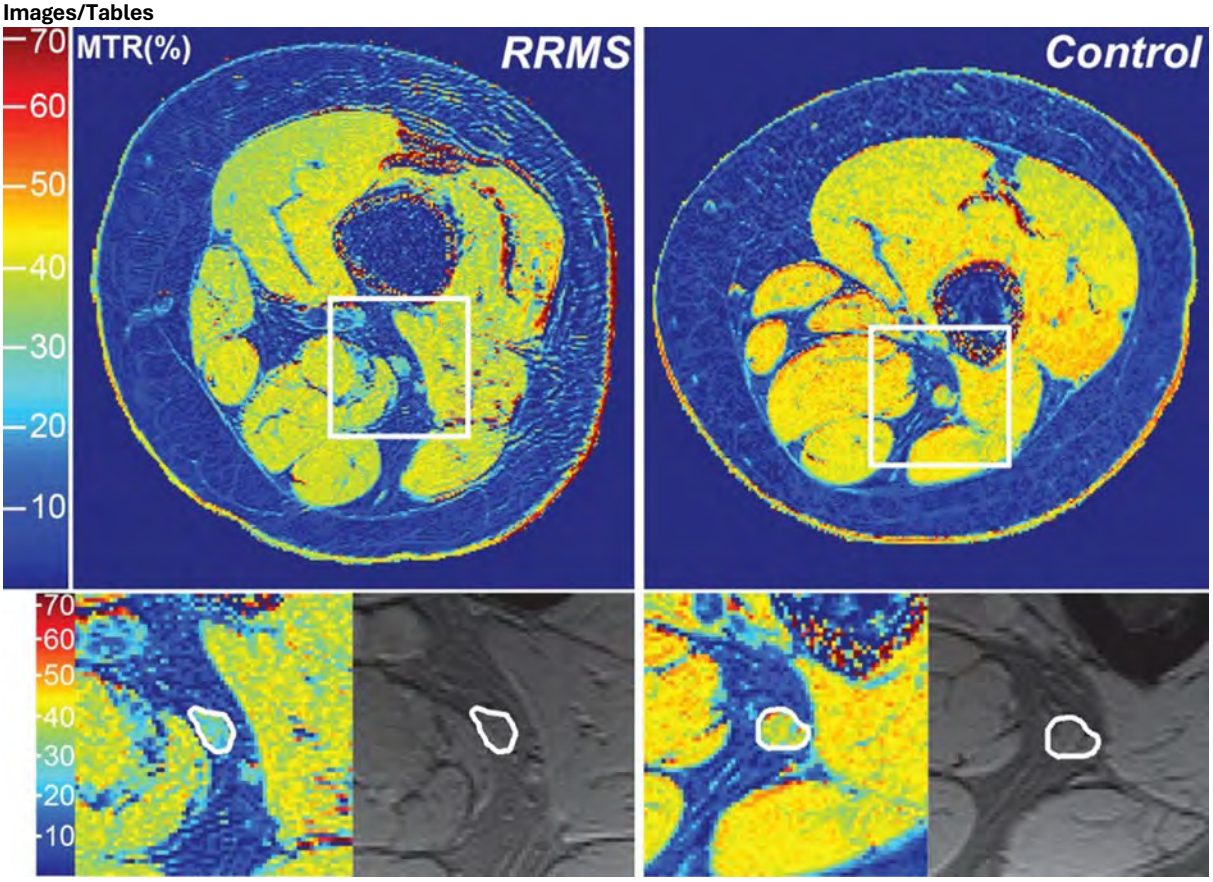

---

103 Composite Arterial and Venous Collateral Score on Single-Phase CTA Predicts 90-Day Outcomes in Anterior Circulation Large-Vessel Occlusion Stroke

Hamza A Salim MD[1], Dhairya A Lakhani MD[2], Jay Kakadiya MD[3], Cynthia Greene MD, PhD[3], Argye E Hillis MD, PhD[4], Tyler McGaughey PhD[2], Kambiz Nael MD[5], Adam A Dmytriw MD, MPH, MSc[6], Jeremy J Heit MD, PhD[7], Tobias D Faizy MD[8], Max Wintermark MD[1], Vivek S Yedavalli MD, MS, FAHA[3]
[1]Department of Neuroradiology, MD Anderson Medical Center, Houston, TX, USA. [2]Department of Neuroradiology, West Virginia University, Morgantown, WV, USA. [3]The Russell H. Morgan Department of Radiology and Radiological Science, Johns Hopkins University School of Medicine, Baltimore, MD, USA. [4]Department of Neurology, Johns Hopkins University School of Medicine, Baltimore, MD, USA. [5]Radiology and Biomedical Imaging, University California, San Francisco, CA, USA. [6]Neuroendovascular Program, Massachusetts General Hospital & Brigham and Women's Hospital, Harvard Medical School, Boston, MA, USA. [7]Department of Radiology, Division of Neuroradiology and Neurointervention, Stanford University, Stanford, CA, USA. [8]Department of Radiology, Neuroendovascular Division, University Medical Center Münster, Münster, Münster, Germany

Purpose

Collateral circulation influences clinical outcomes in patients with acute ischemic stroke due to anterior circulation large-vessel occlusion (LVO). While both arterial and venous collateral assessments on single-phase CTA have prognostic value, they have traditionally been evaluated independently. Purpose: We developed the CTA Collateral Impairment Score (CCIS), a composite measure incorporating arterial (Tan) and venous (COVES) scores, and investigated its association with 90-day functional outcomes.

Materials & Methods

We conducted a retrospective cohort study including 1,080 patients with anterior circulation LVO stroke across four comprehensive stroke centers. Patients were assigned a CCIS of 0 (preserved), 1 (moderate impairment), or 2 (severe impairment) based on predefined thresholds for Tan and COVES scores.

Results

Favorable outcomes (mRS 0–2) occurred in 66% of patients with CCIS 0, 32% with CCIS 1, and 17% with CCIS 2 ($p<0.001$). Mortality increased with higher CCIS (11%, 25%, and 36% for CCIS 0, 1, and 2 respectively; $p<0.001$). In multivariable models, CCIS 0 and 1 were independently associated with greater odds of favorable outcomes compared with CCIS 2 (adjusted OR 5.77 [95% CI, 3.78–8.82] and 1.72 [95% CI, 1.14–2.60], respectively). CCIS also predicted mortality (adjusted OR for CCIS 0 vs. 2: 0.39 [95% CI, 0.25–0.61]; $p<0.001$). The predictive performance of CCIS (AUC 0.73) exceeded that of ASPECTS and occlusion site and approximated NIHSS; inclusion of CCIS improved multivariable model discrimination (AUC 0.84).

Conclusion

CCIS, a composite arterial and venous collateral score derived from single-phase CTA, was strongly and independently associated with 90-day outcomes in anterior circulation LVO stroke. Its integration into acute stroke imaging assessment may improve risk stratification and guide therapeutic decisions.

References

1. Yedavalli VS, Koneru M, Hoseinyazdi M, Greene C, Lakhani DA, Xu R, Luna LP, Caplan JM, Dmytriw AA, Guenego A, Heit JJ, Albers GW, Wintermark M, Gonzalez LF, Urrutia VC, Huang J, Nael K, Leigh R, Marsh EB, Hillis AE, Llinas RH. Prolonged venous transit on perfusion imaging is associated with higher odds of mortality in successfully reperfused patients with large vessel occlusion stroke. J Neurointerv Surg. 2025 Feb 14;17(3):321-326. doi: 10.1136/jnis-2024-021488. PMID: 38471762.
2. Yedavalli V, Salim HA, Mei J, Lakhani DA, Balar A, Musmar B, Adeeb N, Hoseinyazdi M, Luna L, Deng F, Hyson NZ, Dmytriw AA, Guenego A, Faizy TD, Heit JJ, Albers GW, Lu H, Urrutia VC, Nael K, Marsh EB, Hillis AE, Llinas R. Decreased Quantitative Cerebral Blood Volume Is Associated With Poor Outcomes in Large Core Patients. Stroke. 2024 Oct;55(10):2409-2419. doi: 10.1161/STROKEAHA.124.047483. Epub 2024 Aug 26. PMID: 39185560.
3. Lakhani DA, Balar AB, Koneru M, Wen S, Ozkara BB, Caplan J, Dmytriw AA, Wang R, Lu H, Hoseinyazdi M, Nabi M, Mazumdar I, Cho A, Chen K, Sepehri S, Hyson N, Xu R, Urrutia V, Luna LP, Hillis A, Heit JJ, Albers GW, Rai AT, Faizy T, Wintermark M, Nael K, Yedavalli VS. Perfusion-Based Relative Cerebral Blood Volume Is Associated With Functional Dependence in Large-Vessel Occlusion Ischemic Stroke. J Am Heart Assoc. 2024 Dec 3;13(23):e034242. doi: 10.1161/JAHA.124.034242. Epub 2024 Nov 22. PMID: 39575711; PMCID: PMC11681566.
4. Lakhani DA, Balar AB, Koneru M, Hoseinyazdi M, Hyson N, Cho A, Greene C, Xu R, Luna L, Caplan J, Dmytriw A, Guenego A, Wintermark M, Gonzalez F, Urrutia V, Huang J, Nael K, Rai AT, Albers GW, Heit JJ, Yedavalli V. Pretreatment CT perfusion collateral parameters correlate with penumbra salvage in middle cerebral artery occlusion. J Neuroimaging. 2024 Jan-Feb;34(1):44-49. doi: 10.1111/jon.13178. Epub 2023 Dec 6. PMID: 38057941.
5. Lakhani DA, Salim H, Balar AB, Ali S, Wen S, Mei J, Hillis AE, Urrutia VC, Xu R, Broocks G, Fiehler J, Kniep HC, Stracke P, Krähling H, Albers GW, Lansberg M, Wintermark M, Heit JJ, Faizy TD, Yedavalli VS. The Cortical Vein Opacification Score (COVES) is independently associated with good and excellent functional outcomes at 90-days in minor stroke patients with anterior circulation large vessel occlusion: A Multicenter Study. AJNR Am J Neuroradiol. 2025 May 19:ajnr.A8739. doi: 10.3174/ajnr.A8739. Epub ahead of print. PMID: 40389269.

Images/Tables

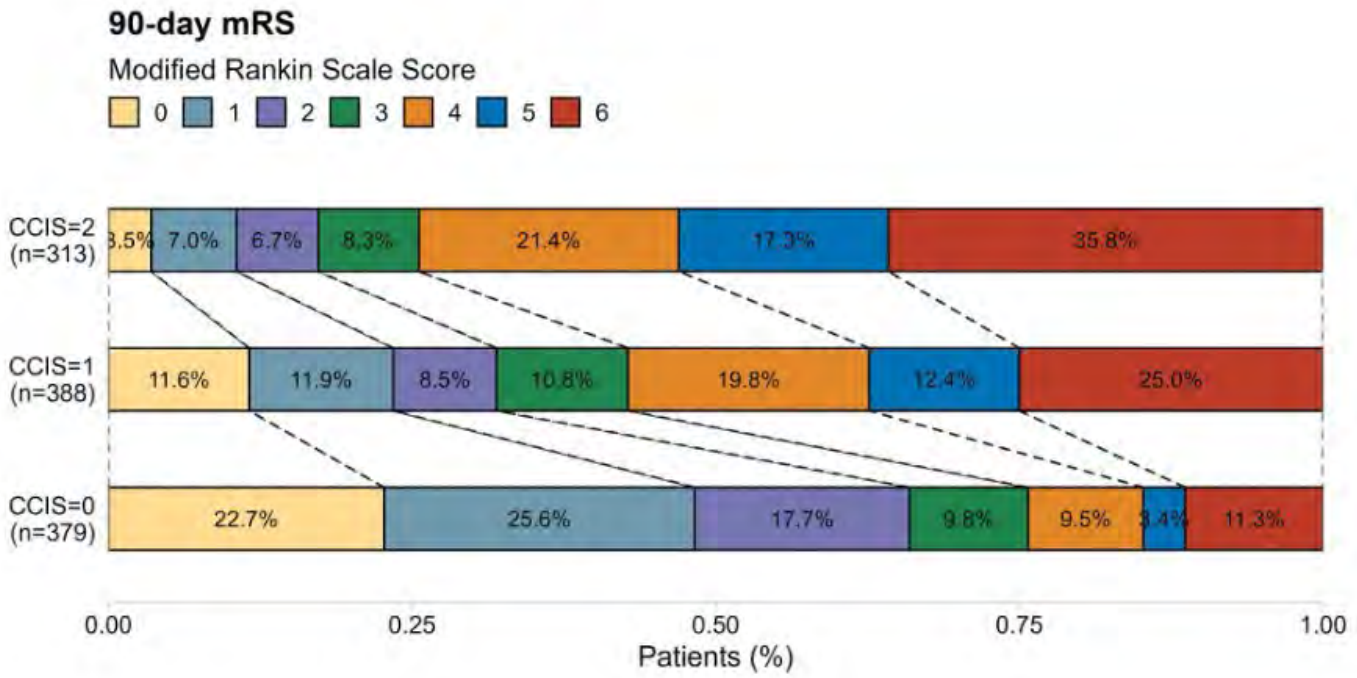

107 Comparison of baseline ASPECTS, Ischemic Lesion Net Water Uptake, and CBF<30% for the Prediction of Failed Recanalization during Mechanical Thrombectomy

Hamza A Salim MD[1], Dhairya A Lakhani MD[2], Jay Kakadiya MD[3], Cynthia Greene MD, PhD[3], Tyler McGaughey PhD[2], Argye E Hillis MD, PhD[4], Adam A Dmytriw MD, MPH, MSc[5], Kambiz Nael MD[6], Jeremy J Heit MD, PhD[7], Max Wintermark MD[1], VIvek S Yedavalli MD, MS, FAHA[3], Tobias D Faizy MD[8]
[1]Department of Neuroradiology, MD Anderson Medical Center, Houston, TX, USA. [2]Department of Neuroradiology, West Virginia University, Morgantown, WV, USA. [3]The Russell H. Morgan Department of Radiology and Radiological Science, Johns Hopkins University School of Medicine, Baltimore, MD, USA. [4]Department of Neurology, Johns Hopkins University School of Medicine, Baltimore, MD, USA. [5]Neuroendovascular Program, Massachusetts General Hospital & Brigham and Women's Hospital, Harvard Medical School, Boston, MA, USA. [6]Radiology and Biomedical Imaging, University California, San Francisco, CA, USA. [7]Department of Radiology, Division of Neuroradiology and Neurointervention, Stanford University, Stanford, CA, USA. [8]Department of Radiology, Neuroendovascular Division, University Medical Center Münster, Münster, Münster, Germany

Purpose

Failed recanalization (Frecan; mTICI 0–2a) after endovascular thrombectomy (EVT) occurs in ≈20% of patients with acute ischaemic stroke due to large-vessel occlusion (AIS-LVO). We compared three admission imaging biomarkers-net water uptake (NWU), Alberta Stroke Program Early CT Score (ASPECTS) and CT-perfusion–derived relative ischemic core volume (relative cerebral blood flow < 30%, rCBF < 30%)-for their ability to predict Frecan.

Materials & Methods

Consecutive anterior-circulation AIS-LVO cases treated within 24 h were retrospectively collected from two comprehensive stroke centers (January 2019–December 2024). NWU and ASPECTS were measured on non-contrast CT; rCBF < 30% volumes were obtained from CT perfusion. Univariable and multivariable logistic regression identified independent predictors of Frecan. Discriminative performance was evaluated with receiver-operatingcharacteristic (ROC) analysis; Youden's index defined optimal cut-offs.

Results

Among 688 patients (median age 75 years; 51.7% women), Frecan occurred in 133 (19.3%). Median NWU was higher in the Frecan group (8.08% vs 5.48%; p<0.001) as was median rCBF < 30% volume (13 mL vs 9 mL; p < 0.001); ASPECTS was lower (8 vs 9; p=0.023). On multivariable analysis, only NWU remained independently associated with Frecan (adjusted OR 1.16 per 1% increase; 95%CI 1.09–1.24; p<0.001). ROC curves showed superior predictive accuracy for NWU (AUC 0.659) compared with rCBF < 30% (AUC 0.542) and ASPECTS (AUC 0.557). An NWU threshold of 5.70% yielded 53.3% sensitivity and 74.4% specificity.

Conclusion

NWU outperforms ASPECTS and rCBF < 30% for predicting failed recanalization after EVT. Quantitative oedema assessment may improve pre-procedural risk stratification in AISLVO.

References

1. Yedavalli VS, Koneru M, Hoseinyazdi M, Greene C, Lakhani DA, Xu R, Luna LP, Caplan JM, Dmytriw AA, Guenego A, Heit JJ, Albers GW, Wintermark M, Gonzalez LF, Urrutia VC, Huang J, Nael K, Leigh R, Marsh EB, Hillis AE, Llinas RH. Prolonged venous transit on perfusion imaging is associated with higher odds of mortality in successfully reperfused patients with large vessel occlusion stroke. J Neurointerv Surg. 2025 Feb 14;17(3):321-326. doi: 10.1136/jnis-2024-021488. PMID: 38471762.
2. Yedavalli V, Salim HA, Mei J, Lakhani DA, Balar A, Musmar B, Adeeb N, Hoseinyazdi M, Luna L, Deng F, Hyson NZ, Dmytriw AA, Guenego A, Faizy TD, Heit JJ, Albers GW, Lu H, Urrutia VC, Nael K, Marsh EB, Hillis AE, Llinas R. Decreased Quantitative Cerebral Blood Volume Is Associated With Poor Outcomes in Large Core Patients. Stroke. 2024 Oct;55(10):2409-2419. doi: 10.1161/STROKEAHA.124.047483. Epub 2024 Aug 26. PMID: 39185560.
3. Lakhani DA, Balar AB, Koneru M, Wen S, Ozkara BB, Caplan J, Dmytriw AA, Wang R, Lu H, Hoseinyazdi M, Nabi M, Mazumdar I, Cho A, Chen K, Sepehri S, Hyson N, Xu R, Urrutia V, Luna LP, Hillis A, Heit JJ, Albers GW, Rai AT, Faizy T, Wintermark M, Nael K, Yedavalli VS. Perfusion-Based Relative Cerebral Blood Volume Is Associated With Functional Dependence in Large-Vessel Occlusion Ischemic Stroke. J Am Heart Assoc. 2024 Dec 3;13(23):e034242. doi: 10.1161/JAHA.124.034242. Epub 2024 Nov 22. PMID: 39575711; PMCID: PMC11681566.
4. Lakhani DA, Balar AB, Koneru M, Hoseinyazdi M, Hyson N, Cho A, Greene C, Xu R, Luna L, Caplan J, Dmytriw A, Guenego A, Wintermark M, Gonzalez F, Urrutia V, Huang J, Nael K, Rai AT, Albers GW, Heit JJ, Yedavalli V. Pretreatment CT perfusion collateral parameters correlate with penumbra salvage in middle cerebral artery occlusion. J Neuroimaging. 2024 Jan-Feb;34(1):44-49. doi: 10.1111/jon.13178. Epub 2023 Dec 6. PMID: 38057941.
5. Lakhani DA, Salim H, Balar AB, Ali S, Wen S, Mei J, Hillis AE, Urrutia VC, Xu R, Broocks G, Fiehler J, Kniep HC, Stracke P, Krähling H, Albers GW, Lansberg M, Wintermark M, Heit JJ, Faizy TD, Yedavalli VS. The Cortical Vein Opacification Score (COVES) is independently associated with good and excellent functional outcomes at 90-days in minor stroke patients with anterior circulation large vessel occlusion: A Multicenter Study. AJNR Am J Neuroradiol. 2025 May 19:ajnr.A8739. doi: 10.3174/ajnr.A8739. Epub ahead of print. PMID: 40389269.

444 Mandibular Arteriovenous Malformation (Yakes Type IIIa/IIIb AVM) Diagnosis and Curative Treatment

Wayne F Yakesq MD, FSIR, FCIRSE, FRSM
The Yakes Vascular Malformation Center, Englewood, CO, USA

Purpose

To determine optimal management strategies for the treatment of intraosseous mandibular AVM.

Materials & Methods

12 patients (9 females, 3 males), age 9 -14; mean age 10, underwent endovascular therapy to treat their mandibular AVMs. 9 patients had distinct intraosseous AVMs. 3 had additional multiple facial and intra-maxillary AVMs requiring treatment. Outside institutions recommended massive hemi-facial resections in these patients. 4 patients had prior PVA and gel foam embolization, 1 patient had a lip graft, 1 had prior mandible surgery, all that had failed.

Results

All 12 patients have demonstrated MR and angiographic cure of their AVMs. 1 patient's therapy is not completed and is on-going. The patients mandibular AVMs cured, a third AVM in this patient in the infratemporal fossa is still undergoing treatment. The follow-up range is 11 months – 41

months, with a mean follow-up of 29 months. No complications were noted in treatment of mandibular AVMS. 1 patient required a minor gingival surgery after treatment of an additional intramaxillary AVM with inferior extension.

Conclusion

Endovascular approaches to manage mandibular AVM can be curative. The mandibular intraosseous variety is largely a vein aneurysm in the mandible with the nidus being the vein aneurysm wall and the bulk are Yakes Type IIIa/IIIb AVMs. All respond and can be cured by endovascular ethanol therapy alone. Surgery was not required in any patient. Surprisingly no complications were encountered in this patient series. Long-term cures are noted in this patient series with endovascular approaches alone. No massive surgical resections in any patient, even in patients with multiple AVMs of the face and scalp soft tissues, mandible and maxilla, was required to effect cure. In patients who suffered hemorrhages from floating teeth, bone formed and stabilized the teeth and no further hemorrhages occurred. Ethanol sclerotherapy proved curative in mandibular intraosseous AVMs in patients who had additional facial soft-tissue and intramaxillary AVMs that were cured as well at long-term follow-up.

---

687 Normative MR Fingerprinting and Cognitive Findings in a Large Cohort of Healthy Older Adults

Douglas J Martin MD, PhD[1], Stephen Jones MD, PhD[1], Ajay Nemani PhD[1], Mark Lowe PhD[1], Christopher MacClugage[1], Yugo Boureima[1], Ketan Fernandes[1], Jessica Padilla[1], Mark Griswold[2], Darlene Floden PhD[1], Imad Najm MD[1]

[1]Cleveland Clinic, Cleveland, OH, USA. [2]Case Western Reserve University, Cleveland, OH, USA

Purpose

Quantitative MRI acquired through MR fingerprinting (MRF) has shown promise as an imaging biomarker in a number of neurologic disorders, including dementia. Successful development of this technique for dementia will require a more thorough understanding of how T1 and T2 relaxation times change in the normal aging brain.

Materials & Methods

The Cleveland Clinic Brain Study is a longitudinal evaluation of healthy aging adults combining extensive laboratory, imaging, and neuropsychologic testing to identify biomarkers for CNS disease. In this initial cohort, a total of 2700 brain MRIs are included in the analysis (1952 females, 748 males), of which 494 are repeated scans. The protocol includes anatomical MPRAGE, 3D T2 GRE, 3D FLAIR, TOF MRA, resting state fMRI, ASL, DTI and 2D MRF (within a 60-minute slot).

T1 and T2 maps are generated from the MRF data and segmented into cortex, white matter, basal ganglia, and CSF spaces as defined from the high-resolution anatomic imaging using Freesurfer. Whole brain histograms of the cortical gray matter and white matter T1 and T2 are analyzed with a bi-gaussian fit in log-normal space (Figure 1A), yielding 4 representative relaxation times for each combination. Multiple neuropsychiatric metrics (e.g., history questionnaire, performance on memory tests, reaction times, etc.) are combined to produce a single predicted probability of cognitive impairment (probCI). Comparison is made between relaxation times derived from MRF, demographic data including age, and probCI using multiple variable regression analysis.

Results

The following are mean MRF values (in milliseconds) across all ages: 1344.5 +/- 31.0 (GM T1); 47.6 +/- 4.2 (GM T2); 901.5 +/- 32.4 (WM T1); 39.1 +/- 3.5 (WM T2). Figure 1B shows the correlation of white matter T1 with age, with overlaid linear fits and confidence intervals. All slopes were statistically different from zero, with the strongest correlation between age and white matter T1 and T2 values. A nonlinear fit of probCI and age is highly predictive ($p<0.001$). Because both probCI and white matter T1 times vary with age, the relationship needs to address the covariance. A simple analysis to covary for age is shown in Figure 1C for T1 values in WM with age groups of <60, 60-70, and >70. Only the slope of the oldest cohort shows significant difference from zero ($p=0.016$ over 70 years of age vs. $p=0.08$ between 60 and 70 and $p=0.46$ under 60), suggesting a small effect correlating T1 WM relaxation times with probCI. Using multiple variable regression to model the log of probCI, GM T1 is also a significant predictor after adjusting for both age and GM T2 ($p=0.025$).

Conclusion

An initial large cohort from the Cleveland Clinic Brain Study demonstrates trends in gray and white matter T1 and T2 relaxation times in healthy aging adults. Preliminary analysis suggests a correlation between white and gray matter T1 values and the probability of cognitive impairment.

References

Keil VC, Bakoeva SP, Jurcoane A, et al. MR fingerprinting as a diagnostic tool in patients with frontotemporal lobe degeneration: A pilot study. *NMR Biomed*. 2019 Nov;32(11):e4157. doi: 10.1002/nbm.4157.

Ma D, Gulani V, Seiberlich N, et al. Magnetic resonance fingerprinting. *Nature*. 2013 Mar 14;495(7440):187-92. doi: 10.1038/nature11971.

Images/Tables

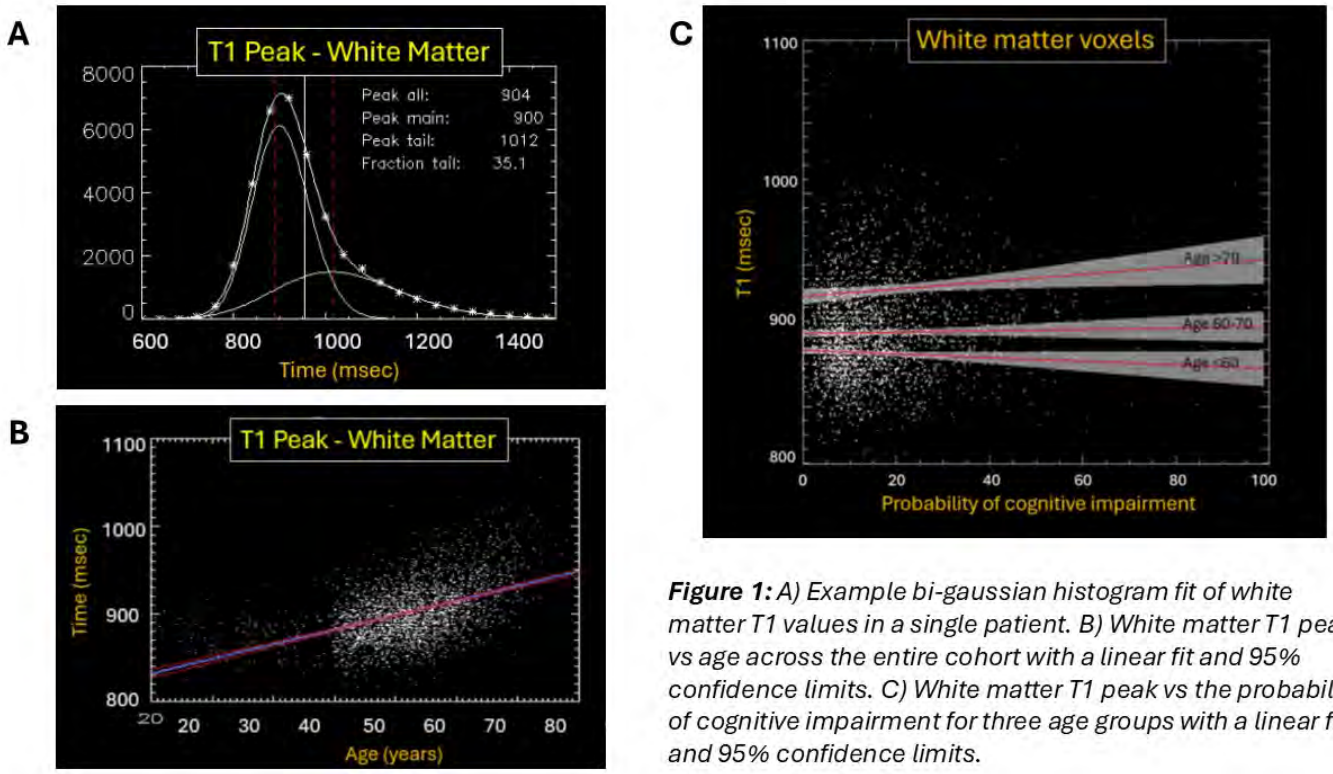

Figure 1: *A) Example bi-gaussian histogram fit of white matter T1 values in a single patient. B) White matter T1 peak vs age across the entire cohort with a linear fit and 95% confidence limits. C) White matter T1 peak vs the probability of cognitive impairment for three age groups with a linear fit and 95% confidence limits.*

---

688 Does Joint Reconstruction of FDG PET-MRI Improve Detection of Insular Abnormalities?

David Ola MD, Gopi Nayak MD, Matthew Breen MD, James R Loftus MD, Kevin Hsu MD, Timothy M Shepherd M.D./Ph.D
NYU Langone Health, New York, New york, USA

Purpose

Insular seizure foci are notoriously difficult to detect using EEG, MRI or FDG PET – the MRI is often negative whereas FDG uptake in the insula is heterogeneous and obscured by partial volume effects with the adjacent FDG-avid putamen using the standard Ordered Subset Expectation Maximization (OSEM) PET image reconstructions. Failure to identify an insular seizure focus or involvement within a larger seizure network can result in failed epilepsy surgery. Joint PET/MR reconstruction improves image resolution and more closely approximates ground truth data [1,2]. We tested the hypothesis that joint PET-MRI image reconstruction can improve recognition of insular abnormalities in epilepsy PET data.

Materials & Methods

This retrospective study identified FDG PET–MRI studies referred from a level IV epilepsy center over the previous 5 years with and without insular FDG abnormalities documented in the radiology report and confirmed by expert consensus (N=12 each). Cases were excluded for motion, diffuse FDG or MRI abnormalities or bilateral insular changes. Four cases from each pool were duplicated to assess intra-rater consistency. For each case, coronal and axial FDG PET data were generated with OSEM and joint reconstruction techniques.

Then, 3 neuroradiologists with extensive PET interpretation experience performed a blinded, independent rater assessment of the images (16x2x2 ~ 64 individual datasets each) for insular abnormalities (none, right, left), image quality (1-4) and diagnostic confidence (1-3). For control subjects we characterized the SUVmax within the anterior, intermediate, and posterior insula relative to the putamen. Regional uptake variation was analyzed using Friedman and Dunn–Bonferroni tests. Other statistical analyses included Wilcoxon signed-rank and evaluation of diagnostic performance and rater agreement.

Results

Joint reconstruction improved aggregate sensitivity and accuracy (100% and 94%) for insular FDG abnormalities versus the OSEM method (69% and 81%), with a slight reduction in specificity. Joint reconstruction was perceived as higher quality by all readers ($p < 0.05$) and produced significantly higher diagnostic confidence for two of three readers and in the aggregate. Inter-rater agreement improved ($\kappa = 0.56$ vs 0.44), with two readers showing increased intra-rater reliability ($\kappa = 0.81/0.62$ vs 0.74/0.43). Significant differences in normalized FDG uptake were found among insular subregions ($p < 0.001$) – e.g. FDG uptake in the posterior insula was approximately 55% higher than in the anterior insula.

Conclusion

Joint PET–MRI reconstruction enhances image quality, reader confidence, and sensitivity for insular lesion detection, with modest gains in agreement and accuracy.

References

1. Knoll, F., Holler, M., Koesters, T., Otazo, R., Bredies, K., & Sodickson, D. K. (2016). Joint MR-PET reconstruction using a multi-channel image regularizer. *IEEE transactions on medical imaging*, *36*(1), 1-16.
2. Ehrhardt, M. J., Thielemans, K., Pizarro, L., Atkinson, D., Ourselin, S., Hutton, B. F., & Arridge, S. R. (2014). Joint reconstruction of PET-MRI by exploiting structural similarity. *Inverse Problems*, *31*(1), 015001.

Images/Tables

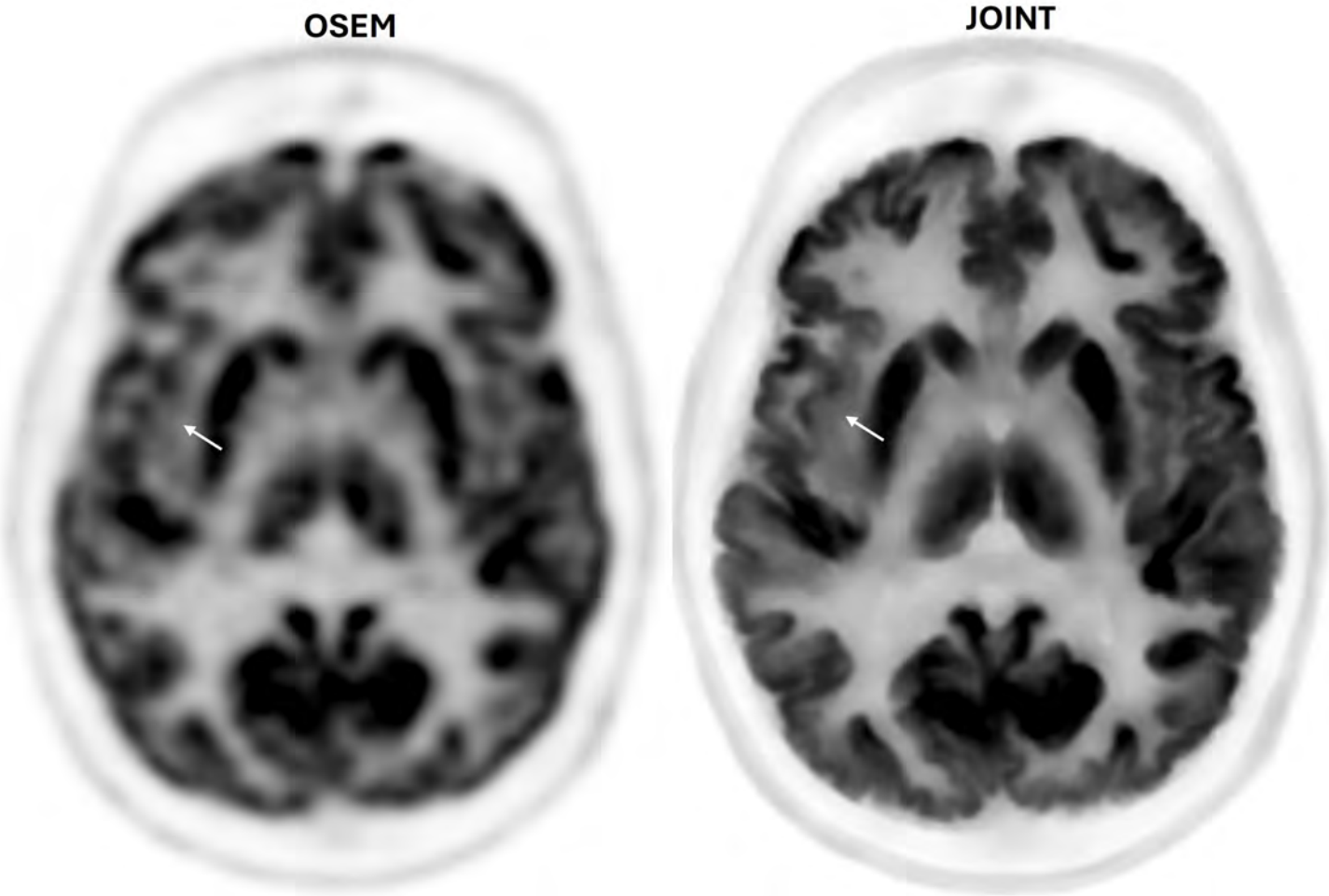

Example image from rater study demonstrating improved detection of right insular FDG hypometabolism (arrows) with joint PET-MRI reconstruction compared to standard reconstruction. Correct identification was achieved by 1 of 3 raters on the standard reconstruction versus 3 of 3 raters on the joint reconstruction.

---

148 Comparison of resting-state fMRI-based dynamic laterality index with task-based fMRI for language lateralization

Shreyas Reddy Kankara, Akshay Kumaar, Sachin Patalasingh, Radha Kumari, Malvika Ganesh, Rimjhim Agrawal
BrainSightAI, Bangalore, Karnataka, India

Purpose

Language mapping with functional magnetic resonance imaging (fMRI) is used in clinical settings to assist in presurgical planning and minimize resection of the eloquent cortex. Task-based functional MRI (tb-fMRI) is routinely used to determine language lateralization. It is, however, limited by many practical challenges, such as patient compliance and pre-existing medical conditions, such as coma, paralysis, age, cognitive response, physical impairment, mental condition, and aphasia. Resting-state fMRI (rs-fMRI) offers an alternative, task-independent technique to evaluate language lateralization. We compared tb-fMRI and various rs-fMRI techniques in studying language hemispheric dominance.

Materials & Methods

We used functional imaging data from 75 participants of the Human Connectome Project (HCP) to compare 5 laterality index (LI) calculation methods based on resting-state fMRI against task-based lateralization using the story-math paradigm. After preprocessing, LI was derived using intensity-based independent component analysis (ICA), connectivity-based, intrahemispheric connectivity, rsLI difference, and dynamic LI (leveraging temporal pattern of LI) approaches, with a lateralization threshold of ±0.15. Kruskal-Wallis and Dunn's tests were used for statistical comparisons, and F1 scores were compared with task-based lateralization as the gold standard.

Results

Bilateral lateralization (-0.15 < LI < +0.15) was most frequent across all rs-fMRI-based LI methods, while left lateralization was predominant in tb-fMRI. The Kruskal–Wallis test showed significant differences in LI across methods ($H = 40.73$, $p = 1.06 \times 10^{-7}$), with tb-fMRI differing from every method except dynamic LI. Dynamic LI achieved the best performance (accuracy 0.74, macro F1 = 0.63), while ICA-intensity showed the lowest accuracy (0.36). All the methods show the best performance in predicting bilateral lateralization as opposed to left or right. Among dynamic LI's 19 discordant cases with tb-fMRI, 37% were ambidextrous, with most mismatches involving bilateral vs. unilateral classifications.

Conclusion

We systematically evaluated five rs-fMRI-based laterality index (LI) methods against tb-fMRI-based LI, identifying dynamic LI as the most accurate approach. Notably, our findings revealed more bilateral lateralization patterns with rs-fMRI, likely attributable to strong homotopic interhemispheric correlations inherent in resting-state data. Factors such as atlas selection, region of interest definitions, and handedness could have contributed to outcome variability. Nevertheless, rs-fMRI-based dynamic LI exhibits the capacity to determine lateralization in situations where tb-fMRI is not

available or feasible, for example, in resource-constrained settings. Future studies should test the potential of the dynamic LI method on clinical data. By leveraging rsfMRI, which is independent of the tasks used to assess language, and by using fixed regions of interest, which have been found to vary across studies, we attempt to standardize language fMRI.

References

1) P. Branco, D. Seixas, and S. L. Castro, 'Mapping language with resting-state functional magnetic resonance imaging: A study on the functional profile of the language network', *Hum. Brain Mapp.*, vol. 41, no. 2, pp. 545–560, 2020, doi: 10.1002/hbm.24821.

2) V. A. Kumar *et al.*, 'The role of resting-state functional MRI for clinical preoperative language mapping', Cancer Imaging Off. Publ. Int. Cancer Imaging Soc., vol. 20, no. 1, p. 47, July 2020, doi: 10.1186/s40644-020-00327-w.

3) J.-M. Lemée et al., 'Resting-state functional magnetic resonance imaging versus task-based activity for language mapping and correlation with perioperative cortical mapping', *Brain Behav.*, vol. 9, no. 10, p. e01362, 2019, doi: 10.1002/brb3.1362.

4) S. Gohel *et al.*, 'Resting-State Functional Connectivity of the Middle Frontal Gyrus Can Predict Language Lateralization in Patients with Brain Tumors', AJNR Am. J. Neuroradiol., vol. 40, no. 2, pp. 319–325, Feb. 2019, doi: 10.3174/ajnr.A5932.

5) D. M. Barch *et al.*, 'Function in the human connectome: Task-fMRI and individual differences in behavior', *NeuroImage*, vol. 80, pp. 169–189, Oct. 2013, doi: 10.1016/j.neuroimage.2013.05.033.

Images/Tables

Table 1: Metrics from different methods of deriving the laterality index (LI) and resultant lateralization. The counts and F1 Scores of bilateral, left, and right lateralization, as well as the accuracy of different resting-state fMRI (rs-fMRI) methods, are shown in the last four columns.

S. no.	Method	LI [mean, median, std]	Bilateral counts | F1_score	Left counts | F1_score	Right counts | F1_score	Accuracy	Macro F1 score
1.	tb-fMRI	[0.12, 0.14, 0.23]	33 | 1.00	36 | 1.00	5 | 1.00	1.00	1.00
2.	rs-fMRI Method 1 ICA-intensity	[0.01,0.01,0.23]	48 | 0.47	13 | 0.24	13 | 0.22	0.36	0.31
3.	rs-fMRI Method 2 connectivity	[0.02,0.02,0.04]	74 | 0.62	0 | 0.00	0 | 0.00	0.45	0.21
4.	rs-fMRI Method 3 intra-hemispheric	[0.03,0.03,0.08]	68 | 0.57	5 | 0.05	1 | 0.33	0.42	0.32
5.	rs-fMRI Method 4 LI difference	[0.03,0.03,0.07]	68 | 0.57	5 | 0.05	1 | 0.33	0.42	0.32
6.	rs-fMRI Method 5 dynamic LI	[0.14,0.10,0.26]	37 | 0.77	30 | 0.79	7 | 0.33	0.74	0.63

1077 Adverse Outcomes Associated with Lumbar Punctures with Concurrent Anticoagulant Use: A Bioinformatics Approach

Mohammad Kassar MD, Justin Addicks MD, Dhairya Lakhani MD, Erin Butcho MD, Melissa Jung MD, Tyler McGaughey PhD

West Virginia University, Morgantown, WV, USA

Purpose

Lumbar Punctures (LP) are one of the most common invasive clinical procedures because of their utility for diagnostics and therapeutics. However, a standing contraindication, active anticoagulant use, limits the use of this procedure in a population who stands to benefit from the timely administration of the procedure. Recent guideline changes by the Society for Interventional Radiology (SIR) support LPs in patients who are taking anticoagulants. Our novel bioinformatics approach provides further support for this finding by surveying patients across our Appalachian health system for adverse outcomes due to concurrent anticoagulant therapy and LP.

Materials & Methods

A Structured Query Language (SQL) query was built to survey all electronic health records across the health system network. We identified patients who had undergone lumbar punctures while taking anticoagulants including: Apixaban, Eliquis, Dabigatran, Pradaxa, Rivaroxaban or Xarelto. To survey for adverse outcomes amongst this patient population, we queried for submitted ICD-10 codes within a year of the LP including paraplegia unspecified (G82.20), contusion of the lower back and pelvis (S30.0XXa), other specified paralytic syndromes (G83.89), postprocedural hematoma (G97.61-62), radiculopathy (M54.1X), and epidural hemorrhage (S06.4X). Expert chart review was then completed by two independent physician reviewers to determine causation.

Results

9892 unique patients underwent a lumbar puncture. 246 of these patients underwent LPs while anticoagulated, of which 21 experienced adverse events within the following year. Expert chart review determined that none of these adverse events were attributable to the procedure itself.

Conclusion

Lumbar punctures (LPs) are a common diagnostic procedure used to confirm central nervous system infections, bleeding, autoimmune disorders, tumors, and other conditions. One of the rare, major complications of LPs includes bleeding into the spinal canal with serious complications of

paralysis, sensory loss, loss of bladder/bowel control, and even death. The use of anticoagulants have largely increased and diagnostic lumbar punctures in patients taking these drugs represents a challenge considering the opposing risks of bleeding and thrombotic complications.
Our study examined the safety of performing LPs in patients on anticoagulants without a washout period. These findings suggest that the perceived risk of severe complications from LPs in anticoagulated patients may be lower than previously thought. This data challenges the conventional approach of holding or delaying anticoagulation prior to LPs in emergent situations. While further research is needed, our results provide reassurance that emergent LPs can often be performed safely, even in the context of anticoagulation therapy, potentially avoiding delays that could jeopardize patient outcomes.

References

Doherty CM, Forbes RB. Diagnostic Lumbar Puncture. *Ulster Med J*. 2014;83(2):93-102.
Domingues R, Bruniera G, Brunale F, et al. Lumbar puncture in patients using anticoagulants and antiplatelet agents. *Arquivos de Neuro-Psiquiatria* 2016;74:679–86.
Epstein N. Neurological complications of lumbar and cervical dural punctures with a focus on epidural injections. *Surgical Neurology International* 2017;8:60.
Patel IJ, Rahim S, Davidson JC, et al. Society of Interventional Radiology Consensus Guidelines for the periprocedural management of thrombotic and bleeding risk in patients undergoing percutaneous image-guided interventions—part II: Recommendations. *Journal of Vascular and Interventional Radiology* 2019;30.

Images/Tables

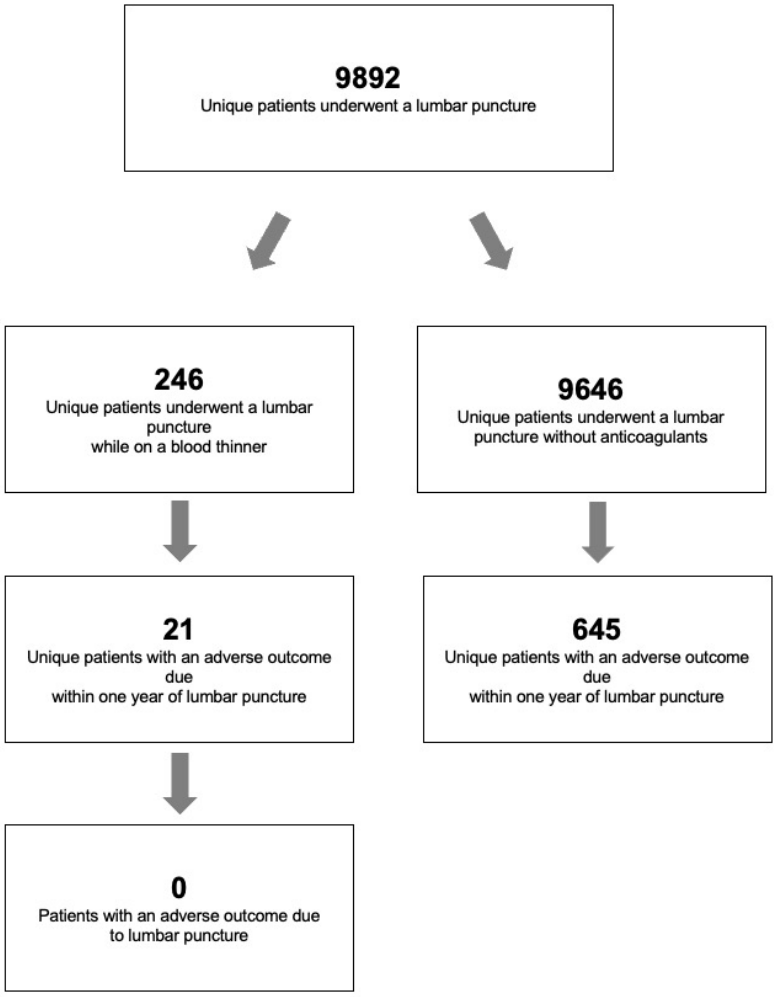

Scientific Abstract Power Pitches & Luminary Speaker: AI-Enhanced Brain MRI: Techniques and Clinical Application

3:20 - 4:20pm Tuesday, 19th May, 2026

614 A Preliminary Comparison of 0.55 Tesla MRI with Deep Learning Reconstruction and 3 Tesla for Diagnostic and Surgical Assessment in Glioma

Jon O Cleary MD-PhD, FRCR[1], Anthony N Price PhD[1], Jonathan Shapey MD, PhD, FRCS[2]
[1]King's College London/Guy's and St. Thomas' NHS, London, London, United Kingdom. [2]King's College London/King's College Hospital NHS Foundation Trust, London, London, United Kingdom

Purpose

Modern wide-bore 0.55T MRI scanners offer greater patient comfort, smaller footprint, flexible installation, and more benign safety profiles than conventional (1.5/3T) systems – benefitting intraoperative applications and lower resource settings[1,2].

High-resolution(~1mm) 3D-imaging is essential for accurate glioma characterization, and surgical/radiotherapy planning. Deep learning (DL) image reconstruction may mitigate longer imaging times necessary to maintain image quality and resolution at 0.55T[3].

We employed DL-enhanced volumetric sequences, devising a 0.55T neuro-oncology protocol, with comparable clinical duration. Performing preliminary comparison with standard-of-care (SoC) 3T, from the same session, we show feasibility of 0.55T for pre-/post-operative glioma assessment, in the first six-patients of this ongoing study.

Materials & Methods

Imaging:Performed on 0.55T MAGNETOM Free.Max and 3T MAGNETOM Vida systems (Siemens Healthineers), using 12 and 20-channel head-neck coils respectively.

0.55T neuro-oncology protocol used prototype DL-reconstruction sequences (Siemens Deep Resolve Boost–DRB, ~1mm isotropic): 3D-FLAIR, T2-SPACE, and T1-SPACE and MPRAGE pre- and post-contrast. Additional sequences included: 2D-T2 (DRB), 2D-EPI-DWI (b=0&1000s/mm2) and 3D-EPI-SWI.

Our institution's 3T protocol was used for comparison and targeted for 0.55T scan time. (Total 3T sequence time:33min10sec; 0.55T:34min52s.)

Patient Imaging:Six IDH-wildtype (mean age 52-years, 5-males) glioblastoma patients gave IRB-approved, written consent.

Imaging session comprised: 1) pre-contrast 0.55T, 2) full SoC 3T protocol (including Gadobutrol) and 3) return to the 0.55T for post-contrast imaging. Five patients, clinically well postoperatively, were imaged again on both systems <48-hours after surgery. (Mean contrast delay before 0.55T post-contrast images after injection: ~22min pre-op; ~18min post-op).

Experienced clinicians – two fellowship-trained attending neuroradiologists and two attending neurosurgeons – assessed images. Domains assessed included diagnostic quality (delineation of DWI, hemorrhagic, enhancing components, T2/FLAIR extent), as well as overall image quality.

Results

*Fig1:*Comparative 0.55/3T images from 50-year-old right insula glioblastoma patient. 0.55T 2D-DL-T2 (top left), b=1000-DWI (top right), and DL-SPACE-FLAIR (bottom left) images show hyperintense tumour extent in insula, basal ganglia and temporal lobe, similar to 3T (green/red arrows). EPI-SWI (bottom right) was sensitive, identifying tiny internal vascular structures within the lesion (blue arrows/inset panel).

*Fig2:*1mm 3D-T2-SPACE images from 48-year-old with left insula glioblastoma. Internal flow voids (blue arrows) and similar posterior deep white matter tumor-oedema extent (green arrows) visible at both fields.

*Fig3:*Pre & post-operative 3D FLAIR, post-contrast MPRAGE and T1-SPACE in 46-year-old with right temporal glioblastoma. 0.55T and 3T FLAIR both depict similar temporal tumor-oedema extent and small areas of ongoing high-signal after resection (green arrows), Post-contrast DL-enhanced 0.55T and standard 3T MPRAGE and SPACE images (middle and right) both similarly delineate thick-walled enhancement pre-op (red arrows) and small post-surgical residuum (orange arrows).

Conclusion

Expert assessment found 0.55T tumor delineation (edema, enhancement, post-operative residual) was similar to 3T, despite slight reduction in perceived image sharpness. This echoes prior positive assessments of 0.55T in brain metastases and other conditions[3,4,5].

0.55T DL-enhanced volumetric scans were shorter (~3-7 minutes) – compared to >10min for non-DL sequences previously[3].

We continue to build experience with ongoing recruitment.

Wide-bore 0.55T MRI, with DL-enhanced 3D-sequences, may provide comparable pre- and post-operative glioma diagnostic information, in similar scan time (~35min), to higher-field SoC systems.

References

1. Campbell-Washburn A *et al.* Opportunities in Interventional and Diagnostic Imaging by Using High-Performance Low-Field-Strength MRI. *Radiology* 293 (2) : 2019
doi: 10.1148/radiol.2019190452

2. Runge VM, *et al.* Advocating the development of next-generation, advanced-design low-field magnetic resonance systems. *Invest. Radiol.* 55(12):747-753 (2020)
doi: 10.1097/RLI.0000000000000703

3. Grigo J, *et al.* Usability of magnetic resonance images acquired at a novel low-field 0.55 T scanner for brain radiotherapy treatment planning. Phys. I*maging Radiat. Oncol.* 13:25:100412. (2023)
doi: 10.1016/j.phro.2023.100412

4. Lavrova A, *et al.* Quality assessment of routine brain imaging at 0.55 T: initial experience in a clinical workflow. NMR Biomed. 2023 e5017 doi: 10.1002/nbm.5017

5. Lavrova A, *et al.* Retrospective comparison of routine brain MRI scans in patients at 0.55 T and 1.5/3T. *Eur. J. Radiol.* 2025;184:111929. doi: 10.1016/j.ejrad.2025.111929

Images/Tables

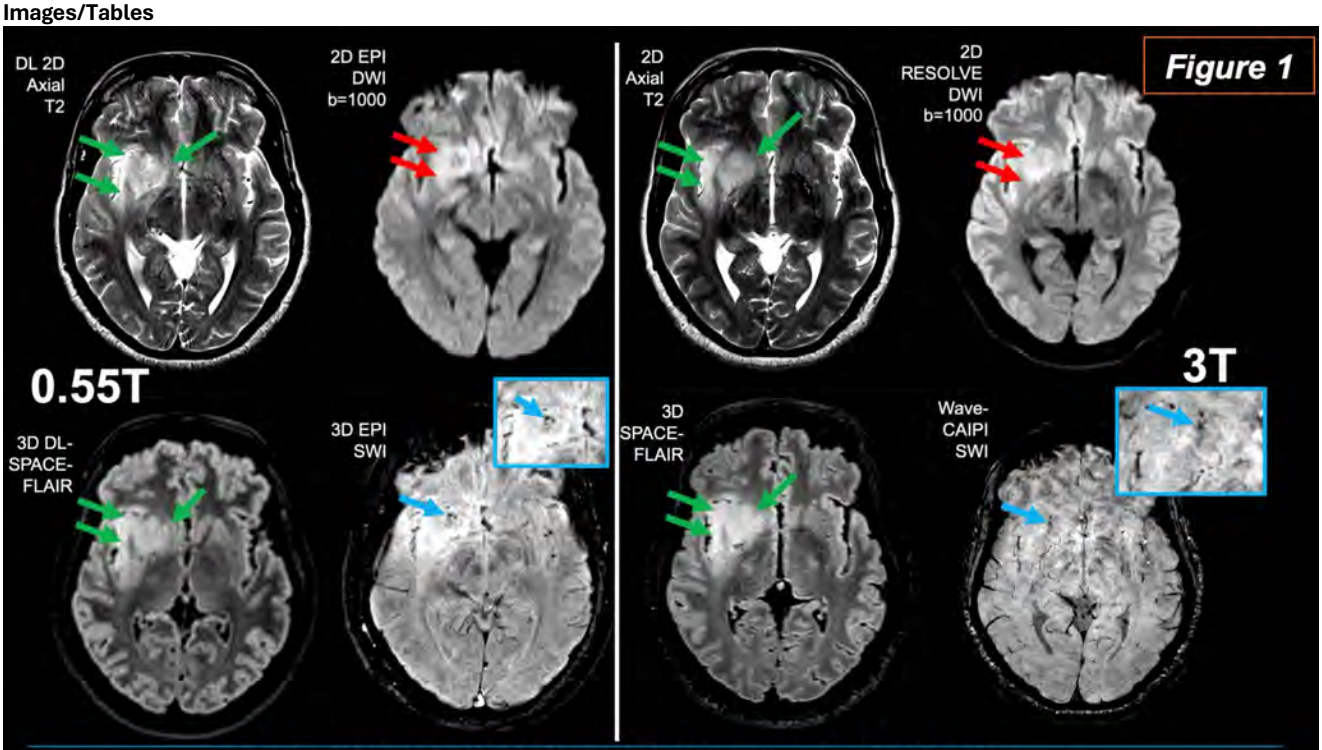

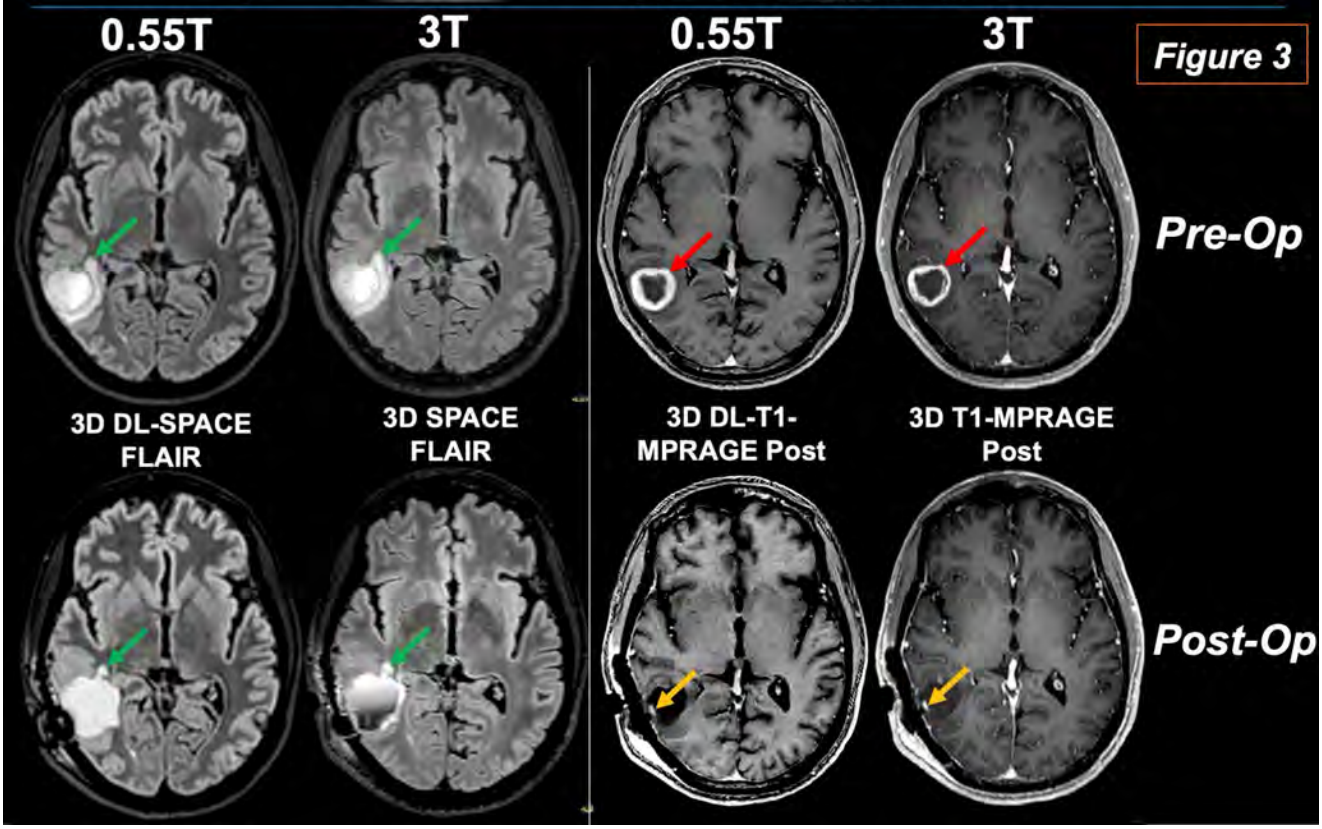

1192 Pathology-Aware Targeted T1 synthesis from T2 and FLAIR images using Deep Learning

Srivathsa Pasumarthi
Subtle Medical Inc, Menlo Park, California, USA

Purpose

Multi-contrast brain MRI images offer complimentary information that aids in differential diagnosis, treatment and surgical planning. The acquisition of multi-contrast images is time consuming and is often susceptible to various artifacts. In this work, we propose the synthesis of T1w weighted images from T2 and FLAIR images using a multi-contrast multi-scale vision transformer, with a pathology-aware loss function. T1w images are usually acquired at the start of any brain protocol and provide the structural baseline for the entire scan. Other contrasts like T2, FLAIR and sometimes T1CE provide additional pathological information that are compared against the T1w. Thus it was inferred that the basic brain structure in the T1w image can be faithfully reconstructed from T2 and FLAIR images alone. Therefore, synthesis of T1w images cuts down on the time required to acquire (~4 mins for 3D and ~1.5 mins for 2D). We quantitatively evaluate the synthesized and acquired T1w images using PSNR, SSIM and RMSE.

Materials & Methods

A generic multi-contrast multi-scale vision transformer (MMT)[1] was trained on all input/output combinations i.e., any subset of T1, T1C ,T2 and FLAIR as input and the missing sequence as the output. This model was further fine tuned by fixing T2 and FLAIR as inputs, and T1 as the output. Lesion masks were generated with the T1 and T1C images as inputs, using an nnUNet[2] based segmentation model trained on the BrATS-GOAT[3] challenge dataset. The training dataset consists of a wide range of lesions including gliomas, meningiomas, metastases and pediatric tumors. The segmented lesion masks were used to weight the L1 reconstruction loss in the T1-synthesis network to make the model pathology-aware. The T1C images are required only for training; at test time, the T2 and FLAIR inputs are sufficient to synthesize the T1 images.

Multi-contrast (T1w, T2 and FLAIR) brain MRI images from 25 patient studies were used for evaluation in this study. The synthesized T1w images were quantitatively evaluated against the acquired T1w images using peak signal-to-noise ratio (PSNR), structural similarity index metric (SSIM) and root mean squared error (RMSE).

Results

Fig 1a shows the overview of the T1 synthesis algorithm. Fig 1b, 1c and 1d show the acquired T2, FLAIR and T1 images with the synthesized T1 images for 3 patients. The average PSNR, SSIM and RMSE over the 25 patient studies are 33.53 ± 1.75, 0.91 ± 0.13 and 0.18 ± 0.02 respectively. It can also be seen in some cases that the synthesized T1w images have better overall image quality with less artifacts.

Conclusion

In this study, we have shown the feasibility of synthesizing T1w images from T2 and FLAIR to reduce the scan time. The synthesized T1w images provide similar structural information as that of the acquired T1w images. Future studies will include downstream tasks such as tissue segmentation and tumor segmentation using the synthesized T1 images to show the clinical performance.

References

1. Liu, J., Pasumarthi, S., Duffy, B., Gong, E., Datta, K., & Zaharchuk, G. (2023). One model to synthesize them all: Multi-contrast multi-scale transformer for missing data imputation. IEEE transactions on medical imaging, 42(9), 2577-2591.
2. Isensee, F., Jaeger, P. F., Kohl, S. A., Petersen, J., & Maier-Hein, K. H. (2021). nnU-Net: a self-configuring method for deep learning-based biomedical image segmentation. Nature methods, 18(2), 203-211.
3. Maani, F. A., Hashmi, A. U. R., Saeed, N., & Yaqub, M. (2024, May). On enhancing brain tumor segmentation across diverse populations with convolutional neural networks. In 2024 IEEE International Symposium on Biomedical Imaging (ISBI) (pp. 1-4). IEEE.

Images/Tables

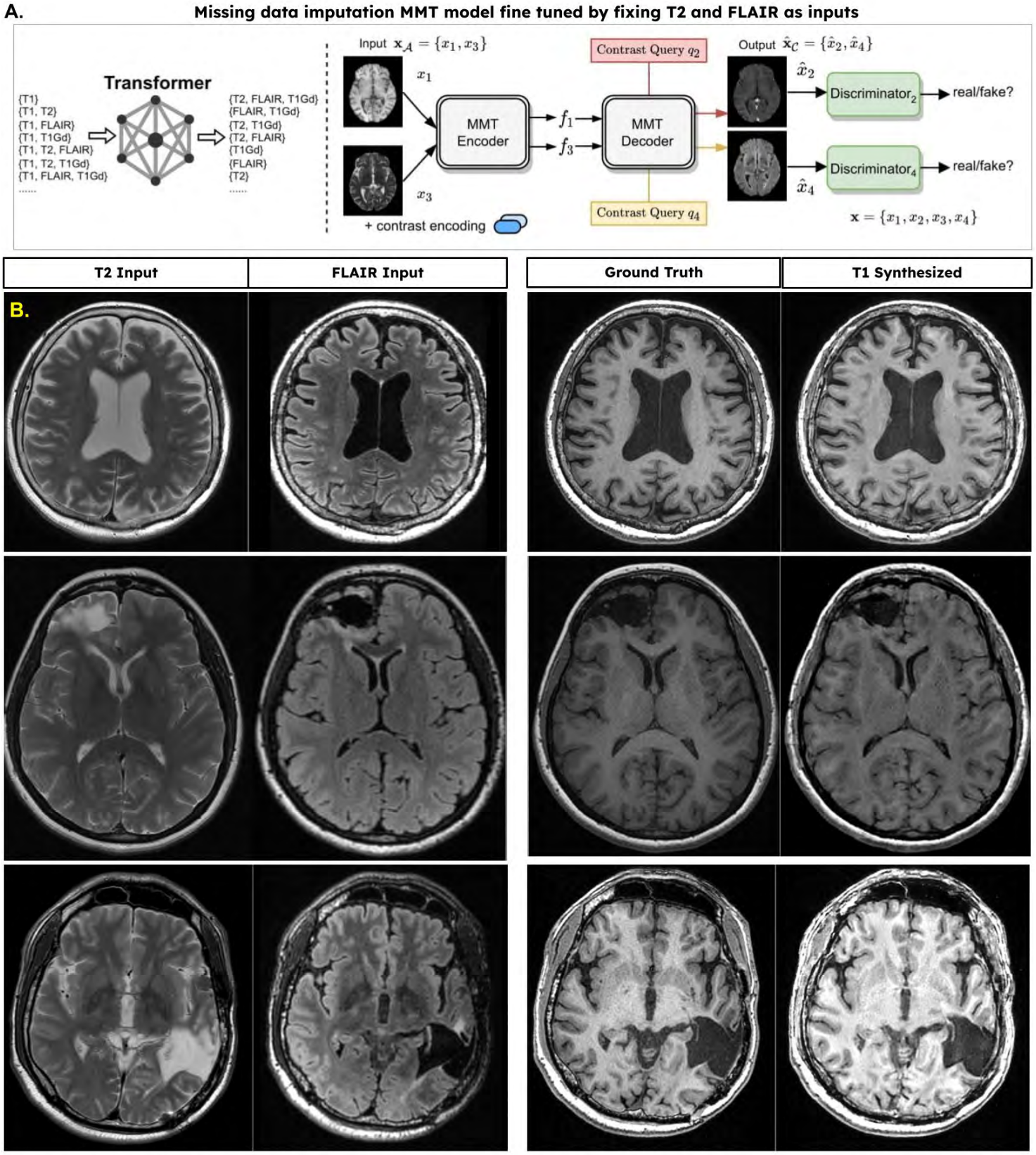

Figure 1: A) Overall schematic of the multi-scale multi-contrast transformer (MMT) used for T1 synthesis **B)** Representative examples of the model outputs shown along with the T2,FLAIR inputs and T1 ground truth.

74 Improved Image Quality of Mean Transit Time via Bayesian Postprocessing: A Comparative Analysis in Patients with Acute Ischemic Stroke

Matthew Halber BS[1], Mona Asghariahmadabad MD[1], Charlie Wang MD[1], Michael Thomas MD[1], Ameera Ismail MD[2], Mersedeh Bahr-Hosseini MD[2], David S Liebeskind MD, MBA[2], Anthony Kim MD[1], Nerissa Ko MD[1], Kazim Narsinh MD[1], Luis E Savastano MD, PhD[1], Daniel L Cooke MD[1], Steven W Hetts MD[1], Matthew R Amans MD[1], S. Andrew Josephson MD[1], Christopher P Hess MD, PhD[1], Kambiz Nael MD[1]

[1]University of California, San Francisco, San Francisco, California, USA. [2]David Geffen School of Medicine, Los Angeles, California, USA

Purpose

CT perfusion (CTP) has been widely used in the triage of patients with acute ischemic stroke (AIS) for treatment selection. While mean transit time (MTT) was initially used as a surrogate for penumbra[1], today estimates of penumbra generally rely on time-to-maximum (Tmax) due to poor image quality of MTT and their noisy nature[2]. Most commercially available software packages for CTP analysis use single value decomposition (SVD), a method that is highly sensitive to noise[3]. The Bayesian approach is a robust probabilistic method with potential in improving image quality of perfusion maps[4]. We aimed to perform a comparative analysis between MTT maps generated using Bayesian and SVD postprocessing to assess differences in diagnostic image quality and estimated penumbral volumes.

Materials & Methods

In this retrospective study, AIS patients with anterior large vessel occlusion stroke who had baseline CTP from two comprehensive stroke centers were included. For routine clinical care, CTP was processed with RAPID software (iSchemaView), which uses SVD method to generate perfusion maps including MTT (SVD-1). All CTPs were also processed in our Lab twice to generate MTT maps, once by SVD using an FDA approved software (Olea Medical) (SVD-2) and once using the Bayesian probabilistic method. Image quality assessment was performed by 2 independent board-certified neuroradiologists blinded to the method of postprocessing for 1) side of hypoperfusion (right, left, can't tell); 2) overall image quality score using a 1-4 scale (1: poor; 2: fair; 3: good; 4: excellent). Differences in image quality were tested by Mann-Whitney test and interobserver agreements were calculated by a kappa test. For quantitative analysis, penumbral volumes were estimated by applying relative MTT (rMTT)> 1.4[5] to both SVD and Bayesian-generated MTT maps and subsequently compared against penumbral volume obtained in routine clinical practice (using Tmax>6 sec). Bland-Altman plots were generated for comparative analysis.

Results

A total of 78 patients were included. The overall image quality was significantly ($p<0.001$) higher for Bayesian-MTT in comparison to SVD-MTT regardless of the commercial software used (Figure 1A and B). There was substantial interobserver agreement for rating image quality scores for Bayesian-MTT ($k=0.70$), SVD-1 ($k=0.69$) and SVD-2 ($k=0.78$). Estimated penumbral volume (median, IQR) using Tmax>6 sec was 103, 67-131 mL, while MTT-estimated penumbral volume was 91, 62-127 mL for Bayesian and 25, 14-37 mL for SVD. The mean (SD) difference of estimated penumbral volume between Bayesian-MTT and Tmax was 3 (8) mL ($p=0.60$), while this difference was significantly ($p<0.001$) higher for SVD-MTT and Tmax (74, 10 mL) (see Bland-Altman plots, Figure 1C).

Conclusion

Results show that MTT maps generated from Bayesian postprocessing significantly outperform SVD which is used in most commercially available software packages. Image quality scores and confidence in delineation of hypoperfusion were rated significantly higher by both neuroradiologists using Bayesian-MTT. Estimated penumbral volumes from Bayesian-MTT were similar to those obtained in routine clinical practice, while estimated penumbral volume from SVD-MTT led to significant underestimation. These findings underscore the viability of the Bayesian method to create high quality MTT maps for routine clinical use.

References

1. Wintermark, M., Flanders, A. E., Velthuis, B., et al. Perfusion-CT assessment of Infarct Core and penumbra. *Stroke*. 2006; *37*(4), 979–985. https://doi.org/10.1161/01.str.0000209238.61459.39

2. Calamante, F., Christensen, S., Desmond, P. M., Østergaard, L., Davis, S. M., & Connelly, A. The physiological significance of the time-to-maximum (TMAX) parameter in perfusion MRI. *Stroke*. 2010; *41*(6), 1169–1174. https://doi.org/10.1161/strokeaha.110.580670

3. Konstas, A. A., Goldmakher, G. V., Lee, T.-Y., & Lev, M. H. Theoretic basis and technical implementations of CT perfusion in acute ischemic stroke, part 2: Technical implementations. *AJNR Am J Neuroradiol*. 2009; *30*(5), 885–892. https://doi.org/10.3174/ajnr.a1492

4. Boutelier, T., Kudo, K., Pautot, F., & Sasaki, M. Bayesian hemodynamic parameter estimation by bolus tracking perfusion weighted imaging. *IEEE Trans Med Imaging*. 2012; *31*(7), 1381–1395. https://doi.org/10.1109/tmi.2012.2189890

5. Edwards, L. S., Cappelen-Smith, C., Cordato, D., et al. Optimal CT perfusion thresholds for core and penumbra in acute posterior circulation infarction. *Front Neurol*. 2023; *14*. https://doi.org/10.3389/fneur.2023.1092505

Images/Tables

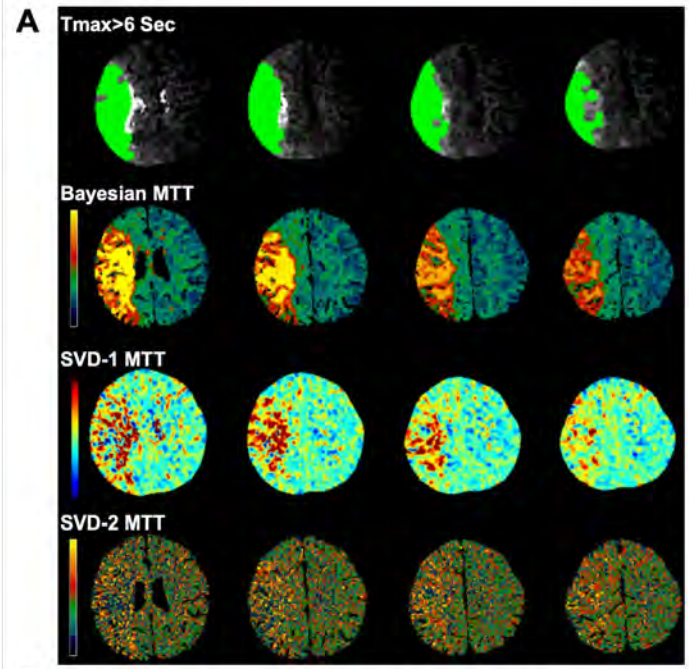

B

Observer-1	Current standard of care (SVD-1)	SVD-2	Bayesian
Correct side (%)	54%	23%	97.5%
Image quality (1-4)	2, 1-2	1, 1-2	3, 2-4
Diagnostic Image quality (%)	11.5%	1%	74.5%
Confidence (1-3)	1, 1-2	1, 1-1	3, 2-3

Data are median, IQR unless stated otherwise

Observer-2	Current standard of care (SVD-1)	SVD-2	Bayesian
Correct side (%)	43.5%	33%	91%
Image quality (1-4)	2, 1-2	1, 1-2	3, 2-4
Diagnostic Image quality (%)	12%	5%	68%
Confidence (1-3)	2, 1-2	1, 1-1	3, 2-3

Data are median, IQR unless stated otherwise

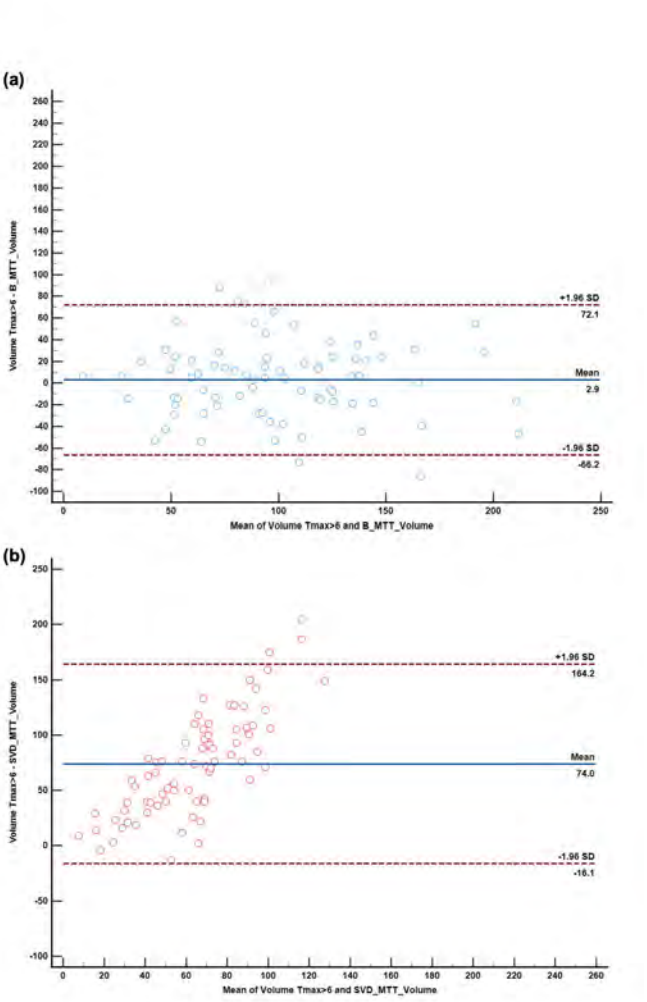

974 Radio-pathomic correlates of progression free survival in post-treatment glioblastoma patients

Samuel Bobholz PhD, Aleksandra Winiarz, Benjamin Chao, Hope Reecher, Daniel Kim, Allison Lowman, Savannah Duenweg PhD, Adam Lahrache, Mrina Mtenga, Fitzgerald Kyereme, Jennifer Connelly MD, Elaine Tanhehco MD, Max Krucoff MD, Mohit Agarwal MD, Rupen Desai MD, Jennifer Tuscher PhD, Peter S LaViolette PhD

Medical College of Wisconsin, Milwaukee, WI, USA

Purpose

Glioblastoma is the most common primary central nervous system tumor, prognostically characterized by a dismal 18 month mean survival time following diagnosis. First line treatment includes maximal safe surgical resection followed by combined radiotherapy and temozolomide use, though these treatments are known to affect the traditional presentation of the tumor on clinical imaging. Therefore, it can be difficult to assess treatment response and disease progression in the post-treatment state, leading to difficulties in assessing disease severity for second-line therapeutics. This study used autopsy-based radio-pathomic maps to test the hypothesis that cell density and extracellular fluid estimates are associated with progression-free survival on post treatment imaging.

Materials & Methods

This study used 63 patients from the publicly available UCSD-PTGBM data with progression free survival data and post-treatment imaging. Pre- and post-contrast T1 weighted images (T1, T1C), T2-weighted FLAIR, and apparent diffusion coefficient (ADC) images derived from diffusion weighted imaging were used as inputs for radio-pathomic map generation. Each image was coregistered to the FLAIR and qualitative images (T1, T1C, FLAIR) were intensity normalized. Our previously published model was then applied for each patient, using 5x5 tiles from each image to predict center voxel cell density (Cell) and extracellular fluid (ECF)[1,2]. The model itself was trained using autopsy tissues samples as ground truth, offering large areas of tissue from near enhancement as well as the peritumoral margin and areas of suspected normal tissue, allowing this model to be particularly sensitive to areas of non-enhancing tumor missed by conventional MRI. Mean values within annotations for contrast enhancement (CE) and non-enhancing FLAIR hyperintensity (FH) were computed for each patient, and Pearson's correlations were used to identify features most associated with progression free survival.

Results

Cell density within contrast enhancement showed a negative association with PFS (R=-0.29, p=0.021), indicating that patients with more hypercellular tumors following treatment tend to recur more rapidly than patients with less cellular tumors (Figure 1A). ECF was not associated with PFS, nor were imaging features from the FH region. Example imaging from short and long PFS patients highlight high overall cellularity within the CE

margin in the short PFS patient, with the long PFS patient showing low cellularity within enhancement, potentially indicating a more promising treatment response.

Conclusion

These results indicate that radio-pathomic estimates of enhancing tumor cellularity on post-treatment imaging are associated with PFS times. This result coincides with our prior work, which has identified cell density within enhancement as predictive of overall survival on pre-treatment imaging as well, even within cases that achieved gross total resection during surgery. Additionally, these results support the hypothesis that these RPMs offer a novel method for assessing treatment response by using sensitive to pathological changes not seen on traditional MRI, with prior studies showing strong performance in delineating therapeutic efficacy during radiotherapy and antiangiogenic therapy[3,4]. Future studies in larger, prospective datasets will allow for finer assessment of the role non-enhancing tumor presence plays in impacting therapeutic resistance and prognosis.

References

1) Bobholz SA, Lowman AK, Brehler M, et al. Radio-pathomic maps of cell density identify glioma invasion beyond traditional MR imaging defined margins. American Journal of Neuroradiology. 2021;(May).2)

2) Bobholz SA, Lowman AK, Connelly JM, et al. Noninvasive Autopsy-Validated Tumor Probability Maps Identify Glioma Invasion Beyond Contrast Enhancement. Neurosurgery. 2024;95(3).
https://journals.lww.com/neurosurgery/fulltext/2024/09000/noninvasive_autopsy_validated_tumor_probability.9.aspx

3) Bobholz SA, Hoefs A, Hamburger J, et al. Radio-pathomic maps of glioblastoma identify phenotypes of non-enhancing tumor infiltration associated with bevacizumab treatment response. J Neurooncol. Published online 2024. doi:10.1007/s11060-024-04593-7

4) Oshima S, Yao J, Bobholz S, et al. Radio-pathomic maps of cell density and cellular growth kinetics estimated using machine learning model predict survival in human recurrent glioblastoma treated with cytotoxic therapy. CNSOncology. Published online 2024.

Images/Tables

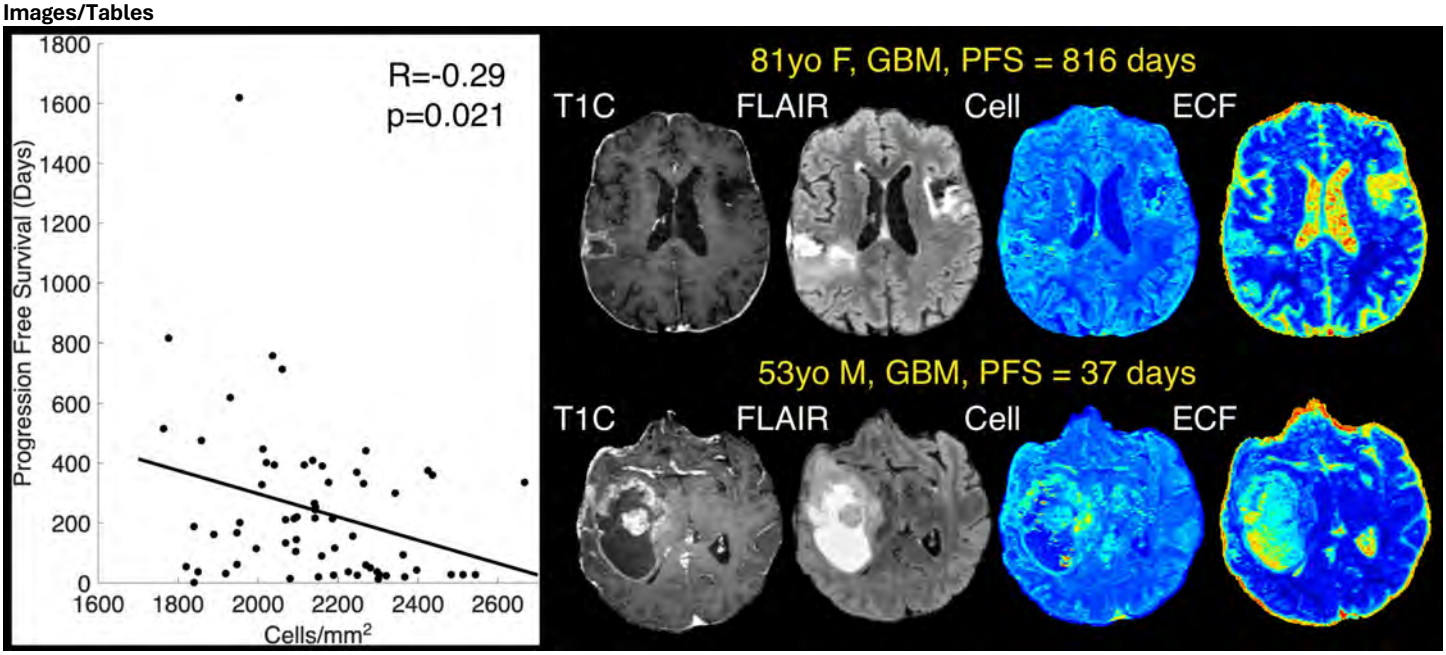

---

912 Radiomic Classification of Primary CNS lymphoma and High-Grade Glioma Using Multiparametric MRI

Sam Cartmell MD[1], Andrew Sharp MS[1], Jacob Zalis[2], Chris Mount MD, PhD[1], Oleg Pianykh PhD[1]

[1]Massachusetts General Hospital, Boston, MA, USA. [2]Emory University, Atlanta, GA, USA

Purpose

Primary Central Nervous System Lymphoma (PCNSL) and High-Grade Glioma (HGG) can demonstrate substantial overlap in their imaging appearance. Nevertheless, it is critical to distinguish between these entities because the treatment for each condition is very different [1,2]. Accordingly, there is significant interest in differentiating PCNSL and HGG using machine learning and radiomics approaches [3]. The current study replicates and extends prior results by classifying these conditions using pretreatment multiparametric MRI from a large retrospective institutional cohort of PCNSL cases (n=112) and a comparable number of HGG cases (n=121).

Materials & Methods

160 tissue-confirmed PCNSL and 203 HGG cases from 2012-2024 were retrospectively identified via an internal pathology database. 112 PCNSL cases and 121 HGG cases had adequate pre-treatment imaging including high-resolution (<2mm isotropic) post-contrast T1-weighted (T1ce), T1-weighted pre-contrast, T2-weighted, Fluid Attenuated Inversion Recovery (FLAIR), and Average Diffusion Coefficient (ADC) maps. Field strength and vendor were recorded.

Images underwent standard preprocessing [4]. After automated initialization, tumor boundaries were manually refined in the 3D slicer software by an attending neuroradiologist (SC).

459 radiomic features, representing properties of the shape, size, and texture of the segmented masses and surrounding areas were computed from each imaging sequence using PyRadiomics and OpenCV, resulting in a total of 2295 features per patient. Masses were randomly split into 80% training and 20% test sets, stratified by mass type. Boolean rule-learning models identified the optimal single-feature model for differentiating lymphomas from gliomas. Multivariate logistic regression models were trained both on features from individual sequences and from the combined feature set from all five sequences. Five-fold cross-validation was used for tuning hyperparameters. To compare the performance of models of different sizes, the top n features were determined using the magnitudes of the full logistic regression model coefficients after feature normalization.

Results

The combined logistic regression model using the optimal number of features (170) achieved 91% test set accuracy ($p<0.001$), which surpassed the performance of models based on individual sequences. Half of the top ten feature coefficients were derived from T1ce images, although each sequence had at least one feature in the top ten. The optimal single-feature model (T1-ce 10th percentile intensity) achieved an accuracy of 85% on the test set ($p<0.001$).

Cases were drawn from 3 vendors (PCNSL: Siemens 37.5%, GE 53.5%, Philips 9%; HGG: Siemens 46.3%, GE 51.2%, Philips 2.5%) and both 1.5 (PCNSL: 64%; HGG: 60%) and 3 Tesla magnets.

Conclusion

PCNSL and HGG can be distinguished with a high degree of accuracy using routinely acquired pretreatment imaging in this retrospective cohort. Radiomic features derived solely from the T1ce image confer high predictive value, but performance improves with the addition of information from other conventional sequences. High accuracy was achieved despite inherent variability in clinically acquired data and heterogeneity among vendors and field strengths. Prospective validation will be needed to confirm feature robustness and clinical generalizability.

References

1. Gerstner ER, Batchelor TT. Primary central nervous system lymphoma. Arch Neurol. 2010 Mar;67(3):291-7. doi: 10.1001/archneurol.2010.3.
2. Stupp R, Mason WP, van den Bent MJ, et al. European Organisation for Research and Treatment of Cancer Brain Tumor and Radiotherapy Groups; National Cancer Institute of Canada Clinical Trials Group. Radiotherapy plus concomitant and adjuvant temozolomide for glioblastoma. N Engl J Med. 2005 Mar 10;352(10):987-96. doi: 10.1056/NEJMoa043330.
3. Cassinelli Petersen GI, Shatalov J, Verma T, et al. Machine Learning in Differentiating Gliomas from Primary CNS Lymphomas: A Systematic Review, Reporting Quality, and Risk of Bias Assessment. AJNR Am J Neuroradiol. 2022 Apr;43(4):526-533. doi: 10.3174/ajnr.A7473.
4. Davatzikos C, Rathore S, Bakas S, et al. Cancer imaging phenomics toolkit: quantitative imaging analytics for precision diagnostics and predictive modeling of clinical outcome. *J Med Imaging (Bellingham)*. 2018 Jan;5(1):011018. doi: 10.1117/1.JMI.5.1.011018.

Images/Tables

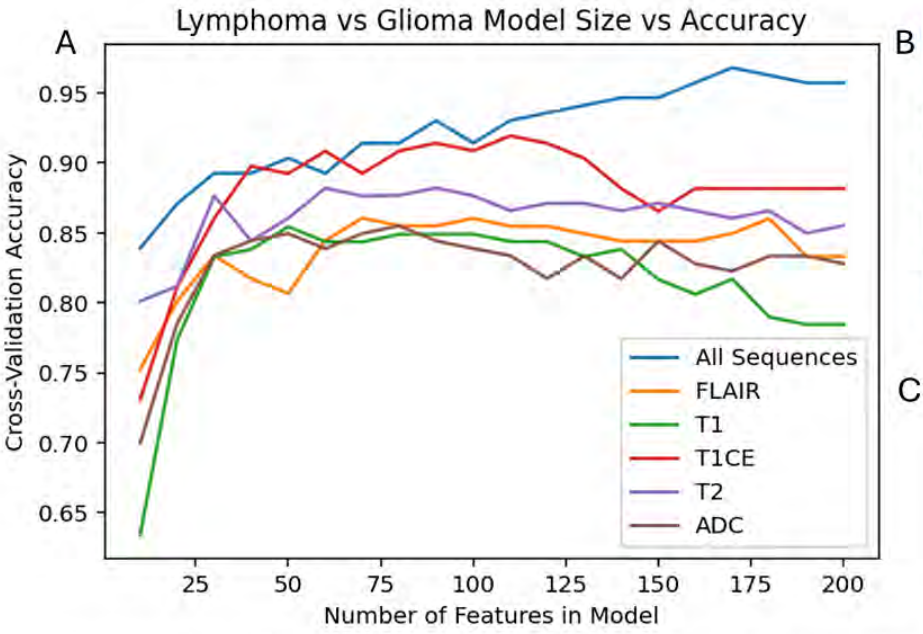

B

Radiomic feature	Sequence	Coefficient
Inverse Difference	T1CE	0.48
Inverse Variance	T1CE	0.47
Minimum	T1	0.46
Inverse Difference Normalized	T1CE	0.44
Kurtosis	T1CE	0.42
Interquartile Range	FLAIR	0.41
Correlation	T2	0.40
Inverse Variance	T1	0.40
Interquartile Range	ADC	-0.39
Difference Average	T1CE	-0.37

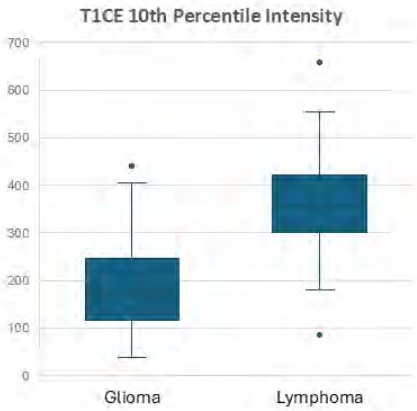

A) Multivariable logistic regression model test set accuracy as a function of model size and sequences used. Optimal results (91% accuracy, $p<0.001$) are achieved at 170 features, after which the model is overfit.

B) Top ten radiomic features by coefficient value from the combined logistic regression model. Positive coefficient values indicate features are more common in PCNSL. Note that although all sequences contribute to the model performance, T1ce features are most predictive.

C) Boolean rule-learning models demonstrate the single best feature distinguishing between PCNSL and HGG, which achieves 85% accuracy ($p<0.001$).

---

847 Impact of Defacement on Deep Learning-Based Prediction of Alzheimer's Disease PET Imaging Biomarkers from MRI

Donghoon Kim Ph.D., Ashwin Kumar MS, Brandon C. Ho BS, Elizabeth Mormino Ph.D., Greg Zaharchuk MD, Ph.D.

Stanford University, Stanford, CA, USA

Purpose

Removing facial information from structural MRI scans, a process known as 'defacement,' has become standard practice to protect patient privacy. Concurrently, deep learning-based predictions are increasingly applied for various applications, including disease diagnosis and classification. Given that deep learning models utilize the whole image, facial regions potentially hold predictive value, as shown in prior MRI-based age-prediction studies.[1] This raises the question of whether facial information in MRI images may contribute to prediction accuracy for Alzheimer's disease related early imaging biomarkers. Thus, we investigated how defacement impacts the deep learning-based prediction of binary amyloid- and tau-PET statues from routine MRIs.

Materials & Methods

Data were obtained from two large publicly available non-defaced neuroimaging datasets: ADNI and OASIS-3. A total of 2,268 MRI–amyloid PET pairs and 2,134 MRI–tau PET pairs were collected. Each MRI exam included T1w and T2-FLAIR images. Amyloid positivity was defined using dataset-

specific Centiloid thresholds, and tau positivity using a cutoff of the mean + 2 standard deviations of tau standardized uptake value ratios (SUVRs) from cognitively normal participants. The data were divided into training, validation, and test sets (64%, 16%, 20%), and all T2-FLAIR images were co-registered to their corresponding T1w images. To evaluate the effect of facial feature removal, four input conditions were analyzed for both amyloid and tau prediction models as shown in **Fig. 1A**: (1) non-processed, (2) refaced (3) defaced, and (4) skull-stripped.[2] Defacement was performed using *pydeface*[3] (facial tissue removal), and refacement using *mri-reface*[4] (replacement with a standardized template face).

Two different 3D convolutional neural networks, EfficientNet-B1 (116 layers) and Squeeze-and-Excitation ResNet-50 (SEResNet50; 50 layers), were trained to mitigate architecture-specific bias. Input intensities were normalized to the 5th–95th percentile range. Each model produced the likelihood of amyloid or tau positivity, and performance was evaluated using the area under the receiver operating characteristic curve (AUC) and balanced accuracy across the four input image conditions. Binary classification was determined using the optimal cutoff derived from Youden's *J* index.[5]

Results

In both amyloid and tau prediction tasks, skull-stripped images achieved the highest performance for both EfficientNet-B1 and SEResNet50 (**Fig. 1B-C**). For amyloid prediction, the AUC was 0.68 with EfficientNet-B1 and 0.69 with SEResNet50, and for tau prediction, the corresponding AUCs were 0.73 and 0.67. The balanced accuracies were 0.63 and 0.65 for amyloid prediction, and 0.68 and 0.66 for tau prediction, respectively. In comparison, non-processed, defaced, and refaced images produced similar performance across models and tasks but consistently underperformed relative to skull-stripped inputs (**Fig. 1B-C**).

Conclusion

Skull-stripped MRI images resulted in the best performance for predicting both amyloid and tau PET positivity, outperforming non-processed, refaced, and defaced images. The inclusion of facial features did not enhance prediction accuracy, suggesting that facial information may have limited relevance for Alzheimer's disease biomarker prediction within the tested deep learning frameworks. Nonetheless, further studies using larger and more diverse datasets, as well as advanced architectures such as Vision Transformers, are warranted to validate these findings and explore potential subtle effects of defacement on other predictive tasks.

References

1. Cali RJ, Bhatt RR, Thomopoulos SI, et al. The Influence of Brain MRI Defacing Algorithms on Brain-Age Predictions via 3D Convolutional Neural Networks. In: *2023 45th Annual International Conference of the IEEE Engineering in Medicine & Biology Society (EMBC)*.; 2023:1–6.
2. Isensee F, Schell M, Pflueger I, et al. Automated brain extraction of multisequence MRI using artificial neural networks. *Human brain mapping* 2019;40:4952–64.
3. Gulban OF, Nielson D, Poldrack R, et al. poldracklab/pydeface: v2.0.0. https://doi.org/10.5281/zenodo.3524401. Accessed November 3, 2025.
4. Schwarz CG, Kremers WK, Wiste HJ, et al. Changing the face of neuroimaging research: Comparing a new MRI de-facing technique with popular alternatives. *NeuroImage* 2021;231:117845.
5. Youden WJ. Index for rating diagnostic tests. *Cancer* 1950;3:32–5.

Images/Tables

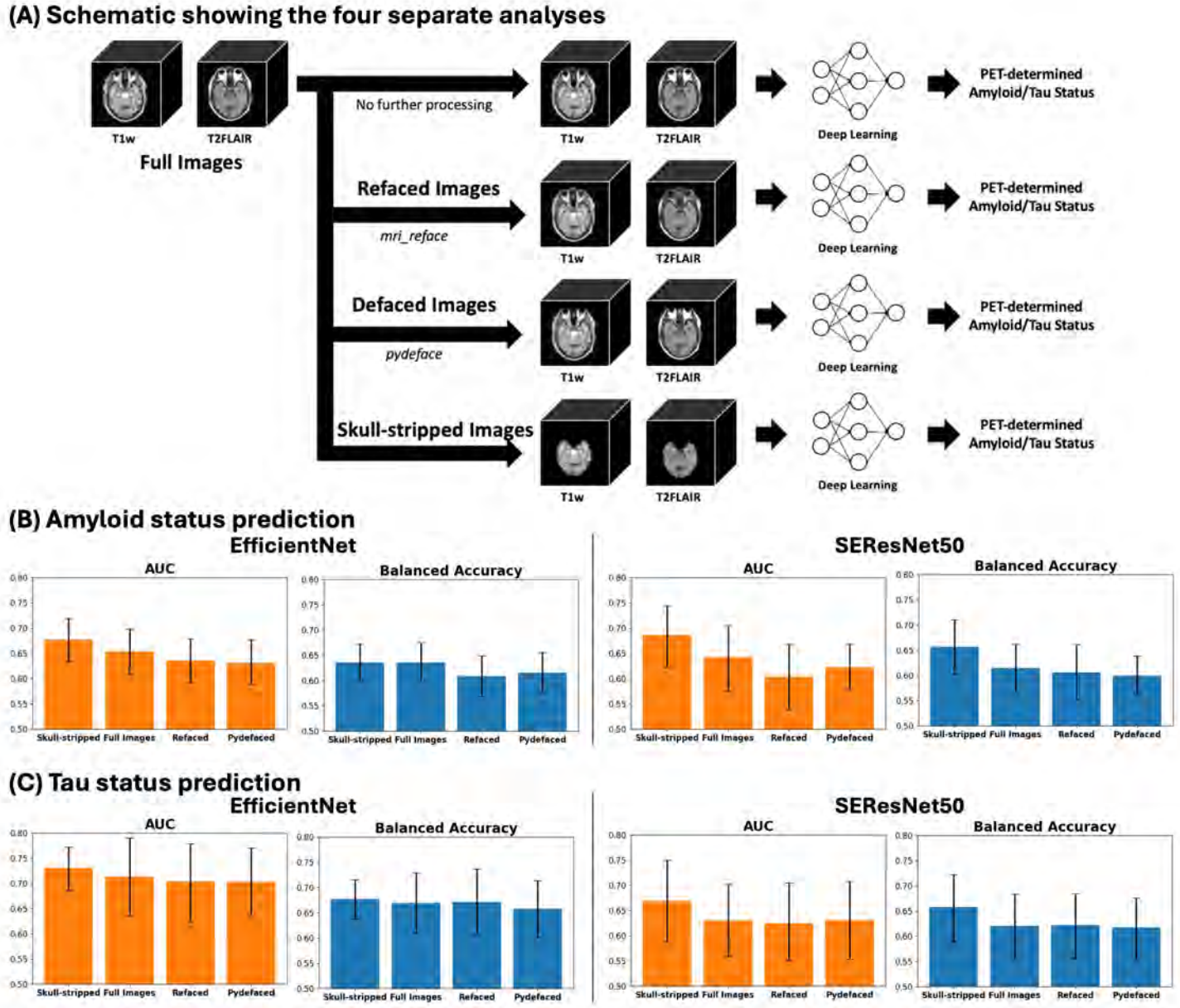

Figure 1. (A) Overview of the four experimental conditions for binary amyloid and tau positivity prediction using T1-weighted (T1w) and T2-FLAIR MRIs: non-processed, refaced, defaced, and skull-stripped inputs. **(B)** Bar plots showing the area under the ROC curve (AUC) and balanced accuracy for EfficientNet-B1 (left) and SEResNet-50 (right) in predicting amyloid positivity. **(C)** Corresponding AUC and balanced accuracy results for EfficientNet-B1 (left) and SEResNet-50 (right) in predicting tau positivity.

---

623 **Validation of Deep Learning Accelerated Post-Contrast Magnetization Prepared Rapid Gradient Echo (MPRAGE) at 1.5 T and 3 T MRI**

Chen-Hua Chiang[1], Eugene Milshteyn[2], Mary Thomas[2], Dan Rettman[3], Susie Huang[4], Ivan Jambor[5]

[1]Shuang Ho Hospital, Taipei Medical University, New Taipei City, N/A, Taiwan. [2]GE HealthCare, Boston, Massachusetts, USA. [3]GE HealthCare, Rochester, Minnesota, USA. [4]Department of Radiology, Massachusetts General Hospital, Boston, Massachusetts, USA. [5]Enterprise Service Group – Radiology, Mass General Brigham, Dover, New Hampshire, USA

Purpose

To evaluate the image quality and diagnostic performance of deep learning (DL) accelerated post-contrast 3D MPRAGE compared with standard MPRAGE at 1.5 T and 3 T.

Materials & Methods

This IRB-approved prospective study included 39 and 49 consecutive patients who underwent brain MRI at 1.5 T (Signa™ Artist) and 3 T (Signa™ Premier), respectively (GE HealthCare, Waukesha, WI). Two 3D MPRAGE acquisitions were obtained:

1. Standard MPRAGE: a commercially available DL Recon algorithm (AIR™ Recon DL), based on a Convolutional Neural Network trained for denoising and sharpening.[1] Acquisition Time (TA) = 2 min 21 s [1.5 T], 2 min 15 s [3 T].
2. DLS MPRAGE: prototypic version of Sonic DL, an acquisition and reconstruction technique that combines highly undersampled data acquisition with an unrolled DL based reconstruction[2-4], then combined with AIR™ Recon DL. TA = 1 min 42 s [1.5 T], 1 min 35 s [3 T].
Two board-certified neuroradiologists independently reviewed paired datasets in randomized order. Qualitative ratings were performed on a 5-point ordinal scale (–2 to +2) across six categories: motion artifact, noise, gray-white matter (GM/WM) differentiation, sharpness, overall diagnostic quality, and visualization of pathological enhancement.
Interrater agreement was assessed using quadratic-weighted Cohen's κ with 95% confidence intervals and percentage agreement. Non-inferiority of DLS MPRAGE versus standard was tested using a one-sided Wilcoxon signed-rank test, with a prespecified non-inferiority margin (Δ) of 0.05 ($p < 0.05$ considered significant). Pooled reader–patient pairs were analyzed as independent observations.

Results

At 1.5 T, moderate interrater agreement was observed for motion (κ = 0.52, 77%), GM/WM differentiation (κ = 0.50, 95%), sharpness (κ = 0.52, 74%), and overall quality (κ = 0.53, 82%). Noise demonstrated poor agreement (κ = –0.04, 44%), while pathological enhancement showed perfect agreement (κ = 1.00, 100%).
At 3 T, moderate agreement was found for motion (κ = 0.57, 84%), noise (κ = 0.52, 65.3%), and sharpness (κ = 0.50, 92%); slight agreement for GM/WM differentiation (κ = 0.00, 98%); fair agreement for overall quality (κ = 0.21, 86%); and substantial for pathological enhancement (κ = 0.72, 86%).
Pooled analysis showed DLS MPRAGE was non-inferior across all six categories at both field strengths. At 1.5 T, significant non-inferiority was demonstrated for motion ($p = 0.01$), GM/WM differentiation ($p < 0.001$), sharpness ($p = 0.04$), overall quality ($p < 0.001$), and pathological enhancement ($p < 0.001$). Noise trended non-significant ($p = 0.45$) but remained within the 95% CI of the non-inferiority margin (Δ = 0.05). At 3 T, DL-MPRAGE was non-inferior for all categories ($p < 0.001$ for all).
Despite low κ values, skewed rating distributions suggested a κ-paradox rather than true disagreement. Importantly, lesion conspicuity and post-contrast enhancement were fully preserved, supporting diagnostic interchangeability (Figure 1).

Conclusion

DLS MPRAGE provided diagnostic image quality statistically non-inferior to standard MPRAGE at both 1.5 T and 3 T, with scan-time reductions of 28% and 27%, respectively—equivalent to roughly 40 seconds per acquisition. High interrater consistency and preserved lesion conspicuity support DLS MPRAGE as a clinically feasible, high-quality alternative for post-contrast brain MRI.

References

1. Lebel RM: "Performance characterization of a novel deep learning-based MR image reconstruction pipeline," Aug. 14, 2020, arXiv: arXiv:2008.06559. doi: 10.48550/arXiv.2008.06559.
2. Ahn S, et al.: "Deep learning-based reconstruction of highly accelerated 3D MRI," Mar. 09, 2022, arXiv: arXiv:2203.04674. doi: 10.48550/arXiv.2203.04674.
3. Ahn S, et al.: Task-based evaluation of deep learning-based reconstruction for highly-accelerated 3D T1-weighted brain MRI scans. ISMRM 2023.
4. Watanabe K, et al.: 0.9mm isotropic 1min MPRAGE using highly-accelerated Deep learning Reconstruction for Brain Structural Analysis. ISMRM 2024

Images/Tables

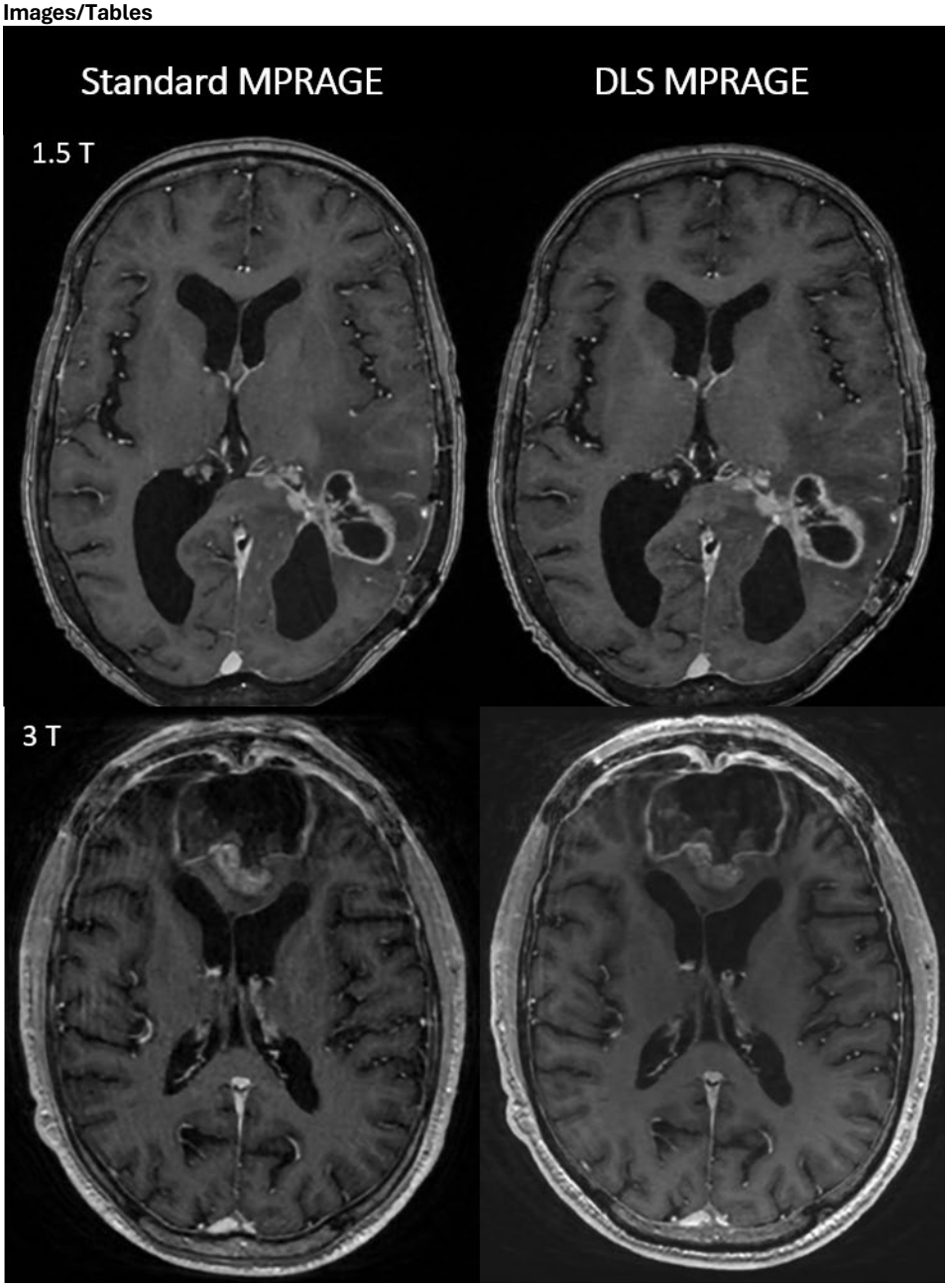

971 Neuroradiology Academic Metrics by Rank: National Benchmarks of Scholarly Productivity

Mahla Radmard M.D.[1], Caline Azzi M.D.[1], Armin Tafazolimoghadam M.D.[2], David M. Yousem M.D., M.B.A.[1], Rohini Nadgir M.D.[1]

[1]Johns Hopkins University School of Medicine, Department of Radiology, Baltimore, Marylan, USA. [2]Tehran University of Medical Sciences, Tehran, Tehran, Iran, Islamic Republic of

Purpose

Academic promotion standards vary widely across U.S. medical institutions, yet publications, citations, and h-indices remain the most quantifiable indicators of scholarly productivity. Despite their importance, national benchmarks for academic output among neuroradiology faculty have not been established. This study aimed to define standardized metrics of academic productivity for U.S. neuroradiologists by faculty rank and to evaluate sex-based differences across academic levels.

Materials & Methods

A point-in-time cross-sectional bibliometric analysis of academic neuroradiology faculty was performed using publicly available data from ACGME-listed neuroradiology programs and departmental websites between July and August 2025. Faculty names, academic rank, and sex were collected and verified through program directors when necessary. Scopus was queried to determine total publications, total citations, and h-index for each individual. Faculty without Scopus records were excluded. Descriptive statistics and percentile distributions were calculated by academic rank (assistant, associate, and full professor). Group comparisons were performed using the Kruskal-Wallis and Mann-Whitney U tests, with statistical significance set at $p < 0.05$.

Results

1,190 neuroradiologists across 94 academic institutions met inclusion criteria (404 male and 152 female assistant professors; 250 male and 81 female associate professors; 231 male and 82 female full professors). Scholarly productivity increased significantly with academic rank ($p < 0.001$). Median citations rose from 105 (assistant) to 555.5 (associate) and 2702 (full professor), while median publications increased from 8 to 30 to 89,

respectively. Corresponding median h-index values rose from 4 to 11 to 27. Sex-based differences were minimal at junior ranks but emerged among full professors, where males had higher median publication counts (92 vs 75.5, $p = 0.04$). No statistically significant sex-based differences in h-index or citations were observed at any other rank. Percentile-based benchmarks were established for each rank, enabling standardized evaluation of scholarly performance within neuroradiology.

Conclusion

This nationwide analysis provides the first percentile-based reference standards for academic productivity among U.S. neuroradiology faculty. Scholarly output—measured by publications, citations, and h-index—increases consistently with academic rank, paralleling trends in other medical specialties but at generally higher levels. Gender differences are negligible at junior ranks but occur (male > female) at the full professor level. These benchmarks offer neuroradiologists, departments, and promotion committees an evidence-based framework for self-assessment, comparison across institutions, and justification for advancement in academic rank.

References

1. Batshaw ML, Plotnick LP, Petty BG, et al. Academic promotion at a medical school: experience at Johns Hopkins University School of Medicine. *N Engl J Med*. 1988;318(12):741–747.

2. Zaorsky NG, O'Brien E, Mardini J, et al. Publication productivity and academic rank in medicine: a systematic review and meta-analysis. *Acad Med*. 2020;95(8):1274–1282.

3. Wang R, Lewis M, Zheng-Pywell R, et al. Using the h-index as a factor in the promotion of surgical faculty. *Heliyon*. 2022;8(4):e09319.

4. Ha GL, Lehrer EJ, Wang M, et al. Sex differences in academic productivity across academic ranks and specialties in academic medicine: a systematic review and meta-analysis. *JAMA Netw Open*. 2021;4(6):e2112404.

Images/Tables

Publication metrics by rank among US academic neuroradiologists, 2025

	Assistant Professor			Associate Professor			Professor		
Metric	Citations	Papers	h-index	Citations	Papers	h-index	Citations	Papers	h-index
Percentile 90th	1,094	41	15	3,298	113	28	13,410	265	59
80th	586	24	10	1,767	66	21	7,704	179	45
70th	317	16	8	1,115	48	17	5,358	133	35
60th	192	11	6	800	38	13	3,546	105	30
50th	105	8	4	556	30	11	2,702	89	27
40th	52	6	3	367	23	9	2,130	70	24
30th	24	3	2	233	17	7	1,536	56	20
20th	4	2	1	153	11	5	943	38	15
10th	0	1	0	55	6	3	561	27	11
Mean	457	17	6	1,250	45	14	5,568	126	31
SD	1,505	26	7	1,925	50	10	10,868	139	20

Scientific Abstract Power Pitches & Luminary Speaker: Tumors and Techniques

3:20 - 4:20pm Tuesday, 19th May, 2026

318 Effects of Meningioma on Blood-Brain-Barrier Permeability in Subjacent Brain Parenchyma

Vince Ly[1], Samantha Keil PhD[2], Kellen Vu[1], Hannah Otis[1], Kate Rosen MD[3], Valentina Marulanda Corzo MD[2], Susan C. Pannullo MD[4], Sadek Nehmeh PhD[2], Joseph R. Osborne MD, PhD[2], Rajiv Magge MD[5], Jana Ivanidze MD, PhD[2]

[1]Weill Cornell Medicine, New York, New York, USA. [2]Weill Cornell Medicine Radiology, New York, New York, USA. [3]Weill Cornell Medicine Neurosurgery, New York, New York, USA. [4]Cornell University, New York, New York, USA. [5]Weill Cornell Medicine Neurology, New York, New York, USA

Purpose

Meningioma is the most common primary brain tumor. WHO grade, the current clinical classification of meningiomas, is primarily based on histomorphology and is limited in predicting treatment response and clinical outcomes. While meningiomas arise from arachnoid cap cells and are themselves outside the blood-brain-barrier (BBB), possible effects of meningiomas on tumor-adjacent brain parenchyma are unknown. Our purpose was to investigate effects of meningiomas on tumor-adjacent blood-brain-barrier (BBB) permeability in the context of tumor grade and clinical outcomes.

Materials & Methods

Patients included on our prospective observational registry who had a diagnosis of meningioma (lesion size ≥ 1 cm in at least 2 dimensions, normal-appearing tumor-adjacent brain parenchyma on conventional MRI) and underwent DCE perfusion MRI as part of their clinical standard-of-care evaluation. Exclusion criteria were history of radiotherapy and presence of tumor-adjacent vasogenic edema. DCE perfusion data were postprocessed using Olea Sphere Medical 3.0 software. For each meningioma as identified on postcontrast T1 MRI, 3 regions of interest (ROI) were placed in brain parenchyma adjacent to the meningioma as well as in the contralateral parenchyma (control). Using the Tofts kinetic model, DCE perfusion parameters (KTRANS, KEP, VE, VP) were derived from each ROI. For each lesion, mean permeability parameters were obtained by averaging the individual ROI values. Statistical analysis was performed using GraphPad Prism. Wilcoxon matched-pairs signed rank test was performed to identify statistically significant differences in the DCE parameters in meningioma-subjacent parenchyma compared to contralateral control parenchyma. Association of DCE parameters and histomorphologic grading (WHO grade) was assessed using 2-way-ANOVA with a multiple comparisons correction.

Results

45 patients with a total of 48 unique meningiomas met inclusion criteria (mean age 55.4 years, 75% female). Among these patients, 40% were WHO grade 1, 33% were WHO grade 2, and 27% were WHO grade unknown. Mean KTRANS, VE, and VP of meningioma-subjacent brain parenchyma were significantly higher compared to contralateral control parenchymal ROI (mean KTRANS 0.15 vs 0.06, mean VE 0.03 vs 0.02, mean VP 0.03 vs 0.02, all $p<0.001$). No significant differences were found between tumor subjacent and contralateral control KEP (3.45 vs 2.94, $p=0.2437$). When stratified by WHO grade, KTRANS, VE, and VP elevation in tumor-subjacent brain parenchyma remained significant in patients with WHO grade 1 meningiomas ($p\leq0.005$). While the trend persisted in WHO grade 2 meningiomas, these differences were no longer significant ($p=0.0526$, $p=0.1128$, $p=0.0693$, respectively).

Conclusion

We report the first study examining effects of meningiomas on tumor-subjacent brain parenchyma. We found BBB disruption in normal-appearing meningioma-subjacent parenchyma relative to contralateral control parenchyma. We further found significant WHO-grade-dependent differences in DCE parameters. Future work will assess effects of meningioma-subjacent BBB disruption on clinical outcomes and treatment response. This study suggests tumor-subjacent BBB permeability as a new potential diagnostic and prognostic biomarker in patients with meningiomas.

References

Roytman M, Kim S, Glynn S, Thomas C, Lin E, Feltus W, et al. PET/MR Imaging of Somatostatin Receptor Expression and Tumor Vascularity in Meningioma: Implications for Pathophysiology and Tumor Outcomes. *Front Oncol* 2022;11:820287. doi:10.3389/fonc.2021.820287

Images/Tables

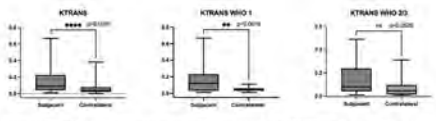

Figure 1. Box plots comparing the volume transfer constant (KTRANS) between parenchyma subjacent to meningioma and contralateral control, a direct measure of blood-brain-barrier permeability. KTRANS values are further stratified by WHO grade.

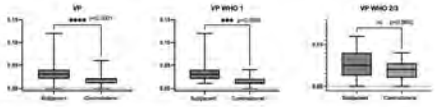

Figure 2. Box plots comparing the plasma volume (VP) between parenchyma subjacent to meningioma and contralateral control. VP values are further stratified by WHO grade.

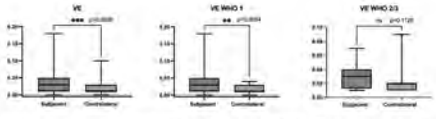

Figure 3. Box plots comparing the extravascular leakage volume (VE) between parenchyma subjacent to meningioma and contralateral control. VE values are further stratified by WHO grade.

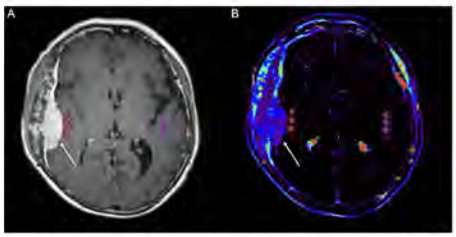

Figure 4. Axial postcontrast-T1-weighted image (A) demonstrates an avidly enhancing dural based mass along the right frontotemporal convexity and extending into the overlying calvarium (subsequently resected with pathology demonstrating CNS WHO grade 1 meningioma); subjacent (1) and contralateral (2) regions of interest are shown. Corresponding VE parametric map (B).

648 Differentiating Diffuse Peripheral Neuropathies Using Quantitative MR Neurography: Insights from Disease-Specific Marker Alterations

Jennifer C Hayes MD, PhD[1], Sabine Heiland PhD[2], Martin Bendszus MD[2], Markus Weiler MD[2]

[1]University of Michigan, Ann Arbor, MI, USA. [2]University Hospital Heidelberg, Heidelberg, Baden-Wuerttemberg, Germany

Purpose

Over the past decade, MR neurography (MRN) has become an important tool for characterizing various polyneuropathies, diffuse neuropathies, and neurodegenerative diseases. Beyond standard semiquantitative assessments based on heavily T2-weighted sequences with fat saturation, advanced techniques such as T2 relaxometry and Magnetization Transfer Contrast (MTC) imaging have been applied. The quantitative MRN markers, proton spin density (ρ), T2 relaxation time (T2app), and magnetization transfer ratio (MTR) serve as sensitive indicators of microstructural integrity, providing detailed information about the macromolecular composition of nerve tissue in vivo. In contrast, cross-sectional area (CSA) serves as a pure morphological quantitative marker. These parameters have been evaluated primarily in the lower extremity peripheral nerves, demonstrating high sensitivity for detecting nerve involvement and allowing for the early detection, characterization, and quantification of peripheral nerve lesions, sometimes even preceding clinical symptom onset. However, while alterations in MRN markers (stable, increased, or decreased) have been described within individual study populations compared to controls, a broader summary of these changes across multiple types of neuropathies could enhance diagnostic differentiation between distinct neuropathic conditions.

Materials & Methods

This single-center retrospective analysis included 337 patients and 99 age- and sex-matched healthy controls, all previously prospectively enrolled in MRN studies at 3T field strength. Subjects were grouped into four disease categories: polyneuropathies (hereditary transthyretin amyloidosis, systemic light chain amyloidosis, diabetic polyneuropathy, and alcohol-related polyneuropathy), demyelinating disorders (multiple sclerosis (MS)), motor neuron diseases (5q-linked spinal muscular atrophy (SMA)), and neurodegenerative diseases (spinocerebellar ataxia, hereditary spastic paraplegia, and Friedreich's ataxia). All patients underwent thorough clinical-neurological examinations and detailed nerve conduction studies for precise disease characterization. Quantitative MRN markers of tibial and sciatic nerves, including ρ, T2app, MTR, and CSA, were extracted and reviewed for each disease and their respective group. For this summary analysis, no additional statistical tests were applied; however, comprehensive statistical analyses, including one-way ANOVA and t-tests, were utilized in the underlying individual studies to evaluate MRN marker differences between patient groups and controls.

Results

Quantitative MRN revealed distinct marker patterns across disease groups (Table 1). In polyneuropathies, early stages showed increased ρ and CSA, alongside decreased MTR. Notably, T2app was elevated only in patients with symptomatic and more advanced disease stages. For demyelinating disorders such as multiple sclerosis, ρ was increased and T2app decreased, accompanied by reduced MTR; CSA was not significantly altered. SMA demonstrated reductions in ρ, MTR, and CSA, with increased T2app. Neurodegenerative diseases, including the various forms of ataxia, exhibited lower ρ, T2app, CSA, and MTR values, except for Friedreich's ataxia, where MTR and CSA did not differ significantly from controls.

Conclusion

Quantitative MR neurography markers exhibit disease-specific changes, likely reflecting distinct underlying neuropathologic mechanisms—such as protein or glycosylated end-product accumulation in amyloidosis and diabetes, demyelination in MS, lower motor neuron decay in SMA, and pure axonopathy in ataxias. This differentiation highlights the potential of MRN to noninvasively identify and characterize peripheral nerve disease etiologies, supporting improved diagnosis and targeted management across neuropathic conditions.

References

1. Jende JME, Hauck GH, Diem R, et al. Peripheral nerve involvement in multiple sclerosis: Demonstration by magnetic resonance neurography. Ann Neurol 2017; 82(5):676-685.

2. Kollmer J, Hilgenfeld T, Ziegler A, et al. Quantitative MR neurography biomarkers in 5q-linked spinal muscular atrophy. Neurology 2019; 93(7):e653-e664.

3. Rother C, Bumb JM, Weiler M. Characterization and quantification of alcohol-related polyneuropathy by magnetic resonance neurography. Eur J Neurol 2022; 29(2):573-582.

4. Kollmer J, Weiler M, Sam G. Quantitative magnetic resonance neurographic characterization of peripheral nerve involvement in manifest and pre-ataxic spinocerebellar ataxia type 3. Eur J Neurol 2022; 29960:1782-1790.

5. Poncelet A, Hegenbart U, Schoenland S, et al. T2-relaxometry in a large cohort of hereditary transthyretin amyloidosis with polyneuropathy. Amyloid 2024; 31(4):309-317.

Images/Tables

Disease Group/Condition	PSD	T2app	MTR	CSA
Polyneuropathies	↑ Early	↑ in symptomatic/advanced stages	↓ Early	↑ Early
Multiple Sclerosis	↑	↓	↓	No change
5q-linked Spinal Muscular Atrophy	↓	↑	↓	↓
Neurodegenerative diseases / Ataxias	↓	↓	↓*	↓*
- Friedreich's Ataxia	↓	↓	No change	No change

1011 Cerebrocerebellar Functional Connectivity Alterations in Patients with Temporal Lobe Glioma: Resting-State fMRI Insights into Language Processing

Sara Naghizadehkashani MD, Kiran Talekar MD, Mahdi Alizadeh PhD, Sahar Darabi Monadi MD, Zahra Sadeghi-Adl MS, Spandana Tammiraju MD, Michael Hoch MD, Feroze Mohamed PhD, Scott Faro MD
Thomas Jefferson University, Philadelphia, PA, USA

Purpose

Glioma in language-eloquent regions can disrupt widespread neural networks, leading to language deficits. Recent evidence highlights the cerebellum's important role in language processing and its potential contribution to compensatory mechanisms supporting recovery in patients with aphasia. In this study, we investigated cerebrocerebellar functional connectivity alterations in patients with left temporal glioma, comparing those with language deficits (LD) to those with normal language function.

Materials & Methods

Twelve minutes Resting-state fMRI was performed on 25 patients with left temporal brain tumor, including 8 males and 6 females (mean age 62 ± 4) with normal language and 4 males and 7 females (mean age 63 ± 5.5) with language deficit (LD). After segmenting and excluding the tumor area, we performed see-to-voxel group analyses, with cerebellum as the seed, using CONN toolbox v18 and the SPM 12 software. (Connectivity and cluster threshold $P< 0.05$).

Results

Seed-to-voxel analysis focusing on the cerebellum revealed increased connectivity in the LD group compared to the normal language group, between the cingulate gyrus and left and right paracingulate gyrus, left caudate, and visual cortices. Networks involving these regions with altered connections to the cerebellum in LD patients are shown in a polar map, with the default mode network (DMN) exhibiting the highest number of voxels.

Conclusion

In LD group, increased cerebellar connectivity with DMN and visual networks suggests adaptive reorganization of higher-order language pathways. Prior studies have shown that DMN contributes to semantic integration and compensatory language processing, while visual and occipitotemporal regions engage in cross-modal recruitment supporting word retrieval and reading. The strengthened cerebrocerebellar coupling with these associative networks may therefore reflect the brain's attempt to sustain language function through distributed, multimodal pathways beyond the damaged temporal cortex. These findings highlight the cerebellum's broader integrative role in language control and underscore the potential value of targeting these circuits in rehabilitation or preoperative mapping.

References

1. Zhou J, et al. Altered cerebello-cerebral functional connectivity in patients with brain tumors: Evidence for cross-network reorganization. NeuroImage: Clinical. 2019;21:101653. PMID: 30599866
2. Yuan L, et al. Disrupted cerebrocerebellar connectivity and language impairment in low-grade glioma. Human Brain Mapping. 2023 Jul;44(10):4129–4144. PMID: 37356540

3. Mao Y, et al. Default mode network reorganization after tumor resection predicts recovery of language function in glioma. Cerebral Cortex. 2023 Sep;33(17):10264–10277. PMID: 37708205
4. Menei P, et al. Cerebello-cerebral functional connectivity supports compensatory mechanisms for language preservation in temporal lobe glioma. Neuro-Oncology Advances. 2024;6(1):vdae004. PMID: 39531223

Images/Tables

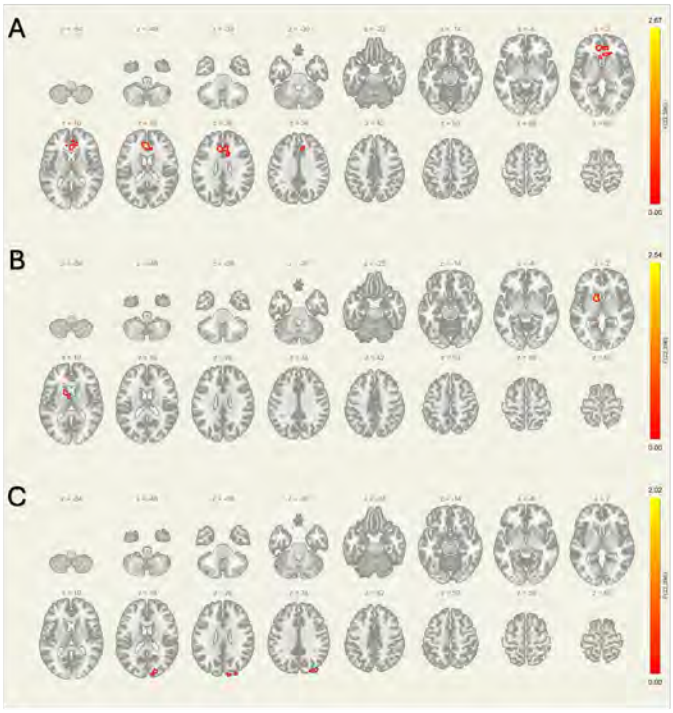

Figure 1. Cerebrocerebellar functional connectivity differences in patients with language deficits compared to those with normal language. (A) Increased cerebellar connectivity with the anterior and paracingulate cortices. (B) Increased cerebellar connectivity with the left caudate and adjacent subcortical regions. (C) Increased cerebellar connectivity with the occipital pole, superior lateral occipital, and cuneal cortices.

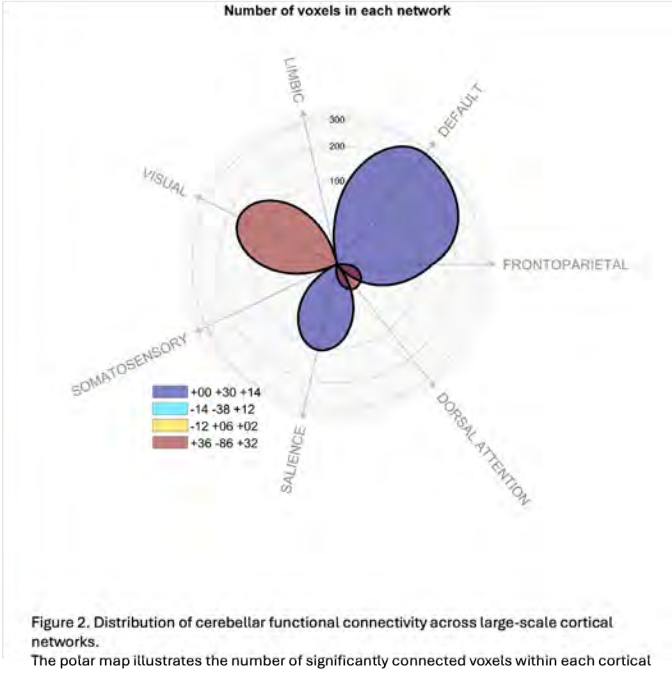

Figure 2. Distribution of cerebellar functional connectivity across large-scale cortical networks.
The polar map illustrates the number of significantly connected voxels within each cortical network for cerebellar seeds, showing altered connectivity in patients with language deficits. Each color represents an area with the corresponding coordinates on the seed (Cerebellum).

1068 Longitudinal Associations Between Vertebral Bone Density and Changes in Brain Microstructural Integrity: Findings from the MESA Cohort

Sara Momtazmanesh MD[1], Quincy A. Hathaway MD, PhD[2], David A. Bluemke MD, PhD[3], Benjamin M. Smith MD, MS[4], Mohamad Habes PhD[5], Ilya M. Nasrallah MD, PhD[2], Susan R. Heckbert MD, PhD[6], R. Nick Bryan MD, PhD[2], Jose A. Luchsinger MD, MPH[4], Shadpour Demehri MD[1]
[1]Department of Radiology and Radiologic Sciences, Johns Hopkins University, Baltimore, MD, USA. [2]Department of Radiology, University of Pennsylvania, Philadelphia, PA, USA. [3]Department of Radiology, University of Wisconsin, Madison, WI, USA. [4]Department of Medicine, Columbia University Medical Center, New York, NY, USA. [5]Neuroimage Analytics Laboratory and Biggs Institute Neuroimaging Core, Glenn Biggs Institute for Neurodegenerative Disorders, University of Texas Health Science Center at San Antonio, San Antonio, TX, USA. [6]Cardiovascular Health Research Unit and Department of Epidemiology, University of Washington, Seattle, Washington, USA

Purpose

Bone loss and brain microstructural decline often co-occur in aging, but their temporal relationship and shared mechanisms remain unclear. Building on our recent experimental evidence of a bone-brain pathway involving senescent marrow adipocytes and amyloid signaling[1], we examined whether vertebral bone mineral density (vBMD) was associated with subsequent microstructural changes in the community-based Multi-Ethnic Study of Atherosclerosis.

Materials & Methods

Among 6,814 participants, 410 (baseline age=69.8±6.9) had repeated fractional anisotropy (FA) from 2D diffusion-tensor imaging (DTI) at Exams 6 (2016–2018) and 7 (2022–2024), and vBMD from chest-CT at baseline quantified across T1-T10 using a validated deep-learning pipeline[2]. Linear mixed-effects models tested the association between baseline vBMD and longitudinal FA change, with random intercepts for participants. Models adjusted for demographics, education, *APOE* genotype, cardiometabolic and lifestyle factors, depressive symptoms, medication use, renal function, C-reactive protein, scanner, and baseline FA. Nonlinearity was assessed with quadratic terms, and regional significance determined after Bonferroni correction.

Results

Twenty-eight regions (59.6%) showed associations of higher vBMD with slower FA decline (Bonferroni-corrected $p<0.036$), spanning association tracts (right external capsule, left superior/inferior fronto-occipital fasciculi, right superior longitudinal fasciculus), cerebellar pathways (right inferior cerebellar peduncle, cerebellum), memory circuits (right fornix), interhemispheric fibers (corpus callosum right genu), and motor-sensory pathways (left retrolenticular internal capsule, left superior/anterior corona radiata, precentral gyrus, posterior thalamic radiation, sagittal stratum, medial lemniscus). Additional associations involved subcortical nuclei (left caudate, right midbrain), frontal executive WM (superior, middle, inferior frontal, lateral fronto-orbital), superior temporal WM, left inferior temporal WM, and right lingual gyrus.
Nineteen regions (40.4%) showed associations of higher vBMD with faster FA decline ($p<0.032$), concentrated in parietal (bilateral superior parietal gyri, right angular gyrus, left supramarginal WM), medial temporal (bilateral amygdalae, right entorhinal cortex, right inferior temporal gyrus),

subcortical (right putamen), occipital (left superior/inferior occipital WM, bilateral middle, left superior occipital gyrus), and frontal (right superior frontal gyrus) regions, as well as association/limbic tracts (right fornix-stria terminalis, superior fronto-occipital fasciculus, tapetum, cingulum WM). All nonlinear tests were significant after Bonferroni correction (p<0.001). Twenty-one showed U-shaped (threshold) patterns (mean inflection 215.8 mg/cm^3; range 152.9-262.4), where higher vBMD was associated with slower FA decline above a physiologic inflection, involving cerebellar-brainstem (left middle cerebellar peduncle, right medulla, pontine crossing tract), hippocampal (left hippocampus, right cingulum-hippocampal, bilateral uncinate fasciculi), motor (bilateral corticospinal tracts, parts of internal capsules, right cerebral peduncle), subcortical (right globus pallidus), association (right inferior fronto-occipital fasciculus, splenium of left corpus callosum), and parietal-occipital (right supramarginal gyrus/WM, left cuneus, lingual gyrus/WM) regions. Nine showed inverted-U (saturation) patterns (mean 224.6 mg/cm^3; range 201.2-248.9), with maximal protection at moderate vBMD, involving cingulum, left fornix, right thalamus, and higher-order association cortices (right precuneus, left angular, middle temporal, and occipital WM).

Conclusion

Higher vBMD was associated with less decline in fronto-subcortical and cerebellar–limbic microstructural integrity. Inverse associations emerged in parietal–occipital and medial temporal regions, indicating region-specific heterogeneity in bone–brain aging pathways. Investigating the mechanisms underlying these region-specific associations may help disentangle systemic risk pathways that differentially contribute to distinct brain degeneration patterns.

References

1. Kumar S, Song K, Wang J, et al. Serum amyloid P secreted by bone marrow adipocytes drives skeletal amyloidosis. *Nature Aging* 2025;5:1771–1789
2. Hathaway QA, Kasaeian A, Pan T, et al. A Deep Learning Model for Three-Dimensional Determination of Whole Thoracic Vertebral Bone Mineral Density from Noncontrast Chest CT: The Multi-Ethnic Study of Atherosclerosis. *Radiology* 2025;314:e242133

Images/Tables

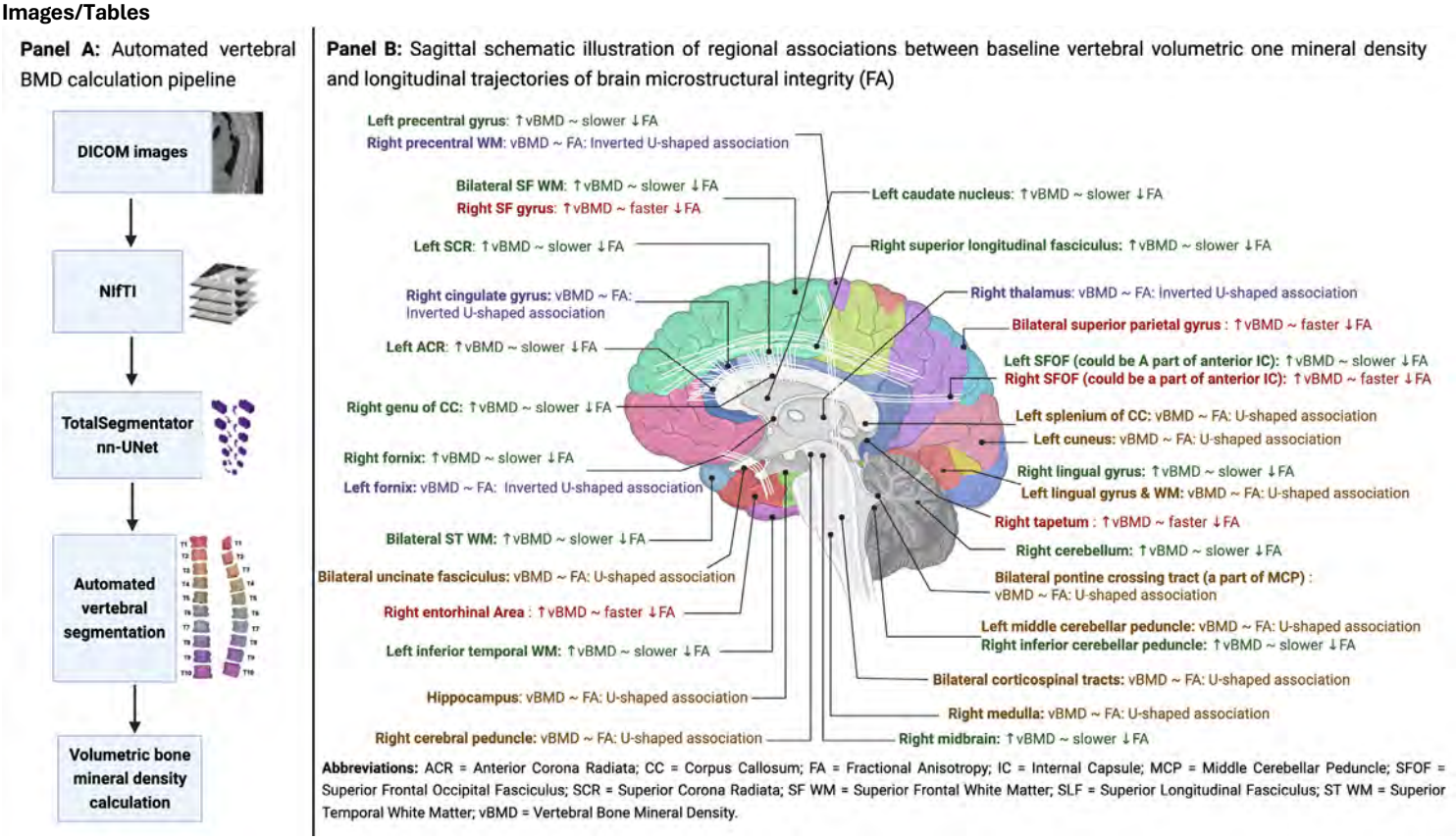

---

496 Physics-Informed Neural Networks Reveal Radiogenomic Determinants of Blood–Brain Barrier Breakdown and Therapeutic Transport in Glioblastoma

Shivi Kumar

Mind Matters Foundation, Flower Mound, TX, USA

Purpose

Glioblastoma (GBM) is characterized by extreme heterogeneity in blood–brain barrier (BBB) permeability, leading to unpredictable drug delivery and recurrence near partially protected tumor margins. Conventional perfusion and diffusion MRI metrics fail to fully capture the underlying biophysical determinants of BBB resistance. This study aimed to develop and validate a Physics-Informed Neural Network (PINN) framework that integrates perfusion-diffusion MRI, radiogenomic data, and vascular transport equations to reconstruct patient-specific maps of BBB transport resistance and identify their prognostic value in predicting recurrence.

Materials & Methods

A retrospective cohort of 78 newly diagnosed GBM patients (2018–2024) with preoperative MRI and follow-up imaging was analyzed. Imaging data included dynamic contrast-enhanced (DCE) MRI, diffusion tensor imaging (DTI), and perfusion-weighted sequences.

DCE-derived permeability (K^trans^), extracellular volume fraction (v_e_), and plasma volume (v_p_) were spatially co-registered with DTI-derived anisotropy maps and tumor masks generated in 3D Slicer.

A PINN was constructed using a 3D diffusion-reaction partial differential equation governing solute transport across the BBB:
where C is drug concentration, D the diffusivity tensor from DTI, k the clearance rate, and S the vascular source term estimated.
The PINN's composite loss combined data fidelity with physical constraint terms to ensure physiologic consistency. Model outputs were voxel-level resistance maps calibrated to normalized permeability indices (0–1). Results were correlated with molecular subtype (MGMT, IDH1), immune gene expression (VEGF, CLDN5, CXCL10), and recurrence regions identified on 6-month follow-up MRI.
Model performance was benchmarked against U-Net and random forest radiomics models using mean absolute error (MAE), Pearson correlation (r), and spatial concordance index (SCI).

Results

The PINN achieved a mean voxel-wise $R^2 = 0.91 \pm 0.02$ for permeability prediction and reduced MAE by 43 % compared with conventional CNN-based radiomics. Spatial resistance maps revealed heterogeneous BBB disruption, with elevated resistance (≥ 0.7 normalized units) in peri-tumoral white-matter tracts.
Regions of high predicted resistance significantly overlapped with early recurrence zones (SCI = 0.79, $p < 0.001$) and correlated with increased expression of tight-junction and hypoxia-response genes ($r = 0.68$, $p < 0.01$).
Patients with median resistance index > 0.6 had shorter progression-free survival (5.6 mo vs 11.2 mo; HR = 2.1; $p = 0.004$). Visualization via 3D resistance cartography demonstrated proximity of resistant regions to eloquent cortices and resection margins, suggesting value for neurosurgical planning and adjuvant therapy targeting.

Conclusion

This study introduces a validated, physics-constrained deep learning framework that links advanced neuroimaging, radiogenomics, and vascular transport modeling to quantify BBB resistance in GBM.
By combining mechanistic equations with data-driven learning, the PINN approach outperforms purely statistical AI models and generates interpretable resistance maps predictive of recurrence and therapeutic response.
Integration of this framework into intraoperative navigation and radiotherapy planning may enhance personalized treatment strategies in glioblastoma.

References

1. Arvanitis CD, Ferraro GB, Jain RK. The blood–brain barrier and blood–tumour barrier in brain tumors and metastases. Nat Rev Cancer. 2020;20(1):26-41. doi:10.1038/s41568-019-0205-x
2. Leow AD, Zhan L, Zhuo J, et al. Physics-informed machine learning for diffusion MRI signal modelling. Magn Reson Med. 2022;87(6):3035-3049. doi:10.1002/mrm.29127
3. Liu Y, Shen H, Zhou J, et al. Radiogenomic mapping of vascular permeability and gene expression in glioblastoma. Neuro Oncol. 2023;25(7):1231-1244. doi:10.1093/neuonc/noad023
4. Raissi M, Perdikaris P, Karniadakis GE. Physics-informed neural networks: A deep learning framework for solving forward and inverse problems involving nonlinear partial differential equations. J Comput Phys. 2019;378:686-707. doi:10.1016/j.jcp.2018.10.045
5. Kumar S, Nguyen S, del Toro C, et al. Integrative modeling of blood–brain barrier resistance in glioblastoma using physics-informed neural networks. Proc ASNR Sci Meet. 2025. (In press; self-cited prior version for continuity).

Images/Tables

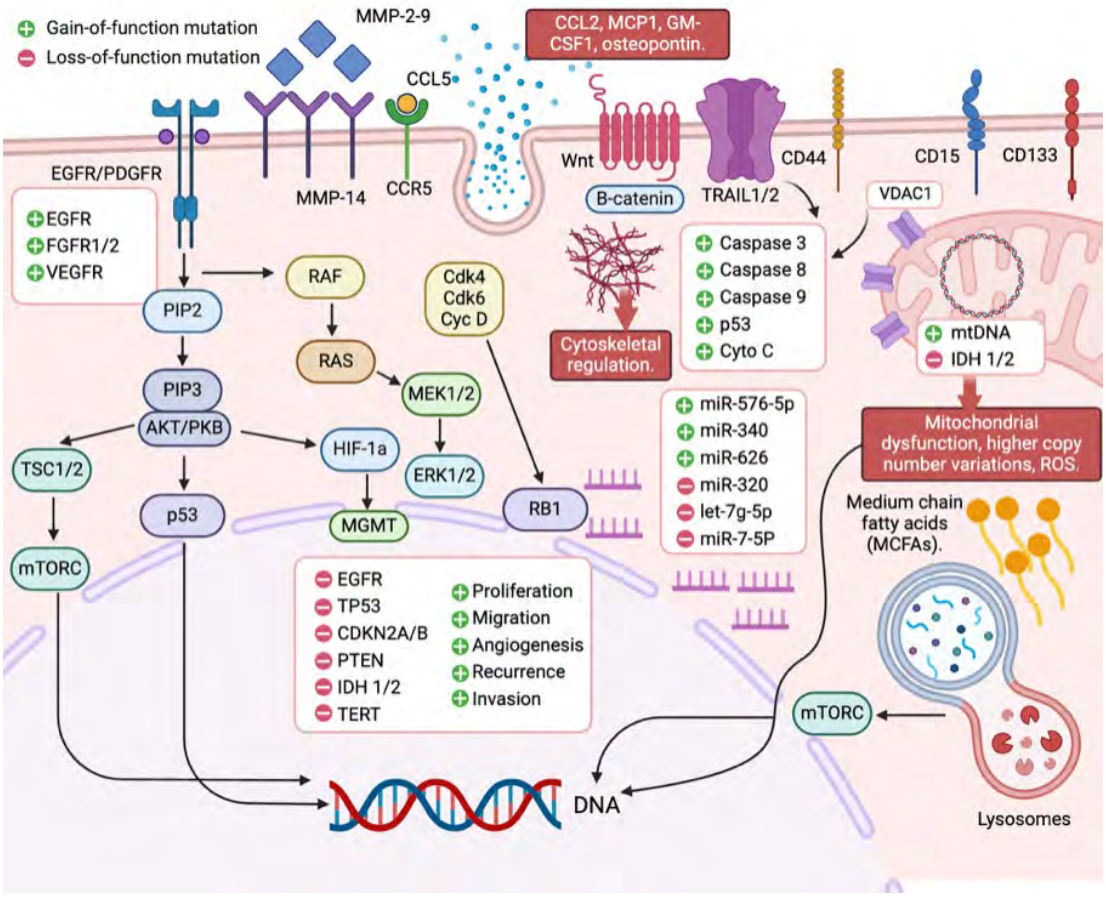

552 Probabilistic Acidity Mapping from Amine CEST-EPI for Improved Assessment of Metabolic Response Following EGFR Inhibition in EGFR-Altered Recurrent Glioblastoma

Omar Ibrahim MS, Jingwen Yao, Francesco Sanvito, Robert Chong, Donatello Telesca, Albert Lai, Phioanh Nghiemphu, David A Nathanson, Timothy F Cloughesy, Benjamin M Ellingson
University of California, Los Angeles, Los Angeles, CA, USA

Purpose

Amine chemical exchange saturation transfer echoplanar imaging (CEST-EPI) is a promising noninvasive, pH-sensitive metabolic imaging technique for assessing brain tumor biology[1]. However, clinical adoption remains limited, in part due to artifacts in the resulting images that complicate interpretation. To distinguish true tissue acidity from artifacts, a probabilistic algorithm was developed to estimate voxelwise uncertainty in CEST measurements and compute probabilistic tissue acidity maps.

Materials & Methods

Amine CEST-EPI data were utilized to simulate four sources of uncertainty: acquisition noise, B_0 field uncertainty, misregistration error, and interpolation error during motion correction. These uncertainties were incorporated into a statistical model to compare against an atlas of healthy volunteers[2] (N=20) to obtain probabilistic acidity maps, which estimate voxelwise probability of CEST contrast elevation compared to the reference population. We then computed probabilistic acidity maps from serial CEST data in a previously reported phase II trial (NCT03732352) evaluating the EGFR inhibitor osimertinib in 12 recurrent EGFR-altered glioblastoma patients[3]. These maps were used to monitor acidic volume changes and metabolic response throughout treatment course, and a biexponential model was used to characterize the acidic volume dynamics within the tumor region.

Results

Simulations identified misregistration and interpolation as the largest sources of uncertainty in CEST images. Probabilistic acidity maps demonstrated reduced artifacts on visual inspection compared to standard CEST contrast. Patients in the osimertinib cohort were classified as CEST responders or non-responders based on the depth of metabolic response obtained from the biexponential fit of tumor acidic volume. Two patients who lacked follow-up CEST data (one withdrew early and the other progressed early and was taken off the drug) were classified as non-responders. Log-rank testing revealed significantly improved survival in CEST responders compared to CEST non-responders ($p = 0.0247$). The depth of metabolic response obtained from the biexponential fits predicted both progression-free survival (HR 0.976, 95% CI [0.953, 0.999], $p = 0.0442$) and overall survival (HR 0.978, 95% CI [0.958, 0.999], $p = 0.0354$).

Conclusion

Probabilistic acidity maps computed from CEST data demonstrate promise for monitoring metabolic treatment response in brain tumors. This approach has the potential to facilitate interpretation of CEST imaging and accelerate its adoption into clinical practice.

References

1. Cho NS, Hagiwara A, Yao J, et al. Amine-weighted chemical exchange saturation transfer magnetic resonance imaging in brain tumors. *NMR Biomed.* 2023 Jun;36(6):e4785. DOI: 10.1002/nbm.4785.
2. Yao J, Hagiwara A, Oughourlian TC, et al. Diagnostic and Prognostic Value of pH- and Oxygen-Sensitive Magnetic Resonance Imaging in Glioma: A Retrospective Study. *Cancers.* 2022;14(10).
3. Ellingson BM, Okobi Q, Chong R, et al. A comparative study of preclinical and clinical molecular imaging response to EGFR inhibition using osimertinib in glioblastoma. *Neurooncol Adv.* 2025;7(1):vdaf022.

Images/Tables

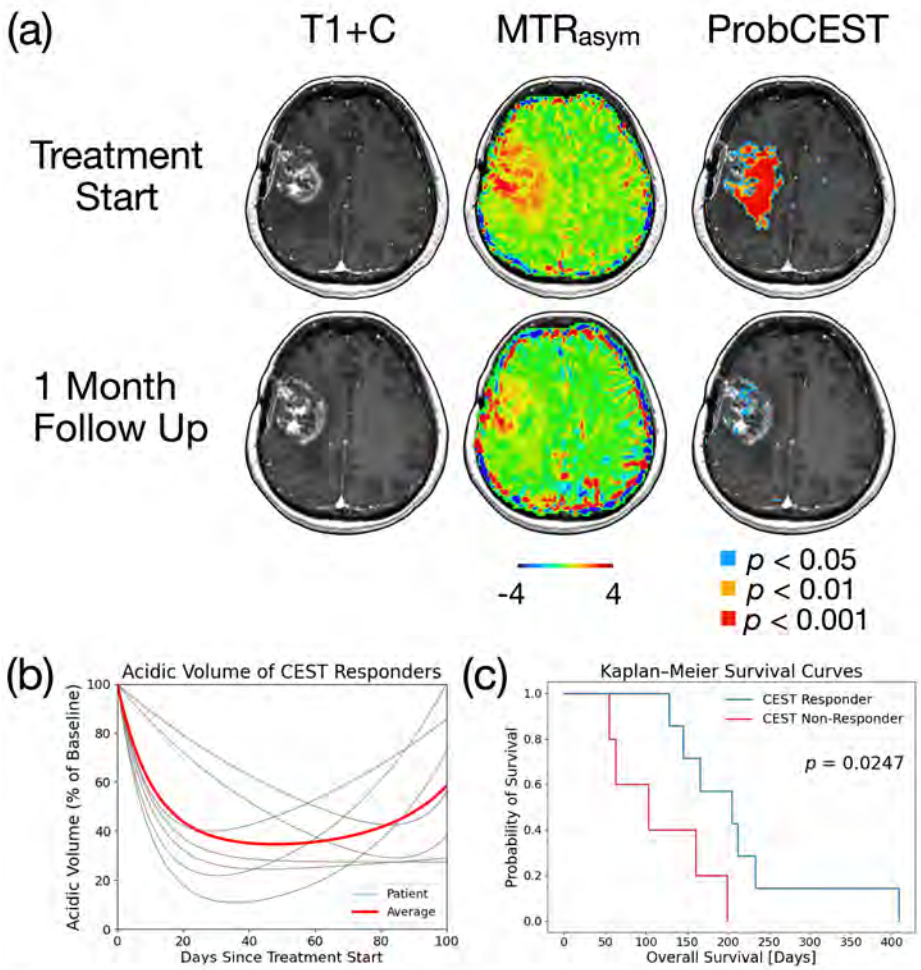

a) Probabilistic acidic volume maps for a sample CEST responder patient in the osimertinib cohort at baseline and after 1 month along with T1 with contrast and MTR_{asym} (at 3 ppm). Lower values of p indicate higher confidence in acidity. (b) Biexponential curve fits of tumor acidic volume of all CEST responders (gray) and average of all curves (red). (c) Kaplan-Meier survival curves of CEST responders (blue) and non-responders (red)

1134 First Report of Visualization of Cardiac Branches of Vagus Nerve in Cadavers using Sub-millimetric CISS MRI with Anatomic–Radiologic Correlation: Initial Experience from SPARC REVA

Shruti Kumari MD, Mridhula Muthukumar MS, Ari Blitz MD
University Hospitals, Case Western Reserve University, Cleveland, Ohio, USA

Purpose

CN X has changed from a structure at potential risk in head and neck surgery, to a target of nerve simulation. Branching of the CN X in the carotid sheath may be related to the side effects or the missing therapeutic efficiency of VNS. CN X is also frequently injured during neck and thoracic surgeries. Due to the extent of its path, and its multiple targets, FDA-approved vagus nerve stimulation (VNS) has been clinically deployed in >125,000 patients worldwide for refractory epilepsy and treatment-resistant depression. This novel technique is not without its limitations, as VNS has been shown to have overall cardiac complication rates of 8.6-9.4% including bradycardia occurring in up to 2.7% during device testing, and late-onset complications like asystole developing years post-implantation in documented cases. Expanding therapeutic applications of VNS are also under investigation for heart failure, atrial fibrillation, and cardiac arrhythmias. Additionally, mediastinal tumors and iatrogenic injury to cardiac branches of CN X during mediastinal procedures may also cause cardiac symptoms like episodic bradycardia, hypotension and asystole. These limitations highlight the necessity for pre-operative MRI of distal CN X branches, specifically the cardiac plexus. We hypothesize that 0.5-0.6 mm CISS MRI can help in the visualization of CN X and its branches.

Materials & Methods

54 embalmed cadavers were scanned with a 3T MRI scanner using 3D isotropic 0.5-0.6 mm resolution CISS sequence; a total of 110 CN X were examined. Identification of branches on CISS MRI was independently evaluated by three readers and confirmed using anatomic dissection. The nerve branch take-off point was noted on the MRI sequence and its distance from a predefined landmark was calculated, followed by anatomic dissection, where each branch was traced up to the target organ for identification. The main trunk of CN X was painted at locations corresponding to the anatomical landmark. The entire nerve with its branches was dissected and placed on a grid where distance of branch takeoff was calculated from the landmark and compared with MRI findings. These findings were confirmed on micro-CT and histology.

Results
We confirmed the visualization of 15 cardiac and cardiopulmonary branches of CN X using CISS MRI. These include the cervical cardiac branch, thoracic cardiac branch, and cardiopulmonary branches.
Conclusion
SPARC-REVA is the most comprehensive mapping of CN X and its branches to date, from the perspectives of sample size, range of imaging modalities, lengths of nerve, and imaging resolutions. The high signal-to-noise ratio, high spatial resolution with isotropic 3D CISS images that can be reconstructed in multiple planes, makes this sequence superior to conventional 2D MRI sequences.**This is the first study showing the visualization of cardiac branches of CN X in cadavers using CISS MRI**. Translation of this work to living subjects and use of CISS MRI for routine clinical imaging of CN X and its branches offers significant potential for enhancing nerve preservation during surgery, optimizing therapeutic procedures targeting and stimulating the cardiac branches, and mitigating side effects associated with VNS.
References

- Wen J, Desai NS, Jeffery D, Aygun N, Blitz A. High-resolution isotropic three-dimensional MR imaging of the extraforaminal segments of the cranial nerves. Magnetic Resonance Imaging Clinics. 2018 Feb 1;26(1):101-19.
- Herzka DA, Markley M, Nuzov NB, Sali G, Kumari S, Pelot NA, Shoffstall AJ, Flask C, Crofton AR, Blitz A. REVA# 3: Magnetic Resonance Imaging (MRI) of Embalmed Cadaver.

Images/Tables

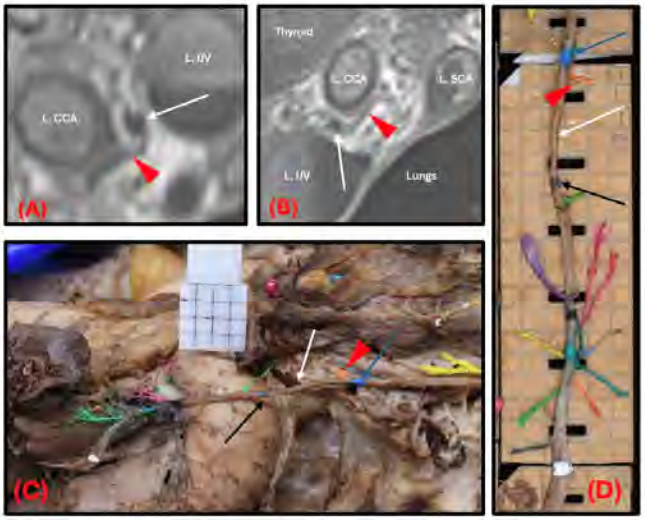

Fig 1.: SR043-(A) Axially reformatted 0.5mm CISS MRI of left CN X (white arrow) in the infrahyoid neck just below superior border of left clavicle giving off a thoracic cardiac branch (white arrowhead) postero-medially which travels medially to supply the left common carotid artery, the great vessels, and anterior surface of the heart; L. IJV-Left Internal Jugular Vein; L. CCA-Left Common Carotid Artery; (B) Sagittally reformatted 0.5mm CISS MRI of left CN X (white arrow) in the infrahyoid neck just below superior border of left clavicle giving off a thoracic cardiac branch (white arrowhead) postero-medially which travels medially to supply the left common carotid artery, the great vessels, and anterior surface of the heart; L. IJV-Left Internal Jugular Vein; L. CCA-Left Common Carotid Artery; L. Subclavian Artery; (C) Cadaveric dissection showing the infrahyoid cervical portion of the left vagus nerve (white arrow) giving off the thoracic cardiac branch (white arrowhead) posteromedially travelling medially and traced up to its target supply to the heart, great vessels and left common carotid artery; blue arrow-vagus nerve at the level of superior border of left clavicle; black arrow-vagus nerve at the level of the jugular notch; (D) Vagus nerve dissected and placed on a grid for anatomic-radiologic correlation where each grid is 5*5 mm and distance of branch from the landmark is calculated;

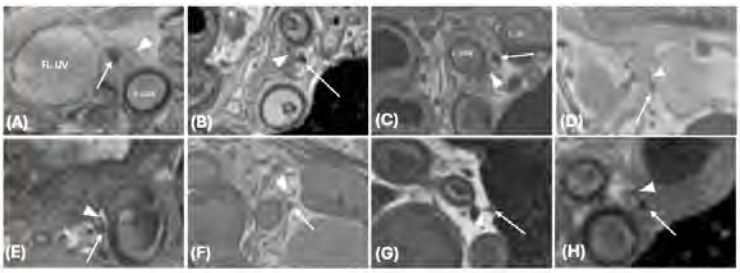

(A) Axially reformatted 0.5mm CISS MRI of right CN X (white arrow) in the infrahyoid neck about 10 mm above the medial end of the clavicle with a cervical cardiac branch (white arrowhead) that branches from the main trunk of CN X postero-medially and travels postero-laterally; (B) Axially reformatted 0.5mm CISS MRI of left CN X in the infrahyoid neck just below the medial end of the superior border of the clavicle with a thoracic cardiac branch that branches from the main trunk of CN X in the posterior direction and travels postero-medially; (C) Axially reformatted 0.5mm CISS MRI of left CN X (white arrow) in the infrahyoid neck just below the medial end of the superior border of the clavicle with a thoracic cardiac branch (white arrowhead) that branches from the main trunk of CN X posteriorly and travels laterally; (D) Axially reformatted 0.5mm CISS MRI of left CN X in infrahyoid neck about 6 mm below the medial end of the superior border of the clavicle with a thoracic cardiac branch that branches from the main trunk of CN X from the anterior direction, and travels infero-medially (E) Axially reformatted 0.5mm CISS MRI of R. CN X in the infrahyoid neck just below the medial end of the superior border of the clavicle with a thoracic cardiac branch that branches from the main trunk of CN X in the anterior direction and travels anterolaterally (F)Axially reformatted 0.5mm CISS MRI of left CN X just below the medial end of the superior border of the clavicle with a cervical cardiac branch that branches from the main trunk of CN X in the anterior direction and travels anterolaterally (G)Axially reformatted 0.5mm CISS MRI of left CN X in the infrahyoid neck about 20 mm above the sternal angle with a thoracic cardiac branch that branches from the main trunk of CN X in the medial direction and travels infero-medially (H) Axially reformatted 0.5mm CISS MRI of left CN X just below the medial end of the superior border of the clavicle with a cervical cardiac branch that branches from the main trunk of CN X in the medial direction and travels infero-medially

---

366 Deep-Learning Accelerated Vessel Wall Imaging Using T1-SPACE at Ultra-High Field Strength MRI

Pranjal Rai MD[1], Vincent Ern Yao Chan FRCR[2], Arien North RT[1], Kristen Betz RT[1], Aaron P. Katzka RT[1], Girish Bathla MBBS, MMed[1]
[1]Mayo Clinic, Rochester, MN, USA. [2]National Neuroscience Institute, Singapore, Singapore, Singapore

Purpose
To evaluate the feasibility and technical performance of a post-contrast T1-SPACE sequence using deep-learning based image reconstruction (DLBIR) for intracranial vessel wall imaging (IC-VWI) at 7T, comparing image quality, artifacts, and acquisition time with the standard T1-SPACE sequence.
Materials & Methods
In this retrospective single-center study, 36 patients (21 women; mean age, 53.3 ± 16.2 years) underwent IC-VWI at 7T using both standard (SOC) T1-SPACE and DLBIR-accelerated T1-SPACE (DL) sequences over 4 months. Two independent neuroradiologists assessed overall image quality (noise, artifacts, sharpness, and overall quality) and wall and lumen visualization along the intracranial vessels using a 4-point Likert scale. A cumulative-logit mixed-effects model (CLMM) of segment ratings was used for intersequence comparison. Segments were also pooled into proximal vs distal and quality compared using exact paired sign test and FDR control. Overall image quality metrics were compared using paired Wilcoxon tests. Inter-reader agreement was summarized as percent agreement; Bland–Altman plots assessed bias.
Results
On segment-level analysis with an ordinal mixed-effects model (CLMM), DLBIR yielded markedly higher ratings than SOC in both domains—wall: OR = 22.79 (95% CI 15.83–32.82), lumen: OR = 97.0 (95% CI 66.8–141.0); both $p<0.001$. Effects remained large when segments were pooled anatomically: for wall, Proximal OR = 297 (95% CI 40–∞) and Distal OR = 71 (28–404); for lumen, Proximal OR = 82 (36–339) and Distal OR = 225 (60–13 350); all FDR-adjusted $p<0.001$. Reader-wise Wilcoxon tests showed higher overall image quality scores across noise, artifacts, sharpness, and overall quality (all $p < 0.001$). Inter-reader agreement was uniformly high, with DLBIR outperforming SOC in distal and posterior circulation

vessels (94–100% vs 64–94%). Bland–Altman analysis demonstrated a positive bias favoring DLBIR. Acquisition time was reduced from 7:30 minutes with SOC to 6:00 minutes (20% reduction) with DLBIR.

Conclusion

DLBIR-accelerated post-contrast T1-SPACE may have potential clinical utility for IC-VWI at 7T, particularly for visualization of medium and small-caliber vessels while significantly improving overall image quality and reducing artifacts as well as scan time.

References

1. Rai P, Chan VEY, Fagan AJ, et al. Vessel Wall Imaging at 7T: State of the Art. American Journal of Neuroradiology. Published online October 24, 2025. doi:10.3174/ajnr.A9065
2. Bathla G, Messina SA, Black DF, et al. Deep Learning-Based Reconstruction of 3D T1 SPACE Vessel Wall Imaging Provides Improved Image Quality with Reduced Scan Times: A Preliminary Study. AJNR Am J Neuroradiol. 2024;45(11):1655-1660. doi:10.3174/ajnr.A8382
3. Seo M, Jung W, Jeong G, et al. Deep learning improves quality of intracranial vessel wall MRI for better characterization of potentially culprit plaques. Sci Rep. 2024;14(1):18983. doi:10.1038/s41598-024-69750-4
4. Zhou Z, Chen S, Balu N, et al. Neural network enhanced 3D turbo spin echo for MR intracranial vessel wall imaging. Magn Reson Imaging. 2021;78:7-17. doi:10.1016/j.mri.2021.01.004
5. Kharaji M, Canton G, Guo Y, et al. DANTE-CAIPI Accelerated Contrast-Enhanced 3D T1: Deep learning-based image quality improvement for Vessel Wall MR. Am J Neuroradiol. Published online July 22, 2024. doi:10.3174/ajnr.A8424

Images/Tables

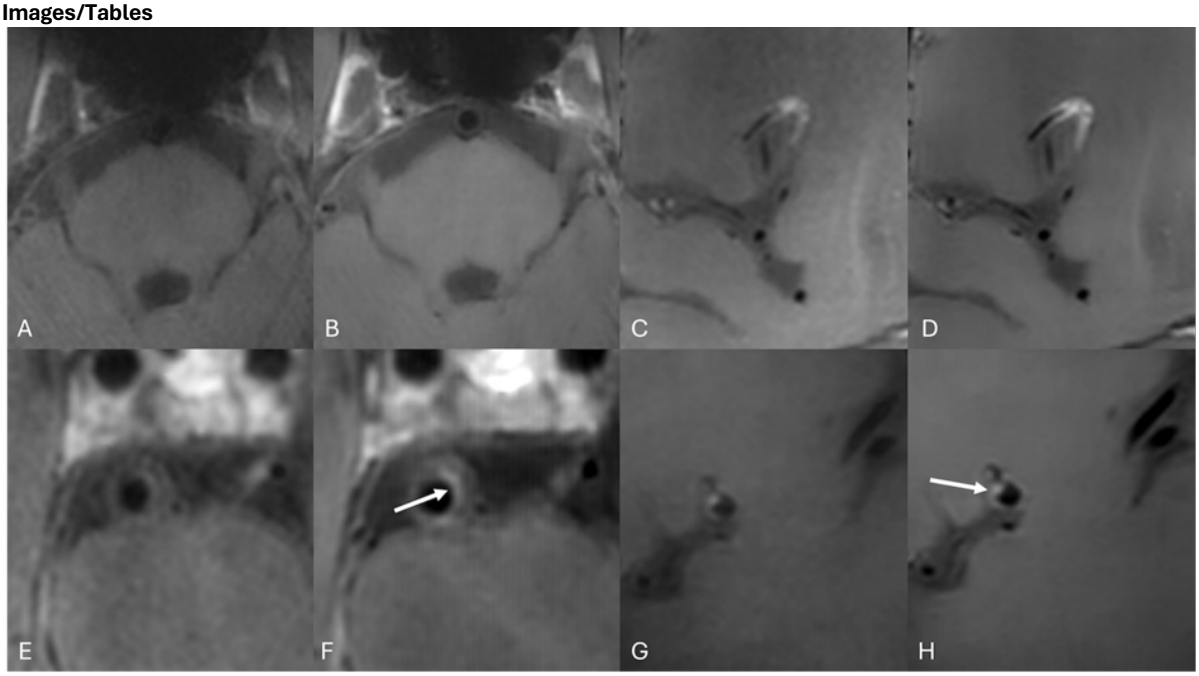

1102 Diagnostic Performance of MRI Contrast Clearance Analysis (Treatment Response Assessment Maps, TRAMs) in Identifying Recurrent Glioblastoma: Histopathologic Correlation and Comparison with Dynamic Susceptibility Contrast Perfusion

Ceylan Altintas Taslicay, Fabricio Feltrin, Toral Patel, Ben Wagner, Joseph Maldjian, Marco Pinho

University of Texas at Southwestern, Dallas, Texas, USA

Purpose

Differentiating true glioblastoma recurrence from post-treatment effects such as pseudoprogression or radiation necrosis remains a major diagnostic challenge on conventional MRI. Dynamic susceptibility contrast (DSC) MR perfusion is widely used to assess tumor vascularity but overlapping imaging characteristics between active tumor and treatment-related changes and technique limitations often limit its practical utility. MRI Treatment Response Assessment Maps (TRAMs), derived from contrast clearance analysis (CCA) using early and delayed post-contrast T1-weighted imaging, represent a novel physiologic imaging technique that characterizes tissue based on gadolinium wash-in and wash-out kinetics. Active tumor typically demonstrates rapid clearance, whereas necrotic or treatment-altered tissue exhibits delayed accumulation. Despite promising initial results, the correlation of TRAM/CCA findings with DSC MR perfusion and histopathologic confirmation of tumor activity has not been fully defined. This study aims to evaluate the diagnostic performance of TRAM/CCA maps in detecting recurrent glioblastoma and to compare their accuracy with DSC MR perfusion using histopathology as the reference standard.

Materials & Methods

This retrospective study included patients with previously treated glioblastoma who underwent MRI for suspected recurrence at a single tertiary care center as part of a clinical trial. TRAM/CCA maps were generated from early (~5 min) and delayed (60–90 min) post-gadolinium T1-weighted images using BrainLab software. DSC MR perfusion datasets were processed on Philips IntelliSpace Portal to calculate relative cerebral blood volume (rCBV) maps. Regions of suspected tumor activity were qualitatively assessed on both TRAM/CCA and rCBV maps, with “hot spots” identified for quantitative rCBV measurement. Lesion patterns were correlated with results from stereotactic biopsy and follow-up imaging. Post-biopsy CT scans were fused with MR datasets to spatially align biopsy sites with imaging findings. The visual agreement between TRAM/CCA and DSC MR perfusion was rated on a 0–10 Likert scale. Statistical correlation between TRAM/CCA visual assessment and rCBV ratios was evaluated using Pearson correlation.

Results

TRAM/CCA maps demonstrated 14 positive findings, all confirmed as tumor recurrence by biopsy, and six negative findings, of which three were verified as treatment-related changes by biopsy and three confirmed by stable follow-up imaging. TRAM/CCA and DSC perfusion findings showed moderate visual agreement; however, a strong correlation was observed between rCBV ratios and TRAM/CCA map intensity (Pearson coefficient, $p < 0.001$). Small lesions were occasionally missed on DSC perfusion but readily detected on TRAM maps. Compared with DSC, TRAM/CCA maps provided superior lesion delineation, improved spatial resolution, and easy to interpret maps with minimal sensitivity to susceptibility artifacts. These features enhanced diagnostic confidence, particularly for small or equivocal lesions.

Conclusion

TRAM/CCA imaging demonstrated high diagnostic accuracy and excellent concordance with histopathologic confirmation in differentiating true glioblastoma recurrence from post-treatment changes. Compared with DSC MR perfusion, TRAMs provided clearer delineation of lesion extent, were less prone to susceptibility artifacts, and allowed reliable detection of small recurrent lesions. These findings suggest that TRAM/CCA imaging is a robust, complementary tool to DSC perfusion in the post-treatment evaluation of glioblastoma and may enhance clinical decision-making in distinguishing recurrence from therapy-related effects.

References

1. Alkhatatneh H, Chen YH, Imhoff S, Fogel L, Yao K, Dubin D, Zhang M, Chen P, Nemade A, Herman M, Khatatneh A, Barnes T, Speiser M, Janosky M. Evaluating the diagnostic ability of treatment response assessment maps (TRAMs)/contrast clearance analysis (CCA) in predicting the presence of active brain tumors. Neuroradiol J. 2025 Feb 26;38(6):19714009251324305. doi: 10.1177/19714009251324305. Epub ahead of print. PMID: 40010303; PMCID: PMC11866328.
2. Khadhraoui E, Schmidt L, Klebingat S, Schwab R, Hernández-Durán S, Gihr G, Paukisch H, Stein KP, Behme D, Müller SJ. Comparison of a new MR rapid wash-out map with MR perfusion in brain tumors. BMC Cancer. 2024 Sep 12;24(1):1139. doi: 10.1186/s12885-024-12909-z. PMID: 39267002; PMCID: PMC11395865.
3. Tahamtan M, Afsharzadeh M, Sarvari M, Rahmani S, Geravandi M, Amiri D, Kolahi S. Contrast clearance analysis in neuro-oncology: A systematic review and meta-analysis on differentiating posttreatment changes from tumor progression. Neurooncol Adv. 2025 Jul 19;7(1):vdaf161. doi: 10.1093/noajnl/vdaf161. PMID: 40746952; PMCID: PMC12311927.
4. Müller SJ, Khadhraoui E, Ganslandt O, Henkes H, Gihr GA. MRI Treatment Response Assessment Maps (TRAMs) for differentiating recurrent glioblastoma from radiation necrosis. J Neurooncol. 2024 Feb;166(3):513-521. doi: 10.1007/s11060-024-04573-x. Epub 2024 Jan 23. PMID: 38261142.
5. Satvat N, Korczynski O, Müller-Eschner M, Othman AE, Schöffling V, Keric N, Ringel F, Sommer C, Brockmann MA, Reder S. A Rapid Late Enhancement MRI Protocol Improves Differentiation between Brain Tumor Recurrence and Treatment-Related Contrast Enhancement of Brain Parenchyma. Cancers (Basel). 2022 Nov 10;14(22):5523. doi: 10.3390/cancers14225523. PMID: 36428617; PMCID: PMC9688406.

Images/Tables

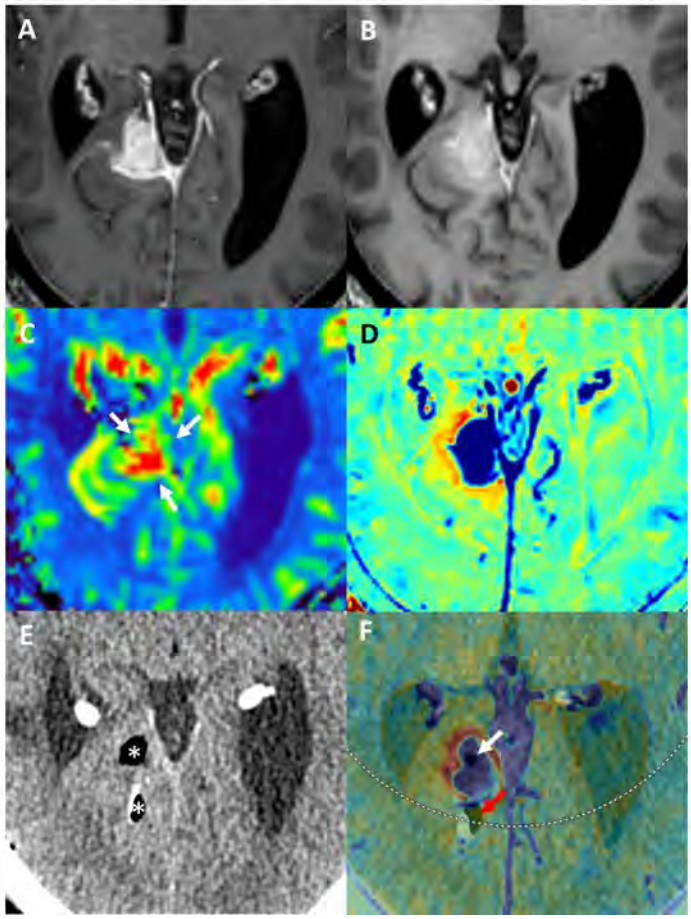

Early (~5 min) post-gadolinium T1-weighted images (A) showing avidly enhancing mass in the right precuneus with relative washout on delayed (60 min) imaging (B). DSC perfusion rCBV map (C) demonstrates low resolution "hot spot" focus (arrows) with adjacent vascular structures. TRAMs/CCA map (C) showing central lesion with washout (blue) consistent with viable neoplasm and peripheral areas of delayed wash in (red) consistent with treatment/reactive changes. Higher resolution allows clearer delineation of tumor margins distinction with adjacent vascular structures. Same-day post-biopsy CT (E) showing biopsy cavities (asterisks). Fused TRAMs and post-biopsy CT (F) showing overlap of the biopsy cavity and the central lesion with washout (white arrow), and overlap of the biopsy cavity and the peripheral area with wash in (red arrow). Path report confirmed recurrent glioblastoma and post-treatment change separately.

Know Your Nodes in the Head & Neck

4:30 - 5:30pm Tuesday, 19th May, 2026

489 Title: Initial Post-treatment NI-RADS 2A surveillance – Emory Experience

Jacqueline Junn MD, Janet S Zhang MD, Sara Tedla MD, Jennifer Becker MD, Kristen Baugnon MD, Ashley Aiken MD, Nicole Schmitt MD, FACS, Wen Wang MBBCh

Emory University Hospital, Atlanta, GA, USA

Purpose

Neck Imaging and Reporting and Data System (NI-RADS) is a standardized reporting system developed by the American College of Radiology for interpreting post treatment imaging in head and neck cancer patients.[1] This serves to standardize radiology reports, stratify risk of residual or recurrent disease, and guide management, including timelines for follow-up imaging or recommending biopsy. There are 4 categories which are used for both the primary and nodal sites which correspond to: no evidence of recurrence, low suspicion of recurrence, high suspicion of recurrence, and definitive recurrence. Within the low suspicion (NI-RADS 2) category for the primary site, there are 2A (superficial focal non-mass-like mucosal enhancement) and 2B (deep ill-defined soft tissue) subcategories.1

Previous research reported a recurrence rate of 18.4% in patients assigned to all NI-RADS 2 category for the primary site, and a negative predictive value of 77%–90% for NI-RADS 2.2-[4] Additionally, among clinically occult recurrences, 38% received a NI-RADS 2 score and 62% received NI-RADS 3.[2-4] Although NI-RADS 2 is described as low suspicion, these findings indicate an intermediate risk of recurrence. However, research stratifying outcomes between 2A and 2B subcategories remains limited, particularly since 2A is thought to reflect mucositis or posttreatment change shortly after therapy.[5] We aimed to evaluate patients in the 2A subcategory within 3 months after completion of treatment, and their subsequent clinical outcomes, with the prediction that recurrence for this cohort will be lower than what has been previously published.

Materials & Methods

We performed a retrospective analysis of patients assigned as NI-RADS 2A who were treated at Emory from 2016 to 2022. Exclusion criteria included patients with another primary cancer, prior head and neck cancer, or reports lacking the NI-RADS template. Initial TNM stage, subsite location, risk factors for aggressive disease, treatment, and outcome data from the EMR will be presented. Patients were followed at least 2 years after completion of treatment.

Results

Initial analysis of 20% of patients with initial baseline post-treatment NI-RADS 2A categorization shows 1.5% with recurrent disease at the primary site at 66 weeks, with NPV of NI-RADS 1 of 98.5%.

Conclusion

In our study, a score of NI-RADS 2A at the primary site on the initial baseline post-treatment study was associated with a very high negative predictive value of 98.5%, with only 1.5% of patients with recurrent or persistent disease at that point. This data differs greatly from prior studies demonstrating a recurrence rate of 18.4%, and NPV ranging from 77-90% for all patients with NI-RAD 2 in the primary site (2a and 2b), as well as NI-RADS 2 for the neck.[2-4] Our improved outcomes are likely because this study focused on NI-RADS 2A at the primary site, assigned to patients within 3 months of completion of treatment. The results of our full analysis may guide future clinical decision making, with the potential for reduced imaging surveillance and unnecessary interventions of patients at this early timepoint.

References

1. Aiken AH, Rath TJ, Anzai Y, Branstetter BF, Hoang JK, Wiggins RH, Juliano AF, Glastonbury C, Phillips CD, Brown R, Hudgins PA. ACR Neck Imaging Reporting and Data Systems (NI-RADS): A White Paper of the ACR NI-RADS Committee. J Am CollRadiol. 2018 Aug;15(8):1097-1108.doi: 10.1016/j.jacr.2018.05.006.Epub2018 Jul 6. PMID: 29983244.
2. Krieger DA, Hudgins PA, Nayak GK,BaugnonKL, Corey AS, Patel MR, Beitler JJ, Saba NF, Liu Y, Aiken AH. Initial Performance of NI-RADS to Predict Residual or Recurrent Head and Neck Squamous Cell Carcinoma. AJNR Am JNeuroradiol. 2017 Jun;38(6):1193-1199.doi: 10.3174/ajnr.A5157.Epub2017 Mar 31. PMID: 28364010; PMCID: PMC7960090.
3. WangaryattawanichP, Branstetter BF 4th, Hughes M, Clump DA 2nd, Heron DE, Rath TJ. Negative Predictive Value of NI-RADS Category 2 in the First Posttreatment FDG-PET/CT in Head and Neck Squamous Cell Carcinoma. AJNR Am JNeuroradiol. 2018 Oct;39(10):1884-1888.doi: 10.3174/ajnr.A5767.Epub2018 Aug 30. PMID: 30166429; PMCID: PMC7410732.
4. Baba A, Kurokawa R, Kurokawa M, Yanagisawa T, Srinivasan A. Performance of Neck Imaging Reporting and Data System (NI-RADS) for Diagnosis of Recurrence of Head and Neck Squamous Cell Carcinoma: A Systematic Review and Meta-analysis. AJNR Am JNeuroradiol. 2023 Oct;44(10):1184-1190.doi: 10.3174/ajnr.A7992.Epub2023Sep 14. PMID: 37709352; PMCID: PMC10549942.
5. Gore A,BaugnonK, Beitler J, Saba NF, Patel MR, Wu X, Boyce BJ, Aiken AH. Posttreatment Imaging in Patients with Head and Neck Cancer without Clinical Evidence of Recurrence: Should Surveillance Imaging Extend Beyond 6 Months? AJNR Am JNeuroradiol. 2020 Jul;41(7):1238-1244.doi: 10.3174/ajnr.A6614.Epub2020 Jun 18. PMID: 32554418; PMCID: PMC7357658.

Zebras Amongst Horses: Challenging Cerebrovascular Imaging Cases

9:20 - 10:20am Wednesday, 20th May, 2026

776 The Asymmetric Brain: Left-Sided Limbic Aging Predicts Cognitive Decline in Parkinson's Disease

Sadegh Ghaderi PhD[1], Ali Fathi Jouzdani MD[2], Ali Mohammad Pourbagher-Shahri MD[3], Sana Mohammadi MD[1]

[1]Tehran University of Medical Sciences, Tehran, Tehran, Iran, Islamic Republic of. [2]Institute for Research in Fundamental Sciences, Tehran, Tehran, Iran, Islamic Republic of. [3]Mashhad University of Medical Sciences, Mashhad, Mashhad, Iran, Islamic Republic of

Purpose

While pathological aging is a known component of Parkinson's disease (PD), it is unclear if this process is global or region-specific. We aimed to use MRI-derived brain structure age (BSA) to identify patterns of accelerated aging in PD patients with mild cognitive impairment (PD-MCI) versus normal cognition (PD-NC) and healthy controls (HC). This study sought to: (1) compare global and regional subcortical BSA across groups, and (2) identify localized networks of accelerated aging.

Materials & Methods

We conducted a cross-sectional analysis of structural MRI data from 55 participants (22 HC, 18 PD-NC, 15 PD-MCI). Global and subcortical BSA estimates (for accumbens, amygdala, basal forebrain, caudate, hippocampus, pallidum, putamen, and thalamus) were generated using the deep-learning volBrain platform . Group differences in chronological age, global BSA, and regional BSA were assessed using non-parametric Kruskal-Wallis tests. Pearson correlations were used for follow-up analyses on significant regions.

Results

There were no significant group differences in chronological age ($p=0.111$) or global BSA ($p=0.143$), suggesting preserved global brain aging. However, regional analysis revealed a highly localized and asymmetric pattern of accelerated aging. Significant group differences were found in the predicted age of the left amygdala ($p=0.040$) and the left basal forebrain ($p<0.050$) . The predicted ages of these two structures were almost perfectly correlated ($r=0.992$), indicating a shared pathological signal. No other subcortical regions showed significant differences after correction.

Conclusion

Accelerated brain aging in PD appears to be a localized and asymmetric process rather than a global phenomenon. We found that cognitive impairment is linked to accelerated aging confined to the limbic-cholinergic network, specifically the left amygdala and left basal forebrain. This finding, in the absence of global BSA differences, suggests that regional brain-age metrics are more sensitive biomarkers for tracking early cognitive vulnerability in PD.

References

1. Nguyen H, Clément M, Mansencal B, et al. Brain structure ages—A new biomarker for multi-disease classification. Hum Brain Mapp. 2024;45(1):e26558
2. Manjón JV, Coupé P. volBrain: An Online MRI Brain Volumetry System. Front Neuroinform. 2016;10:30
3. Kemp AS, Eubank AJ, Younus Y, et al. Sequential patterning of dynamic brain states distinguish Parkinson's disease patients with mild cognitive impairments. Neuroimage Clin. 2025;46:103779
4. Braak H, Braak E, Yilmazer D, et al. Amygdala pathology in Parkinson's disease. Acta Neuropathol. 1994;88(6):493-500
5. Ray NJ, Bradburn S, Murgatroyd C, et al. In vivo cholinergic basal forebrain atrophy predicts cognitive decline in de novo Parkinson's disease. Brain. 2018;141(1):165-176

Images/Tables

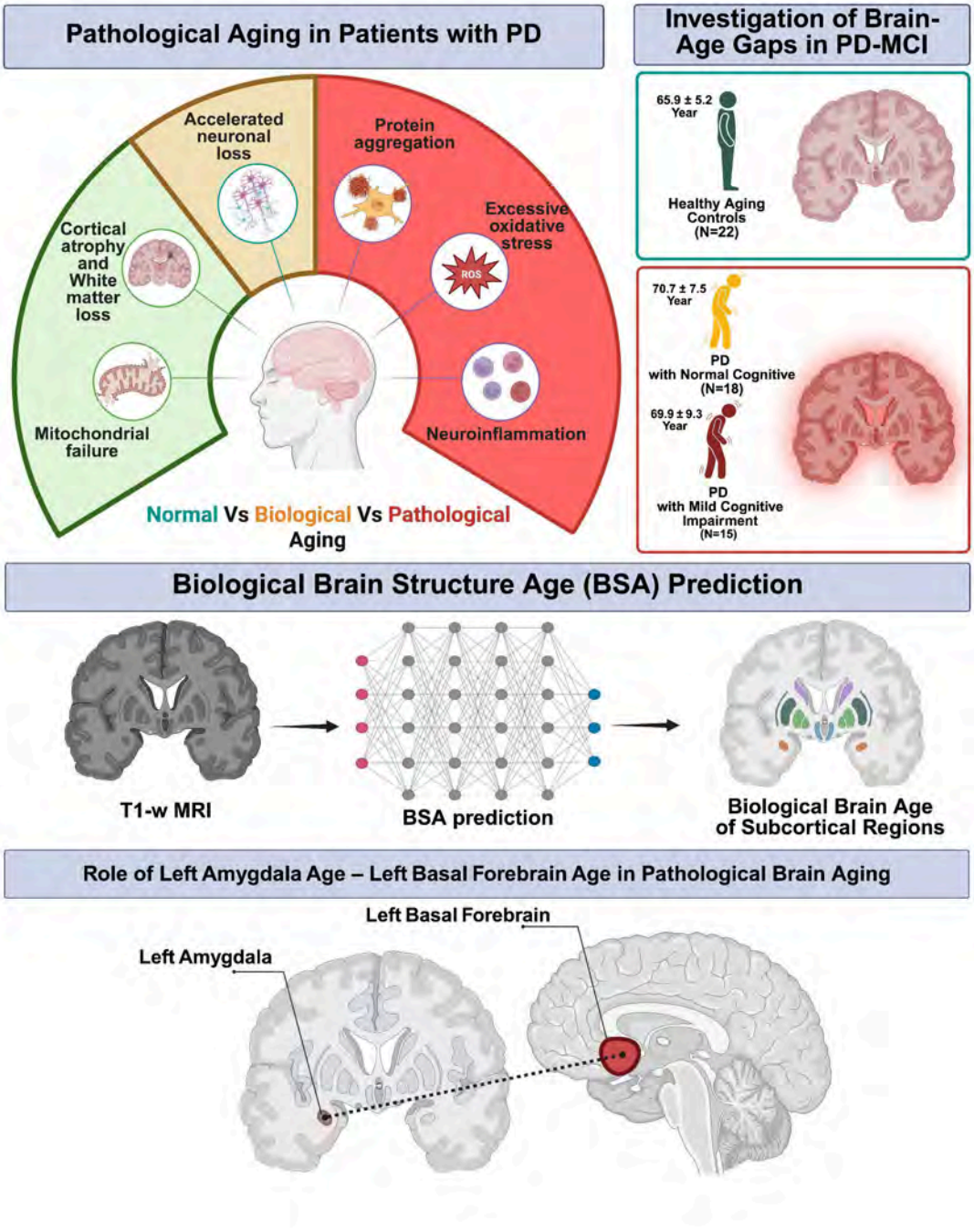

Skull Base Imaging: Skull Base Osteomyelitis, Pre-op Evaluation of Skull Base Tumors, Post-op Skull Base Imaging and Complications

10:25 - 11:25am Wednesday, 20th May, 2026

999 Segmental Visualization of Cadaveric Hypoglossal Nerve on High Resolution 3D Isotropic CISS MRI

Shruti Kumari MD, Mridhula Muthukumar MS, Ari Blitz MD
University Hospitals, Case Western Reserve University, Cleveland, Ohio, USA

Purpose

The hypoglossal nerve (CN XII) principally innervates the intrinsic and extrinsic tongue muscles (except the palatoglossus). CN XII in the tongue supplies lateral branches (CN XII-Lat) to the extrinsic tongue retractors (styloglossus and hyoglossus) and medial branches (CN XII-Med) to the extrinsic tongue protrusor genioglossus. Targeted Hypoglossal Nerve Stimulation (THS) therapy directed at CNXII-Med with tongue protrusion has recently been developed for obstructive sleep apnea (OSA) . We hypothesized that 0.5-0.6 mm CISS MRI in cadavers would enable visualization of CN XII and its branches in the sublingual space, atopic of potential relevance for surgical planning in this region.

Materials & Methods

54 embalmed cadavers were scanned with a 3T MRI scanner using 3-D isotropic 0.5-0.6 mm resolution CISS; a total of 108 CN XII were examined. Two readers (one radiology resident and one physician) independently evaluated visualization of CN XII anterior to the apparent origin from the medulla according to a qualitative scale ranging from 0 to 3, with 3 being the best. MRI was followed by dissection, allowing for anatomic-radiologic correlation.

Results

- Distal to the brainstem the cadaveric CN XII is well visualized on CISS MRI along the remainder of its entire course. Table 1. summarizes the segment-wise CISS MRI visibility scores (0–3 scale).
- There is no significant difference between the visibility of the left and right CN XII.
- Out of 54 cadavers, we confidently identified the distal branches (CN XII-Med and CN XII-Lat) in 34 right CN XII and 31 left CN XII showed excellent visualization of CN XII-Med as it branches from the main trunk of CN XII near the hyoglossus muscle to travel medially and supply the geinoglossus and the transverse/vertical muscle via its multiple branches.

Conclusion

- Sub-milimetric CISS sequence allows for visualization of all CN XII segments beyond the brainstem.
- Terminal branches of CN XII innervating the tongue protrusors (CN XII-Med) and retractor (CN XII-Lat) were visible within the tongue musculature. This to our knowledge is the first report of visualization of the lingual branches of CN XII within the tongue musculature.
- Translation of this imaging protocol to living subjects perhaps with motion compensation techniques and/or contrast administration may help us map out the innervation of the tongue prior to procedures including THS for OSA.

References

- Mu L, Sanders I. Human tongue neuroanatomy: Nerve supply and motor endplates. Clinical Anatomy2010;23:777–91.
- Wen J, Desai NS, Jeffery D, et al. High-Resolution Isotropic Three-Dimensional MR Imaging of the Extraforaminal Segments of the Cranial Nerves. Magn Reson Imaging Clin N Am 2018;26:101–19.

Images/Tables

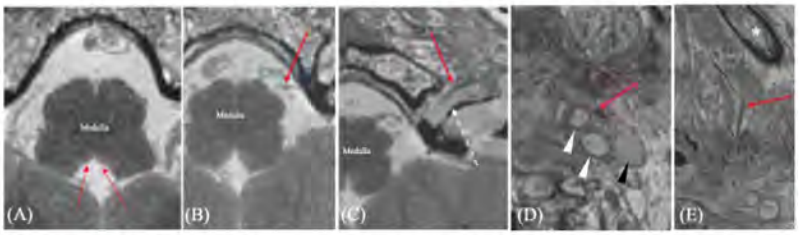

Fig. 1 : Axially reformatted CISS MRI of segments of CN XII (red arrow) (A) Hypoglossal trigone (dotted red arrow) (B) Cisternal segment (C) Foraminal segment (CN XII inside the hypoglossal canal) (D) Extra-foraminal-carotid space segment (E) Extra-foraminal-anterior segment; *: mandible; hypoglossal canal (white dashed arrow); left internal and external carotid arteries (white arrowheads); left internal jugular vein (black arrowhead)

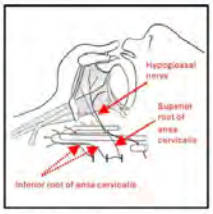

Fig. 2 : Schematic figure showing CN XII and corresponding anatomic dissection in a cadaver.

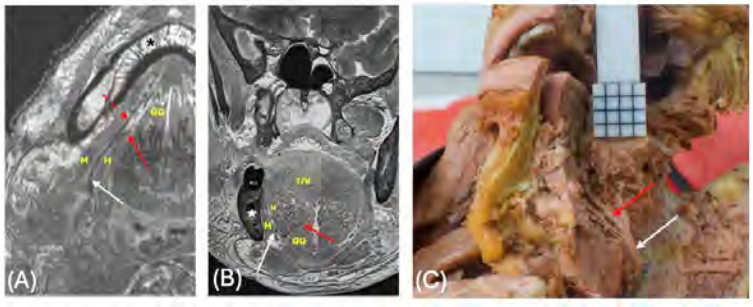

Fig. 3 (A) Axially reformatted CISS MRI of extracranial anterior segment of CN XII (white arrow) with its medial (solid red arrow) and lateral (dotted red arrow) lingual branches; M: Mylohyoid muscle; H: Hyoglossus muscle; GG: Geinoglossus muscle, *: Mandible; (B) Coronally reformatted CISS MRI showing m-CN XII, at the anterior edge of the Hyoglossus muscle: the m-XII turns medially and enters the GG at the boundary between its oblique (GGo) and horizontal (GGh) compartments, passes between these layers, ascends to the transverse and vertical (T/V) intrinsic muscles, and finally turns anteriorly to supply them. (C) Anatomic dissection of left CN XII (white arrow) in a cadaver in the anterior segment as it branches and supplies the tongue muscles; medial branch supplying the genioglossus (red arrow);

Average ± SD	Cisternal segment	Foraminal segment	Carotid space segment	Anterior segment
Combined Average ± SD	3.0 ± 0	3.0 ± 0	2.48 ± 0.15	2.64 ± 0.35
Average ± SD R. CN X	3.0 ± 0	3.0 ± 0	2.45 ± 0.08	2.5 ± 0.26
Average ± SD L. CN X	3.0 ± 0	3.0 ± 0	2.52 ± 0.23	2.61 ± 0.36

Table 1: Segmental scoring of CN XII on CISS MRI on a scale of 0-3 with 3 being the best.

Scientific Abstract Power Pitches & Luminary Speaker: Advanced Neuroimaging: AI and Biomarker Innovations

10:25 - 11:25am Wednesday, 20th May, 2026

232 Title: GRACIE: An AI Agent for Automated Generation of Customized Patient Summaries in Neuroradiology

David F Black MD, Carrie M Carr MD, Timothy J Kaufmann MD, Kara M Schwartz MD, Theodore Passe MD, Charlotte H Rydberg MD, John D Port MD, PhD, Ian T Mark MD, Steven A Messina MD, Daniel J Blezek PhD
Mayo Clinic, Rochester, MN, USA

Purpose

Neuroradiologists face increasing patient volumes and data complexity within fragmented electronic health records (EHRs), resulting in time-intensive chart review that can delay or compromise interpretation of advanced imaging.[1] We developed GRACIE (Generative Radiology AI for Clinical Information Extraction), an AI agent that automatically synthesizes comprehensive, neuroradiology-specific patient summaries overnight, ensuring summaries are ready for review at the time of patient encounter.[2]

Materials & Methods

Our Neuroradiology Advanced Imaging Lab developed an AI agent integrated directly into the EHR patient context via an intermediary program. The system employs a large language model with specialist-designed prompts and custom coding optimized for neuroradiology workflows including specific outputs for the following clinical scenarios: Primary Brain Tumors, Epilepsy, Spontaneous Intracranial Hypotension, Multiple Sclerosis, Pain Injections, Neuro Procedures, Dementia, Head and Neck, Neurofibromatosis type 2, Metastasis, and General Neuroradiology. Each output contains standard sections as well as data unique to the clinical context. Following institutional Software as a Medical Device (SaMD) committee approval, we conducted multi-faceted validation: (1) prospective review by 6 radiologists who each evaluated 25 AI-generated summaries against source EHR data; (2) independent retrospective review by 4 radiologists; (3) output consistency analysis using a separate LLM to assess agreement among 5 summaries generated for each of 100 patients; and (4) automated verification that all generated content was supported by cited source material (100 outputs). Inter-rater reliability was assessed using Gwet's AC2 statistic.

Results

Radiologist evaluation demonstrated high performance across all metrics: Useful (100%), Trustworthy (99%), Accurate (98%), and Satisfactory (96%). Inter-rater reliability was excellent (Usefulness: 0.98; Trust: 0.96; Satisfaction: 0.97; Accuracy: 0.95). Consistency analysis revealed mean agreement >85% across multiple summaries generated for identical patients. Radiologists reported time savings of 1-10 minutes per case with improved data accessibility. GRACIE has been successfully integrated into daily clinical practice, including two weekly tumor boards and one multidisciplinary epilepsy conference-with very favorable feedback from the presenting radiologists.

Conclusion

AI-generated patient summaries provide accurate, well-organized clinical information that enhances efficiency and supports high-quality neuroradiologic interpretation. Following successful single-site implementation, enterprise-wide deployment is planned pending resolution of scaling infrastructure requirements.

References

[1]**Lee C, Vogt KA, Kumar S.** Prospects for AI clinical summarization to reduce the burden of patient chart review. *Front Digit Health* 2024 Nov 6;6:1475092. doi:10.3389/fdgth.2024.1475092

[2]**Black DF, Carr CM, Kaufmann TJ, et al.** Initial experience with generative AI for clinical summarization in glioma MR interpretation. Presented at: 2025 WFNOS and SNO Annual Meeting; 2025.

Images/Tables

Summary of Care

Mr. Doe has a six-year history of debilitating orthostatic headaches due to SIH from recurrent CSF-venous fistulas. Despite numerous diagnostic studies identifying fistulas at various thoracic and lumbar levels, multiple interventions—including at least four separate transvenous embolizations and numerous multi-level, high-volume epidural blood patches—have failed to provide a durable solution. His clinical picture is complicated by a history of IIH and significant rebound CSF hypertension following procedures. Due to the failure of standard targeted treatments, his functional status remains poor, and he is being considered for more experimental therapies.

Current Plan

Given the failure of multiple targeted embolizations and the ongoing severe symptoms, the current plan is to proceed with another ultra-high-resolution dynamic photon-counting CT myelogram to search for any small, previously undetected fistulas. If no new target is identified, the discussion will move towards palliative strategies and a potential referral for experimental surgical dural repair techniques, acknowledging the high risks and uncertain outcomes.

Key Takeaways

- Chronic, severe, and treatment-refractory SIH with debilitating orthostatic headaches since 2018.
- Extensive history of multiple, recurrent CSF-venous fistulas identified on both the left and right sides of the thoracic and lumbar spine.
- Multiple failed interventions, including numerous multi-level blood patches and targeted transvenous embolizations.
- Significant history of rebound intracranial hypertension post-procedure, complicating management.
- Severely impaired functional status, requiring near-constant recumbency.
- Imaging demonstrates classic signs of SIH and post-procedural changes.

Surgery

DATE	SURGERY TYPE	SURGICAL SITE	HOSPITAL/SURGEON	DETAILS/EXTENT OF RESECTION
11/15/2023	Transvenous Embolization	Right T10 paraspinal vein	Mayo Clinic / Dr. Smith	Onyx embolization of confirmed fistula.
05/10/2023	Transvenous Embolization	Left L1 paraspinal vein	Mayo Clinic / Dr. Smith	Onyx embolization of confirmed fistula.
08/20/2022	Transvenous Embolization	Left T7 and T9 paraspinal veins	Mayo Clinic / Dr. Jones (CE)	Onyx embolization of two fistulas identified on DSM.
02/05/2021	Transvenous Embolization	Right T11 paraspinal vein	Mayo Clinic / Dr. Jones (CE)	Initial Onyx embolization. Complicated by severe RIH.

Myelography

DATE	TYPE	FINDINGS	LEAK LOCATION
03/02/2024	Digital Subtraction Myelogram	Negative study. Extensive post-embolization artifact noted at multiple levels. No new fistula identified.	NA
11/01/2023	Digital Subtraction Myelogram	Subtle but conclusive evidence of a CSF-venous fistula at the right T10 nerve root.	Right T10
04/18/2023	CT Myelogram (Photon Counting)	Confirmed active CSF-venous fistula at the left L1 level.	Left L1
07/25/2022	Digital Subtraction Myelogram	Identification of two separate CSF-venous fistulas at left T7 and left T9.	Left T7, Left T9
01/15/2021	Digital Subtraction Myelogram	Clear evidence of a high-flow CSF-venous fistula at the right T11 level.	Right T11
09/10/2020	CT Myelogram	Equivocal for a leak; suggestive subtle pooling near the right thoracic nerve roots, but no definitive fistula seen.	Indeterminate

Blood Patches

DATE	PROCEDURE	EFFECT
06/15/2024	Multi-level CT-guided EBP (T7-8, L1-2)	Minimal (1-2 days) improvement in headache intensity.
09/05/2023	Multi-level CT-guided EBP (T9-10, L2-3)	No appreciable benefit.
12/12/2022	CT-guided EBP (L4-5)	Performed for post-dural puncture headache; effective for that indication only.
04/01/2022	High-volume EBP (40 mL, Thoracic)	Less than one week of partial relief.
06/10/2020	Multi-level CT-guided EBP (C7-T1, T10-11)	Induced severe rebound intracranial hypertension lasting 5 days.

Imaging Summary

MRI

DATE	MODALITY/BODY PART	SUMMARY	BERN SCORE
03/01/2024	MR Brain w/wo Contrast	Persistent diffuse pachymeningeal enhancement and mild brainstem sagging, consistent with ongoing SIH. Stable compared to prior.	3 out of 9
04/17/2023	MR Spine (Cervical, Thoracic, Lumbar)	No extradural fluid collections. Extensive Tarlov cysts throughout the sacrum without evidence of nerve root compression.	NA
01/14/2021	MR Brain w/wo Contrast	Prominent dural enhancement, venous distention, and notable sagging of the cerebellar tonsils and brainstem.	6 out of 9

547 Precision Lesion Burden Mapping in Familial CCMs - Self-supervised and Morphology-aware Deep Learning

Jenny Lee[1], Marc Mabray[2], Joshua Fortriede[3], Jeffrey Nelson[4], Helen Kim[5], Janine M Lupo[6]

[1]University of California San Francisco, San Francisco, CA, USA. [2]Department of Radiology, University of New Mexico,, Alburquerque, NM, USA. [3]Information Services for Research, Cincinnati, Ohio, USA. [4]Department of Anesthesia and Perioperative Care, University of California, San Francisco, San Francisco, CA, USA. [5]Department of Anesthesia and Perioperative Care, University of California, San Francisco, CA, USA. [6]Department of Radiology and Biomedical Imaging, University of California, San Francisco, CA, USA

Purpose

Cerebral cavernous malformations (CCMs) are vascular malformations of the central nervous system characterized by dilated, thin-walled capillary cavities. Quantitative imaging markers derived from MRI, particularly lesion count and volume, reflect total disease burden that is predictive of future hemorrhagic events. Reliable identification and quantification of all lesions are therefore crucial for precision diagnostics, individualized risk assessment, and evaluation of emerging treatments, but remains a challenge due to the number of lesions and variability of their size, shape, and manual delineation. This study aims to leverage a novel, 2-staged deep learning approach that incorporates self-supervised pretraining and shape-aware loss functions to create an accurate tool for automatic quantification of CCM lesion burden.

Materials & Methods

Data curation and preprocessing: The primary dataset is from Brain Vascular Malformations Consortium (BVMC) CCM project, including 178 participants from six institutions who underwent susceptibility-weighted imaging (SWI). Reference annotations were created via a semi-automated annotation protocol and adjusted by a neuroradiologist. To build a model robust to real world clinical variability, we assembled a large, unlabeled pre-training cohort by retrospectively querying our institution's electronic health records archive, comprised of 3,523 unique SWIs from 1,884 patients. Deep learning model training and evaluation: Our 2-staged approach leveraged nnU-Net's 3D full-resolution architecture to first perform self-supervised pre-training on a large unlabeled dataset before fine-tuning the model using the expert-annotated dataset (Figure 1A). The goal of the pretraining stage was to guide the model to learn a generalizable representation of 3D SWI neuroanatomy. A Model Genesis framework was employed to train the model to restore original images from corrupted versions using MSE reconstruction loss. The segmentation network's weights were then initialized from the best pretraining checkpoint. A sphericity regularization loss was implemented to boost sensitivity for the smaller, low-contrast, compact lesions that were difficult to detect without additional false-positives by penalizing predictions that were not spherical. a morphological property not captured by standard volumetric Dice or cross-entropy loss functions.

Results

Figure 1B demonstrates the efficacy of self-supervised pretraining via UMAP, where our pretrained model naturally clustered patches by disease severity, a structure not present in the default nnUNet's feature space. For the primary segmentation task, our method showed a 4.0% increase in sensitivity for small lesions (10-50mm^3, p=0.013) compared to the default nnUNet (Figure1C,D). Although this was accompanied by a 5.4% decrease in precision (p=0.002), the majority of resulting false positives visually appear as true lesions, highlighting the benefit of our model over human delineation. Our model achieved reduced boundary error for small lesions(Average surface distance: 0.44mm vs. 0.47mm, p=0.09) without negatively impacting the segmentation of large lesions (>50mm^3), with Dice (0.77) and IoU (0.65) scores remaining statistically identical to the baseline.

Conclusion

We developed a 2-stage deep learning pipeline for precise detection and segmentation of CCM lesions. Self-supervised pretraining on nearly 4000 unlabeled scans built a highly robust feature foundation. A novel, shape-aware loss improved detection of small lesions with higher sensitivity. This tool provides a fully automated, precise, and sensitive metric for tracking lesion burden, essential for patient monitoring and therapeutic trials.

References

Scerrati A, Mantovani G, Travaglini F, Bradaschia L, De Bonis P, Farneti M, et al. Bleeding risk evaluation in cerebral cavernous malformation, the role of medications, and hemorrhagic factors: a case-control study. Neurosurgical Focus. 2023;55(4):E15

Shenkar R, Shi C, Rebeiz T, Stockton RA, McDonald DA, Mikati AG, et al. Exceptional aggressiveness of cerebral cavernous malformation disease associated with PDCD10 mutations. Genetics in medicine. 2015;17(3):188-96.

Zhou Z, Sodha V, Pang J, Gotway MB, Liang J. Models genesis. Medical image analysis. 2021;67:101840.

Isensee F, Jaeger PF, Kohl SA, Petersen J, Maier-Hein KH. nnU-Net: a self-configuring method for deep learning-based biomedical image segmentation. Nature methods. 2021;18(2):203-11

Images/Tables

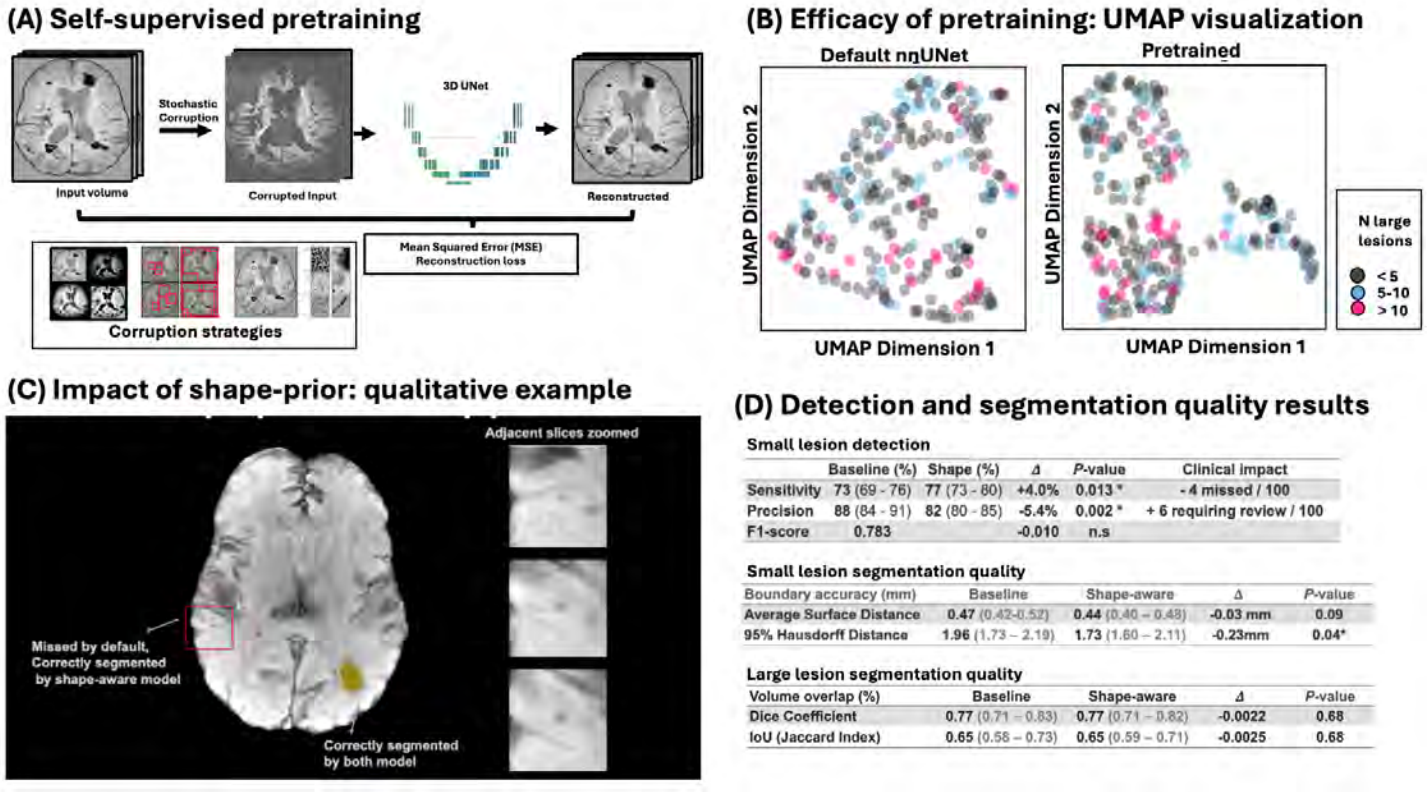

	Baseline (%)	Shape (%)	Δ	*P*-value	Clinical impact
Sensitivity	73 (69 - 76)	77 (73 - 80)	+4.0%	0.013 *	- 4 missed / 100
Precision	88 (84 - 91)	82 (80 - 85)	-5.4%	0.002 *	+ 6 requiring review / 100
F1-score	0.783		-0.010	n.s	

Boundary accuracy (mm)	Baseline	Shape-aware	Δ	*P*-value
Average Surface Distance	0.47 (0.42-0.52)	0.44 (0.40 – 0.48)	-0.03 mm	0.09
95% Hausdorff Distance	1.96 (1.73 – 2.19)	1.73 (1.60 – 2.11)	-0.23mm	0.04*

Volume overlap (%)	Baseline	Shape-aware	Δ	*P*-value
Dice Coefficient	0.77 (0.71 – 0.83)	0.77 (0.71 – 0.82)	-0.0022	0.68
IoU (Jaccard Index)	0.65 (0.58 – 0.73)	0.65 (0.59 – 0.71)	-0.0025	0.68

766 Radiomics Based Characterization of Secondary Structures Involved in TBI-related Intracranial Hemorrhage Detection

Anusha Kanagala M.S, Stephanie M Aguilera B.S, Jonah Barrett B.A, Lora D Bozeman B.S, John Eddins B.S, Sabrina Goddard M.D, Sandeep Bodduluri Ph.D, Manoj Tanwar M.D
University of Alabama at Birmingham, Birmingham, Alabama, USA

Purpose

Traumatic brain injury (TBI) remains a major cause of morbidity and mortality worldwide, making timely diagnosis critical for improving outcomes. Timely and accurate diagnoses of TBI rely on the rate and efficiency of CT scan interpretation, which in turn depend heavily on radiologist expertise, and are often limited by inter-observer variability and workforce shortages. This study aimed to develop and validate a comprehensive radiomics-based machine learning model for hemorrhage detection and to characterize secondary brain structures affected by TBI-related intracranial hemorrhages as surrogate structures for complete observation.

Materials & Methods

In this retrospective study approved by IRB, we analyzed head CT scans from 1,592 patients (1,092 with confirmed TBI and 500 controls) collected from a level 1 trauma center and the UAB clinical imaging database. The overall cohort had a mean age of 45.2 ± 18.7 years (range, 18–98 years). The TBI group consisted of 715 males (65.6%), 374 females (34.0%), and 3 individuals with unknown sex (0.4%), while the control group (n = 500) included 160 males (32.0%) and 340 females (68.0%). Seventeen anatomical structures were segmented for each patient: brain, brainstem, caudate nucleus, central sulcus, cerebellum, frontal lobe, insular cortex, internal capsule, lentiform nucleus, occipital lobe, parietal lobe, septum pellucidum, subarachnoid space, temporal lobe, thalamus, venous sinuses, and ventricles using open-source TotalSegmentator package. A comprehensive set of radiomics features was extracted from each segmented region, including first-order density statistics and texture features derived from gray-level matrices using PyRadiomics library. LightGBM (Gradient Boosting Machine) was utilized as the classification model. The patients were divided into 70:30 (n = 1114, n=478) train-test split, and the model performance was evaluated using area under the receiver operating characteristic curve (AUC) and precision-recall curve (PR-AUC).

Results

The radiomics based machine learning model achieved an AUC of 0.97 (95% CI: 0.94-0.97), NPV of 0.86 and PPV of 0.95 for TBI related hemorrhage detection. Key discriminative radiomics analysis of secondary structures included texture changes in the subarachnoid space (gray level non-uniformity normalized) and the central sulcus (gray level variance), density changes in venous sinuses (total energy), and the caudate nucleus (kurtosis). Lobar-level findings included density changes in the occipital lobe and texture changes in the temporal lobe (gray level variance). On a more global scale, texture changes were noticeable in the brain (cluster shade). As a result, these textural and intensity-based heterogeneity in secondary structures demonstrates the composite effects of TBI-related injuries on the brain parenchyma.

Conclusion

This study demonstrates that a radiomics-based machine learning model using multi-regional brain segmentation can not only accurately detect TBI on head CT but also demonstrates the damaging effects on adjacent brain and extra-cranial structures. Radiomic features, especially from the subarachnoid space and venous sinuses, emerged as potential biomarkers reflecting TBI-related pathophysiological changes. The model shows promise as a clinical decision support tool to augment radiologist interpretation, potentially improving diagnostic accuracy and efficiency in emergency settings.

References

Chilamkurthy S, Ghosh R, Tanamala S, Biviji M, Campeau NG, Venugopal VK, Mahajan V, Rao P, Warier P. Deep learning algorithms for detection of critical findings in head CT scans: a retrospective study. Lancet. 2018 Dec 1;392(10162):2388-2396. doi: 10.1016/S0140-6736(18)31645-3. Epub 2018 Oct 11. PMID: 30318264.

Images/Tables

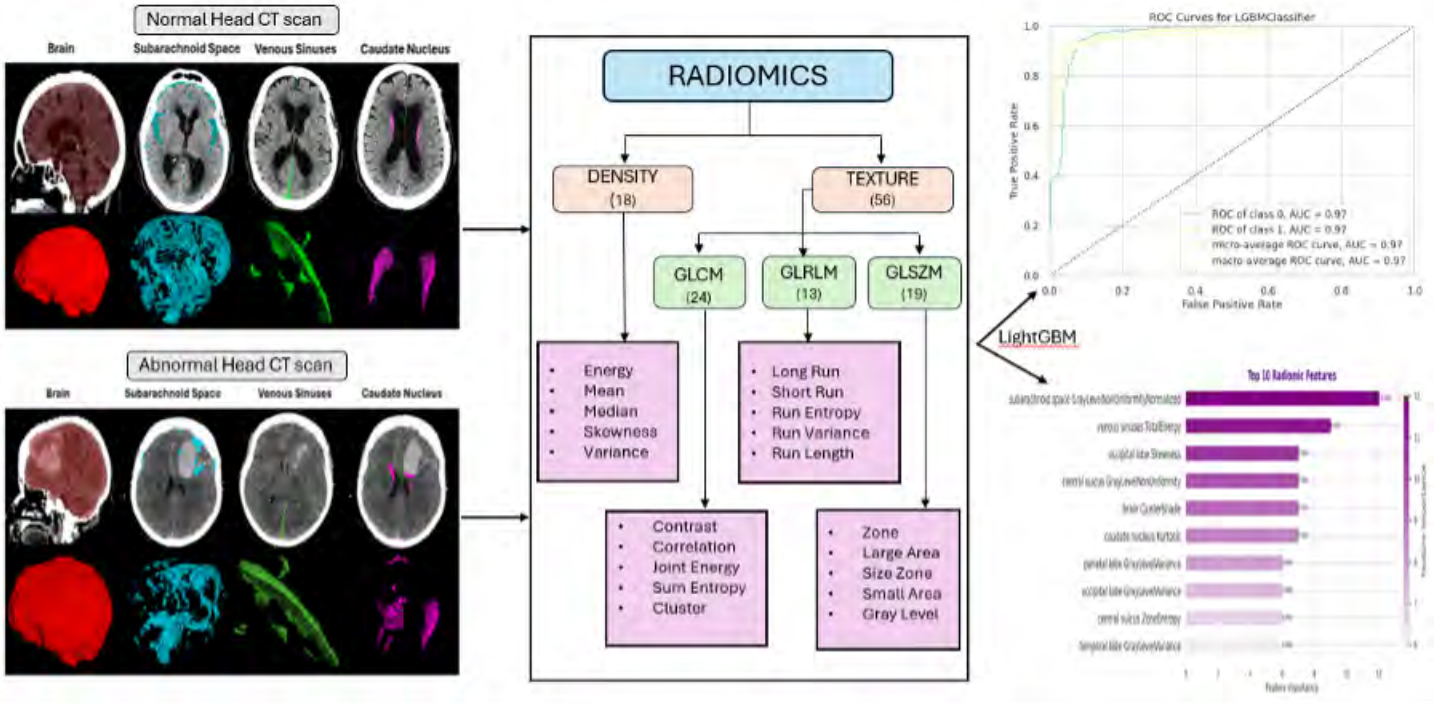

---

815 Population-Scale Artificial Intelligence Enables Highly Accurate Brain-Age Prediction from Routine CT

Yongkai Liu PhD[1], Bin Jiang MD[1], Donghoon Kim PhD[1], David Liebeskind MD[2], Max Wintermark MD[3], Michael Mosley PhD[1], Greg Zaharchuk MD, PhD[1]
[1]Stanford University, Stanford, California, USA. [2]University of Southern California, Stanford, California, USA. [3]University of Texas MD Anderson, Houston, Texas, USA

Purpose

Non-contrast head CT (NCCT) is the most widely performed clinical neuroimaging study, yet it remains underutilized for quantitative assessment of brain aging. This study aimed to develop and validate a population-scale artificial intelligence (AI) model, trained on **over 300,000 NCCT volumes**, to predict brain age, quantify prediction error relative to chronological age, and evaluate the brain-age gap (BAG) as an imaging biomarker.

Materials & Methods

Data Acquisition and Preprocessing: After obtaining IRB approval, we identified more than 300,000 NCCT volumes from Stanford University Hospital (310,303 for training, 3,112 for validation, and 3,330 for internal testing). External evaluation included **72,949 separate NCCT studies from external sites** including other academic centers, community or integrated health systems, and private/specialty imaging centers. Soft tissue kernel NCCT studies were de-identified, standardized to RAS orientation with 1 × 1 × 3 mm^3 voxel spacing using trilinear interpolation, then padded and center-cropped to 224 × 224 × 64 voxels. Each study was then window/leveled using soft-tissue, subdural, and bone settings, which were concatenated to form a three-channel 3D volume for model input.

Model: A vision transformer with a patch size of 16 × 16 × 8, 12 layers, 12 attention heads, a hidden size of 768, and three input channels was first pretrained in a self-supervised manner using a masked autoencoder to learn representations from unlabeled CT data. Following this, fine-tuning of the pre-trained vision transformer was performed by regression on chronological age.

Evaluation: The primary performance metric was the mean absolute error (MAE, in years) between predicted and chronological age. To account for age-related bias, the BAG was bias-corrected using a linear regression between predicted and chronological age. The corrected BAG was then analyzed in relation to the severity of cerebral atrophy as determined from clinical reports for the internal test set.

Results

On the internal test set (n = 3,330), the model achieved a **MAE of 3.20 years** (95% CI, 3.10–3.31). On the external test set (n = 72,949), the MAE was 3.92 years (95% CI, 3.86–3.98), substantially outperforming prior CT-based brain-age models, which typically report errors exceeding 10 years (1–3). Among scans without focal pathology (i.e., no lesions or infarcts), the MAE was 3.14 years (95% CI, 2.98–3.31), while for scans with focal pathology, it was 3.25 years (95% CI, 3.07–3.44).

In addition, among scans without focal pathology, when stratified by global atrophy severity, the average **BAG was +2.1 years for severe atrophy** (n = 28), +0.8 years for moderate atrophy (n = 63), and 0 years for mild or no atrophy (n = 834).

Conclusion

A population-scale AI model accurately predicts brain age from non-contrast CT (average error ≈3.2 years), for the **first time achieving MRI-comparable** performance and demonstrating robust generalization across diverse institutions. The brain–age gap increased with atrophy severity, highlighting its potential as a scalable biomarker of accelerated or atypical brain aging.

References

1. Cole JH, Franke K. Predicting age using neuroimaging: innovative brain ageing biomarkers. Trends in neurosciences. Elsevier; 2017;40(12):681–690.

2. Jónsson BA, Bjornsdottir G, Thorgeirsson TE, et al. Brain age prediction using deep learning uncovers associated sequence variants. Nature communications. Nature Publishing Group UK London; 2019;10(1):5409.
3. Levakov G, Rosenthal G, Shelef I, Raviv TR, Avidan G. From a deep learning model back to the brain—Identifying regional predictors and their relation to aging. Human brain mapping. Wiley Online Library; 2020;41(12):3235–3252.

Images/Tables

Dataset Summary

	CT Volumes	Source Institutions
Train	310303	Stanford Medicine
Validate	3112	Stanford Medicine
Test	3330	Stanford Medicine
External	72949	*Multiple (Comprehensive, Community, and Private Hospitals)*

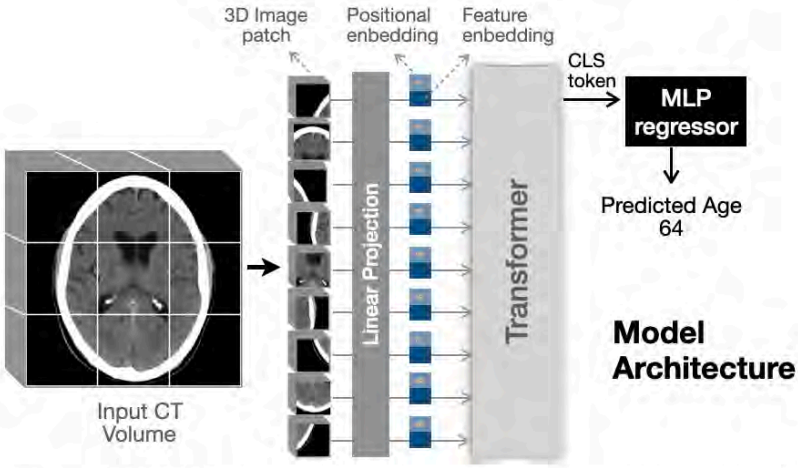

EVALUATION

Performance on Test Sets

Test sets	Mean absolute error
Internal Test	**3.2 years**
External Test	**3.9 years**
Most Prior Studies	> 10 years

Lower mean absolute error indicates better age prediction accuracy

Predicted vs. Chronological Age

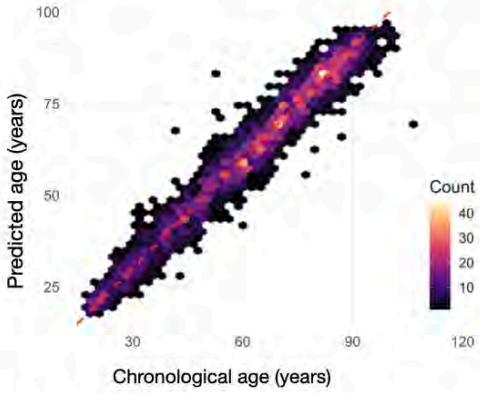

Hex-bin plot showing correlation between predicted and chronological age (internal test set)

Brain Age Gap (BAG) vs. Atrophy Severity

Brain age gap increases with atrophy severity (internal test set)

1010 Cerebrovascular Collateral Circulation Predicts Treatment Outcomes in Patients with Medium and Distal Vessel Occlusion

Aditi Deshpande PhD[1], Aysha Jadran MD[2], Pouya Tashili Fahadan MD, MBA, FAHA[2], Krzysztof Bochenek MD[3], Patrick Oliverio MD[3], Noushin Yahyavi MD, MBA[4], Kaveh Laksari PhD[5]
[1]University of California, Riverside, CA, USA. [2]Inova Fairfax, Fairfax, VA, USA. [3]Fairfax Radiology, Fairfax, VA, USA. [4]Univesity of Maryland, Baltimore, MD, USA. [5]Univesity of California, Riverside, CA, USA

Purpose

Medium and distal vessel occlusions (MeVO/DiVO) account for 25–40% of acute ischemic strokes (AIS). The benefits of endovascular thrombectomy (EVT) in MeVO/DiVO patients remain uncertain. Cerebrovascular collateral circulation status plays a critical role in mediating treatment response. We hypothesized that quantitative analysis of collateral circulation and vascular morphology may refine EVT candidacy and inform individualized treatment decisions for MeVO/DiVO patients.

Materials & Methods

This retrospective study analyzed prospectively collected data from MeVO/DiVO patients who underwent EVT at our comprehensive stroke center between 2019 and 2024. MeVO was defined as occlusion at the M2/3 segment of the middle cerebral artery (MCA), A2 segment of the anterior cerebral artery (ACA), and P1 segment of the posterior cerebral artery. DiVO was defined as occlusions distal to the M2/3 segments. Collateral circulation and vascular morphometry was quantified using our validated and fully automated machine-learning algorithm applied to presentation computed tomography angiography (CTA).

Results

Patients with medium and distal vessel occlusions were included in the analysis. Favorable outcomes, defined as discharge to home, were significantly associated with younger age (mean 66 vs. 74 years; $p < 0.0001$), lower admission NIHSS (mean 11 vs. 16; $p < 0.0001$), successful recanalization (TICI ≥2B; $p = 0.0038$), higher total length of vascular tree ($p = 0.033$) and higher qCI ($p = 0.056$) compared to those discharged to rehabilitation, nursing care, hospice, or deceased. No statistically significant differences were observed between groups in terms of sex, race, core infarct volume, penumbra volume, time from symptom onset to recanalization and ASPECTS. Multivariate logistic regression analysis identified

younger age (OR = 1.03; 95% CI: 1.009–1.066; p = 0.0092), lower NIHSS at admission (OR = 1.08; 95% CI: 1.027–1.138; p = 0.0029), and successful recanalization (TICI ≥2B) (OR = 0.154; 95% CI: 0.042–0.569; p = 0.0050) as independent predictors of favorable discharge disposition.

Conclusion

Among MeVO/DiVO patients, favorable discharge outcomes following EVT were associated with younger age, lower NIHSS on presentation, successful recanalization, higher collateralization as estimated by qCI and higher total length of the vessel network. These findings suggest that application of clinical and imaging-based factors, including collateral circulation and quantitative features of cerebrovascular morphology can improve the prediction of MeVO/DiVO outcomes after EVT.

References

Deshpande A, Elliott J, Kari N, Jiang B, Michel P, Toosizadeh N, Fahadan PT, Kidwell C, Wintermark M, Laksari K. Novel imaging markers for altered cerebrovascular morphology in aging, stroke, and Alzheimer's disease. *J Neuroimaging* 2022;32:956–967. doi:10.1111/jon.13023

1018 Cerebrovascular Morphology as a Predictor of Early Neurological Deterioration After Thrombectomy Introduction

Aditi Deshpande PhD[1], Aysha Jadran MD[2], Pouya Tahsili Fahadan MD, MBA, FAHA[2], Krzysztof Bochenek MD[3], Patrick Oliverio MD[3], Noushin Yahyavi MD, MBA[4], Kaveh Laksari PhD[1]

[1]University of California, Riverside, CA, USA. [2]Inova Fairfax, Fairfax, VA, USA. [3]Fairfax Radiology, Fairfax, VA, USA. [4]University of Maryland, Baltimore, MD, USA

Purpose

Early neurological deterioration (END) affects 10–30% of patients with acute ischemic stroke (AIS) despite successful recanalization. END impacts mortality and long-term outcomes after AIS. We hypothesize that collateral cerebrovascular circulation impacts END occurrence and functional outcomes following endovascular thrombectomy (EVT).

Materials & Methods

We performed a retrospective analysis of prospectively collected data of AIS patients that underwent EVT from 2019 to 2024 at our comprehensive stroke center. END was defined as a ≥4 points increase in the total National Institutes of Health Stroke Scale (NIHSS) score within 24 hours after the initial stroke. Collateral circulation was quantified using our validated and fully automated machine-learning algorithm applied to presentation computed tomography angiography (CTA).

Results

Among patients who experienced END, admission NIHSS scores were significantly lower compared to those without END (mean NIHSS 10 vs. 16; p < 0.0001). No statistically significant differences were observed between groups in terms of age, race, sex, core infarct volume, penumbra volume, time from symptom onset to recanalization, ASPECTS, successful recanalization (TICI ≥2B). Quantitative collateral index was significantly higher in the group without END as compared to patients with END (p = 0.021). Multivariate logistic regression analysis identified lower NIHSS at admission (OR = 1.114; 95% CI: 1.019–1.218; p = 0.0174) and lower collateralization or qCI (OR = 1.27; 95% CI: 0.99-1.62; p = 0.05) as an independent predictor of END.

Conclusion

Among AIS patients undergoing EVT, lower NIHSS scores at admission and an underdeveloped collateral network on the quantitative collateral assessment were independently associated with the occurrence of early neurological deterioration. These findings suggest that clinical characteristics and collateral circulation, may play a greater role in predicting END, and further studies are needed to refine risk stratification in this population.

References

Deshpande A, Elliott J, Kari N, Jiang B, Michel P, Toosizadeh N, Fahadan PT, Kidwell C, Wintermark M, Laksari K. Novel imaging markers for altered cerebrovascular morphology in aging, stroke, and Alzheimer's disease. *J Neuroimaging* 2022;32:956–967. doi:10.1111/jon.13023

---

246 Cerebral Aneurysm Detection via an Agentic AI Committee

Jax Luo PhD, Satyam Ghodasara MD, Chintan Shah MD, Scott Raymond MD/PhD

Cleveland Clinic, Cleveland, OH, USA

Purpose

Accurate detection of cerebral aneurysms on Time-of-Flight Magnetic Resonance Angiography (TOF-MRA) is critical for early treatment and rupture prevention. Conventional deep learning (DL) models, such as U-Net–based architectures, depend on large, well-annotated datasets and consistent imaging protocols, but suffer from limited generalizability and potential model drift.

When will general-purpose multimodal language models (MLMs) advance far enough to outperform tailor-made DL models for aneurysm detection? This study introduces a training-free, agentic AI paradigm that leverages a committee of popular MLMs to detect aneurysms on TOF-MRA. We test whether such an agentic reasoning approach can achieve clinically competitive performance on standard benchmarks compared with traditionally trained DL models.

Materials & Methods

In this exploratory study, 3D TOF-MRA volumes from the ADAM dataset (93 subjects) were first pre-processed with decomposition into 2D 512×512 axial slices and intensity normalization. High-signal range (0.65–0.95) pixels were clustered using DBSCAN to generate candidate bounding boxes representing potential aneurysms (Step 1). The resulting coordinates were converted into continuous physical space to enable precise localization. Next, three AI agents forming an agentic committee were instantiated from different MLMs and prompted with a structured template outlining aneurysm morphology, size, signal intensity, and common vascular sites (Step 2). Each agent independently analyzed which bounding boxes corresponded to true aneurysms and provided reasoning for its decisions (Step 3). Through a majority-voting process (Step 4), the agents reviewed one another's rationales and refined their predictions; a candidate aneurysm was accepted if at least two agents reached consensus. Finally, overlapping detections across consecutive slices were aggregated into 3D bounding boxes to obtain volumetric predictions (Step 5). Aneurysm-level sensitivity and false positive count (FPC) were calculated as performance metrics in both the 2D and 3D settings.

Results
In the 2D slice-based evaluation, individual agents achieved sensitivities of 0.42 (GPT-5 and Gemini-2) and 0.54 (Claude-3.5). Incorporation of the majority-voting ensemble substantially improved performance, attaining a sensitivity of 0.62 with an FPC of 0.38, outperforming all single-agent baselines. When extended to the 3D volumetric setting, sensitivity marginally declined to 0.58 with an FPC of 0.33. Nevertheless, despite the complete absence of task-specific training, the proposed agentic, reasoning-based approach demonstrated performance comparable to the ADAM Challenge benchmark winner (sensitivity = 0.66, FPC = 0.14).
Conclusion
Current multimodal language models working as an agentic AI committee, when guided by structured clinical knowledge, can achieve performance approaching domain-specific deep learning models through reasoning alone. The simplicity, interpretability, and training-free design of this approach make it highly amenable to clinical and research deployment. With further refinement, such as enhanced prompting strategies and optimized anatomical priors, the agentic AI committee holds promise as a flexible and augmentative paradigm capable of automated image analysis.
References
1 Kimberley M. Timmins, Irene C. van der Schaaf, Edwin Bennink, et.al “Comparing methods of detecting and segmenting unruptured intracranial aneurysms on TOF-MRAS: The ADAM challenge," Neuroimage (2021)
Images/Tables

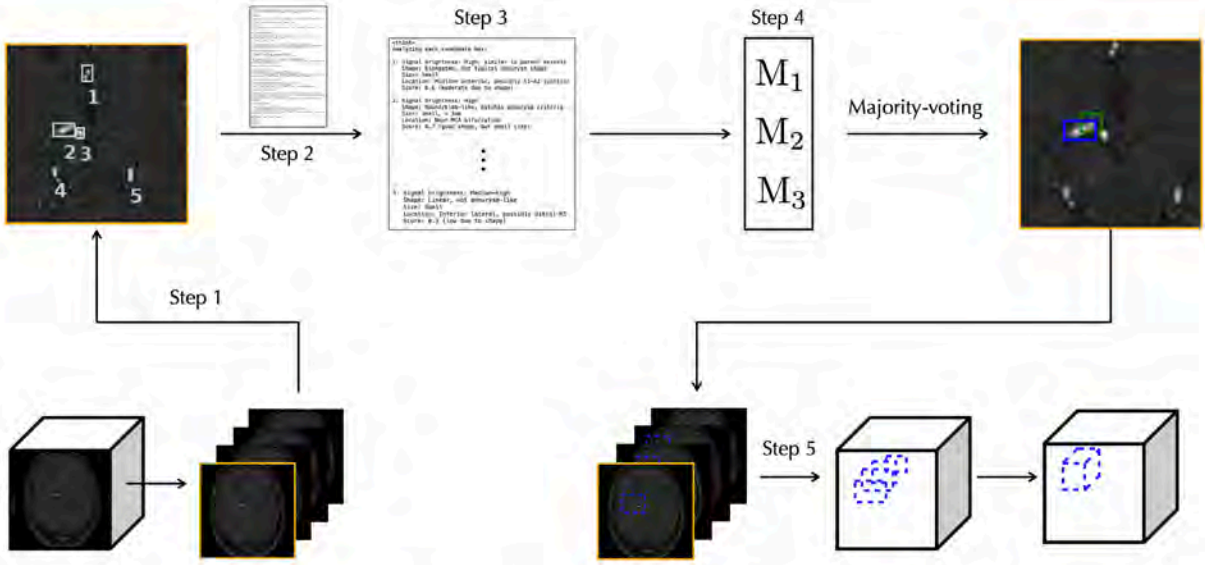

Figure 1: Overview of the Aneurysm Detection by Agentic AI framework. M_1, M_2, and M_3 represent the three AI Agents.

---

920 Value of Cine and 3D Ultrasound Data in the Diagnostic Performance of Deep Learning Models for Thyroid Nodule Classification: A Systematic Review and Meta-analysis
Marcus Jun Rui Lee MBBS[1], Zayin Tan MBBS[1], Ling Ling Chan MBBS, FRCR, FAMS[2]
[1]Yong Loo Lin School of Medicine, National University of Singapore, Singapore, Singapore, Singapore. [2]Singapore General Hospital, Singapore, Singapore, Singapore
Purpose
High-resolution ultrasound (US) is the primary imaging modality for triaging thyroid nodules with suspicious features for further investigation.[1] However, feature interpretation is highly operator-dependent and may lead to unnecessary fine-needle aspiration (FNA) biopsies.[2] Recent video-based deep learning (DL) models that capture spatiotemporal features have been proposed to more closely replicate radiologists’ diagnostic reasoning process than conventional models using static image input.[3,4] However, their diagnostic value for thyroid nodule analysis in US remains unclear. This is the first systematic review and meta-analysis that evaluates the diagnostic performance of DL models using exclusively video-based US data for thyroid nodule classification.
Materials & Methods
A systematic search of PubMed, Cochrane Library, Embase and Scopus was conducted to identify appropriate studies. Our inclusion criteria were: use of 1) video-based US data as input, 2) a diagnostic AI model for thyroid nodule analysis, and 3) surgical histopathology or Bethesda-classified FNA cytology as the reference standard. The primary outcome was Area Under the Receiver Operating Characteristic curve (AUROC). Secondary outcomes included sensitivity, specificity, positive predictive value and negative predictive value. Subgroup analyses evaluated the effects of training dataset size, model dimensionality, and model architecture on classification accuracy. Model inference speed was noted where available. Study bias and quality were assessed using RSNA’s 9 key considerations for evaluating AI research.[5]
Results
Of 233 screened studies, eight were eligible for analysis (Fig. 1). The pooled AUROC across test sets was 0.896 (95% CI, 0.854–0.937; n=8), exceeding that of radiologists (0.820 [95% CI, 0.770–0.870; n=4]) and conventional-input models (0.810 [95% CI, 0.636–0.984; n=3]). Pooled sensitivity and specificity were 0.834 (95% CI, 0.751–0.918) and 0.850 (95% CI, 0.798–0.901), respectively. The mean training dataset size was 867 ± 526 nodules (range: 192–1882) and showed no significant association with AUROC (R^2 = 0.057, p = 0.571). Model dimensionality also did not influence classification performance (p = 0.90), with 3D CNNs (AUROC = 0.898) performing comparably to 2D CNNs with temporal layers (AUROC = 0.892). When internal and external comparators were included, 2D CNNs achieved significantly higher AUROCs than both hybrid and 3D

architectures ($p < 0.01$). Funnel plot analyses (Egger's $t = -0.91$, $p = 0.40$; Begg's $z = -0.99$, $p = 0.32$) showed no evidence of publication bias. Of the eight studies, computational speed was reported in three. Only two studies reported external testing, and four fulfilled at least five of the nine RSNA AI evaluation criteria.

Conclusion

DL models using spatiotemporal US data outperformed radiologists and static 2D models in thyroid nodule classification. Increased model complexity and larger training datasets did not significantly enhance performance. More standardized, prospectively validated studies with multicenter external validation and attention to explainability, fairness and generalizability are required. Future work should also justify dataset adequacy, promote open-source publication of models for accessibility, and report model processing speed for clinical feasibility.

Clinical Relevance Statement

Video-based DL models are increasingly accurate in thyroid nodule diagnosis, showing promise in supporting US interpretation and reducing unnecessary biopsies. Clinicians should understand these tools to effectively integrate them into practice.

References

1. Brander A, Viikinkoski P, Nickels J, Kivisaari L. Thyroid gland: US screening in a random adult population. *Radiology* 1991;181:683-87. DOI: https://doi.org/10.1148/radiology.181.3.1947082
2. Hoang JK, Middleton WD, Farjat AE, et al. Interobserver variability of sonographic features used in the American College of Radiology Thyroid Imaging Reporting and Data System. *AJR Am J Roentgenol* 2018;211:162-67. DOI: https://doi.org/10.2214/AJR.17.19192
3. Fadaei AH, Dehaqani MRA. Going beyond still images to improve input variance resilience in multi-stream vision understanding models. *Sci Rep* 2024;14:15366. DOI: https://doi.org/10.1038/s41598-024-66346-w
4. Yamashita R, Kapoor T, Alam MN, et al. Toward reduction in false-positive thyroid nodule biopsies with a deep learning-based risk stratification system using US cine-clip images. *Radiol Artif Intell* 2022;4:e210174. DOI: https://doi.org/10.1148/ryai.210174
5. Bluemke DA, Moy L, Bredella MA, et al. Assessing radiology research on artificial intelligence: a brief guide for authors, reviewers, and readers—from the *Radiology* Editorial Board. *Radiology* 2020;294:487-89. DOI: https://doi.org/10.1148/radiol.2019192515

Images/Tables

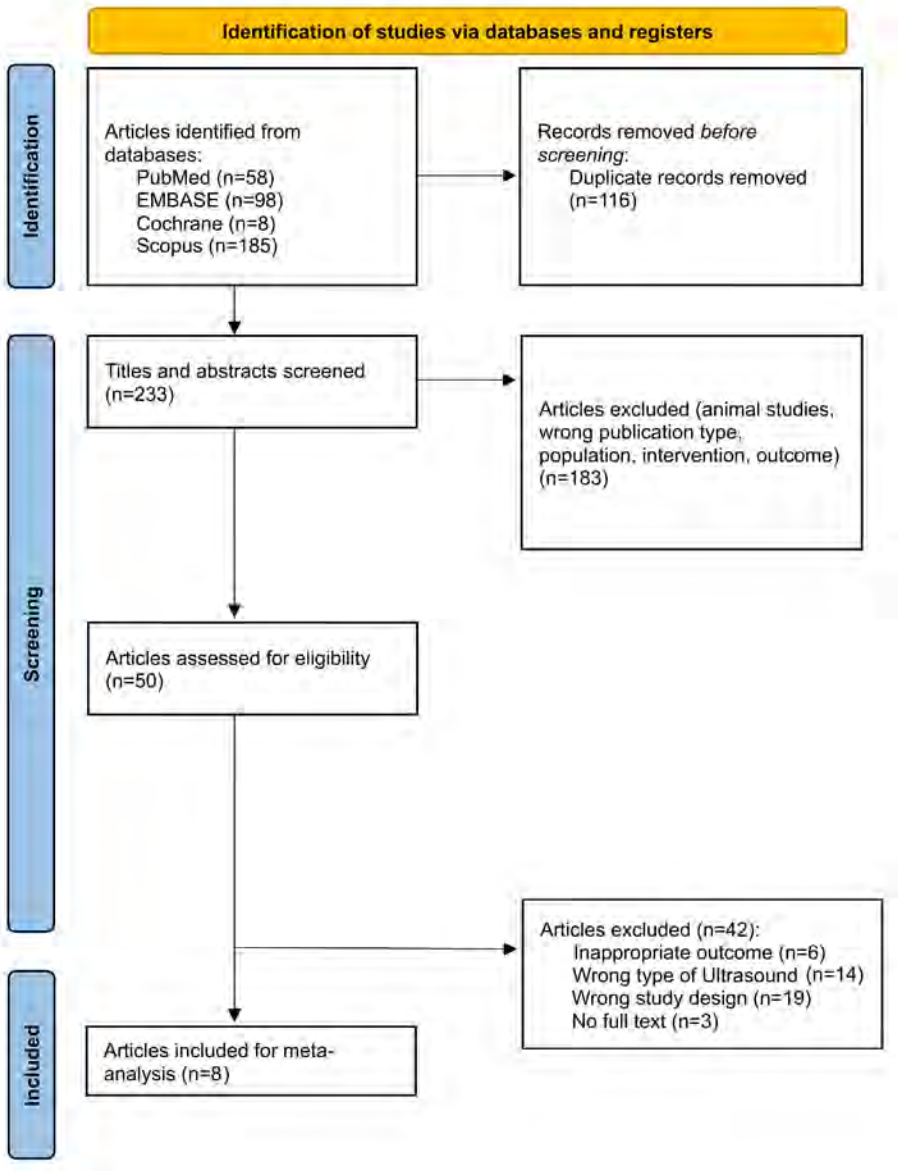

1014 Improved diagnostic performance of automated ARIA detection when harnessing real-world data

Simon Van Eyndhoven PhD, Ricardo Magalhaes PhD, Diana Sima PhD, Rafay A Khan PhD, Arno Liseune PhD, Arne Brys, Dirk Smeets PhD
icometrix, Leuven, Flemish Brabant, Belgium

Purpose

With increasing usage of amyloid-targeting therapies for Alzheimer's disease, timely and accurate detection of amyloid-related imaging abnormalities (ARIA) is crucial to guarantee patients' safety. icobrain aria is an FDA-approved medical device designed for automated detection and grading of ARIA on MRI images (Sima et al., 2024). Its first released version (v1.1; Magalhaes et al., 2024) included deep learning (DL) models that were trained exclusively on clinical trial data with a harmonized MRI protocol, which hampers generalizability to clinical practice, where heterogeneous protocols are used. To address this gap, the most recent version of icobrain aria, v1.2, incorporated additional real-world clinical data for re-training the DL models. The present study investigated the impact of the extension of the training data on the diagnostic performance of icobrain aria.

Materials & Methods

The original training+tuning data, sourced from 277 patients from the EMERGE (NCT02484547) and PRIME (NCT01677572) clinical trials, were extended with real-world data from 343 patients. Retrained models were then optimized for balanced performance on tuning data from both sources, where v1.1 fell short. Sensitivity, specificity, and area under the curve (AUC) for detection of ARIA-E (n=199, 123 positive cases), ARIA-H microhemorrhages (MH; n=199, 82 positive cases) and ARIA-H superficial siderosis (SS; n=199, 78 positive cases), as well as the mean true positive rate (TPR) and mean false positive rate (FPR) of the number of ARIA-E sites and new incidents of MH and SS were compared across icobrain aria versions on a fixed test dataset with expert consensus ground truth.

Results

Sensitivity for ARIA-E decreased only slightly (icobrain aria v1.2=0.93, icobrain aria v1.1=0.95), while specificity (v1.2=0.78, v1.1=0.74) and AUC (v1.2=0.90, v1.1=0.89) increased. TPR remained constant (78.3%), while FPR decreased (v1.2=0.44, v1.1=0.52).
Sensitivity for MH also decreased just slightly (v1.2=0.87, v1.1=0.89), while specificity (v1.2=0.73, v1.1=0.63) and AUC (v1.2=0.83, v1.1=0.81) increased. TPR increased (v1.2=68.7%, v1.1=68%), while FPR (v1.2=0.62, v1.1=0.96) decreased in the new version.
Sensitivity for SS remained constant (0.72 for both versions), while specificity (v1.2 = 0.93, v1.1 = 0.89) and AUC (v1.2 = 0.83, v1.1 = 0.82) increased. TPR increased (v1.2 = 73%, v1.1 = 72%), while FPR (v1.2 = 0.17, v1.1 = 0.23) decreased in the new version.

Conclusion

Adding real-world clinical data to the training data of icobrain aria v1.2 led to a meaningful overall improvement in diagnostic performance compared to v1.1. There were small decreases in sensitivity of ARIA-E and MH detection, but these were likely as a result of decreasing FPR. The increased specificity and reduction in FPR for ARIA-E, MH, and SS suggest that v1.2 is a more robust and clinically useful tool. By providing high sensitivity coupled with a lower false positive burden, icobrain aria v1.2 can enhance the efficiency and accuracy of ARIA detection in clinical practice, ultimately supporting safer and more effective management of patients receiving amyloid-targeting therapies.

References

- Sima, D.M., Vân Phan, T., Van Eyndhoven, S., Vercruyssen, S., Magalhães, R., Liseune, A., Brys, A., Frenyo, P., Terzopoulos, V., Maes, C. and Guo, J., 2024. Artificial intelligence assistive software tool for automated detection and quantification of amyloid-related imaging abnormalities. *JAMA Network Open*, 7(2), pp.e2355800-e2355800.
- Magalhaes, R., Van Eyndhoven, S., Khan, R.A., Phan, T.V., Liseune, A., Brys, A., Sima, D.M., Smeets, D. Enhanced ARIA detection with icobrain aria v1.1: a validation study. ASNR 2025

Images/Tables

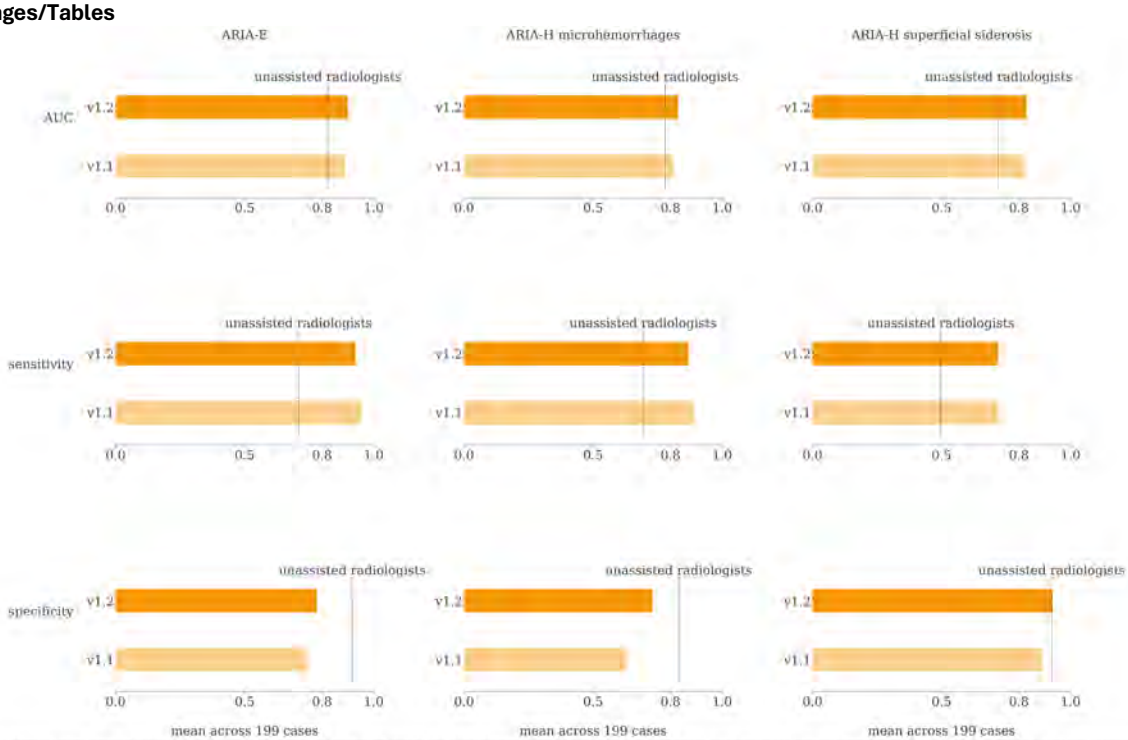

Figure 1. icobrain aria v1.2 improves upon v1.1 (Magalhaes et al., 2025, ASNR Annual Meeting) in terms of specificity and AUC, while maintaining a high sensitivity for the detection of amyloid-related imaging abnormalities (ARIA). Reaching a higher sensitivity and AUC than unassisted radiological readers, icobrain aria permits radiologists to attain a higher reading performance when used as an assistive device (Sima et al., 2024, JAMA Network Open).

Scientific Abstract Power Pitches & Luminary Speaker: Neurodegenerative Disease

10:25 - 11:25am Wednesday, 20th May, 2026

472 A Multi-Contrast 3D MRI Sequence for Simultaneous Whole-Brain FGATIR, MPRAGE, and Neuromelanin Imaging

Jinsuh Kim MD, MS[1], Hahnsung Kim PhD[1], Chan Hong Moon PhD[2]
[1]Emory University, Atlanta, GA, USA. [2]University of Pittsburgh, Pittsburgh, PA, USA

Purpose

Neuromelanin-sensitive (NM) MRI enables visualization of the substantia nigra pars compacta (SNc) and locus coeruleus (LC)—key brainstem nuclei implicated in neurodegenerative and psychiatric disorders associated with dopamine deficiency.

The NM contrast arises from a combination of magnetization transfer (MT) and T_1 effects but typically requires long scan times due to a low SNR, often necessitating multiple signal averages. Consequently, most NM imaging protocols restrict acquisition to a brainstem-only field of view, which limits anatomical context and increases the risk of misregistration with separately acquired structural images. In presurgical MRI for DBS planning, additional FGATIR and MPRAGE acquisitions are also required, further prolonging total scan time.

To overcome these limitations, we developed a novel MRI sequence that simultaneously acquires whole-brain T_1-weighted MPRAGE, FGATIR, and NM contrasts within a single repetition time (TR).

Materials & Methods

MRI data were acquired on a Siemens Prisma 3T scanner equipped with a 64-channel head/neck receive coil. Three healthy volunteers were scanned using the newly developed sequence. Whole-brain imaging was performed with a simultaneous FGATIR–MPRAGE–NM sequence comprising three turbo FLASH readout blocks following a single adiabatic inversion pulse, each with different inversion times (TIs) empirically optimized for FGATIR, T_1-weighted, and NM contrasts.

Sequence parameters were: $TR/TI_1/TI_2/TI_3$ = 5000/422/1300/3500 ms, GRAPPA acceleration factor = 2, 1-mm isotropic resolution, whole-brain field of view, flip angle = 8°, and total acquisition time = 11 min 17 s. Six Gaussian-shaped MT saturation pulses (total flip = 1275°) were applied at a 1200 Hz frequency offset (Fig. 1). The NM imaging block employed a centric-out k-space sampling order to maximize the MT effect and enhance SNR. Image contrast for the whole brain and NM-rich regions (SNc and LC) was visually assessed.

Results

The sequence successfully produced whole-brain 3D images (Fig. 2A) exhibiting distinct FGATIR, MPRAGE, and NM contrasts comparable to conventional single acquisitions. Measured SNRs for FGATIR, MPRAGE, and NM components were 19.4, 57.6, and 295.1, respectively. Gray–white matter CNRs were 8.8, 9.2, and 0.4, while the SN–white matter CNR in the NM image reached 78.7. The NM module's centric k-space sampling achieved high SNR, and the long TI (3500 ms) effectively suppressed CSF signal in the fourth ventricle, improving LC delineation (Fig. 2B).

Conclusion

This multi-contrast MRI sequence offers substantial advantages in efficiency and data consistency. The total acquisition time for all three contrasts was approximately 11 minutes—nearly threefold shorter than acquiring them separately (~30 minutes). Because all contrasts are obtained within a single TR, the resulting images are inherently co-registered, eliminating misalignment due to patient motion or session variability.

This approach provides comprehensive anatomical and functional information in a single scan—whole-brain structure (MPRAGE), midbrain subnuclei delineation (FGATIR), and neuromelanin integrity (NM)—which could be particularly valuable for DBS planning and for research in disorders such as Parkinson's disease. Future work will focus on further optimizing sequence parameters to enhance contrast and balance SNR among the three components.

References

1. Moon et al. (2025), Simultaneous T1-MPRAGE, FGATIR and Neuromelanin Acquisition of Whole Brain at 3 T, Proc. Intl. Soc. Mag. Reason. Med., 2025.
2. Sudhyadhom, A., et al. (2009). A high resolution and high contrast MRI for differentiation of subcortical structures for DBS targeting: the Fast Gray Matter Acquisition T1 Inversion Recovery (FGATIR). NeuroImage 47 Suppl 2: T44-52.
3. Lakhani, D. A., et al. (2024). Diagnostic utility of 7T neuromelanin imaging of the substantia nigra in Parkinson's disease. NPJ Parkinsons Dis 10(1): 13.
4. Cassidy, C. M., et al. (2019). Neuromelanin-sensitive MRI as a noninvasive proxy measure of dopamine function in the human brain. Proceedings of the National Academy of Sciences 116(11): 5108-5117.

Images/Tables

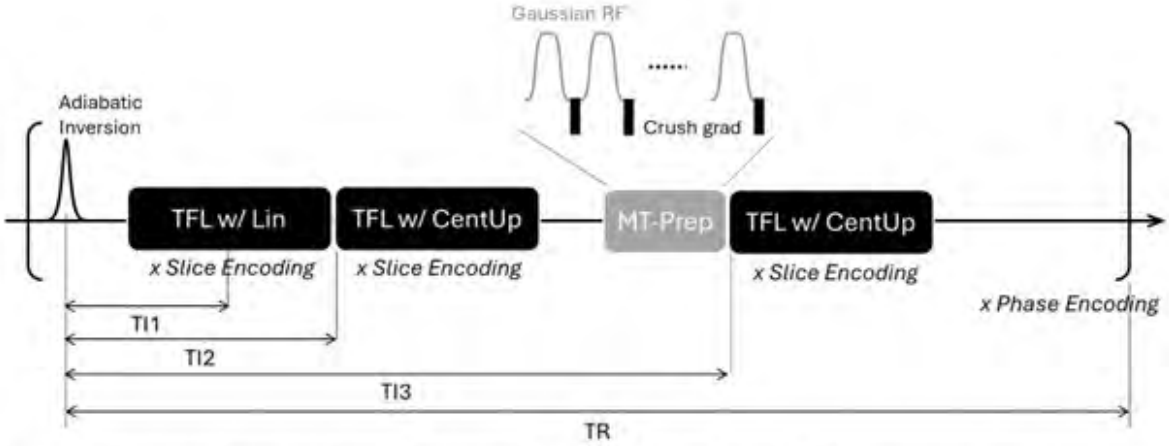

Figure 1. Schematic diagram of simultaneous T1MPRAGE, FGATIR, and NM acquisition in single sequence.

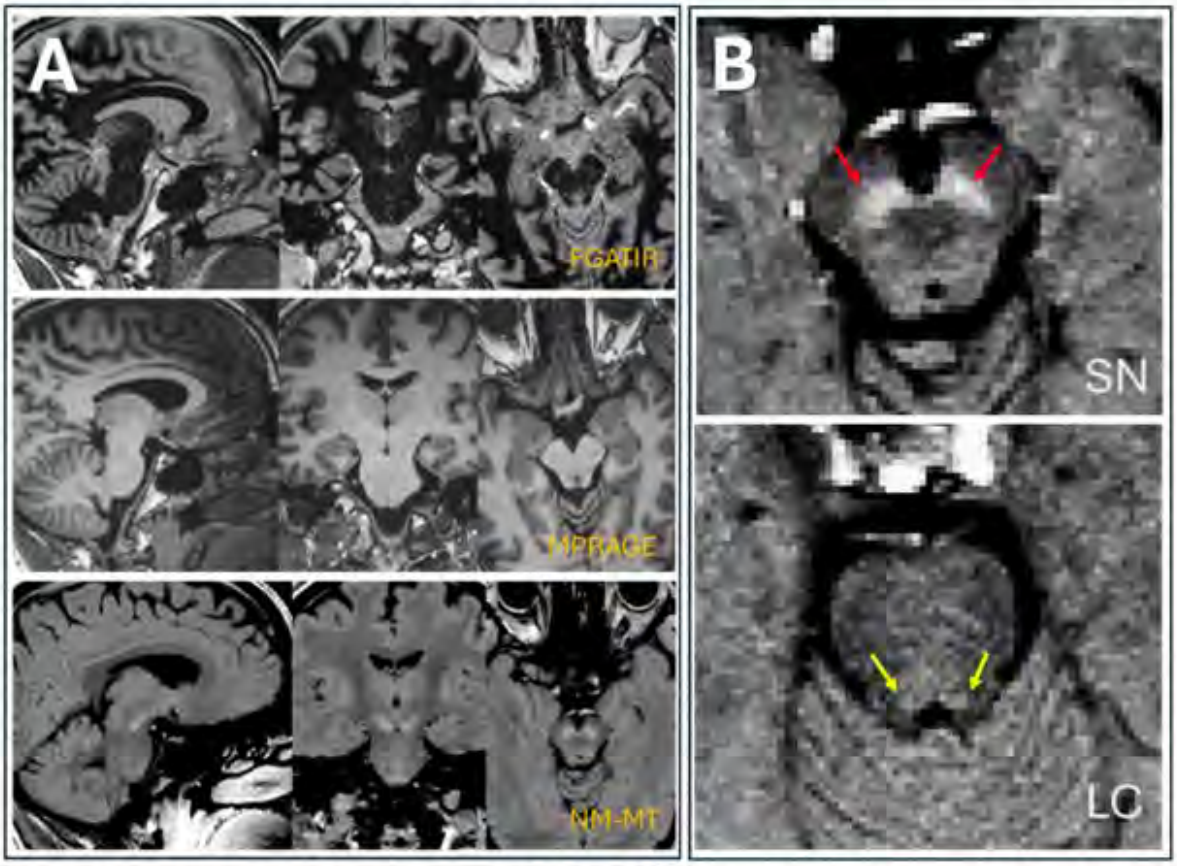

Figure 2. Simultaneous whole-brain T_1MPRAGE, FGATIR, and NM MRI (A) with zoomed views demonstrating the substantia nigra and locus coeruleus (B).

560 Using Arterial Spin Labeling MRI to Investigate Cerebral Blood Flow Changes in Alzheimer's Patients Undergoing Lecanemab Anti-Amyloid Therapy

Elena R Andree[1], Conan Chen[2], Katherine Bangen[3], Ryan Barnes[2], Jason Handwerker[4], Eric Wong[2], Thomas Liu[2], Divya Bolar[2]

[1]University of Oxford, Oxford, England, United Kingdom. [2]Center for Functional MRI, Department of Radiology, University of California San Diego, La Jolla, CA, USA. [3]Department of Psychiatry, University of California San Diego, La Jolla, CA, USA. [4]Department of Radiology, University of California San Diego, La Jolla, CA, USA

Purpose

This study aimed to measure cerebral blood flow (CBF) using arterial spin labeling (ASL) MRI in Alzheimer's patients receiving anti-amyloid therapy with Lecanemab. CBF measurements were obtained at baseline and after multiple infusions to assess associations with cognitive response.

Materials & Methods

A retrospective analysis was conducted using MRI data from AD patients undergoing biweekly Lecanemab therapy, acquired on GE Premier 3T systems.

Methods are summarized in Figure 1. ASL data were acquired using a pseudocontinuous ASL (PCASL) sequence. Quantitative CBF maps were generated using PCASL data calibrated with an M_0 scan and modeled using the ASL signal equation [1]. CBF data were registered to MNI space using high-resolution T1 MPRAGE images and parcellated into regions of interest (ROI) using Harvard-Oxford and MNI atlases for mean CBF calculation across ROIs.

Longitudinal CBF data were analyzed for 18 patients (61-82 yo, 14F, 4M). Inclusion criteria required clinical diagnosis of early AD based on neuropsychological assessment and confirmation of amyloid pathology by PET or CSF biomarkers (per Clarity trial [2]).

Scans were typically obtained at baseline and between infusions 4-7, 12-14, and 24-26; due to the limited number of data points over infusions, intervening CBF values were linearly interpolated. One patient was excluded due to a fetal PCA causing artifactual hypoperfusion [3].

Patients were classified as Lecanemab responders (stable or improved Mini-Mental State Examination (MMSE) or Montreal Cognitive Assessment (MoCA) scores) and non-responders (declining scores). Analyses were performed with FSL (FMRIB, Oxford, UK) and MATLAB (Mathworks, Natick, MA).

Results

Figure 2 shows average ΔCBF as a function of infusion number for the 18 patients who received at least 13 Lecanemab infusions, divided into responders and non-responders. In all six regions, responders demonstrated mildly increased CBF, whereas non-responders demonstrated overall decreased CBF; Figure 3 demonstrates that this difference was statistically significant for the posterior cingulate cortex (PCC) and precuneus regions ($p < 0.05$, Wilcoxon Rank Sum).

Figure 4 shows average ΔCBF as a function of infusion number for 9 cognitive non-responders receiving all 25 infusions. An initial drop in CBF is seen through the sixth infusion, followed by a stabilized negative ΔCBF through infusion 25.

Conclusion

Our findings suggest that longitudinal changes in CBF during Lecanemab treatment may reflect both therapeutic and neurovascular processes. Responders demonstrated increases in CBF across the first 13 infusions relative to CBF decreases in non-responders, particularly in the precuneus and PCC, regions known to be vulnerable in AD. This pattern may indicate some degree of amyloid-β clearance, resulting in restorative vascular and metabolic changes that support cognitive improvement.

In contrast, non-responders exhibited early CBF decline followed by partial normalization. This initial reduction could reflect acute vascular or inflammatory responses to amyloid mobilization, or inadequate plaque removal, leading to persistent neurovascular compromise. Only partial improvement in CBF through infusion 25 suggests stabilization at sub-baseline CBF levels rather than true recovery, possibly relating to continued cognitive decline.

These findings underscore the potential of CBF as an imaging biomarker for monitoring anti-amyloid treatment response, predicting early responders, and informing risk stratification for amyloid-related imaging abnormalities (ARIA).

References

1. Alsop DC, Detre JA, Golay X, et al. Recommended implementation of arterial spin-labeled perfusion MRI for clinical applications: A consensus of the ISMRM perfusion study group and the European consortium for ASL in dementia. *Magn Reson Med* 2015 Jan;73(1):102-16. DOI 10.1002/mrm.25197.
2. Van Dyck CH, Swanson CJ, Aisen P, et al. Lecanemab in early Alzheimer's disease. *New England Journal of Medicine* 2023. 388 (1), 9-21. DOI: 10.1056/NEJMoa2212948.
3. Noorbakhsh A, Farid N, Bolar DS. Apparent posterior cerebral artery territory perfusion asymmetry on arterial spin labeling MRI is a common non-pathologic finding in patients with a unilateral fetal posterior cerebral artery. *Neuroradiology*. 2022 Mar;64(3):513-520. DOI 10.1007/s00234-021-02794-9.

Images/Tables

Figure 1

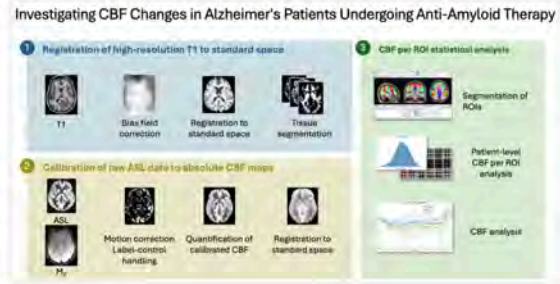

Figure 2

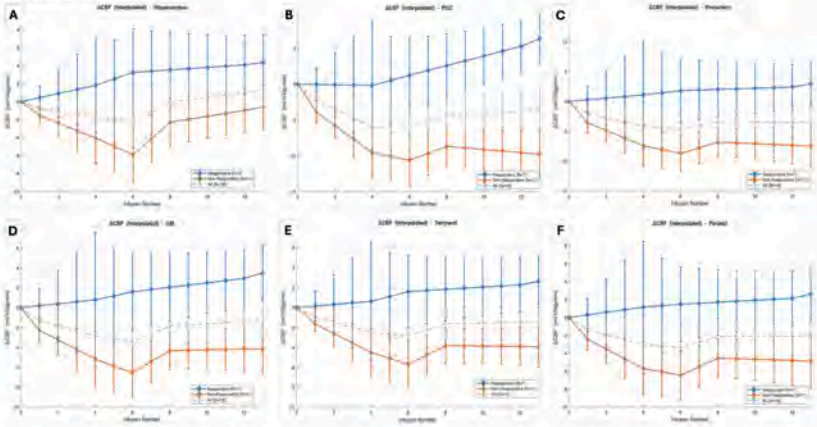

Figure 3

ROI	*Responders (N=7)* Mean ΔCBF	*Non-Responders (N=11)* Mean ΔCBF	p-value
Gray Matter	3.48 ± 7.22	-4.17 ± 8.34	0.069
Hippocampus	4.38 ± 8.10	-0.62 ± 8.28	0.126
PCC	**6.37 ± 9.11**	**-9.81 ± 10.97**	**0.003****
Parietal	2.61 ± 7.68	-4.90 ± 9.97	0.085
Precuneus	**2.92 ± 9.22**	**-7.52 ± 11.31**	**0.035***
Temporal	2.60 ± 6.82	-3.94 ± 6.71	0.104

Figure 4

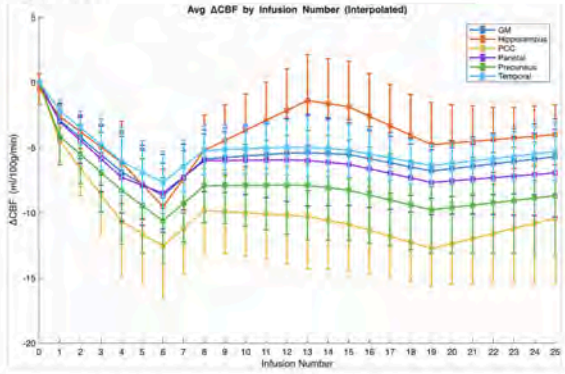

Figure 1: Workflow for investigating CBF changes in AD patients undergoing anti-amyloid therapy (Lecanemab). The pipeline involved (1) preprocessing and registration of structural images to standard space, (2) calibration and processing of arterial spin labeling (ASL) data to generate absolute CBF maps, and (3) ROI-based statistical analysis to quantify and compare longitudinal CBF changes across patients.

Figure 2: Longitudinal changes in CBF across 13 Lecanemab infusions in responders (blue line, N=7) and non-responders (orange line, N=11) for regions shown to be associated with AD pathology (upper panel): (A) Hippocampus, (B) Posterior Cingulate Cortex (PCC), and (C) Precuneus, in addition to regions not typically associated with AD pathology (bottom panel): (D) Gray Matter (GM), (E) Temporal Lobe, and (F) Parietal Lobe. Error bars represent the standard error of the mean (SEM).

Figure 3: Mean change in cerebral blood flow (ΔCBF, ml/100 g/min) at infusion 13 for Lecanemab responders (N=7) and non-responders (N=11) across regions of interest. Values represent mean ± standard deviation. Responders exhibited higher ΔCBF compared with non-responders, with the posterior cingulate cortex (PCC) and precuneus showing statistically significant group differences based on the Wilcoxon rank-sum test ($p < 0.05$*, $p<0.005$**).

Figure 4: Average change in CBF across 25 Lecanemab infusions for cognitive non-responders (N = 9). Responders were not included as there were only 2 patients meeting this criteria. Mean ΔCBF (ml/100 g/min) was calculated relative to baseline and averaged across all patients for Gray Matter (GM, dark blue), Hippocampus (orange), Posterior Cingulate Cortex (PCC, yellow), Parietal Lobe (purple), Precuneus (green), and Temporal Lobe (light blue). Error bars represent the standard error of the mean (SEM).

---

591 **Impaired Glymphatic Flow in Alzheimer's Disease: A Systematic Review and Meta-Analysis of DTI-ALPS Studies**

Sadegh Ghaderi PhD, Sana Mohammadi MD
Tehran University of Medical Sciences, Tehran, Tehran, Iran, Islamic Republic of

Purpose

The DTI-ALPS index is a widely used, non-invasive biomarker for glymphatic system activity, but its consistency across Alzheimer's disease (AD) cohorts is debated. We aimed to systematically review and meta-analyze the existing literature to quantify the precise magnitude of glymphatic flow dysfunction in AD patients compared to healthy controls (HC) using this specific DTI-ALPS method.

Materials & Methods

A comprehensive, PRISMA-compliant systematic search was conducted in four major databases (PubMed, Scopus, Embase, Web of Science) for studies published up to April 27, 2025. We included 22 case-control studies comparing DTI-ALPS indices in 1163 AD patients and 1565 HCs. A random-effects meta-analysis was performed to pool Standardized Mean Differences (Hedges's g). We conducted extensive subgroup analyses (by age, cognition, and technical MRI parameters), leave-one-out sensitivity analyses, and comprehensive assessments of publication bias (Egger's/Begg's tests, trim-and-fill) and Risk of Bias (ROB) using the Newcastle-Ottawa Scale.

Results

A large and highly significant reduction in the DTI-ALPS index was found in AD patients versus HCs (Hedges's g = −1.00; 95% CI: −1.42 to −0.57; p<0.001). Significant, high heterogeneity was observed (I^2=95.7%). This finding remained consistent and significant across all examined subgroups, including age (<70 vs. ≥70), cognitive status (MMSE >20 vs. ≤20), and various MRI technical parameters. Stratification by quality revealed that high-quality (low ROB) studies showed an even stronger effect (g = −1.17). While publication bias was detected, leave-one-out sensitivity analysis confirmed the overall findings' robustness.

Conclusion

This meta-analysis confirms that glymphatic flow, as measured by the DTI-ALPS index, is significantly impaired in Alzheimer's disease with a large and robust effect size. The finding is consistent across diverse study cohorts and technical acquisition parameters. Although interpretation requires caution due to methodological confounders , DTI-ALPS stands as a consistent biomarker of glymphatic dysfunction in AD pathophysiology.

References

1. Taoka T, Masutani Y, Kawai H, et al. Evaluation of glymphatic system activity with the diffusion MR technique: diffusion tensor image analysis along the perivascular space (DTI-ALPS) in Alzheimer's disease cases. Jpn J Radiol. 2017;35(4):172–8

2. Iliff JJ, Wang M, Liao Y, et al. A Paravascular Pathway Facilitates CSF Flow Through the Brain Parenchyma and the Clearance of Interstitial Solutes, Including Amyloid β. Sci Transl Med. 2012;4(147):147ra111
3. Kamagata K, Andica C, Takabayashi K, et al. Association of MRI Indices of Glymphatic System With Amyloid Deposition and Cognition in Mild Cognitive Impairment and Alzheimer Disease. Neurology. 2022;99(24):e2648–60
4. Ringstad G. Glymphatic imaging: a critical look at the DTI-ALPS index. Neuroradiology. 2024;66(2):157–60
5. Page MJ, McKenzie JE, Bossuyt PM, et al. The PRISMA 2020 statement: an updated guideline for reporting systematic reviews. BMJ. 2021;372:n71

Images/Tables

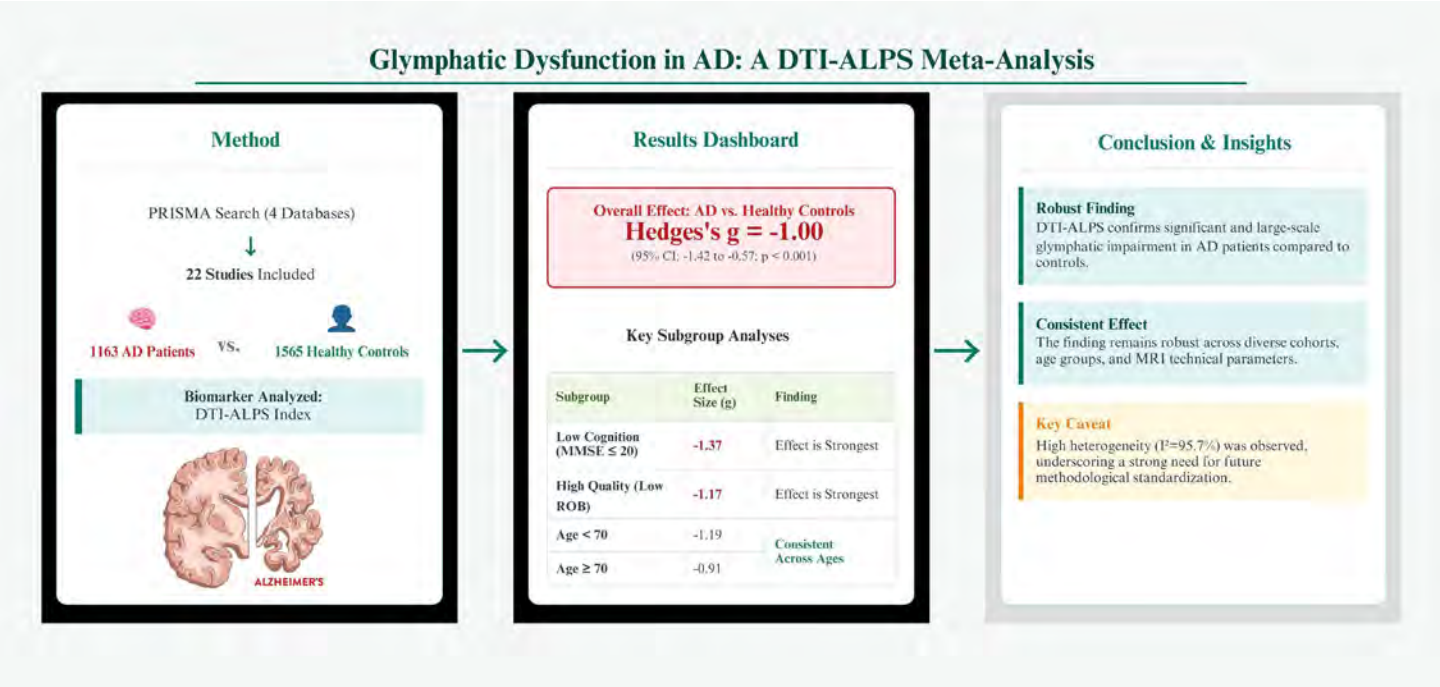

663 Nanobodies Delivered with Focused Ultrasound, Enhances Human Tau Detection in-vivo

Deepshikha Bhardwaj PhD, Ankit Gupta PhD, Wojciech Lesniak PhD, Sandi Terpack, Marc Diamond MD, Bhavya R Shah MD
UT Southwestern Medical Center, Dallas, Texas, USA

Purpose

The restricted permeability of the blood–brain barrier (BBB) poses a major challenge for diagnosing and treating Alzheimer's disease (AD). Majority of small-molecule drugs and almost all macromolecular therapeutics fail to reach the brain in effective doses due to this barrier. Hence, non invasive and targeted methods such as Focused Ultrasound (FUS) are being actively investigated to achieve transient and reversible BBB disruption. FUS is a noninvasive, image-guided technology capable of modulating BBB permeability in specific brain regions with high spatial accuracy. Because AD remains undetected during its preclinical stage-the efficacy of potential diagnostic and therapeutic approaches is greatly reduced. Detecting tau pathology, a defining feature of AD and related tauopathies, at early stages is therefore critical. This study examines whether FUS can be used to deliver Tau-specific nanobodies (Tau-VHH) across the BBB in a mouse model, enabling early visualization of tau aggregates that are otherwise inaccessible under normal barrier conditions.

Materials & Methods

Tau-VHH nanobodies were conjugated with Alexa Fluor 488 (AF488) Maleimide, and successful labeling was verified by Matrix-Assisted Laser Desorption/Ionization Time-of-Flight (MALDI-TOF) mass spectrometry. P301S transgenic mice, which develop tau aggregation, along with their wild-type (WT) littermates, underwent FUS (RK50-MR Guided) sonication targeting the right hippocampus to induce localized BBB opening. BBB disruption was confirmed using magnetic resonance imaging (MRI). Afterward, 1 mg of AF488-labeled Tau-VHH (510 nM) was administered intravenously, and animals were sacrificed at predetermined time points. Following cardiac perfusion, brains were collected, sectioned, and analyzed by tissue cytometry to determine nanobody distribution.

Results

Relative to WT controls, P301S mice displayed significantly increased hippocampal Tau-VHH fluorescence. Within these transgenic mice, the FUS-treated hippocampus exhibited markedly greater fluorescent intensity than the untreated side at 90 minutes post-injection ($p < 0.05$), confirming both BBB opening and selective binding of Tau-VHH to tau aggregates.

Conclusion

FUS-induced BBB modulation allows precise delivery of Tau-specific nanobodies to the hippocampus, enabling in vivo detection of tau pathology in P301S mice. This strategy offers a potential platform for early, noninvasive identification of tauopathies and for the advancement of image-guided diagnostic and therapeutic approaches for Alzheimer's disease.

References

Ankit G, Richard L, Devin K et al. Selective Targeting of Pathogenic Tau Seeds via a Novel VHH
bioRxiv 2025.01.13.632833; doi: https://doi.org/10.1101/2025.01.13.632833

1055 Noninvasive PET-Guided Assessment of Amyloid-Beta Clearance and Cognitive Outcomes in a Clinical Real-World Cohort of Patients With Alzheimer Disease Undergoing Anti-Amyloid Therapy

Jae Gardella[1], Ahlanna Olson[2], Blake Gershon MD[3], Divya Yadav MD[4], Samantha A Keil PhD[2], Anna S Nordvig MD[2], Miran Salgado MD[2], Adina Alport MD[5], Moath A Hamed MD[5], Silky Pahlajani MD[3], Gloria C Chiang MD[3], Sonja Blum MD/PhD[2], Jana Ivanidze MD/PhD[3]

[1]MD Program, Weill Cornell Medicine, New York, NY, USA. [2]Department of Neurology, Weill Cornell Medicine, New York, NY, USA. [3]Department of Radiology, Weill Cornell Medicine, New York, NY, USA. [4]Department of Radiology, Moffitt Cancer Center, Tampa, FL, USA. [5]NewYork-Presbyterian Brooklyn Methodist Hospital, New York, NY, USA

Purpose

Amyloid PET has assumed a central role in confirming Alzheimer disease (AD) before treatment initiation with anti-amyloid therapies (AAT). Our aim was to investigate the use of beta-amyloid (Aβ)-PET as a measure of treatment response in AD patients undergoing treatment with AAT. Associations between magnitude of Aβ-clearance, demographic variables including APOE4 status, cognitive function, and occurrence of amyloid-related imaging abnormalities (ARIA), and clinical outcomes were assessed.

Materials & Methods

In this retrospective IRB-approved study, we identified individuals diagnosed with mild cognitive impairment due to AD (MCI/AD) who underwent Aβ-PET after treatment with AAT (Lecanemab or Donanemab). Aβ-PET studies were evaluated visually by a board certified neuroradiologist and nuclear medicine physician. Additionally, quantitative Aβ-PET analysis was performed to determine centiloid values (CL) which provide a numerical magnitude of Aβ-PET signal according to two anchor points (0CL: cognitively unimpaired; 100CL: mild-moderate AD). Cognitive function was assessed by mini-mental status exam (MMSE) or Montreal Cognitive Assessment (MoCA) test.

Results

Forty-four patients met inclusion criteria; 28 treated with Lecanemab and 16 with Donanemab AAT. Across all patients, we found a median ΔCL of 58.38 ($p < 0.0001$). A complete response to AAT, defined as a grade 1 brain amyloid plaque load (BAPL1) or CL <20 post-AAT PET, was seen in 50% of patients. An additional seven patients had a partial response, but with a ΔCL above the median. There was no significant difference in ΔCL between Lecanemab and Donanemab ($p = 0.481$). An association between at least one copy of the APOE ε4 variant and ΔCL approached significance ($U = 59.0$, $p = 0.079$). Despite its known association with cerebral angiopathies[1], APOE4 status did not predict higher rates of ARIA ($p = 0.374$). No significant association between change in pre- and post-AAT cognitive scores and either ΔCL ($\tau b = 0.305$, $p = 0.205$) or post-AAT amyloid burden ($r = 0.240$, $p = 0.196$) was appreciated.

Conclusion

Robust Aβ-clearance post-AAT was seen in the majority of patients in this pilot clinical real-world study, with neither agent proving superior to the other. APOE4 status trended toward a higher degree of Aβ clearance, although this did not reach significance. APOE4 carriers did not experience higher rates of ARIA. A weak association between treatment response and cognitive outcomes was detected but did not reach statistical significance, likely due to small sample size and cohort heterogeneity.

References

1) Jackson RJ, Hyman BT, Serrano-Pozo A. Multifaceted roles of APOE in Alzheimer disease. Nat Rev Neurol. 2024 Aug;20(8):457-474.

Images/Tables

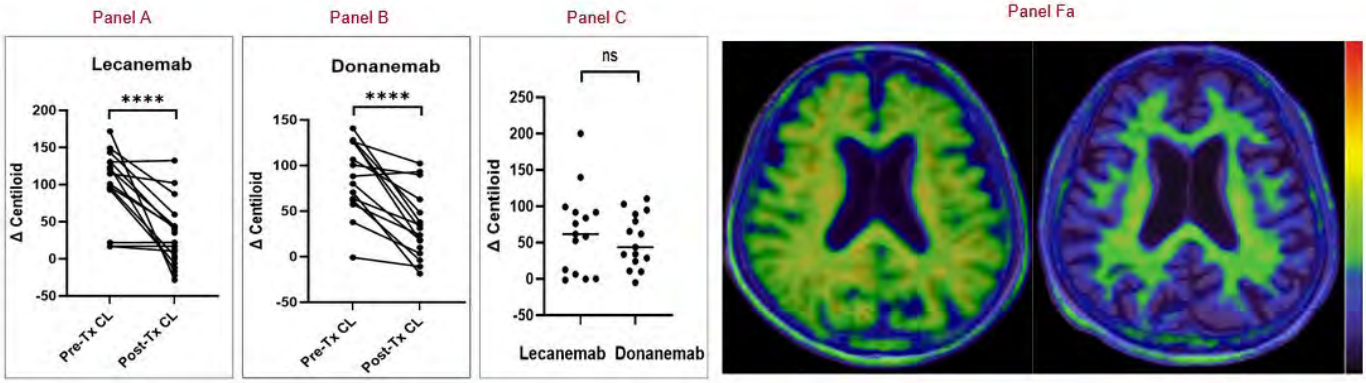

Legend. Panel A: Pre- and Post-AAT CL for Lecanemab (ΔCL = 64.8, p < 0.001). Panel B: Pre- and Post-AAT CL for Donanemab (ΔCL = 52.2, p < 0.001). Panel C: ΔCL comparison between AAT agents (p = 0.481). Panel D: ΔCL comparison by APOE4 status (U = 59.0, p = 0.079). Panel E: ΔCL vs Change in Pre- and Post-AAT MMSE (r = 0.240, p = 0.196). Panel Fa: Complete Aβ clearance in patient treated with Lecanemab [Pre-AAT (Left) CL = 123.28 | Post-AAT (Right) CL = -16.61 | ΔCL = 139.89 | PET Rainbow color scale (Far-Right): 0-4 maximum SUV]. Panel Fb: Unchanged diffuse Aβ positivity in patient treated with Donanemab [Pre-AAT (Left) CL = 88.25 | Post-AAT (Right) CL = -93.33 | ΔCL = -5.08 | PET Rainbow color scale (Far-Right): 0-4 maximum SUV].

---

579 **Cross-Platform Concordance of Quantitative Amyloid PET Z-Scores in a Real-World Clinical Cohort of Patients with Cognitive Impairment and Suspected Alzheimer Disease.**

Edward J Ebani M.D.[1], Divya Yadav[2], Gloria Chiang M.D.[1], Jana Ivanidze M.D. Ph.D.[1], Anna Nordvig MD, MS[3]

[1]Weill Cornell Medicine, New York, NY, USA. [2]Moffitt Cancer Center, Tampa, FL, Tampa, Florida, USA. [3]Weill Cornell Medicine, New York, New York, USA

Purpose

With the advent of anti-amyloid therapies for patients with cognitive impairment and/or suspected Alzheimer disease (CI/AD), clinical use of amyloid PET has rapidly expanded in recent years. Quantification of cortical tracer avidity can increase diagnostic confidence, reduce inter-reader variability, and guide treatment eligibility and response assessment. Database comparison tools are FDA-approved, clinically integrated software applications that enable quantitative PET analysis in routine clinical practice. However, differences in implementation across packages may yield non-interchangeable Z-scores, with potential consequences for diagnosis, treatment planning, and trial eligibility. This study evaluated the agreement of Z-scores derived from two widely used clinical software packages in a real-world cohort of patients with CI/AD.

Materials & Methods

Amyloid PET from 100 consecutive patients with CI/AD obtained as part of clinical standard-of-care evaluation at a single institution (August to October 2024) were retrospectively reviewed. 6 scans were excluded due to poor registration, leaving 94 evaluable studies. Amyloid PET data were post-processed using syngo.via MI Neurology (Siemens Healthineers) and separately, MIMneuro (MIM Software/ GE Healthcare) packages, respectively, by a board-certified neuroradiologist with one year of dedicated clinical amyloid PET experience. Regional Z-scores were obtained for the temporal, precuneus, posterior cingulate, parietal, frontal, and anterior cingulate cortices. Regional Z-scores were compared on a per-patient and per-region basis, and stratified by Centiloid burden. Agreement was evaluated using Bland-Altman analysis, simple linear regression, and Deming regression.

Results

Agreement between Syngo.via and MIMneuro varied by region. When regional Z-scores were averaged into a per-patient composite measure, overall bias was near-zero, with tight limits of agreement (slope = 0.97 [95% CI 0.93–1.02], intercept = 0.11 [95% CI –0.05–0.26]), indicating minimal proportional and constant bias between platforms. Bland–Altman analysis showed small bias and narrow limits of agreement (LoA) in the low amyloid group (<20 Centiloids; mean bias –0.19, 95% LoA –0.93 to +0.55). In the intermediate group (20–30 Centiloids), bias was larger (–0.44) and variability increased (LoA –2.02 to +1.14), representing the greatest divergence between platforms. In the high amyloid group (>30 Centiloids), bias reversed but remained small (+0.16) with wider LoA (–1.92 to +2.24). Region-stratified Deming regression showed both proportional and constant bias in the temporal cortex (slope = 0.70 [95% CI 0.66–0.74], intercept = 0.34 [95% CI 0.07–0.61]), indicating systematic underestimation of high Z-scores by MIM relative to Syngo.via.

Conclusion

Our findings demonstrate overall concordance between Syngo.Via and MIMneuro quantitative amyloid PET analysis software packages, however with significant region- and amyloid burden-dependent variability that becomes more pronounced near the positivity threshold. These differences may influence interpretation and determination of treatment eligibility in borderline cases, emphasizing that Z-scores from different commercial platforms should not be used interchangeably without cross-validation. Limitations include the lack of correlation with clinical outcomes and the focus on Z-scores rather than alternative quantitative metrics. In summary, our work underscores the need for standardization and calibration across software tools as amyloid PET becomes increasingly embedded in therapeutic decision-making.

References

Sabri O, Seibyl J, Rowe C, et al. Beta-amyloid imaging with florbetaben. *Clin Transl Imaging*. 2015;3(1):13-26. doi:10.1007/s40336-015-0102-6

Nayate AP, Dubroff JG, Schmitt JE, et al. Use of Standardized Uptake Value Ratios Decreases Interreader Variability of [18F] Florbetapir PET Brain Scan Interpretation. *AJNR Am J Neuroradiol*. Jul 2015;36(7):1237-44. doi:10.3174/ajnr.A4281

Chapleau M, Iaccarino L, Soleimani-Meigooni D, et al. The Role of Amyloid PET in Imaging Neurodegenerative Disorders: A Review. *J Nucl Med*. Jun 2022;63(Suppl 1):13s-19s. doi:10.2967/jnumed.121.263195

Pemberton HG, Collij LE, Heeman F, et al. Quantification of amyloid PET for future clinical use: a state-of-the-art review. *Eur J Nucl Med Mol Imaging*. Aug 2022;49(10):3508-3528. doi:10.1007/s00259-022-05784-y

Pontecorvo MJ, Arora AK, Devine M, et al. Quantitation of PET signal as an adjunct to visual interpretation of florbetapir imaging. *Eur J Nucl Med Mol Imaging*. May 2017;44(5):825-837. doi:10.1007/s00259-016-3601-4

Images/Tables

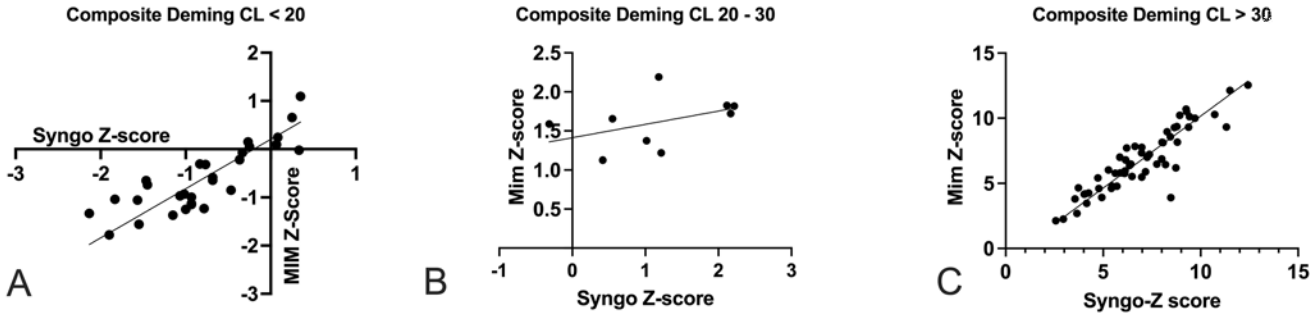

885 Regional ^{18}F-Flortaucipir Standardized Uptake Value Ratio (SUVR) Patterns in Clinical Tau PET: Implications for Expanded Treatment Eligibility

Michelle Chen MD[1], Graham Keir[2], Christopher Caravella[1], Josephine Rini MD[1], Sean A. P. Clouston[3], Ana M. Franceschi MD, PhD[1]

[1]Donald and Barbara Zucker School of Medicine at Hofstra/Northwell, New York, NY, USA. [2]Piedmont South Imaging, Atlanta, GA, USA. [3]Stony Brook University, Stony Brook, NY, USA

Purpose

Flortaucipir F18 (TAUVID), the first FDA-approved PET radiotracer for imaging tau neurofibrillary tangles, has transformed Alzheimer's disease (AD) diagnostics. Regional TAU-PET patterns predict cognitive decline more accurately than amyloid PET or volumetric MRI, establishing tau imaging as a superior prognostic biomarker. The 2025 appropriate use criteria designate TAU-PET for determining eligibility for anti-amyloid and emerging anti-tau therapies. However, ^{18}F-flortaucipir demonstrates reduced sensitivity for early-stage tau pathology (Braak I-IV), particularly in mild cognitive impairment, with visual interpretation frequently yielding indeterminate results. These diagnostic uncertainties potentially exclude patients with intermediate but treatable pathology from accessing disease-modifying interventions during optimal therapeutic windows. We investigated whether quantitative SUVR analysis may help identify distinct uptake patterns in visually indeterminate cases to differentiate true early-stage AD pathology from non-specific uptake, thereby clarifying treatment eligibility for patients at stages most amenable to intervention.

Materials & Methods

Following IRB approval, we retrospectively analyzed 23 patients (mean age 74±5.8 years, 13F/10M) who underwent clinical 18F- flortaucipir (TAU) PET/CT and MRI brain at our institution. TAU-PET and MRI were fused using MIMNeuro software (version 7.3.2). Amyloid status was determined using Centiloid scale when available (34.9±41.4 CL, n=5). A board-certified neuroradiologist with 10 years of experience in brain PET interpretation visually analyzed ten brain regions (mesial temporal, anterolateral temporal, posterolateral temporal, frontal, parietal, precuneus, posterior cingulate, occipital, basal ganglia, dentate nucleus), classifying scans as negative (n=10), indeterminate (n=7), or positive for AD pattern (n=6). SUVmean and SUVmax values were recorded. SUVR were calculated, using SUVmax values in cortex and SUVmean in cerebellar gray matter as the reference region, as these estimates provided the largest effect sizes.

Results

Visual assessment classified 10/23 (43%) TAU-PET scans as negative, 7/23 (30%) as indeterminate, and 6/23 (26%) as positive, demonstrating that nearly one-third of clinical scans yield diagnostic uncertainty directly impacting treatment eligibility. Positive cases showed markedly elevated SUVR across posterolateral temporal, parietal, and posterior cingulate regions. Negative cases demonstrated minimal SUVR elevation across all regions. Indeterminate cases often exhibited distinct intermediate patterns with elevated mesial and anterolateral temporal SUVR but preserved neocortical regions, consistent with Braak III-IV pathology. The correlation matrix revealed strong positive correlations between posterior cingulate, precuneus, and parietal regions, suggesting synchronized progression across these areas. Indeterminate cases showed a distinct pattern of elevated mesial and anterolateral temporal SUVR with preserved neocortical regions.

Conclusion

Our findings demonstrate that 30% of clinical TAU-PET scans yield indeterminate visual interpretations, representing a substantial population with intermediate tau pathology consistent with Braak III-IV stages who remain ineligible for current disease-modifying therapies. The distinct pattern observed, with elevated temporal but preserved neocortical SUVR, suggests quantitative analysis could transform diagnostic uncertainty into

actionable staging information. Implementation of region-specific quantitative thresholds may expand treatment eligibility to include patients at optimal/early intervention stages when disease-modifying therapies are most beneficial. While specific cutoff values require validation in larger cohorts, this approach addresses a critical gap between pathological burden and treatment access, ensuring patients with early but clinically significant tau accumulation aren't excluded from therapeutic opportunities due to limitations in visual interpretation alone.

References

1. Groot C, Smith R, Collij LE, et al. Tau Positron Emission Tomography for Predicting Dementia in Individuals With Mild Cognitive Impairment. JAMA Neurol. 2024;81(8):845-856. doi:10.1001/jamaneurol.2024.1612
2. Jack CR Jr, Andrews JS, Beach TG, et al. Revised criteria for diagnosis and staging of Alzheimer's disease: Alzheimer's Association Workgroup. Alzheimers Dement. 2024;20(8):5143-5169. doi:10.1002/alz.13859
3. Rabinovici GD, Knopman DS, Arbizu J, et al. Updated appropriate use criteria for amyloid and tau PET: A report from the Alzheimer's Association and Society for Nuclear Medicine and Molecular Imaging Workgroup. Alzheimers Dement. 2025;21(1):e14338. doi:10.1002/alz.14338
4. Sims JR, Zimmer JA, Evans CD, et al. Donanemab in Early Symptomatic Alzheimer Disease: The TRAILBLAZER-ALZ 2 Randomized Clinical Trial. JAMA. 2023;330(6):512-527. doi:10.1001/jama.2023.13239
5. Soleimani-Meigooni DN, Rabinovici GD. Tau PET Visual Reads: Research and Clinical Applications and Future Directions. J Nucl Med. 2023;64(5):822-824. doi:10.2967/jnumed.122.265017

Images/Tables

^{18}F-flortaucipir SUVR	Amyloid Positive	Amyloid Negative
Dentate	1.02 (0.14)	0.83 (0.08)
Occipital	1.42 (0.45)	0.83 (0.06)
Basal Ganglia	1.55 (0.31)	1.21 (0.13)
Mesial Temporal	1.34 (0.34)	0.91 (0.22)
Anterior Lateral	1.74 (0.35)	0.89 (0.11)
Posterior Lateral Temporal	1.72 (0.71)	0.93 (0.09)
Frontal	1.23 (0.44)	0.79 (0.11)
Parietal	1.2 (0.73)	0.71 (0.13)
Precuneus	1.29 (0.82)	0.8 (0.06)
Posterior Cingulate	1.41 (0.62)	0.83 (0.08)

Table 1. Regional ^{18}F-flortaucipir SUVR in Amyloid positive and Amyloid negative subjects.

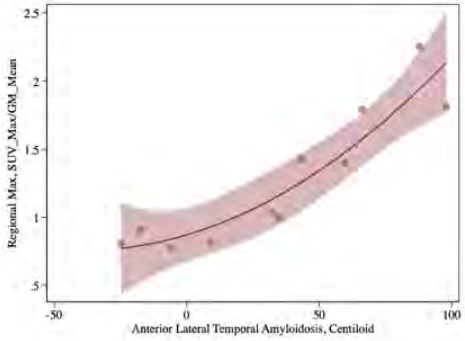

Figure 1. Correlations between ^{18}F-flortaucipir SUVR and Centiloid values in the anterior lateral temporal region (Spearman's rho = 0.96, P<0.05).

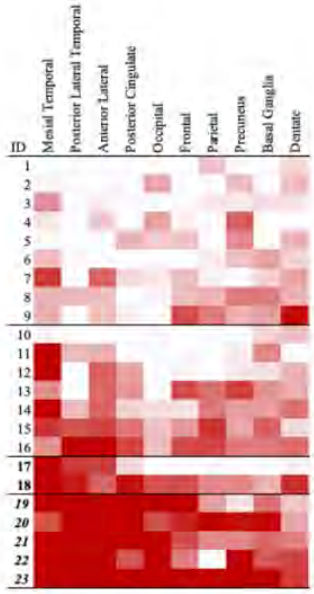

Figure 2. ^{18}F-flortaucipir burden in study subjects ranked by average SUVR across all measured regions. Note, tau-positive subjects are highlighted using bold typeface in the ID column. The five subjects with amyloid-positive centiloids (Centiloid > 40) are italicized.

---

819 Functional Connectomics of Neurodegeneration and Cognitive Dysfunction in Multiple Sclerosis

Elias A. Khan, Diana A. Hobbs Ph.D., Danielle M. Royer M.S., Khushi C. Hiremath B.S., Anahita Samadi Ph.D., Florence L. Chiang M.D., Ph.D.
UT Southwestern, Dallas, Texas, USA

Purpose

Neurodegeneration is a key component of clinical disability in multiple sclerosis (MS). However, the underlying mechanism of localized gray matter (GM) atrophy in MS remains unknown. Recently, an atrophy-based functional network (AFN) model was described, which identifies a network-mediated pattern of neurodegeneration in MS.[1] Specifically, the AFN model defines nodes as regional hubs that show localized patterns of GM atrophy in MS. The goal of this study was to assess nodal contributions to network-mediated neurodegeneration. We leveraged computational neuroimaging approaches via graph theoretical constructs to capture the relationships between nodes and their influence on network dynamics, which extends prior observations of altered cortical-subcortical connectivity in other network disease populations.[2] Our hypothesis was that cortical nodes will exhibit a greater influence on network organization compared to subcortical nodes and that these changes would be associated with cognitive impairment in MS. Findings of this study would support further development of the AFN model toward biomarker qualification for clinical trial use.

Materials & Methods

Whole-brain structural and resting-state functional MRI (rsfMRI) data were collected on a 3T MRI scanner (Tim Trio; Siemens Medical Solutions). All 18 AFN nodes were used to sample the rsfMRI timeseries data, and graph-theoretical metrics (i.e. community, participation coefficient, modularity, clustering coefficient, local efficiency, eigenvector centrality, degree, and edge strength) were computed via an 18x18 correlation matrix for each subject using the Brain Connectivity Toolbox[3]. Statistical analyses included Wilcoxon signed-rank tests to compare network measures of eigenvector,

strength, degree, and participation between cortical and subcortical AFN nodes. Partial correlations corrected for age, sex, and disease duration were computed between working memory and eigenvector centrality for both cortical and subcortical AFN nodes.

Results

Participants included 20 relapsing remitting MS (M/F: 8/12; age 36.3±8.94 years; EDSS 4.03±2.09; disease duration 7.85±5.45) and 20 age-matched healthy controls (HC; Table 1). For MS, subcortical nodes showed significantly lower eigenvector centrality (0.18 ± 0.05; 0.22 ± 0.03), participation coefficient (0.22 ± 0.12; 0.27 ± 0.12), degree (9.70 ± 1.58; 10.73 ± 1.72), and edge strength (5.40 ± 0.95; 6.27 ± 1.55) when compared to cortical nodes (Figure 1). No significant differences were found for HC for any graph theoretical measure. Partial correlations between working memory and eigenvector centrality revealed strong positive associations within subcortical nodes ($r=0.59$, $p\leq 0.01$) and a strong negative association within cortical nodes ($r=-0.56$, $p\leq 0.01$) (Figure 2).

Conclusion

Results of this study demonstrate increased network-wide influence of AFN cortical nodes compared to subcortical nodes in MS. Further, strong associations between network alterations and cognitive impairment (i.e. working memory) were observed. Our findings suggest that cortical GM plays a role in maintaining network integrity and driving network reorganization in response to neurodegeneration in MS [4,5]. These findings encourage future studies in probing local functional connectivity fluctuations of network-mediated damage and further investigations of brain structure-function relationships in MS.

References

[1] Chiang FL, Feng M, Romero RS, et al. Disruption of the atrophy-based functional network in Multiple Sclerosis is associated with clinical disability: Validation of a meta-analytic model in resting-state functional MRI. *Radiology* 2021;299(1):159-66. DOI: https://doi.org/10.1148/radiol.2021203414

[2] Ajilore O, Lamar M, Leow A, et al. Graph theory analysis of cortical-subcortical networks in late-life depression. *AJGP Am J Geriatr Psychiatry* 2014;22(2):195-206. DOI: https://doi.org/10.1016/j.jagp.2013.03.005

[3] Rubinov, M., & Sporns, O. (2010). Complex network measures of brain connectivity: Uses and interpretations. *NeuroImage, 52*(3), 1059–1069. https://doi.org/10.1016/j.neuroimage.2009.10.003

[4] Mangeat G, Badji A, Ouellette, R, et al. Changes in structural network are associated with cortical demyelination in early multiple sclerosis. *Hum Brain Mapp* 2018;39(5):2133-46. DOI: https://doi.org/10.1002/hbm.23993

[5] Fleischer V, Gröger A, Koirala N, Droby A, Muthuraman M, Kolber P, Reuter E, Meuth SG, Zipp F, Groppa S. Increased structural white and grey matter network connectivity compensates for functional decline in early multiple sclerosis. *Mult Scler J* 2016; 23(3):432-441. DOI: https://doi.org/10.1177/1352458516651503

Images/Tables

Characteristic	HC	MS	Group differences (P-value*)
Demographics			
Age	36.20 ± 9.75	36.30 ± 8.94	0.9732
Sex (M/F)	8/12	8/12	—
EDSS	—	4.03 ± 2.09	—
Disease Duration (yr)	—	7.85 ± 5.45	—
Cognition			
NLV (mL)	0.05 ± 0.17	5.89 ± 8.02	0.0041
Brain volumes			
GM (L)	0.52 ± 0.11	0.46 ± 0.07	0.0524
WM (L)	0.61 ± 0.13	0.59 ± 0.08	0.4973
WBV (L)	1.35 ± 0.26	1.27 ± 0.17	0.2260
Cognition			
Processing Speed	—	-2.02 ± 2.46	—
Executive Function	—	-1.53 ± 2.36	—
Verbal Memory	—	-1.27 ± 1.53	—
Working Memory	—	-0.42 ± 0.71	—
Verbal Fluency	—	-1.05 ± 0.97	—
Global Cognitive Score	—	-2.10 ± 2.52	—

Table 1. Characteristics of Participants. Demographics, EDSS scores, and disease duration were obtained. Brain volumes and lesions were normalized for head size. Cognitive domain scores and global scores were normalized to healthy controls. Variables are reported as mean (SD) unless otherwise indicated. EDSS, Expanded Disability Status Scale; GM, gray matter; WM, white matter; WBV, whole brain volume; NLV, normalized lesion volume. P-values from two-tailed independent samples t-test.

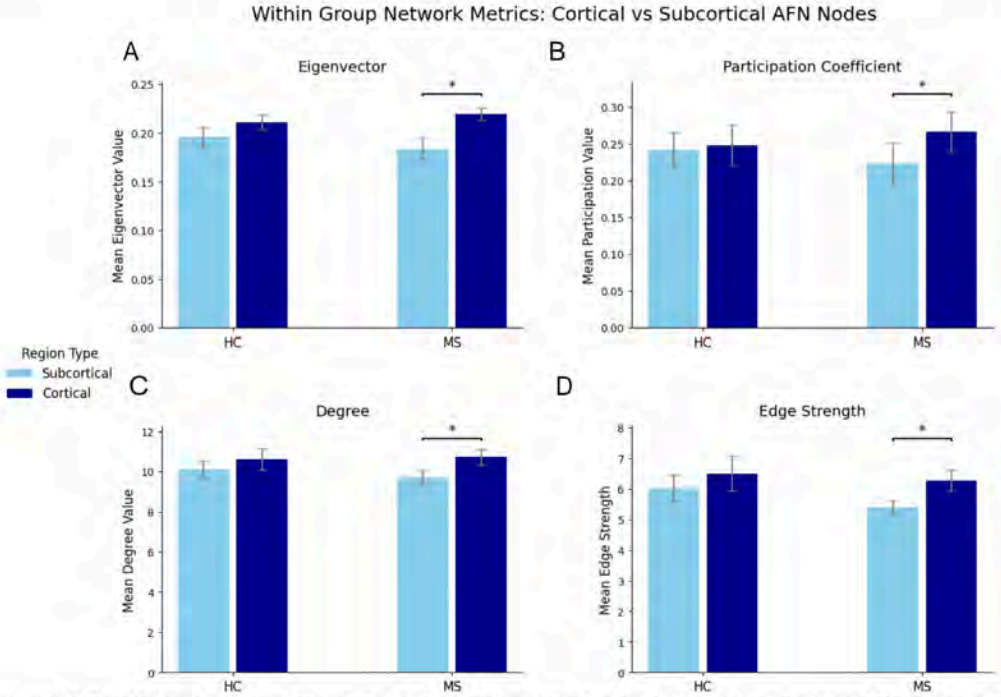

Figure 1. Boxplots showing Wilcoxon Signed Rank tests comparing cortical to subcortical node network metrics of A) Eigenvector Centrality, B) Participation Coefficient, C) Degree, and D) Edge Strength for healthy controls (HC) and individuals with multiple sclerosis (MS). * p<0.05.

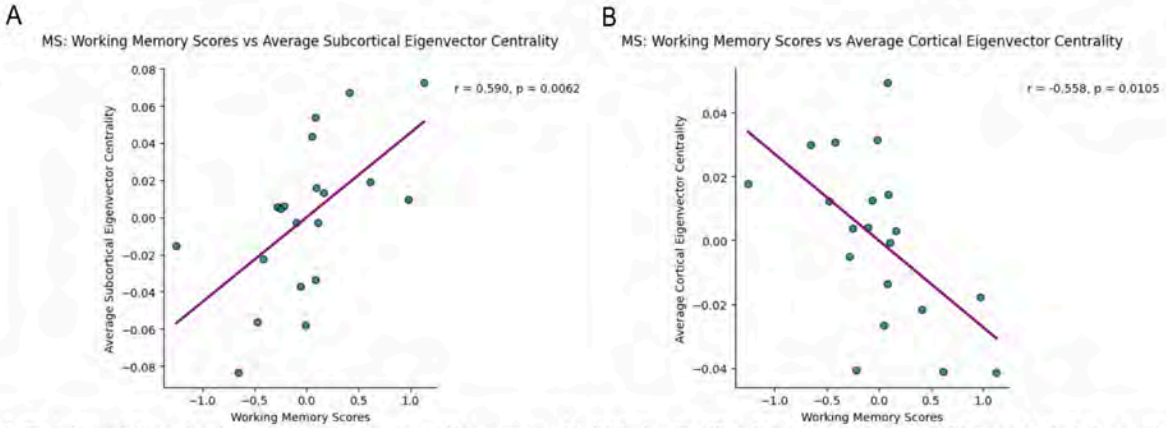

Figure 2. Partial correlations showing association between working memory of individuals with MS to A) mean subcortical and B) mean cortical eigenvector centrality.

Emergency Neuroimaging: Appropriateness, Protocols, Recommendations, & Utilization ... Value Added?

11:30am - 12:30pm Wednesday, 20th May, 2026

640 Clinical History and Neurologic Exam Findings are Highly Associated with Acute Central Pathology in Emergency Department Patients Presenting with Vertigo: 10 Year Retrospective Analysis in a Large Health System

Raven Spencer MD[1], Charles Li MD[1], Michael Goldberg MD, MPH[1], Matthew Kulzer[1], Laura Eisenmenger MD[2], Warren Chang MD, MBA[1]
[1]Allegheny Health Network, Pittsburgh, PA, USA. [2]University of Wisconsin, Madison, WI, USA

Purpose

This study aims to quantify the diagnostic yield and clinical relevance of neuroimaging for emergency department (ED) patients presenting with vertigo in a large health system, examining the real-world concordance between bedside risk stratification, imaging findings, and current guideline recommendations.

Materials & Methods

A retrospective cohort analysis was performed on adult patients who underwent neuroimaging for vertigo in 14 EDs in a large health system between May 2016 and January 2025. ED patients scanned for the provided diagnosis of vertigo were included. Electronic medical records were reviewed by board-certified neuroradiologists and neurologists. 4,135 unique patients (5,445 imaging exams; mean age 62.5 ± 16.9, 62% female, 38% male) were included; imaging reports were reviewed and flagged when potentially clinically relevant findings were present.

291 patients (5.3%) were flagged with potentially relevant imaging findings. These findings were categorized as 1) acute actionable contributory to vertigo (acute contributory findings), 2) acute actionable not contributory to vertigo (acute non-contributory findings), 3) non-acute actionable, or 4) non-actionable. Clinical variables were also gathered from the electronic medical record in these cases, including vertigo quality, acuity, physical examination findings (including HINTS and cerebellar signs), specialty consultations, and interventions. Statistical analyses employed Chi-square and Fisher's exact tests with Holm-Bonferroni corrections for multiple comparisons. The study was performed under the supervision of the local institutional review board.

Results

Neuroimaging revealed acute actionable findings deemed contributory to vertigo in just 1.2% of exams, while 94.7% demonstrated normal or chronic non-contributory findings. Acute contributory findings most frequently included posterior fossa infarcts (0.9%), hemorrhage, neoplasm with mass effect, and vertebral artery dissection. Constant vertigo was highly predictive of acute central pathology (98.5% in acute contributory group vs. 6.0% in others, $p<0.0001$, RR 16.4), while intermittent/positional vertigo or symptoms that resolved spontaneously were associated with peripheral etiologies or non-actionable findings.

Acute symptom onset (<24h prior to presentation) further stratified risk (63.1% in contributory group vs. 40.8% in others, $p=0.0006$). Abnormal HINTS and/or focal cerebellar signs were also strongly linked with acute contributory findings (44.6% in contributory group vs. 6.0% in the other groups, RR 7.4, $p<0.0001$). Nearly all patients with acute contributory findings underwent specialty consultations and interventions (95.4% vs. 34.2% in others, RR 2.8, $p<0.0001$).

A small subset of patients (27 patients, 0.5%) had acute non-contributory findings, including supratentorial infarcts, hemorrhage, and neoplasms, that required hospitalization or changes in management.

23 patients (0.4%) had non-acute contributory findings, mostly chronic vertebrobasilar insufficiency without evidence of acute occlusion or high grade stenosis.

176 patients had non-actionable findings; most of these patients were diagnosed with peripheral etiology such as benign paroxysmal peripheral vertigo.

Conclusion

The diagnostic yield of neuroimaging for ED patients with vertigo remains low, with <2% demonstrating acute central pathology requiring urgent intervention. Symptom quality and acuity—specifically, constant and acute onset vertigo—along with abnormal neurological examination, are closely associated with acute central pathology and should guide selective imaging to optimize resource utilization and patient outcomes. These findings support the prioritization of bedside risk assessment and continued alignment with evidence-based imaging guidelines in the emergency setting.

References

1. Shah VP, Oliveira JS, Farah W, et al. Diagnostic accuracy of neuroimaging in emergency department patients with acute vertigo or dizziness: A systematic review and meta-analysis for the guidelines. Academic Emergency Medicine. 2023;30(5):517–530. doi:10.1111/acem.14561
2. Ohle R, Montpellier R,MarchadierV, et al. Can Emergency Physicians Accurately Rule Out a Central Cause of Vertigo Using the HINTS Examination? A Systematic Review and Meta-analysis. Academic Emergency Medicine. 2020;27(9):887–896. doi:10.1111/acem.13960
3. Wang LL, Thompson TA, Shih RY, et al. ACR Appropriateness Criteria Dizziness and Ataxia 2023 Update. Journal of the American College of Radiology. 2024;21(6S):100–125.doi:10.1016/j.jacr.2024.02.018
4. Edlow JA, Carpenter C, Akhter M, et al. Guidelines for reasonable andappropriate carein the emergency department 3 (GRACE-3): Acute dizziness and vertigo in the ED. Academic Emergency Medicine. 2023;30(5):442–486. doi:10.1111/acem.14728
5. Kerber KA, Brown DL, Lisabeth LD, Smith MA, Morgenstern LB. Stroke among patients with dizziness, vertigo, and imbalance in the emergency department: a population-based study. Stroke. 2006;37(10):2484–2487.doi:10.1161/01.STR.0000240329.48263.0d

Images/Tables

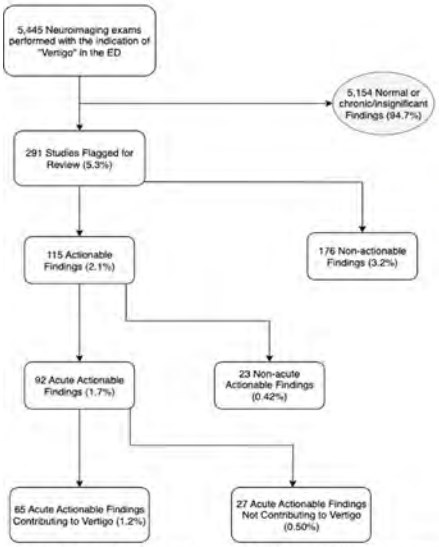

Figure 1: Study flowchart depicting selection and classification of 5,445 neuroimaging exams performed with the indication of vertigo in the emergency department. The diagram summarizes imaging modalities and outcomes, highlighting the proportion with actionable versus non-actionable findings.

	Number of Exams	% of Total Exams
Total Number of Exams	5,445	100
Exams Flagged for Review	291	5.3%
Total Actionable Findings	115	2.1%
Acute Actionable Findings	92	1.7%
Acute Contributory Findings	65	1.2%
Posterior fossa/vestibular cortex infarct	51	0.9%
Posterior fossa hemorrhage	5	0.09%
Posterior fossa neoplasm with mass effect	6	0.09%
Vertebral Artery Dissection	3	0.06%
Acute Non-contributory Findings	27	0.50%
Non-vertiginous infarct	16	0.29%
Non-vertiginous hemorrhage	7	0.13%
Active Demyelination/CJD/Neoplasm/Hydrocephalus	4	0.07%
Non-acute Actionable Findings	23	0.42%
Vertebrobasilar artery insufficiency	14	0.25%
Posterior fossa neoplasm without mass effect	1	0.02%
Vestibular/facial nerve schwannoma	2	0.04%
Labyrinthitis	2	0.04%
Inactive Demyelination/Susac Syndrome	3	0.06%
Semicircular canal dehiscence	1	0.02%
Non-actionable Findings	176	3.2%
BPPV/Peripheral Vertigo	100	1.8%
Orthostatic hypotension/vasovagal/nonspecific dizziness	34	0.62%
Other (unrelated hospital diagnosis)	42	0.77%

Table 1. Classification of exams flagged for review (N = 291), including breakdown of acute and non-acute actionable findings, and non-actionable diagnoses such as peripheral vertigo and unrelated hospital diagnoses.

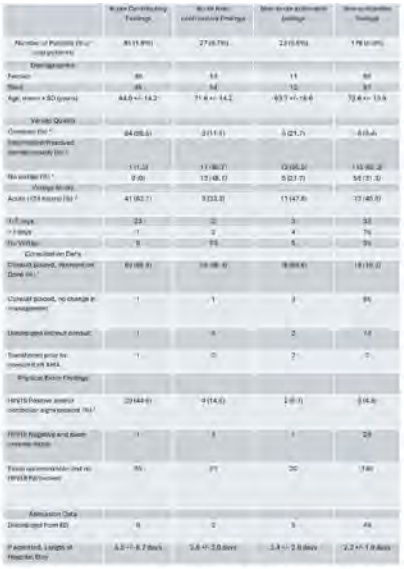

Table 2. Clinical comparison between groups of patients (total N = 4,135) with abnormal imaging findings based on vertigo relevance and acuity of imaging findings: acute contributory findings, acute non-contributory findings, non-acute actionable findings, and non-actionable findings. Includes demographic, clinical, physical exam, consultation, and admission data.

	Constant	Intermittent/Resolved Spontaneously	No Vertigo
Number of Patients (N = 291)	78	140	73
Demographics			
Female	36	81	32
Male	42	59	41
Age, mean ± SD (years)	65.1 +/- 14.1	72.1 +/- 13.8	70.7 +/- 15.8
Physical Exam Findings			
Abnormal HINTS and/or Cerebellar Signs [1]	33 (42.3%)	36 (25.7%)	5 (6.8%)
Unremarkable exam	45	104	68
Consultation Data			
Discharged without consult	3 (3.8%)	40 (28.6%)	34 (46.6%)
Consulted, no change in management	1	69	20
Consulted, intervention done [2]	74 (94.9%)	31 (22.1%)	19 (26.0%)
Diagnoses			
Acute Diagnoses [3]			
Acute/subacute infarct	55 (70.5%)	5 (3.6%)	8 (11.0%)
Intracranial Hemorrhage	5 (6.4%)	1 (0.7%)	2 (2.7%)
Intracranial Neoplasm/Cerebral Edema	8(10.3%)	2 (1.4%)	1(1.4%)
Vertebral artery dissection	2 (2.5%)	1 (0.7%)	0 (0%)
Non-Acute Diagnoses			
Demyelination	0	2	2
TIA/Hypertensive Urgency	3	17	4
BPPV/Peripheral Vertigo [4]	5 (6.4%)	95 (67.9%)	—
Non-vertigo Diagnosis	0	17	56

Table 3. Comparisons of patient characteristics and outcomes stratified by vertigo symptom quality: Constant, intermittent/resolved spontaneously, or no vertigo. Analyses include demographics, physical exam, consultation outcomes, and central versus peripheral etiologies.

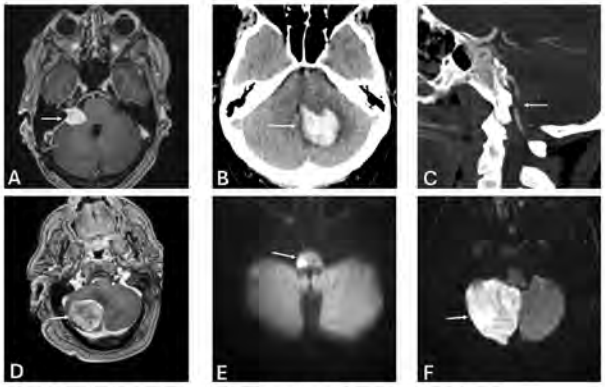

Figure 2: Neuroimaging examples of actionable pathologies detected in patients presenting with vertigo.
(A) Right-sided vestibular schwannoma (axial contrast-enhanced T1-weighted MRI);
(B) Left cerebellar intraparenchymal hemorrhage causing fourth ventricular compression (non-contrast CT);
(C) Occlusive thrombus in left vertebral artery V4 segment (sagittal CTA maximal intensity projection);
(D) Right cerebellar metastasis with mass effect (axial contrast-enhanced T1-weighted MRI);
(E) Right lateral medullary infarct (axial DWI MRI);
(F) Extensive right cerebellar infarct (axial DWI MRI)

Scientific Abstract Power Pitches & Luminary Speaker: Advanced Neuroimaging of Vascular, Traumatic, and Neurodegenerative Disorders

11:30am - 12:30pm Wednesday, 20th May, 2026

401 Leveraging Fluid-Sensitive Imaging to Evaluate Perivascular Spaces in Alzheimer's Disease

Arun Venkataraman MD, PhD, Manuel Taso PhD, Ilya M Nasrallah MD, PhD, Christopher A Brown MD, PhD
Hospital of the University of Pennsylvania, Philadelphia, PA, USA

Purpose

Amyloid-β deposition in the brain is a characteristic finding in Alzheimer's Disease (AD)[1]. Evidence suggests that amyloid-β may be cleared through a glial-lymphatic ("glymphatic") pathway along cerebral perivascular spaces (PVS). Enlarged PVS are considered a biomarker of dysfunctional PVS, thus potentially a measure of impaired clearance of amyloid-b in AD[2,3]. MRI methods have been developed to leverage anatomical imaging to segment PVS[4]; however, imaging methodologies have not been designed specifically to evaluate PVS. In this study, we test a high-resolution fluid-sensitive MRI sequence to segment PVS and evaluate its utility in AD.

Materials & Methods

High-resolution volumetric T1 MPRAGE and T2 images were collected on clinically diagnosed patients with Mild Cognitive Impairment (MCI) or Dementia due to Alzheimer's disease (AD) and cognitively unimpaired (CU) older adults. The T2 sequence was modified with a longer echo time (TE = 792 ms) to suppress background tissue signal and increase the contrast of fluid in the brain.

MRI data was then processed through a pipeline similar to Sepherband et al.[4], with some modifications. Briefly, the T1 and T2 images were preprocessed and registered to MNI space. A T1 by T2 quotient image was then calculated. PVS were segmented and using FreeSurfer parcellation with the Desikan-Killiany atlas. PVS data was segmented by lobe. Metrics extracted included PVS volume, PVS count, and average PVS volume (PVS volume/PVS count).

Results

A total of 21 subjects with AD (MCI or Dementia) and 37 CU were included for analysis. We found no statistically significant changes in the total PVS volume in any of the lobes (Figure 1). However, there was a nonsignificant trend of increasing PVS volume in the AD cohort in the parietal and temporal lobes. Figure 2 shows results of average PVS volume, which was increased in the frontal and parietal lobes in AD compared to CU (p=0.03 for both).

Conclusion

We found significant group-wise differences in metrics extracted from our PVS segmentation method. Despite a small sample size, there were statistically significant differences of the average PVS volume between CU older adults and individuals with MCI or dementia due to AD in the frontal and parietal lobes. This study suggests that average PVS volume may be a more sensitive biomarker of AD compared to overall PVS volume. Average PVS may be elevated due to distended PVS becoming confluent, resulting in fewer overall PVS with slightly increased overall volume. This study was limited by the sample size. Future directions include evaluating AD patients receiving anti-amyloid therapy to assess the impact of therapy on PVS and how PVS change in patients with amyloid-related imaging abnormalities.

References

1. Kinney, Jefferson W., et al. "Inflammation as a central mechanism in Alzheimer's disease." Alzheimer's & Dementia: Translational Research & Clinical Interventions 4 (2018): 575-590.
2. Mestre, H., Mori, Y., and Nedergaard, M. (2020). The brain's glymphatic system: Current controversies. Trends Neurosci. 43, 458–466. doi: 10.1016/j.tins.2020.04.003
3. Lynch, Miranda, et al. "Perivascular spaces as a potential biomarker of Alzheimer's disease." Frontiers in neuroscience 16 (2022): 1021131.
4. Sepehrband, Farshid, et al. "Image processing approaches to enhance perivascular space visibility and quantification using MRI." Scientific reports 9.1 (2019): 12351.

Images/Tables

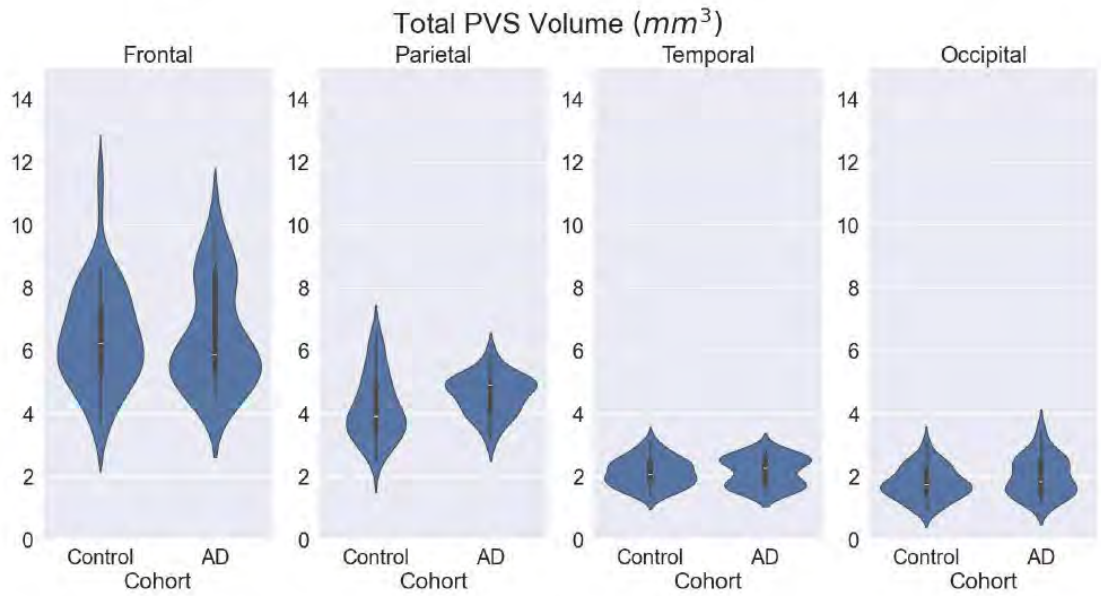

Figure 1. Violin plots of total lobar PVS volume comparing CU (control) and AD cohorts.

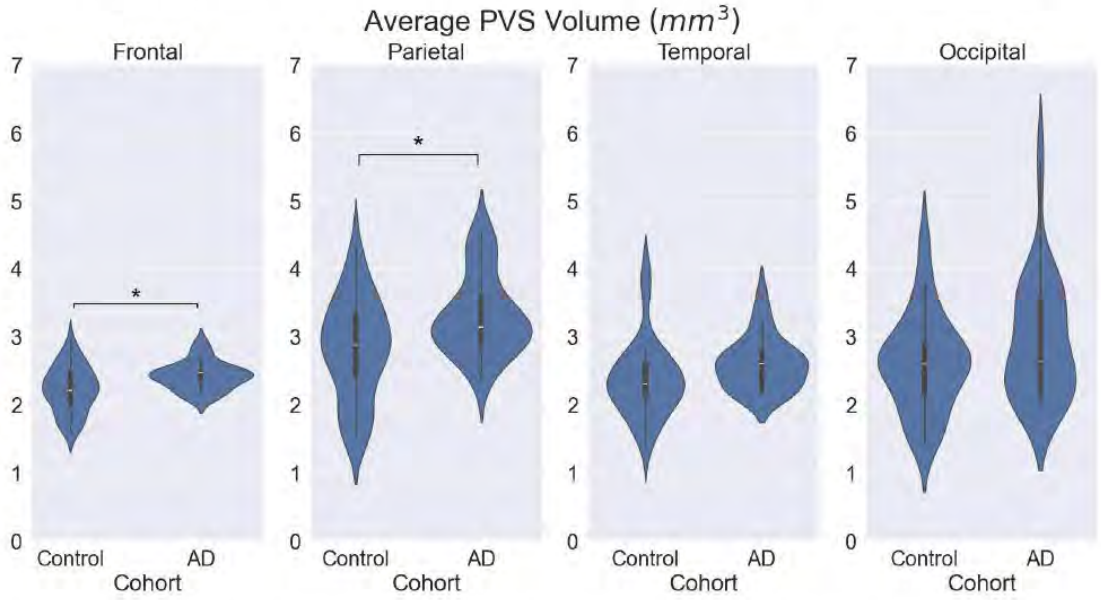

Figure 2. Violin plots of average PVS volume between CU (control) and AD groups.

659 Quantitative MRI of Blood-Brain-Barrier Permeability to Water in Alzheimer's Disease Continuum: WEPCAST in relation to Amyloid PET

Behnaz Khazai MD[1], Wen Shi[2], Bashar Kako[1], Hanzhang Lu[2], Jeremy Ford MD[1]
[1]Massachusetts General Hospital, Boston, MA, USA. [2]Johns Hopkins, Baltimore, MD, USA

Purpose

Blood brain barrier (BBB) integrity has been shown to play a role in various pathologies including Alzheimer's disease (AD), the most common type of dementia. While various imaging markers of BBB permeability have been promising, yet discrepancies in findings point out presence of gaps in our knowledge. We question whether the measures derived from different methods highlight different pathophysiological processes. This study focuses on quantifying BBB permeability to water derived from WEPCAST (Water Extraction with Phase Contrast Arterial Spin Tagging) in healthy controls and AD continuum (mild cognitive impairment (MCI) and AD) and in correlation with cognitive performance and Amyloid PET.

Materials & Methods

A total of 54 subjects were enrolled for the study: 37 subjects with suspected cognitive impairment and 17 age matched healthy controls. Cardiovascular risk factors were defined as hypertension, diabetes type 2, and history of tobacco smoking. Cognitive performance was evaluated using Clinical Dementia Rating (CDR) and Montreal Cognitive assessment— (MoCA). Subjects had amyloid PET using ^{18}F Florbetaben PET and Centiloid scores were obtained. MR imaging was performed with focus on WEPCAST to measure permeability surface area product of water (PS_w) based on water extraction fraction. A total of 39 subjects were included in the final analysis: 26 subjects on AD continuum (MCI-AD) with CDR of 0.5-1 and positive p-tau217 and/or amyloid PET (8 had CDR of 1 (AD) and 18 had CDR of 0.5 (MCI)); and 13 subjects with CDR of 0 and negative p-tau217 and amyloid PET (healthy controls—HC). Image processing and statistical analysis were performed using MATLAB R2025 and Python 3.8.10.

Results

PS_w and Centiloid score had non-normal distributions on Shapiro-Wilk test (P: 0.022 and 0.026) therefore nonparametric statistics were applied to be consistent across the analyses. There was a positive correlation between PS_w and Centiloid score across HC, MCI and AD (Spearman $\rho = +0.395$, $P = 0.015$). PS_w had a negative correlation with MoCA score across HC, MCI and AD (Spearman $\rho = -0.461$, $P = 0.003$). PS_w was significantly different between HC and AD continuum (MCI-AD) on Mann-Whitney test with a median of 114.5 ml/min in HC and a median of 144.1 ml/min in MCI-AD ($p = 0.003$, $U = 70.0$).

Conclusion

The demonstrated positive correlation between WEPCAST-derived measure of BBB permeability to water (PS_w) and Centiloid score which is supported on the clinical grounds by the notable negative correlation of PS_w and MoCA score is in line with the previous literature on BBB dysfunction in AD. Findings suggest potential application of PS_w as a quantitative imaging marker correlating with amyloid burden and clinical severity in AD continuum.

References

1. *Lin Z, Li Y, Su P, et al. Non-contrast MR imaging of blood-brain barrier permeability to water. Magn Reson Med. 2018;80(4). doi:10.1002/mrm.27141*
2. *Lin Z, Jiang D, Liu D, et al. Noncontrast assessment of blood–brain barrier permeability to water: Shorter acquisition, test–retest reproducibility, and comparison with contrast-based method. Magn Reson Med. 2021;86(1). doi:10.1002/mrm.28687*
3. *Lin Z, Sur S, Liu P, et al. Blood–Brain Barrier Breakdown in Relationship to Alzheimer and Vascular Disease. Ann Neurol. 2021;90(2). doi:10.1002/ana.26134*
4. *Ford JN, Zhang Q, Sweeney EM, et al. Quantitative Water Permeability Mapping of Blood-Brain-Barrier Dysfunction in Aging. Front Aging Neurosci. 2022;14. doi:10.3389/fnagi.2022.867452*

Images/Tables

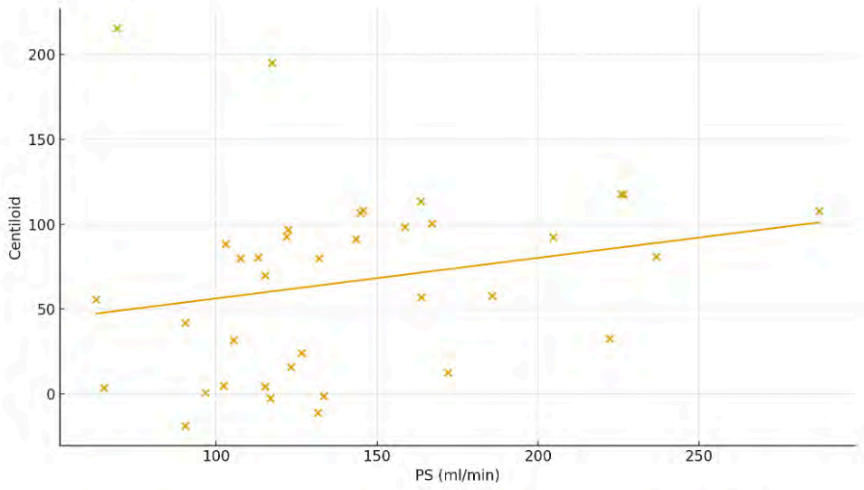

Figure 1 Centiloid score correlation with PS_w (permeability surface area product of water)

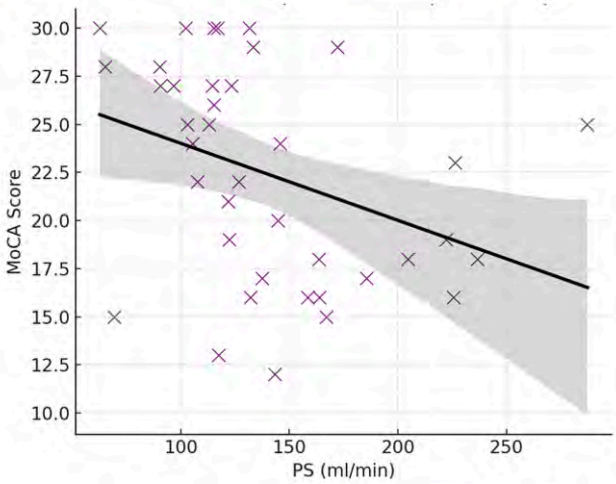

Figure 2 MoCA (Montreal cognitive assessment) score correlation with PS_w (permeability surface area product of water)

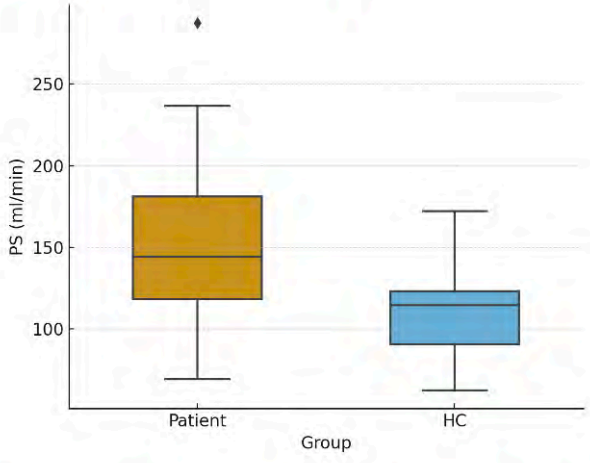

Figure 3 PS_w (permeability surface area product of water) in healthy controls (HC) vs patients on the MCI-AD continuum

463 Frequency-Dependent Neural Activation During Subthalamic Nucleus Deep Brain Stimulation in Parkinson's Disease

Garene A Matossian MSc[1], Brendan Santyr MD, PhD[1], Jianwei Qiu[2], Afis Ajala PhD[2], Jürgen Germann PhD[1], Alfonso Fasano MD, PhD[1], Andres M Lozano MD, PhD[1], Alexandre Boutet MD, PhD[1]

[1]Toronto Western Hospital, Toronto, Ontario, Canada. [2]GE HealthCare Technology and Innovation Center, Niskayuna, New York, USA

Purpose

Deep brain stimulation (DBS) of the subthalamic nucleus (STN) is an established treatment for the motor symptoms of Parkinson's disease (PD)[1]. The therapeutic effects of DBS depend, in part, on stimulation frequency. Stimulation frequency may be adjusted to achieve optimal outcomes: low-frequency stimulation (LFS; 60–80 Hz) has been linked to gait improvement[2], whereas high-frequency stimulation (HFS; >100 Hz) more effectively alleviates tremor[3]. However, the broader neural networks engaged by different frequencies remain poorly understood. Previous work by our group identified a stereotypical fMRI activation pattern associated with optimized outcomes in STN-DBS[4]. The present study tested whether this pattern is preserved across frequencies under clinically optimal settings and whether distinct regions are differentially engaged by LFS and HFS.

Materials & Methods

Eleven participants were prospectively recruited, including four who achieved optimal symptom control with LFS and seven with HFS during standard-of-care programming[5]. Functional MRI (fMRI) was acquired as DBS was delivered in a block design (30 s ON/30 s OFF; total 6.5 min) at 60 Hz and 180 Hz for each participant. Stimulation amplitude was adjusted to maintain equivalent total electrical energy delivered (TEED) across frequencies, and TEED was entered as a covariate of no interest at the group level. fMRI activation patterns were compared between (1) optimal HFS vs. LFS, (2) optimal vs. non-optimal HFS, and (3) optimal vs. non-optimal LFS.

Results

The optimal HFS > LFS revealed significant activation in the left motor cortex, right superior parietal lobule, and bilateral occipital cortices (lingual gyrus and cuneus; $p < 0.001$ uncorrected; Figure 1), indicating frequency-dependent recruitment of motor and posterior cortical networks during high-frequency stimulation. The optimal > non-optimal HFS showed activation in the right occipital cortex, bilateral superior parietal lobules, left sensorimotor cortex, and cerebellar hemispheres ($p < 0.001$ uncorrected; Figure 2). No significant clusters were observed for optimal > non-optimal LFS at this threshold.

Conclusion

These results demonstrate that stimulation frequency and parameter optimization shape cortical recruitment during STN-DBS. Compared with LFS, HFS elicited broader activation encompassing posterior parietal, occipital, cerebellar, and motor regions, extending prior work emphasizing subcortical and motor effects[3,4]. Within HFS, optimal stimulation further enhanced activation across these regions, suggesting that effective settings engage a more integrated visuomotor–cerebellar network. The absence of significant clusters for optimal vs. non-optimal LFS may indicate more localized cortical effects at lower frequencies.

The overlap between optimal stimulation patterns and our previously described "optimal network"[4], including parietal, cerebellar, and medial frontal regions, supports the concept of a distributed therapeutic circuit modulated by frequency and clinical state. Together, these findings highlight that STN-DBS influences widespread cortical and subcortical systems rather than isolated sites. Future connectivity-based analyses may clarify how frequency-dependent network recruitment contributes to distinct clinical outcomes and guide individualized DBS programming.

References

1. Hariz M, Blomstedt P. Deep brain stimulation for Parkinson's disease. *J Intern Med*. 2022;292(5):764-778. doi:10.1111/joim.13541

2. Tortato NCB, Ribas G, Frizon LA, Farah M, Teive HAG, Munhoz RP. Efficacy of subthalamic deep brain stimulation programming strategies for gait disorders in Parkinson's disease: a systematic review and meta-analysis. *Neurosurg Rev*. 2024;47(1):525. doi:10.1007/s10143-024-02761-x

3. Dayal V, Limousin P, Foltynie T. Subthalamic Nucleus Deep Brain Stimulation in Parkinson's Disease: The Effect of Varying Stimulation Parameters. *J Park Dis*. 2017;7(2):235-245. doi:10.3233/JPD-171077

4. Boutet A, Madhavan R, Elias GJB, et al. Predicting optimal deep brain stimulation parameters for Parkinson's disease using functional MRI and machine learning. *Nat Commun*. 2021;12(1):3043. doi:10.1038/s41467-021-23311-9

5. Picillo M, Lozano AM, Kou N, Puppi Munhoz R, Fasano A. Programming Deep Brain Stimulation for Parkinson's Disease: The Toronto Western Hospital Algorithms. *Brain Stimulat*. 2016;9(3):425-437. doi:10.1016/j.brs.2016.02.004

Images/Tables

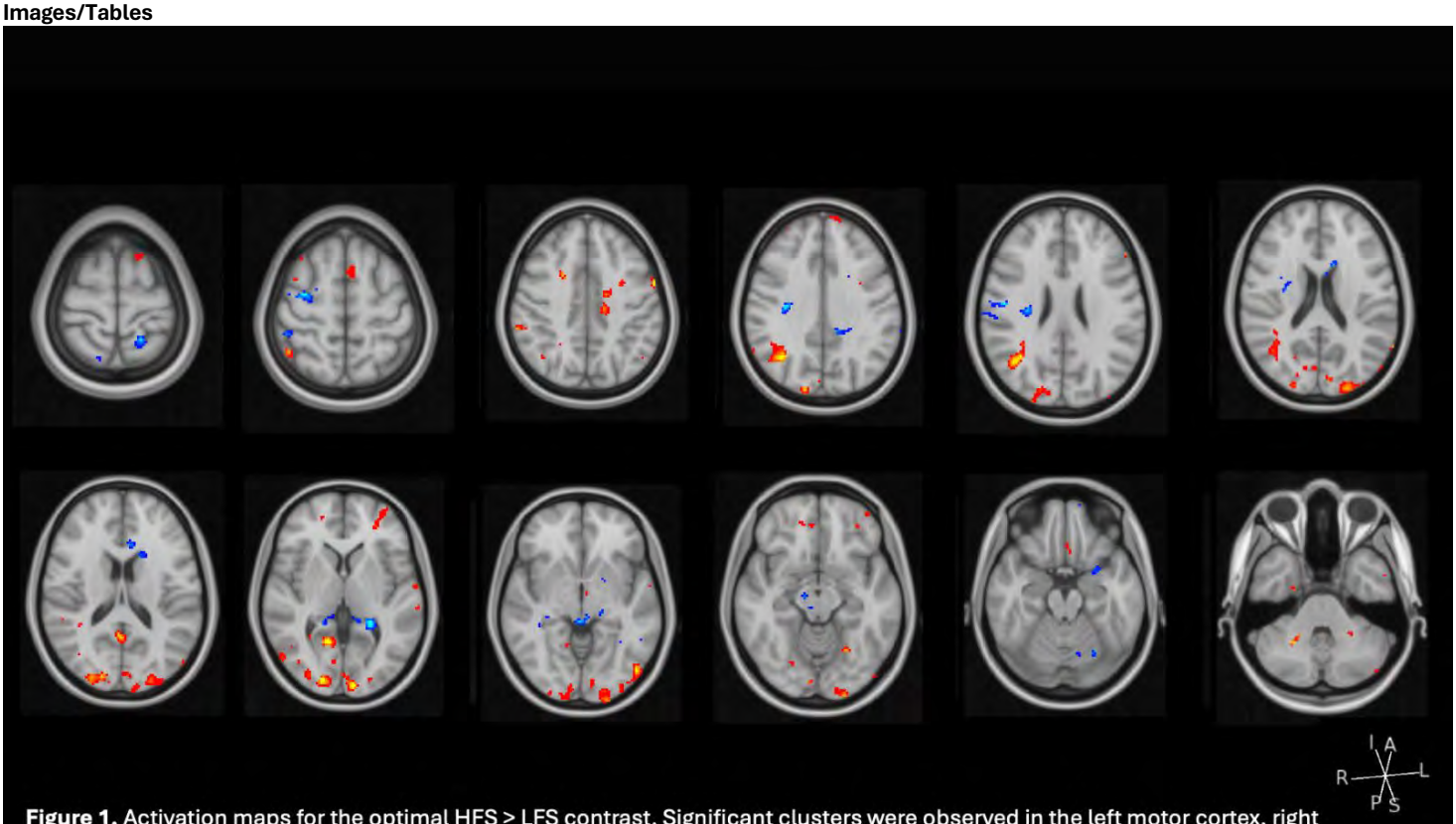

Figure 1. Activation maps for the optimal HFS > LFS contrast. Significant clusters were observed in the left motor cortex, right superior parietal lobule, and bilateral occipital cortices (lingual gyrus and cuneus). Statistical threshold: t = 2-4.5, p > 0.001, (uncorrected)

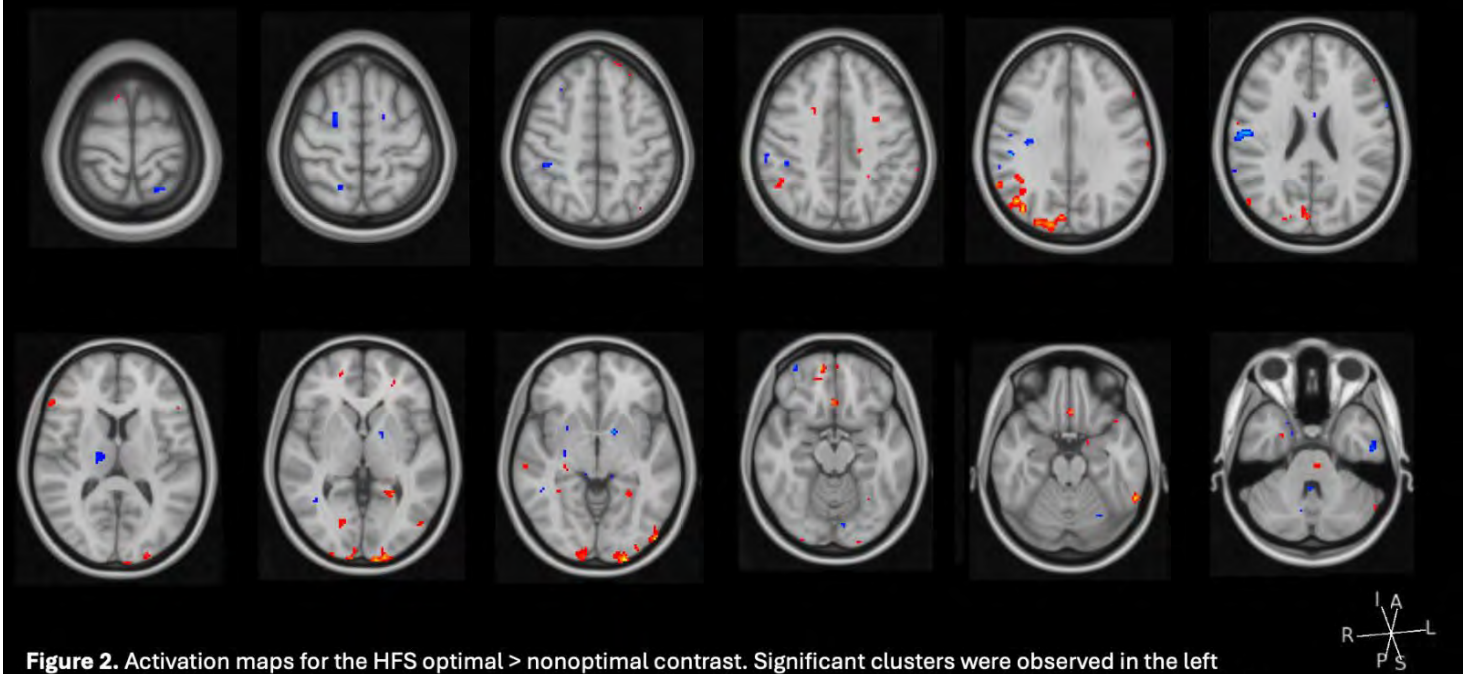

Figure 2. Activation maps for the HFS optimal > nonoptimal contrast. Significant clusters were observed in the left sensorimotor cortex, parietal and occipital association areas, and cerebellar hemispheres. Statistical threshold: $t = 2–4.5$, $p < 0.001$ (uncorrected).

715 Association of choroid plexus volume with brain atrophy and glucose metabolism in multiple system atrophy

CHAE JUNG Park MD, PhD
Yongin Severance hospital, Seoul, Seoul, Korea, Republic of

Purpose

The choroid plexus (CP), a component of the glymphatic system, is essential in maintaining homeostasis and producing cerebrospinal fluid. Although previous studies have reported associations between CP and neurodegenerative diseases, its role in multiple system atrophy (MSA) remains unclear. This study aimed to investigate the implication of the CP in patients with MSA.

Materials & Methods

This retrospective cross-sectional study searched MSA patients who underwent Unified MSA Rating Scale (UMSARS), brain MRI, and ^{18}F-FDG PET scan, along with 84 healthy controls (HCs). Multivariate linear regression analyses were performed to examine the associations between CP volume (CPV) and UMSARS scores, as well as the volumes and regional cerebral metabolism of subcortical structures.

Results

: A total of 87 patients with MSA (39 with the parkinsonian subtype [MSA-P] and 48 with the cerebellar subtype [MSA-C]) (mean age, 60.6 ± 8.8 [standard deviation]; 43 men) were evaluated. Compared with HCs, patients with MSA had significantly reduced CPV (1.00 ± 0.27 vs. 1.30 ± 0.26, $P <$ 0.001). CPV showed no association with UMSARS scores, however, it was positively correlated with regional cerebellar volumes. Smaller CPV was also associated with decreased cerebral metabolism in MSA-susceptible regions. Notably, CPV positively correlated with glucose metabolism in the brainstem (β = 0.110, P = 0.003) and cerebellar white matter (β = 0.080, P = 0.004).

Conclusion

This study suggests that choroid plexus volume is positively associated with disease burden in multiple system atrophy, with choroid plexus volume decreasing as disease severity increases. Further research is warranted to determine whether choroid plexus volume could serve as a potential biomarker for multiple system atrophy.

References

1. Kratzer I, Ek J, Stolp H. **The molecular anatomy and functions of the choroid plexus in healthy and diseased brain**. *Biochim Biophys Acta Biomembr* 2020;1862:183430
2. Harrison IF, Ismail O, Machhada A, et al. **Impaired glymphatic function and clearance of tau in an Alzheimer's disease model**. *Brain* 2020;143:2576–93
3. Liu L, Weng Q, Cai Q, et al. **Choroid plexus enlargement contributes to motor severity via regional glymphatic dysfunction in Parkinson's disease**. *NPJ Parkinsons Dis* 2025;11:134
4. Shi C, Guo G, Wang W, et al. **Impaired glymphatic clearance in multiple system atrophy: A diffusion spectrum imaging study**. *Parkinsonism Relat Disord* 2024;123:106950

Images/Tables

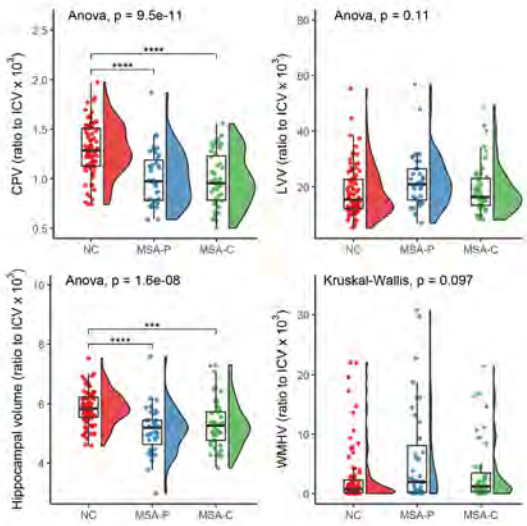

Figure 1. Rain-cloud plots of MR volumetric imaging markers, including CPV, LVV, hippocampal volume, and WMHV in the HC, MSA-P, and MSA-C groups

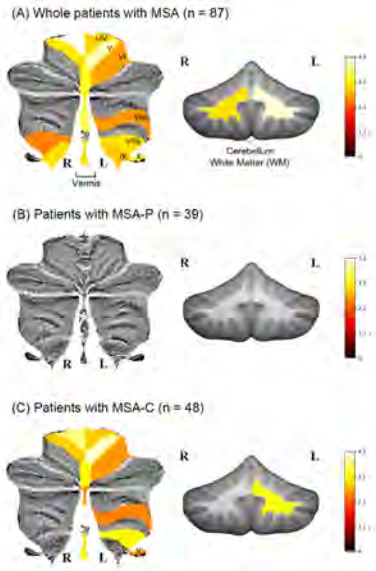

Figure 2. Relationship between CPV and cerebellar brain volumes. Regions showing a significant association between CPV and regional cerebellar volume are visualized on a cerebellar heatmap template, with color indicating t-values derived from a multivariate linear regression model in (A) all patients with MSA, (B) patients with MSA-P, and (C) patients with MSA-C.

1006 Multimodal Non-Contrast MRI in Midlife Adults: Relationships with Neurodegeneration from ASL-Derived CBF, Cortical Thickness, and Thigh FMR

Mahshid Naghashzadeh MSc, Paul Commean, Mahsa Dolatshahi, LaKisha Lloyd, Soheil Mohammadi, Mobina Amanollahi, Mona Mirbeyk, Bettina Mittendorfer, Tammie L.S Benzinger1, Hongyu An, Cyrus A Raji
Washington University in St. Louis, St. Louis, Missouri, USA

Purpose

Midlife obesity is linked to neuroinflammation, vascular dysfunction, and metabolic dysregulation, yet the contribution of body fat distribution—beyond BMI—to neurodegeneration remains under explored. This study examines, in cognitively normal midlife adults, whether thigh body composition measured with Dixon MRI (fat and muscle volumes summarized as fat-to-muscle ratio, FMR) relates to arterial spin labeling (ASL)–derived cerebral blood flow (CBF) and MRI-based cortical thickness, including regions vulnerable to Alzheimer's disease. By testing relationships among body composition, metabolic status, and multimodal neuroimaging measures, we assess links between midlife adiposity patterns and AD-relevant structural and perfusion alteration.

Materials & Methods

We studied 104 cognitively normal midlife adults (49.8 ± 6.0 y; 65% female; 55% obese; BMI 32.0 ± 7.3). Cognitive status was screened with MMSE. All imaging was acquired on Siemens 3T scanners. Brain MRI included pCASL for absolute CBF maps (SPM12 single-compartment model, M0-normalized) and T1-weighted imaging for cortical thickness (FreeSurfer v7.1.1 with manual QC). Thigh composition was measured with VIBE Dixon; nine mid-thigh slices were selected reproducibly, N4ITK bias correction applied, and an in-house MATLAB pipeline segmented subcutaneous, intermuscular, and intramuscular fat and muscle to compute the fat-to-muscle ratio (FMR = total fat volume ÷ muscle volume). Amyloid ($[^{11}C]$PiB) and tau (AV-1451) PET SUVRs were computed with the PET Unified Pipeline using a cerebellar reference and region-based partial-volume correction. Whole-brain and AD-vulnerable regional CBF, cortical thickness, and PET measures were related to FMR, BMI, and HOMA-IR using age/sex-adjusted Spearman partial correlations with Benjamini–Hochberg FDR control ($q<0.05$). Analyses were performed in MATLAB/SPM12 and R (v4.4.2).

Results

Individuals with obesity showed higher BMI (36.6 ± 4.9 vs 25.6 ± 4.1), higher HOMA-IR (4.8 ± 3.8 vs 2.2 ± 2.2), lower HDL (50.7 ± 12.8 vs 63.5 ± 16.6), higher cholesterol/HDL ratio (3.76 ± 1.16 vs 3.09 ± 1.07), and higher amyloid centiloids (−0.4 ± 8.9 vs −4.4 ± 7.0; all $p \le 0.027$). Thigh composition also differed (greater total fat, total muscle, and FMR in obesity; all $p < 0.001$). In age/sex-adjusted partial Spearman analyses with FDR control, higher FMR was associated with thinner cortex in AD-vulnerable regions, including left middle temporal, left precuneus, left temporal pole, left transverse temporal, and right middle temporal, temporal pole, lateral occipital, superior/inferior parietal, supramarginal, and precuneus (all $q \le 0.017$). Perfusion analyses showed that higher BMI was linked to lower whole-brain aCBF ($\rho=-0.24$, $q=0.014$) and reduced regional CBF across limbic/default-mode nodes (amygdala, hippocampus, posterior cingulate, precuneus; all $q < 0.05$). Total fat and total muscle volumes showed weaker, region-limited inverse CBF associations, whereas FMR was not significantly related to global or regional CBF. Amyloid measures were not significantly correlated with FMR, BMI, or other thigh metrics.

Conclusion

This study shows that an unfavorable thigh composition links with thinner cortex in AD-vulnerable temporal and parietal regions, while greater absolute adiposity (BMI/total fat) is accompanied by widespread reductions in ASL-derived cerebral blood flow, in the absence of amyloid associations. Together, these patterns point to early, potentially modifiable links between peripheral body composition, metabolic status, and AD-relevant structural and perfusion vulnerability in midlife.

References

1. Dolatshahi, M. Alzheimer Disease Pathology and Neurodegeneration in Midlife Obesity: A Pilot Study. *Aging Dis.* (2024) doi:10.14336/AD.2023.0707.
2. Dolatshahi, M. *et al.* Relationships between abdominal adipose tissue and neuroinflammation with diffusion basis spectrum imaging in midlife obesity. *Obesity* **33**, 41–53 (2025).
3. Dincer, A. *et al.* Comparing cortical signatures of atrophy between late-onset and autosomal dominant Alzheimer disease. *NeuroImage Clin.* **28**, 102491 (2020).
4. Su, Y. *et al.* Quantitative Analysis of PiB-PET with FreeSurfer ROIs. *PLoS ONE* **8**, e73377 (2013).
5. Swinford, C. G. *et al.* Altered cerebral blood flow in older adults with Alzheimer's disease: a systematic review. *Brain Imaging Behav.* **17**, 223–256 (2023).

Images/Tables

Figure 1. Segmentation pipeline for muscle and adipose tissue analysis. **A** The yellow line denotes the distance from the bottom of the ischial ramus to the center of the medial knee condyle, serving as a reference for mid-thigh slice selection. **B** First of the nine selected mid-thigh Dixon fat slices prior to inhomogeneity correction. **C** The same slice after inhomogeneity correction using the N4ITK method with a spline value of 100. **D** Subcutaneous fat mask. **E** Muscle compartment mask. **F** Inhomogeneity corrected Dixon water image. **G** Segmented muscle compartment mask with muscle boundaries following automatic removal of the subcutaneous with connected intermuscular adipose tissue. **H** Muscle compartment mask segmentation of intramuscular fat (green) and intermuscular fat (green) inside muscle mask (red). **I** Final segmentation mask integrating bone (blue), muscle (red), intermuscular and intramuscular fat (green), and subcutaneous fat (yellow).

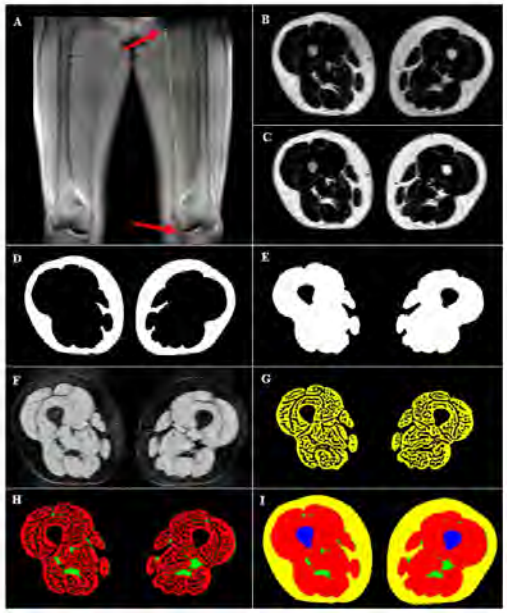

Figure 2. Brain regions negatively associated with fat-to-muscle ratio (FMR) in late-onset Alzheimer's disease (LOAD). **A** Left hemisphere regions include the middle temporal gyrus, precuneus, temporal pole, and transverse temporal gyrus. **B** Right hemisphere regions include the fusiform gyrus, temporal pole, inferior temporal gyrus, lateral occipital cortex, superior parietal lobule, inferior parietal lobule, and precuneus.

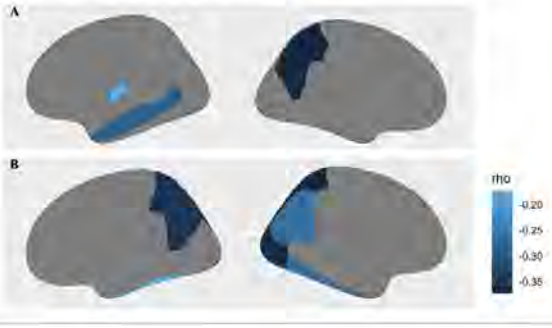

Table 1. Demographic and clinical characteristics of study participants stratified by obesity status. Continuous variables are presented as mean (standard deviation), and categorical variables as n (%).

Variable	Group	Non-Obese (N = 47)	Obese (N = 57)	p-value
Sex	Male	16 (34)	20 (35.1)	N/A
	Female	31 (66)	37 (64.9)	N/A
Age		48.64 (5.91)	50.89 (6.12)	0.06
BMI		25.60 (4.10)	36.63 (4.86)	<0.001
Total Cholesterol (mg/dL)		182.98 (33.95)	182.00 (36.34)	0.894
Triglycerides (mg/dL)		88.91 (52.94)	105.59 (49.70)	0.121
HDL Cholesterol (mg/dL)		63.45 (16.58)	50.67 (12.76)	<0.001
LDL Cholesterol (mg/dL)		101.70 (28.79)	110.33 (35.16)	0.186
Non-HDL Cholesterol (mg/dL)		119.18 (32.32)	131.33 (35.97)	0.092
Cholesterol/HDL Ratio		3.09 (1.07)	3.76 (1.16)	0.005
HOMA-IR (Insulin Resistance)		2.20 (2.22)	8.78 (5.84)	<0.001
Amyloid Centiloid Score		-4.42 (6.99)	-0.42 (8.85)	0.027
Total Muscle Volume (cm^3)		634.14 (146.67)	784.25 (202.42)	<0.001
Total Fat Volume (cm^3)		525.00 (241.84)	944.03 (443.01)	<0.001
Fat-to-Muscle Ratio		0.86 (0.41)	1.36 (0.86)	<0.001

Table 2: Association between Cortical Thicknesses in 22 LOAD Brain Regions with FMR

Brain Hemisphere	Brain Region	Spearman's Rho	Adjusted p-value
Left	Banks of the Superior Temporal Sulcus	-0.1214	0.0840
	Entorhinal	0.0951	0.6781
	Middle Temporal	-0.2651	0.0032
	Medial Orbitofrontal	-0.0769	0.2017
	Precuneus	-0.2383	0.0060
	Superior Temporal	-0.1483	0.0515
	Temporal Pole	-0.1653	0.0343
	Transverse Temporal	-0.3131	0.0008
Right	Entorhinal	-0.0527	0.3015
	Banks of the Superior Temporal Sulcus	-0.1361	0.0662
	Middle Temporal	-0.1696	0.0338
	Fusiform	-0.1323	0.0681
	Temporal Pole	-0.2151	0.0090
	Inferior Temporal	-0.1134	0.0958
	Lateral Occipital	-0.2295	0.0069
	Parahippocampal	-0.0218	0.4717
	Posterior Cingulate	0.1084	0.6054
	Superior Parietal	-0.2544	0.0038
	Supramarginal	-0.1935	0.0170
	Inferior Parietal	-0.2198	0.0086
	Precuneus	-0.3044	0.0008

Table 3. Associations between body composition measures and cerebral perfusion across limbic and default mode network regions.

Brain Region	BMI (ρ, p-adj)	Total Fat (ρ, p-adj)	Total Muscle (ρ, p-adj)	FMR (ρ, p-adj)
Amygdala (L)	−0.281, 0.012	−0.186, 0.032	−0.241, 0.014	−0.067, 0.233
Amygdala (R)	−0.210, 0.022	−0.165, 0.047	−0.152, 0.057	−0.079, 0.197
Precuneus (L)	−0.178, 0.036	−0.090, 0.167	−0.227, 0.017	0.023, 1.000
Precuneus (R)	−0.167, 0.047	−0.048, 0.296	−0.202, 0.025	0.061, 1.000
Hippocampus (L)	−0.271, 0.012	−0.181, 0.034	−0.159, 0.049	−0.094, 0.158
Hippocampus (R)	−0.221, 0.020	−0.145, 0.065	−0.110, 0.117	−0.073, 0.213
Middle Temporal (L)	−0.273, 0.012	−0.191, 0.029	−0.252, 0.013	−0.075, 0.209
Middle Temporal (R)	−0.249, 0.013	−0.149, 0.061	−0.196, 0.026	−0.038, 0.337
Posterior Cingulate (L)	−0.279, 0.012	−0.163, 0.047	−0.246, 0.013	−0.049, 0.296
Posterior Cingulate (R)	−0.259, 0.013	−0.098, 0.147	−0.195, 0.026	0.002, 1.000
Whole-brain aCBF	−0.240, 0.014	−0.134, 0.079	−0.197, 0.026	−0.028, 0.386

1058 Substantia Nigra Neuromelanin Volume Loss and Its Relation to Motor Features in Early Parkinson's Disease Using Semi-Automated Neuromelanin MRI Quantification

Arturs Silovs
Riga Stradins University, Riga, Latvia, Latvia

Purpose

The hallmark of Parkinson's disease (PD) is progressive loss of dopaminergic neurons in the substantia nigra pars compacta (SNpc). Neuromelanin-sensitive MRI (NM-MRI) offers a non-invasive way to quantify neuromelanin (NM) in vivo, potentially serving as a biomarker of neuronal integrity. We aimed to (1) quantify SNpc NM volume in early-stage PD using a semi-automated segmentation workflow, (2) compare corrected NM volumes between PD patients and healthy controls, and (3) explore associations between NM volume, motor severity and disease stage.

Materials & Methods

In a prospective case-control design, 68 participants were recruited; after exclusion for motion artefacts, 64 subjects remained (32 PD patients, mean age 64.9 ± 12.3 yrs; 32 healthy controls, mean age 50.8 ± 11.1 yrs). Imaging was performed on a 3 T scanner using a high-resolution T1-weighted spin-echo NM-MRI sequence. Semi-automated segmentation of SNpc NM volume was performed using Mango v3.5.1, and intracranial volume correction applied via FreeSurfer v7.3. Clinical assessment included the Unified Parkinson's Disease Rating Scale part III (UPDRS-III) and Hoehn & Yahr (H&Y)

staging. Statistical analyses comprised independent-samples t-test and Mann–Whitney U for group comparisons, receiver-operating characteristic (ROC) analysis for diagnostic performance, and intraclass correlation coefficient (ICC) to assess segmentation reliability.

Results

Corrected SNpc NM volume was significantly lower in PD patients (0.0276 ± 0.0058 mm^3) compared to controls (0.0337 ± 0.0102 mm^3), representing ~18 % reduction (p = 0.014, t-test; p = 0.039, Mann-Whitney U). ROC analysis yielded an area under the curve (AUC) of 0.700, with sensitivity 68.4 % and specificity 74.1 % for differentiating PD from controls. A progressive reduction in NM volume was observed across H&Y disease stages: stage 1 (0.0285 ± 0.0054 mm^3) and stage 2 (0.0279 ± 0.0064 mm^3), both significantly lower than controls ($p < 0.05$). No significant correlation emerged between corrected NM volume and UPDRS-III motor scores. The semi-automated segmentation method demonstrated excellent agreement with manual measurement (ICC = 0.945).

Conclusion

Semi-automated NM-MRI reliably detects SNpc neuromelanin volume loss in early-stage Parkinson's disease with moderate diagnostic accuracy. While NM volume did not significantly correlate with motor severity (UPDRS-III), it did reflect disease stage, supporting its potential as a non-invasive biomarker for early PD diagnosis, stratification and monitoring. Longitudinal studies with age-matched cohorts are warranted to establish the temporal dynamics and prognostic value of NM volume decline.

References

1. Sulzer D, Cassidy C, Horga G, et al. Neuromelanin detection by magnetic resonance imaging (MRI) and its promise as a biomarker for Parkinson's disease. *Brain*. 2018;141(8):1996-2017.

---

549 Regional Post-Contrast T1 Alterations in the Choroid Plexus, Perivascular Space, and Cortex in Parkinson's Disease and Essential Tremor

Yangsean Choi MD

Department of Radiology, Asan Medical Center, Seoul, Seoul, Korea, Republic of

Purpose

To quantitatively assess post-contrast T1 changes (ΔT1) in the brain and choroid plexus (CP) among patients with idiopathic Parkinson's disease (IPD) and essential tremor (ET).

Materials & Methods

This retrospective, single-center cohort study recruited patients who underwent brain MRI for suspected movement disorders between November 2023 and February 2025. Patients were classified into three groups: ET (n=109), early IPD (n=81), and advanced IPD (n=87). Post-contrast ΔT1 was calculated by subtracting pre-contrast from post-contrast T1 values. Post-contrast ΔT1 of CP, basal ganglia perivascular space, cerebral cortex, cerebellar cortex, and thalamus were assessed and compared among groups via one-way analysis of variance.

Results

The study included 277 patients: 109 with ET (mean age, 67 ± 10 years; 70 female), 81 with early IPD (mean age, 69 ± 10 years; 42 female), and 87 with advanced IPD (mean age, 70 ± 10 years; 43 female). Mean post-contrast ΔT1 of CP in advanced IPD (–902.2 ± 106.7 ms) was significantly shortened compared to that in ET (–859.6 ± 116.9 ms; p =.02). However, patients with advanced IPD demonstrated significantly prolonged mean post-contrast ΔT1 of cerebellar cortex (–167 ± 24.6 ms) and thalamus (–86.5 ± 12.5 ms) compared to those of ET (–175.7 ± 24.7 ms; p =.03 and –91.5 ± 13.8 ms; p =.02, respectively).

Conclusion

Advanced IPD demonstrated significantly greater post-contrast T1 shortening in the CP and reduced T1 shortening in the cerebellar cortex and thalamus compared with ET. These regional differences in contrast distribution may reflect disease-related alterations in cerebrospinal fluid dynamics and microvascular exchange.

References

1. Klostranec JM, Vucevic D, Bhatia KD, et al. Current Concepts in Intracranial Interstitial Fluid Transport and the Glymphatic System: Part II—Imaging Techniques and Clinical Applications. *Radiology* 2021;301:516–32.

2. Bae YJ, Kim J-M, Choi BS, et al. Glymphatic function assessment in Parkinson's disease using diffusion tensor image analysis along the perivascular space. *Parkinsonism Relat Disord* 2023;114:105767.

3. Lee S, Yoo R-E, Choi SH, et al. Contrast-enhanced MRI T1 Mapping for Quantitative Evaluation of Putative Dynamic Glymphatic Activity in the Human Brain in Sleep-Wake States. *Radiology* 2021;300:661–8.

4. Alisch JSR, Kiely M, Triebswetter C, et al. Characterization of Age-Related Differences in the Human Choroid Plexus Volume, Microstructural Integrity, and Blood Perfusion Using Multiparameter Magnetic Resonance Imaging. *Front Aging Neurosci* 2021;13:734992.

5. Sun Y, Cao D, Pillai JJ, et al. Rapid imaging of intravenous gadolinium-based contrast agent (GBCA) entering ventricular cerebrospinal fluid (CSF) through the choroid plexus in healthy human subjects. *Fluids Barriers CNS* 2024;21:72.

Images/Tables

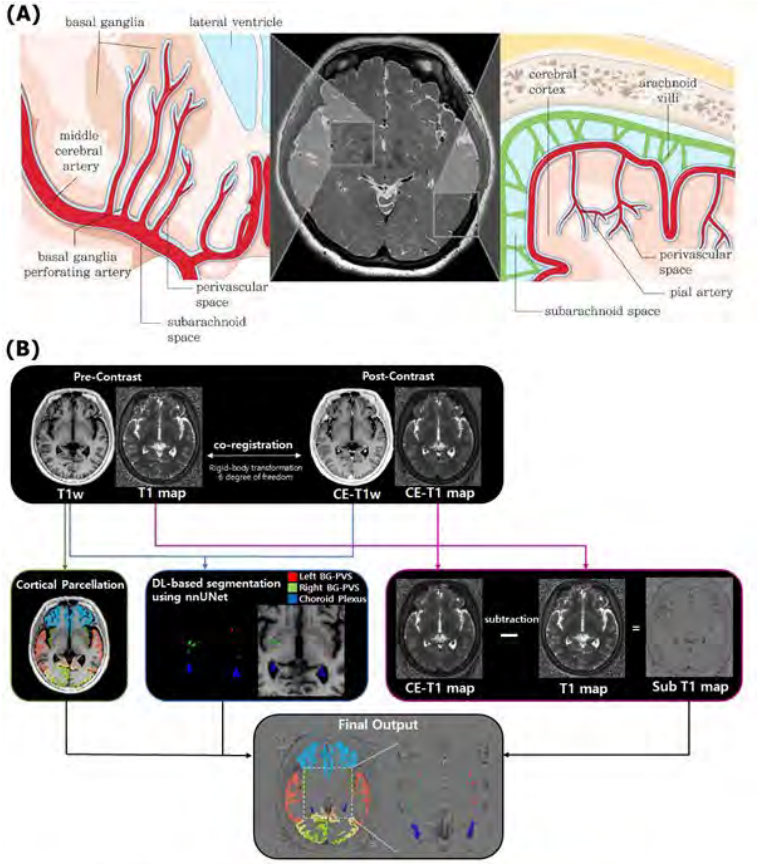

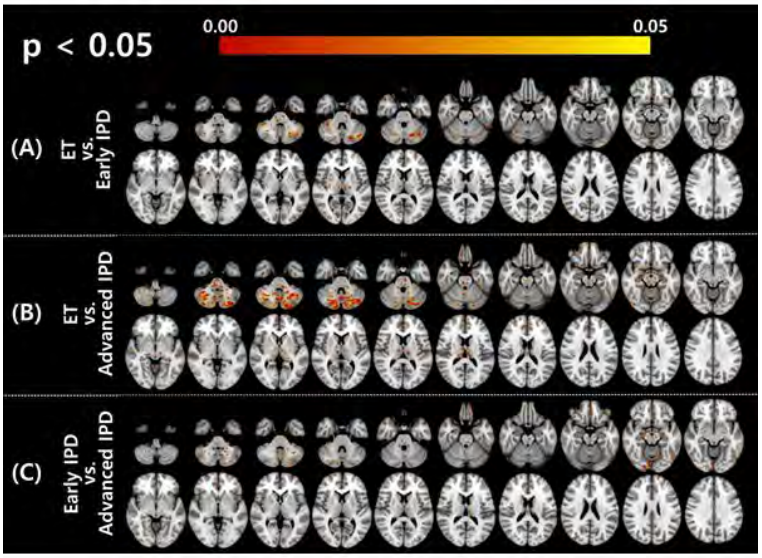

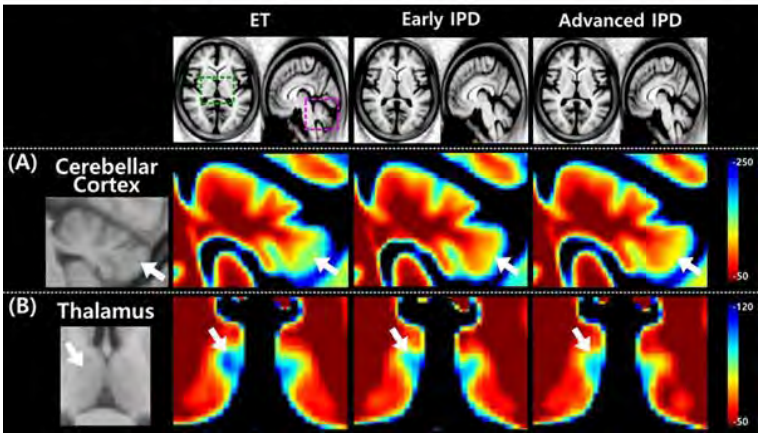

863 Association of Glymphatic Flow at Diffusion-Tensor MRI with Clinical Symptoms and Dopaminergic Degeneration in Parkinson's Disease

CHAE JUNG Park MD, PhD
Yongin Severance hospital, Seoul, Seoul, Korea, Republic of

Purpose

Dysfunction of the glymphatic system may contribute to neurodegeneration in Parkinson's disease (PD). We aimed to investigate the association between the diffusion tensor image (DTI) analysis along the perivascular space (ALPS) index, striatal dopamine transporter (DAT) availability, and baseline motor and cognitive function in patients with PD.

Materials & Methods

This retrospective study included newly diagnosed patients with PD who underwent brain MRI and ^{18}F-FP-CIT PET between January 2015 and December 2020. The ALPS index was used to assess glymphatic system function. Motor function was assessed using the Unified Parkinson's Disease Rating Scale Part III (UPDRS-III), and cognitive function was measured using the Mini-Mental State Examination (MMSE). Multiple linear regression and mediation analyses were performed to evaluate their associations.

Results

The study included 207 consecutive patients (mean age 71.6 ± 8.9 years; 118 females). The ALPS index and DAT availability in the posterior putamen were negatively associated with UPDRS-III scores. The ALPS index affected UPDRS-III scores both directly (β = −10.116, *P* = .002) and indirectly via DAT availability in the posterior putamen (β = 2.509, *P* = .036). Furthermore, the ALPS index and DAT availability in the associative striatum were positively associated with the MMSE-scores. The ALPS index affected MMSE scores both directly (β = 1.317, *P* = .003) and indirectly via DAT availability in the anterior putamen (β = −0.169, *P* = .047). An interaction effect was observed between the ALPS index and striatal DAT availability, and the relationship between ALPS index and baseline motor or cognitive function was significant only when striatal dopamine was severely depleted.

Conclusion

Glymphatic dysfunction is associated with worse motor and cognitive function in Parkinson's disease and may exert stronger effects when striatal dopamine is severely depleted.

References

1. Rasmussen MK, Mestre H, Nedergaard M. **The glymphatic pathway in neurological disorders**. *Lancet Neurol* 2018;17:1016–24
2. Taoka T, Masutani Y, Kawai H, et al. **Evaluation of glymphatic system activity with the diffusion MR technique: diffusion tensor image analysis along the perivascular space (DTI-ALPS) in Alzheimer's disease cases**. *Jpn J Radiol* 2017;35:172–78
3. Bae YJ, Kim J-M, Choi BS, et al. **Glymphatic function assessment in Parkinson's disease using diffusion tensor image analysis along the perivascular space**. *Parkinsonism & Related Disorders* 2023;114:105767
4. Marecek S, Rottova V, Nepozitek J, et al. **Exploring glymphatic system alterations in iRBD and Parkinson's disease using automated DTI-ALPS analysis**. *npj Parkinson's Disease* 2025;11:76
5. He P, Shi L, Li Y, et al. **The Association of the Glymphatic Function with Parkinson's Disease Symptoms: Neuroimaging Evidence from Longitudinal and Cross-Sectional Studies**. *Ann Neurol* 2023;94:672–83

Images/Tables

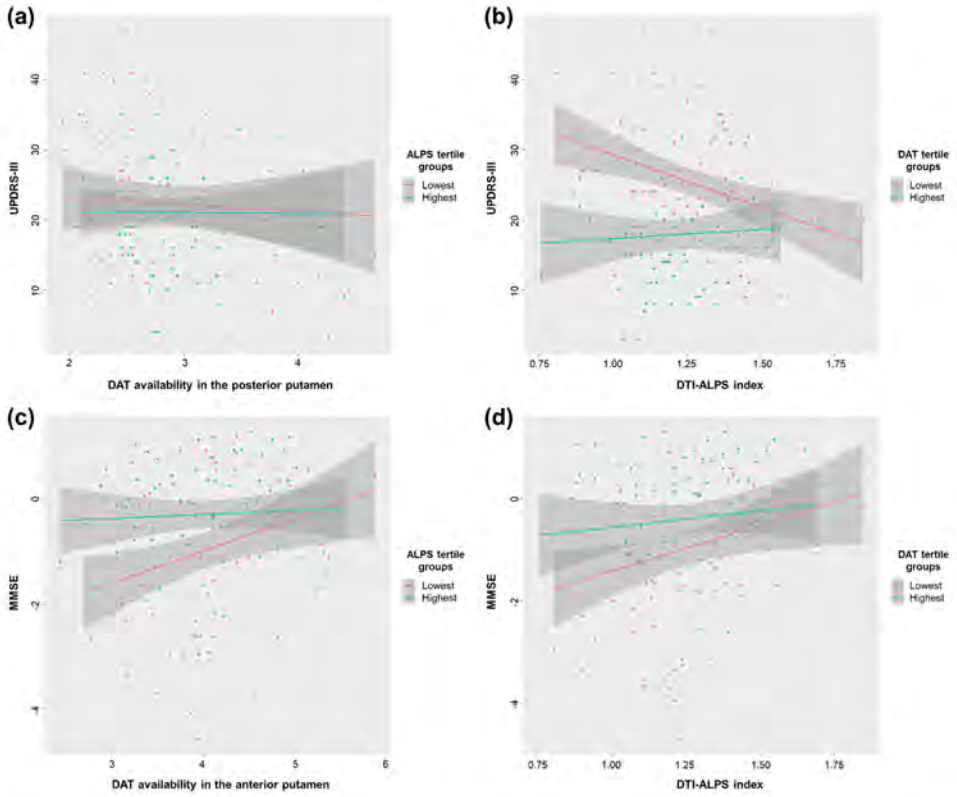

Figure. Interaction effects between of Diffusion Tensor Image (DTI) Analysis aLong the Perivascular Space (ALPS) index and striatal dopamine transporter (DAT) availability on clinical features of Parkinson's Disease

(a) The UPDRS-III score was substantially affected by DAT availability in the posterior putamen in the status of low ALPS indices

(b) The UPDRS-III score was substantially affected by ALPS index in the status of severely decreased DAT availability in the posterior putamen

(c) The MMSE score was substantially affected by DAT availability in the anterior putamen in the status of low ALPS indices

(d) The MMSE score was substantially affected by ALPS index in the status of severely decreased DAT availability in the anterior putamen

---

1048 Increased perivascular spaces burden in parkinson's disease: quantitative mri assessment as a potential neuroimaging biomarker

Arturs Silovs[1], Nauris Zdanovskis[1], Ardis Platkajis[1], Jurgis Skilters[2], Santa Bartusevica[2], Janis Mednieks[1], Aleksejs Sevcenko[1], Edgars Naudins[1], Solvita Umbrasko[2], Liga Zarina[2], Laura Zelge[2], Agnese Anna Pastare[2], Jelena Smilga[2], Elza Batraga[2], Evelina Stagisa[1], Baingio Pinna[3]

[1]Riga Stradins University, Riga, Latvia, Latvia. [2]University of Latvia, Riga, Latvia, Latvia. [3]Università degli Studi di Sassari, Sassari, Italy, Italy

Purpose

Parkinson's disease (PD) is characterized by progressive neurodegeneration involving accumulation of alpha-synuclein and other pathogenic proteins. The glymphatic system, comprised of perivascular spaces (PVS) and aquaporin-4 water channels, mediates cerebrospinal fluid circulation through the brain parenchyma to clear metabolic waste and neurotoxic proteins. Impaired glymphatic function and reduced PVS patency have been implicated in multiple neurodegenerative diseases. While enlarged PVS have been documented in cerebral small vessel disease, vascular dementia, and Alzheimer's disease as markers of impaired clearance, their prevalence and significance in PD remain poorly characterized. This study hypothesizes that PD patients exhibit increased PVS burden compared to healthy controls, reflecting compromised brain clearance mechanisms. We aimed to quantitatively assess PVS burden in multiple brain regions using complementary quantification methods and examine relationships with cognitive function.

Materials & Methods

Cross-sectional study of 49 participants (25 PD patients, 24 healthy controls) underwent 3T MRI imaging. PVS were independently quantified in basal ganglia (BG) and centrum semiovale (CS) regions bilaterally using: (1) absolute manual PVS counts and (2) Potter visual rating scale (1-4). Neuroradiologists performed blinded assessments. Groups were compared using Mann-Whitney U tests ($p<0.05$). Effect sizes were calculated with Cohen's d. Pearson correlations examined relationships between PVS burden and Montreal Cognitive Assessment (MoCA) scores.

Results

PD patients demonstrated significantly elevated PVS burden across all regions. Total basal ganglia PVS: 84.8±41.3 versus 48.0±24.5 in controls ($p=0.0002$, $d=1.14$, 77% increase). Centrum semiovale PVS: 290.6±116.3 versus 143.9±80.5 ($p=0.0001$, $d=1.52$, 102% increase). Potter scale

median scores showed excellent discrimination: basal ganglia right (2.0 vs 1.0, p=0.0002), basal ganglia left (2.0 vs 1.0, p=0.025), centrum semiovale right (3.0 vs 2.0, p=0.0003), centrum semiovale left (3.0 vs 2.0, p=0.001). PVS burden negatively correlated with MoCA scores (r=-0.381 to -0.447), suggesting clinical relevance to cognitive decline.

Conclusion

PD patients exhibit significantly increased PVS burden, particularly in white matter regions, with large effect sizes. Potter rating scale provides reliable, reproducible quantification for clinical research. PVS burden represents a potential neuroimaging biomarker for PD, offering mechanistic insights into impaired glymphatic clearance in neurodegeneration and potential for monitoring disease progression and evaluating neuroprotective interventions. Limitations: Cross-sectional design precludes causality assessment. Age difference between groups (PD: 65.8±12.6 vs controls: 51.7±9.8 years, p=0.0003) is a potential confounder; however, diagnosis-related differences substantially exceeded age-related correlations with PVS burden. Modest sample size limits subgroup analyses.

References

1. Potter GM, Chappell FM, Morris Z, et al. Cerebral perivascular spaces visible on magnetic resonance imaging: development of a qualitative rating scale and its observer reliability. Cerebrovasc Dis 2015;39:224–31
2. Zhang Y, Zhang X, Qu S. Interaction between the glymphatic system and α-synuclein in Parkinson's disease. Mol Neurobiol 2023;60:2209–22
3. Lian X, Wang R, Yao Y, et al. Targeting the glymphatic system to promote α-synuclein clearance in Parkinson's disease: opportunities and challenges. Neurosci Biobehav Rev 2024;157:105522
4. Cao X, Ren Y, Chen K, et al. Altered perivascular spaces in subcortical white matter in Parkinson's disease patients with levodopa-induced dyskinesia. NPJ Parkinsons Dis 2024;10:84
5. Si X, Guo T, Wang Z, et al. Neuroimaging evidence of glymphatic system dysfunction in possible REM sleep behavior disorder and Parkinson's disease. NPJ Parkinsons Dis 2022;8:54

Current Perspectives on MS and New McDonald Criteria

1:25 - 2:25pm Wednesday, 20th May, 2026

550 Assessment of cortical myelination in patients with multiple sclerosis via T1w/FLAIR ratio: a longitudinal follow-up study

Yangsean Choi MD

Department of Radiology, Seoul, Seoul, Korea, Republic of

Purpose

The T1-weighted (T1w)/fluid-attenuated inversion-recovery (FLAIR) ratio may reflect cortical myelin integrity in patients with multiple sclerosis (PwMS). This study aimed to investigate the longitudinal significance of the cortical T1w/FLAIR ratio in PwMS.

Materials & Methods

Brain MRI data were obtained from PwMS and clinically isolated syndrome (CIS) patients between September 2021 and December 2023. Three-dimensional T1-weighted and FLAIR images were preprocessed to calculate gray matter (GM) and superficial white matter (WM) T1w/FLAIR ratios across cerebral regions. Baseline and follow-up MRI scans were analyzed for T1w/FLAIR ratio changes and correlations with clinical parameters [Expanded Disability Status Scale (EDSS) and disease duration]. Cortical T1w/FLAIR ratio changes were compared with WM lesion changes (new, developing, or decreased lesions) on follow-up MRI scans.

Results

In total, 63 MS and 5 CIS patients (mean age: 40.5 years; 73.5% female) were evaluated. The baseline median EDSS score was 1.5, and median MRI interval was 13.5 months. GM T1w/FLAIR ratio changes were negatively correlated with EDSS changes in whole-brain ($r = -0.201$, $p = 0.020$), occipital ($r = -0.269$, $p = 0.002$), and insular ($r = -0.18$, $p = 0.038$) cortices. Patients with stable or improved EDSS scores exhibited significant GM T1w/FLAIR ratio increases ($p = 0.044$ and $p < 0.001$, respectively). T1w/FLAIR ratio changes were positively correlated with disease duration ($r = 0.285$, $p = 0.018$) but not WM lesion changes.

Conclusion

Longitudinal GM T1w/FLAIR ratio changes were associated with disease severity in PwMS, supporting its potential role as a biomarker for cortical myelination and disease monitoring.

References

1. Glasser MF, Goyal MS, Preuss TM, et al. Trends and properties of human cerebral cortex: correlations with cortical myelin content. *Neuroimage* 2014;93 Pt 2:165–75.

2. Righart R, Biberacher V, Jonkman LE, et al. Cortical pathology in multiple sclerosis detected by the T1/T2-weighted ratio from routine magnetic resonance imaging. *Ann Neurol* 2017;82:519–29.

3. Nakamura K, Chen JT, Ontaneda D, et al. T1-/T2-weighted ratio differs in demyelinated cortex in multiple sclerosis. *Ann Neurol* 2017;82:635–9.

4. Hannoun S, Kocevar G, Codjia P, et al. T1/T2 ratio: A quantitative sensitive marker of brain tissue integrity in multiple sclerosis. *J Neuroimaging* 2022;32:328–36.

5. Pareto D, Garcia-Vidal A, Alberich M, et al. Ratio of T1-Weighted to T2-Weighted Signal Intensity as a Measure of Tissue Integrity: Comparison with Magnetization Transfer Ratio in Patients with Multiple Sclerosis. *AJNR Am J Neuroradiol* 2020;41:461–3.

Images/Tables